TESIS DOCTORAL

2018

DESIGN AND APPLICATION OF AN OPTIMIZED ADAPTIVE CONTROL SYSTEM FOR THE SUPERCONDUCTING CAVITIES OF A LINAC

D. ISAÍAS MARTÍN HOYO
INGENIERO INDUSTRIAL Y MÁSTER EN INVESTIGACIÓN EN INGENIERÍA ELÉCTRICA, ELECTRÓNICA Y CONTROL INDUSTRIAL

PROGRAMA DE DOCTORADO EN TECNOLOGÍAS INDUSTRIALES

DIRECTOR: JOSÉ CARPIO IBAÑEZ
CO-DIRECTOR: JUAN MANUEL MARTÍN SÁNCHEZ

TESIS DOCTORAL

AÑO
2018

TÍTULO DE LA TESIS
DESIGN AND APPLICATION OF AN OPTIMIZED ADAPTIVE CONTROL SYSTEM FOR THE SUPERCONDUCTING CAVITIES OF A LINAC

NOMBRE Y APELLIDOS DEL AUTOR/A
ISAÍAS MARTÍN HOYO

TITULACIÓN DEL AUTOR
(PREVIA AL DOCTORADO)
INGENIERO INDUSTRIAL Y MÁSTER EN INVESTIGACIÓN EN INGENIERÍA ELÉCTRICA, ELECTRÓNICA Y CONTROL INDUSTRIAL

PROGRAMA DE DOCTORADO
TECNOLOGÍAS INDUSTRIALES

REALIZADO EN:
DEPARTAMENTE DE INGENIERÍA ELÉCTRICA, ELECTRÓNICA Y DE CONTROL (DIEEC) -
ESCUELA TÉCNICA SUPERIOR DE INGENIEROS INDUSTRIALES (ETSII)

DIRECTOR:
JOSÉ CARPIO IBAÑEZ
CO-DIRECTOR:
JUAN MANUEL MARTÍN SÁNCHEZ

ABSTRACT

Research works presented in this Ph.D thesis have been performed in the framework of the successive EU R&D projects devoted to the development of the MYRRHA transmutation facility for the incineration of nuclear waste. Reliability is a crucial requisite for MYRRHA to become the first midsize demonstrator of the feasibility of industrial transmutation. The research endeavor presented in this thesis has focused on the development of an Optimized Adaptive Control System (OACS) providing hi-reliability to the superconducting (SC) cavities of the proton accelerator driving the transmutation reaction. Thus, this study merges two forefront research disciplines: particle acceleration and advanced control methodologies.

The OACS is based on Adaptive Predictive Expert (ADEX) control methodology and its operation responds to an Optimized Control Strategy (OCS) that comprises the main original contributions of this thesis. The OCS has introduced the combination of notch filters and ADEX controllers, and added an anticipation of the effects of Lorentz forces and a compensation technique based in Chebyshev filters which was previously used for SC cavities. Thus, the OCS gathers the tools to attenuate the excitation of the cavity´s resonant modes that could be caused by the ADEX controller's actions, compensate in advance for Lorentz forces and minimize the known microphonics induced by external perturbations.

The OACS, defined according to the OCS, has undergone a series of evaluation phases in which it has been compared to advanced PID-based systems. Firstly, its performance was thoroughly evaluated in a 704.4 MHz cavity simulation developed by CNRS. The successful outcome of these tests allowed to embed the OCS in the appropriate hardware and asses the resulting OACS in a room temperature (RT) spoke cavity. These RT tests yielded promising results and the OACS was approved for its evaluation in a SC elliptical cavity.

Simulation tests and the actual application on RT and SC cavities yielded that the OACS achieved a significant reduction in the oscillations of the resonance frequency (or other indirect measurements of this magnitude) around its setpoint in comparison to the previously mentioned advanced PID-based systems. Namely, the simulation showed how this performance maintained the power consumption nearly at its minimum throughout the test. Additionally, the OACS proved, both in simulation and on the SC cavity tests, that under the effect of unexpected perturbations it modified its behavior and delivered the adequate control actions that maintained the resonance frequency within its operational limits and the cavity under control. On the other hand, similar unexpected perturbations caused advanced PID-based control to lose control of the cavity.

These results can be explained by the fact that unforeseen perturbations, not only deviate the variables under control, but also change the processes dynamics, which makes the parameters of a well-tuned PID controller to become detuned for the new dynamics and the controller performance deteriorate. ADEX controllers adjust themselves to changes in the process dynamics and, therefore, can deal with uncertainty scenarios and unforeseen perturbations, increasing in this way significantly the reliability of cavities and therefore of the linac operation.

RESUMEN EN ESPAÑOL

Los trabajos de investigación presentados en esta tesis doctoral han sido realizados en el marco de sucesivos proyectos de I+D financiados por la Comisión Europea y dedicados al desarrollo del reactor de transmutación MYRRHA que poseerá la capacidad de incinerar residuos nucleares. La fiabilidad es un requisito crucial para que MYRRHA pueda convertirse en la instalación que demuestre la viabilidad del proceso de transmutación a escala industrial. El esfuerzo investigador presentado en esta tesis se ha centrado el desarrollo de un Sistema de Control Optimizado Adaptativo (SCOA) que dote de una elevada fiabilidad a las cavidades supercondutoras (SC) del acelerador de protones que conduce la operación del MYRRHA. Por consiguiente, el presente estudio combina dos campos a la vanguardia de la investigación: la aceleración de partículas y las metodologías de control avanzado.

El SCOA desarrollado está basado en la metodología de control Adaptativo Predictivo Experto (ADEX) y su operación responde a una Estrategia de Control Optimizada (ECO) que comprende las principales aportaciones originales de esta tesis. A este respecto cabe destacar que el diseño de la ECO ha introducido la combinación de filtros notch y controladores ADEX, a la que se ha añadido un bloque de anticipación de las fuerzas de Lorentz y una técnica de compensación basada en filtros de Chebyshev y que ha sido previamente utilizada en cavidades SC. De esta forma, la ECO reúne las herramientas para, respectivamente, atenuar la excitación de modos resonantes que pudieran causar las propias acciones del controlador ADEX, compensar anticipadamente las fuerzas de Lorentz y minimizar las microfonías causadas por perturbaciones externas.

El SCOA definido de acuerdo a la ECO ha sido sometido a rigurosas fases de evaluación en las que ha sido comparado con sistemas avanzados basados en PIDs. En primer lugar, se analizó el rendimiento de la ECO en una simulación de la cavidad elíptica de 704,4 MHz desarrollada por el CNRS. La evaluación favorable de la ECO propició que esta se embebiera en el hardware adecuado dando lugar a un SCOA plenamente funcional destinado a ser probado en una cavidad radial a temperatura ambiente (TA). Las pruebas a TA dieron lugar a resultados prometedores y finalmente se procedió a probar el SCOA en una cavidad elíptica operada a temperatura criogénica (TC).

Las pruebas en simulación y la aplicación del SCOA en las cavidades a TA y TC mostraron que el SCOA consigue una reducción considerable de las oscilaciones de la frecuencia de resonancia (o de otras medidas indirectas de esta magnitud) alrededor de su consigna en comparación con los sistemas avanzados basados en PID. Esto implica que la operación del SCOA minimiza el consumo energético de la cavidad como demostraron los estudios en simulación. Adicionalmente, el SCOA demostró, tanto en simulación como en las pruebas a TC, que, bajo el efecto de perturbaciones inesperadas, es capaz de modificar su comportamiento y devolver acciones de control adecuadas para las nuevas circunstancias, siendo capaz de mantener la frecuencia de resonancia dentro de sus límites operacionales y la cavidad bajo control. Por otro lado, este mismo tipo de perturbaciones inesperadas provocaron que los sistemas avanzados basados en PID perdieran el control de la cavidad.

Estos resultados se pueden explicar por el hecho de que las perturbaciones inesperadas, no solo desvían las variables bajo control, sino que también modifican la dinámica del proceso. Esto hace que controladores PID cuyos parámetros habían sido convenientemente ajustados, se encuentren deficientemente ajustados para la nueva dinámica, deteriorándose su rendimiento. Los controladores ADEX se auto-ajustan a los cambios en la dinámica del proceso y, es por ello que pueden hacer frente a escenarios de operación inciertos con perturbaciones no previstas, incrementando considerablemente la fiabilidad operativa de las cavidades y, por tanto, de la operación del linac.

ACKNOWLEDGEMENTS

I gratefully acknowledge the Open University of Spain (UNED) where I have performed this PhD program in industrial technologies, and in particular my thesis director Dr. José Carpio for his generous help, advices and his revision of my work.

I am deeply grateful to the ADEX Company, the living dream of building a hi-tech company in Spain, which allowed me to work in fascinating areas of technology and industry and, above all, forged me as a professional. Acknowledging ADEX is impossible without expressing my gratitude to my father, the soul of the company, and to Hector Pastor, whose strength keeps the dream alive. Thank you for your invaluable lessons about process control and life.

I profoundly acknowledge the CNRS of France for allowing me to perform a crucial part of my investigations in its facilities. A special mention must be made to Dr. Jean-Luc Biarrotte who supervised my works in CNRS. His support and wise council enlightened my way throughout my research, especially during my sojourns at Orsay. I must also acknowledge the rest of CNRS personnel who hosted and helped me during this time, most of whom are coauthors of the paper “Optimized Adaptive Control for the MYRRHA Linear Accelerator”.

Dr. Frédéric Bouly has truly earned a separate acknowledgment note. Thank you for everything Fred, without your help and acceleration lessons this thesis would have simply not been possible.

Finally, I want to thanks my friends, my family and Carolina for their support throughout these years.

CONTENTS

LIST OF FIGURES

ANNEX A:

ANNEX B:

ANNEX C:

LIST OF TABLES

LIST OF ACRONYMS AND ABREVIATIONS

MA - minor actinides
ADEX - Adaptive Predictive Expert
OACS - Optimized Adaptive Control System
SC - Superconducting
OCS - Optimized Control Strategy
PID – Proportional Integral Derivative
LLFPs - Long-lived fission products
PDS-XADS - Preliminary Design Studies of an eXperimental Accelerator Driven System
ADS - Accelerator Driven System
EUROTRANS - European Research Programme for the TRANSmutation of High Level Nuclear Waste in an Accelerator Driven System
FP7 – Framework Package 7
MAX - MYRRHA Accelerator eXperiment, research & development program
MYRRHA - Multi-purpose hybrid research reactor for high-tech applications
CTS - Cold Tuning Systems
LMS - Least Minimum Squares
RF - Resonance Frequency or Radio Frequency (depending on the context)
CNRS - Centre National de la Recherche Scientifique
IPNO - Institut de Physique Nucléaire d'Orsay
UOX- Uranium oxide
MOX - Mixed Oxides
P&T - Partitioning and Transmutation
JAEA - Japan Atomic Energy Agency
LBE - Lead-Bismuth Eutectic
ESFRI - European Strategy Forum for Research Infrastructures
ERC - Electron Cyclotron Resonance
LEBT - Low Energy Beam Transfer
LPSC Grenoble - Laboratoire de Physique Subatomique et Cosmologie de Grenoble
AC - Alternating Current
LLRF - Low Level Radio Frequency
DLLRF - Digital Low Level Radio Frequency system
FTS - Frequency Tuning System
PV - Process Variable
SP - Setpoint
MPC - Model Predictive Control
APC- Adaptive Predictive Control
AP - Adaptive Predictive
MRAS - Model Reference Adaptive Systems
I/O - Input and Output
PDT - Projected Desired Trajectory
DDT - Driving Desired Trajectory
MIMO - Multi-Input, Multi-Output
SISO - Single-Input, Single-Output
ARMAX - Autoregressive-moving average with exogenous terms
FFT - Fast Fourier Transform
ADEX COP - ADEX control and Optimization Platform

ADEX SCS - Supervisory and Configuration System of ADEX COP
ADEX COS - Control and Optimization System of ADEX COP
IDE - Integrated Development Environment
GUI - Graphical User Interface
OUTs - Outputs of the ADEX controller
AIs - Actual Input of the ADEX controller
PSS - Perturbed Simulated Scenario
Linac - Linear accelerator
cRIO - CompactRIO
RT - Real-Time
HiL - Hardware in the Loop
PLL - Phase Locked Loop
CPS - Cavity Phase Shift
RFD - Resonant Frequency Detuning

CHAPTER I:

INTRODUCTION

Energy forecasts [1] indicate that world primary energy consumption will increase significantly (approximately 37%) by 2040, despite potential improvements in energy efficiency. World electricity demand is expected to increase to almost 80% by 2040 [1], thus the share of electricity in the energy mix will increase more rapidly than the share of other energies, even more so when carbon-avoiding technologies are implemented. The security of the energy supply is, and will be, a major concern for the world.

In this context, the use of nuclear energy must be consistent with sustainable development goals. Besides concern about potential proliferation, there also exists the challenge of raising nuclear safety levels even higher while improving the economic competitiveness of nuclear power. Using technologically reliable and socially acceptable nuclear waste solutions is crucial. At present the European Union relies on nuclear fission for approximately 25% of its electricity supply, leading to an approximate annual production of 2,500 t of used fuel, containing 25 t of Plutonium, 3.5 t of minor actinides (MA, namely Np,

Am, Cm) and 3 t of long-lived fission products (LLFPs) [2], [3]. These MA and LLFP stocks need to be managed in an appropriate way.

Used fuel reprocessing followed by geological disposal, or direct geological disposal are today the envisaged solutions depending on national fuel cycle options and waste management policies. However, the time scale presently considered for geological disposal causes problems of public acceptance and exceeds the one that may be accomplished with the current accumulated technological knowledge. In addition, radiotoxic nuclear waste generates a significant amount of heat, which directly impacts the size of deep geological repositories. Indeed, the maximum density of nuclear waste that can be stored is essentially limited by the thermal load which the geological soil can support [4].

In an attempt to formulate an answer to these concerns, studies, [5]–[7], pointed out the adequate separation of nuclear waste, referred to as partitioning, and the transmutation of some of them (MA, LLFPs,...) as the strategy of choice that can relax the time constraints on geological disposal (from 200,000 - 2,000,000 years) to technologically relevant and manageable time scales (≈250 years).

The PDS-XADS (Preliminary Design Studies of an eXperimental Accelerator Driven System) [8] European funded project produced a sound basis for the design of an Accelerator Driven System (ADS), a reference solution for the transmutation of nuclear waste. Further development towards the demonstration of the ADS transmutation concept were achieved throughout the EUROTRANS (European Research Programme for the TRANSmutation of High Level Nuclear Waste in an Accelerator Driven System) project [6] launched under the workscope of the FP6 European integrated effort to enhance research on strategic issues. One of the results of EUROTRANS was the delivery of the preliminary design file of an experimental ADS facility intended to demonstrate and validate the incineration and transmutation of nuclear wastes (MA, LLFPs).

An ADS consists of a transmutation reactor, bearing the nuclear waste to be burned, driven by a particle accelerator. The accelerator is a key element in ADS technology. Its function is to generate a high energy proton beam that collides with a spallation target thus producing the fast neutrons necessary to induce the transmutation reaction inside the

reactor. In this way the processed fission products and the minor actinides are incinerated, i.e. converted into shorter radioactive half-life elements.

EUROTRANS's outcome preceded the FP7 MAX (MYRRHA Accelerator eXperiment, research & development program) project [9] aimed at performing and/or pursuing the component related R&D to set the design details for the accelerator of MYRRHA (Multi-purpose hybrid research reactor for high-tech applications). MYRRHA is intended to be the first medium power transmutation reactor (100 MWth) and will be placed in the Belgian Nuclear Research Center at Mol (Belgium).

The reference solution for MYRRHA's accelerator is a linear proton accelerator using superconducting (SC) cavities for beam acceleration in high energy sections. In the operating context of this accelerator, the essential role of the control system can hardly be overemphasized. When the proton beam acceleration in SC cavities takes place, precise control of the field amplitude and phase is of paramount importance for obtaining required stability levels in terms of beam power and position on target. Nevertheless, SC cavities' acceleration processes, characterized by being designed to operate in optimal conditions at a certain electromagnetic resonance frequency, are non-linear and time varying. The resonance frequency is a very sensitive feature that depends on the shape of the SC cavity, which may be modified by operating conditions and different kinds of stochastic and unmeasured perturbations, as well as by the excitation of the mechanical vibrating modes of the cavity itself. Maintaining the resonance frequency in its optimal operating value is critical. Mechanical devices named Cold Tuning Systems (CTS) driven by piezoelectric actuators have been developed for this purpose. Nevertheless, resonance frequency control still presents multiple difficulties that have challenged the research efforts of numerous scientists in the accelerator community, i.e. [10]–[18]. These works describe different control system designs that rely on PID controllers, but enhance their performance with advanced control techniques, or just propose these techniques to be used with ad-hoc controllers. Among this kind of approaches, adaptive feedforward techniques have been proposed [10]–[14] in which a reference signal attempts to compensate for periodic perturbations previously recorded in the facility. This reference signal is processed, prior to its application to the CTS, by an inverse adaptive algorithm obtained with techniques such as the Least Minimum Squares (LMS) method. However, it has been reported that this approach is limited [10] by the lack of

capacity of PID controllers to achieve the desired level of disturbance attenuation, since their controller gains are limited by stability requirements. Recently, a feedback alternative using a series of bandpass filters operating in parallel with a PID controller to enhance compensation at determined critical frequencies was proposed in [14]–[18]. This bandpass filters technique has yielded good results and will be considered in the following chapters.

Due to their control difficulty, SC cavities presented a control scenario suitable for testing the performance of a new Adaptive Predictive Expert (ADEX) control methodology [19], [20], that has already been applied to challenging-to-control processes in the industrial field with excellent results [21]–[24]. ADEX methodology uses Adaptive Predictive control [25], [26], that includes an adaptive self-tuning feature able to deal automatically with process and environmental uncertainties, and identify and track actual process dynamics in real time. According to EUROTRANS recommendations, "both standard and ADEX control technologies should be thoroughly evaluated as alternative solutions to the ADS control/command system". Consequently, the MAX project carried out a dedicated task on this experimental evaluation, whose results are presented in Chapter 10 of this report.

In the MAX project, an Optimized Adaptive Control System (OACS) [27] defined by an optimized control strategy in which ADEX controllers were integrated, has been specifically developed for the Resonance Frequency (RF) loop, and applied to a high fidelity simulation of the SC cavity provided by the Centre National de la Recherche Scientifique (CNRS) of France. The optimized control strategy for the resonance frequency of the SC cavity has taken into account the associated instrumentation and the SC cavity's dynamic nature. An essential part of it, is the filtering and signal processing tools used to avoid exciting the inherent mechanical vibration modes and to compensate for them if externally excited. The OACS performance has been evaluated and compared in the same context with that of some of the most significant control systems [15]–[17] based on PID controllers previously applied to the RF loop. The favorable evaluation of the OACS performance in simulation has allowed for its implementation in the prototypical cavities being currently studied at the Institut de Physique Nucléaire d'Orsay (IPNO) facility of CNRS [28].

In the following, Chapter 2 presents the transmutation concept and the Accelerator Driven System approach towards an industrial transmutation facility, the MYRRHA project. In

this chapter, the key concepts of the MYRRHA accelerator's operation are explained intuitively. Chapter 3 describes the insights of the proton beam acceleration process and the operation of SC cavities. Chapter 4 reviews the acceleration processes form a control perspective, defining the control loops and highlighting the main control challenges in the resonance frequency loop. This chapter also describes the Cold Tuning Systems (CTS) and the Frequency Tuning Systems (FTS) required by this loop. Chapter 5 presents previous approaches considered in literature and based on PID for the design of the FTS. Chapter 6 is dedicated to Optimized Adaptive Control Systems (OACS) and the ADEX control methodology, while Chapter 7 reviews the design of the specific Optimized Control Strategy for the acceleration process. Chapter 8 describes the ADEX OACS performance evaluation in a simulation of the cavity provided by CNRS when compared to that of some of the advanced control systems based on PIDs and previously considered in Chapter 5. In Chapter 9, the successive hardware implementations in which the OACS has been embedded prior to testing it on the prototypical cavities are presented. Chapter 10 is devoted to the experimental campaign. This last chapter starts by describing the different setups used during the campaign, as well as the practical aspects that differed between simulation and real implementation, to present afterwards the experimental results and a comparative analysis between the ADEX OACS' performance and that of an advanced PID based system.

CHAPTER II:

THE ADS TRANSMUTATION CONCEPT AND THE MYRRHA PROJECT

2.1 ALTERNATIVES TO MILLENNIAL GEOLOGICAL DISPOSAL FOR FISSION PRODUCTS

According to the survey presented in [29], each year, nuclear power generation facilities worldwide produce about 10,000 m^3/ 12,000 tons of hi-level radioactive waste. This waste with variable levels of nuclear activity presents biological risks and can harm human beings.

Radiotoxicity is a measure of the potential biological hazard of a nuclear material based on its radioactive quality rather than on its chemical toxicity or radioactivity alone. Radiotoxicity is commonly expressed in “Sieverts”. Figure 1 represents the reduction of radiotoxicity of the different elements present in a nuclear power plant’s waste with time. The radiotoxic elements considered are mayor actinides (essentially plutonium and uranium), minor actinides (neptunium, americium, curium, etc.) and other fission products. The

radiotoxicity of nuclear fuel “uranium ore”, present in nature, is also represented in the figure for comparison.

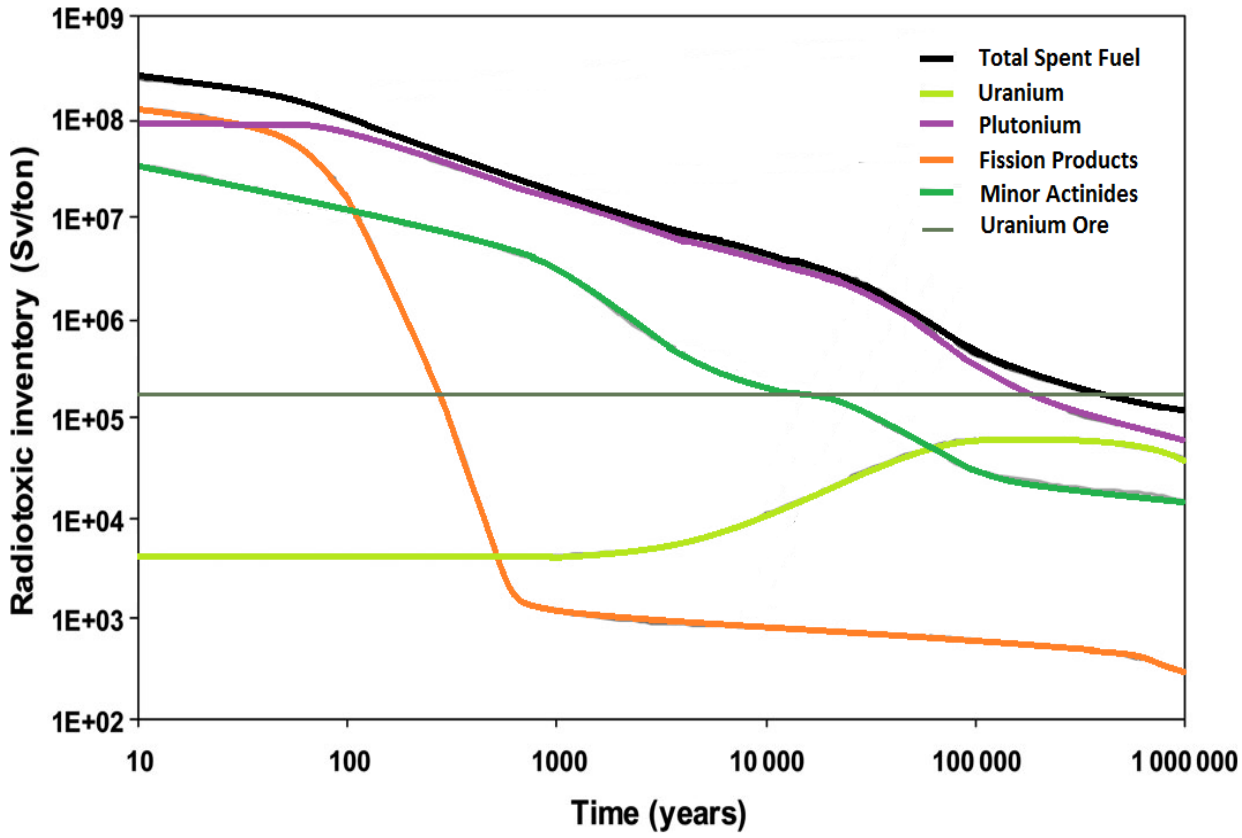

Figure 1. Radiotoxicity of spent nuclear fuel components with time [30]

It can be noted that after the first couple of centuries the radiotoxicity of fission products decreases steeply and minor actinides and plutonium dominate the radiotoxicity of spent fuel.

Mayor Actinides

Nuclear fuel is generally composed of a basis of uranium oxide (UOX) whose content is enriched with uranium 235 (235U) up to 3.5% (for electricity production), being the rest of it composed of a more stable isotope uranium 238 (238U).

235U is necessary for the fission reaction to take place and to generate the necessary heat to produce electricity. Nevertheless 235U is not totally consumed in the reactors core

and one quarter remains after every batch. Reprocessing procedures are capable of recovering this material and recycling it into new fuel.

Unaltered 238U is also recycled. However, a part of it is transformed during irradiation, into uranium 239 by capturing a neutron. This unstable form of uranium emits β rays and briefly transforms into neptunium 239 (during an average of 2.35 days) and finally into plutonium 239 (239Pu). Many isotopes of plutonium coexist in the final mixture, although 239Pu remains the most plentiful.

As represented in Figure 1 plutonium dominates in the long term the radiotoxicity of spent nuclear fuel after the decay of fission products. Paradoxically plutonium is a hi-energy fissible mater, and is considered more profitable in terms of neutrons than 235U.

239Pu can be reprocessed alone or joint with uranium in Mixed Oxides (MOX) fuel for fast neutrons reactors. However, plutonium generates a higher amount of minor actinides and other Long Life Fission Products (LLFP) than uranium. Indeed, the production of americium and curium is ten times higher in reactors using MOX fuel [17].

Minor Actinides (MA) and other Fission Products

Minor actinides and fission products cannot be reprocessed with current reactors, and, are considered nuclear waste. Minor actinides such as neptunium 237 with a radioactive half-life of 2.14 million years are created by disintegration of 238U. Nevertheless its radiotoxicity is smaller than that of the isotopes of americium, 241Am and 243Am, whose half-lives are 430 and 7,400 years respectively. Both are transformations of isotopes of plutonium (241Pu and 242Pu), for this reason their concentration is high in spent MOX fuel. Curium is less harmful as its isotopes have short half-lives, except 245Cm, with a half-life of 8,500 years, but which is scarcely generated in comparison with other fission products.

Finally, other fission products such as isotopes 135 and 137 of cesium, iodine 129, technetium 99 and zirconium 93, with variable disintegration periods ranging from 200,000 years up to 2,000,000 years, are also considered as high activity radioactive waste.

A promising alternative to millennial geological disposal

Modern studies ([6], [7], [9]) have proven that there exists the possibility of artificially transforming highly radiotoxic elements into short radioactive half-life elements. These studies have determined partitioning, meaning the adequate separation of different components of nuclear spent fuel, and transmutation, term that refers to nuclear reactions eliminating the most hazardous among these components, as key techniques for the reduction of time and space constraints in the geological repositories. For these reason, Partitioning and Transmutation (P&T) have been studied throughout the last twenty years [4] – [9] and are an ongoing matter of research.

Figure 2 illustrates the reported [4] capacity to reduce radiotoxicity and time of geological disposal in several orders of magnitude ([4], [31], [32]) with Partitioning and Transmutation (P&T) techniques. In the figure, the evolution of radiotoxicity, measured in Sieverts per ton of radioactive material, is represented along the years of geological disposal by the black, orange and green lines, where each of them corresponds to a different reprocessing procedure of spent fuel before its storage. The black line shows the radiotoxicity decrease when spent fuel is directly accumulated in conventional facilities. The orange line represents the radiotoxicity decrease after the spent fuel has been reprocessed in closed cycle in a Gen-IV reactor where Pu, MA and LLFP are burnt together. The green line shows the radiotoxicity decrease after the spent fuel has been reprocessed in two different reactors one for Pu fission and other for MA and LLFP transmutation, this technique is called “double strata” and considers Pu a resource rather than a waste. Finally, the radiotoxicity of uranium ore found in nature has also been represented in the horizontal green line for comparison.

It can be noted that both techniques considered in the figure obtain similar results according to radiotoxicity and time constrains, thus, the choice between them will depends on other technical or economic issues and is a matter of debate [4]. Regarding the figure it can be concluded that P&T techniques are expected to yield a significant drop of the radiotoxicity of nuclear waste and reduce the associated storage time necessary for the spent fuel to reach radiotoxicity levels found in nature. While radiotoxicity decreases in more than a couple of orders of magnitude with these techniques, the time it takes for nuclear waste radiotoxicity

to reach uranium ore levels, which are found in nature, is reduced by almost three orders of magnitude.

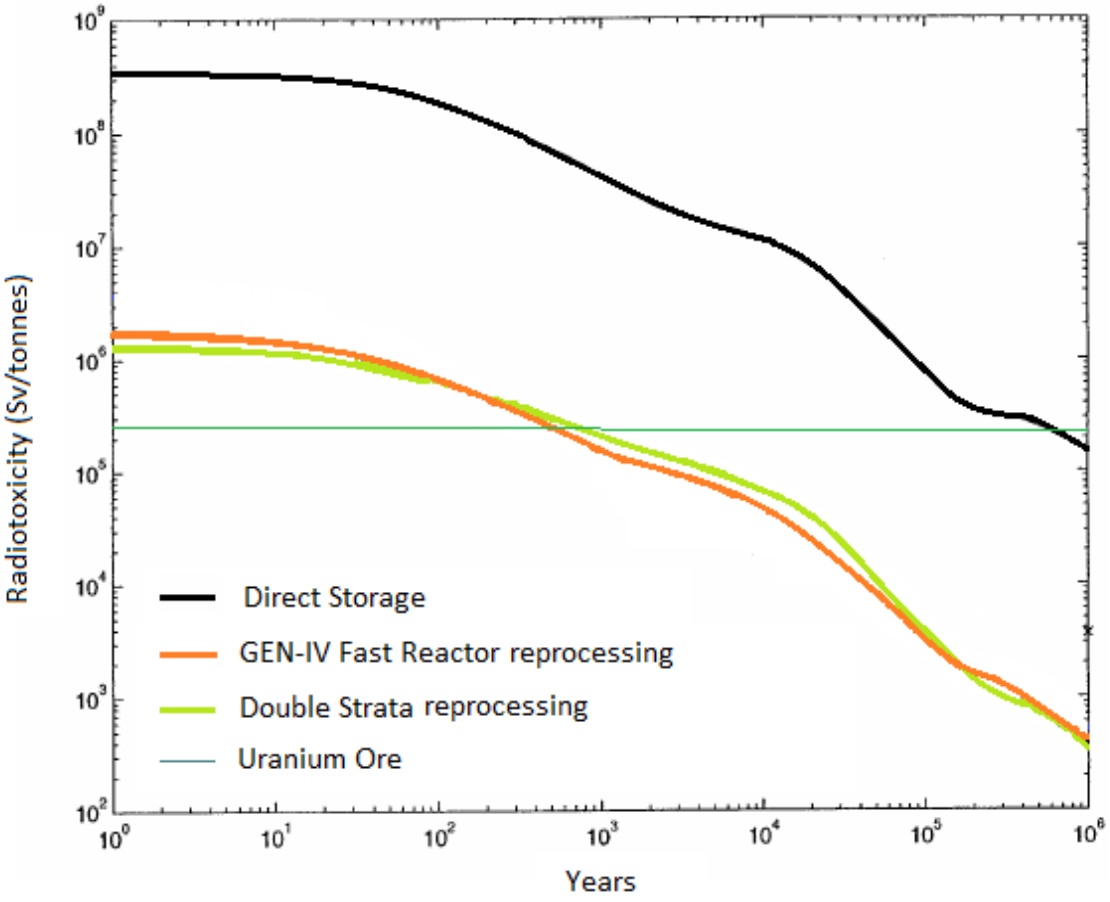

Figure 2. Expected evolution of spent fuel radio toxicity after different reprocessing options [4]

Arguments such as those previously described have encouraged the scientific community to enhance research efforts and experimental studies to demonstrate the industrial feasibility of P&T procedures. Consistent technical progress has brought forth optimism in developing facilities for the incineration of nuclear waste. Currently, prototypical machines have been built [33], are under construction or in a design phase, looking towards the development of a large-scale industrial demonstrator for the transmutation of nuclear waste [34].

2.2 PRINCIPLE OF TRANSMUTATION AND SPENT NUCLEAR FUEL INCINERATION

A chemical element transmutes when it is transformed into another element due to the modification of the structure of its nucleus. As it is not possible to modify the time constants of emitting particles such as MA or LLFP, the transmutation of these particles into more stable or fissionable elements remains an interesting alternative to reduce the radiotoxicity of spent nuclear fuel.

The use of different types of particles (hadrons, photons, etc.) to trigger transmutation reactions in radioactive nucleus has been reported [17]. Currently, neutrons are widely acknowledged as the most efficient particle for the transmutation of MA and LLFP.

Simplified representations of transmutation and incineration reactions are presented in Figure 3 where technetium 99 is transformed into a ruthenium 100 stable nucleus and neptunium 237 is transformed in fissionable 239Pu which can be used as new fuel.

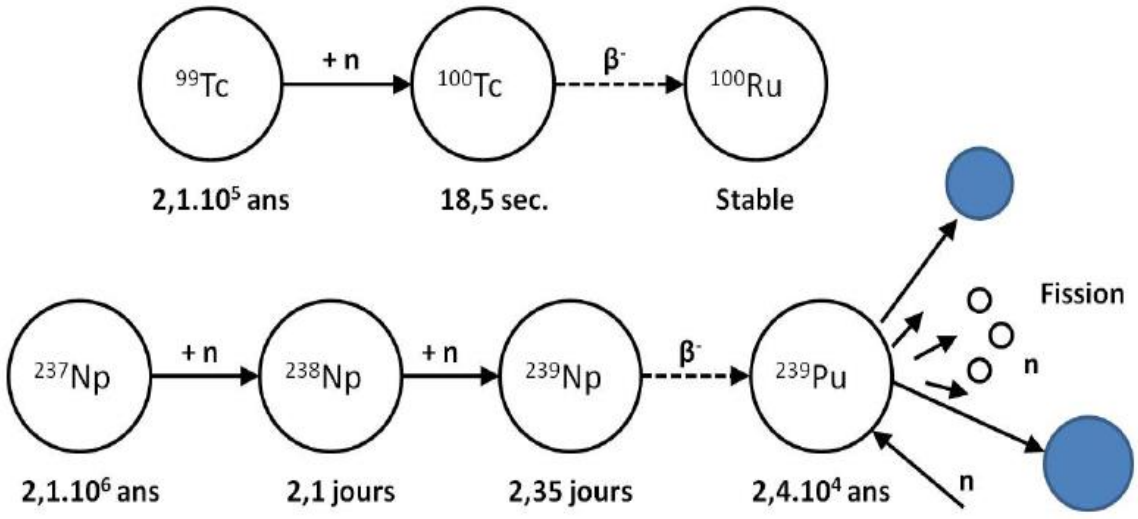

Figure 3. Transmutation reaction of technetium 99 and incineration of neptunium 237 [17].

Incineration of minor actinides by fission implies two major advantages, the first one is that the products of this reaction have a shorter radioactive half-life, as indicated in the figure, while the second one is that they produce new fission reactions which generate new

neutrons that allow for the transmutation of other nucleus. Thus a chain reaction could be achieved and this would be interesting for energy production purposes.

However, in practice, transmutation of minor actinides requires of high amount of fast neutrons to take place. Hence, today's envisaged option is to force transmutation of MA and LLFP inside a reactor by feeding it with a flow of high energy neutrons provided by an external source.

It must be noted that the speed of neutrons is crucial to the predominant reaction that will take place on the nucleus of a particle. The probability of fission of an atom depends on the energy of the neutron, being the alternative the capture of the neutron by the atom. This is illustrated in Figure 4 that shows the variation with the neutron's energy of the effective sections of an atom, namely americium 241. These sections will determine the probability that a certain reaction will take place.

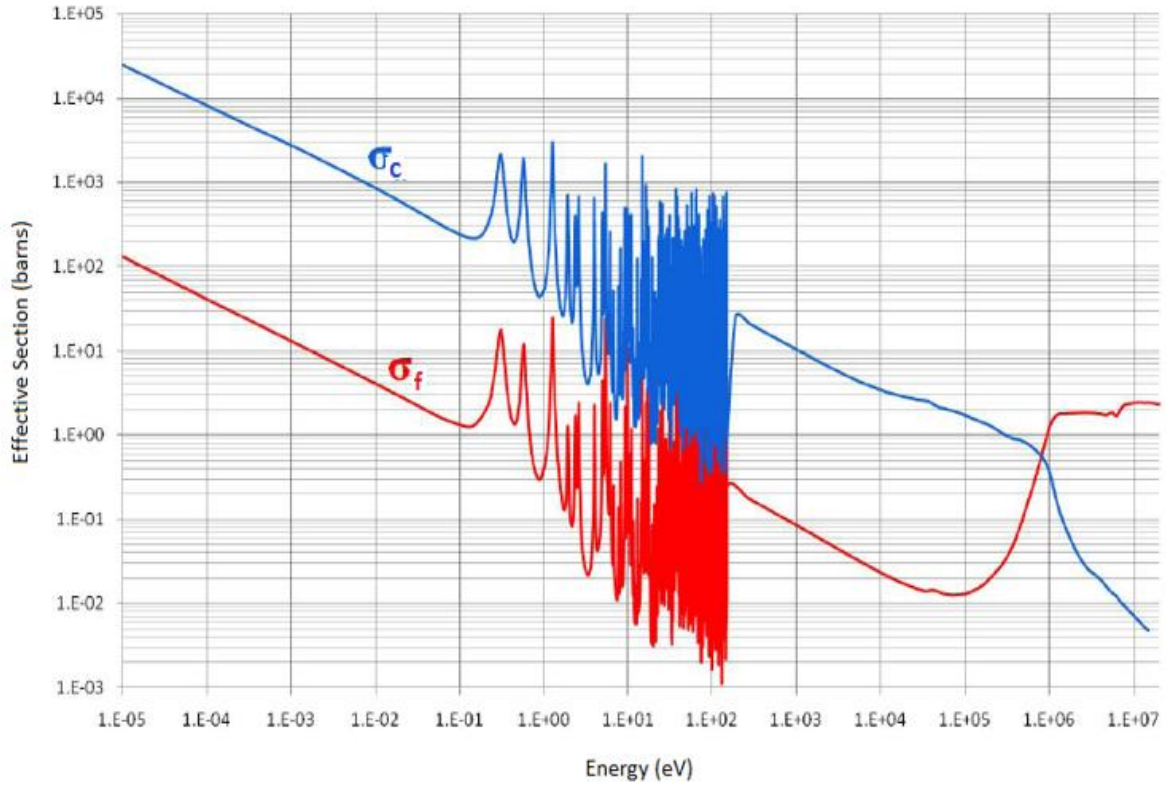

Figure 4. Effective Sections of capture and fission of 241Am depending on the neutron speed [17]

According to the figure for neutrons of energy lower than 1 eV (in the domain of thermal neutrons) the effective section for the capture (σ_c) is predominant, namely, two orders of magnitude bigger than the effective section for fission (σ_f). Thus, the capture of the neutron is more probable than the fission in this range of energy. This remains similar for energies from 1 eV to 1 MeV (in the epithermal neutrons domain). For more than 1 MeV (on the fast neutrons domain) fissions become more probable than captures. Logically, the external source providing neutrons to the transmutation reaction shall be conceived to produce fast neutrons with higher energy.

Introducing minor actinides or LLFP in a reactor influences the reactivity of the fission reactions taking place inside. Reactivity (K) is expressed as:

$$K = \frac{Number\ of\ neutrons\ produced}{Number\ of\ neutrons\ absorbed} \tag{2.1}$$

This coefficient determines the evolution of the neutron population and the number of fission reactions taking place, which will increase if $K > 1$ (supercritical reaction), remain stable if $K = 1$ (critical reaction), or decline when $K < 1$ (subcritical reaction). $K < 1$ is always the case in a subcritical reactor that needs of a continuous flow of neutrons to sustain the reaction.

The same idea is also explained by the concept of economy of neutrons (D) expressed as the difference between the number of neutrons consumed and the number of neutrons produced by fission. This can be written as a function of the effective sections of capture (σ_c), fission (σ_f), and the mean number of neutrons produced by fission (γ).

$$\mathrm{D} = \sigma_c - \gamma\sigma_f \tag{2.2}$$

Recalling the analysis of Figure 4 it seems clear that working on the thermal neutrons has an adverse effect on the neutron population. Indeed, in the thermal spectrum the neutron capture is favored and the burning spent fuel becomes too demanding on neutrons. Burning spent fuel in the fast neutron spectrum (>1 MeV) improves the reactivity of the reaction to

the point that some nucleus like neptunium 237 and americium 241 when incinerated by fission provide new neutrons and get to cause chain reactions.

Exposing fission products to a neutron flow in the fast spectrum is the best solution to incinerate them. Nevertheless, this fast electron flow affects the reactors dynamics making the core's reactivity difficult to control. Assuring the safety of a fast spectrum critical reactor is complicated.

However today's geological disposal, in different sites around the planet, causing proliferation risks and maintaining these sites polluted for millenniums, demands for a solution. The use of a transmutation reactor to incinerate nuclear waste requires of a compromise between processing capacity and safety. However, this compromise could be achieved using a subcritical reactor, which intrinsically assures operational safety, with an external neutron source providing a high energy continuous neutron flow that would allow to sustain the chain reaction. The next subsection will explain how a high energy continuous beam of neutrons can be provided by a linear accelerator or linac, capable of driving the subcritical reaction in a transmutation facility. This concept is referred to as an Accelerator Driven System (ADS).

2.3 THE ACCELERATOR DRIVEN SYSTEM (ADS) CONCEPT

An Accelerator Driven System (ADS) is a fast spectrum nuclear fission reactor, piloted by a particle accelerator. Unlike conventional critical reactors where the neutron population is sufficient to self-sustain the nuclear reaction, the subcritical core of an ADS requires an external neutron source to maintain the reactor's operation. These additional neutrons are provided by a high energy proton accelerator. The protons hit a specific target and produce neutrons by the spallation process [35]. Figure 5 presents a schematic view of an ADS.

An ADS basically consists of three main elements, a proton accelerator, a spallation target and, a sub-critical core which will be discussed in the following:

I. The *accelerator* is the driver of the ADS. It provides the high energy protons that hit the spallation target to create fast neutrons which in turn feed the sub-critical core.

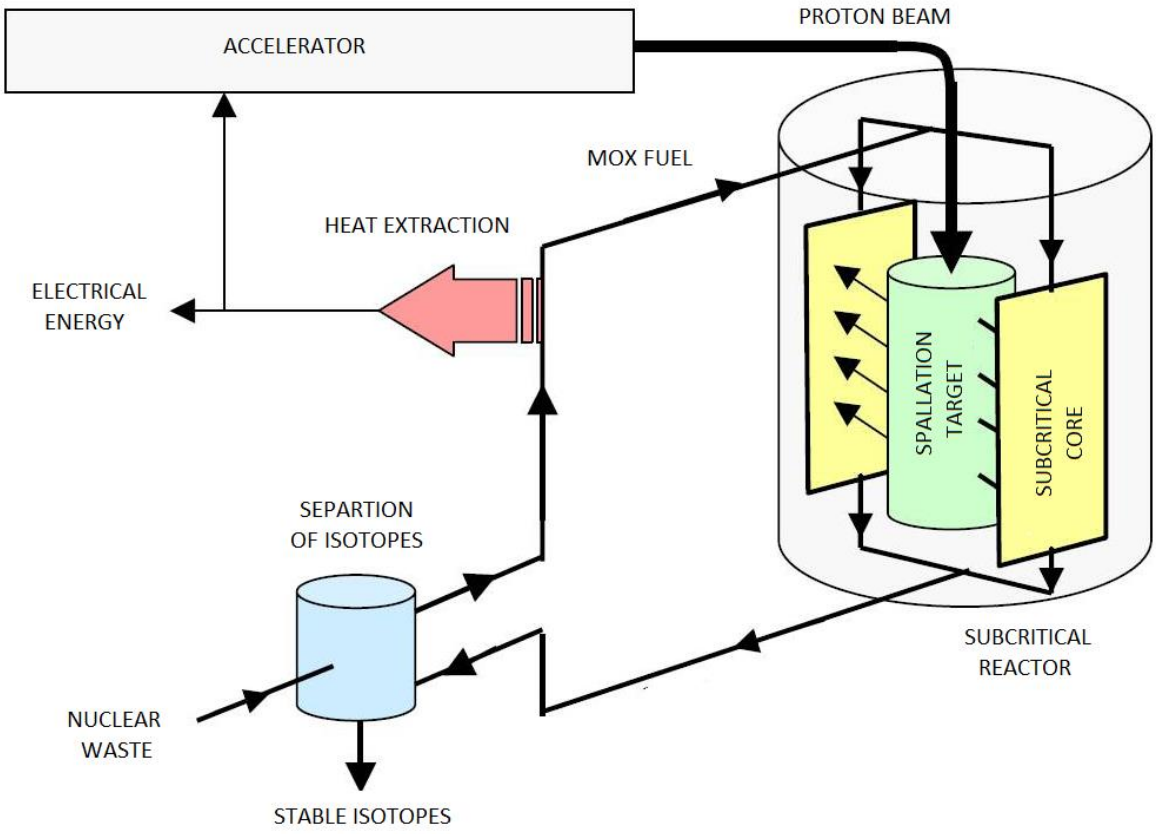

Figure 5. Schematic View of an ADS [34]

II. In the spallation target the interaction of high energy protons (of at least several hundreds of MeV) with a thick target causes a significant emission of neutrons. Since the energy of the protons is higher than the Coulomb barrier (energy barrier due to electrostatic interaction that two nuclei need to overcome so they can get close enough to undergo a nuclear reaction) of the nuclei of the target, they cause by intra-nuclear elastic scattering the ejection of nucleons and the excitation of the nuclei, which de-energize either by fission or by new emissions of nucleons.

The excited nuclei can also interact with other nuclei of the target, and thus cause an inter-nuclear cascade reaction. These chain reactions also cause nucleon

emissions. Overall, these interactions are largely dominated by neutron emission. The production of neutrons is all the more effective when the nuclei are heavy and the incident energy of the protons is large (see Figure 6).

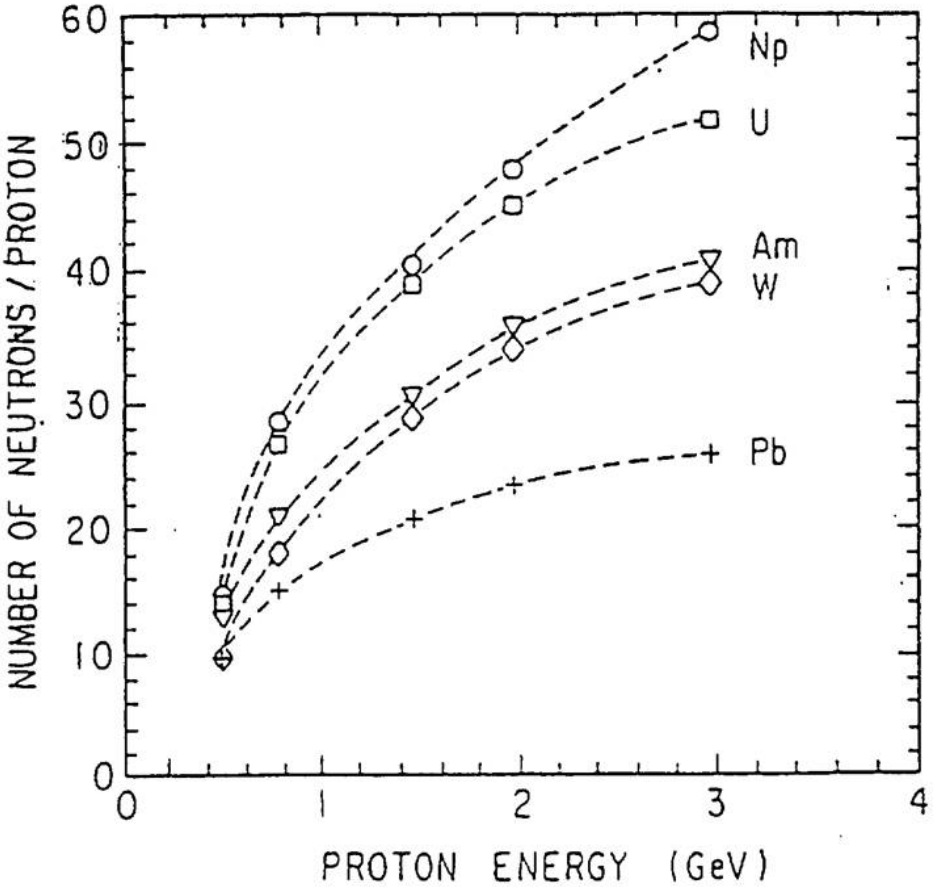

Figure 6. Number of neutrons generated by spallation depending on the proton energy [17]

Thus, in the spallation target primary neutrons are produced by the spallation reaction of heavy-metal target nuclei bombarded by hi-energy protons generated by the accelerator. The spallation target then becomes a neutron source providing primary neutrons that are multiplied by the surrounding sub-critical core.

III. The *sub-critical core* of an ADS is constructed in such a way that it does not have enough fissile material to reach criticality, this means neutrons are needed as an input. One dominant feature of an ADS is its inherent safety: the reactor is switched off at the moment the proton beam is switched off. A key aspect of the sub-critical

core is the cooling system as the heat produced by the transmutation reactions must be safely evacuated from the core. Recent studies [36], point out that the alternative of using an ongoing flow of a low boiling point heavy metal (such as Na or lead-bismuth eutectic) for the dual purpose of producing the spallation reaction and cooling the ADS reactor's core is envisaged as a simple constructive solution. In this case a secondary circuit removing heat from the heavy metal flow is necessary. This secondary circuit could be made of oil or pressurized water, similarly to that of coal fired power plants and used for power generation.

ADS devices are considered as a potential solution to reduce the volume and the radiotoxicity of the accumulated nuclear waste: in particular MA and LLFPs [37]. Nuclear waste reduction can be achieved by transmutation and fission of these wastes under a high neutron flux [36]. In principle, such a process can be achieved with both critical reactors or subcritical ADSs dedicated for transmutation, by mixing the waste with nuclear fuel.

Consequently, the ADS concept offers a promising alternative. It is intrinsically safe in terms of criticality and it can be controlled by the intensity of the external neutron source, and not just through the reactivity adjustment of the fuel (which is the case in conventional nuclear reactors). Therefore, a higher "waste loaded" nuclear fuel can be envisaged. It also offers a better freedom of choice for fuel composition to optimize the transmutation. In other words the main ADS advantages for waste incineration, with regard to conventional reactors, are their operational safety and design flexibility.

2.4 ADS CONCEPT: CONCERNS AND CHALLENGES

An ADS operation and performance depends on the quality of the continuous proton beam provided by the linac. However, medium size linac facilities around the world have proven that the current state of the art of this kind of machines does not warrant sufficient reliability to consider the ADS concept industrially feasible. Figure 7 shows the frequency of beam trips against the duration of these trips in representative accelerating facilities.

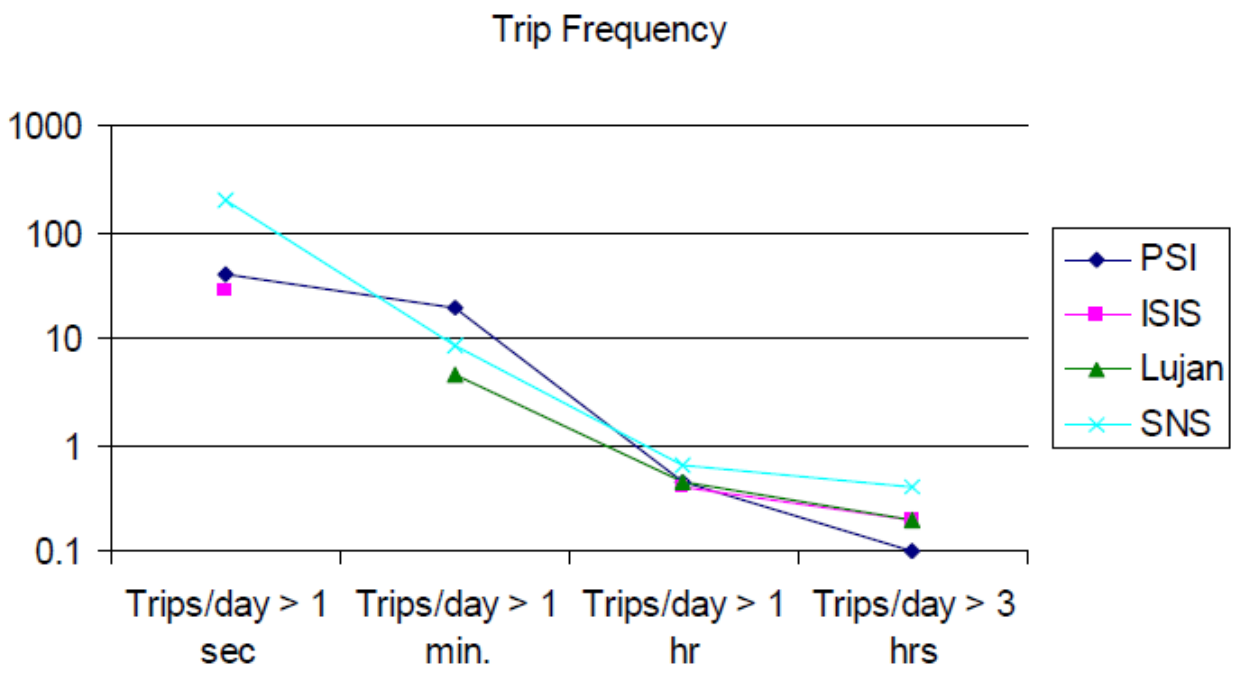

Figure 7. Trip frequency vs. trip duration for high power accelerators (Data from 2008) [38]

Frequent beam trips as experienced in existing high power proton accelerators may cause thermal fatigue problems in ADS components which may lead to degradation of their structural integrity and a reduction of their lifetime. The allowable beam trips should make a compromise between an efficient and reliable subcritical reactor and a reasonable cost of an accelerator.

Japan Atomic Energy Agency (JAEA) has been performing thermal transient analyses to investigate the effects of beam trips on the reactor components, with the objective of formulating ADS design considerations, and to determine the requirements for accelerator reliability. These analyses were made on the thermal responses of reactor components. The results indicate that the acceptable frequency of beam trips ranges from 50 to 2.5×10^4 times per year, depending on the beam trip duration [39].

These findings were supported by a work performed by B. Giraud (Areva) [40] during the course of the PDS-XADS project [8]. He quoted the final statements: “For the lead-bismuth eutectic cooled ADS, limitations are likely to be imposed by the structures exposed to the fluctuating free level, such as the main vessel, which require detailed thermal-hydraulic and structural analyses. Beam trips with time duration of less than 10 s would have no effect on

the reactor structures. A number of allowable beam trips of significant duration for the reactor structures of 5,000 is a reasonable target value for accelerator designers."

These JAEA and Areva analysis yielded larger values than those taken form PHENIX. PHENIX was a small-scale (233 MWe) prototype fast breeder reactor, located at the Marcoule nuclear site, near Orange, France. PHENIX operated using liquid metal as coolant (Na) and can, consequently, be considered a reference of the expected behavior of other reactors using melted metallic coolants such as Lead-Bismuth Eutectic (LBE). For PHENIX, 5 beam trips per cycle of 3 months (15 trips per year) were enough to reach the recommended maximum number of emergency stops (≈200) in 20 years [41]. This lifetime span should be at least doubled for an industrial facility.

The design approach taken by PHENIX developers to define the number of allowable quick or emergency stops is very much based on a demonstration that a restricted number of stops are acceptable and that periodic check of the components is not leading to any degradation of the plant integrity. However, the experience has shown that this process has led to the replacement of some initially designed components by less sensitive ones and, above all, to the reduction of the plant's lifetime.

More recently, SCK-CEN attempted to find the number of allowed beam trips for a medium size industrial demonstrator of an ADS according to the RCC-MR code for "Design and Construction Rules for Mechanical Components in high-temperature structures, experimental reactors and fusion reactors" [42], assessing the maximum allowed number of cycles during lifetime and considering a safety factor of 10, which is the usual recommended practice. Results are shown in Table 1.

Trip duration	Allowed number (Trips/year)
<10 sec	2,500
10 sec – 5 min	250
> 5 min	25

Table 1. Recommendations for the maximum number of allowable beam trips

The results of the three studies (Areva, SCK·CEN and JAEA) considered above are devoted to experimental ADS and do not fit with the PHENIX plant safety dossier in which values of 2,000 stops (normal, quick and emergency ones) are quoted for its entire life of 20 years.

The reason of such differences does not seem to be related to the way irradiation has been taken into account since the approach has been the usual one in these studies. It is surprising that such margins exist between results yielded from PDS-XADS and from PHENIX operational experience when specific problems due to the use of metallic coolant at low temperature should be similar.

The consequence of a bad prediction in the induced stress of quick or emergency stops is either leading to the replacement of a components (heat exchangers for instance) with an associated reduction of the plant availability or a reduction in the plant lifetime and, in any case, to an extra operational cost. Hence, increasing the maximum number of beam trips is not an issue which has minor consequences on the plant operation. This is to say that the objective to keep the number of beam trips to an absolute minimum is mandated by the need to guarantee the availability of the machine.

Indeed, the PHENIX recommendations [41] regarding 10 transients per cycle of 3 months as the permitted number of the quick transients for a medium size ADS with metallic coolant, are more restrictive and might be considered as the procedural indication.

Following this indication, the MYRRHA ADS has been conceived to be an industrial demonstrator of an ADS and is currently under construction in Mol (Belgium). Figure 8 allows to compare the MYRRHA reliability goals to the data gathered from the Spallation Neutron Source's (SNS) operation in the period ranging from 2006 to 2008 and in the period ranging from 2010 to 2013 and to the Japan Atomic Energy Agency (JAEA) specifications for an industrial ADS.

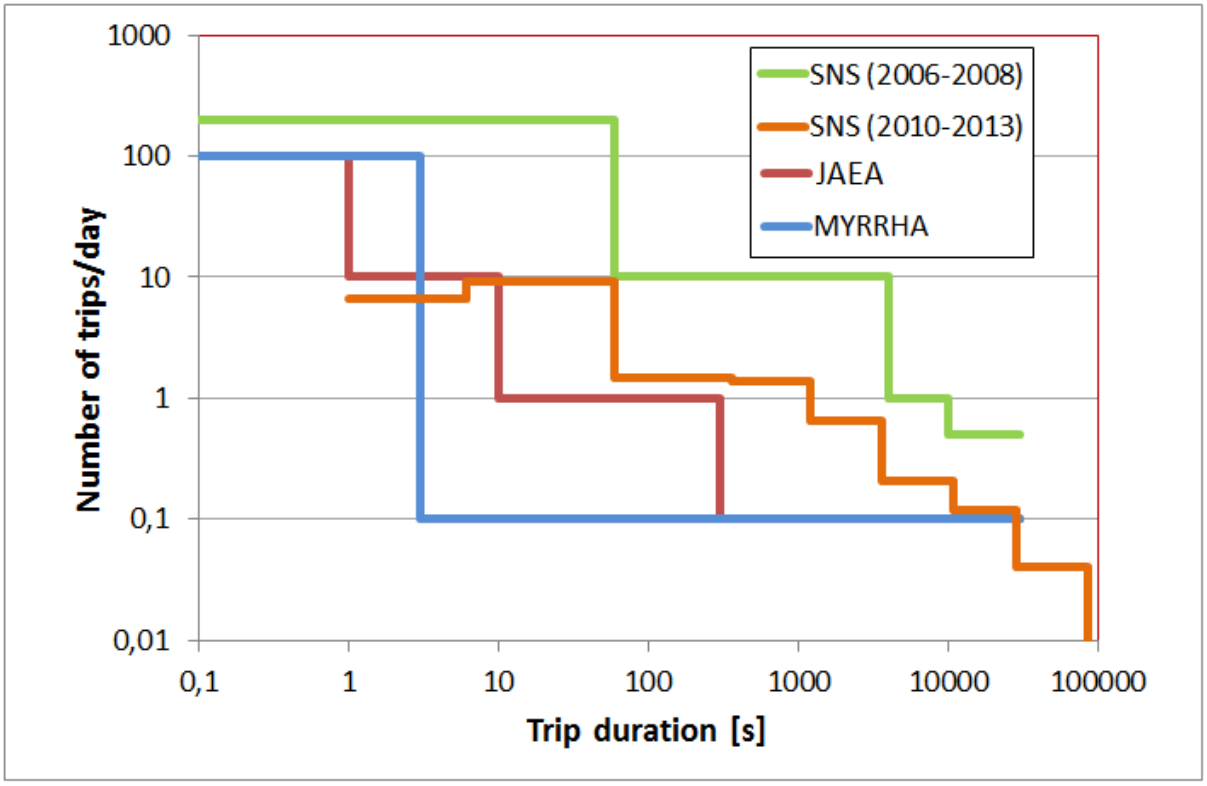

Figure 8. MYRRHA reliability goals as regards to other comparable facilities [33]

Analyzing the figure it must be noted that MYRRHA's reliability challenge, as regard to the data from SNS and JAEA, is to reduce to its minimum the number of beam trips lasting between 3 and 300 seconds. The following subsection describes the MYRRHA design that targets to overcome this ambitious reliability challenge and the fault-tolerance strategy chosen to accomplish this objective.

2.5 MYRRHA ADS OVERVIEW

The MYRRHA project, led by SCK-CEN, aims at the construction of a new nuclear ADS facility in Mol (Belgium) [34]. MYRRHA is supported by the European Commission and has been funded throughout the successive FP6, FP7 and H2020 European Union research frameworks. Furthermore, MYRRHA has been identified by the European Commission as one of the 50 ESFRI (European Strategy Forum for Research Infrastructures) projects which are considered necessary to maintain the European Union on the cutting edge of research during the next 20 years.

This large scale ADS reactor prototype is especially designed to demonstrate industrially feasible the ADS concept for the transmutation of high level radioactive waste. Under this premise the projects in charge of MYRRHA's design, [6], [8] and [9], established the envisaged features for the MYRRHA ADS that are presented in Table 2.

Features	Design Specification
Power	50-100 MW_{th}
Spectrum	Fast (flexible)
Fuel	MOX
Coolant	LBE
Particles	Protons
Particles energy	600 MeV
Peak beam current	0,1 to 4 mA
Bunch Repetition rate	CW 176,1 MHz
Beam duty cycle	10^{-4} to 1
Beam power stability	< ±2 % on a time scale of 100ms
Beam footprint on reactor window	Circular 85 mm diameter
Beam footprint stability	< ±10 % on a time scale of 1s
Number of allowed beam trips longer than 3 seconds	10 maximum per 3 month operation period
Number of allowed bean trips longer than 0,1 seconds	100 maximum per day
Number of allowed bean trips shorter than 0,1 second	Unlimited

Table 2. Design Specifications for the MYRRHA ADS [17]

Figure 9 shows a schematic view of the MYRRHA, which will be an ADS conceived for research use (50 - 100 MWth) and intended to operate during 3 month periods, normally in subcritical mode.

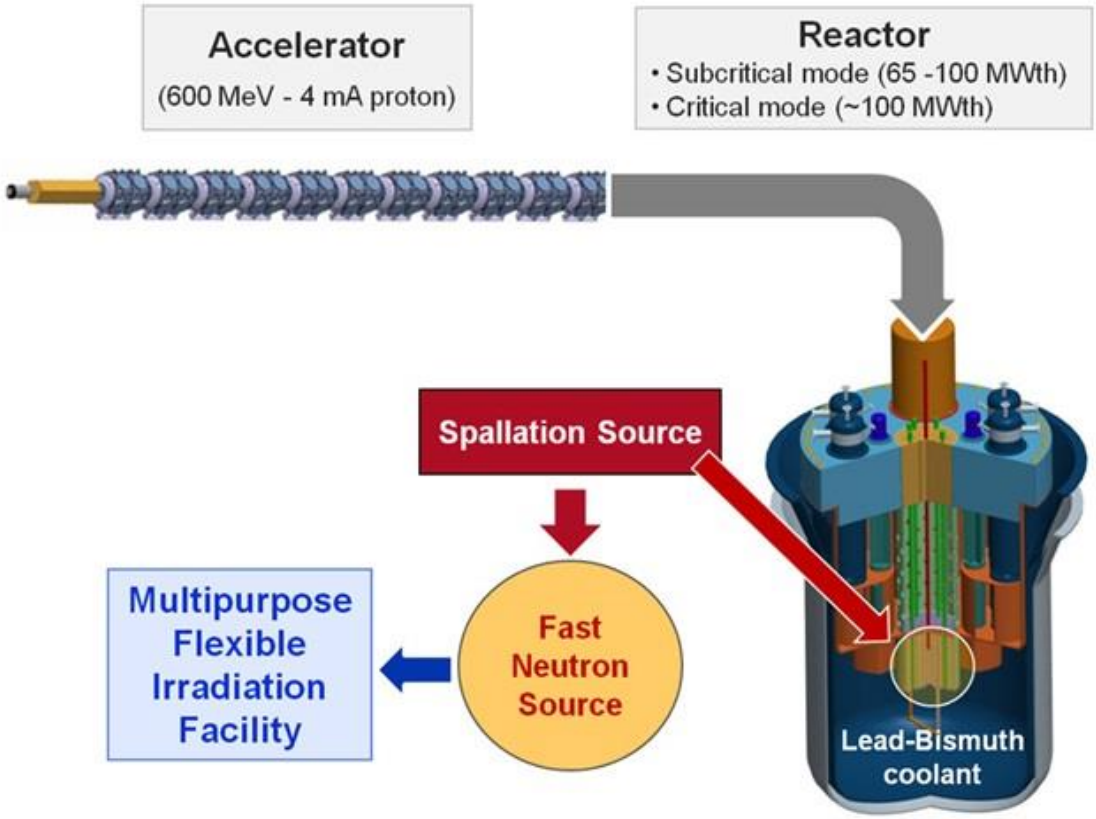

Figure 9. MYRRHA layout [34]

MYRRHA's reactor will bear the transmutation of nuclear waste products when fed by a neutron source created by coupling a linear proton accelerator, a spallation target and a sub-critical core. These concepts are reviewed giving specific details of MYRRHA's design:

- The **linear accelerator** is the driver of the ADS. It provides the high energy proton beam that collides with the spallation target to create fast neutrons which feed the sub-critical core. The linac accelerates particles from 30 Kev to 600 MeV by subjecting them repeatedly to longitudinal electric fields. MYRRHA's accelerator will require around 150 cavities (normal conducting and superconducting) arranged in series, bearing inside electromagnetic fields of oscillating nature, for the consecutive acceleration of

the proton bunches. The frequency of these oscillations is in the Radio Frequency (RF) domain (50 MHz to 1 GHz).

- MYRRHA can work in critical or sub-critical mode depending on the composition of fuel. However, its main operation mode will be subcritical, meaning that a **subcritical core** will be designed in such a way that it does not have enough fissile material to reach criticality, this means neutrons will be needed as an input to maintain the reaction. One dominant feature of an ADS is its inherent safety: the reactor is switched off at the moment the proton beam is switched off. MYRRHA's subcritical reactor will be made of MOX fuel, in which the high amount of plutonium favors the production of fast neutrons and inside which there will be irradiation cells composed by other materials such as MA. The MYRRHA subcritical core will be cooled by a liquid lead-bismuth eutectic (LBE).

- The spallation target is envisaged to be the LBE coolant that will act as a neutron source providing primary neutrons that will be multiplied by the surrounding sub-critical core. The primary neutrons are produced by the spallation reaction of the heavy-metal (namely LBE) target nuclei, bombarded by hi-energy protons generated by the accelerator.

The following section describes MYRRHA's accelerator design features, derived from MYRRHA's operational requirements, and its global design conceived in accordance with them. Descriptions of the accelerator components and their functions will be found in the following.

2.6 THE MYRRHA ACCELERATOR AND THE FAULT-TOLERANCE CONCEPT

To prove industrially feasible the transmutation concept MYRRHA is intended to work uninterruptedly during operational periods of 3 months. This imposes a level of availability onto its driver accelerator significantly higher than what is currently achieved in accelerator installations of comparable complexity and performances.

An accelerator's availability is expressed as a limit upon the integrated number of beam trips that last longer than a predefined reactor time constant. The allowable number of beam trips is determined by the endurance of the oxide layer protecting the fuel clads and their resistance to thermal stress. While thermal stress caused by beam trips lasting less than the reactor time constant, 3 seconds for MYRRHA, can be considered negligible, the maximum number of beam trips lasting longer should not surpass 10 per operational period according to EUROTRANS recommendations [36]. These goals directly address the accelerator's reliability that must be stressed since the accelerator's conception.

The MYRRHA accelerator will be a high power proton linac (600 MeV, 4 mA) with strongly enhanced reliability. The adopted technical solution [43], [44] is that of a superconducting linac. To implement a strong reliability scheme, the linac consists of two clearly distinct sections, as illustrated on Figure 10.

- A low energy section (injector or linac front end) in which the modularity and fault tolerance are not applicable since the beam velocity is too low. Here the number of elements is minimized using multi-cell cavities, and redundancy is applied in its parallel form so that two complete proton injectors with fast switching capabilities are foreseen.

- The high energy section (main linac or independently-phased SC section), highly modular, based on individual, independently controlled accelerating cavities. In this section a serial redundancy is applied so as to yield a strong fault tolerance. The function of a faulty cavity may typically be taken over by 4 adjacent cavities.

Thus the injector's design [45] is conceived to provide a continuous proton beam of 4 mA to the main linac. The beam's transition energy between the sections has been set to 17 MeV. The main linac is then intended to accelerate the beam up to 600 MeV.

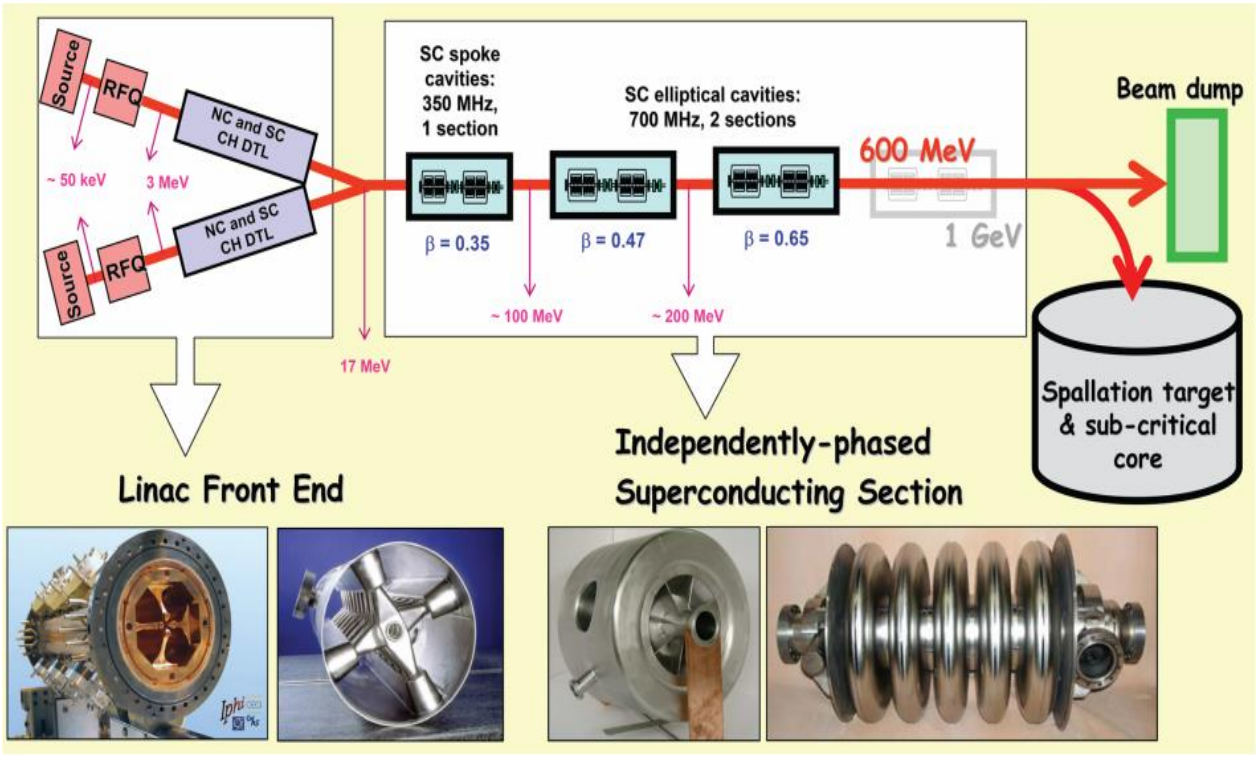

Figure 10. Conceptual scheme of the MYRRHA accelerator [17]

The injector will be composed of two identical branches. In operation only one of them will be in use, while the other will stand to take over in case of an unforeseen stop of the first one. Fast switching capabilities between the two branches are being studied. This redundant choice is based on the accumulated experience of several accelerating facilities [46] and, particularly the start-up of the SNS accelerator [47].

Experience gathered on these facilities yields that injection branches are the origin of numerous beam interruptions, causing time costly repairs and long periods of machine inactivity. Hence, doubling the elements of this branch seems indispensable to attend the reliability requirements.

In the injector, an Electron Cyclotron Resonance (ECR) source will produce a 30 keV beam. The prototype including a “Low Energy Bem Transfer” (LEBT) line has already been built and is currently being tested in the “Laboratoire de Physique Subatomique et Cosmologie de Grenoble” (LPSC Grenoble). Figure 11 shows the prototype of the ion source and the LEBT.

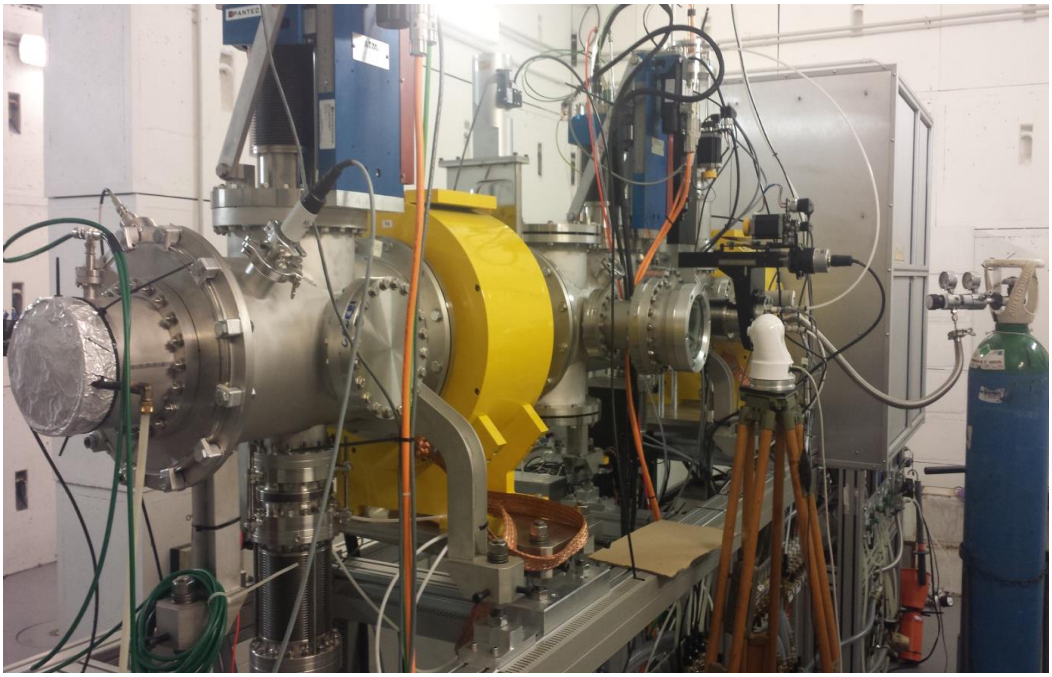

Figure 11. Ion source and LEBT

It is foreseen that the injection line will also be composed of cavities “Crossbar-H-Type” to accelerate the beam up to 17 MeV. Figure 12 illustrates this type of CH-DTL structure as described in [48].

Figure 12. Picture of the inside of a CH-DTL Cavity

Between the source and the cavities a Radio Frequency Quadrupole RFQ allows to convert the continuous particle flow produced by the source into bunches with a repetition cycle of 176,1 MHz. Figure 13 shows a section of this kind of RFQ.

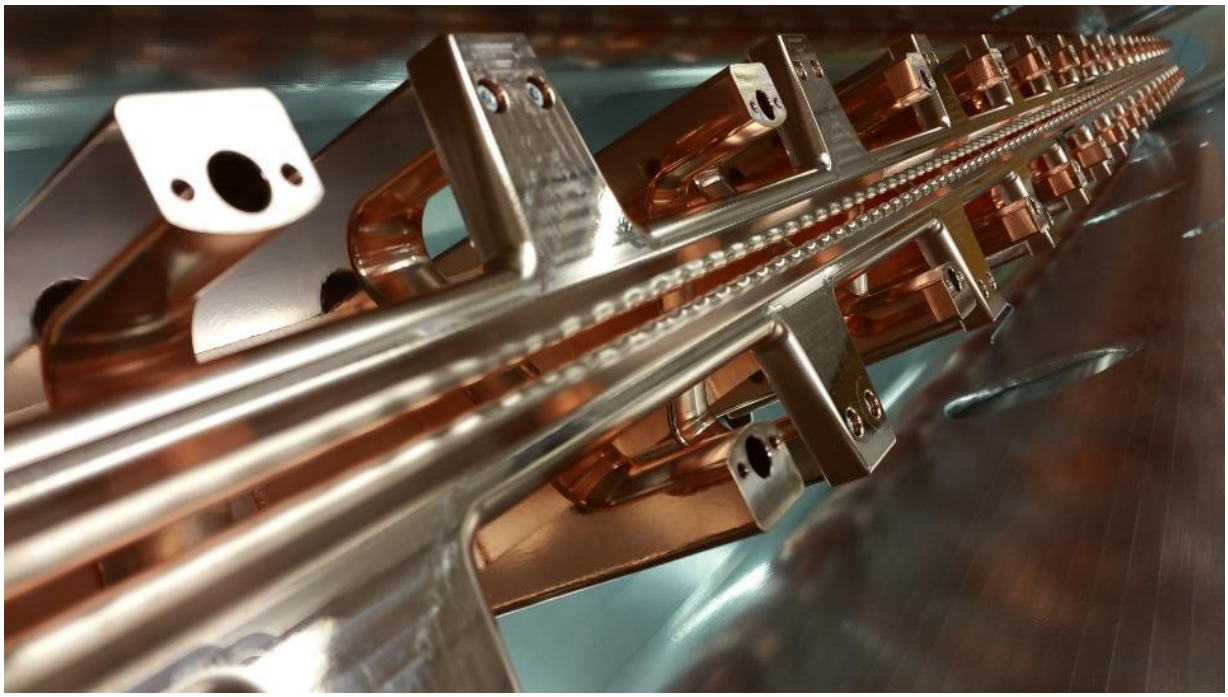

Figure 13. Four Rod RFQ [33]

After the injector, the beam will be injected into the superconducting linac, which will be composed of two types of accelerating cavities. The medium energy section of the superconducting linac will be composed of simple or double Spoke cavities with a working frequency of 352,2 MHz in correspondence with twice the repetition rate of the bunches. 5 cells elliptical cavities are envisaged for the high energy superconducting section. Elliptical cavities will work at a frequency of 704.4 MHz. The functioning principle of resonant cavities and a deeper introduction to the types of cavities are presented in the next chapter.

The MYRRHA accelerator superconducting line design [36] has been conceived following the guidelines of a fault-tolerant scheme, meaning that the conception has been performed taking into account procedures providing operational robustness in case of unforeseen events and breakdowns. In a fault-tolerant scheme redundancy of all elements is a key aspect. As already commented, parallel redundancy is considered for the injector line, while serial redundancy is envisaged for the superconducting line. For this reason when the

accelerator is in normal operational, superconducting cavities will not work at their maximum capacity. Thus, if a cavity suffers a breakdown, the neighboring cavities will compensate its absence with their overhead power.

The present adopted strategy in the main linac is to use a local compensation method to compensate for failures of: cavities, their associated control systems and their power supply.

To recover such fault conditions, the philosophy is to re-adjust the operational parameters (accelerating gradient, synchronous RF phase and resonance frequency) of some non-faulty RF cavities to recover the nominal beam characteristics at the end of the linac. A way to proceed is to readjust the accelerating cavities neighboring the failing one. The advantage of the local compensation method is involving a small number of elements, and, therefore, being able to compensate multiple faults in different sections of the machine at the same time. This is illustrated on Figure 14, where the black element is the faulty cavity, the red ones the compensating cavities and quadrupole doublets for beam focusing are represented in blue. These same elements when represented in white are not be affected by the local compensation. If cavity #n is faulty, the (i.e.) 4 surrounding cavities (#n-2, #n-1, #n+1, #n+2) are retuned to recover the nominal beam energy & phase at the end of the following lattice (point M), and by consequence, at the linac end. It can of course be done with more (or less) cavities when necessary. In this case, the fault of a cavity is compensated by acting on the accelerating gradient and the phase of the 4 nearest neighboring cavities operating de-rated (i.e. not already used for compensation). During this retuning procedure the beam is switched-off.

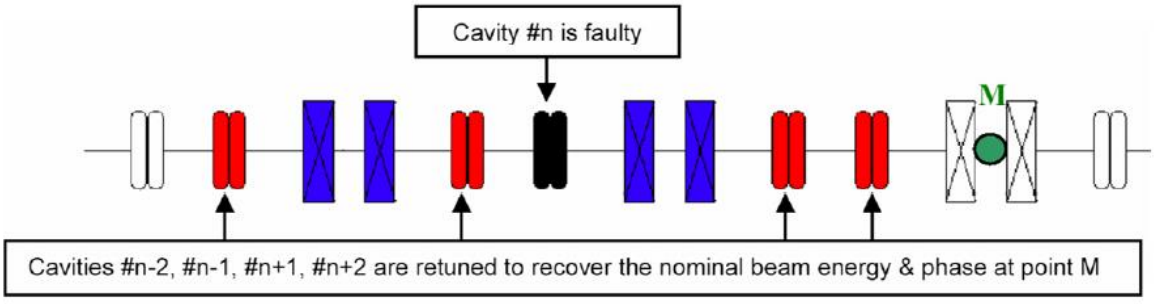

Figure 14. Principle of the local compensation method in the main superconducting linac [39].

Therefore, the retuning procedure has to be sufficiently fast to resume the beam in less than 3 seconds, so the beam interruption remains “transparent” for the ADS operation. This retuning scheme can only be achieved by providing significant power and accelerating gradient overhead throughout the three superconducting sections. As a consequence, the operating accelerating gradients of the MYRRHA cavities have been chosen on the conservative side to enable the compensation procedures under nominal conditions, the cavities operate with an accelerating gradient which is 30% below its maximum capabilities (details in [49] and [50]).

Beam physics studies have been carried out to evaluate the feasibility of the retuning procedures. The results obtained tend to show that it is possible to apply the local compensation method without substantially perturbing the beam transport and acceleration [51].

As previously mentioned, when a retuning procedure takes place the cavities setpoints have to be changed in less than 3 seconds. To assess the feasibility of such a procedure, a model of the cavity and its control loops have been developed with Matlab Simulink [52]. The model includes the RF control of the cavity, which is the control of the stored electromagnetic wave inside the cavity that provides the accelerating field, as well as the resonance frequency control, which is a variable dependent on the mechanical behavior of said cavity. This model enabled the setting of specific requirements for the hardware platforms used for the dynamic adjustment of the cavity resonance frequency, which are described in Chapter 9.

The RF control and the resonance frequency control are in charge of driving the cavities main operating variables (accelerating voltage and phase) to new nominal conditions after a cavity failure in the linac in less than three seconds. Consequently, the linac design intends to provide a high energy acceptance and moderate energy gain per cavity. The goal is to increase as much as possible the tuning flexibility and to provide sufficient margins for the implementation of the fault-tolerance capability by serial redundancy.

To assure the superconducting condition of cavities they are grouped inside cryomodules. During normal operation, liquid helium is pumped across the cryomodules so that it flows between its inner walls and the cavity, keeping temperature at 2 K. At this temperature cavities become superconductors avoiding energy losses caused by surface

currents on the cavity walls. Beam focusing is performed with 52 room-temperature quadrupoles doublets (i.e. 104 magnets) located in between the cryomodules. In the present scheme, the main linac is about 220 meters long with 157 cavities and 52 cryomodules.

At the linac hi-energy end [53], a final beam line injects the proton beam onto a full power beam dump and on the spallation target located inside the reactor vessel. This beam line to reactor is composed of two 45° bending magnets going up from the linac tunnel, and a last 90° dipole bending the beam down through the reactor hall to the sub-critical core. This is represented in Figure 15. The linac hi-energy end has achromatic and telescopic optics in order to guarantee the beam stability on target and to ease the tuning, and it houses AC magnets which allow scanning the beam on target.

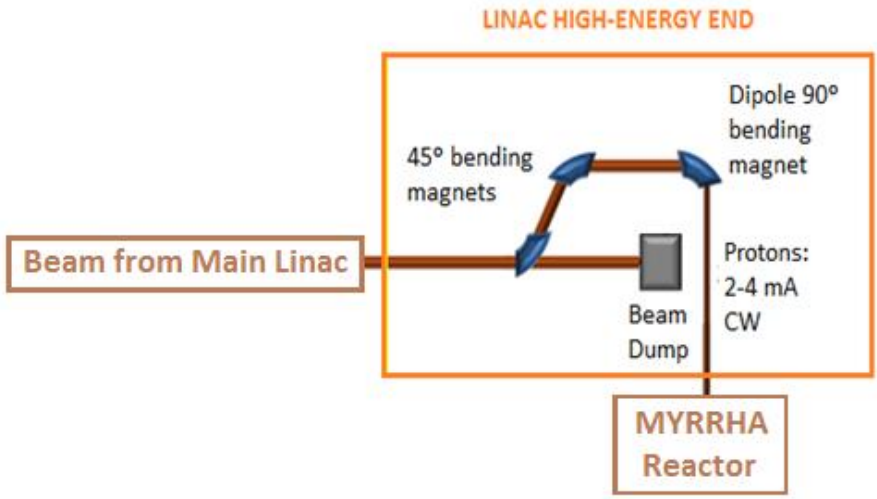

Figure 15. Hi-energy end of the MYRRHA linac.

Summarizing this section the MYRRHA accelerator is composed of a dual proton injector delivering a 4 mA beam at 17 MeV to the main linac where the beam is accelerated in cavities grouped in cryomodules up to 600 MeV. Figure 16 shows a detailed scheme of the MYRHA's accelerator composition.

In the following section the principle of beam acceleration inside the cavities of the superconducting linac will be presented. Later the families of cavities considered for MYRRHA and their main operational elements will also be described.

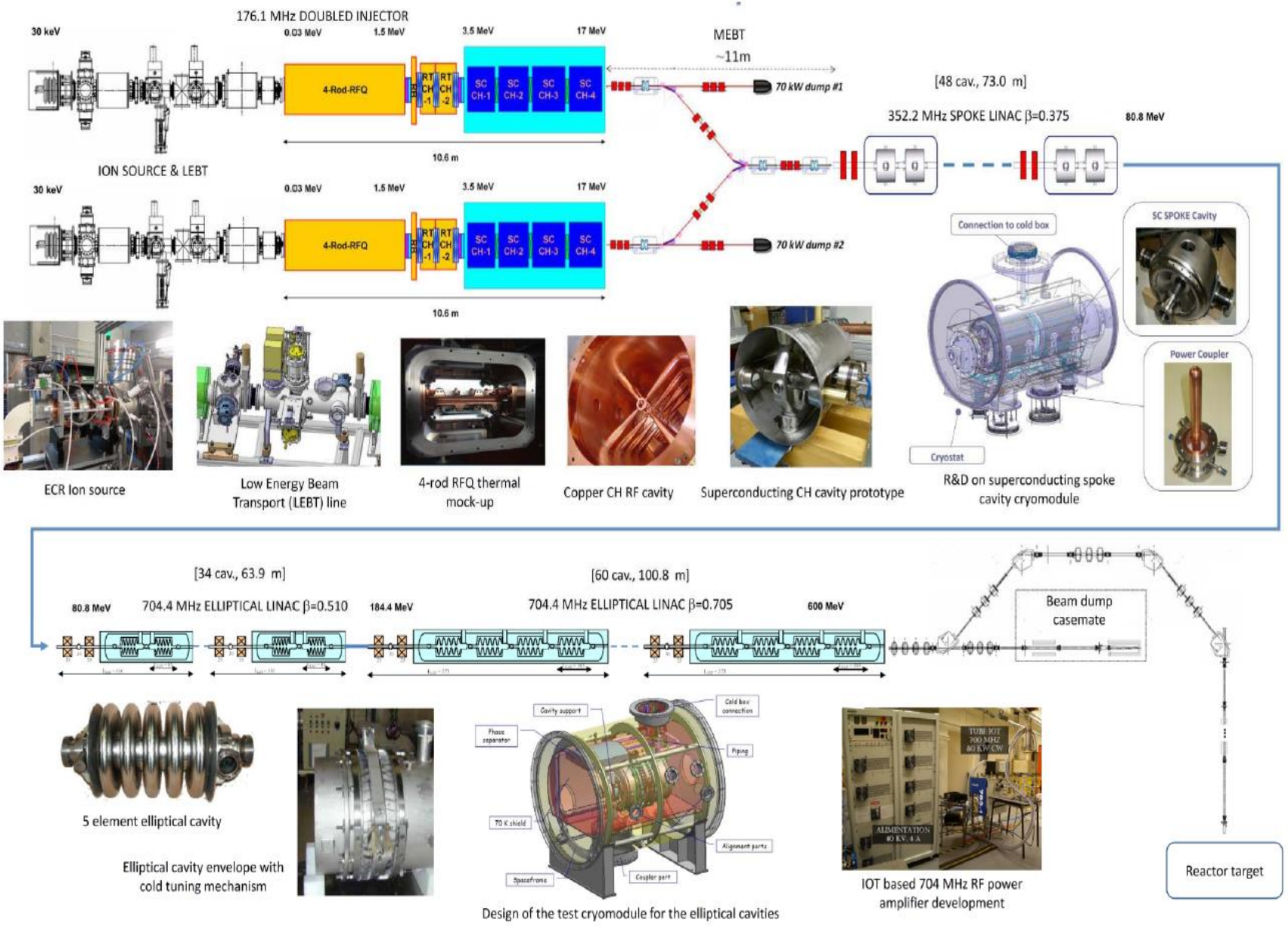

Figure 16. Detailed scheme of MYRRHA's accelerator [54]

CHAPTER III:

PARTICLE ACCELERATION AND SUPERCONDUCTING CAVITIES

3.1 ACCELERATION PRINCIPLE

The movement in vacuum of a charged particle subjected to the effect of electromagnetic fields or, otherwise said Lorentz forces, is described by the fundamental principle:

$$\vec{F} = \frac{d\vec{p}}{dt} = q\left(\vec{E} + \vec{v}\ x\ \vec{B}\right) \tag{3.1}$$

where $\vec{F}$ is the force on the particle (N), $\vec{p}$ is the momentum (kg.m/s), t is time (s), q is the charge of the particle (C), $\vec{E}$ is the electric field (V/m), $\vec{v}$ is the velocity of the particle (m/s) and $\vec{B}$ is the magnetic induction (T).

Additionally, the evolution of the total energy of a relativistic particle (W_{tot}) subject to the effect of an electromagnetic field is given by the equation [35], [17]:

$$\frac{dW_{tot}}{dt} = q\vec{E}.\vec{v} \tag{3.2}$$

From the equation it must be noted that the energy gain of a particle is only due to the electric field and that an electric filed parallel to the particle's velocity is optimal for the particle's acceleration.

It is on this principle that the electrostatic acceleration is based: a set of electrodes of increasing tension is placed along the accelerator line and a constant gradient of electric power is created between each of them. Several types of accelerators are based on this principle, i.e. Cockcroft-Walton [55] and the Van de Graaf [56]. In these kinds of machines the beam energy gain is directly proportional to the voltage between the electrodes. It is, indeed, for this reason that these machines are limited by electrical breakdowns, which occur, in the best case, around of the ten megavolts. Thus, these instruments are generally dedicated to the acceleration of very low energy ions or used as injectors in electromagnetic accelerators, since they provide an uninterrupted flux of particles.

The following section explains how acceleration can be performed using electric fields of oscillating nature enclosed in resonant structures, thus overcoming the limitations of electrostatic accelerators.

3.2 RESONANT STRUCTURES FOR ACCELERATION

Pill-box cavity

For the understanding of the acceleration principle of different resonant structures it is first convenient to comprehend the pill-box cavity which is the simplest resonant structure. The resonant phenomena inside a pill-box cavity can be explained through that of a geometrical ideal capacitor like the one represented in Figure 17. In the following, the main concepts presented in [57] will be reviewed.

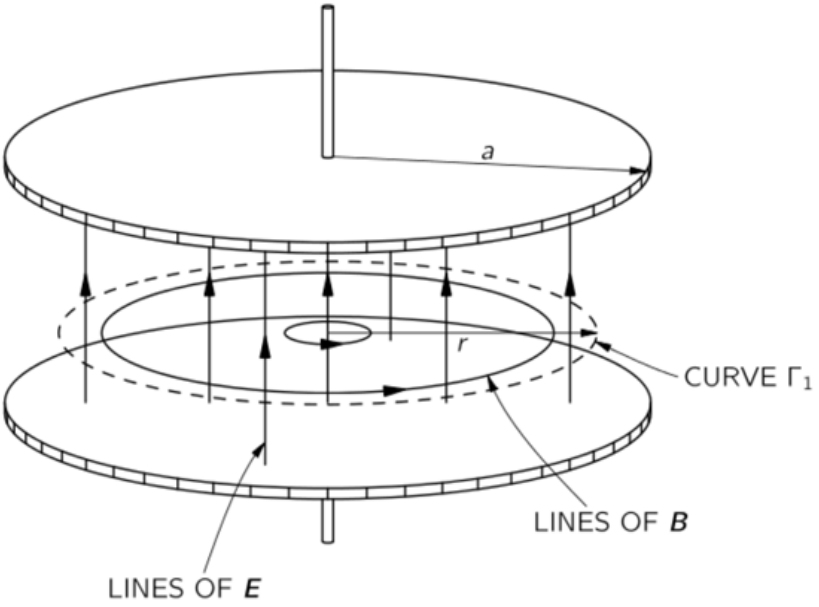

Figure 17. Ideal Capacitor [57]

If an alternating current (AC) generator is connected to the circular plates of the capacitor of Figure 17, as the voltage of the plates alternates, the direction of the electric field ($\vec{E}$) between de plates will also alternate. However, at each instant, the electric field between the plates will be uniform except for negligible differences at the edge of the plates. The electric field can be written as function of the AC generator frequency in the following way:

$$\vec{E} = \vec{E}_0 e^{iwt} \tag{3.3}$$

being $\vec{E}_0$ a vector with the maximum amplitude and direction of $\vec{E}$, w the frequency of the AC generator and t the time.

It is sufficiently well-known that an electric field of oscillating nature produces a perpendicular oscillating magnetic field. This circumstance is determined by one of Maxwell's equations which establishes that the rate of change of the electric flux through a given area, if there are no currents crossing the area, is equal to the integral of the magnetic field ($\vec{B}$) around the boundary of that area multiplied by the square of the speed of light (c).

Regarding Figure 17, the oscillating field represented by equation (3.3) will create an electric field flux through the loop Γ_1. This flux will consequently generate a magnetic field $\vec{B}$ on the loop Γ_1, which according to Maxwell's equation is determined by:

$$c^2 \oint_{\Gamma_1} \vec{B} \cdot d\vec{s} = \frac{d}{dt} \iint_{\Gamma_1} \vec{E} \cdot \vec{n}\, da \tag{3.4}$$

Taking into account $\vec{B}$ and $\vec{E}$ are perpendicular and considering Γ1 a circle of radius r the equation (3.4) can be simplified into:

$$2\pi r c^2 B = \frac{d}{dt} E \pi r^2 \tag{3.5}$$

The derivative of E with time expressed in equation (3.5) is equal to $iwE_0 e^{iwt}$, thus:

$$B = \frac{iwr}{2c^2} E_0 e^{iwt} \tag{3.6}$$

It must be noted that the magnetic field is oscillating and increases proportionally to the radius and to the frequency of oscillation.

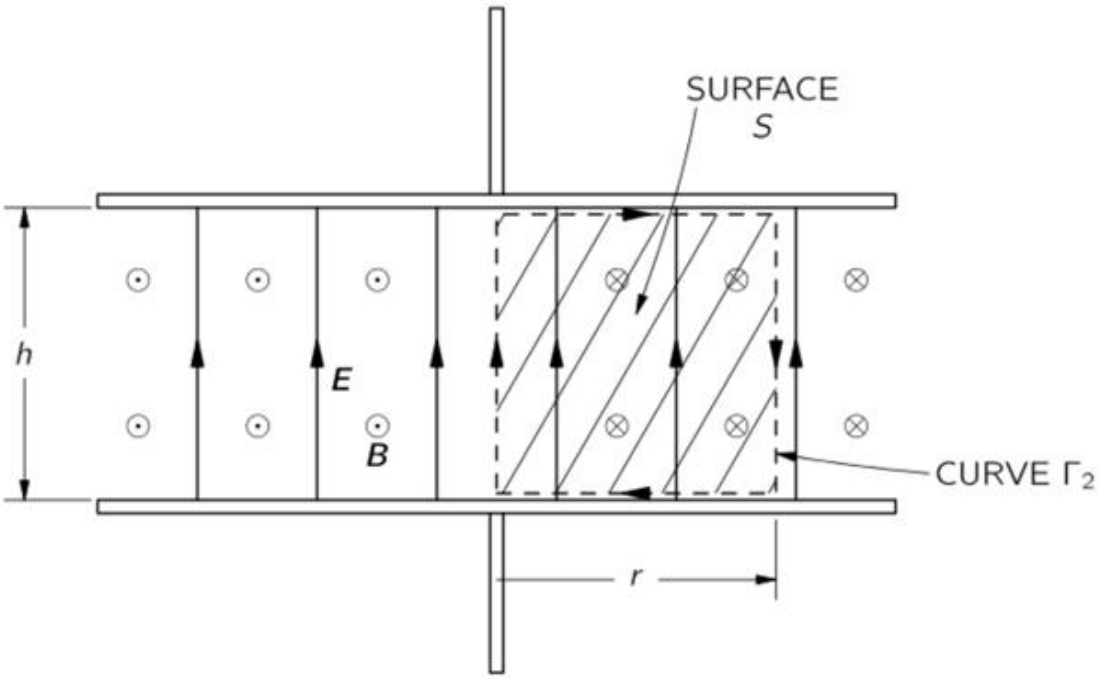

Figure 18. Side view of the ideal capacitor [57].

Figure 18 shows the side view of the capacitor, considering the fields $\vec{B}$ and $\vec{E}$ that have been described. As considered in equation (3.6), the higher the oscillation frequency, the stronger the oscillating magnetic field will be. An oscillating magnetic field causes the appearance of an oscillating electric field in the perpendicular direction of the magnetic field. This effect cannot be neglected at a high oscillation frequency because the magnetic field becomes too strong and the electric field is significantly modified from the one considered in

equation (3.3). The resulting modified electric field $\vec{E}$ can be expressed as a function of the previously considered field $\vec{E_1} = \vec{E_0}e^{iwt}$ and a correction field $\vec{E}_2$:

$$\vec{E} = \vec{E}_1 + \vec{E_2} \tag{3.7}$$

The maximal amplitude of the field $\vec{E}$ in the axis of the capacitor (r =0) will be considered E_0, which implies no correction is considered at the axis of the capacitor. This is $\vec{E}_2$=0 at r =0.

According to Faraday's law the rate of change of the flux of the magnetic field ($\vec{B}$) through an area is equal to the integral of the electric field it creates $\vec{E}_2$ in the boundary of that area. Considering the area delimited by Γ_2 in Figure 18 this is written as:

$$\oint_{\Gamma_2} \vec{E_2} \cdot d\vec{s} = -\frac{d}{dt}\iint_{\Gamma_2} \vec{B} \cdot \vec{n}\, da \tag{3.8}$$

Being the produced electric field $\vec{E_2}$ perpendicular to $\vec{B}$ and one of the sides of Γ_2 in the axis of the plates (r =0) the first part of the equation can be simplified as:

$$\oint_{\Gamma_2} \vec{E_2} \cdot d\vec{s} = -E_2(r)h \tag{3.9}$$

where h is the space between plates. On the other hand

$$\iint_{\Gamma_2} \vec{B} \cdot \vec{n}\, da = h\int B(r)dr \tag{3.10}$$

Thus:

$$-E_2(r)h = -\frac{d}{dt}\, h\int B(r)d\boldsymbol{r} \tag{3.11}$$

Using equation (3.6) for $B(r)$:

$$E_2(r) = \frac{d}{dt}\frac{iwr^2}{4c^2}E_0e^{iwt} = -\frac{w^2r^2}{4c^2}E_0e^{iwt} \tag{3.12}$$

The resulting field will be:

$$\vec{E} = \vec{E}_1 + \vec{E}_2 = \left(1 - \frac{1}{4}\frac{w^2 r^2}{c^2}\right)\vec{E}_0 e^{iwt} \tag{3.13}$$

The corrected field is represented in Figure 19.

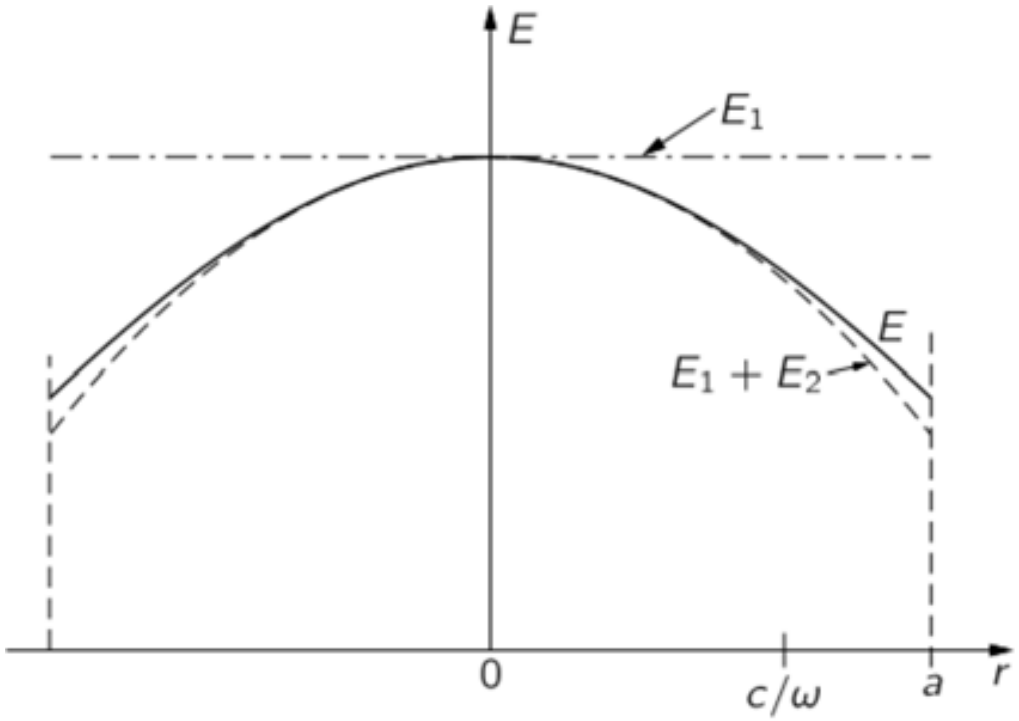

Figure 19. Field amplitude as a function of the radius of an ideal capacitor [57].

It may be observed that the correction makes the field decrease when it approaches the edge of the plate. Note that this correction process is on-going as the new electric field component $\vec{E}_2$ will generate a new magnetic field correction component $\vec{B}_2$, and this one a new electric field correction component and so on.

If the process was continued [52] it would be concluded that the resulting electric field is given by the series:

$$\vec{E} = \vec{E}_0 e^{iwt}\left[1 - \frac{1}{(1!)^2}\left(\frac{wr}{2c}\right)^2 + \frac{1}{(2!)^2}\left(\frac{wr}{2c}\right)^4 - \frac{1}{(3!)^2}\left(\frac{wr}{2c}\right)^6 + \cdots\right] \tag{3.14}$$

which is the product of $\vec{E}_0 e^{iwt}$ by the function of Bessel:

$$J_0(x) = 1 - \frac{1}{(1!)^2}\left(\frac{x}{2}\right)^2 + \frac{1}{(2!)^2}\left(\frac{x}{2}\right)^4 - \frac{1}{(3!)^2}\left(\frac{x}{2}\right)^6 + \cdots \tag{3.15}$$

Thus the electric field can be expressed by the following equation:

$$\vec{E} = \vec{E}_0 e^{iwt} J_0\left(\frac{wr}{c}\right) \tag{3.16}$$

Figure 20 represents the values of the Bessel function:

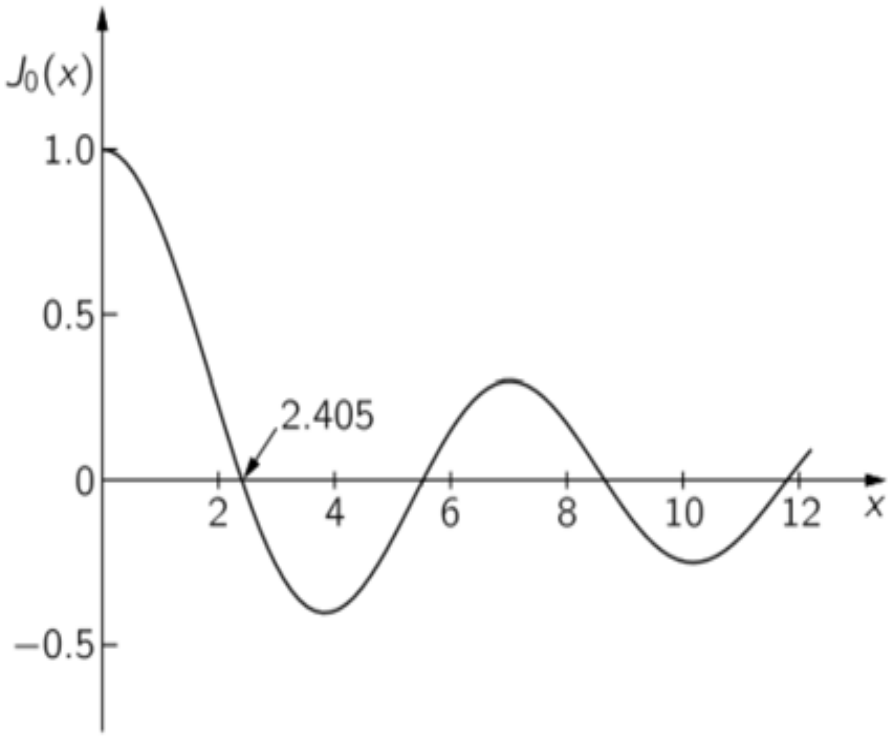

Figure 20. Bessel function [57].

Note that the first zero of the Bessel function comes for $x = 2.405$. This means that $\vec{E} = 0$ when $\frac{wr}{c} = 2.405$. Thus, for a given frequency w_0, at a radius $r_0 = \frac{2.405c}{w_0}$ there will not exist electrical field.

Establishing a conducting cylindrical wall of radius r_0 concentrically to the plates and between them the result would be a cylindrical cavity with oscillating electric and magnetic fields inside and no current on its cylindrical walls ($E(r_0) = 0$). Note that if the plates finished in the cylindrical wall there would be no propagation of the fields inside the cavity to the outside world. This kind of cavity is called a pill-box cavity and it is represented in Figure 21.

In the ideal pill-box cavity model electric fields will be oscillating back and forth at the frequency w_0 that has determined the diameter of the cavity. Note that, as long as there is a charge flow between the plates, the fields will maintain themselves without the help of the

external AC generator that was considered at the beginning of this description: the changing electric field $\vec{E}$ will induce a changing magnetic field $\vec{B}$, and the changing magnetic field $\vec{B}$ will induce the changing electric field $\vec{E}$. This is the resonance phenomenon inside a cavity.

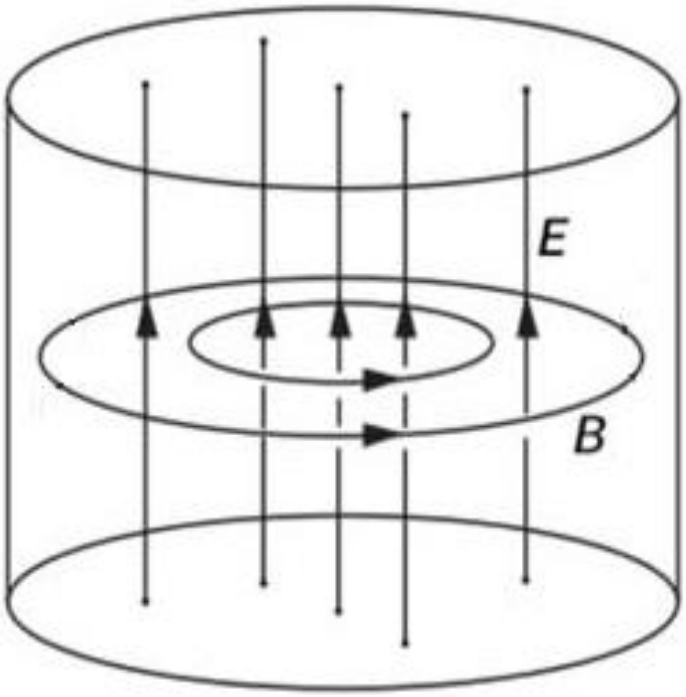

Figure 21. Pill-box cavity model [57].

However the charge flow between the upper and lower plates is needed for the electric field to oscillate. If the AC generator is removed, “parasite currents” will appear along the inner surface of the cylindrical wall of the cavity allowing for charges to flow between the plates and keep the resonance between the fields. However, these currents will also gradually mitigate the resonance phenomenon due to the energy losses in the cavity walls caused by the oscillating currents.

Hence, an external power source is needed to compensate for energy losses. This power can be provided by an antenna introduced in the inside of the cavity inducing RF power. If the field induced by the antenna is at the wrong frequency the electric and magnetic fields will not resonate and will fade away. For this reason the frequency of the field induced by the

antenna has to be coupled to that of the resonance of the cavity. This driving antenna that allows for on-going resonance is called “power coupler”. A receiving antenna can also be used to measure the evolution of the electric field inside the cavity.

Higher order modes (Resonant Modes)

In this reasoning it has been stated that for a determined radius of a pill-box cavity there exists a resonance frequency at which electric and magnetic fields will resonate. However, regarding again the Bessel function drawn in Figure 20 it can be noted that there are several zeros of the function after the first one. Recalling equation (3.16), it is clear that at a given radius r_0, the electric field will satisfy that $\vec{E}(r_0) = 0$ for several values of the resonance frequency w. This means that a determined pill-box cavity will have several resonance frequencies or “resonant modes”.

For a cavity of a certain radius as the one shown in Figure 22, resonances will occur for values of the frequencies corresponding to the zeros of function J_0, in which the electric field ($\vec{E}$) changes its sign in the radial direction. Thus, the second resonance mode is found for the frequency $w = 5{,}52c/r$. However, there exists plenty of intermediate resonant modes that have not been considered. Indeed, up to now only the only oscillations considered have been in the plane (O, $\overrightarrow{\boldsymbol{u_r}}$, $\overrightarrow{\boldsymbol{u_z}}$) considering a revolution symmetry around the z axis. Nevertheless, fields can arrange themselves in different periodic structures in the azimuth direction (as a function of θ) and in the longitudinal direction (as a function of z). This is demonstrated when solving the wave’s equations, resulting from the combination of Maxwell's four equations [35], for oscillating fields at a pulsation w (in e^{iwt}):

$$\Delta\vec{E} + \left(\frac{w}{c}\right)^2 \vec{E} = 0 \; ; \; \Delta\vec{B} + \left(\frac{w}{c}\right)^2 \vec{B} = 0 \qquad (3.17)$$

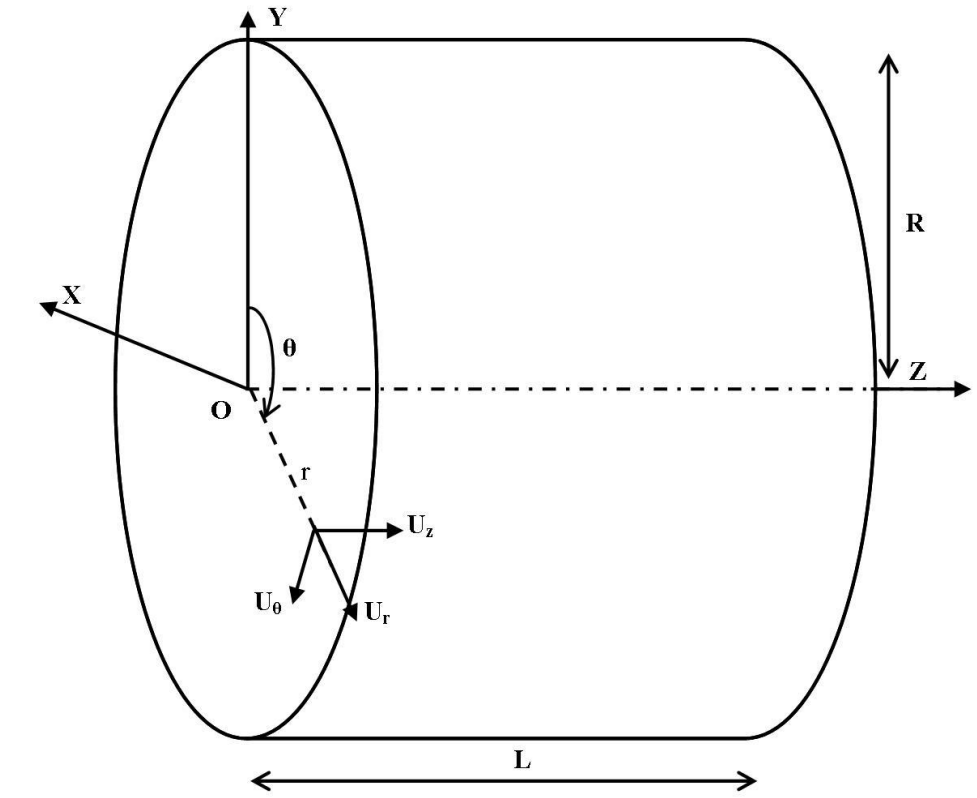

Figure 22. Coordinates in the pill-box cavity model [17]

Applying these equations to every component of the fields in cylindrical coordinates ($\overrightarrow{\boldsymbol{u_z}}, \overrightarrow{\boldsymbol{u_r}}, \overrightarrow{\boldsymbol{u_\theta}}$), and stating the conditions in the limits of the metallic walls of the cavity ($\vec{n}.\vec{E} = 0$ and $\vec{n}\ x\ \vec{B} = 0$, with $\vec{n}$ being the vector normal to the cavity walls), all possibilities in which an electromagnetic wave can establish in the cavity can be deduced [58]. These waves correspond to two families:

i) The electric transversal waves (TE), for which the electric field is null in the longitudinal direction ($E_z = 0$).

ii) The magnetic transversal waves (TM), for which the magnetic field is null in the longitudinal direction ($B_z = 0$).

For a determined type of wave, the equation's system is verified by particular frequencies f_{mnp} corresponding to a mode TE_{mnp} or TM_{mnp}. The indexes m, n and p describe the periodicity of the fields in the three directions of the cylindrical system of coordinates:

- m, indicates the exact number of oscillation periods of the field in the azimuthal direction (between $\theta = 0$ and $\theta = 2\pi$).
- n, indicates the exact number of times the field is null in the radial direction (between $r = 0$ and $r = R$).
- p, indicates the exact number of semi periods of field in the longitudinal direction (between $z = 0$ and $z = L$).

As considered, each resonant mode corresponds to a different geometrical distribution of the electric and magnetic fields inside the cavity. The main resonant mode, TM_{010}, is determined by the first zero of the Bessel function (J_0) and is the mode typically used for particle acceleration, for the adequateness of the distribution of its fields. The electric and magnetic fields for TM_{010} are the ones that were represented in Figure 21.

Beam acceleration considerations

Up to now, the resonance phenomenon in a pill-box cavity has been presented. It has been stated that the diameter of the cavity depends on the resonant frequency of the cavity and on the resonant mode chosen for the cavity. For TM_{010} the radius of the cavity will be determined according to the following equation (3.18):

$$r = \frac{2.405c}{w} \tag{3.18}$$

This information is sufficient to create the resonance phenomenon in a cavity. However, new constraints appear when the particle accelerating purposes are considered.

The proper functioning of accelerating cavities requires that charged particles cross the cavity when the field favors their acceleration. The pill-box cavity is an ideal model on which the functioning of accelerating cavities is based. In practice the cavity is opened for the beam to enter and exit. This is done by means of tubes that can simultaneously be used to place the RF antennas in the cavity. These tubes will act thus as waveguides. Figure 23 shows a schema of an accelerating cavity with its beam tubes and its antennas. The bigger antenna (Q_i) induces

the RF field into the cavity, the smaller (Q_t) allows measuring the resulting electric field inside the cavity. In the figure the accelerating field is also represented by the colored arrows. The proton beam will cross the cavity through the z axis represented, in the same direction as the electric field.

Obviously the electromagnetic field should not propagate through the beam tubes. It can be determined that only electromagnetic fields corresponding to a limited range of frequencies can propagate through tubes. Furthermore, the cutoff frequency, which is the lowest frequency at which the wave will still propagate, is inversely proportional to the radius of the tube [59]. It is, therefore, necessary to assure that the radius of the beam tubes is sufficiently small to avoid the propagation of the electromagnetic field out of the cavity.

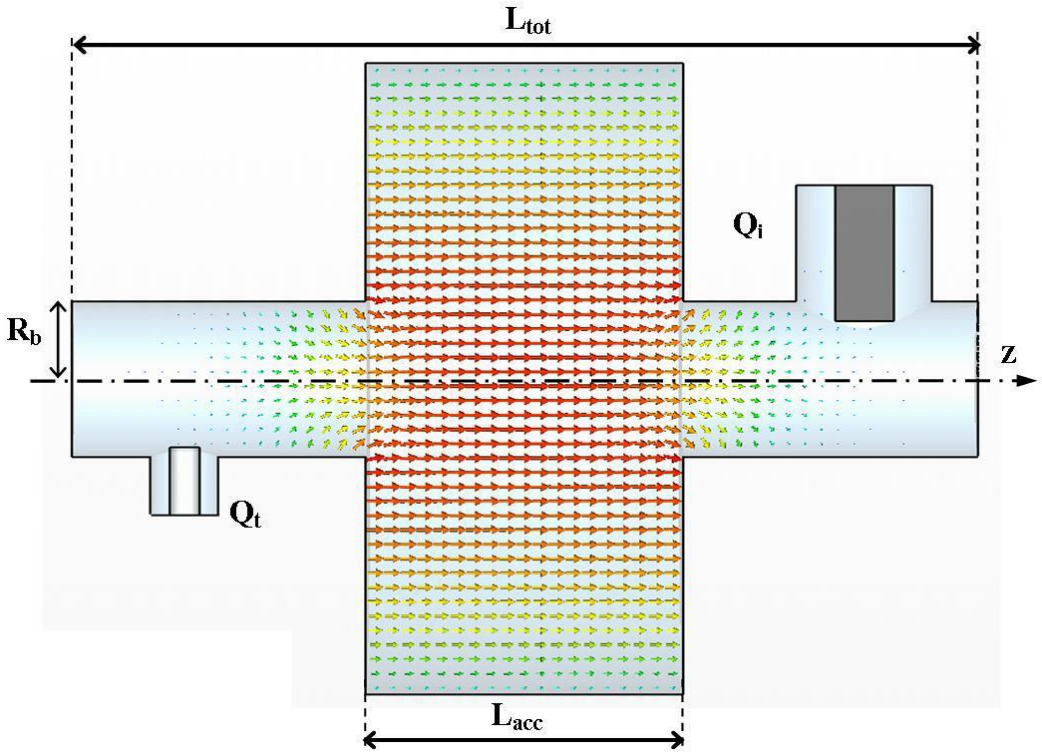

Figure 23. Static field distribution in the cavity [17]

The cutoff frequency f_c can be expressed [17] by:

$$f_c = \frac{1{,}841c}{2\pi R_b} \tag{3.19}$$

where R_b is the radius of the beam tubes. In a proper design, the resonance frequency of the cavity shall be lower than that of cutoff frequencies of the tubes.

3.3 MAIN PARAMETERS OF ACCELERATING CAVITIES

Synchronism Conditions

The acceleration induced in the beam by the oscillating fields depends on the synchronism between the passing of particles through the cavity and the oscillations of the electric field. In the beam, particles are grouped in periodical "packages". Logically, these proton packages must cross the cavity while the field is favoring the acceleration. This gets more complex when considering multiple cell cavities such as the one shown in Figure 24.

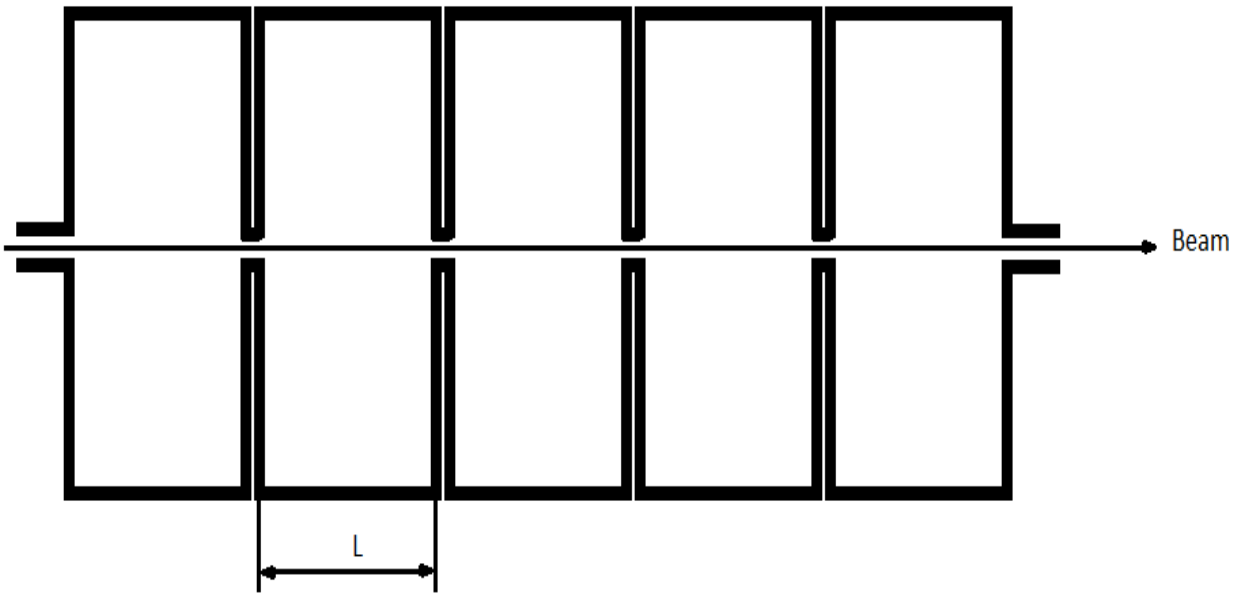

Figure 24. Multiple cell pill-box cavity [35]

Due to the periodical nature of the fields it is convenient that the accelerating length L is a fraction of the wavelength of the accelerating field. Thus several operation modes are can be envisaged:

i. Mode 2π: the length of the cells is equal to the wavelength of the field $L = \lambda$.

ii. Mode π: the length of the cells is equal to half the wavelength of the field $L = \frac{\lambda}{2}$.

iii. Mode 2π/N: the length of the cells is equal to the N[th] part of wavelength of the field $L = \lambda/N$.

A simple way of assuring synchronization between the proton bunches and the accelerating fields is to have a TM_{010} electric field with a phase velocity equal to the speed of the beam, operating in <<mode π>>, and the periodicity of the bunches being equal to the fields wavelength λ. Note the synchronization would still be assured if the period of the bunches was equal to N times λ, being N an integer.

Figure 25 shows the distribution of the electric fields inside the cavity for the <<mode π>>.The resonant cavity represented in the figure is composed of several cells. For a determined time moment t, the electric field's E_z direction will be opposite in adjacent cells. For correct synchronization the phase velocity and the beam velocity shall be equal, this is:

$$v_{beam} = \ v_{phase} = \frac{\lambda}{T} = \beta c$$

$$v_{beam} = \beta c \tag{3.20}$$

$$v_{phase} = \frac{\lambda}{T}$$

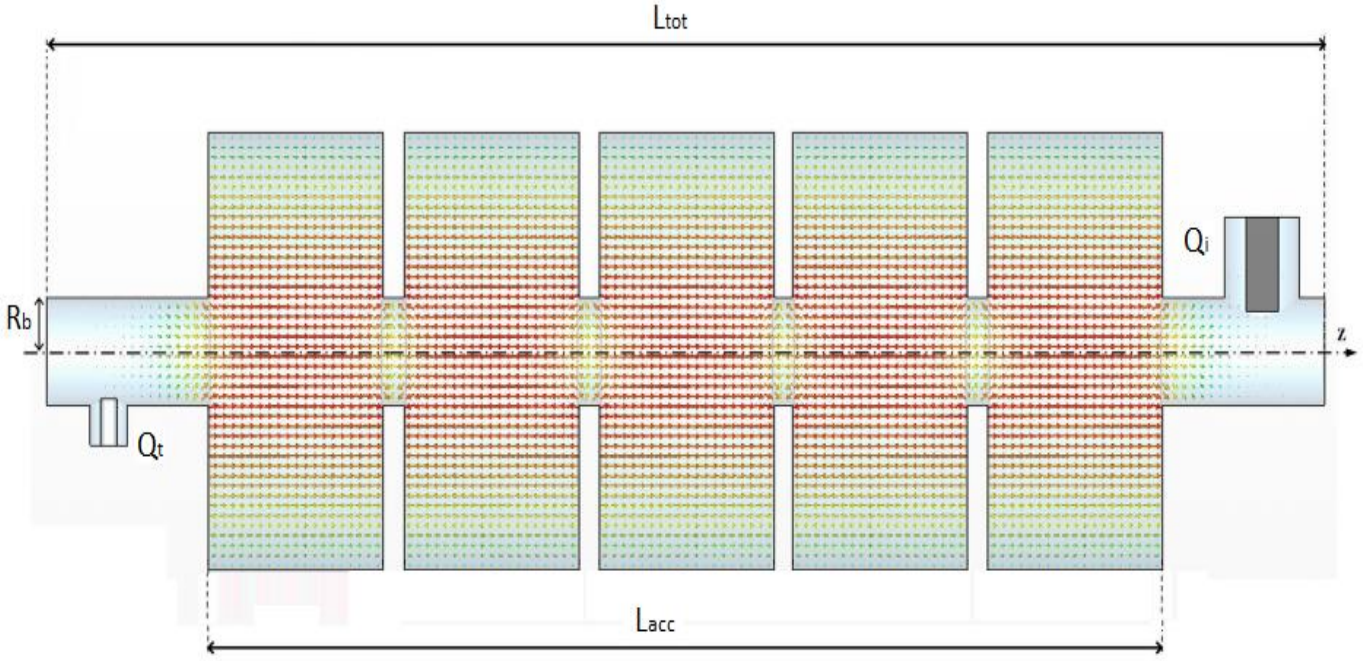

Figure 25. Field distribution in a multiple cell pill-box working in TM_{010} mode [17]

Recalling that for <<mode π>> acceleration the length of the cavity is $L = \lambda/2$, it can be derived that the time it takes for a particle to cross a cell is:

$$t_{cell} = \frac{\lambda}{2\beta c} = \frac{\pi}{w_0} \tag{3.21}$$

Note that a particle arriving at the first cell will at time t_0 will see an accelerating field E_z and when it arrives at the second cell at time $t_0 + \frac{\pi}{w_0}$ it will find the same accelerating field E_z, although in this second cell the field was decelerating at time t_0.

Regarding the previous considerations it is clear that the length of a cell working in <<mode π>> will depend on the speed of the particle it intends to accelerate. Thus:

$$L_{cell} = \frac{\beta c}{2f_0} \tag{3.22}$$

This last equation (3.22) is called the synchronism condition.

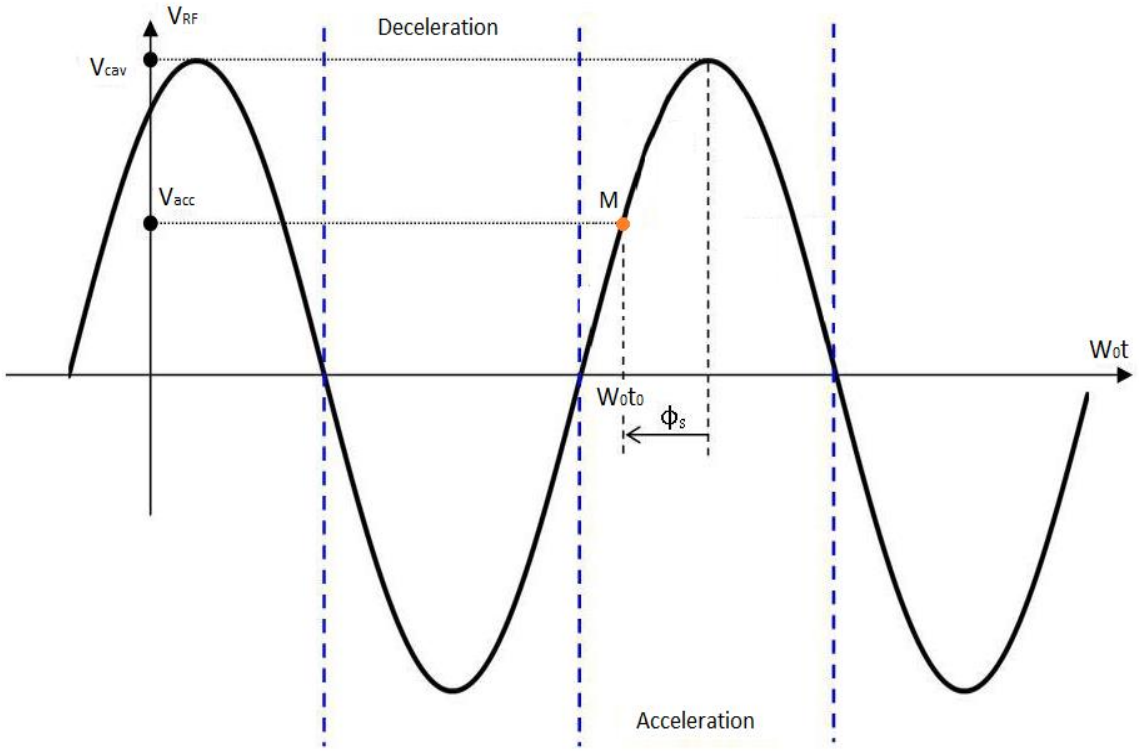

Figure 26. Synchronous particle entering the cavity at a synchronous phase with respect to the accelerating field

Another important aspect for synchronism purposes is the moment at which the particle will enter the cavity. By convention a reference particle representative of the charge of a proton package and entering the cavity at an average moment is considered for the definition of the synchronous phase. The reference particle is called the synchronous particle. The synchronous phase is the phase shift between the electromagnetic wave at its highest value and at the moment the particle enters the cavity. Figure 26 represents the evolution of the accelerating tension with time and illustrates the synchronous phase of a particle M entering the cavity at time $w_0 t_0$.

Considering the synchronous phase (ϕ_s), and the tension induced in the cavity (V_{cav}), the accelerating tension applied to the particle entering the cavity can be expressed by:

$$V_{acc} = V_{cav} \cos(\phi_s) \tag{3.23}$$

Taking into account the charge of the particles q, the instantaneous energy gain delivered by the cavity is:

$$\Delta W = qV_{acc} = qV_{cav}\cos(\phi_s) \tag{3.24}$$

Accelerating field and synchronous phase

The electric field profile inside the cavity along the z axis when the particle enters the cavity is represented by $E_z(z, r = 0)$. $E_z(z, r = 0)$ will be stronger at the middle of the cavity and will weaken as it approaches the beam tubes. However, for the energy gain calculation it cannot be consider that E_z is independent of time, as the field intensity is bound to change during the transit time of the particle through the cavity. The average accelerating field that will accelerate the particle while crossing the cavity can be expressed as:

$$E_{acc} = \frac{1}{L_{acc}}\left|\int_{t_0}^{t_1} \boldsymbol{E_z}(z, r = 0)e^{iw_0 t}\, dt\right| \tag{3.25}$$

where L_{acc} is the accelerating length, t_0 is the time at which the proton enters the cavity, t_1 the time when it quits the cavity and $e^{iw_0 t}$ the factor of decay of $\boldsymbol{E_z}(z, r = 0)$ due to the transit time. Note the resulting E_{acc} is expressed as the module of a complex number. Hence it represents the maximum average acceleration achievable, rather than the one really seen by the particle.

Considering the velocity of the beam can be expressed by β, where $\beta = \frac{v}{c}$, being v the speed of the beam and c the speed of light, equation (3.17) can be rewritten on the following way:

$$E_{acc} = \frac{1}{L_{acc}}\left|\int_{0}^{L_{tot}} E_z(z, r = 0)e^{\frac{iw_0 z}{\beta c}}\, dz\right| \tag{3.26}$$

Note that by convention E_{acc} is normalized by L_{acc}, although L_{tot} is considered for its calculation. It must also be noted that the real accelerating field affecting the synchronous particle depends on the synchronous phase, thus:

$$E_{acc}^{real} = E_{acc}\cos(\phi_s) \tag{3.27}$$

Transit time Factor

The "transit time factor" (TTF) is the relation between the total amount of accelerating field affecting particles at a determined speed β and the maximum amount of accelerating field available in the cavity. This is:

$$TTF = \left| \frac{\int_0^{L_{tot}} E_z(z, r=0) e^{\frac{i w_0 z}{\beta c}} dz}{\int_0^{L_{tot}} |E_z(z, r=0)| dz} \right| \leq 1 \tag{3.28}$$

Regarding (3.26) and (3.28) and considering $E_z(z, r=0) = E_0$ constant and $L = L_{acc} = L_{Tot}$, which means dismissing the drift tube effects on the field, the average accelerating field can be expressed as:

$$E_{acc}(\beta) = E_0 \frac{\sin\left(\frac{w_0 L}{2\beta c}\right)}{\frac{w_0 L}{2\beta c}} = E_0 \cdot TTF(\beta) \tag{3.29}$$

$E_{acc}(\beta)$ is the maximum average acceleration achievable for a cavity working at a frequency w_0, an accelerating length L and a beam traveling at a speed β. For a given particle speed β the transit time factor is indicative of the quality of the acceleration.

Geometrical β and optimal β

The transit time factor, $T(\beta)$, can be defined for a determined β. For each type of cavity there exists an optimal value of the speed, β_{opt}, for which the transit time factor is highest. The optimal value of β depends on the electric field in the axis of the cavity, on the cavity's frequency and on its length.

However, as already considered the value of β is related to the length of a cell of the cavity by the synchronism condition of equation (3.22). The value that can be derived for a

determined cell length from the synchronism condition is usually called the geometrical β, β_g, and calculated according to the following equation:

$$\beta_g = \frac{2f_0 L_{cell}}{c} \tag{3.30}$$

For a pill-box cavity without beam tubes the geometrical β and the optimal β are coincident. However for cavities with more complex geometries this two values can be significantly different.

Quality factor

The quality factor is the parameter of a cavity that defines the relation between the RF power inside the cavity and the power dissipated in the cavity for a determined operational frequency. This is expressed in the following equation:

$$Q_0 = w_0 \frac{W}{P_{cav}} \tag{3.31}$$

where w_0 is the operational frequency, W is the RF power in the cavity and P_{cav} is the power dissipated in the cavity.

The ways in which power might be dissipated in a cavity are losses in the dielectric volume inside the cavity and losses caused by the Joule effect in the cavity walls. Considering there is vacuum inside the cavity, losses in the dielectric volume can be neglected and the only source of losses becomes currents in the internal surface of the cavity, S, induced by the magnetic field H. Thus, the losses will be proportional to the surface resistance R_S:

$$P_{cav} = \frac{1}{2}\int_S R_S |H|^2 dS \tag{3.32}$$

Similarly the RF power inside the volume V of the cavity can be expressed by the following equation:

$$W = \frac{1}{2}\epsilon_0 \int_V |E|^2 dV \tag{3.33}$$

where E is the electric field inside the cavity and ϵ_0 is the vacuum permittivity. This is the same as:

$$W = \frac{1}{2}\mu_0 \int_V |H|^2 \, dV \tag{3.34}$$

being μ_0 the magnetic permeability of vacuum.

If the surface resistance of the cavity is considered homogeneous then the quality factor can be expressed as:

$$Q_0 = w_0 \frac{\mu_0 \int_V |H|^2 \, dV}{R_S \int_S |H|^2 \, dS} \tag{3.35}$$

and the geometrical factor of the cavity, G, which is measured in Ohms can be defined as:

$$G = \; R_S Q_0 = w_0 \mu_0 \frac{\int_V |H|^2 \, dV}{\int_S |H|^2 \, dS} \tag{3.36}$$

Shunt Impedance

Similarly to an electrical circuit, the dissipated power (P_{cav}) in the cavity walls is produced by an impedance summited to the cavity's tension (V_{cav}). This impedance is called shunt impedance (r_{shunt}) and is calculated by:

$$r_{shunt} = \frac{{V_{cav}}^2}{2P_{cav}} = \frac{(E_{acc}L_{acc})^2}{2P_{cav}} \tag{3.37}$$

This impedance, also expressed in Ohms, will have higher values when the RF losses are lower. As in the case of the quality factor, r_{shunt} is indicative of the cavity losses. The shunt impedance and the quality factor are commonly related in literature by the expression $\left(\frac{r}{Q}\right)$:

$$\left(\frac{r}{Q}\right) = \frac{(E_{acc}L_{acc})^2}{2w_0 W} \tag{3.38}$$

Thus, for a determined value of power in the cavity, the higher the value of $\left(\frac{r}{Q}\right)$ the higher the accelerating field obtained inside the cavity. This relation allows to compare cavities with different shapes.

3.4 SUPERCONDUCTING CAVITIES

Superconducting advantages

The main advantage of the resonance phenomenon is that, ideally, an RF field can be kept enclosed and oscillating inside a cavity with a very low energy input. However, as already commented, currents appear on the walls of the cavity and dissipate energy by the Joule effect. This constant losses decrease the energy stored in the electromagnetic field inside the cavity, which eventually fades away. For this reason a continuous energy input is needed to maintain the field inside the cavity.

As the resonating electromagnetic fields become stronger in cavities with hi-energy accelerating purposes, the power dissipated increases steeply and the energy input to compensate for this loses becomes too costly. Furthermore, the amount of dissipated energy could eventually damage the cavity walls. However, there exists the possibility of reducing significantly the value of the surface resistance of a cavity (R_S), which, as explained in the previous section, determines the losses of a cavity (P_{cav}), by transforming the material of the cavity walls into a superconductor. However in order to do this cavities have to be submitted to extremely low temperatures. Thus superconducting cavities at cryogenic conditions can be used to minimize the Joule effect of parasite currents in hi-energy sections of an accelerator.

Superconductivity is a phenomenon of extremely low electrical resistance and expulsion of magnetic flux fields occurring in certain materials, called superconductors, when cooled below a characteristic critical temperature. It was discovered by Dutch physicist Heike Kamerlingh Onnes on April 8, 1911, in Leiden. [17] gives a detailed overview on the superconductivity phenomenon.

Cavities made of superconductors cooled below their critical temperature can maintain resonating electromagnetic fields with minimal energy input even in presence of hi-energy fields. However, fields cannot be higher than a certain value. As a matter of fact, the

existence of the superconducting state depends not only on temperature but also on the magnetic field on the surface and the induced current running through it. Both the magnetic field and the density of current, as in the case of temperature, have to be kept bellow a determined critical value for the superconducting state to exist. The critical temperature, critical magnetic field and critical current density are parameters that depend on the superconductor material.

As cavities conceived for hi-energy acceleration purposes will bear strong magnetic fields, when planning to use a superconducting material to build a cavity, it has to be chosen regarding that it has a high critical magnetic field ($\mu_0 H_{C1}$). It is also beneficial that the chosen material has the highest possible critical temperature (T_C) to avoid excessive energy consumption in the cooling of the cavity and minimize problems associated to cryogenic technologies. Another desirable property would be that the material has the lowest residual resistance (R_S) in the superconducting state. Finally, other mechanical aspects are to be considered such as machinability, resistance rigidity, etc.

Considering these criteria the most suitable material is Niobium, mainly for its high critical magnetic field, as described in [17]. Niobium has been used for the development of superconducting cavities for several decades and is envisaged as one of the reference solutions for building cavities for hi-energy accelerators. Table 3 allows to compare the most important properties for the construction of SC cavities of Niobium with those of some other well characterized materials for this purpose:

Material	$\mu_0 H_{C1}(mT)$	T_C (K)	R_S $(n\Omega)$
Nb	170	9,2	~30
Nb_3Sn	50	18	~0,4
MgB_2	30	40	$\sim 2{,}4 \cdot 10^{-5}$
NbN	20	16,2	~5
NbTi	10	9,5	~/
YBaCuO	10	93,4	~0,4

Table 3. Properties of superconducting materials [17].

The most outstanding property of pure Niobium is its high critical magnetic field. This makes this material ideal for the construction of SC cavities intended to bear strong electromagnetic fields.

The acceleration process efficiency is a key parameter to understand the benefits of using SC cavities. The efficiency (η_{cav}) of a cavity can be calculated as:

$$\eta_{cav} = \frac{P_b}{P_b + P_{cav}} \tag{3.39}$$

where P_b is the power transmitted to the beam and P_{cav} is the power dissipated in the cavity walls. The low energy losses in superconducting cavity walls can yield an efficiency of nearly 100 %, which means that, during the cavity's operation, all the energy introduced in the cavity is transferred to the beam and no energy is lost in the cavity walls. In contrast, the efficiency of a room temperature cooper cavity drops to a value between 15 and 25%.

However, the overall acceleration process efficiency in a cavity not only depends on the cavities efficiency, but also on the efficiency of the cryogenic system and the power sources. A study of the acceleration process efficiency considering a normal conducting and a SC cupper cavity is presented in [60]. The equation used to calculate the acceleration process efficiency in the cavity is:

$$\eta = \eta_{RF} \frac{P_b}{P_b + \frac{P_{cav} + P_{cryostat}}{\eta_{cryo}}} \tag{3.40}$$

being the efficiency of the power sources η_{RF}, the efficiency of the cryogenic system η_{cryo} and the power losses in the cryostat used to cool down the cavity $P_{cryostat}$ (a thorough description of the cryostat can be found in the next subsections of this report). The efficiency of the cryogenic system can be calculated according to equation:

$$\eta_{cryo} = \eta_{carnot} . \eta_{plant} \tag{3.41}$$

being η_{carnot} the efficiency of the Carnot cycle for cooling and η_{plant} the efficiency of the cryogenic plant. Considering that for the Carnot cycle the hot reservoir is 300 K and the cold reservoir (the cavity) is working at 2 K:

$$\eta_{carnot} = \frac{2}{300 - 2} = 0{,}00671 \tag{3.42}$$

For a reasonable value of the cryogenic plants efficiency like 25%, the efficiency of the cryogenic system is $\eta_{cryo} = 0{,}16\%$. Additionally, experimental results allow to consider the efficiency of the power sources, η_{RF}, around 60% and the power losses in the cryostat, $P_{cryostat}$, approximately 10 W.

	Normal conducting cavity (300K)	SC cavity (2K)
Surface Resistance (R_S)	6mΩ	30nΩ
Quality Factor $(Q_0 = G/R_S)$	2.10^4	$3{,}5.10^9$
Shunt Impedance of a cavity $(r_{shunt} = \left(\frac{r}{Q}\right).Q_0)$	$4{,}4.10^6$Ω	$7{,}7.10^{11}$Ω
Accelerating Field (E_{acc})	5 MV/m	5 MV/m
Dissipated power $(P_{cav} = (E_{acc}L)^2/2r_{shunt})$	291kW	1,662W
Power delivered to the beam $(P_{beam} = E_{acc}.L.I_{beam})$	16 KW	16 KW
Cryogenic system efficiency (η_{cryo})	--	$0{,}16\%$
Power losses in cryostat $(P_{cryostat})$	0 W	10 W
Efficiency $(\eta = \eta_{RF}\frac{P_b}{P_b + \frac{P_{cav}+P_{cryostat}}{\eta_{cryo}}})$	3%	41%

Table 4. Comparison between Cu cavity in normal conducting and SC states [35].

Thus, for a cupper cavity with $\left(\frac{r}{Q}\right) = 220\ \Omega$, $G = 110\ \ \Omega$ and $L_{acc} = 0{,}32$ m, accelerating a proton beam of 10 mA at β=0,37 with a field of E_{acc} =5 MV/m, calculations presented in Table 4, on the basis of the surface resistance, R_S, of the cavity in normal conducting and SC states, allow to evaluate the overall efficiency of the cavity in these states.

In this example it has been determined that the cupper cavity increases its efficiency from 3% up to 41% in SC state. In general for medium and high beam power the SC state can significantly enhance the efficiency of the acceleration process. This difference is crucial when considering facilities like MYRRHA that are bound to work during tens of years.

Multipacting

Multipacting [35] is an undesirable phenomenon found in cavities operating with hi-energy fields. This phenomenon takes place when an electron is dragged from the cavity walls or the free space by the electric fields inside the cavity and then hits another point in the cavity, causing new electrons to abandon the cavity surface and starting a chain reaction. It is particularly critical in the case of superconducting cavities, as it is capable of absorbing a high quantity of RF power, hampering the capability to increase the field and limiting the performance of the cavity. This phenomenon is called a cavity "quench".

In some resonance conditions multipacting causes a large flux of electrons, steeply increasing power consumption and heat generated in the cavity walls. The development of multipacting has a very close relation with the cavity's shape. As a matter of fact, this phenomenon is favored [61] in surfaces with no magnetic field gradient and when two surfaces are separated by a very short distance. Both situations occur in the pill-box cavity model where the magnetic field is the same in the cylindrical wall and where separation between walls is small in the corners.

In order to minimize the risk of multipacting a simple solution [62] is rounding the cavity walls as shown in Figure 27. This way the resulting profile turns out to be spherical/elliptical. Note that the electric field in the cavity which is represented in the figure by the field lines remains similar to that of the pill-box model shown in Figure 21. Also, this geometry suppresses corners and the magnetic field's gradient remains non-null throughout

all the shape when the magnetic field inside the cavity is not null. Other geometries have been adopted under these same premises giving shape to families of cavities whose performance varies depending on the speed of the particles they are intended to accelerate. The next Section of this report starts with an overview of the main families of cavities and their purposes in a linac.

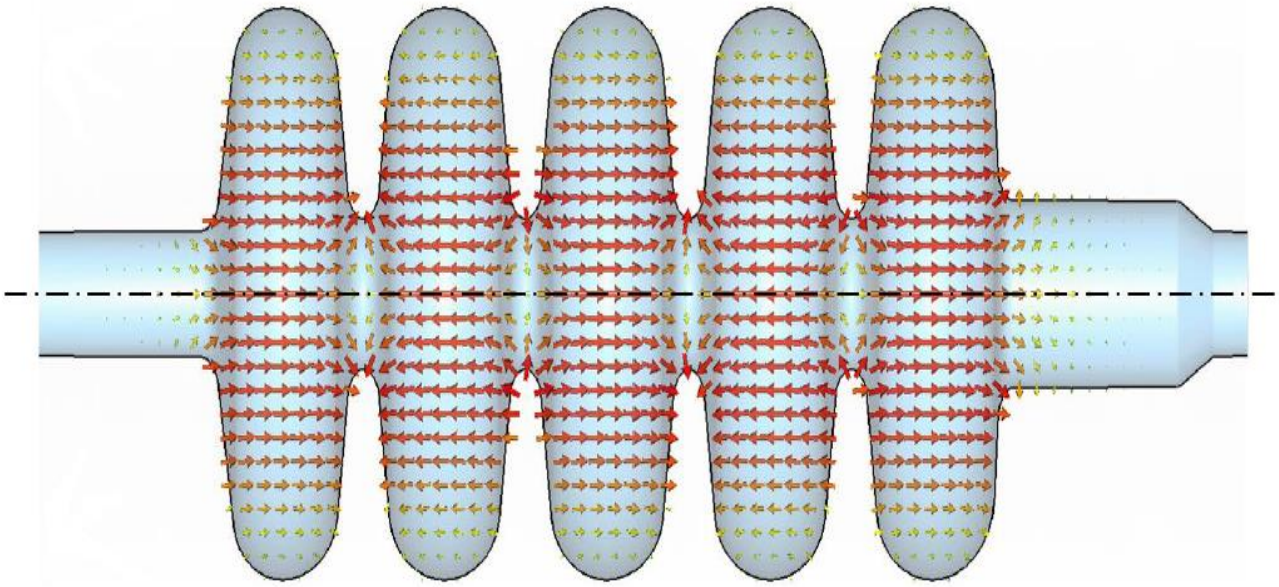

Figure 27. Elliptical cavity profile [17].

3.5 MAIN RESONANT STRUCTURES AND CRYOMODULES FOR THE MYRRHA LINAC SUPERCONDUCTING SECTION

Main families of cavities

As in the case of the pill-box cavity, the operational frequency of a cavity is closely linked to its resonance volume. However, the choice of this frequency depends on the speed of the particles that the cavity is intended to accelerate. Indeed, recalling equation (3.2), for a kinetic energy gain, dW, the duration of the path of the particle in the cavity, dt, can be defined as:

$$dt = \frac{dW}{qE(w_0 t)\beta c} \tag{3.43}$$

As a consequence, for a determined field E, in order for the particle to gain dW kinetic energy, it will have to travel through the cavity an amount of time dt that will be larger if the speed of the particle is lower. Logically, for particles with smaller speed it will also be necessary that the frequency of the electric field E is also slower.

Otherwise said, lower frequencies are more suitable for lower speeds at the beginning of the acceleration line and vice versa. This also affects the design of the cavity. Four main families of cavities are commonly used for proton beam acceleration with β <0.1: quarter-wave, half-wave, spoke and elliptical cavities. These families of cavities are depicted in Figure 28 along with their particle speed range and described in the following.

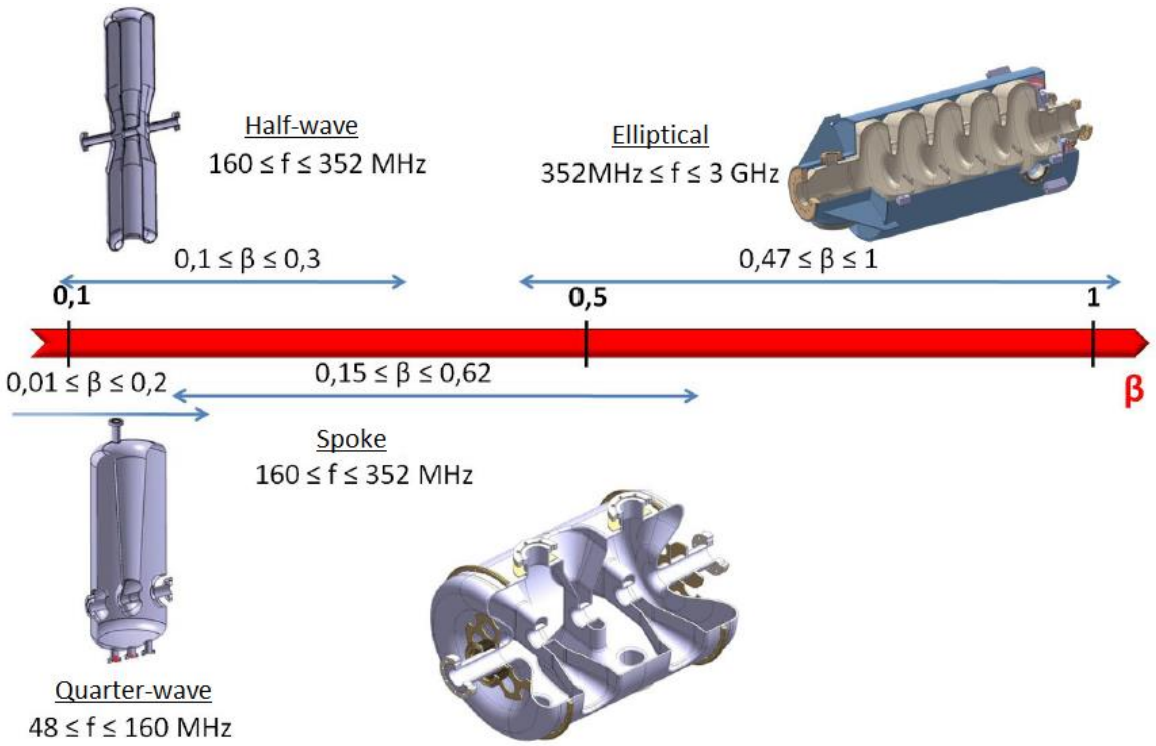

Figure 28. Elliptical cavity profile [17].

- For β~0.15 it is preferable to use quarter-wave cavities, which are compact, modular and built with well-known and economical methods. This kind of cavities allow to obtain high accelerating gradients at low β [63].

- The advantage of half-wave cavities is that they reduce the electric field in the cavity surface. Nevertheless, these cavities are complicated to manufacture and their resonance frequency is difficult to adjust due to rigid mechanical structure. Therefore these cavities are scarcely used.

- Spoke cavities have a multiple gap structure that allows to work at frequencies of up to 800 MHz and to accelerate particles over $\beta = 0.5$. This kind of cavity is more stable mechanically than elliptical cavities but its fabrication is complex and expensive.

- Finally for $\beta > 0.5$ the preference is to use elliptical cavities. This kind of cavity is the most effective for the acceleration of particles at high energy (β≈1). Nevertheless, they are more sensible to mechanical vibrations and this causes operational inefficiencies.

Normal conducting spoke and SC elliptical cavities have been used for the experimental phase described in Chapter X of this thesis. Consequently, the next subsections are dedicated to describe in detail these cavities and their operation, as well as the cryogenic system for the SC elliptical cavity.

Spoke Cavities

As commented in the previous subsection, due to the excellent performance of the elliptical cavity, it is unanimously recognized that this cavity is the best choice for high energy proton beam acceleration. However, the performance of this kind of cavity is limited by the speed of the beam being accelerated [58]. In fact, for β≈0.5, the accelerating length of the cavity, L_{acc}, becomes too small, according to eq. (3.22), and the cavity walls too vertical weakening the cavity structure. This type of cavities must be stiffened by increasing the thickness of walls or reinforcing them with additional systems conceived with this purpose.

However, for β smaller than 0.5, this type of cavity can simply not be used because of its structural instability under vacuum conditions. In this case, means to stiffen the cavity are either inefficient or too costly (i.e. increasing the thickness of Niobium). For this reason spoke

cavities were brought forth at the beginning of the nineties to work between 300 and 400 MHz. Their shape is depicted in Figure 29.

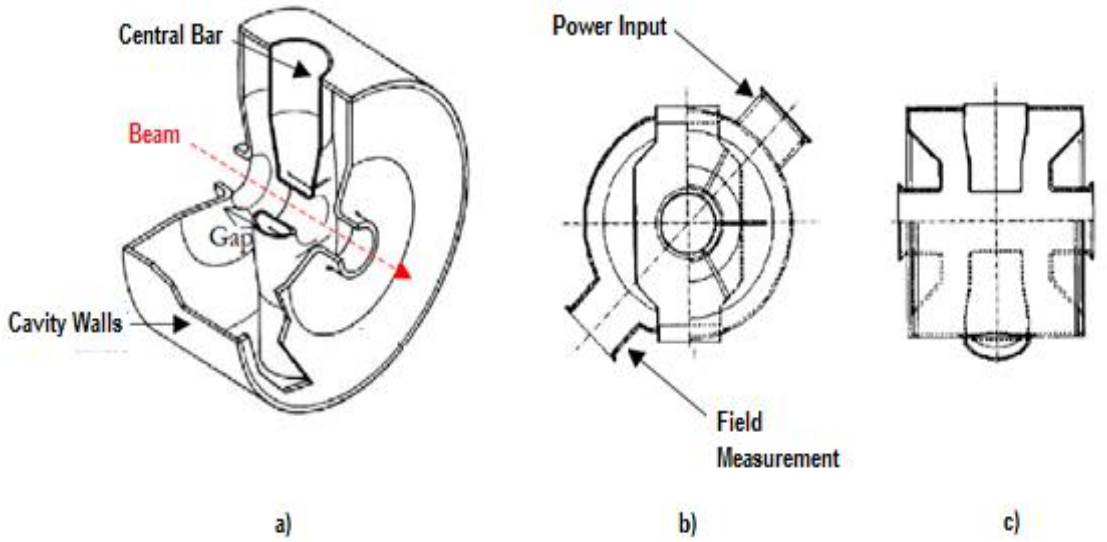

Figure 29. Scetch of a spoke cavity. Subfigure a) Scetch of the spoke cavity. Subfigure b) Front view of the spoke cavity. Subfigure c) Side view of the spoke cavity [64].

As shown in the figure a spoke cavity has a similar structure to that of a pill-box cavity but with a vertical bar on the center. Figure 30 illustrates the electric and magnetic field lines on a spoke cavity operating in TM_{010} mode.

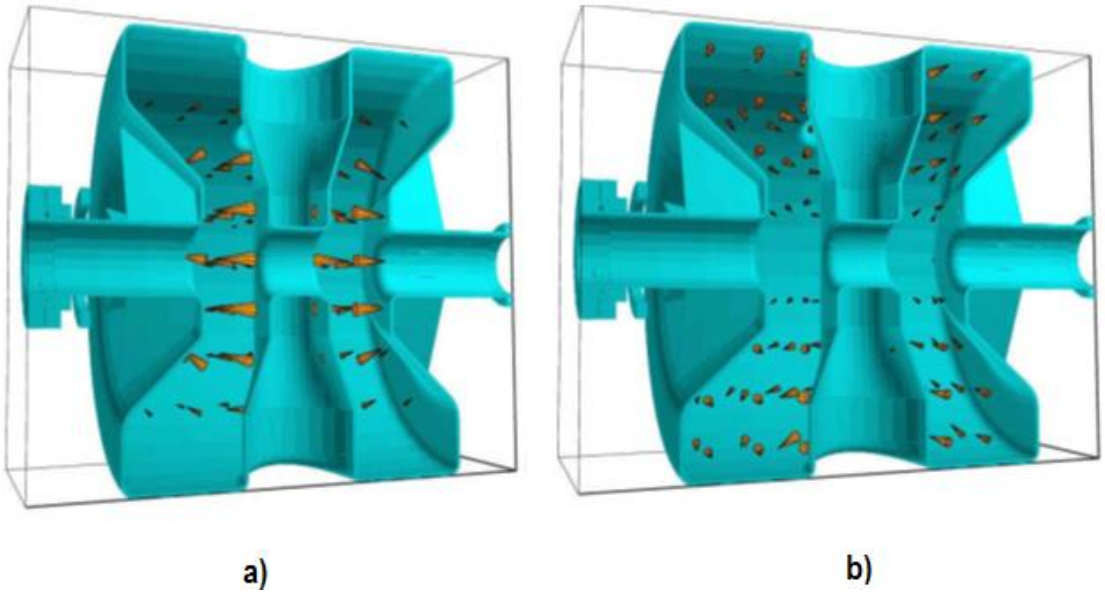

Figure 30. Electric and magnetic fields in a spoke cavity at TM_{010} mode. Subfigure a) electric field lines. Subfigure b) magnetic field lines [64].

Spoke cavities have been envisaged to work in the superconducting part of the MYRRHA linac. The basic operating features of a prototype of these cavities are presented in the following:

- Resonance frequency : 352.2 MHz
- Structure: 2 gaps.
- Optimal β= 0.35
- Eacc≈6.3 MeV; EaccMax≈8.18 MeV
- Quality factor Q_0=1.9·10^9 (2K)

The structural features of the cavity depend on the synchronism condition and on optimization considerations which will be briefly commented in the following. In this kind of cavities, due to the synchronism condition, the distance between the centers of the gaps will be equal to

$$d_{gaps} = \frac{\beta c}{2 f_0} \tag{3.44}$$

as depicted in the basic representation of a spoke cavity of Figure 31.

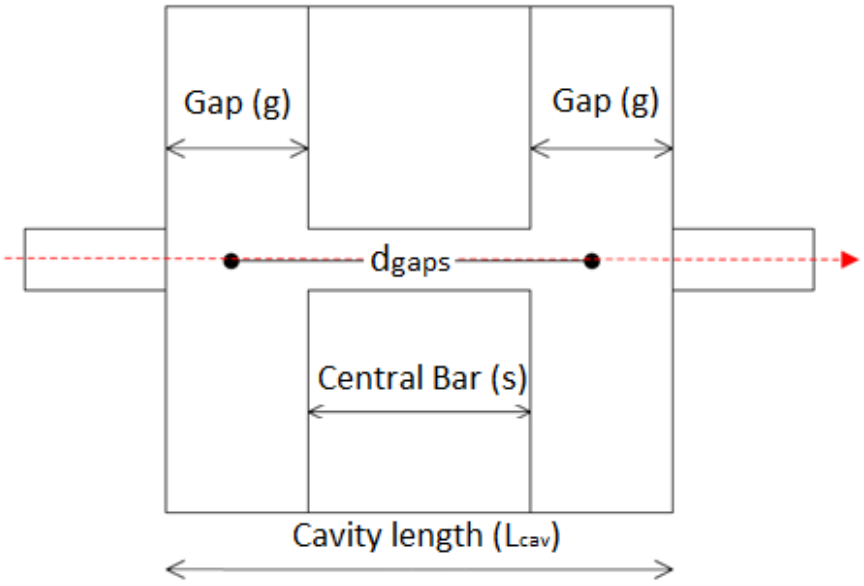

Figure 31. Basic representation of a spoke cavity [64].

Having established the value of d_{gaps}, it is still not possible to determine the length of the cavity (L_{cav}), without information about the relation between the size of the bar (s) and the size of the gaps (g), as function of the optimum β of the cavity. If the diameter of the central bar (s) is considered equal to twice the length of a gap then $\beta c/2f_0 = g + s = 3/4L_{cav}$. In this case the cavity length will be

$$L_{cav} = \frac{2\beta c}{3f_0} \tag{3.45}$$

Note that this length is not fixed and depends on the relation chosen during the design of the cavity between the gap length and the central bar diameter. For an optimal β = 0.35 and a resonance frequency of 352.2 MHz the cavity length will be L_{cav}=200 mm.

Further decisions concerning the optimization of the shape of the spoke cavity have been subject of numerous research efforts and discussions. Among the optimization criteria the peak field's values in the surface of the cavity are particularly important. While high electric fields cause electron emissions and parasite currents, high magnetic fields can surpass the critical magnetic field above which Niobium is not superconductive any more. Both effects cause a significant temperature and RF power consumption increment. However these are not the only optimization criteria considered, obtaining the maximum accelerating field and obtaining good structural resistance are also important.

Maintaining the cavity shape relatively simple is also important so that fabrication costs do not increase excessively. [64] presents an optimization analysis that yields an optimized structural configuration for the spoke cavity presented in Table 5 which can be better understood with the help of Figure 32.

Cavity Parameters	Dimensions (mm)
Cavity diameter	408
Top cavity length	354
Spoke base diameter	118
Spoke center thickness	67
Spoke center width	147
Gap-center to gap-center length	150
Iris-to-iris length	200
Tube length (from iris to flange)	150
Beam tube aperture	60

Table 5. Optimization features for a spoke cavity [58]

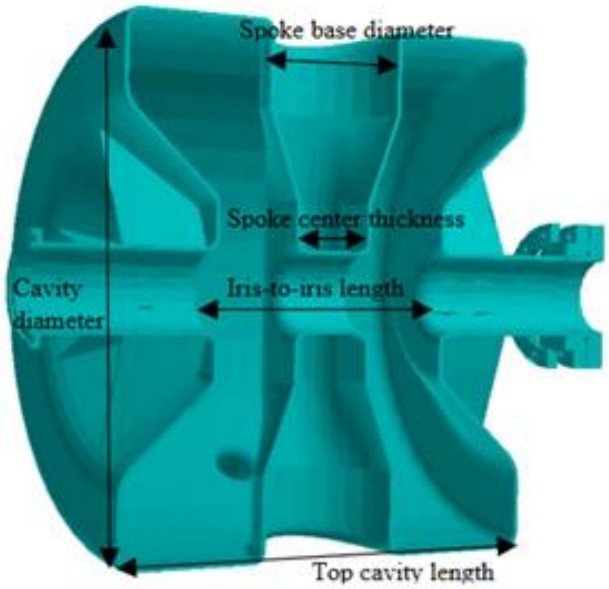

Figure 32. Cross-section of the spoke cavity [65].

Note that the cavity structure changes significantly from the one considered in the basic cavity scetch of Figure 36 due to optimization considerations. Nevertheless, the distance from iris-to-iris remains 200 mm as calculated for the “cavity length” of the basic cavity scetch and as reported in [59]. Figure 39 shows a MYRRHA accelerator single spoke currently in *Institut de Physique Nucleaire d’Orsay* in Paris.

Figure 33. Spoke cavity prototype [64].

Elliptical Cavities

Elliptical cavities are an "evolution" of the pill-box model to avoid the multipacting effect. These cavities are envisaged to operate on the superconducting hi-energy part of the linac. The analysis performed in [17] established the main features of an elliptical cavity prototype for the MYRRHA accelerator. These features are listed in the following:

- Resonance frequency : 704.4 MHz
- Structure: 5 cells.
- $\beta_g = 0.47$ and $\beta_{opt} = 0{,}51$
- Quality factor Q_0=5·10^9 (2K)

In the classical elliptical profile of superconducting cavities, cavity walls have to be inclined by an angle α [35], as shown in Figure 34.

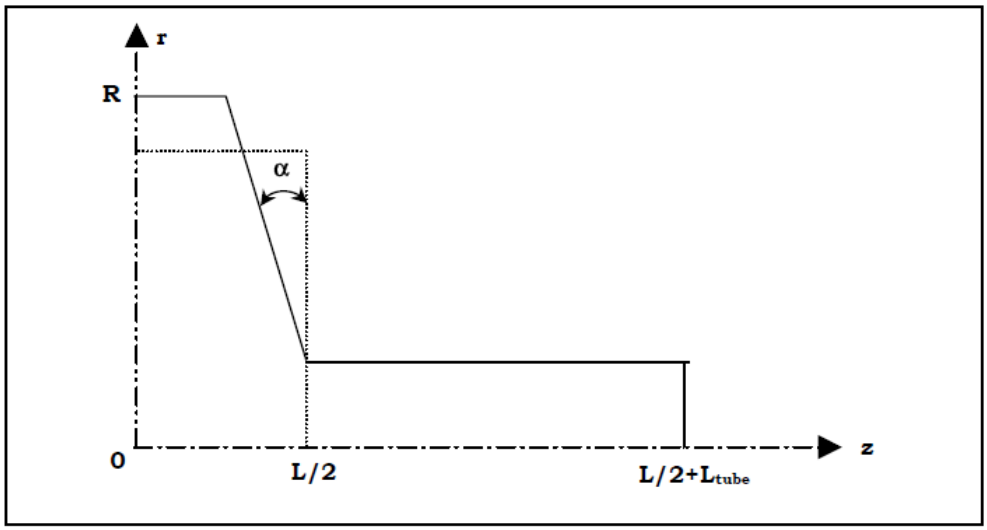

Figure 34. Inclination of the walls of an elliptical cavity [35].

However, a volume variation in the cavity ΔV causes a variation of resonance frequency Δf. This phenomenon is predicted by the following equation (3.46), known as the Slater's theorem [66]:

$$\frac{\partial f}{f} = \frac{1}{4W}\int_{\partial V}(\varepsilon_o E^2 - \mu_0 H^2)dV \qquad (3.46)$$

where f is the initial frequency, W the energy stored in the cavity, E the electric field, $\varepsilon_o$the permittivity of vacuum, H the magnetic field and μ_0 permeability of vacuum.

This theorem yields that:

- A volume increase in zones covered by electric field raises the cavity resonance frequency.
- A volume increase in zones covered by magnetic field reduces the cavity resonance frequency.

According to these statements wall inclination tends to increase the resonance frequency of the cavity, as the volume reduced by this inclination which was covered by magnetic field outweighs that which was covered by electric field. In order to maintain the cavity resonance frequency the radius may be increased, expanding the zones where the magnetic field is dominant.

Nevertheless, the value of α also plays an important role affects the mechanical behavior of a cavity. The following is considered in the cavity design:

- Bigger values for α yield resistant structures.
- The cavity resonance frequency is more sensitive to Lorentz forces in bigger α structures.

Other important structural parameters are show in Figure 35:

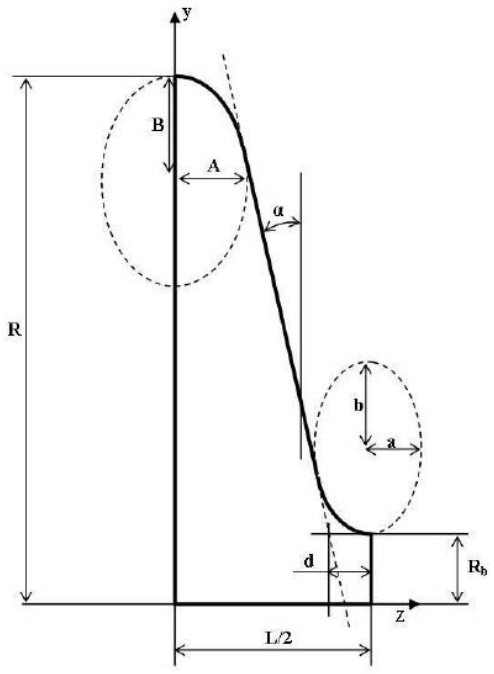

Figure 35: Other influential parameters in a cavity design [35].

In [17] a cavity optimization analysis regarding the appropriate choice of these values for each cell to fulfill a compromise between several performance criteria was presented. As in the case of spoke cavities, among these criteria the maximal values of peak fields in the surface of the cavity are particularly important as well as obtaining the maximum accelerating field. Figure 36 shows the MYRRHA accelerator 5-cell elliptical cavity prototype that was constructed according to this optimization analysis and that is being studied in *Institut de Physique Nucleaire d'Orsay* in Paris.

Figure 36. Prototype of the 5-cell Elliptical cavity developed by IPNO [17]

Cryomodule for the 5 cell elliptical cavity prototype

In this chapter the properties of superconductivity and the functioning and conception of an elliptical cavity have been explained. In the rest of it, the cryomodule developed by "Istituto Nazionale di Fisica Nucleare (INFN)" [17] for cooling down and keeping the elliptical cavity under 2 K will be described.

In order to cool down cavities to temperatures lower than 2 K the use of a cryomodule capable of hosting one or more cavities is necessary. The cryomodule developed by INFN is

composed of a cryostat, a Helium tank, and a valve box, this last one developed by IPNO, which manages the cryomodule's operation. These elements are described in the following.

- The Helium tank:

  The Helium tank is a metallic cylindrical container that surrounds the cavity. Two holes at the straight walls of the tank allow for enough space to fit the beam tubes of the cavity. To enclose the area between the Helium tank and the walls of the cavity two flanges welded to the beam tubes are also welded to the Helium tank. Additionally, the tank has input and output holes to allow, in case there are no leaks in the welding's or the cavity walls, a Helium flow between the cavity walls and the tank.

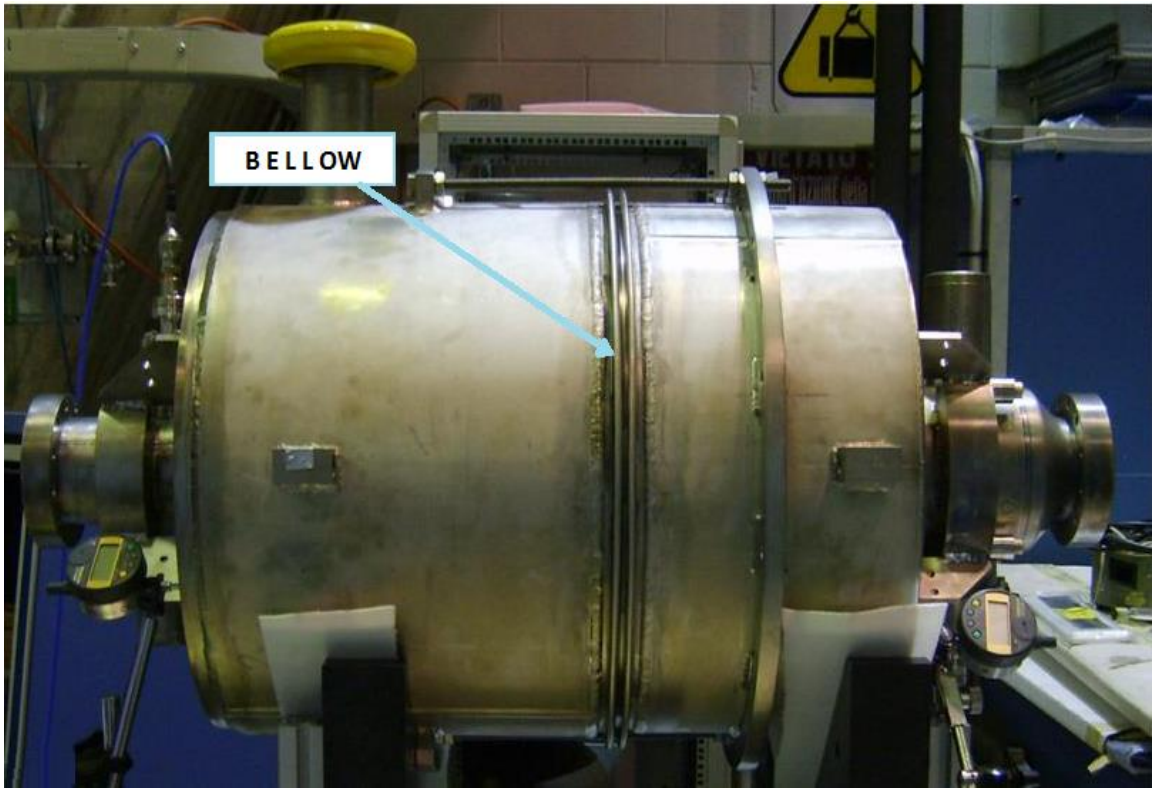

Figure 37. Prototype of the Helium tank developed by INFN [17]

Another important constructive aspect of the Helium tank is the bellow installed in the middle of the tank. This feature provides flexibility to the structure that can be shortened or stretched by applying external forces. Chapter 4 will explain that the flexibility granted by the bellow to the Helium tank is the basis of innovative cavity control systems. Figure 37 shows a picture of the Helium tank developed for the elliptical cavity and its bellow.

The Helium tank is made of titanium since this material has an expansion coefficient similar to that of the Niobium of the cavity and this is convenient to limit the thermal stresses when cooling down to 2 K.

Finally, it is important to note that inside the Helium tank and surrounding the cavity, a magnetic shield has been introduced. This shield allows to intercept the earth's magnetic field that can get trapped inside Niobium during the cool down, when it becomes superconducting. Without shielding, this magnetic field can deteriorate the conductivity of Niobium in its superconducting state. The magnetic shield is a cylinder surrounding the cavity composed of a thin layer (1mm) of Cryoperm® [67]. The magnetic shield is almost in contact with the Helium tank walls and never touches the cavity. Small holes in the magnetic shield allow for the Helium to flow, thus, the shielding remains "invisible" to the cavity and the Helium tank's operation.

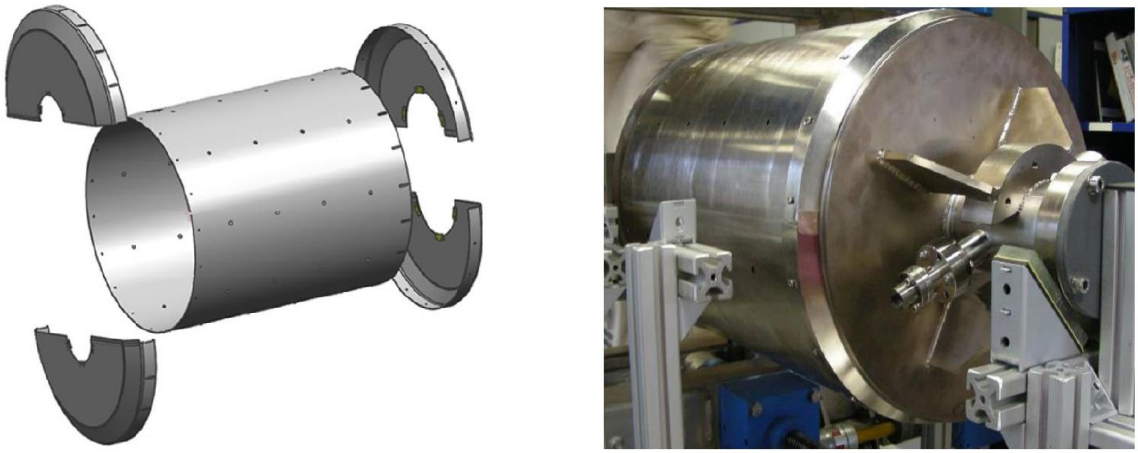

Figure 38. Magnetic shielding scetch and real picture [17]

- The Cryostat:

  The Helium tank remains inside the cryostat during operation. In other words, the cryostat acts as the envelope between the He tank and the rest of the world. Note that between the Helium tank and the external world there exists a temperature difference of approximately 300 K. To maintain the Helium tank in a controlled environment with manageable temperature fluctuations a thermal screen working at 80K has been placed inside the cryostat and surrounding the Helium tank. Thus, temperature in the Helium tank is controlled by the action of two different cooling circuits, a primary

circuit feeding the Helium tank with a flow of liquid Helium and a secondary circuit providing a flow of liquid nitrogen to the thermal screen. Hence, the thermal screen is intended to stabilize the conditions of operation of the Helium tank.

Figure 39. Cryostat Prototype [17]

The primary cooling circuit is composed of a first deposit that accumulates liquid Helium before feeding the Helium tank. Pumps are installed outside the cryostat to maintain a certain helium flow and a certain pressure inside the Helium tank. The secondary cooling circuit feeds a sole liquid nitrogen a deposit from which the thermal screen is cooled. Finally, it must be noted that a 10^{-6} bars vacuum is created inside the cryostat to avoid heat flows due to convection.

Figure 39 shows the cryostat while Figure 40 shows a scetch of this cryostat with transparent walls and bearing the helium tank inside.

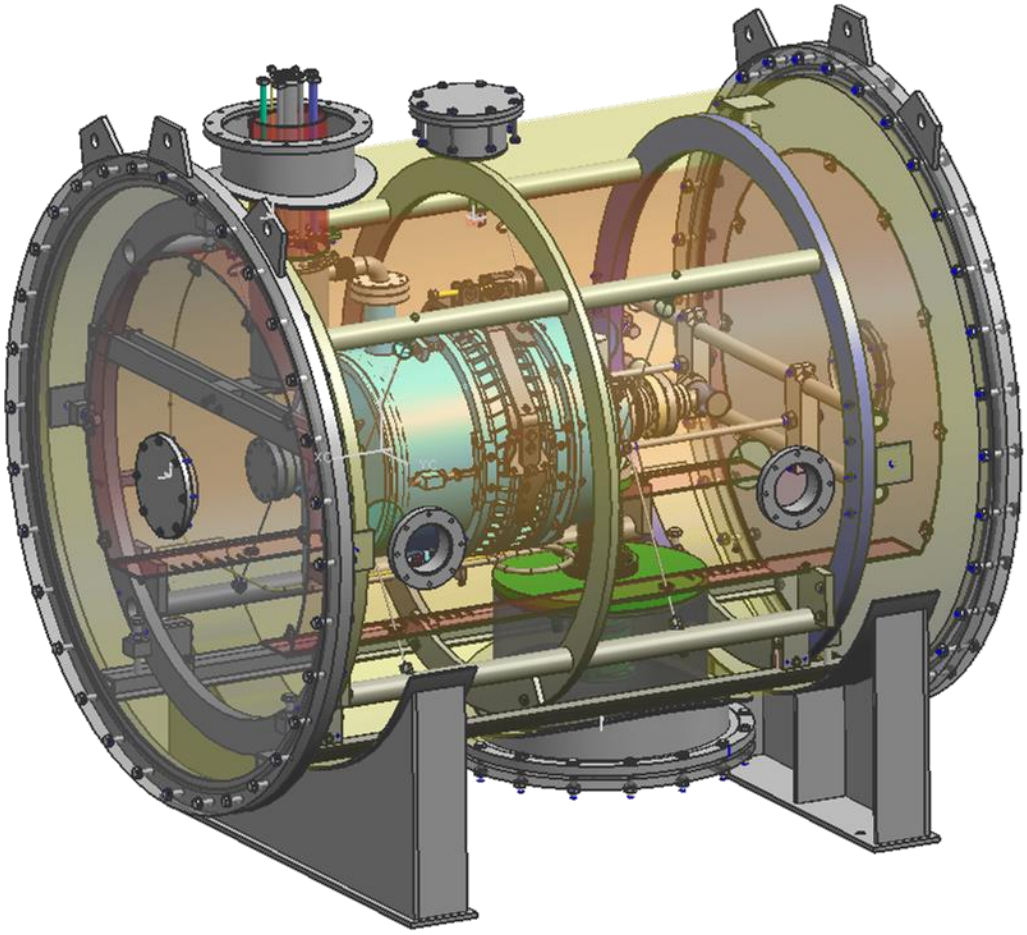

Figure 40. Transparent scetch of the prototype of the cryostat [17]

Note that in Figure 40 the transparent walls of the cryostat have been shaded in green. Inside them, the walls of the thermal screen are also transparent but have been shaded in orange. Finally, the Helium tank, painted in blue stands inside the thermal screen. At the upper left hand side of the figure there is a hole containing a series of tubes for the cryogenic feed of the primary and secondary circuits which are managed by the valve box.

- The valve box:

  As already commented, the valve box manages the flow of nitrogen and Helium into the cryostat. It is placed at the top of the cryostat, as shown in Figure 34, so that the flow of nitrogen and helium is favored by the effect of gravity.

In the accelerator, the valve box allows to isolate a single cryomodule form the rest of the refrigerating lines for operational or maintenance purposes and performs the temperature control of the elements inside the cryostat by managing the flows of the primary and secondary cooling circuits.

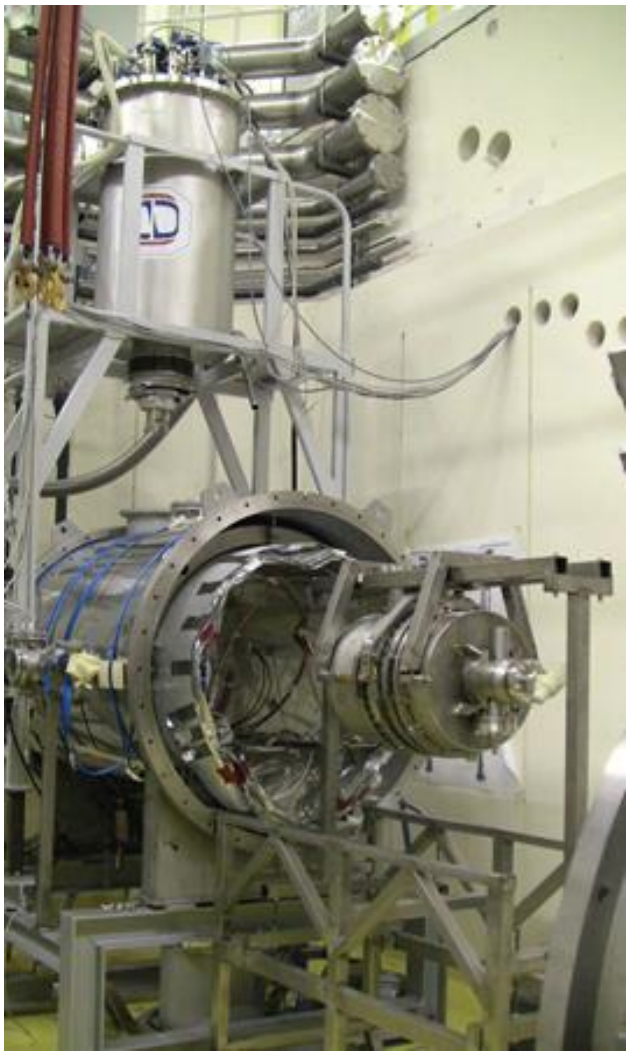

Figure 41. Valve box on top of the open cryostat at Institut de Physique Nucléaire d'Orsay

The primary circuit provides liquid helium to the helium tank, thus, it maintains the cavity temperature lower than 2 K (≈1,8K) while assuring a stable pressure of around 1 mbar inside the helium tank. Pressure control requires a regulation loop acting on the valves of the valve box driving the primary circuit for the compensation of perturbations affecting the helium tank pressure. During the accelerators operation these perturbations will be produced mostly from interactions between the valves of

the valve boxes of different cryomodules fed by the same refrigerating line. Additionally, the valve box also performs the pumping of the helium flow in order to assure the necessary depression to obtain superfluid helium under 2 K.

The secondary circuit provides a nitrogen flow at a temperature of 77 K and a pressure of 1 bar. This flow is intended to refrigerate the thermal screen up to 80K and set stable conditions for the operation of the helium tank. The thermal screen temperature could also be controlled with regulation valves in the valve box allowing to reduce considerably the helium consumption.

Both the normal conducting spoke and the superconducting 5 cell elliptical cavity have been already explained. The cryomodule, composed of a helium tank, a cryostat and a valve box, which allows for the elliptical cavity to become superconducting has also been described. Both structures will also be part of the MYRRHA linac and have played a fundamental role in the research works that will be presented in the following chapters of this thesis.

CHAPTER IV:

CAVITY CONTROL OVERVIEW: DYNAMIC ANALYSIS, CONTROL LOOPS, CHALLENGES AND SYSTEMS

In order to accelerate adequately the proton beam the amplitude and the phase of the field, measured by a receiving antenna inside each cavity, will have to be precisely controlled, in real time, within a narrow margin around their set points by varying the phase and the amplitude of the field emitted by the power coupler. The positions of the power coupler and the receiving antenna are represented in the schematic drawing of a 5 cell elliptical SC cavity shown in Figure 42. Note that the induced field inside the cavity, shaded in green on the figure, will not be the same as the field emitted by the power coupler. As a matter of fact, the amplitude and the phase of the field inside the cavity will differ from those of the field emitted by the power coupler due to: i) the resonance effect that takes place inside the cavity, and; ii) the effect of the beam crossing the cavity. Amplitude and phase setpoints for each cavity are calculated so that the electric field is synchronous with the beam and acceleration takes place gradually in each cavity to achieve the necessary beam energy at the end of the linac.

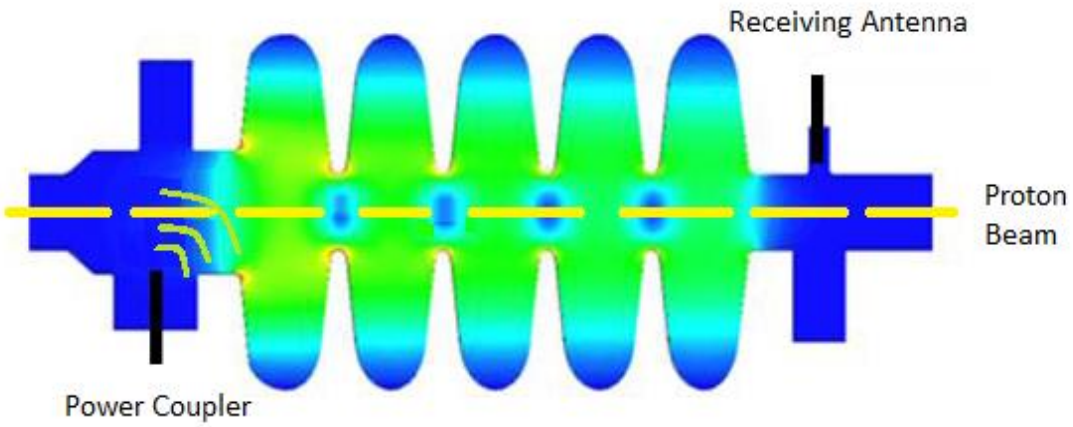

Figure 42. 5 Cell Elliptical Cavity Scheme

Nevertheless, an acceptable control of amplitude and phase by itself isn't enough to accelerate in the desired manner the proton beam. The electromagnetic resonance frequency of the cavity, which is a property closely related to its structure, will vary because of the effect of Lorentz forces, microphonic vibrations and other perturbations which may affect the cavity's structure. Thus deviations from the design resonance frequency will cause drifts of both the amplitude and the phase of the field inside the cavity. These drifts will have to be compensated by varying the field emitted by the power coupler in order to maintain the cavity's phase and amplitude on their targets or setpoints and this will increase the power consumed. Since power consumption should not exceed reasonable limits, it is necessary to compensate for resonance frequency drifts caused by perturbations.

In the following the behavior of the cavity is going to be described with the help of a model based on the analogy of a cavity and an electric circuit. This model will help to explain the phenomena that have been described in this introduction and their relation with external components and perturbations.

4.1 DYNAMIC MODEL OF A CAVITY AND ITS ENVIRONMENT

Analogy to RLC circuits

This section reviews a part of the works of [17] and [68] that describe the very interesting analogy between the operation of a cavity and a RCL circuit. These analyses are based on the fact that the cavity acts as a bandpass resonator, allowing for the resonance of

waves at a certain frequency. Similarly a RLC circuit, as the one shown in Figure 43, allows for the resonance of current at a determined frequency of the generator.

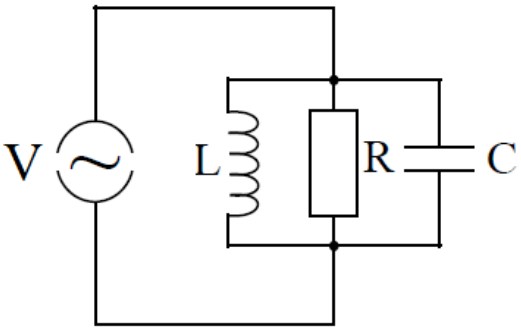

Figure 43. Electric model of a cavity

The resonance frequency of the RLC circuit of the figure is determined by the value of the inductance L and the capacitance C and given by

$$w_0 = \frac{1}{\sqrt{LC}} \tag{4.1}$$

while R determines the energy losses of the circuit. Considering that the resistance R represents the surface resistance of the cavity walls in which a part of the RF power, P_{cav}, is dissipated, then the voltage between the ends of the resistance can be considered V_{cav} and these magnitudes obey the following relation:

$$P_{cav} = \frac{{V_{cav}}^2}{2R} \tag{4.2}$$

In this cavity/ RLC circuit analogy, the energy stored in the cavity is equivalent to that stored in the condenser described by the following equation:

$$W = \frac{1}{2} C {V_{cav}}^2 = \frac{1}{2} \frac{{V_{cav}}^2}{{w_0}^2 L} \tag{4.3}$$

and, recalling equations (3.31), (4.2), (4.3), the quality factor can be expressed as

$$Q_0 = w_0 \frac{W}{P_{cav}} = \frac{R}{w_0 L} = w_0 RC \tag{4.4}$$

Of course when aiming to model the operation of a cavity, further considerations are necessary. In an operational cavity, a RF power source is connected through a transmission line to a power coupler. In the transmission line there will exist a circulator that deviates reflected waves to a load in order to prevent damage in the RF source. Finally, the beam crossing the cavity also needs to be considered in the model. Figure 44 presents a model that takes into account all these considerations.

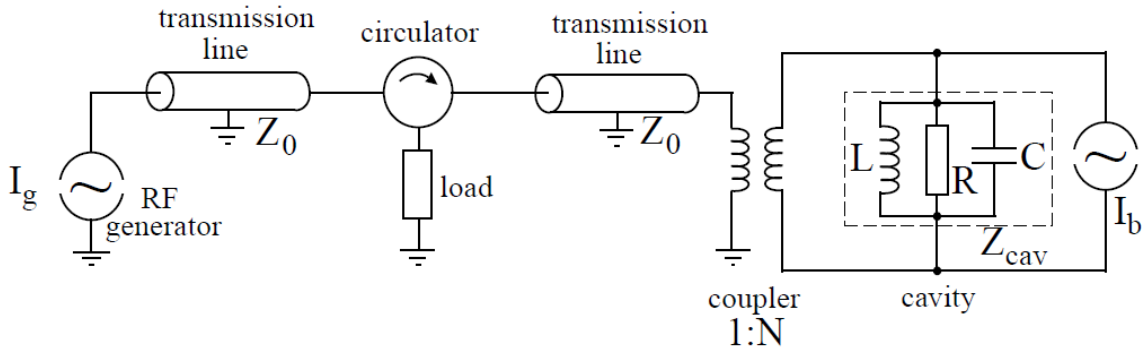

Figure 44. Full electric model of a cavity operation [68].

The full model of the cavity operation considers an RF source attached to a transmission line of impedance $2Z_0$. To simplify, the circulator and its load have been placed at the middle of the line. The power coupler at the end of the transmission line is represented in the model by an ideal transformer with a relation 1:N (meaning that there are N spirals at the side of the cavity for each spiral at the side of the generator). After the coupler, the cavity has been represented as in Figure 43 and the beam crossing it as a power source opposing the current generated in the transformer. With this model it can be considered that energy is not only dissipated in the cavity walls but also on the transmission line and in the load of the circulator. Thus, an external quality factor can be defined by the following equation:

$$Q_{\text{ext}} = w_0 \frac{W}{P_{ext}} \tag{4.5}$$

being P_{ext} the power dissipated in all external devices. The external power and the total power can be calculated through the following equations:

$$P_{ext} = \frac{{V_0}^2}{2Z_{ext}} \tag{4.6}$$

$$P_{tot} = \frac{{V_0}^2}{2R_L} \tag{4.7}$$

where V_0 is the tension of the RF generator, $Z_{ext}$the impedance of the external charge of the circuit (this is the impedance due to the transmission line, the coupler, the circulator and the load) and R_L the total load of the circuit ($\frac{1}{R_L} = \frac{1}{R} + \frac{1}{Z_{ext}}$).

The resulting loaded quality factor will then be:

$$Q_{\mathrm{L}} = w_0 \frac{W}{P_{cav} + P_{ext}} = w_0 \frac{W}{P_{tot}} \tag{4.8}$$

being P_{tot} the total power dissipated in the model.

The relation between Q_L, Q_{ext} and Q_0 and their associated powers can be deduced considering equations (4.4), (4.5) y (4.7):

$$Q_0 P_{cav} = Q_{\mathrm{ext}} P_{ext} = Q_{\mathrm{L}} P_{tot} \tag{4.9}$$

Up to now, the cavity/ RLC circuit analogy applied to the computation of the quality factor has been analyzed. In order to understand how this analogy is applied to the shunt impedance it can be derived from equations (4.1), (4.4) and (4.8) that:

$$\frac{R}{Q_0} = \sqrt{\frac{L}{\mathrm{C}}} \tag{4.10}$$

and

$$\frac{Z_{ext}}{Q_{\mathrm{ext}}} = \frac{R_L}{Q_{\mathrm{L}}} = \sqrt{\frac{L}{\mathrm{C}}} \left(\frac{{V_0}^2}{{V_{cav}}^2}\right) \tag{4.11}$$

Note that this $\frac{R}{Q_0}$ relation only depends on L and C. In other words, the relation is independent of the surface resistance and characteristic of the geometry of the cavity. It is therefore possible to link this relation, devised form an "electrical" analysis, with the relation $\left(\frac{r}{Q}\right)$ defined in the previous Chapter and derived from an "energetic" analysis. Actually, form equation (3.38) it can be derived that:

$$\left(\frac{r}{Q}\right) = \frac{{V_{cav}}^2}{2w_0 \frac{1}{2} C {V_{cav}}^2} = \frac{1}{w_0 C} \tag{4.12}$$

Considering equation (4.9) it can be deduced that:

$$\left(\frac{r}{Q}\right) = \frac{R}{Q_0} \tag{4.13}$$

These are the coupling relations for the cavity/RLC circuit analogy, and the links between the values that characterize a cavity, like Q_0 and (r/Q), and the parameters of the electric model R, L, and C. The next subsection will focus on the behavior of the current sources of the RLC model that represent the RF generator and the particle beam. Thus, the cavity/ RLC circuit analogy will allow to describe how a cavity can be considered a bandpass resonator and its consequences.

The RF source and the beam current generator

This subsection will focus on the modeling aspects of the RF generator and the particle beam. For the following dissertation two equivalent circuits to the one represented in Figure 44 are going to be used.

- The circuit of Figure 45 is equivalent to that of Figure 44 from the transmission line perspective. It considers the tension V'_{ind} induced by the generator, the reflected tension V'_{ref} and the equivalent elements to the circuit after the circulator (from the second half of the transmission line up to the power source that represents the beam current in Figure 44).

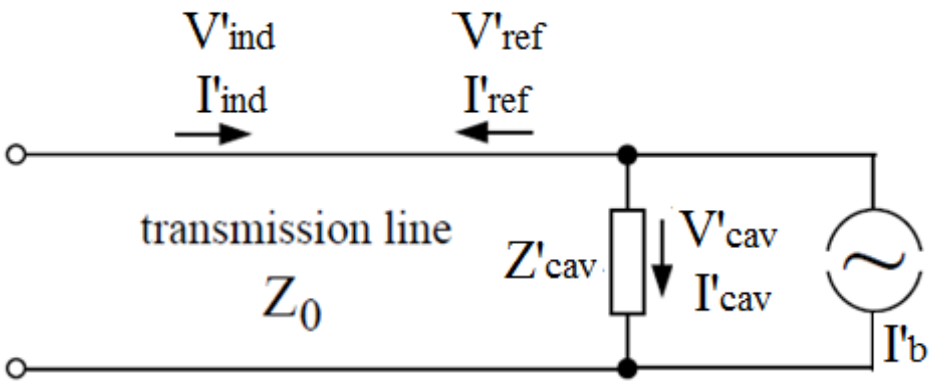

Figure 45. Equivalent electric circuit from the transmission line perspective [68]

- Figure 46 represents another equivalent circuit to the one represented in Figure 44 but from the perspective of the RLC circuit representing the cavity.

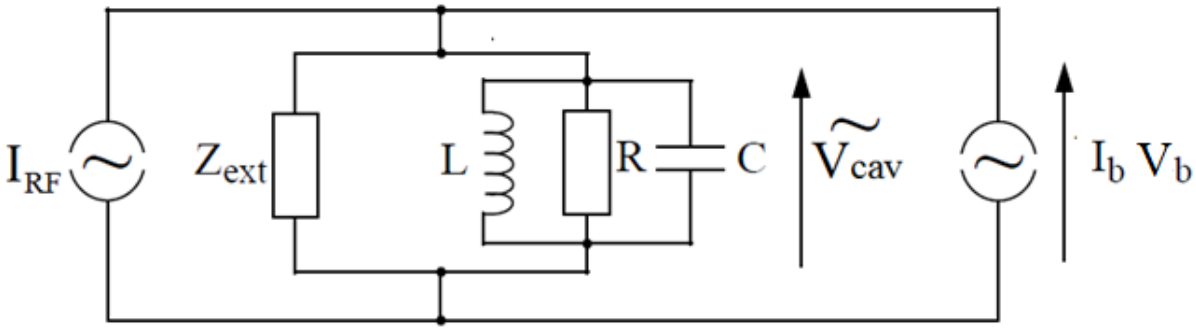

Figure 46. Equivalent electric circuit from the RLC circuit perspective [17]

In Figure 45, the different signals written with an apostrophe, << ' >> indicate that they belong to the equivalent circuit from the transmission line perspective. Thus, the only value that remains unchanged in this circuit is, indeed, the impedance of the transmission line (Z_0). In the circuit, two superposed signals will go across the transmission line, the induced tension V'_{ind}, traveling towards the cavity, and the tension reflected in the cavity V'_{ref}, traveling towards the circulator. The tension of the cavity, V'_{cav} can be expressed as a function of these two tensions

$$V'_{cav} = V'_{ind} + V'_{ref} \tag{4.14}$$

and the current of the cavity I'_{cav}, can be expressed as a function of the currents represented in Figure 45:

$$I'_{cav} = I'_{ind} + I'_{ref} + I'_b \tag{4.15}$$

Taking into account that $V'_{ind} = Z_0 I'_{ind}$ and $V'_{ref} = -Z_0 I'_{ref}$, the current crossing the cavity can be expressed as:

$$I'_{cav} = \frac{V'_{ind}}{Z_0} - \frac{V'_{cav} - V'_{ind}}{Z_0} + I'_b \tag{4.16}$$

Applying Ohms law it is possible to express the cavity tension as a function of the incoming current and the current of the beam:

$$V'_{cav} = \frac{Z'_{cav} Z_0}{Z_0 + Z'_{cav}} (2 I'_{ind} + I'_b) \tag{4.17}$$

This relation links the currents and the cavity tension from the perspective of the transmission line. However, it is interesting to know the relation of these values from the cavity's perspective. To do this, it is necessary to recall the passing relations for an ideal transformer:

$Transmission\ line$		$Cavity$
V'	$\rightarrow$	$V = NV'$
I'	$\rightarrow$	$I = \frac{I'}{N}$

These transformation laws allow to relate the impedance of the cavity and of the transmission line in the perspectives considered in Figures 44 and 45:

$$Z'_{cav} = \frac{Z_{cav}}{N^2} \tag{4.18}$$

$$Z_{ext} = Z_0 N^2 \tag{4.19}$$

Applying these transformation equations and considering that the induced current I'_{ind} is the same as the generator current I_g, and that $I'_b = I_b$ (because the coupling is direct since there is no intermediate transformer between the beam and the cavity), the expression of V_{cav} can be written as:

$$V_{cav} = \frac{N^2 Z_{cav} Z_0}{N^2 Z_0 + Z_{cav}} (2\, I_g + I_b) \tag{4.20}$$

However, as expressed in Figure 46, the generator current from the cavity perspective is I_{RF} and its relation with the tension of the cavity can be expressed as:

$$V_{cav} = \frac{Z_{cav} Z_{ext}}{Z_{ext} + Z_{cav}} (I_{RF} + I_b) = \frac{N^2 Z_{cav} Z_0}{N^2 Z_0 + Z_{cav}} (I_{RF} + I_b) \tag{4.21}$$

Thus, comparing equation (4.20) and (4.21) it can be determined that:

$$I_{RF} = 2\, I_g \tag{4.22}$$

Focusing at this point on the other current generator, the beam, it must be noted that it has been considered an AC generator. Nevertheless, the structure of the beam current is not exactly the same as this kind of generator. In fact its structure can be considered as a succession of Gaussian "bunches" with standard deviation σ_t and spaces of period T, as shown in Figure 47.

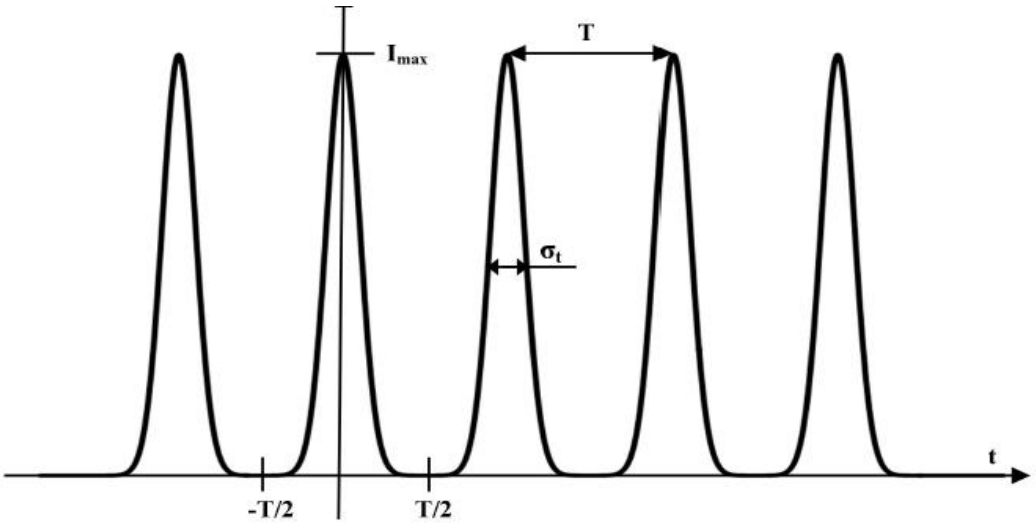

Figure 47. Temporal structure of the beam current [17]

The current delivered by a “bunch” of total charge q can be expressed as:

$$I(t) = \frac{q}{\sqrt{2\pi}\,\sigma_t} e^{-\frac{t^2}{2\,\sigma_t^2}} = I_{max} e^{-\frac{t^2}{2\,\sigma_t^2}} \tag{4.23}$$

In order to identify its harmonic components, this periodic function can be decomposed in a Fourier series in the interval $[-T/2, T/2]$:

$$I(t) = \frac{a_0}{2} + \sum_{n=1}^{\infty} a_n \cos(n\Omega t) + b_n sin(n\Omega t) \tag{4.24}$$

with,

$$\Omega = (\frac{2\pi}{T})$$

$$a_0 = (\frac{2q}{T})$$

$$a_n = \left(\frac{2q}{T}\right) e^{-\frac{(n\Omega\sigma_t)^2}{2}}$$

$$b_n = 0 \tag{4.25}$$

The values of the Fourier coefficients result from Gauss’ integral calculus [17]. The current of the beam in a period T, can be defined by:

$$I_{b0} = \frac{q}{T} \tag{4.26}$$

This leads to writing the pair coefficient of the Fourier series as:

$$a_n = 2I_{b0} e^{-\frac{(n\Omega\sigma_t)^2}{2}} \tag{4.27}$$

Generally, for particle bunches with a low dispersion $\sigma_t \ll T$ it can be considered that:

$$a_n \approx 2I_{b0} \tag{4.28}$$

Another reasonable simplification is to consider that, since the bandwidth of an accelerating cavity is very narrow (especially if it is superconducting) [35], then the only significant harmonic will be the one corresponding to its resonance frequency $w_0 = n\Omega$. Thus, the beam can actually be modeled as an AC generator where:

$$I_b(t) = 2I_{b0}\cos(w_0 t) \tag{4.29}$$

The cavity modeled as a bandpass resonator

The cavity has been modeled as an RLC circuit which is known to act as a bandpass filter. In this section the bandwidth of this bandpass filter will be characterized. Going back to the equivalent circuit of the model from the cavity perspective shown in Figure 46 and recalling equation ($I_{RF} = 2I_g$), it can be established that:

$$I_{RF} + I_b = 2I_g + I_b = I_C + I_{RL} + I_L \tag{4.30}$$

From this expression, the differential equation that relates currents and tensions in a RLC circuit can be deduced:

$$\frac{dI(t)}{dt} = C\frac{d^2V_{cav}(t)}{dt^2} + \frac{1}{R_L}\frac{d\,V_{cav}(t)}{dt} + \frac{1}{L}V_{cav}(t) \tag{4.31}$$

In order to solve this equation, the current can be considered in its complex form $\tilde{I}(t) = I_0 e^{iwt}$. Thus, a solution for the cavity tension is $\widetilde{V_{cav}}(t) = V_{cav}e^{iwt+\psi}$, being ψ the phase shift between current and tension induced by the RLC circuit. This two expressions for current and tension can be related by the following equation:

$$\widetilde{V_{cav}} = \frac{R_L}{1 + iR_L(wC - \frac{1}{wL})}\tilde{I} \tag{4.32}$$

Using equations (4.1) and (4.11), together with the previous expression, and considering $V_0 \approx V_{cav}$, the relation between current and tension can be expressed as a function of the loaded quality factor and the resonance frequency of the cavity:

$$\widetilde{V_{cav}} = \frac{R_L}{1 - jQ_L(\frac{w_0}{w} - \frac{w}{w_0})}\tilde{I} \tag{4.33}$$

Therefore, the phase shift can be written as

$$\psi = Arg(\widetilde{V_{cav}}) \leftrightarrow \tan\psi = Q_L\left(\frac{w_0}{w} - \frac{w}{w_0}\right) = Q_L\left(\frac{{w_0}^2 - w^2}{ww_0}\right) \tag{4.34}$$

When the frequency of the generator w is close to the resonance frequency of the cavity w_0 a reasonable approximation to the last expression is [17] and [68]:

$$\tan\psi = 2Q_L\left(\frac{\Delta w}{w}\right) = 2Q_L\left(\frac{\Delta f}{f}\right) \tag{4.35}$$

where $\Delta w = w_0 - w$ and $\Delta f = f_0 - f$, being w and f the frequency of the generator and $w_0$and f_0 the resonance frequency of the cavity in radians and Hertz respectively.

Considering the previous dissertation and equations (4.33) and (4.34) the amplitude of the cavity tension as a function of the generator frequency can be written as:

$$V_{cav}(w) = \frac{R_L}{\sqrt{1 + (\tan\psi)^2}}I_0 \tag{4.36}$$

Thus, both, V_{cav} and ψ, depend on the frequency of the generator, w, and this relation is shown in Figure 48:

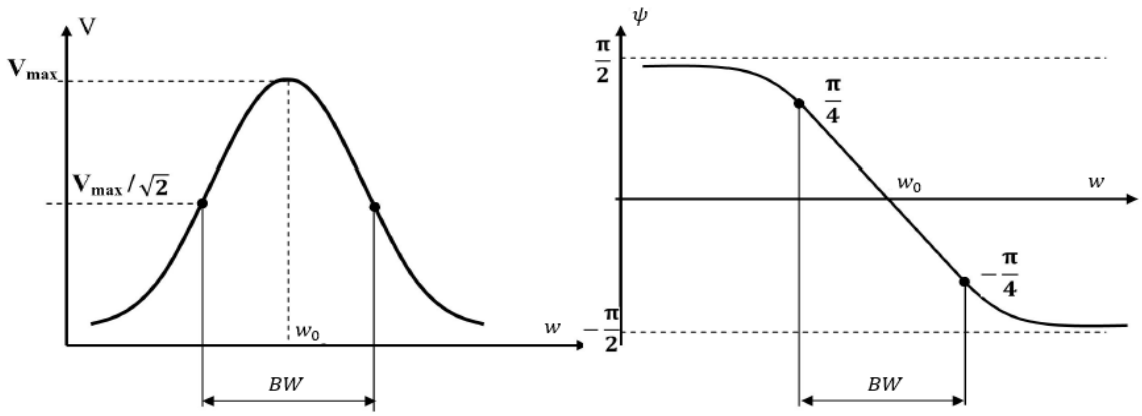

Figure 48. Bode diagram of the cavity model [17]

Figure 48 corresponds to a Bode diagram in which both the amplitude and the phase of an outgoing signal, namely $\widetilde{V_{cav}}(t)$, are described by the frequency, w, of the incoming signal, namely $\tilde{I}$. This behavior corresponds to that of a bandpass filter, in which the outgoing signal only has a significant magnitude for a determined set of frequencies.

The bandwidth of a cavity is, by convention, defined as the set of frequencies for which the power stored in the cavity is higher than half the maximum power that can be stored, which corresponds to a -3dB drop in power. For such a drop in the power stored inside the cavity, $V_{cav}(w)$ becomes equal to $V_{max}/\sqrt{2}$, being V_{max} the maximum tension that can be achieved in the cavity. Figure 48 illustrates these concepts and the cavity bandwidth.

It is important to note that, for a determined frequency w_{bw}, the bandpass filter described by equations (4.35) and (4.36) yields that:

$$V_{cav}(w_{bw}) = \frac{V_{max}}{\sqrt{2}} \leftrightarrow |\tan\psi| = 1 \leftrightarrow \ \psi = \pm\frac{\pi}{4}. \tag{4.37}$$

Thus, going back to equation (4.35) with this value of ψ it can be determined that

$$\Delta w_{bw} = \frac{w_{bw}}{2Q_L} \tag{4.38}$$

being $\Delta w_{bw} = w_0 - w_{bw}$. Since the bandwidth BW_w in radians described in Figure GG is twice the value of Δw_{bw} then:

$$BW_w = \frac{w_{bw}}{Q_L} = \frac{2\pi f_{bw}}{Q_L}. \tag{4.39}$$

This same bandwidth BW_f in Hertz will be:

$$BW_f = \frac{f_{bw}}{Q_L}. \tag{4.40}$$

A reasonable approximation to the real values of the bandwidths of the spoke and elliptical cavities can be made considering that $f_{bw} \approx f_0$ and that $Q_L \approx Q_0/1000$ (losses in the

RF cycle are considerably higher than losses in a cryogenic cavity). Calculated in this way, the bandwidth of the elliptical and spoke cavities will theoretically be around 185 and 90 Hertz, respectively. As it will be explained later on, the experimental test on the spoke cavity were performed in room temperature conditions. In this case, Q_0 can be considered to be $2 \cdot 10^4$ (see Table 4) and, thus $Q_0 \ll Q_{ext}$, so $Q_L \approx Q_0$. Consequently, the bandwidth of the spoke cavity at room temperature increases in several orders of magnitude.

Resonance Frequency Perturbations

However, as already considered, the resonance frequency of a cavity is strongly dependent on the shape of the cavity which, in the case of SC cavities, is built in expensive materials such as Niobium. Therefore cavity walls are usually thin and their shape is sensitive to environmental perturbations. These perturbations modify slightly the shape of the cavity and, thus, its resonance frequency. The most common perturbations affecting the operation of a cavity are described in the following.

➔ The Lorentz forces - The electromagnetic field stored inside the cavity induces a radiation pressure on its walls. This results in a small deformation of the cavity resulting in a resonance frequency detuning [42]. The accelerating field inside a cavity, Eacc, can be defined from the accelerating voltage, Vacc, according to the following equation:

$$E_{acc} = \frac{V_{acc}}{L_{acc}} \tag{4.41}$$

where L_{acc} is the accelerating lenght.

The static detuning, Δf_L, can be expressed as a function of the accelerating field, E_{acc}, and the Lorentz factor, k_L. The Lorentz factor can be estimated with mechanical and electromagnetic simulations. It can also be measured during cavity tests and is given in $Hz/(MV/m)^2$. The static detuning amplitude due to Lorentz forces increases with the square root of E_{acc}:

$$\Delta f_L = -k_L E_{acc}^2 \tag{4.42}$$

➔ The Microphonics - Vibrations due to the environmental systems of the cavity can excite its mechanical modes and create some dynamic detuning. They are

barely predictable and can become very critical for the cavity control. In general, the frequency range for microphonics is from ~1 Hz to ~1 kHz. Beyond that range, vibrations are damped by the mechanical elements. The total perturbations due to microphonics can be modelled as:

$$\Delta f_{mic} = \sum_i \Delta f_i(t) \sin(w_i t) \tag{4.43}$$

with w_i the angular frequency of the mechanical excitation and Δf_i the detuning amplitude the cavity resonance frequency.

➔ The helium bath - Some detuning can also be observed due to variations in the helium bath pressure, Δf_{He}. Nevertheless, these variations are very slow: the order of magnitude for such time variations is from a few seconds to minutes.

The effects of the listed perturbations can be described with the help of Figure 49, where, similarly to Figure 48, the resonating phenomenon of a cavity on an electromagnetic wave induced in it is represented in a bode diagram. The left side of Figure 49 shows that at time t_0 the cavity's electromagnetic resonance frequency $w_0(t_0)$ is equal to that of the injected field w_{RF}. For $w_0 = w_{RF}$, the amplification of any induced electromagnetic field whose frequency was surrounding w_{RF} is represented by the black line, being the maximum amplification the one obtained for a field of frequency equal to w_{RF} and decreasing as the distance with w_{RF} increases. However, due to the effect of a perturbation at time t_1 the resonance frequency of the cavity could vary and its value could move to $w_0(t_1)$. In this case, the black line representing the amplification of fields with different frequencies would move with the resonance frequency and would become the one represented by the blue dotted line. For a field induced in the cavity with a frequency w_{RF} the consequence of this variation of the cavity resonance frequency would be a drop of the accelerating voltage (ΔV). In the same manner, at the right side of the figure the phase variation of the field induced inside the cavity is represented by the black line when the cavity resonance frequency is $w_0(t_0) = w_{RF}$ and by the blue dotted line when it is $w_0(t_1)$. The variation of the cavity's resonance frequency from $w_0(t_0)$ to $w_0(t_1)$ causes also a drift $\Delta\psi$ in the phase of the electromagnetic wave ψ inside the cavity.

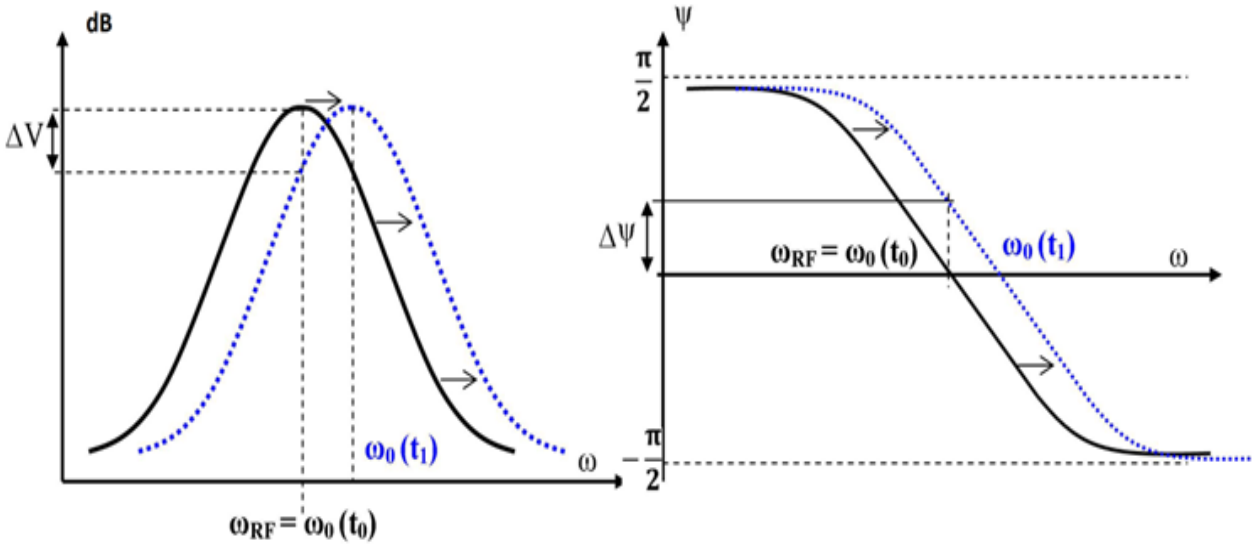

Figure 49. Resonance phenomenon and perturbations effect

As illustrated in the bode diagram, deviations from the design resonance frequency, which in operation shall be equal to that of the RF field injected in the cavity w_{RF}, will cause drifts of both the amplitude and the phase of the field inside the cavity. These drifts will have to be compensated by varying the field emitted by the power coupler in order to maintain the cavity's phase and amplitude on their targets or setpoints and this will increase the power consumed.

Since power consumption should not exceed reasonable limits, the idea of compensating for resonance frequency drifts caused by perturbations such as microphonics, Lorentz forces, variations of the helium tank pressure, etc, is being studied. Mechanical devices that compress or expand the cavity walls, modifying the cavity resonance frequency and thus capable of compensating for perturbations causing resonance frequency drifts have been studied and developed [69], [70]. Their goal is to keep the resonance frequency of each cavity under control. These systems have been named Cold Tuning Systems (CTS) for their capacity to modify the resonance frequency of a cavity working close to a cryogenic environment. However, the design of CTS has not only dealt with the extreme temperature requirements, but has also considered other "aggressive" operational circumstances such as vacuum, X radiation, produced by the interaction of strong magnetic fields and the cavity walls, and the proximity of these strong magnetic fields themselves. For instance, X radiation

avoids the use of semiconductors in the CTS and the presence of strong magnetic fields requires the use of non-magnetic materials.

CTS are usually composed of a non-magnetic metallic structure able to compress or expand the cavity walls when driven either by the stepper motor or by a piezoelectric actuator. The stepper motor is a slow actuator that will be used to compress or expand the cavity under certain circumstances but will be kept constant in normal operating conditions. The piezoelectric are fast actuators whose size will increase when excited by a voltage signal, thus, acting on the metallic structure that will modify the resonance frequency of the cavity. Hence, with these piezoelectric actuators the real-time control of the cavity's resonance frequency can be performed.

The following subsection presents an analysis of the optimal operating point for the resonance frequency of a cavity, which will minimize the reflected power for a determined synchronous phase. Afterwards, an overview of the control systems that address the control needs of the processes discussed will be presented and the main control challenges of the system in charge of performing the cavity resonance frequency regulation will be commented. A later subsection describes the functioning principle and the features of the two CTS that are the main instruments used for frequency tuning control tests in the Spoke and Elliptical prototypical cavities.

4.2 OPTIMAL FREQUENCY DETUNING

The idea of using CTS to compensate for perturbations has been introduced. Nevertheless, CTS is not only envisaged for real-time compensation of perturbations, but also for driving the resonance frequency of a cavity to its optimal operating point during accelerator startups and during cavity failure procedures. The optimal operating point for the resonance frequency detuning is the value that minimizes the power consumption in the generator and the power reflected to the circulator for a determined field in the cavity. In this situation, the power transmitted to the beam is maximized. The following mathematical digression determines the resonance frequency value that assures these conditions.

For a superconducting cavity (with Q_0 >> Q_L), in steady state (that is when the accelerating field has been ramped up to a stable value) the power from the generator, P_g, the power stored in the cavity, P_{cav}, the power transmitted to the beam, P_b, and the reflected power at the power coupler port, P_{ref} , can be written as follows ([17], [68]):

$$P_g = \frac{V_{acc}^2}{8(\frac{r}{Q})Q_L}\left(1 + (2Q_L\frac{\Delta f}{f_0})^2\right) + \frac{I_{b0}V_{acc}}{2}\left(\cos(\phi_s) + \sin(\phi_s)(2Q_L\frac{\Delta f}{f_0})^2\right) + \frac{(\frac{r}{Q})Q_L}{2}I_{b0}^2$$

$$P_{cav} = \frac{V_{acc}^2}{2(\frac{r}{Q})Q_0}$$

$$P_b = I_{b0}V_{acc}\cos(\phi_s)$$

$$P_{ref} = \frac{V_{acc}^2}{2\left(\frac{r}{Q}\right)}\left[\frac{1}{4Q_L}\left(1 + \left(2Q_L\frac{\Delta f}{f_0}\right)^2\right) - \frac{1}{Q_0}\right]$$
$$+ I_{b0}V_{acc}\left[\frac{1}{2}(\cos(\phi_s) + \sin(\phi_s)2Q_L\frac{\Delta f}{f_0}) - \cos(\phi_s)\right]$$
$$+ \frac{(\frac{r}{Q})Q_L}{2}I_{b0}^2. \qquad (4.44)$$

In addition, by ignoring the power in the pick-up antenna,

$$P_g = P_{cav} + P_b + P_{ref} \qquad (4.45)$$

It can be noticed that the powers P_g and P_{ref} depend on:

- the voltage V_{acc} in the cavity,
- the beam current I_{b0} and the synchronous phase ϕ_s,
- the loaded coupling Q_L and the cavity detuning Δf.

So, for a given V_{acc}, I_{b0} and ϕ_s the power delivered by the generator depends on the cavity detuning. The power transmission of P_g will be optimal while P_{ref} will be minimized.

According to the system of equations (4.41), the optimal detuning which minimizes the reflected power is:

$$\Delta f_{opt} = -f_0 \frac{I_{b0}(\frac{r}{Q})}{V_{acc}} \sin(\phi_s) \tag{4.46}$$

To illustrate the importance of the optimal detuning one can consider the example with a cavity of the linac that operates to a nominal accelerating field E_{acc} = 8,2 MV/m (Lacc = 0,5 m), and with a synchronous phase ϕ_s = -25°. The beam current is I_{b0} = 4 mA and (r/Q) = 80. According to equation (4.43) the cavity optimal detuning, in steady state, is $\Delta f_{opt} \approx 24$ Hz.

To ensure the optimal detuning, the tuning system has to compensate the perturbations and in particular the Lorentz forces. In this example, without considering the influence of the microphonics and the helium bath, the contribution of the CTS has to be:

$$\Delta f_{CTS} = -\Delta f_{opt} - \Delta f_L \left(E_{acc} = \frac{8{,}2MV}{m}\right) \tag{4.47}$$

On Figure 50, P_g, P_{ref} and P_b (for a superconducting cavity P_{cav} is small) are plotted as a function of the accelerating field in the cavity. It is considered that the cavity frequency is tuned to compensate for the Lorentz forces at the nominal operation point E_{acc} = 8,2 MV/m (solid line curves on Figure 50): here $k_L = 10\ \mathrm{Hz/(MV/m)^2}$ and $\Delta f_L \left(E_{acc} = \frac{8{,}2MV}{m}\right) = -538$ Hz. Two settings of static detuning are represented, one with the solid line and another with the dotted line. Initially the tuning system is set to get an optimal operation at 8.2 MV/m. But, to increase the field value to 10.7 MV/m, the tuning system has to move its position in order to compensate for the Lorentz detuning increase and to reach the new Δf_{opt} .

The operation is indeed optimal at 8.2 MV/m because the reflected power is minimized. However, around this point, the RF power supply has to furnish more power than necessary if the accelerating field has to be changed. In addition the maximum power (30 kW)

that the generator can deliver is quickly reached. As a consequence, if the field has to be increased to 10.7 MV/m (dashed line curves on Figure 50) it is necessary to re-optimize the frequency detuning of the cavity at the same time as the field is ramped up into it. In this way the Lorentz detuning is compensated and there is no power saturation of the generator. So, when the steady state is reached the RF power consumption is minimized.

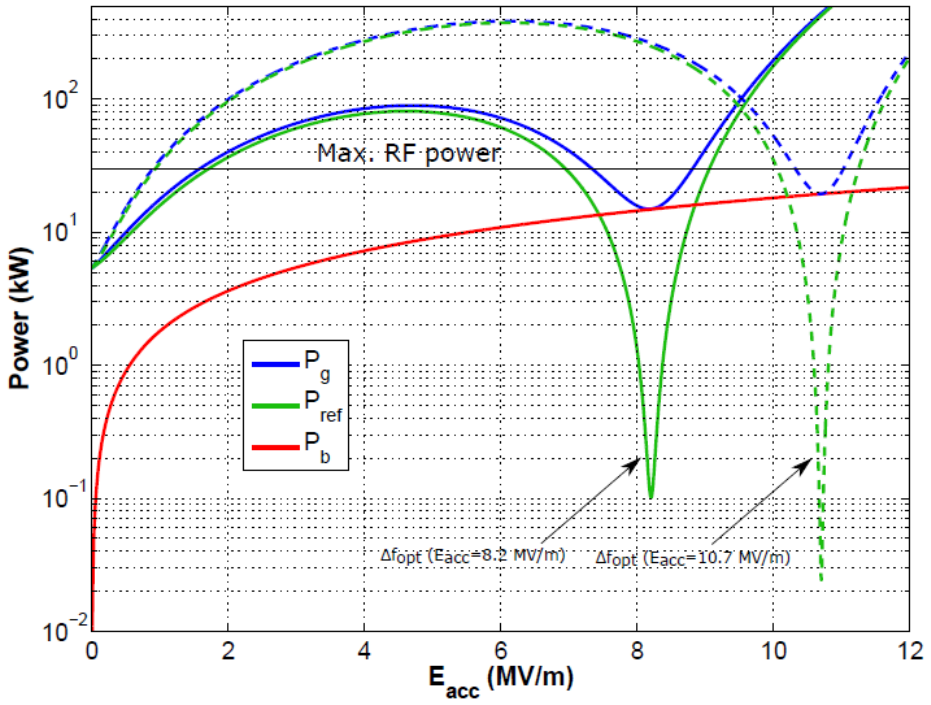

Figure 50. Evolution of the generator power, Pg, the reflected power, Pref and of the power delivered to the beam, Pb, as function of the accelerating field Eacc.

As a conclusion, to operate a superconducting cavity in a CW mode, it is necessary to use a tuning system, which can be dynamically controlled, in order to help the LLRF feedback loop that enables the stabilization of the accelerating field and phase inside the cavity. The tuning system control loop has to enable the compensation of all the perturbations. The Lorentz forces may bring a high cavity detuning, which leads to power saturation. Microphonics, which may appear randomly, can also strongly perturb the cavity operation. It is therefore essential to use a system which can compensate for detuning caused by perturbations and keep track of the resonance frequency dynamic evolution.

4.3 CONTROL LOOPS

Reviewing the previous concepts it can be concluded that an accelerating cavity will require both a loop controlling the RF field inside the cavity and a loop controlling the cavity electromagnetic resonance frequency. These control loops are summarized in the following:

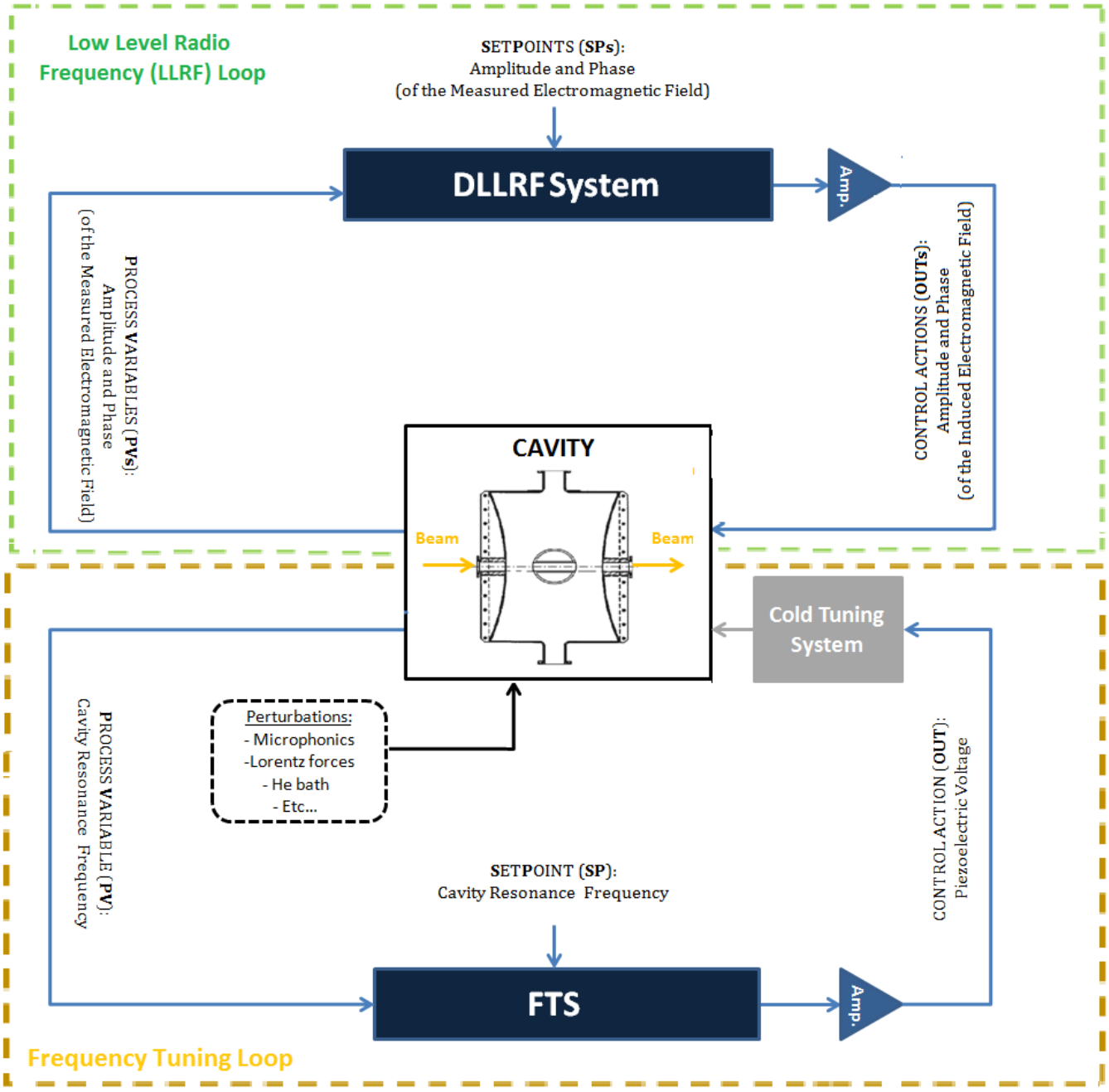

Figure 51. Cavity Control System Strategy

- The **Low Level Radio Frequency (LLRF) loop** has the objective of maintaining the phase and the amplitude of the field measured inside the cavity controlled around their setpoints by acting on the amplitude and the phase of the field induced by the power coupler.
- The **Frequency Tuning (FT) loop** has the objective of maintaining the resonance frequency of the cavity as close as possible to its optimum value or setpoint, by acting on the voltage applied to the piezoelectric actuator via the amplifier (Amp.). However, the cavity's resonance frequency will be affected by several perturbations such as microphonics or Lorentz detuning. The FT loop will have to compensate for these variations acting on the CTS so that it retunes the cavity.

The control strategy that has been envisaged for the two control loops described above is to use two independent control systems: the Digital Low Level Radio Frequency system (DLLRF) and the Frequency Tuning System (FTS). This strategy is illustrated along with the control loops described in Figure 51. At the center of the figure the cavity is represented by the picture of a spoke cavity. Uncertain perturbations affecting the cavity's operation are considered next to it.

As already considered, the DLLRF will be a control platform with two process variables, phase and amplitude, that will command an RF generator or amplifier to drive these variables to their nominal operation values.

The control actions of the FTS will modify the resonance frequency of the cavity throughout operation and as previously considered will modify the amplitude and the phase of the field inside the cavity. Therefore there will be a certain interference of the FTS in the performance of the DLLRF. This may lead to think the strategy of using two independent control systems may not be appropriate. However, in practice, dynamic changes in the LLRF loop take place within μs while dynamic changes in the frequency tuning loop occur in ms, thus the DLLRF system has enough time to recover adequately field control between succesive control actions of the FTS, making this control strategy adequate for these processes.

Another important aspect of resonance frequency control is that the cavity resonance frequency cannot be directly measured. Thus the control strategy represented in Figure 51 is

valid for example in simulations where the resonance frequency is accessible but not for a real implementation with beam.

An alternative approach for the control of resonance frequency relies on the fact that its deviation with respect to its setpoint (or optimal value) is closely related to the deviation of the phase of the field induced in the cavity (computed by the DLLRF) with respect to its nominal value (the one it would have if the cavity frequency was on its setpoint). This relation between the resonance frequency and the emitted field's phase is a consequence of the DLLRF system's actions to compensate for phase deviations caused by resonance frequency drifts, consequently, for a determined value of the resonance frequency there will be a corresponding value of the emitted field phase in steady state. Therefore, for the optimal resonance frequency of the cavity there will be a nominal value of the emitted field's phase that can be calculated by means of physics equations. Therefore, in practice, the FTS intends to drive the phase of the field induced in the cavity to its theoretically calculated nominal value.

Figure 52 shows the block diagram of the cavity control strategy with the new approach explained in the previous paragraph. At the top, the LLRF control system block receives the amplitude and the phase of the field measured inside the cavity and computes the induced field's amplitude and phase that will drive the measured variable to their set points. The field computed by the LLRF is then amplified before being sent to the cavity. At the bottom the FTS control system block receives the phase of the field induced in the cavity by the LLRF and modifies the voltage applied to the piezoelectric actuator in order to drive the phase already mentioned to its nominal value.

The complexity of the processes involved in beam acceleration is high and the control challenges for the DLLRF loop and the FTS will be different and depend on the nature of the process controlled by each system and the dynamics of their critical variables. Research works presented in this thesis focus mainly in developments made for the FTS, although certain issues in relation with the LLRF loop will be commented depending on their influence in the FTS performance. The next sections will describe the different CTS used for the experimental campaign described in the future Chapters of this thesis and the main control challenges the FTS will encounter throughout its operation.

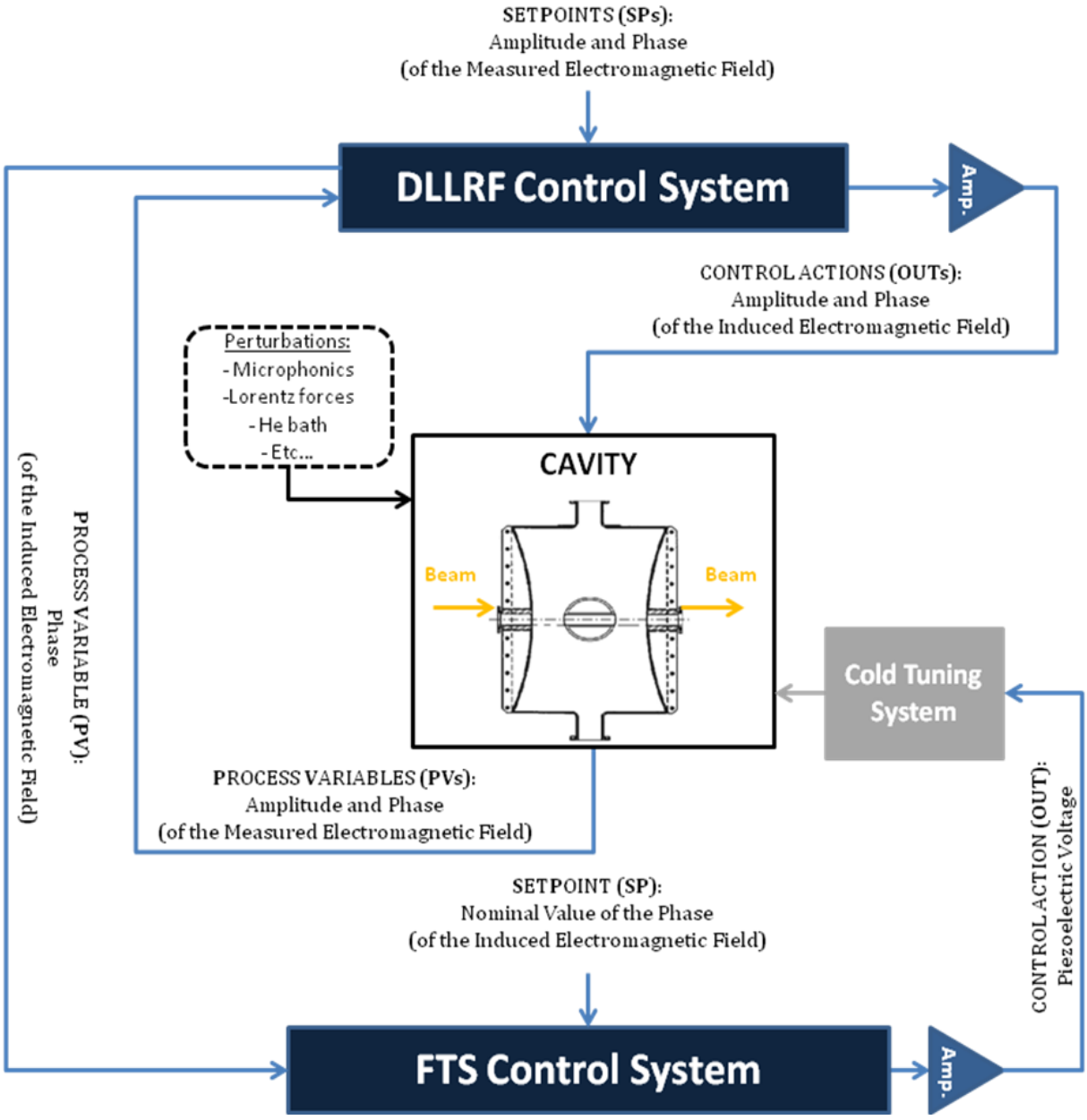

Figure 52. Cavity control system strategy when resonance frequency is not available

4.4 COLD TUNING SYSTEMS

Cold Tuning Systems (CTS) are a mechanism conceived for the cavity frequency tuning. CTS allow to apply small mechanical deformations to the cavity during operation, in order tune its resonance frequency and drive it to its optimal operating point. The operation of the CTS

is based on the already commented Slater Theorem that states that a volume variation in the cavity ΔV causes a variation of resonance frequency Δf. This phenomenon can be predicted by the following equation already considered in the previous chapter:

$$\frac{\partial f}{f} = \frac{1}{4W}\int_{\partial V}(\varepsilon_o E^2 - \mu_0 H^2)dV \qquad (4.48)$$

where f is the initial frequency, W the energy stored in the cavity, E the electric field, $\varepsilon_o$the permittivity of vacuum, H the magnetic field and μ_0 permeability of vacuum.

Two CTS are going to be reviewed in the following, the first was developed for the spoke cavity prototype while the second was used in the elliptical cavity prototype. Both are based on the same principle considering two actuators: (i) a "slow" motor capable to achieve several kHz detuning (SC state) within seconds and (ii) a "fast" piezoelectric actuator that can detune several hundreds of Hz (also SC state) in milliseconds.

Cold Tuning System for a spoke cavity

For the prototypical spoke cavity a CTS designed by IPNO which allows to deform voluntarily the cavity to regulate its resonance frequency is used [69]. The first constraint of a CTS is to allow a range of deformation while remaining in the elastic domain of the cavity materials, thus, avoiding failures due to fatigue. For this reason it is beneficial to deform the cavity in the more resistant direction which in this case is the longitudinal direction.

Figure 53 shows in subfigure 53.a the Helium (He) tank bearing the spoke cavity and in subfigure 53.b the same He tank "dressed" with the CTS designed by IPNO. The CTS considered in the subfigure 53.b is composed of a stepper motor coupled to an endless screw, two arms that will move through the endless screw, four connecting rods pushing the He tank and a mechanical structure that holds a plate and two piezoelectric actuators. In operation the plate will be screwed to the corresponding opening of the He tank which is shown at the left side of subfigure 53.a. This opening is intended to allow the passing of the beam through the cavity.

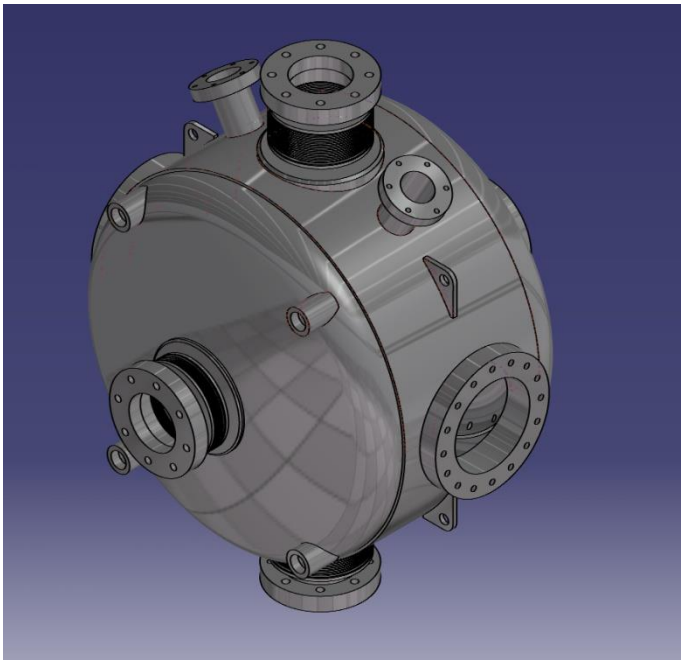

a)

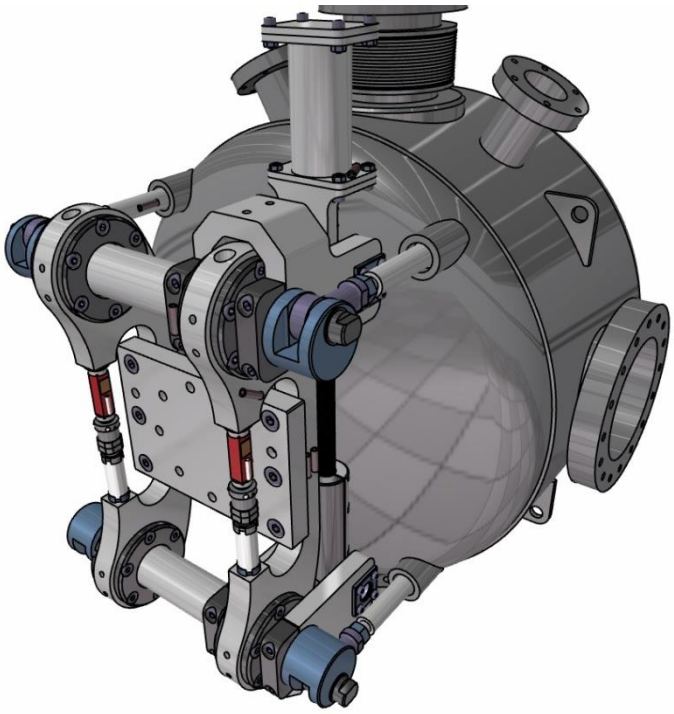

b)

Figure 53. He tank and CTS for the spoke cavity. Subfigure a) Helium (He) tank bearing the spoke cavity. Subfigure b) He tank "dressed" with the CTS [62].

Note that the plate would seal this opening. For use with beam the plate should be drilled to let the beam through, but this is not the case because the cavity is used for tests and research purposes without beam.

When the plate is screwed to the end of the He tank, the CTS remains encased between the contact of the rods with the He tank and the plate. The end of each of the four connecting rods pushes a conical bumper welded to the He tank. These rods will be maintained in contact with the bumpers throughout operation by working all the time around a compression offset. If the opposite beam opening of the He tank to the one screwed to the plate is fixed, the compression effort of the rods will transmit a traction effort, through the CTS structure, in the longitudinal direction of the tank. Thus, there will be a compression effort in the outer part of the tank and a longitudinal traction effort in the middle. This efforts will be transferred to the cavity through the tank walls.

As presented in [69], the CTS movement is driven by a stepper motor. The stepper motor for this CTS is the model VSS32.200.1,2-UHVC –VGPLC of the brand TSA. The main advantage of this type of motor is that its position is not controlled by means of a sensor of any type (optical, magnetic, etc.). This kind of sensors rely on semi-conductors and are unreliable under X radiation due to field emission. Instead the position is controlled by the number of steps of the motor. The chosen motor belongs to an extremely reliable kind which is conceived for aeronautical applications guarantying optimal performance in the expected low temperature working conditions. Figure 54 shows a picture of the stepper motor.

Figure 54. Stepper motor (brand TSA) [69]

The functioning principle when the CTS is driven by the stepper motor is represented in Figure 55. In this case an elliptical cavity has been sketched inside the He tank to simplify the drawing although this kind of CTS has been applied to a spoke cavity in the works reported on this thesis.

The figure represents two situations for a different number of turns of the stepper motor M. When the motor rotates the endless screw moves the two arms drawn in light blue in both subfigures in opposite directions, depending on the sense of rotation. Hence distance dx can be modified. This distance dx can modulate the compression effort F transmitted from the connecting rods to the He tank.

The bigger dx the bigger the force exerted by the arms (represented in light blue) on the plate (upper figure) and the bigger the traction effort of the structure of the cavity. Thus, for a smaller distance dx the cavity will be less stretched than for a bigger one, as it can be seen comparing both situations shown on the figure. On the other hand the outer part of the He tank will be more compressed for a smaller dx. The subfigures show how for a smaller dx distance L_1 will be shorter than L_2 which is the cavity distance corresponding to a larger dx.

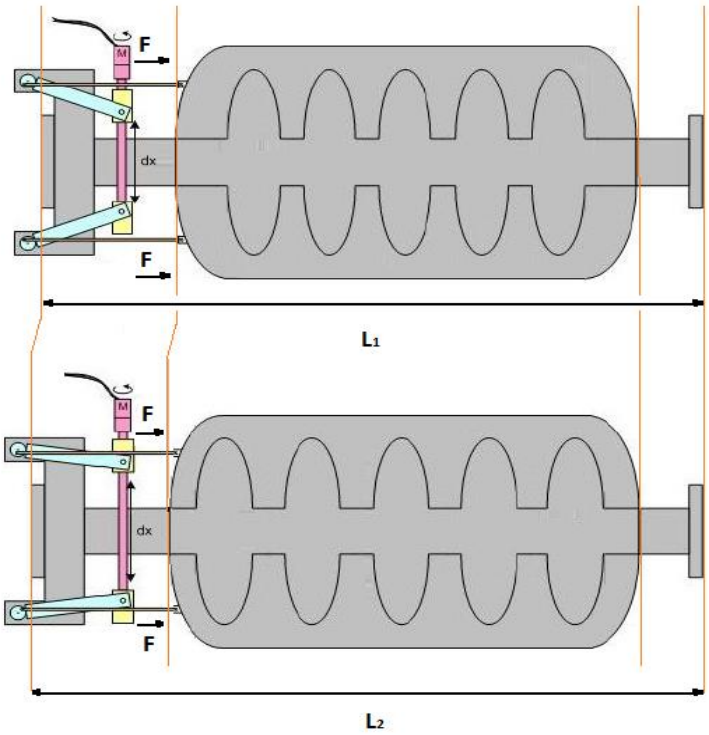

Figure 55. Deformation produced by the CTS in a cavity when driven by the stepper motor [69]

On the other hand the CTS can also be driven by the piezo electric actuator. The piezoelectric is envisaged to perform fast compensation (ms) for which the motor is not prepared. This actuator has to be capable to support very low temperatures in vacuum and under the effect of magnetic fields and X-ray radiation. In general these kinds of systems can yield a very low displacement (40 μs at room temperature) but they are capable to generate forces of several kN in a response time which is inferior to a millisecond.

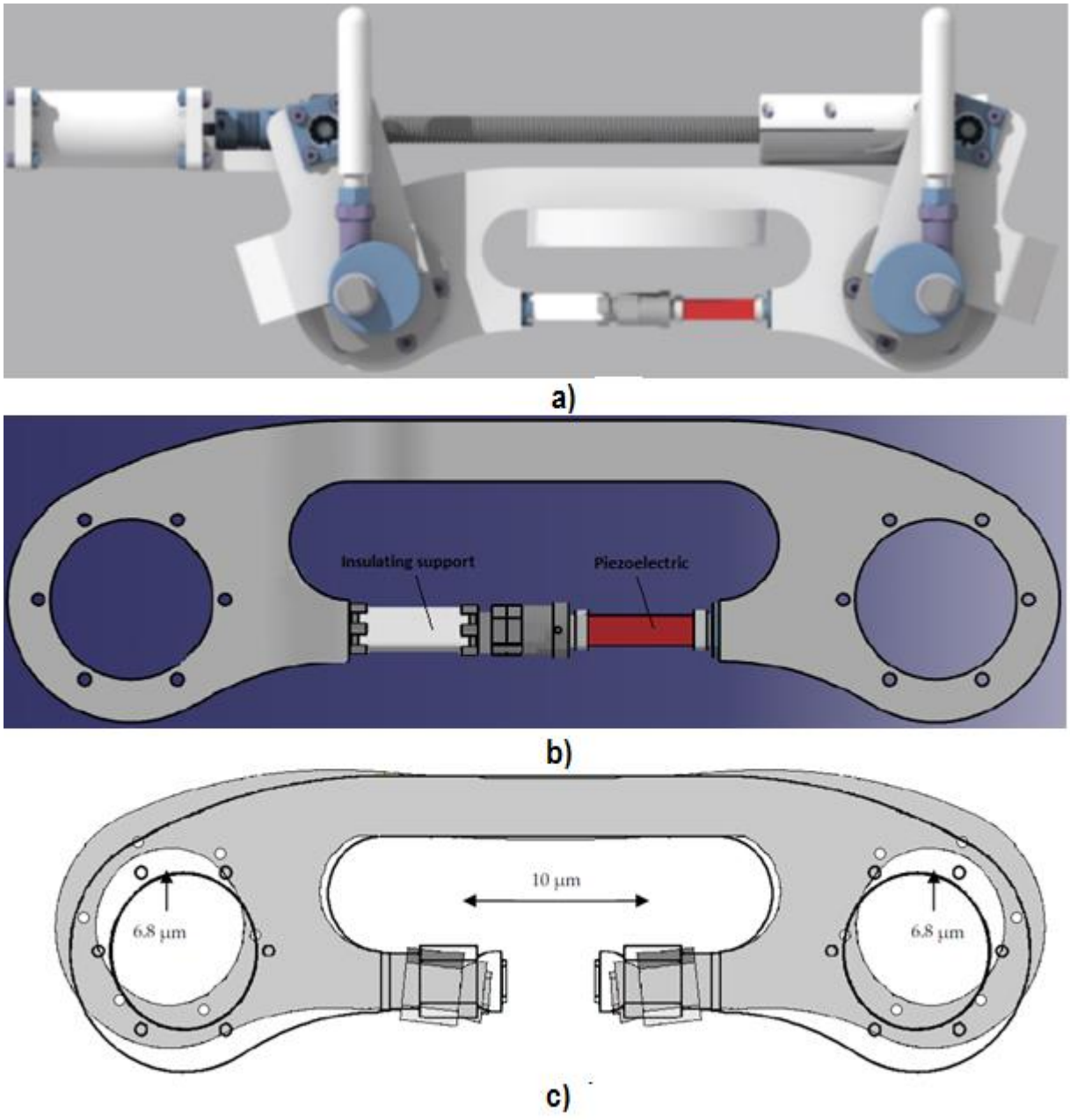

Figure 56. Deformation produced by the Piezoelectric in the CTS. Subfigure a) Side view of the whole CTS. Subfigure b) Part of the CTS that holds a piezoelectric actuator. Subfigure c) Deformation of the Part of the CTS holding the piezoelectric actuator. [69]

Among the piezoelectric actuators available in industry a “naked” model must be chosen because it is the only one that will tolerate the extreme working conditions in which the actuator is intended to perform its task. “Encapsulated” models are commonly used in industry and easier to put into operation but materials other than the piezoelectric will cause problems in the CTS very “aggressive” work environment. These problems will be magnified due to the scarce maintenance these systems are expected to have.

The chosen actuator is a sandwich type piezoelectric composed of multiple piezoelectric material layers separated by a thin film of resin. This actuator presents a relation between compression force and displacement that is ideal for this application. Generally the piezoelectric displacement in vacuum depends mostly on its length and the force it generated depends on its section. The piezoelectric actuator size was 36x10x10 mm.

The functioning principle when the CTS is driven by the piezo actuator depends on the deformation produced in the structure of the parts of the CTS by the voltage applied to the piezo actuator. Figure 56 is divided into 3 subfigures. Subfigure 56.a shows a side view of the whole CTS, subfigure 56.b shows one of the parts of the CTS that holds a piezolectric actuator and subfigure 56.c shows an illustration of the deformation the actuator can produce.

Subfigure 56.a shows a lateral view of the CTS while subfigure 56.b shows the detail of the part holding the piezoelectric actuator. Note that there is an insulating support helping the piezoelectric to fill the gap. This way, different size piezoelectric actuators can be used. Finally, subfigure 56.c depicts in black the original contour of the part before a 10 μm increase in the piezoelectric actuator and the new position after the deformation in grey. Note that the 10 μm increase in the piezoelectric actuator moves forward 6.8 μm the holes supporting the bar (calculations are reported in [69]) to which the connecting rods are linked. Logically, the rods will push the outer part of the He tank and consequently stretch it longitudinally in its axis.

Piezoelectric actuators are symmetrically installed in the CTS as show in Figure 56. The two piezo unit installed are 36 mm long multi-layer piezoelectric with a maximum displacement of 36 μm, having the spoke cavity a sensibility of 1 MHz/mm.

Cold Tuning System for an elliptical cavity

For the 5 cell elliptical cavities a coaxial piezoelectric blade tuner was developed during the EUROTRANS project [6] and a broader design report can be found in [71]. This tuning system is based on a flexible structure of the helium tank bearing the cavity. The helium tank has to allow longitudinal elongation required by the installed tuning mechanism in order to change the cavity frequency. Thus, the helium tank has been designed installing a bellow in the middle of the tank as represented in Figure 57.

Apart from the bellow in the middle of the tank, two rings welded to the surface are necessary for the functioning of the blade tuner. The compression or traction efforts performed on the welded rings will be transferred to the cavity through the walls of the tank, correctly shaped for this purpose, and the pressure of liquid Helium to the cavity walls modifying their resonance frequency.

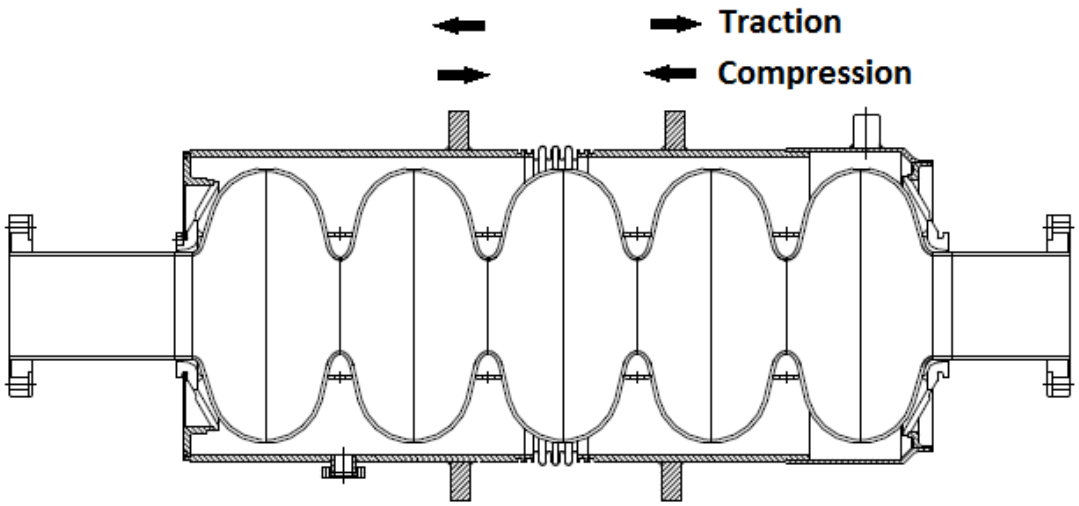

Figure 57. Scetch of the cross-section of the He tank bearing the cavity assembly [70]

The blade tuners objective is therefore to transfer traction or compression efforts to the welded rings. The system consists of three main components:

- the rings-blades assembly, that provide the cavity slow tuning action;
- the leverage mechanism, that, equipped with a stepping motor, drives the rings-blade assembly;
- the piezo actuator part, that, during operation, provides the fast tuning action necessary for Lorentz force and microphonics detuning compensation.

The rings-blades assembly consists of three different rings: the two external rings, which are rigidly connected to the welded rings of the He tank, and the one at the center, symmetrically divided in two halves. Figure 58 shows a scetch of the blade tuners rings:

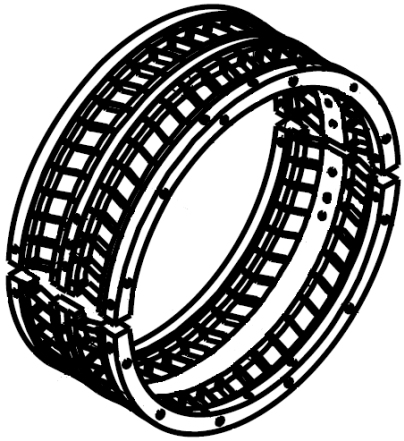

Figure 58. Scetch of the rings-blades assembly [70]

As shown in the figure, the rings are connected between them by thin plates or blades made of titanium. The external rings have several nuts so that they can be screwed to the rings welded to the He tank and for fixing the leverage mechanism. Central rings have several nuts also for the fixing of the leverage mechanism.

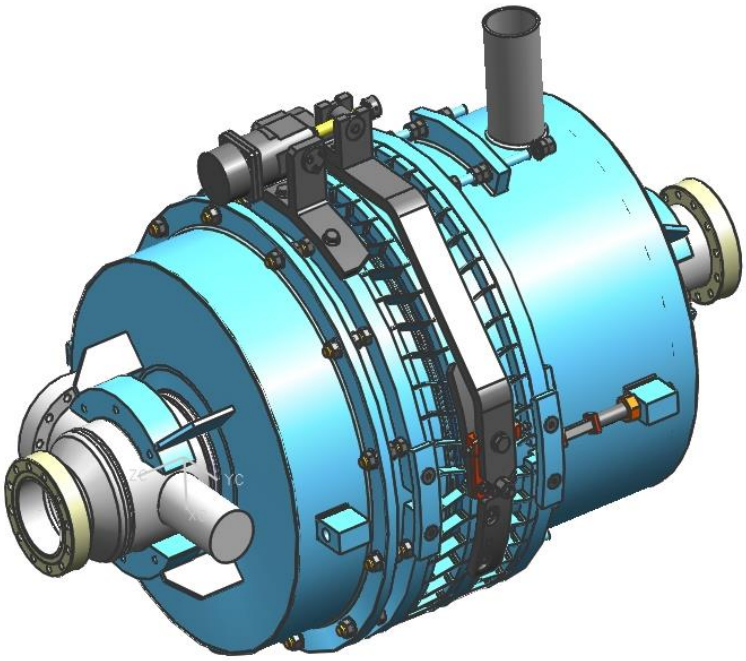

Figure 59. Scetch of the leverage mechanism, the rings-blades assembly and the He tank [17]

Figure 59 shows the leverage mechanism on top of the rings to which it is connected, and these connected to the He tank through the welded rings, as envisaged for operation. The leverage mechanism is composed of a stepper motor driving a big central arm connected to the central ring.

The rotation of the stepper motor will move longitudinally the upper part of the central arm producing a torque in its lower part which is connected to the central ring. The central arm is connected to the central ring through the plate shown in Figure 60.

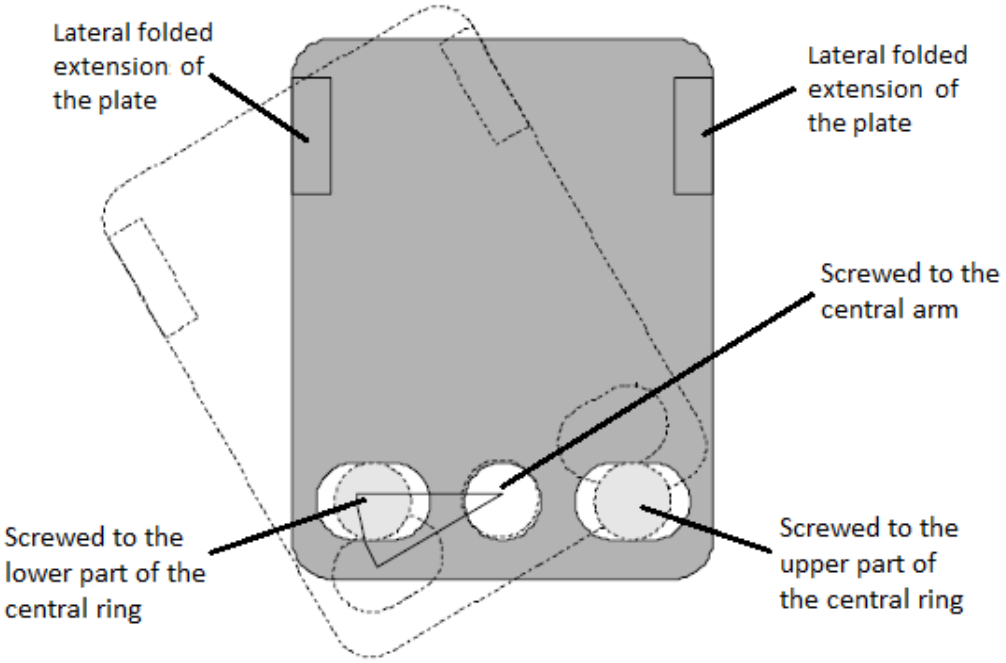

Figure 60. Details of the connecting plate [70]

Figure 60 shows the plate between the central arm and central ring. The holes at the sides of the plate are screwed to the upper part and to the lower part of the central ring, as commented in the drawing, and the central hole is screwed to the central arm. The plate is also fixed to the central arm by the two lateral folded extensions and moves jointly with it as suggested by the dotted drawing in the figure.

The kinematics of the whole system with the leverage mechanism, the rings-blades assembly and the He tank is explained with the help of Figure 61. This figure represents in two subfigures how the force **F** transmitted by the stepper motor to the central arm in form of a

longitudinal effort is transferred to the rings welded to the He tank, and, thus compresses or expands the cavity. In the left part of the figure it can be seen how the force **F** moves a distance **u** the upper part of the central arm. This causes a torque at the lower part of the central arm which is transferred through the plate of Figure 53 to the upper and lower parts of the central ring in form of the vertical efforts **v** shown in the right side of Figure 54. As the external rings are fixed to the welded rings of the He tank, efforts **v** will bend the blades between the central and external rings causing longitudinal efforts **w** in opposite directions on each external ring. In this way force **F** of the stepper motor is transmitted to rings welded to the He tank and through the tank to the cavity.

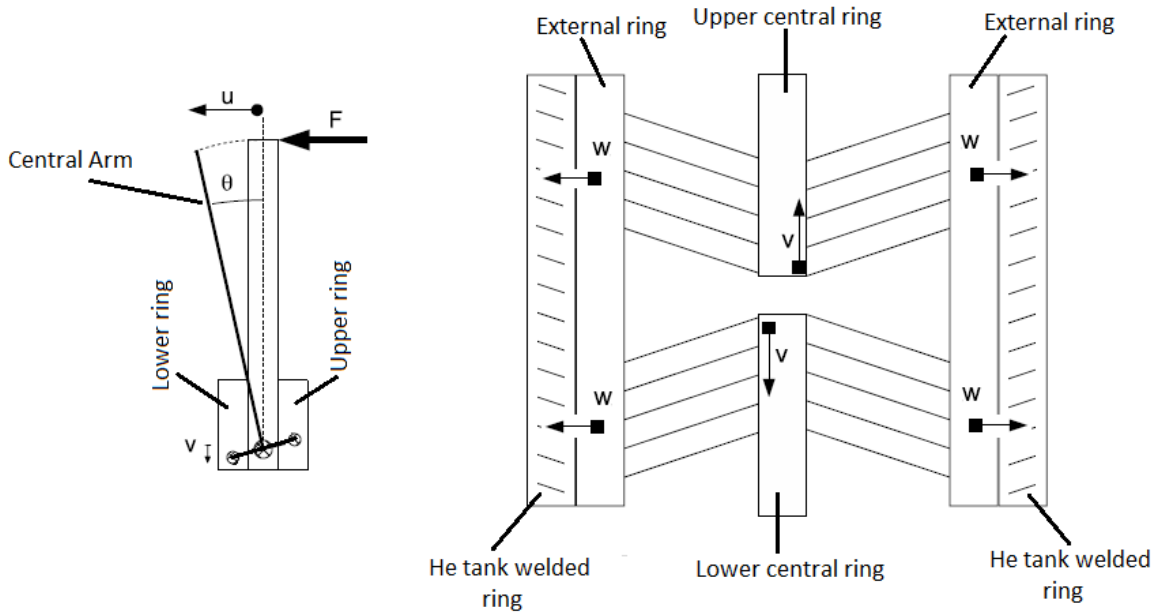

Figure 61. Kinematics leverage mechanism and the rings-blades assembly [70]

The last part of the blade tuner system is the piezo actuator part which is in fact the simplest as it is based on using a piezoelectric actuator to push one of the welded rings from a fixed point as shown in Figure 62.

This figure shows the whole blade tuner system installed on the He tank of the 5 cell elliptical cavity. This setup enables the control of the resonance frequency within a range up to 350 kHz and the static compensation of Lorentz's force detuning. Piezoelectric actuators are symmetrically installed on both sides of the tank along the tuner force line. The two piezo unit installed, 70 mm long multi-layer ceramic stack with 100 mm nominal stroke at 200 V

driving voltage, provide capability to dynamically adjust the cavity frequency within 10 kHz range with nanometric resolution.

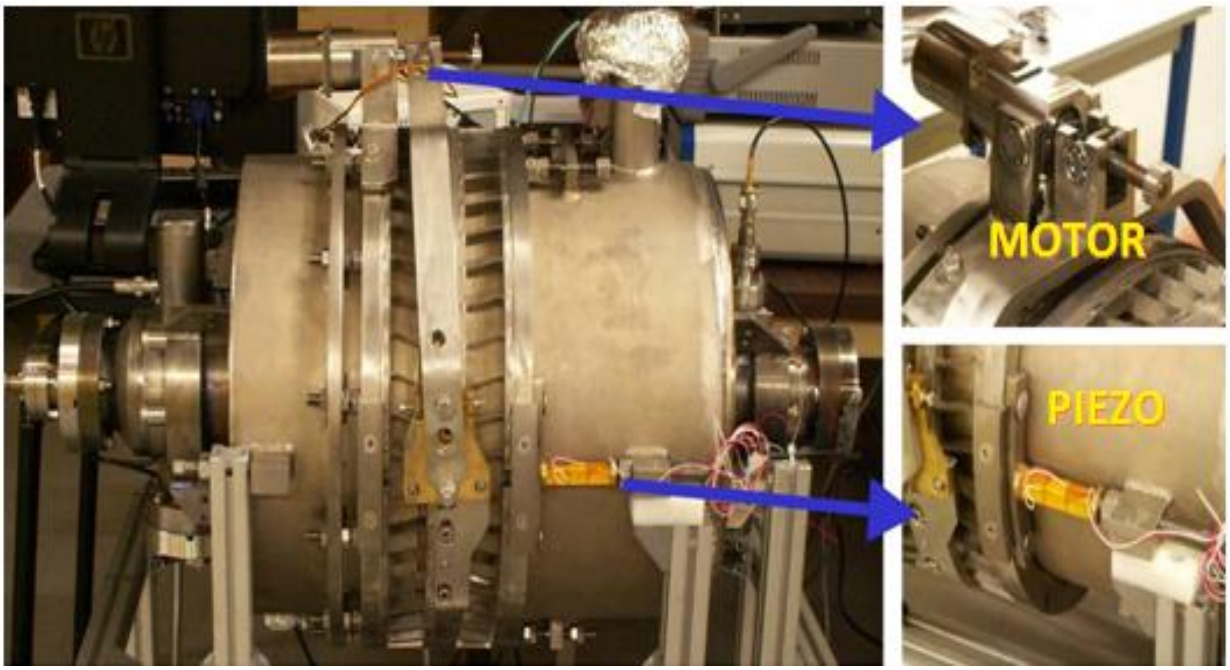

Figure 62. Cold Tuning System for the elliptical cavity [17]

4.5 CONTROL CHALLENGES FOR THE FTS

Reviewing the strategy for the cavity control, two independent control systems, one for the LLRF loop, and another for the FT loop will operate the cavity. As previously commented this thesis will focus mainly in developments made for the FTS of the FT loop. Therefore, in the following the main control challenges related to this loop are presented.

Frequency tuning loop's main control challenges

The FT loop is a vital part of the acceleration structure. As already commented precise control of the cavity detuning can significantly reduce the RF power consumption, which is about 30% of the total amount of energy foreseen for the accelerators operation. This issue has dragged the attention of researchers and several works, i.e. [10]–[17], have focused on developing different control strategies and systems in order to achieve a suitable control solution.

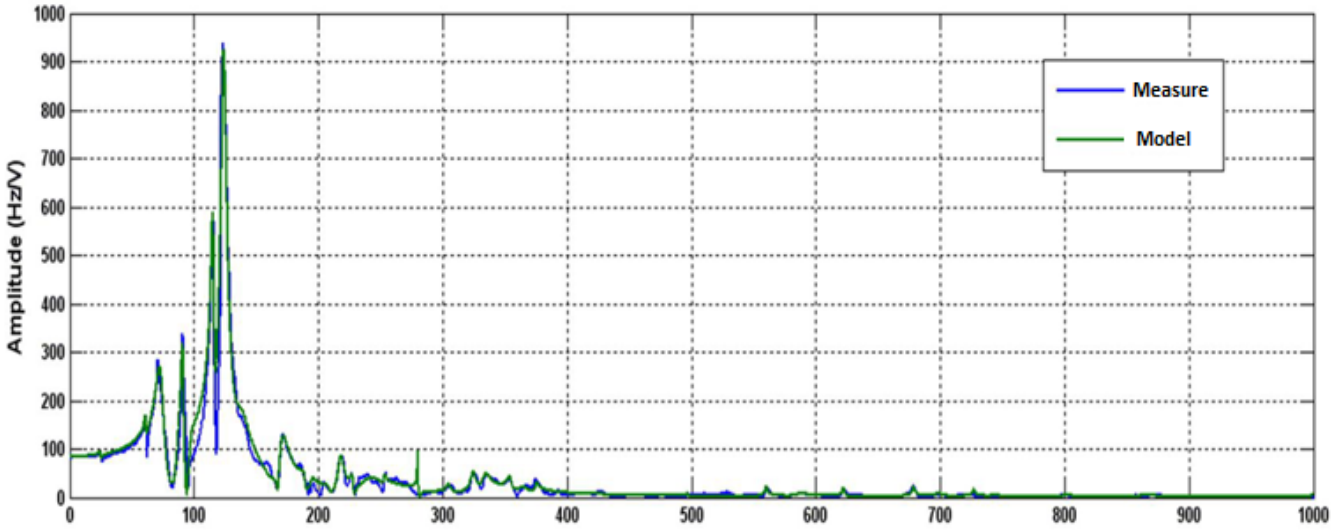

Figure 63. Cavity´s detuning produced by sinusoidal excitations [17]

However, due the control complexity of the FT loop no control solution has yet obtained general recognition from the accelerator community as an acceptably reliable technique for robust implementation of FTSs. The complexity of the FT loop, for which a strategy of choice has not been currently found, is based on the following control challenges:

1) **Dynamics of the cavity resonance frequency** - When driven by piezoelectric actuators, the CTS can excite some mechanical vibrating modes of the cavity. The dynamic response of the 704.4 MHz 5-cell elliptical resonance frequency detuning when excited by the piezoelectric actuator was measured and modelled [17]. Figure 56 shows (in blue) the cavity's detuning produced by a sinusoidal excitation with 1 V amplitude on the piezos and frequencies varying from 0 to 1000 Hz. These measurements aimed at evaluating the vibrating mechanical modes of the cavity and to model (green curve on Figure 56) the transfer function of the CTS acting on the cavity resonance frequency.

   Regarding this figure it may be seen that the cavity presents a high number of mechanical resonant modes with different resonant magnitudes. These resonant modes can be excited by the piezoelectric actuator movement or by external vibrations which might also excite other modes in an unknown manner, producing strong perturbations on the cavity detuning.

2) **Time Constrains.** Although these are not as strict as for the LLRF loop control system, the FTS control period should be in the range of a few ms to obtain an adequate control performance.

3) **Significant delay.** There exists a pure time delay (≈1ms) between the control actions applied to the piezoelectric actuator and the dynamic response that they cause on the frequency detuning. This delay is due to the piezo's movement transmission across the mechanical system.

4) **Lorentz forces.** High variations of the RF field inside the cavity will induce forces in the cavity walls that will slightly deform them. However small, these deformations will cause significant variations in the cavity frequency detuning.

5) **Microphonic perturbations.** Produced by environmental noise or other vibrations, i.e. pumps operation or seismic activity, which may cause drifts from the optimal cavity detuning and excite the resonant modes deteriorating the control performance.

6) **Uncertainty in the cavity´s operation**. The time-varying environment (microphonics, Lorentz forces, beam intensity, etc.) will not only tend to deviate the cavity´s critical variables from their set points, but also will change the dynamics or cause-effect relationship of cavity´s processes.

In order to address the control challenges here considered for the FTS an Optimized Adaptive Control System has been developed and tested on a CNRS simulation of the 704.4 MHz elliptical SC cavity [17] and its performance has been compared to that of previously proposed [10] – [14] PID-based control systems as the following sections present.

Some of the most successful advanced control systems based on PIDs reviewed in the following section will be taken as a reference for comparison with the Optimized Adaptive Control System object of the study here presented.

CHAPTER V:

PID CONTROL APPROACHES FOR THE FREQUENCY TUNING SYSTEMS

5.1 ADVANCED PID BASED SYSTEMS

Different control system designs for the FTS rely on PID controllers, but enhance their performance with advanced control techniques, or just propose these techniques to be used with ad-hoc controllers. Among this kind of approaches, an adaptive feedforward technique has been proposed [10] – [14] in which a reference signal attempts to compensate for periodic perturbations previously recorded in the facility. This reference signal is processed, prior to its application to the cavity, by an inverse adaptive model of the cavity obtained with techniques such as the LMS method. The main limitation of this kind of approach was related to the lack of capacity of PID controllers to achieve the desired level of disturbance attenuation, since their controller gains are limited by stability requirements.

Recently, a feedback alternative using a series of bandpass filters operating in parallel with a PID controller to enhance compensation at determined critical frequencies was proposed in [15] – [18]. This bandpass filters technique, has yielded good results which shall be considered as a reference in the following.

5.2 THE USE OF CHEBYSHEV FILTERS

The original implementation of this latest approach [15] considered Chebyshev type II bandpass filters acting in parallel with a PID controller in order to compensate for persistent microphonics. Phase shifters were added [16], [17] in series with the filters enabling the adjustment of filter delay in order to enhance microphonic compensation. This last approach is represented in the block diagram of Figure 64.

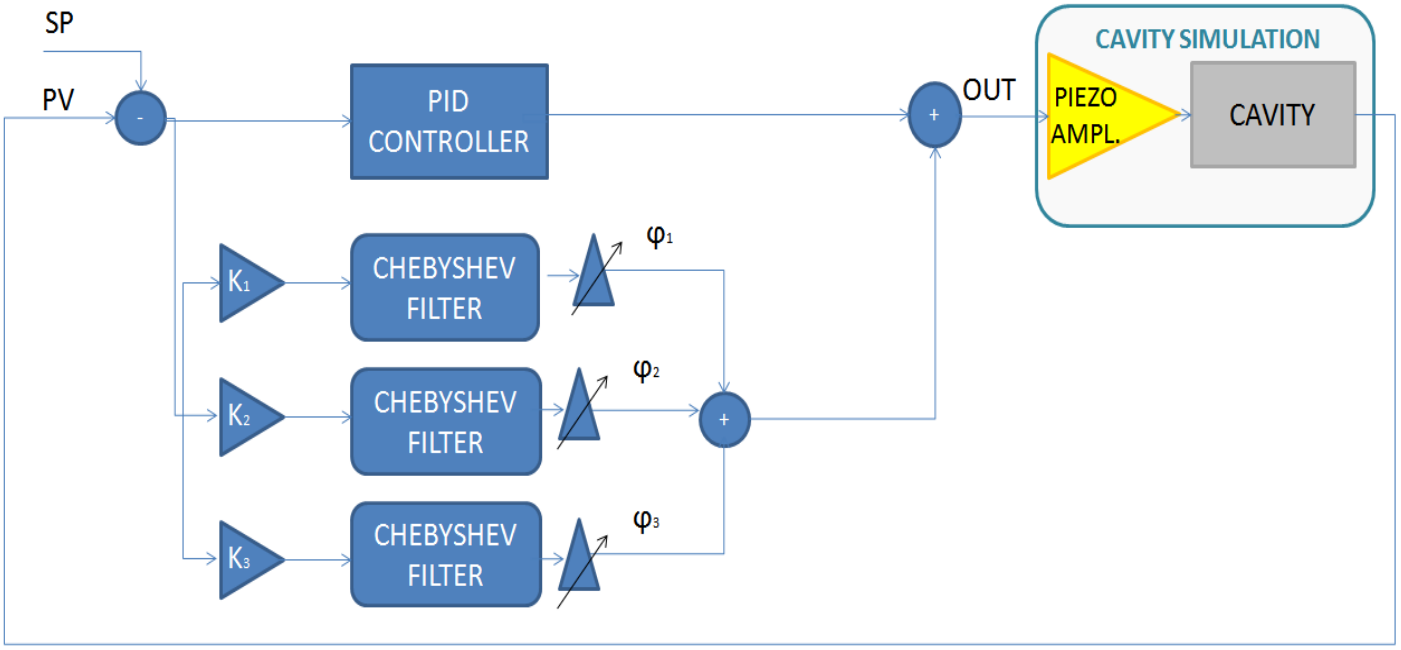

Figure 64. Block diagram of an advanced PID-based system

In the control system represented in Figure 64 several filters can work in parallel with the PID controller being fed by the error signal computed as the difference between the process variable (PV), which is the cavity's resonant frequency, and its setpoint (SP). Gains K_i and phase shifts φ_i, where i is the number of the filter, are placed in series with the filters. These parameters have been considered separately given the importance of their tuning to

the control system's performance. Under this scheme bandpass filters act as a feedback mechanism that, prior to applying the error signal to the process, isolates the microphonic frequency. These signals corrected by the filters can be tuned to maximize microphonics compensation by modifying the phases (φ_i) and the gains (K_i). [16] and [17] considered fourth order Chebyshev type II bandpass filters represented by the following equation:

$$\begin{aligned} y(k) = {} & a_1 y(k-1) + a_2 y(k-2) + a_3 y(k-3) + a_4 y(k-4) + b_0 u(k) + b_1 u(k-1) \\ & + b_2 u(k-2) + b_3 u(k-3) \\ & + b_4 u(k-4) \end{aligned} \quad (5.1)$$

where u(k) is the original signal before filtering sampled at time k and a_i and b_i are the filters coefficients and y(k) is the signal after filtering.

The coefficients shown in Table 6 define the Chebyshev type II bandpass filter designed for a frequency of 71 Hz with a sampling time of 2s. At this frequency a microphonic perturbation has been implemented in the simulation and the filter here considered has been used to obtain the simulation results presented in Chapter 8.

Coeffs. Cheby Type II	Value	Coeffs. Cheby Type II	Value
a_1	3.98214754	b_0	0.00999999
a_2	-5.96237521	b_1	-0.03984043
a_3	3.97816630	b_2	0.05968248
a_4	-0.99800146	b_3	-0.03984238
		b_4	0.01000097

Table 6. Chebyshev type II filter's coefficients for 71 Hz for a sampling time of 2 μs.

The recursive filter (5.1) with the coefficients defined in Table 6 corresponds to the following discrete transfer function for a sample time of 2μs:

$$C(z) = \frac{0.0099999z^4 - 0.0398404z^3 + 0.0596824z^2 - 0.0398423z + 0.01000097}{z^4 - 3.98214754z^3 + 5.96237521z^2 - 3.9781663z + 0.99800146} \quad (5.2)$$

Figure 65 shows the classical shape of the step response of a Chebyshev filter, in this case the one determined by (5.2).

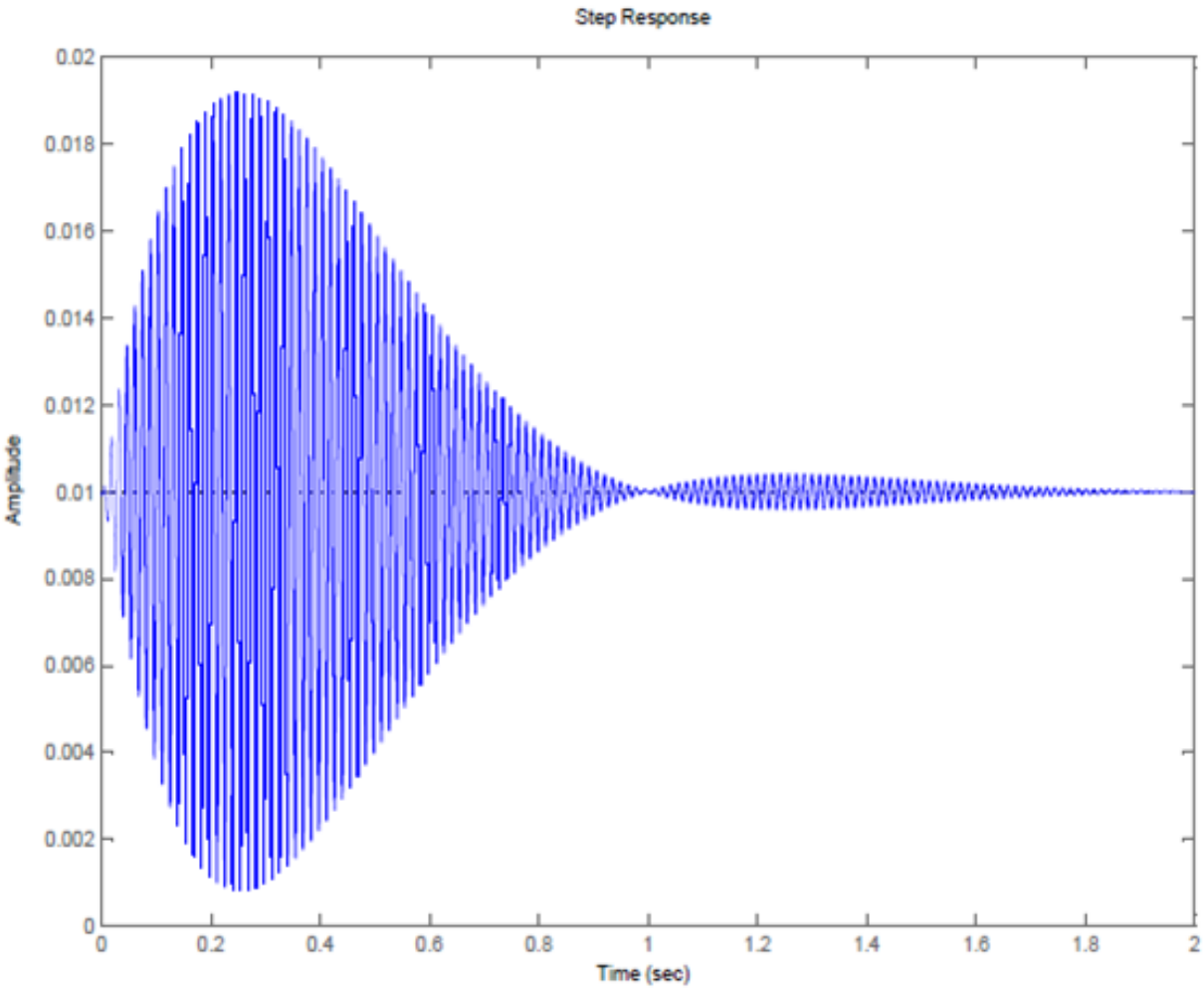

Figure 65. Step filtered with a Chebyshev filter designed for 71 Hz. The filtered step response is a sinusoidal wave of 71 Hz whose amplitude depends on the magnitude of this harmonic component in the step.

The figure shows a sinusoidal wave of 71 Hz whose amplitude depends on the magnitude of this harmonic component on the filtered signal (in this case a step). The computed Bode diagram of this filter is shown in Figure 66.

The Bode diagram of Figure 66 shows the magnitude of attenuation and the phase shift caused by the filter in the harmonic components of the incoming signal as a function of their frequency. The figure shows that for 71 Hz, there is no attenuation (0 dB) while for the rest of

the frequencies there is considerable attenuation. In this manner Chebyshev filters separate their design frequency from the rest of the signal.

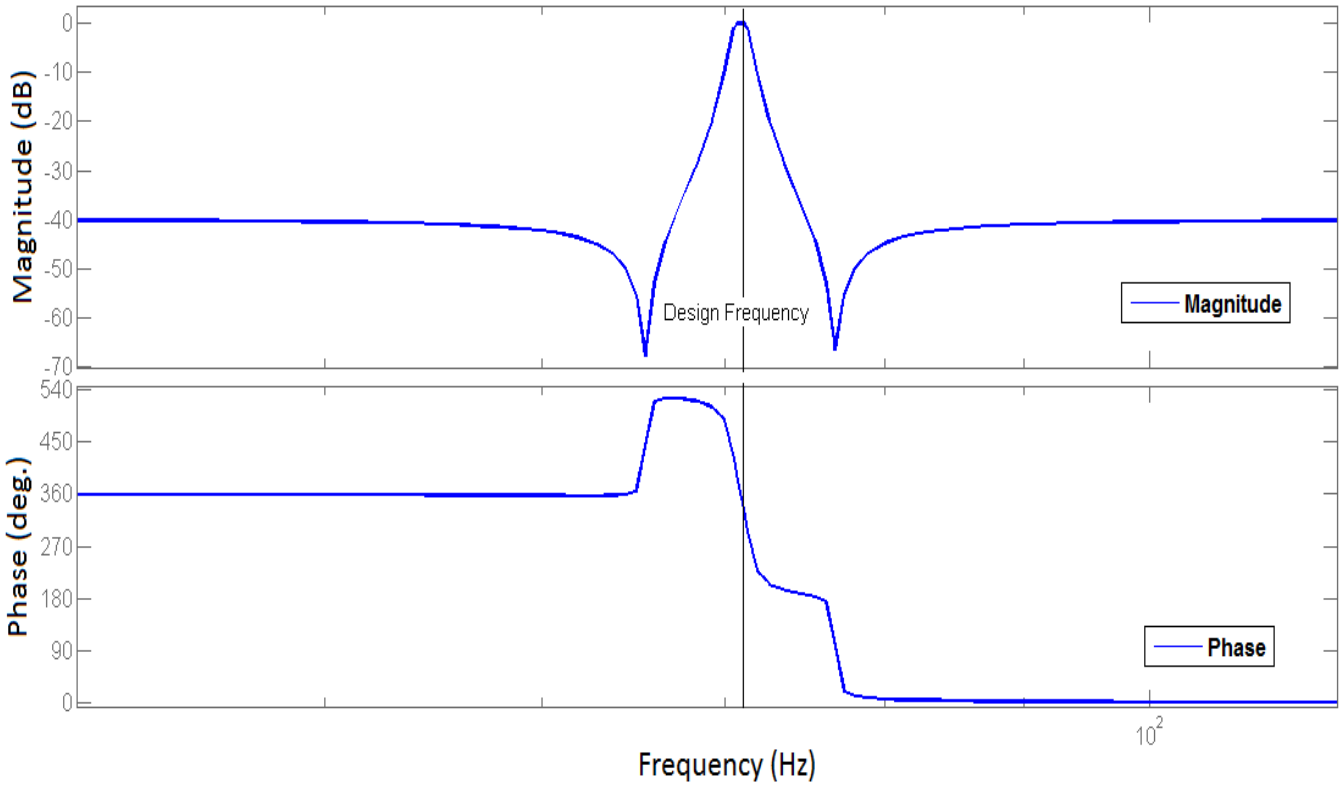

Figure 66. Bode diagram of a Chebyshev type II filter designed for a 71 Hz frequency.

Chebyshev filter performance has been described in [15] and they appear to be an appropriate tool for the compensation of microphonics which cause sinusoidal drifts at a determined frequency in the cavity's detuning. Nevertheless, these kinds of filter have been conceived for microphonic perturbations which occur in a certain scenario, this means at a given moment, in a particular facility and with a particular setup. However, the way in which microphonic perturbations alters the cavity detuning will depend and change according to random factors such as the equipment (pumps, motors, etc) in the facility or the transports surrounding it. Thus, the performance of this type of filter when facing the uncertainties of a continuous operating facility such as MYRRHA, in which operating circumstances will change throughout the years while filter parameters remain unchanged, may deteriorate.

The research works performed in this thesis intend to enhance the performance of the existing FTSs reported in literature so far, and that have been commented at the beginning of

this chapter, by applying the modern Adaptive Predictive Expert control (ADEX) methodology to the FT loop. Based on said ADEX methodology, an Optimized Adaptive Control System (OACS) has been developed and tested, first in simulation, and afterwards on the real prototypical setups. The next chapter reviews the main features of the family of Optimized Adaptive Control Systems (OACS) and therefore of the OACS developed for the FTS and presented in this thesis.

CHAPTER VI:

OVERVIEW OF OPTIMIZED ADAPTIVE CONTROL SYSTEMS

A state of the art analysis of industrial control methodologies would report that the main tool currently used to control process variables is the PID controller. It could also report that PID controllers require a manual adjustment, which is tedious and consumes start-up time, and that their performance is sometimes satisfactory but in many other cases it is not. Consequently there are, at this moment, plenty of industrial processes being controlled manually by a human operator.

Lack of effectiveness of PID in certain processes or operational scenarios brought forth the development of advanced control techniques of which Model Predictive Control (MPC) is the most popular. Nowadays, advanced control systems are expensive solutions sold worldwide by well-known brands. These systems require a highly specialized staff to build a model of the plant and then use this model to perform control. This kind of systems often work satisfactorily, but when the plant dynamics gradually varies, due to changing operating

conditions, aging of the facility, instrumentation renewal, etc, the dynamics of the model starts to differ from the real dynamics of the plant and the performance of the system deteriorates. Consequently, many plant owners demand themselves if these investments are worthwhile.

Therefore the state of the art of industrial control systems can be summarized by stating that industry plant operators and owners are demanding a control solution (requiring no manual and tedious adjustment) capable of guiding the process variables to their setpoints with stability and precision along desired trajectories in a permanent manner. Modern Optimized Adaptive Control Systems (OACS) were conceived to respond to these demands and are currently spreading through numerous industries with successful results [21] – [24].

In the following subsection a historical overview of the evolution of control systems starting in the second half of last century is presented, and will serve as an introduction to the Adaptive Predictive Control (APC) methodology. The latest evolution of APC, Adaptive Predictive Expert (ADEX) control, will be presented afterwards. Finally, the current status of the development of OACS based on ADEX control will be reviewed.

6.1 HISTORICAL EVOLUTION OF CONTROL METHODOLOGIES

This section gives a brief historical review of the technological evolution of process control in order to guide the reader towards the development of the latest control methodologies which are spreading through industry.

- Manual control:

Before the advent of automation and electronics, industrial process control was carried out manually by operators who took measurements and made the necessary adjustments by hand. Furnace control, for example, required operators to measure temperature and adjust heating levels manually. When the temperature was too high the operator would turn down the heating or vice versa. The operator often gained an intuition about the changing dynamics of the process under his control and was able to make adjustments through intimate knowledge gained over years of experience, but, basically, he reacted to the error already produced.

- Automation and PID control:

At the beginning of the fifties of the last century, with the advent of electronics, automation became possible, and PID (Proportional, Integral and Derivative) controllers came into industrial use reducing the need for full time operator attention and have become the standard tool for industrial process control. These controllers invoked PID control actions based on the error between the “set point”, permanent value desired for the variable under control, and actual measurements of this variable. Thus, PID controllers react to the error already produced (known as “negative feedback”) just as human operators did under manual control.

As industrial processes usually behave according to an unknown, complex and time-varying cause-effect relationship, PID control applications require in many cases a lengthy manual “tuning” procedure and often the performance of the controller is less than satisfactory. Thus, although PID controllers are currently the standard automatic tool used for process control, there exists a gap which these controllers have been unable to cover for many years.

- Expert systems:

The attempt to overcome the gap left by PID controllers, led to the development of Expert systems which emulated the expertise of the skilled operator by applying rules to control processes. They were ad hoc systems, difficult to develop and maintain, and vulnerable to changes in process dynamics. They were therefore of limited success in industrial process control.

- Advanced control systems:

In control theory, advanced process control refers to a broad range of techniques and technologies. Advanced process control is usually deployed optionally and in addition to basic (PID) process control. Basic process control is designed and built with the process itself, to facilitate basic operation, control and automation requirements. Advanced process control is typically added subsequently, to address particular performance or economic improvement opportunities in the process.

Within the context of advanced control systems a patent application filed in 1976 introduced the methodology of APC [25], which included the innovative principle of predictive control, also called Model Predictive Control (MPC). MPC makes the predicted process output equal to the desired process output and uses a model for predictions, which may or may not be “adapted” (adjusted in real time).

The following subsection is devoted to advanced control methods studied before the introduction of APC and that where the origin of modern Optimized Adaptive Control Systems.

6.2 BACKGROUND TO OPTIMIZED ADAPTIVE CONTROL

Optimized Adaptive Control considers methods relying on a predictive model of the plant, whose parameters are adjusted in real time by an adaptive mechanism in such a way that the prediction error converges towards zero. Additionally, this predictive model is used at every control instant to derive a desired future process output trajectory by minimizing an index that is chosen according to a performance criterion.

Development of optimized adaptive control had as background the stability approach used previously by Model Reference Adaptive Systems (MRAS). The following subsections reviews this background upon which Adaptive Predictive Control (APC) was introduced. Later developments also belonging to the set of methods defined as Optimized Adaptive Control [27] are reviewed afterwards.

Model Reference Adaptive Systems

A significant research perspective for the design of adaptive systems has been based on stability theory [26]. Under this perspective the adaptive system had to verify certain stability conditions to perform satisfactorily. The performance criterion was established by means of a reference model with desired dynamics.

In this context, the objective of the adaptive system operation was to reduce the error between the process output and a model reference output. In the ideal case, if the adaptive system was designed to be asymptotically stable, the previously mentioned error will tend

asymptotically towards zero. In the real case, if the adaptive system was stable, the error will remain bounded.

This kind of adaptive systems became quite popular for the research community under the name of MRAS. The state of the art of MRAS, previous to the introduction of predictive control, was presented in a famous survey paper in 1974 [72]. The basic scheme of a MRAS is presented in Figure 67.

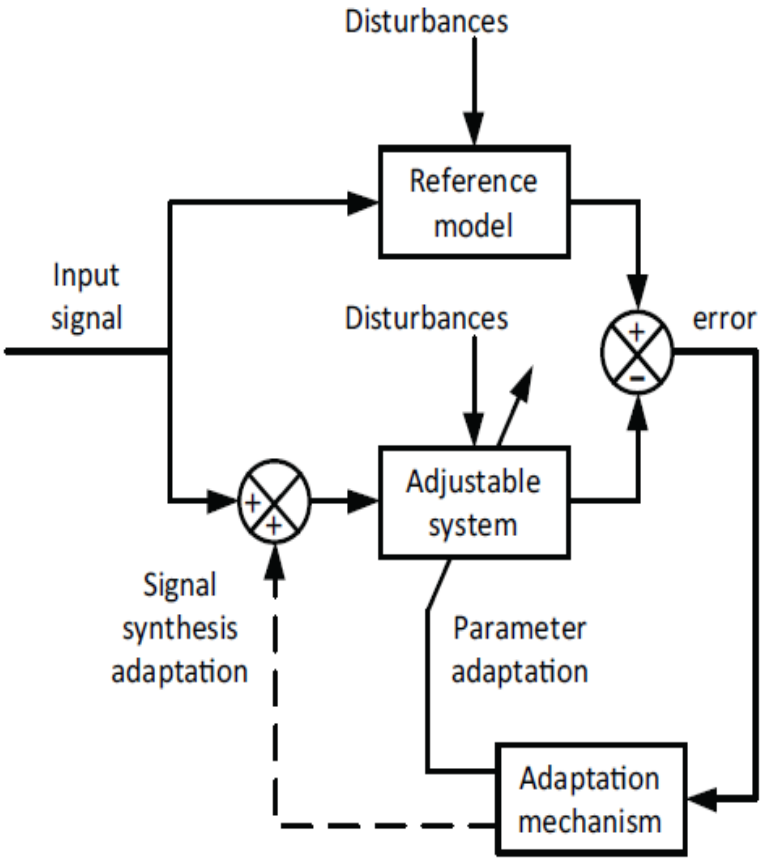

Figure 67. Block diagram of a model reference adaptive system (MRAS).

The reference model gives the desired response of the adjustable system, and the task of the adaptation is to minimize a function of the difference between the outputs, or the states, of the adjustable system and those of the reference model. This was done by the adaptation mechanism that modified the parameters of the adjustable system or generated an auxiliary input signal.

MRAS had a “dual” character in the sense that they were used for applications in the field of adaptive control systems and also for applications in the field of process identification. When used for process identification, the process played the role of reference model and the adjustable model was replaced by an adaptive model, whose parameters were adjusted by the adaptation mechanism in order to obtain a dynamic characteristic similar to those of the process.

Three different configurations of the MRAS for process identification were possible depending on the adaptive model structure: a) a “parallel” configuration, also called “output error method”, b) a “series-parallel” configuration, also known as the “equation error method” [73] – [75], and c) a “series” configuration called “the input error method”. A unified approach to the analysis and the synthesis of these different structures was presented from the stability perspective in [76] using hyperstability concepts [77]. The stability result guaranteed that, after a given time instant, the adaptation mechanism ensures that the absolute value of the error considered in Figure 67 is bounded by a limit that depends on the level of noise and perturbations acting on the process. If no noise or perturbations are involved, the error tends asymptotically towards zero.

While the synthesis of stable parallel and series MRAS for process identification required certain knowledge of the process parameters and the verification of a positivity condition [78], [79], the series-parallel structure was free of these conditions [80] and was later used on the adaptive predictive control formulation, as considered in the following.

When applied to adaptive control systems, MRAS did not consider a change in previous control strategies, but only an adaptation of the controller parameters to prevent a decrease in the global performance of the control system in the presence of changes in the process dynamics. Thus, MRAS used traditional negative feedback methodology as the basic control strategy and adapted the controller parameters using different algorithms. This is probably one of the reasons for the lack of successful industrial control applications of these techniques. In the conclusions of [72] it is written: “The growth of applications of MRAS will be determined in part by new improvements of the design methods and the development of implementation techniques”.

6.3 THE INTRODUCTION OF ADAPTIVE PREDICTIVE CONTROL

Predictive Control: Origin and Basic Concepts

The methodology of predictive control was introduced in 1974 in a doctoral thesis [81]. Subsequently, the original basic principle was formally defined in a US patent [25] and presented in [82]. This principle may be expressed in the following way: 'Based on a model of the process, predictive control is the one that makes the predicted process dynamic output equal to a desired dynamic output conveniently predefined'. Defined in this way, predictive control is straight common sense and its objective of control has a clear physical meaning.

This predictive control strategy can be implemented through a predictive model and a driver block, as presented in the block diagram of Figure 68.

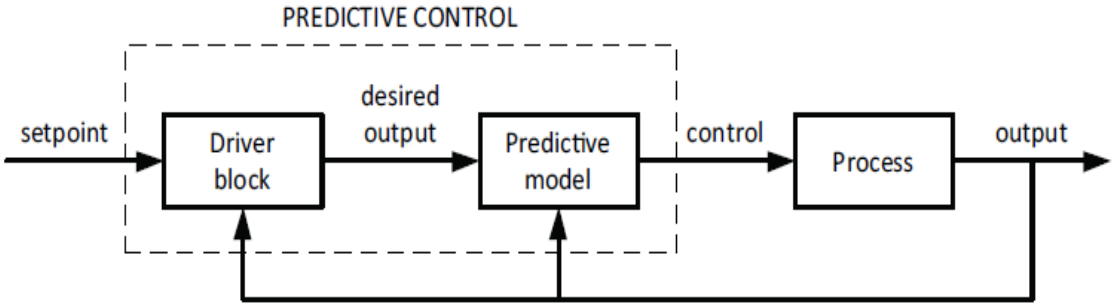

Figure 68. Block diagram of predictive control.

As already mentioned, the predictive model generates, from the previous input and output (I/O) process variables, the control signal that makes the predicted process output equal to the desired output. This will be generated by the driver block which is an essential concept in predictive control.

The original driver block design generated a desired output trajectory that, starting from the actual values of the process output, converged towards the set point following desired dynamics. This trajectory was produced at every control instant and was named projected desired trajectory (PDT). One simple way of generating it consists of using the

output of a stable model with desired dynamics, having the set point as input and the actual process outputs as initial conditions.

From the driver block operation described above, the concept of the driving desired trajectory (DDT) was derived. This is produced from the first values of each of the projected desired trajectories that are redefined at the consecutive control instants. Then, the DDT is generated point-by-point in real time and, from its values, the control action will be computed according to the predictive control principle. Consequently, this trajectory is the one which has to guide the process output to the set point in the desired way: rapidly, without oscillations and, moreover, compatible with a bounded control action.

The fact that the DDT was redefined, at each control instant, from the actual process output was a key factor to obtain satisfactory results in many practical applications, since it helped the DDT to approach a physically feasible process output trajectory. The concept of physical realizability of the DDT is of great theoretical and practical relevance and may be defined as follows: “It is said that a DDT is physically realizable if, at any control instant, it can be realized through the application of a control signal that always remains bounded”.

The driver block concept as defined in [25] was different from the previous MRAS reference model concept, where the reference model output was generated from previous model reference outputs without redefinition. Also, it distinguished predictive control from the minimum variance control strategy of previous self-tuning controllers [83], [84].

The original formulation of predictive control considered only a single step prediction for the computation of the control action and the driver block design did not use the information available from the process dynamics in the predictive model. This way of applying predictive control is known as the basic strategy of predictive control. Although successful in many practical applications in the context of adaptive control, it had important limitations that will be considered later.

The need for adaptation

It is not generally reasonable to expect excellent performance of predictive control in an industrial context, mainly due to the unknown and time-varying nature of industrial process

dynamics. Obviously, when the predictions are not satisfactory due to 'unadjusted' model parameters, it would be convenient to have an adaptation mechanism able to adjust the parameters of the predictive model in order to reduce the prediction error towards zero.

Accordingly, predictive control was already introduced in the framework of adaptive predictive control (APC) [81], [25], [82], by combining the predictive control system with an adaptive system as represented by Figure 69. It can be observed that the right half of this figure represents an adaptive system similar to those used for process identification within the MRAS context.

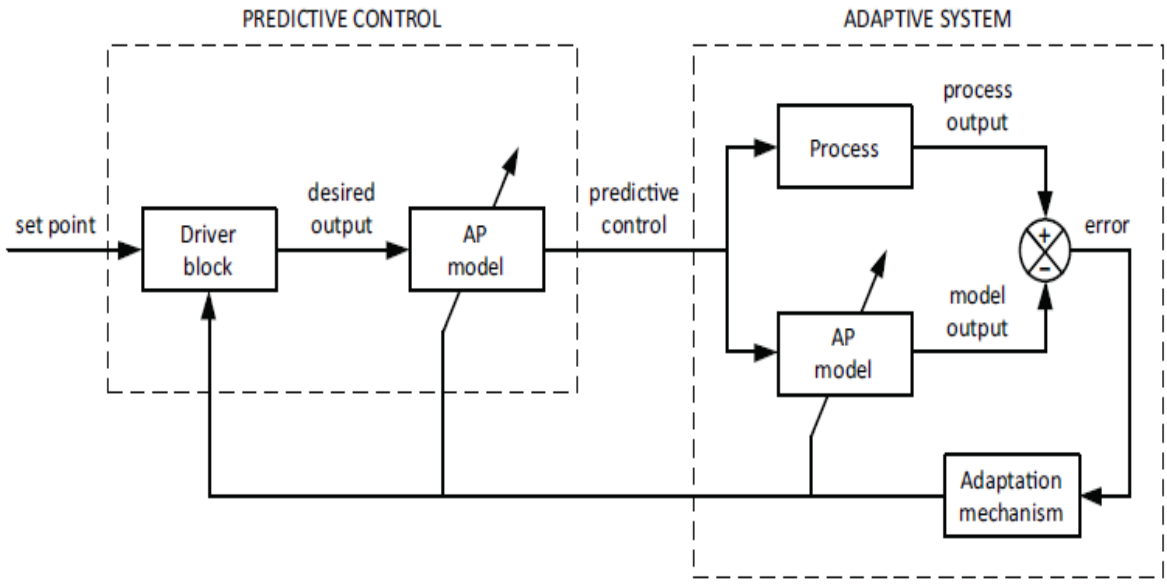

Figure 69. Block diagram of an adaptive predictive control system.

Since the knowledge gained in the adaptive system from the process dynamics should be immediately used for prediction in the predictive scheme, in both cases the same adaptive-predictive (AP) model should be used. Thus, an AP model with a series-parallel structure performs the following two roles:

1. Within the adaptive system, the AP model receives the same input signal as the process and generates the model output that, compared with the process output, allows the adaptation mechanism to adjust its parameters in order to obtain a stability result in the sense previously considered in MRAS.

2. Within the predictive part of the scheme, the AP model calculates the control signal from the desired output generated by the driver block. This computation, carried out according to the predictive control principle, renders the desired output equal to the predicted process output.

Consequently, when the adaptation mechanism makes the difference between the process and the model outputs tend towards zero, the difference between the process output and the desired output also tends towards zero. In this way global stability of the adaptive predictive control system can be achieved under an appropriate driver block design.

Thus, adaptive predictive control was introduced with a perspective of stability similar to that considered in the context of MRAS, but extended to the closed loop APC system, unifying the global stability result with the desired control system performance. In fact at the same time that the methodology was formally presented in [25], a first analysis of stability was published [82].

Basic implementation of APC

This section presents a general description of the original formulation of APC, by assigning to the different blocks in Figure 69 equations that conceptually rule their operation, without going into the detail of the practical implementation which will be seen in the next Chapter of this thesis report.

The dynamics of the generic process considered in Figure 69 can be described by multi-input, multi-output (MIMO) difference equations of the form:

$$Y(k) = \sum_{i=1}^{h} A_i(k)Y(k-i-r) + \sum_{i=1}^{f} B_i(k)U(k-i-r) + \sum_{i=1}^{g} C_i(k)W(k-i-r) + \Delta(k) \quad (6.1)$$

where $Y(k-i-r)$, $U(k-i-r)$ and $W(k-i-r)$ are, respectively, the increments at time $k-i-r$ of the measured output, input and measurable disturbance vectors of the process

with respect to its steady state values. $A_i(k)$, $B_i(k)$ and $C_i(k)$ are time variant matrices of appropriate dimensions which determine the most significant dynamics of the process. $\Delta(k)$ is the perturbation vector, where measurement noises, non-measurable perturbations and other process dynamics are considered, and r represents the pure process time delay.

The AP model used in the adaptive system of Figure 69 calculates an *a priori* estimation of the process output $Y(k)$ as follows:

$$\hat{Y}(k|k-1) = \sum_{i=1}^{h} \hat{A}_i(k-1)Y(k-i-r) + \sum_{i=1}^{f} \hat{B}_i(k-1)U(k-i-r) + \sum_{i=1}^{g} \hat{C}_i(k-1)W(k-i-r) \quad (6.2)$$

The adaptation mechanism uses the error of the a priori estimation, $Y(k) - \hat{Y}(k|k-1)$, to adjust the AP model parameter matrices $\hat{A}_i$, $\hat{B}_i$ and $\hat{C}_i$, at each control time k, according to the previously considered stability perspective.

It may be observed that the AP model of (6.2) is, in the context of the adaptive system, a series-parallel model [80] that produces the model output from the previous process outputs. A parallel model would have produced the model output from the previous model outputs [82]. This kind of series-parallel model was chosen in the formulation of APC because of two reasons:

a) The desired stability result for the adaptive system was obtained by means of a rather simple adaptive mechanism that reduced the estimation error in the gradient direction [75], and

b) It makes the computation of the predicted process output and of the predictive control signal straightforward, as considered in the following.

The previously considered AP model is also used to predict, at time k, the process output for time $k + r + 1$ as follows:

$$\hat{Y}(k+r+1|k) =$$

$$= \sum_{i=1}^{h} \hat{A}_i(k) Y(k-i+1) + \sum_{i=2}^{f} \hat{B}_i(k) U(k-i+1)$$

$$+ \sum_{i=1}^{g} \hat{C}_i(k) W(k-i+1) \qquad (6.3)$$

From the above prediction, the basic strategy of predictive control computed the control vector that renders the predicted output $\hat{Y}(k+r+1|k)$ equal to the desired output $Y_d(k+r+1)$ by means of

$$\mathrm{U(k)} = \hat{B}_1(k)^{-1} Y_d(k+r+1)$$

$$- \hat{B}_1(k)^{-1} \left[\sum_{i=1}^{h} \hat{A}_i(k) \hat{Y}(k-i+1) + \sum_{i=2}^{f} \hat{B}_i(k) \hat{U}(k-i+1) \right.$$

$$\left. + \sum_{i=1}^{g} \hat{C}_i(k) W(k-i+1) \right] \qquad (6.4)$$

where the desired output $Y_d(k+r+1)$ is computed by the driver block at time k as follows:

$$Y_d(k+r+1) = \sum_{i=1}^{t} F_i(k) Y(k-i+1) + \sum_{i=1}^{s} H_i(k) Y_{SP}(k-i+1) \qquad (6.5)$$

where $Y_{SP}(k-i+1)$ represents the value of the set point vector at time $k-i+1$, and matrices F_i and H_i are chosen to take into account the desired dynamics.

The basic implementation of APC presented in [25] and previously considered, was described with particular emphasis on its practical issues in [85], where a successful application to the multivariable control of a distillation column was presented.

Block diagram

The diagram in Figure 69 can be simplified to the one shown in Figure 70, which is the diagram generally used to represent the APC methodology. The functional description of the blocks in this diagram may be summarized as follows:

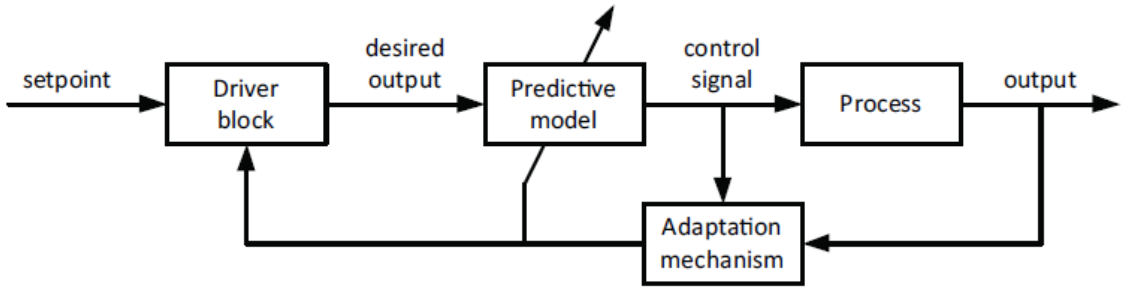

Figure 70. Simplified block diagram of the adaptive predictive control system.

- The driver block. Generates the DDT that will guide the process output to the set point in an "optimal" way.

- The predictive model. Calculates the control signal that ensures that the predicted process output follows the desired trajectory generated by the driver block.

- The adaptation mechanism. Adjusts the predictive model parameters from the prediction errors in order to make these errors tend towards zero efficiently. Likewise, it informs the driver block of the deviation of the process output with respect to the desired trajectory. In this way, the driver block can redefine the desired trajectory from the actual process output.

After the introduction of the basic adaptive predictive control concepts, considerable research effort was devoted to the development of:

a) Adaptive mechanisms in different operating contexts for adjusting the AP model parameters in real time in such a way that the prediction error is reduced toward zero according to various criteria, and

b) Predictive control strategies to derive optimal desired future process output trajectories at every control instant a receding prediction horizon verifying various performance criteria.

This research effort gave rise to the industrial optimized adaptive control techniques that are considered in the next sections.

6.4 OPTIMIZED ADAPTIVE CONTROL FROM THE STABILITY PERSPECTIVE

This section recalls firstly the stability results that led to the development of the body of APC stability theory which supports optimized adaptive control systems designed from the stability perspective. Next, starting from conditions for the driver block and the adaptive mechanism that can guarantee the desired stability result, it describes the syntheses of the driver block and adaptive mechanism, and interprets the results obtained from an intuitive perspective. Finally, it recalls the steps involved in the development and validation of standard systems for the optimized adaptive control of industrial plants and the applications carried out by a first generation of these kinds of systems.

Stability Results for Adaptive Control

The APC principles were key factors in the proof of the existence of simple, globally convergent adaptive control algorithms for discrete systems. The main results of the progress made towards the creation of the body of APC stability theory that supports industrial application, is considered in the following, taking into account both the various subjects.

- Stable-Inverse Processes

The first analysis of stability for an adaptive predictive control algorithm [82] was based on the convergence properties of the a posteriori estimation error and the AP model parameters of a stable adaptive system, under the assumption of a bounded desired output. These conditions were sufficient to prove stability of the APC closed loop in the case of a first order process, but the extension of the stability result to a more general order required a restrictive assumption on the stable-inverse nature of the process [86].

Since the convergence result on the prediction or control error in [82] was valid for a more general order in spite of the unstable-inverse nature of the process, in order to overcome the considered restriction in the global proof of stability, it was suggested in [87] a new driver block design capable of generating a desired output trajectory physically realizable by a bounded control signal for the kind of unstable-inverse processes. The suggested driver block design was formally introduced in a patent application [88] and defined the so called extended strategy of predictive control.

The restrictive assumption on the stable inverse nature of the process was introduced in [89], where the challenging proof of stability, for the same adaptive predictive control algorithm considered in [82], was rigorously obtained for discrete deterministic systems. Analogous global stability results were also obtained for continuous systems [90], [91] and hybrid systems [92].

- Stochastic Processes

Once the above results were known, interest in the analysis of stability focused on the stochastic aspects of a system. Some stability results in the discrete stochastic case required that the disturbance acting on the system verified the statistical properties of a moving average of independent zero mean random variables [93]. In practice such conditions were generally very restrictive. Less restrictive assumptions led to the stability analysis in the presence of bounded disturbances. Results derived for this case [94] suffer from certain restrictions on the a priori estimate of the process parameters, and the proof of stability is technically very involved. Shorter proofs of analogous stability results were obtained for continuous [95] and discrete [96] systems, but these proofs also suffer from a condition on the a priori estimate of a process parameter. All of these results [94] - [96] used as a main argument in their proofs, the boundedness of the rate of growth in the system signal.

Global stability results for a general class of time-invariant stable-inverse in the presence of bounded noises and disturbances were presented in [97], [98]. These results proved the minimization of the control error and, unlike earlier results, did not depend on any previous estimation of the process parameters nor use the argument of a limited divergence rate for the system signals. It is interesting to note that the proof introduces a criterion for

continuing or stopping parameter adaptation and is derived directly from the same conditions considered in [82], plus the assumption of inverse stability.

- Unstable-Inverse Processes

All the previous stability results assumed the process to have a stable-inverse and to be time-invariant. Global convergence for deterministic continuous systems not requiring inverse stability was reported in [99], but this is conditional on convergence of the estimated parameters to their true values. Local stability results for non-minimum-phase discrete systems [100] were based on adaptive pole assignment algorithms, but required a priori knowledge of initial parameter estimates.

The stability of the extended strategy of predictive control, under some specific choices of driver block design, was proved in [101], although the complete proof of stability, including the adaptive mechanism, was not considered. Global stability results, also based on adaptive pole-assignment, were reported in [102] but they required a persistency-of-excitation condition.

- Time-Variant Processes

The stability of algorithms designed for the time-invariant case [103] was analyzed in the time variant case as a preliminary result of convergence. Other studies analyzed the robustness of adaptive schemes where external exciting signals help to keep the parameter estimates close to the true process parameters [104]. Also the performance of previous algorithms [93], developed for the time-invariant case, were analyzed as applied to systems with converging martingale parameters [105] and exponentially convergent parameters [106].

Conditions for the design of globally stable APC in the multivariable stochastic time-variant case were established in [107]. These conditions are quite general, in the sense that the only restrictive assumption on the process equation is its stable-inverse nature, and basically rely on assumed convergence properties of the estimation system. Therefore, research into stability proofs in the time-variant case may, using this approach, proceed to consider different models of the process, for which estimation systems that satisfy the required convergence properties exist or may be derived.

It is clear that restrictive assumptions on the considered models of the process are necessary [108].A methodology used to derive the required properties of the estimation system is also presented in [107] and is based on a theorem closely related to hyperstability [109] and input-output passivity theories [110].

- Unmodeled Plant Dynamics

The stability problem related to the model-process order mismatch in the control scheme was illustrated in [111], where it was demonstrated that straightforward application of stable algorithms found in the literature may lead to instability when said mismatch is present. Stability results reported in the presence of unmodeled dynamics, [112] and [113], are based on the following assumptions: i) the a priori knowledge or existence of a tuned set of controller parameters that guarantee the stability result and ii) the modeling error is relatively bounded. Also, the results in [113] required of an additional projection in the adaptive law.

A generalization of previous stability analysis for APC is combined in [114] with a normalized parameter estimation system to prove global stability for stable-inverse processes in the presence of bounded disturbances and unmodeled dynamics. The generalization of the stability analysis states a single condition for stability in terms of convergence properties of the a posteriori estimation error and the AP model parameters. The normalized parameter estimation system allows a formal proof that the modeling errors can be treated as a bounded disturbance. Thus, the on/off mechanism considered in [97], [98] is valid and the normalized estimation system verifies the convergence properties that guarantee global stability.

The results presented in [114] prove that the control system converges to a tuned set of parameters and guarantees stability without the need for any assumption on the knowledge or existence of such a tuned set, neither the assumption of a relatively bounded modeling error nor the need of an additional projection in the adaptive law. However, it shows that there is a stability limit in the process-model mismatch that depends on the process dynamics itself.

- APC Stability Theory

The stability results presented in [26] encompass, unify and generalize all the previous stability results on APC and form a theoretical body of stability both in the context of predictive control and APC. This body of stability theory considers three different class of processes taking into account their stability nature:

(1) Processes of a linear and stable-inverse nature;

(2) Processes of a linear and stable nature; and

(3) Unstable processes with an unstable inverse.

All of them are represented by autoregressive-moving average with exogenous terms (ARMAX) type equations with time-varying parameters, including a term for unmeasured perturbations, and are characterized for verifying input/output properties previously derived for the same kind of linear processes in the case of constant parameters. Process class (1) and (2) can describe the dynamic behavior of almost the entire set of industrial processes.

Class (3) was included for the sake of completion of the theoretical analysis. For each of these process classes, a stability condition was established related to the boundedness and/or physical realizability of the driving desired trajectory (DDT). In the first class, where the process inverse is stable, the corresponding condition (DDT boundedness) may easily be satisfied using the basic or the extended strategy of predictive control in the driver block. In the second class, where the process inverse may be unstable, the satisfaction of the condition (DDT physical realizability) requires in practice the use of the extended strategy. These conditions unified the analysis performed for each class of processes, and gave general validity to the stability results derived, irrespective of the specific driver block design used.

The general global stability results obtained in this context rely only on convergence properties of the a posteriori estimation error and of the AP model parameters of a stable adaptive system, similar to those already considered in [82]. These convergence properties can be reduced to a single convergence condition that has to be verified by the adaptive system. The analysis of the verification of the convergence or stability condition by the adaptive system progresses within APC stability theory from the simplest formulation (no

noises, perturbations, model-process mismatch and constant process parameters of the ideal case) to a formulation defined by hypotheses that describe an industrial environment. Thus, in addition to the ideal case, three scenarios are considered: (i) the real case with no difference in structure (no process-model mismatch and time-invariant process parameters, but presence of bounded noises and unknown perturbations); (ii) the real case with difference in structure (adds the process-model mismatch), and (iii) the time-varying parameters case.

In the context of predictive control, where there is no adaptive system, the stability result depends on a measure of the modeling error that was mathematically formulated in relation to the process dynamics. This result was intuitive and could reasonably be expected. The basic motivation for adaptive predictive control has been to overcome the stability problem due to the modeling error. In the ideal case, the expected result for APC was obtained, that is to say asymptotic stability guaranteeing that the process output converges towards the DDT with a bounded control signal.

As expected, asymptotic stability was not possible in the real case with no difference in structure due to the existence of the unknown and unpredictable perturbation vector ($\Delta(k)$). Nevertheless, the results obtained proved stability for this case in terms of the boundedness of the control or tracking error, approaching the corresponding boundary that would be obtained if the process parameters were known and used in the predictive control law.

In the real case with difference in structure, it seems logical that stability may not always be guaranteed and that there must be stability limits in terms of the model order reduction. The stability results for this case derived the mathematical formulation of these limits and their relationship with the process dynamics. When the model order reduction is compatible with these limits, APC guarantees the stability result and the control error can be minimized by appropriate selection of the adaptation mechanism. These stability limits were also analyzed in [115] and their practical consequences were illustrated by means of simulation examples.

In the case of time-varying parameters, APC adaptation mechanisms guarantees tracking of the process parameters by the AP model parameters until the stability result is

reached, which has been repeatedly confirmed by good practice in the implementation of the methodology.

The APC stability theory considered here has also been presented with minor changes in [116]. It has determined the design of the driver block and the adaptive mechanism from the perspective of stability and provides theoretical support for the industrial application of APC methodology as a whole, that is, both for predictive control and for adaptive predictive control. Those areas of theoretical analysis which are still an open subject for research were also indicated in [26], but it is important to emphasize that the results arising from the APC stability theory already developed have clear implications in a widespread practical context.

In the following, the main concepts of the APC stability theory will be reviewed and interpreted in a simple but illustrative way, and their practical implications in their application to industrial plants will be analyzed.

Stability Conditions for the Design of Adaptive Predictive Controllers

As a starting argument for the development of APC stability theory presented in [26], [116], a Conjecture formulates conditions for the design of the driver block and the adaptive mechanism that guarantee the global stability result under hypotheses that accord with an industrial environment.

In this section, we will consider these hypotheses, a description of the process and the adaptive predictive control system, and state and prove the Conjecture, using a single-input single-output (SISO) formulation and simplifying the notations. The extension of the results to the multivariable case is direct and easy.

- Conjecture Hypotheses

The Conjecture departing hypotheses are the following:

a) The process is described by linear equations with time varying parameters.

b) There exist measurement noises and unmeasurable disturbances randomly acting on the process.

c) The process and model equations may have different orders.

- Process Description

The process can be described by the following equation:

$$y(k) = \theta(k)^T \phi(k - d) + \Delta(k) \quad (6.6)$$

It may be observed that (6.6) is the SISO case of (6.1), where y(k) is the measured process output at time k, $\theta(k)$ is the process parameter vector, $\phi(k - d)$ is the regression vector that includes process input, output and measurable disturbances, d represents the process time delay that includes the discretization delay plus the pure delay, that is, $d = r + 1$, and $\Delta(k)$ is the perturbation signal that represents the effect of the unmeasured perturbations and measurement noise acting on the process.

It is interesting to note that Equation 6.6 verifies the above conjecture hypotheses (a) and (b).

- Adaptive System

In the adaptive system shown in Figure 69, the AP model can give an estimation of the process output at instant k using the AP model parameters also estimated at instant k, which will be denoted by $\hat{\theta}_r(k)$, and the signals included in the regression vector. This estimation is expressed in the form

$$\hat{y}(k|k) = \hat{\theta}_r(k)^T \phi_r(k - d) \quad (6.7)$$

The dimensions of ϕ_r and $\hat{\theta}_r$ are usually less than or equal to the dimensions of ϕ and θ. ϕ_r contains a subset of the most recent process inputs and outputs included in ϕ. These assumptions account for conjecture hypothesis (c).

The estimated parameter vector $\hat{\theta}_r$ (k) is generated by the adaptation mechanism using the information available on the process inputs and outputs up to instant k. The following notation is adopted for the estimation error, the difference between the process and model outputs:

$$e(k|k) = y(k) - \hat{y}(k|k) = y(k) - \hat{\theta}_r(k)^T \phi_r(k - d) \tag{6.8}$$

$\hat{y}(k|k)$ and $e(k|k)$ are called respectively the *a posteriori process output estimation* and the *a posteriori estimation error* because both of them are calculated after the model parameters have been adjusted at instant k. Another estimation error, extremely important in the analysis and synthesis of adaptive systems, is the *a priori estimation error*, which is defined by the equation

$$e(k|k-1) = y(k) - \hat{y}(k|k-1)$$
$$= y(k) - \hat{\theta}_r(k-1)^T \phi_r(k - d) \tag{6.9}$$

where $\hat{y}(k|k-1)$ is the a priori estimation for the process output $y(k)$ calculated from the model parameter vector adjusted at instant $k-1$, that is, $\hat{\theta}_r(k-1)$.

- Predictive Controller

The predictive model calculates the control action $u(k)$ to make the predicted output at instant $k + d$ equal to the DDT at the same instant. The predicted output can be expressed in the form

$$\hat{y}(k+d|k) = \hat{\theta}_r(k)^T \phi_r(k) \tag{6.10}$$

Denoting now the DDT as $y_d(k+d)$ and applying the principle of predictive control, it is obtained that

$$y_d(k+d) = \hat{\theta}_r(k)^T \phi_r(k) \tag{6.11}$$

This equation may also be written in the form

$$y_d(k+d) = \hat{\theta}_{r0}(k)^T \, \phi_{ro}(k) + \hat{\theta}_1(k)^T \, u(k) \tag{6.12}$$

where $\hat{\theta}_1(k)$ is the parameter included in vector $\hat{\theta}_r(k)$ in equation (6.7) that corresponds to the control signal $u(k)$ in the inner product. The predictive control law can be written from equation (6.12) in the form

$$u(k) = \frac{y_d(k\ +\ d) - \hat{\theta}_{r0}(k)^T \phi_{ro}(k)}{\hat{\theta}_1(k)^T} \tag{6.13}$$

The difference between the process output and the DDT is defined as the control or tracking error

$$\epsilon(k) = \ y(k) - \ y_d(k) \tag{6.14}$$

which plays an important role in characterizing the performance of APC systems.

- Design from a Stability Perspective

Definition 1

An adaptive predictive control system is said to be globally stable if the following conditions are satisfied:

1) $|\epsilon(k)| \ \leq M < \ \infty \qquad \forall k \geq k_f > 0$

2) $\|\phi(k)\| \leq \ \Omega \ < \infty \qquad \forall k \geq k_f > 0$

where $\| \cdot \|$ denotes the Euclidean norm.

The above definition corresponds to the stability result that will represent the desired control performance for APC in its application to industrial processes. It is implicitly expected that the limit M on the absolute value of the control or tracking error is reduced to a minimum value that depends on the level of noise and unmeasured perturbations acting on the process, and the unmodeled dynamics. For the ideal case, the expected result corresponds to that of

asymptotic stability, where the regression vector remains bounded and the tracking error converges to zero.

- Stability Conditions

The design principles for APC systems are stated by means of a Conjecture in terms of specific conditions that, if satisfied by the driver block and the adaptation mechanism, would make the APC system globally stable.

Conjecture 1

If the Driver Block verifies that the DDT $y_d(k+d)$ is:

i. physically realizable, and

ii. bounded,

and that, for certain values M and k_f , the adaptive system satisfies the following conditions:

a) $\hat{\theta}_r(k) = \hat{\theta}_r(k-d) \qquad \forall k \geq k_f > 0.$

b) $|e(k|k)| \leq M < \infty \qquad \forall k \geq k_f > 0.$

Then, the APC system represented in Figure 69 will have the following properties:

I. $|\epsilon(k)| = |y(k) - y_d(k)| \leq M < \infty \qquad \forall k \geq k_f > 0.$

II. $\|\phi(k)\| \leq \Omega < \infty \qquad \forall k \geq k_f > 0.$

□

Although we are going to prove the above proposition, it was called a 'conjecture' since conditions (i), (ii) and a), b) need to be satisfied through an appropriate synthesis of the driver block and the adaptation mechanism, respectively.

Equation (6.11) can be written in the delayed form

$$y_d(k) = \hat{\theta}_r(k - d)^T \ \phi_r(k - d) \tag{6.15}$$

By comparing (6.7) and (6.15) it is clear that, if condition a) holds, then it may be written that

$$y_d(k) = y(k|k) \tag{6.16}$$

From this result and condition b), along with equation (6.16), property I) of the Conjecture immediately follows. Property II) is derived solely from the boundedness and physical realizability of the DDT.

Once it has been verified that the control objectives are achieved if the conditions of the conjecture hold, the problem to solve is that of the synthesis of the driver block and the adaptation mechanism that are able to satisfy these conditions.

Driver Block Design

- Basic Strategy of Predictive Control

For stable-inverse processes, a bounded DDT is always physically realizable. Therefore, using the basic strategy of predictive control in the driver block design will make it satisfy, in this case, the Conjecture stability conditions (i) and (ii). However, for unstable-inverse processes, to make the process output follow a bounded DDT may require an unbounded process input sequence, not applicable in practice. In this case, a driver block based on the basic strategy of predictive control may violate the DDT physical realizability stability condition. As previously mentioned the need for an extended strategy of predictive control was first considered in [87] and later formalized methodologically in [88].

- Extended Strategy

The extended strategy of predictive control uses the same basic principles of predictive control, but the driver block generates a desired output trajectory at each control instant that verifies a certain performance criterion in a fictitious prediction horizon, taking into account the process dynamics as considered in the following.

The predictive model defines the available knowledge from the process dynamics and it can, at each control instant be used for one step ahead prediction of the process output (basic strategy) or to predict the effect on the process output of a sequence of control actions in a certain prediction horizon. A predicted process output trajectory will correspond to each possible sequence of control actions, and the convenience of applying each one of these sequences can be evaluated according to a certain performance criterion. The extended strategy of predictive control defines as Projected Desired Trajectory (PDT) the predicted output trajectory that corresponds to the sequence of control actions which minimizes a certain performance index in a chosen prediction horizon. The following quadratic cost function was considered by the way of example in [88] as performance index:

$$J_k = \sum_{j=r+1}^{r+\lambda} Q_j[\hat{y}(k+j|k) - y_r(k+j|k)]^2 + \sum_{j=0}^{\lambda-1} R_j \Delta\hat{u}(k+j|k)^2 \qquad (6.17)$$

where $\hat{y}(k+j|k)$ and $\Delta\hat{u}(k+j|k)$ are the predicted output and incremental input sequences in the prediction horizon, respectively; r is the process pure time-delay, and $y_r(k+j|k)$ is a reference trajectory which can be generated in a form equivalent to the way that the PDT for the basic strategy was generated, irrespective of the dynamic nature of the process to be controlled. The cost function (6.17) imposes a compromise between the resultant PDT being as close to the reference trajectory as possible and the required control action not being excessive. Q_j and R_j are weighting factors which are chosen to weight the tracking of the reference trajectory and the magnitude of the incremental control action, respectively. Within this criterion, a predicted trajectory which requires an unlimited control sequence can obviously not be the resulting PDT. By selecting the reference trajectory, the designer can define, in a simple way and independently of the dynamics of the process, the time response and damping that would be desirable for the PDT. The index of performance (6.17) was also used to describe the extended strategy of predictive control and some practical applications in [117] and analyzed as an optimal design for the driver block in [101].

The PDT determines the control action to be applied to the process, which is the first control action of the corresponding predicted control sequence. A new PDT is defined at each control instant and the corresponding sequence of PDT determines the sequence of control actions actually applied to the process. The envelope of the first values of the sequence of PDT, which correspond to the control actions being applied to the process, is known as Driving Desired Trajectory (DDT).

- A solution for industrial applications

The performance criterion of the extended strategy may include a condition to make the predicted control sequence constant along the prediction horizon. A particular case of the performance criterion, already considered in [88], [117] and [101], adds to the previous condition that of making the PDT value at the end of the prediction horizon equal to the value at the same instant of a reference trajectory that, starting from the actual process outputs, converges to the set point according to dynamics chosen by the designer. This kind of performance criterion has been successfully used when applying the extended strategy, in an adaptive predictive context, to a wide variety of industrial plants.

In order to explain the physical meaning for the APC operation of the choice of the prediction horizon under the previously considered performance criterion, let us assume the ideal case in which there is no prediction error and the process initially at steady state. Then, let us analyze the following three alternatives to the prediction horizon choice in the predictive controller operation when a setpoint change is undertaken:

1) If the chosen prediction horizon is greater than the process time response and greater than the settling time of the reference trajectory, i.e. the reference value at the end of the prediction horizon equals the set point value, the first PDT will reach the set point value following a natural process step response. All the subsequent PDT will follow the same path and the DDT and the process output trajectory will also follow this process natural response.

2) If the prediction horizon is chosen equal to 1, the DDT and the process output will follow the previously considered reference trajectory, which in this case will also be equal to the PDT.

3) If the value of the prediction horizon lies between the two previous choices, the DDT and the process output will follow a trajectory in between the process natural response and the reference trajectory, i.e. the dynamics of this trajectory will approach those of the natural process step response as the prediction horizon grows and those of the reference trajectory as it gets closer to 1.

- Physical realizability of the DDT

As explained above, the choice of the prediction horizon will determine the DDT and, therefore, the control law stability, since the physical realizability of the DDT will depend on the stability nature of the process as considered in the following.

Processes of a linear and stable-inverse nature have the bounded input-bounded output property and its inverse. Therefore, the control law stability is guaranteed for any choice of the prediction horizon, with the only condition of a bounded reference trajectory.

Processes of a linear and stable nature do not have the bounded output-bounded input property and, in order to follow certain bounded output trajectories, these processes may require unbounded control sequences. When the prediction horizon is “large enough” and the DDT matches the natural process step response, a bounded control sequence is guaranteed with the only condition of a bounded reference trajectory. However, when the prediction horizon is equal to 1, the process output to follow the DDT, which matches the reference trajectory, may require an unbounded control sequence and the stability of the control law is not guaranteed.

Consequently, for processes of a linear and stable nature, the choice of a large prediction horizon can guarantee stability, but the process output trajectory will approach the natural process response. On the other hand, a small prediction horizon can result in the process output trajectory approaching the reference trajectory, but stability may not be guaranteed.

The above reasoning, which assumes the ideal case with no prediction error, is also consistent in the industrial context. Industrial practice in the operation of APC has

demonstrated that, using the driver block design previously considered in combination with a stable adaptive system, it is easy to find a prediction horizon experimentally that makes the process output dynamics approach the reference trajectory dynamics at the same time that stability is guaranteed in a desired manner.

Adaptation Mechanism Design

In this section the synthesis of an adaptive mechanism is first outlined in the ideal case, and the way it approaches the conjecture stability conditions is described. Next, modifications on this adaptive mechanism are considered to meet the conjecture stability conditions under different hypotheses that approach the operation in an industrial context.

- Synthesis in the Ideal Case

In the ideal case there is neither process-model order mismatch nor noises nor unmeasured perturbations acting on the process, and therefore the process and AP model can be described by the following equations

$$\mathrm{y(k)} = \theta^{\mathrm{T}}\phi(\mathrm{k}-\mathrm{d}) \tag{6.18}$$

$$\hat{y}(k|k) = \hat{\theta}(k)^{T}\,\phi(k-d) \tag{6.19}$$

and the a posteriori estimation error by

$$e(k|k) = \tilde{\theta}(k)^{T}\phi(k-d) \tag{6.20}$$

where $\tilde{\theta}(k) = \theta - \hat{\theta}(k)$ is the parameter estimation error vector. The desired stability result is defined in the form

$$\lim_{\mathrm{k}\to\infty} e(k|k) = 0 \tag{6.21}$$

The following proposition defines the design strategy for the adaptive system.

Proposition 1

Property (6.21) holds if the following condition is satisfied:

$$s(k_t) = \sum_{k=1}^{k_t} e(k|k)^2 \leq \delta^2 \qquad \forall k_t > 0 \qquad (6.22)$$

Proof 1

Clearly, since it sums the squares of the error, $s(k_t)$ is a non-decreasing sequence that may begin to grow from the instant at which the adaptation mechanism starts to operate, as is illustrated in Figure 71. If condition (6.22) holds, this sequence is bounded by δ^2 and thus its increments must tend to zero, that is, $e(k|k)^2 \rightarrow 0$ as $k \rightarrow \infty$.

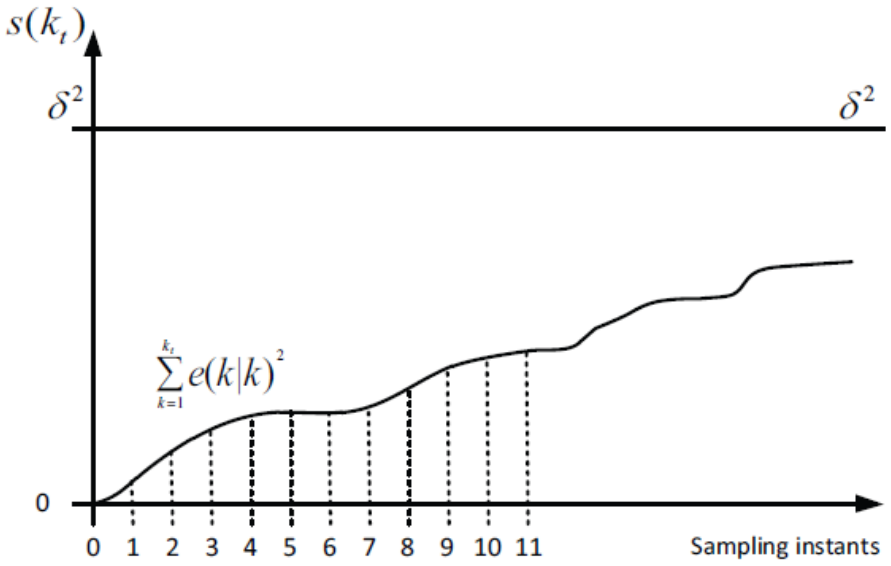

Figure 71. Graphical illustration of condition (6.22).

Therefore, an adaptive system satisfying (6.22) will be asymptotically stable.

It is proven that condition (6.22) is satisfied if the AP model parameter vector is generated at instant k by means of algorithms of the form:

$$\hat{\theta}(k) = \mathrm{e(k|k)B}\phi(\mathrm{k} - \mathrm{d}) + \hat{\theta}(\mathrm{k} - 1) \tag{6.23}$$

where B is a positive definite matrix.

Also it is proven that the relation between the a posteriori estimation error and the a priori estimation error, $e(k|k-1) = y(k) - \hat{\theta}(k-1)^T \phi(k-d)$, is expressed by

$$e(k|k) = \frac{e(k|k-1)}{1 + \phi(k-d)^T B \phi(k-d)} \tag{6.24}$$

and the adaptive algorithm can be written in the form

$$\hat{\theta}(k) = G(k)[y(k) - \hat{\theta}(k-1)^T \phi(\mathrm{k} - \mathrm{d})] + \hat{\theta}(\mathrm{k} - 1) \tag{6.25}$$

where

$$G(k) = \frac{B\phi(k-d)}{1 + \phi(k-d)^T B \phi(k-d)} \tag{6.26}$$

With this formulation, equation (6.23) takes the form of a linear recursive filter with a variable gain: the new vector of the estimated parameters is obtained by adding to the previous one an increment equal to the estimation error obtained using the preceding vector multiplied by the gain vector G(k).

Other techniques of parametric estimation, such as those of the gradient [75], which minimize a function of the square of the prediction error in the direction of the gradient (from which the name is derived), or the estimation techniques based on optimization criteria [118], converge with small differences towards the general expression that has been derived in this case from a perspective of stability.

- Interpretation of the synthesis of the adaptive mechanism

The interpretation of the previous synthesis of the adaptive mechanism is summarized in the following points:

1. The upper limit δ^2 of the non-decreasing sequence $s(k_t)$ is a quadratic function of the Euclidian norm of the initial parameter estimation error vector, $\tilde{\theta}(k)$.

2. If the initial value of the parameter estimation error vector were equal to zero, i.e. $\hat{\theta}(0) = \theta$, then δ^2 would be zero and so would be for all k_t the non-decreasing sequence $s(k_t)$, that would follow the X axis in Figure 71.

3. At any other time k_t, the difference between the upper limit δ^2 and the value of the non-decreasing sequence $s(k_t)$ is a quadratic function of the Euclidian norm of the parameter estimation error vector at time k_t, $\tilde{\theta}(k_t)$. Therefore, when the sequence $s(k_t)$ increases, the length of the parameter estimation error vector decreases. If the sequence $s(k_t)$ were to reach the upper limit δ^2, the parameter estimation error vector would be zero and the AP model would have identified the process equation, i.e. $\hat{\theta}(k_t) = \theta$.

4. When the a posteriori estimation error $e(k|k)$ is zero, the increment between $k - 1$ and k of the parameter estimation vector, $\hat{\theta}(k)$, is also zero, and therefore the conjecture stability conditions are verified.

5. The a posteriori estimation error $e(k|k)$ would be zero, only if the process parameters have been identified by the AP model parameters or if the parameter estimation error vector, $\tilde{\theta}(k_t)$, and the regression vector, $\phi(k - d)$, are orthogonal.

6. In fact, when the non-increasing sequence $s(k_t)$ remains constant, the conjecture stability conditions are verified and the parameter estimation and regression vectors are orthogonal.

7. The parameter estimation algorithm (6.23) of the adaptive mechanism efficiently achieves the result of stability, $e(k|k)^2 \to 0$ as $k \to \infty$, because the updating increments of the estimated parameters look for the orthogonality condition

between the parameter estimation error vector and the regression vectors, by reducing the square of the a posteriori estimation error in the gradient direction.

8. Therefore, the parameter estimation performed by the adaptive mechanism produces an identification of the process dynamics with a view to control. This concept introduced in [82] is of paramount importance in understanding the performance of stable APC systems, as outlined in the following points.

9. The first goal of the identification with a view to control is to achieve the above mentioned orthogonality condition, which results in the verification of the conjecture stability conditions and guarantees the desired control system performance. Looking for the orthogonality condition, the parameter estimation error vector is projected to the plane orthogonal to the regression vector and, in this way, the length of the parameter estimation error vector is reduced. At the same time, the non-increasing sequence $s(k_t)$ increases and approaches the upper limit δ^2.

10. Figure 72 illustrates the performance of the adaptive mechanism. When the regression vector, $\phi(k-d)$, changes from ϕ_1 to ϕ_2 and ϕ_3, the adaptive mechanism updates the AP model parameters in such a way that the corresponding parameter estimation error vector, $\tilde{\theta}(k_t)$, changes from $\tilde{\theta}_1$ to $\tilde{\theta}_2$ and $\tilde{\theta}_3$, respectively, looking for the desired orthogonality.

11. Practical application of APC demonstrates that the considered orthogonality condition is much easier to attain than process parameter identification. This is particularly relevant when considering changes in the process dynamics, where the control performance may not significantly deteriorate if this adaptive mechanism is applied.

12. Therefore, the identification with a view to control provides satisfactory APC performance without the need of identifying the process parameters.

The proof of stability for the adaptive mechanism, derived in the ideal case, implies the verification of the conjecture stability conditions when the regression vector is bounded. Obviously, the adaptive system does not produce the control signal and therefore, it cannot ensure the boundedness of the regression vector. However, the stability properties, derived for this and the following real cases, combined with the conjecture conditions on the DDT, allow APC stability theory to prove the boundedness of the regression vector and, as a result, to attain the desired global stability.

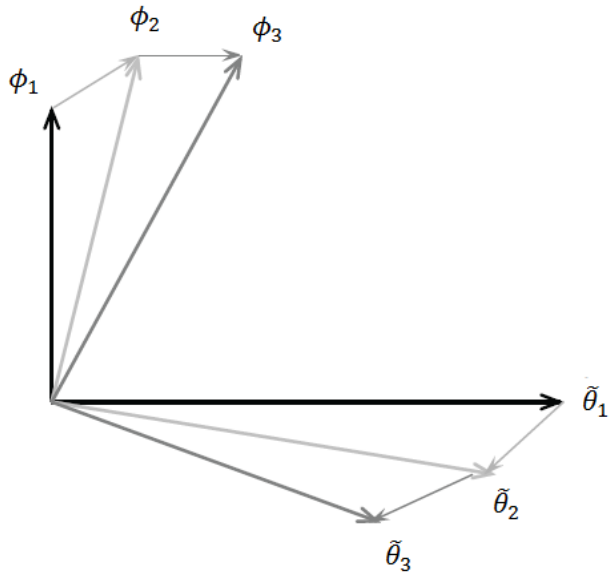

Figure 72. Tracking the orthogonality condition for identification with a view to control.

- Synthesis in the Real Case with no Difference in Structure

In the real case with no difference in structure, the process and AP model can be described by the following equations

$$\mathrm{y(k)} = \theta^T \phi(\mathrm{k-d}) + \Delta(\mathrm{k}) \tag{6.27}$$

$$\hat{y}(k|k-1) = \hat{\theta}(k-1)^T \, \phi(k-d) \tag{6.28}$$

Equation (6.28) gives the a priori process output estimation and (6.27) is equal to (6.18), but in this case it is assumed that there is a boundary Δ_b such that

$$\Delta_b \geq |\Delta(\mathrm{k})| + \delta \qquad \forall \mathrm{k}, \quad \delta > 0 \tag{6.29}$$

From equations (6.27) and (6.28), the a priori estimation error can be derived

$$\begin{aligned} e(k|k-1) &= y(k) - y(k|k-1) \\ &= \left(\theta - \hat{\theta}(k-1)\right)^T \phi(k-d) + \Delta(k) \end{aligned} \tag{6.30}$$

It can be observed in (6.30) that the a priori estimation error is the sum of two terms. The first one depends on the parameter estimation error vector, while the second is the perturbation signal.

In the ideal case the only source contributing to the a priori estimation error is the parameter estimation error vector. Thus it is logical to have a continuous adaptation in order to make the convergence as fast as possible. The situation is different when noise and disturbances are present, since they are unpredictable and also contribute to the estimation error.

It seems logical that the information given by the a priori estimation error may or may not be useful for adaptation depending on whether the estimation error is mainly due to the parameter identification error or to the effect of noise and disturbances, respectively. When the estimation error is due mainly to noise and disturbances, the information on which the parameter adaptation is based will be misleading. On the other hand, if the estimation error is due mainly to the parameter estimation error vector, this information is probably useful for adaptation. This fact suggests the convenience of performing the adaptation only when the second case occurs, instead of doing it continuously.

This idea, first presented for the real case with no difference in structure in [97], [98], is the core of the approach followed by APC stability theory. It is essentially based on the introduction of a criterion that allows the adaptation of the model parameters only when it is certain that this adaptation will lead to a reduction in the norm of the parameter estimation

error vector. This criterion is based on some estimated knowledge about the size of the noise and disturbances that can influence the process output unpredictably, and can be described in the following simple terms:

1) If the a priori estimation error is equal or smaller than a function of the maximum level that the perturbation signal can reach (Δ_b), it may be possible that such an error is due more to the perturbation signal than to the parameter estimation error vector. In such a case, the adaptation should be stopped.
2) If the a priori estimation error is greater than such a function, such an estimation error is mainly due to the parameter estimation error vector and, consequently, the adaptation should be performed.

The problem of synthesis was solved by using the same gradient parameter estimation algorithms derive for the ideal case and determining and applying the aforementioned function to perform or stop adaptation [97], [98], [26], [116].

Using this adaptive mechanism, it was proved that

a) When adaptation is stopped, the a priori and a posteriori estimation errors are bounded.
b) When adaptation is performed, the norm of the parameter estimation error vector decreases.
c) The number of adaptations is bounded when the regression vector is bounded. Therefore in this case the conjecture stability conditions are met.
d) When the bound Δ_b approaches the maximum absolute value of the perturbation signal $\Delta(k)$, the limit on the control error approaches the maximum control error obtained if the process parameters were known and used in the AP model.

At this point it is important to note that the effect of the unmeasured disturbances in the process output is only totally unpredictable at an initial stage. However, since disturbances

contribute to the evolution of the process output, their effect can subsequently be predicted in part by the AP model itself. Therefore, the contribution of unmeasurable disturbances to the maximum level of the perturbation signal is not usually as large as it might seem a priori. Thus, determining a reasonable value for Δ_b is usually not difficult in practice.

The interpretation of the synthesis results obtained for this case can be summarized as follows:

1) The adaptive mechanism looks permanently for an extended orthogonality condition in which the zero value for the ideal case is replaced by a dead band around zero.
2) When the a priori estimation error, which contains the inner product between the parameter estimation error vector and the regression vector, enters the dead band, the extended orthogonality condition is attained and adaptation is stopped.
3) The dead band is determined by the level of noise and unmeasured disturbances acting on the process.
4) The limit on the dead band can be chosen to make the control error to approach that obtained if the process parameters were known and used in the predictive control law.
5) The norm of the parameter estimation error vector becomes a non-increasing function that determines stability.

- Synthesis in the Real Case with Difference in Structure

The synthesis of adaptive systems able to handle not only the problem of noise and unmeasurable disturbances, but also the problem of difference in structure, i.e. process-model order mismatch, uses within APC stability theory the strategy introduced in [114] and outlined in the following:

1) Definition of a normalized adaptive system, so that all the process input/output signals become bounded, allowing dynamic terms of the process equation to be

included in an extended perturbation signal that remains bounded. In this way, the process order in the normalized system is reduced to match the AP model order.

2) Similar to the case with no difference in structure, an adaptation mechanism is defined which guarantees that the norm of the reduced parameter estimation error vector is a non-increasing function.
3) From the result obtained in point 2, the properties of convergence of the a posteriori estimation error and the AP model parameters are derived for the normalized adaptive system.
4) Finally, by the inverse process to normalization, the corresponding convergence properties are derived for the adaptive system without normalization.

Using the previously considered normalized adaptive mechanism it is proven [26], [116]:

a) When adaptation is stopped, the a priori and a posteriori estimation errors of the normalized system are bounded, and the a posteriori estimation error of the adaptive system without normalization is bounded by a function proportional to the norm of the regression vector, where the proportionality depends on the norm of the unmodeled parameter vector.
b) When adaptation is performed, the norm of the reduced parameter estimation error vector decreases.
c) The number of adaptations is bounded, independently of the boundedness of the regression vector.

Therefore in this case the conjecture stability conditions for the adaptive system are also met when the regression vector is bounded. However, APC stability theory establishes limits on the stability result for the close loop control system in the presence of unmodeled dynamics. The existence of these limits, which depend on the process dynamics and the norm of the unmodeled process dynamics included in the extended perturbation signal, was analyzed and illustrated in [115].

The stochastic and unmodeled dynamics hypotheses considered in this case for the synthesis of the adaptive system are closer to a real industrial context. In this sense, the results obtained approach the desired control objectives for a realistic environment and encompass previous stability results obtained for the ideal case and the real case with no difference in structure. It can be interpreted in this case that the adaptive mechanism looks permanently for an extended normalized orthogonality condition between the reduced regression vector and the reduced parameter estimation error vector, and the norm of this vector becomes a non-increasing function that guarantees stability.

An important practical advantage is that, while precise knowledge of the structure of the process equations was required before in order to define the AP model, a reduced-order AP model can now be chosen without requiring such knowledge.

- Time-Varying Parameters

The dynamic nature of industrial processes is basically non-linear, but it is known that in general, their behavior can be described approximately by linear equations, such as those previously considered, with time varying parameters. These parameters usually undergo variations due to the effect of external perturbations acting on the process or changes in the point or conditions in which the process is operating; but these variations generally stop when the context of operation stabilizes and the process approaches steady state.

APC stability theory shows that the adaptive mechanism, previously considered in the presence of unmodeled dynamics, when applied in the time-varying parameter case, maintains the property that the norm of the reduced parameter estimation error vector decreases when adaptation is performed.

Therefore, although in this case the proof of global stability requires logically some restrictive assumptions on the process parameter changes [107], there is a guarantee that the adaptive mechanism will adjust the AP model parameters in order to track the previously considered orthogonality condition and reduce the parameter estimation error vector. In the following section, the methodological evolution of APC will be considered. Certain limitations of APC methodology were detected while applying this technique in industry.

Adaptive Predictive Expert Control was brought forth as a technique that overcomes this limitations guarantying optimal performance throughout operation.

6.5 ADAPTIVE PREDICTIVE EXPERT CONTROL

Adaptive Predictive Expert Control (ADEX) domains

ADEX control was introduced in an international patent application [119] and accepted in both the USA [19] and Europe [120]. This new control methodology combined adaptive predictive control with rule-based expert control through the definition of operating domains for both, in one integrated control structure.

Given an operating range for the variable under control, the ADEX methodology divides this range into different domains, corresponding to adaptive predictive control (AP) and expert control (EX). Figure 73 shows an example in which 3 AP domains are defined: one located in the central part (AP-C) of the variable variation range, another above the centre (AP-S), and one below the centre (AP-I). There are two expert domains as well, one above the variation range (EX-S) and one below it (EX-I).

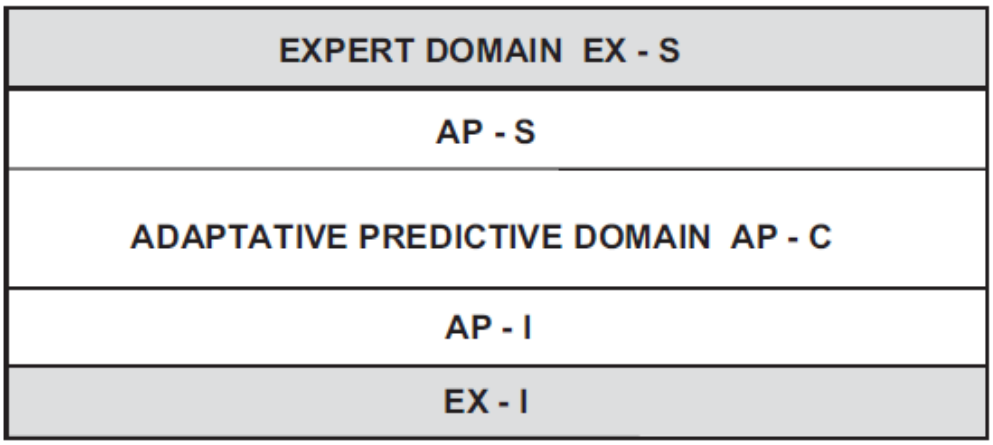

Figure 73. Adaptive Predictive Expert Control (ADEX) domains.

The AP domains are those in which the dynamic cause-effect relationship between the input and output variables of the process can be identified by means of an adaptive system. In these domains AP control is applied and the operation of the process can generally be controlled in an optimal way. As shown in Figure 73, different AP domains can be defined, and each domain can define a different way of applying AP, depending on which is most suitable in each case.

Expert domains are operating domains where manual control can provide a more robust and efficient control than AP control. This situation can arise when there does not exist a cause-effect relationship between the input and output variables, or it cannot be obtained in real time, or obtaining this information would take too much time and would not deliver a substantial improvement over manual control. These domains are usually located in the extremes of normal operating ranges of the process variables, and in these domains, operator experience is used to define rules that imitate the intelligence of manual control. ADEX control applied in expert domains is designed to drive the process variables back to the AP domains, were AP control is applied.

Block diagram and functional description

The ADEX block diagram is presented in Figure 74 and, as can be observed, it is equivalent to the AP control diagram with the exception that an Expert Block has been added to the top level. This expert block, based on the information that it receives from the process variables, is capable of determining and modifying the operation of the controller block, the driver block, and the adaptation mechanism as is described below.

- **Controller Block**: Depending on whether the operating domain of the output variable is found to be AP or EX, the expert block determines which type of control to apply. In the first case, the controller block acts like a predictive model within its own AP control scheme, and calculates the predictive control to be applied to the process. If expert control has to be applied, the controller block will act like a rule-based system, imitating the actions of a human operator, and apply expert control to the process. This function of the expert block prevents the application

of AP control when it is not appropriate, resulting in a deterioration of the application, and in these cases, enables a reasonable control action similar to that which would be taken by a human operator. This function of the expert block greatly increases both the robustness of the ADEX controller and its industrial reliability.

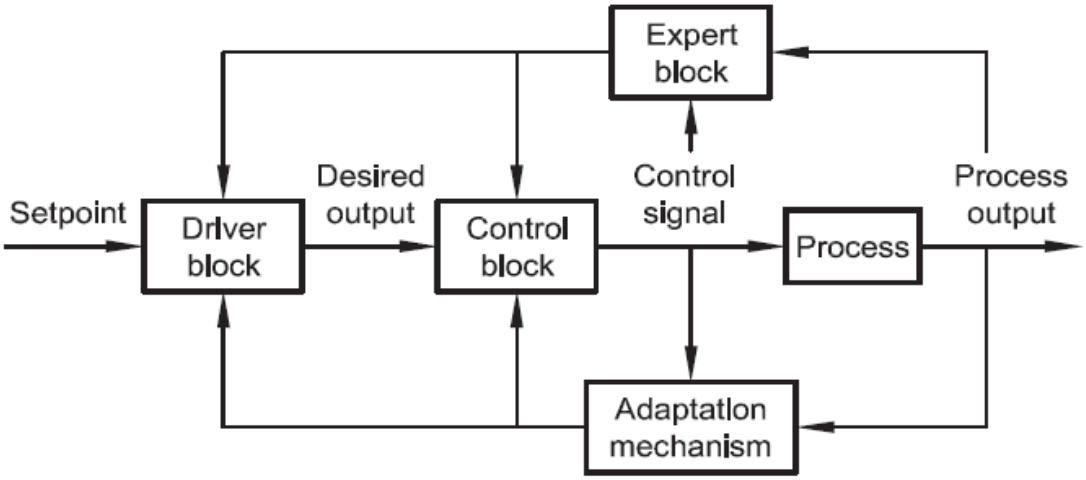

Figure 74. Adaptive predictive expert control block diagram.

- **Driver Block**: In its interaction with the driver block, the expert block can determine the performance criteria required for the generation of the most suitable desired trajectory for each AP domain. So, for example, it could determine the rate of change or the slope of the desired trajectory in reaching the setpoint. If the domain was far from the setpoint it could require a large rate of change, but if the domain contains the setpoint, a smaller rate of change could be required so that the setpoint be reached smoothly and without oscillations.

- **Adaptation Mechanism:** Interacting with the adaptation mechanism, the expert block can determine: (a) when it is appropriate to activate or deactivate the adaptation of the AP model parameters, depending on operating conditions, and (b) the reinitialization of the AP model parameters when the operating domain changes. In the first place, by introducing criteria for starting or stopping the adaptation in accordance with operating conditions, the expert block makes the

adaptation mechanism more robust, thus avoiding deterioration in the parametric identification of the AP model. Secondly, for example, if we have approximate knowledge of the main changes in process dynamic of the various operating domains, the expert block can assist the adaptation mechanism to reinitialize appropriately the AP model parameters when the process output changes from one domain to another. Processes involving pH control are a typical example where these circumstances can occur. In short, the operation of the export block enables the utilization of prior process knowledge, by means of applying rules, for both expert and adaptive predictive control of ADEX.

With this, the controller can use the knowledge to advantage and apply the appropriate control to the various operating domains, and particularly to the AP domains by choosing the most appropriate performance criteria for the driver block and/or adapting and reinitializing the parameters of the AP model when appropriate.

Conceptual example of an application

A simple conceptual example of the ADEX performance can be seen in Figure 75. It will be considered that an intelligent building which has not been heating overnight, in order to save energy, initiates the heating process early in the morning before the staff starts to arrive. The initial temperature is 10°C and the target or setpoint of the heating control system, which should be reached in more or less half an hour, is 22°C.

Figure 75 represents the start of the heating control signal and its evolution just as the evolution of the temperature reaches the setpoint (22 °C), after a night where no energy is used to heat the building, that is to say, the control signal is equal to zero. The variation range of the temperature, from its initial value of 10 °C divides itself into an expert domain and an AP domain. As may be observed, the expert domain is defined in a zone away from the setpoint where control precision is not critical. The AP domain however, is defined around the setpoint where the precision of control is important.

As shown in Figure 75, once the operation of the ADEX controller is initiated, and while the temperature variable remains in the expert domain, expert control is applied imitating the

action of a human operator, which consists of maintaining a constant control action. But when the variable enters the AP domain, at minute 15, adaptive predictive control is initiated to guide the trajectory to the desired temperature setpoint, smoothly and without oscillations.

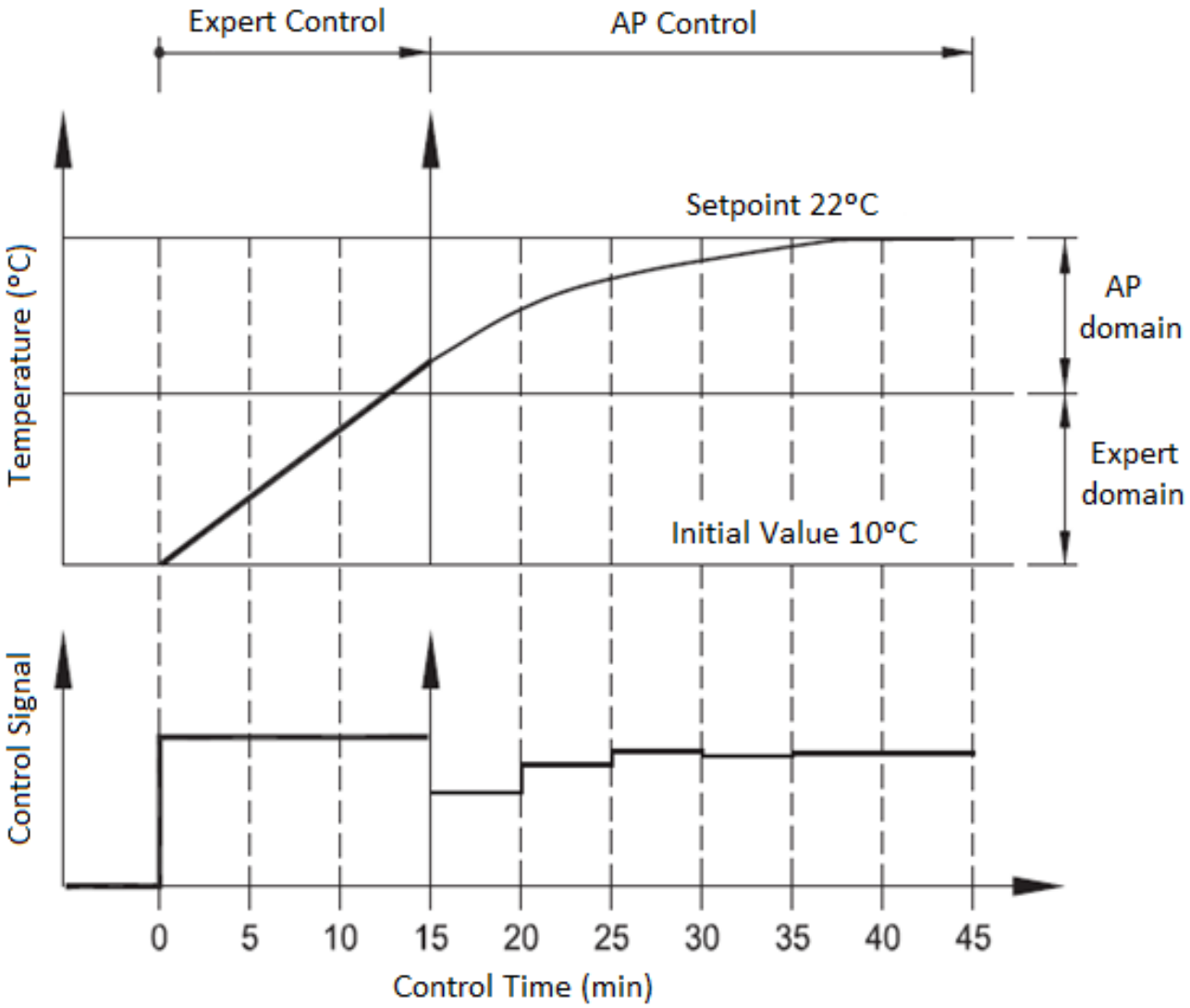

Figure 75. Conceptual example of the application of ADEX.

6.6 ADEX OPTIMIZED ADAPTIVE CONTROL SYSTEMS

This section will introduce and distinguish between the concepts of optimized adaptive controller and optimized adaptive control system, as defined previously in [20], [121], and relate these concepts with the control solutions that have been used throughout the research works of this thesis.

ADEX optimized adaptive controllers

Adaptive Predictive Control methodology [20], [121] set up the bases for a large class of controllers characterized by:

1) An adaptive predictive (AP) model of the plant whose parameters are adjusted in real time by an adaptive mechanism in such a way that the prediction error converges towards zero.

2) This AP model is used at every control instant to derive a desired future process output trajectory by minimizing an index that is chosen according to a performance criterion.

This class was named "optimized adaptive controllers" [121] since in their design adaptive systems theory is complemented by optimal control theory. In this context, adaptive predictive expert (ADEX) control methodology adds to the bases of adaptive predictive or optimized adaptive control, the capability of using the available process knowledge (through intelligent tools) to provide precise and stable control for a wide variety of difficult-to-control processes. Thus, for these processes, ADEX optimized adaptive controllers are able to overcome the inherent instability problems of classical PID controllers and can be an efficient tool to achieve plant optimization and to improve the reliability of its operation, as described below.

Optimized process control system

The concept of "Optimized Process Control System" was introduced in [121] as that capable of verifying the following optimized process control performance conditions:

1) An optimized process control system must be able to achieve the dynamic stabilization of process, i.e. this means be able to maintain, in the range of attainable operating points, the process variables under precise control around their set points with adequately bounded control signals, in spite of changes in

process dynamics, context of operation and noise and perturbations acting on the process.

2) It must be able to achieve transitions between the attainable operating points in which the process variables are driven through desired trajectories with adequately bounded control signals.
3) It has to be able in real time to look when necessary for the process operating point that 10 satisfies a criterion for the optimization of the process performance and drive the process variables towards this optimal operating point.

Obviously, the previous concepts of dynamic stabilization of the process and optimized process control performance are not well-defined mathematical concepts. Due to the usual complexity of the industrial operating context, these concepts have been derived from an industrial application perspective, where the best possible control performance can only be defined in a qualitative manner and be confirmed by the common sense criteria of the human process operator.

Optimized process control strategy

The design of industrial control systems, and particularly those aimed at optimizing process control performance, is necessarily based on available knowledge of the process dynamics and the use of a control methodology. A complete knowledge of the process dynamics may not satisfactorily solve the control problem. Also, the simple use of controllers based on a control methodology is not often able to achieve what has been defined as optimized process control performance.

From available process knowledge we can derive guidelines and rules which can facilitate the desired control of the process by defining process control strategies in which the controllers, designed according to a certain control methodology, can be integrated in order to achieve the best process control and performance. When the combination of process control strategy and control methodology enables optimized process control performance, we will talk about optimized process control strategy and optimized process control system.

ADEX optimized adaptive control systems

Due to the time-varying nature of industrial processes, the desired objective of process dynamic stabilization is often difficult to attain and maintain using fixed parameter controllers. But currently industrial operating applications have demonstrated that the use of optimized adaptive controllers integrated in the appropriate control strategy can solve the process dynamic stabilization problem and approach optimized process control performance in industry [21] – [24]. This kind of system is referred to as Optimized Adaptive Process Control Systems. When ADEX is the kind of optimized adaptive controller used in the optimized control strategy, we will talk about ADEX Optimized Adaptive Control Systems or simply ADEX systems.

The following Chapter presents the design of the optimized control strategy that has defined the ADEX system applied for the FTS control.

CHAPTER VII:

DESIGN OF THE OPTIMIZED CONTROL STRATEGY

The control strategy for the FTS has been designed in order to address the main control challenges, previously described in Chapter 4. The following list recalls the main challenges previously considered and describes the bases for addressing said main control challenges:

1. **Complex dynamics of the cavity resonance frequency** - Due to the time-varying dynamic nature of the cavity´s processes, the optimized process strategy considers the integration of ADEX controllers for the guidance of the critical process variables. However, it has been studied that the cavities frequency detuning cause-effect relationship with the actions of the CTS has an extremely hi-order transfer function [17], that is described by the bode diagram of Figure 63. Hence the ADEX controller will require a very hi-order model of this cause-effect relationship to perform adequate control of the frequency detuning. The problem is that this model might not be executable within the necessary time to maintain satisfactory control performance.

Nevertheless, if the resonant peaks shown in Figure 63 were removed the remaining dynamics would resemble that of a smaller order model. Consequently, a promising approach would be to include in the optimized control strategy mechanisms to attenuate the excitation of the resonance modes of the cavity, taking into account that these modes might be excited by the controller´s actions themselves.

2. **Time Constrains -** Execution time requirements have been studied in a time scaled simulation and all the algorithms that employed are conceived bearing in mind that there exists strict time constrains that will have to be met after their implementation on a hardware solution. Particularly, the ADEX controller has yielded satisfactory performance in the high fidelity simulation of the FT loop with a control period of 2 ms, which makes the execution time required compatible with any adequate processing hardware.

3. **Significant delay -** The pure time delay between the control action applied to the piezo and its effect on the frequency detuning is a control problem found in plenty of industrial processes. This kind of delays is usually well managed by predictive controllers. Unlike PIDs, a predictive controller has the capability of dealing with the pure time delays and considering their effects during the control action computation. Particularly, the time delay recorded of 1 ms in the CTS is absorbed by the control period of 2 ms used by the ADEX controller. Thus, there is no pure time delay in the discrete description of the process dynamics under this control period. The parameters of the AP model adjusted by the adaptation mechanism consider implicitly this time delay.

4. **Lorentz forces -** The optimized control strategy will have to consider the effects derived from an adjacent cavity failure. This event will activate a retuning procedure of the cavity changing the set points of the frequency detuning and the RF field's amplitude and phase. The RF field amplitude will be highly increased in order to compensate for the faulty cavity and this will cause strong detuning due to Lorentz forces. Therefore, an adjacent cavity failure is a perturbation that will deeply affect the FTS performance but that can be anticipated as soon as the cavity failure is detected. For this reason,

the optimized control strategy design has to consider mechanisms to perform the adequate control actions that may prevent the detuning from taking place.

5. **Microphonic perturbations -** caused by environmental noise, vibrations near the cavity or even by the pressurized liquid Helium flow around the cavity, produce two main problems. On the one hand, they can directly affect the cavity's mechanical shape causing a drift of the frequency detuning from its set point. On the other hand, some microphonics, i.e. microphonics caused by the noise of the pumping system, could excite some of the main resonant modes in a continuous manner during the cavity's operation causing permanent oscillations at certain frequencies. The drifts of the frequncy detuning can be compensated by an adaptive controller action, but the continuous excitation of resonance modes previously considered should be taken into account by the optimized control strategy, which has to incorporate some smart mechanism to compensate for them.

6. **Uncertainty in the cavity´s operation -** The time-varying environment (microphonics, Lorentz forces, beam intensity, etc.) will not only tend to deviate the cavity's critical variables from their set points, but to change cavity dynamics. The ADEX adaptation mechanism can keep track of the cavity dynamics, avoiding deterioration experienced by fixed parameters control systems and optimizing the FTS control performance.

Summarizing the previous considerations, the optimized control strategy should consider:

a) The integration of ADEX controllers able to deal with the time varying and uncertain nature of the cavity´s process dynamics.

b) A mechanism to either avoid exciting the resonant modes by the controller´s actions, or to damp or attenuate efficiently the excitation of the modes caused by them.

c) A feed-forward mechanism to perform the adequate control actions that will compensate for drifts in the frequency detuning caused by Lorentz forces in the presence of an adjacent cavity failure.

d) A smart mechanism to compensate for permanent oscillations at resonant frequencies caused by consistent microphonics noise excitation of the resonant modes.

The following Section describes the design of the optimized control strategy that will take into consideration the above points, integrating ADEX controllers and defining the ADEX system applied during the tests in simulation and in the prototypes of the spoke and elliptical cavities.

7.1 THE MAIN CONTROL TOOL: THE ADEX CONTROLLER

Many of the previous control challenges (1, 3 and 6 of the previous list) have directly addressed by the choice of an ADEX controller as the main control tool to be used in the optimized process control strategy. The ADEX controller guarantees operational stability, control precision and robustness against the complex dynamics of the resonance frequency, the uncertainties involved in the cavity's operation and the time delays caused by the movement of the CTS. This section describes the ADEX controller used and in particular de AP algorithm that was conveniently reduced to the minimum expression to address control challenge number 2 of the list: the execution time constraints. Time constraints will be discussed further in Chapter 9, related to the implementation of the OACS.

While Chapter 6 has described the general methodology of Adaptive Predictive Expert ADEX control, this section will describe the "compact" operation algorithm in an Adaptive Predictive (AP) domain of the ADEX controller applied to the FT regulation loop.

The ADEX controller was programmed with three different control domains, two expert domains and an AP domain corresponding respectively to the upper, lower and central parts of the range of operation of the cavity frequency detuning. Expert control, using the operator knowledge from the process dynamics, is applied in the expert domains while Adaptive Predictive Control (APC) is applied in the AP domain. The block diagram of the APC algorithm applied to the FT loop is shown in Figure 76.

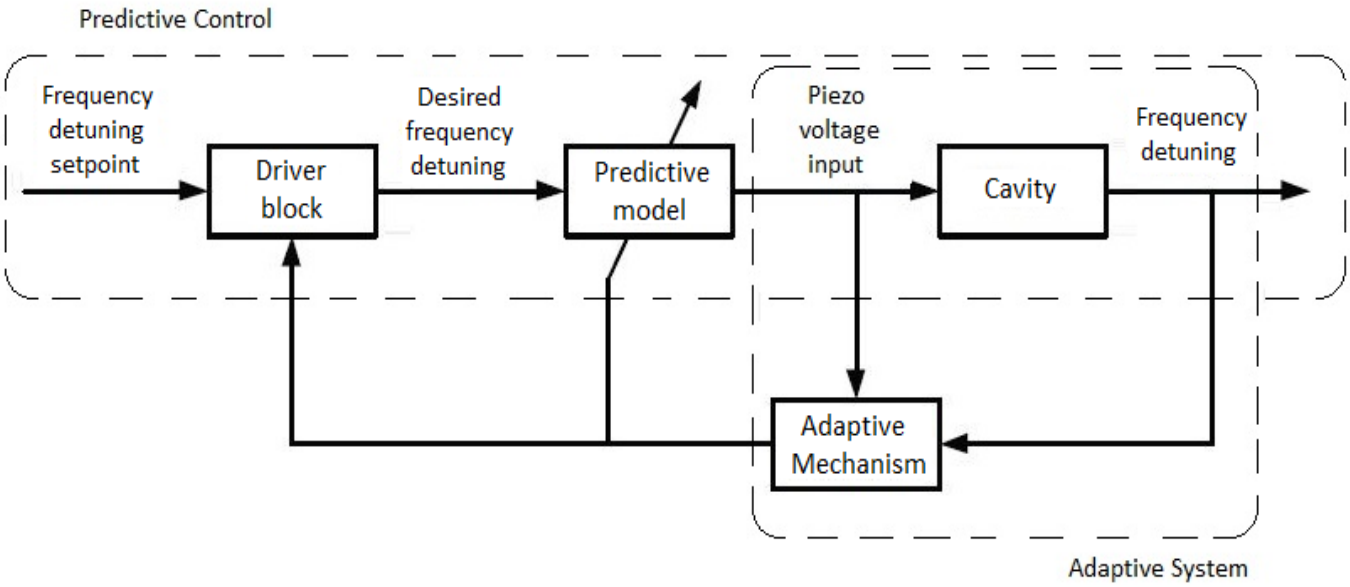

Figure 76. Adaptive Predictive Control (APC) for the Frequency Tuning System (FTS).

APC results from the combination of a predictive control scheme, with an adaptive system. As shown in the forward path of this figure, at each control instant k, a driver block generates a desired process output value (desired frequency detuning value in this case) from a setpoint value (the setpoint value for the frequency detuning) and the currently measured process output (frequency detuning measurement). A predictive model is then used to compute the control signal applied to the process (voltage applied to the piezoelectric actuator), according to the predictive control principle [119], that makes the predicted process output equal to the desired process output, i.e. this voltage signal makes the predicted frequency detuning equal to the desired frequency detuning computed by the driver block.

An Adaptation Mechanism in the feedback path updates the parameters and variables of the Driver Block and the Predictive Model. This adaptive (self-tuning) mechanism makes the prediction error on the process output tend towards zero and ensures stability and optimized performance of APC.

AP controllers are called optimized adaptive controllers [27] when, according to the extended predictive control strategy [25], [122], [123], the desired value for the process output previously considered is the first one of a future desired process output trajectory that optimizes a performance criterion in a selected prediction horizon λ. In this case, the

predictive control signal is the first one of a corresponding future control sequence that the predictive model predicts will cause said desired process output trajectory. The APC algorithm was applied to the FT loop with a control period of 2 ms, used the extended strategy of predictive control and is described as follows.

In order to generate the desired process trajectory (DPT) for the frequency detuning, at each control time k, the driver block uses a particular case of the generic AP model (II) described in Chapter 6, customized for the FT loop. Since the time delay in the caused by the CTS (1ms) is shorter than the control period, the AP model does not consider any pure time delay and the prediction at time $k+1$ of the process output made by the FT AP model is as follows:

$$\hat{y}(k\ +\ 1|k) = \hat{a}_1(k)y(k) + \hat{a}_2(k)y(k-\ 1) + \hat{b}_1(k)u(k)\ + \hat{b}_2(k)u(k-1) + \hat{b}_3(k)u(k-2) \tag{7.1}$$

where $\hat{a}_1(k)$, $\hat{a}_2(k)$, $\hat{b}_1(k)$, $\hat{b}_2(k)$ and $\hat{b}_3(k)$ are the AP model parameters as updated by the adaptation mechanism at time k, $y(k)$ and $y(k-1)$ are the values of the frequency detuning at times k and $k-1$, and $u(k)$, $u(k-\ 1)$ and $u(k-\ 2)$ represent the voltage values applied to the piezoelectric at times k, $k-\ 1$ and $k-\ 2$ respectively. Two parameters $\hat{a}_i(k)$ and three $\hat{b}_i(k)$ were chosen empirically to define the structure of the AP model for this application after trying different AP model configurations in the control simulation.

The recursive prediction of future process output values $\hat{y}(k\ +\ j\,|\,k)_{(j=1,\lambda)}$ in the prediction horizon $[k\ +1, k\ +\lambda]$, is given by:

$$\hat{y}(k\ +\ j|k) = \hat{a}_1(k)\hat{y}(k+j-1|k) + \hat{a}_2(k)\hat{y}(k+j-2|k) + \hat{b}_1(k)\hat{u}(k+j-1|k) + \hat{b}_2(k)\hat{u}(k+j-2|k) + \hat{b}_3(k)\hat{u}(k+j-3|k) \qquad for\ j=1,\lambda \tag{7.2}$$

where $\hat{u}(k+j|k)_{(j=0,\lambda-1)}$ represents the corresponding process input sequence and

$$\hat{y}(k\ +\ 1-i|k) = y(k+1-i), \qquad for\ i=1,2$$
$$\hat{u}(k\ +\ 1-i|k) = u(k+1-i), \qquad for\ i=1,3 \tag{7.3}$$

The driver block, under its general formulation [25], selects, at each time k, a desired output trajectory y_d, a predicted process output sequence in the prediction horizon $[k + 1, k + \lambda]$, which is caused by a predicted process input sequence in the interval $[k, k + \lambda - 1]$, in such a way that both sequences satisfy a certain performance criterion. A performance criterion generally used in practical applications [26] has been chosen for this implementation. It is defined by the following two conditions:

Condition 1: $\hat{y}_d(k + j|k)_{(j=1,\lambda)} = \hat{y}(k + j|k)_{(j=1,\lambda)}$, where:

a) $\hat{y}_d(k + j|k)$ is the value of the desired output trajectory at time $k + \lambda$. This value is computed at time k as the output value at time $k + \lambda$ of a model reference with a chosen desired dynamics, the same setpoint input as the driver block and the same initial values as the predicted output sequence; and
b) $\hat{y}(k + j|k)$ is the process output sequence predicted by the AP model at time k from the values of the process input sequence $\hat{u}(k + j - 1|k)_{(j=0,\lambda-1)}$.

Condition 2: The process input sequence $\hat{u}(k + j - 1|k)_{(j=0,\lambda-1)}$ is constant in the interval of prediction $[k, k + \lambda - 1]$, i.e. $\hat{u}(k|k) = \hat{u}(k + j - 1 \,|\, k)_{(j=0,\lambda-1)}$.

The dynamic of the model reference considered in "Condition 1" was chosen for this application of second order with a gain of 1, a damping ratio of 1 and a time constant of 1.5 control periods. Parameter λ defining the prediction horizon was chosen equal to 10 control periods.

Under "Condition 2", the prediction at time k of the process output at time $k + \lambda$, $\hat{y}(k + \lambda|k)$, obtained by the AP model (7.1), may be computed by:

$$\hat{y}(k + \lambda|k) = \hat{a}_{1\lambda}(k)y(k) + \hat{a}_{2\lambda}(k)y(k - 1) + \hat{b}_{1\lambda}(k)\hat{u}(k|k) + \hat{b}_{2\lambda}(k)u(k - 1) + \hat{b}_{3\lambda}(k)u(k - 2) \quad (7.4)$$

where the parameters $\hat{a}_{1\lambda}(k)$, $\hat{a}_{2\lambda}(k)$, $\hat{b}_{1\lambda}(k)$, $\hat{b}_{2\lambda}(k)$ and $\hat{b}_{3\lambda}(k)$ are obtained by means of recursive algorithms from the AP model parameters in (7.1), $\hat{a}_1(k)$, $\hat{a}_2(k)$, $\hat{b}_1(k)$, $\hat{b}_2(k)$ and $\hat{b}_3(k)$, as shown in [101]. This last equation (7.4) may be written in the form:

$$\hat{y}(k+\lambda|k) = \hat{\theta}_{0\lambda}(k)^T \ \phi(k) + \hat{\theta}_{1\lambda}(k)\hat{u}(k|k) \tag{7.5}$$

where

$$\begin{gathered}\hat{\theta}_{0\lambda}(k)^T = [\hat{a}_{1\lambda}(k), \hat{a}_{2\lambda}(k), \hat{b}_{2\lambda}(k), \hat{b}_{3\lambda}(k)] \\ \hat{\theta}_{1\lambda}(k) = \hat{b}_{1\lambda}(k) \\ \phi(k)^T = [y(k), y(k-1), u(k-1), u(k-2)]\end{gathered} \tag{7.6}$$

Taking into account "Condition 1" and using (7.5) the control signal $u(k)$ is computed as follows:

$$u(k) = \hat{u}(k|k) = \hat{\theta}_{1\lambda}(k)^{-1}\left[y_d(k+j|k) - \hat{\theta}_{0\lambda}(k)^T\phi(k)\right] \tag{7.7}$$

In the implementation performed for the FT loop, the sequence of operations required to implement (7.7) is executed under the incremental approach described in [85].

In order to estimate the process output, at each control time k, the AP model uses a particular case of the generic AP model described in Chapter 6 and customized for the FT loop. Thus the a priori process output estimation $\hat{y}(k|k-1)$ made by the FT AP model is as follows:

$$\begin{aligned}\hat{y}(k|k-1) = \hat{a}_1(k-1)y(k-1) + \hat{a}_2(k-1)y(k-2) + \hat{b}_1(k-1)u(k-1) \\ + \hat{b}_2(k-1)u(k-2) + \hat{b}_3(k-1)u(k-3)\end{aligned} \tag{7.8}$$

and the error of this estimation is given by

$$e(k) = y(k) - \hat{y}(k|k-1) \tag{7.9}$$

The adaptive algorithms used in the adaptation mechanism of the present implementation are similar to those considered in [85] but include a criterion for stopping parameter adaptation of the type used in [97], [98]. Thus, the estimated error drives the computation of the parameters $\hat{a}_i(k)$ and $\hat{b}_i(k)$ by gradient parameter algorithms of the form:

$$\hat{a}_i(k) = \beta_{ai}\alpha(k)e(k)y(k-i) + \hat{a}_i(k-1) \qquad for\ i = 1,2$$
$$\hat{b}_i(k) = \beta_{bi}\alpha(k)e(k)u(k-i) + \hat{b}_i(k-1) \qquad for\ i = 1,2 \tag{7.10}$$

where

$$\alpha(k) = \left(1 + \sum_{i=1}^{2} \beta_{ai}\, y(k-i)^2 + \sum_{i=1}^{3} \beta_{bi}\, u(k-i)^2\right)^{-1} \tag{7.11}$$

and the values of the coefficients β_{ai} and β_{bi} are conveniently chosen [85] when adaptation takes place, but become equal to zero, at any time k, when a criterion to stop parameter adaptation is fulfilled. This criterion complies with the stability requirements for the adaptive predictive controller in an industrial context ensuring that the norm of the parameters error vector, i.e. the difference between a vector formed by the process parameters and a vector formed by the AP model parameters, is always reduced when parameter adaptation takes place [20].

Experimental Interpretation of APC Operation in the FT Loop

In this section, an illustrative example of the APC algorithm, described in the previous section, applied to a FT loop simulation without microphonics is described. The simulation scenario considers a field increase inside the cavity, which will be a frequent procedure when the accelerator is in service. The main variables of the cavity and the AP algorithm operation are depicted in Figure 77.

The variables of the trend curves in the different subfigures of Figure 77 are explained as follows:

- The green line in Subfigure 77.a is the evolution of the field inside the cavity.
- The blue and red lines in Subfigure 77.b represent the cavity frequency detuning and its setpoint values respectively.
- The blue line in Subfigure 77.c shows the voltage applied by APC to the piezoelectric actuator.
- The blue and red lines in Subfigure 77.d show the prediction error computed as in (7.9), and the zero value respectively.
- The blue and green lines in Subfigure 77.e show the evolution of the $\hat{a}_1(k)$ and $\hat{a}_2(k)$ AP model parameters respectively.
- The blue, green and yellow lines in Subfigure 77.f show the evolution of the $\hat{b}_1(k)$, $\hat{b}_2(k)$ and , $\hat{b}_3(k)$ AP model parameters respectively.

After 20 ms from the beginning of the simulation the field starts to increase (Subfigure 77.a). 40 ms later it stops increasing. It starts to increase again around 70 ms to stop definitely around 90 ms. Note that when the field slope changes Lorentz Forces deviate the frequency detuning from its setpoint (Subfigure 77.b). These forces act as unknown perturbation whose dynamics are not considered into the AP model. They have two effects; the first one is deviating the frequency detuning under control and, the second is changing the process dynamics, changing the dynamic relationship between voltages applied to the piezoelectric and frequency detuning. Each time that the frequency detuning is deviated from the setpoint by the Lorentz forces, the absolute value of the prediction error increases (Subfigure 77.d). Then the adaptation mechanism, driven by this error, adjusts the AP model parameters (Subfigures 77.e and 77.f). This makes the prediction error return towards zero as the frequency detuning stabilizes for a short time until the new field slope changes, which produces again new Lorentz forces. Along with the adaptation mechanism operation, predictive control is applied on the piezoelectric voltage (Subfigure 77.c) and stabilizes the frequency detuning close to its setpoint when the prediction error comes back to zero and the AP model parameters stabilize their values. This situation is an indication that the new process

dynamics has been “identified with a view to control” by the AP model parameters. This kind of identification was considered in [26], [82].

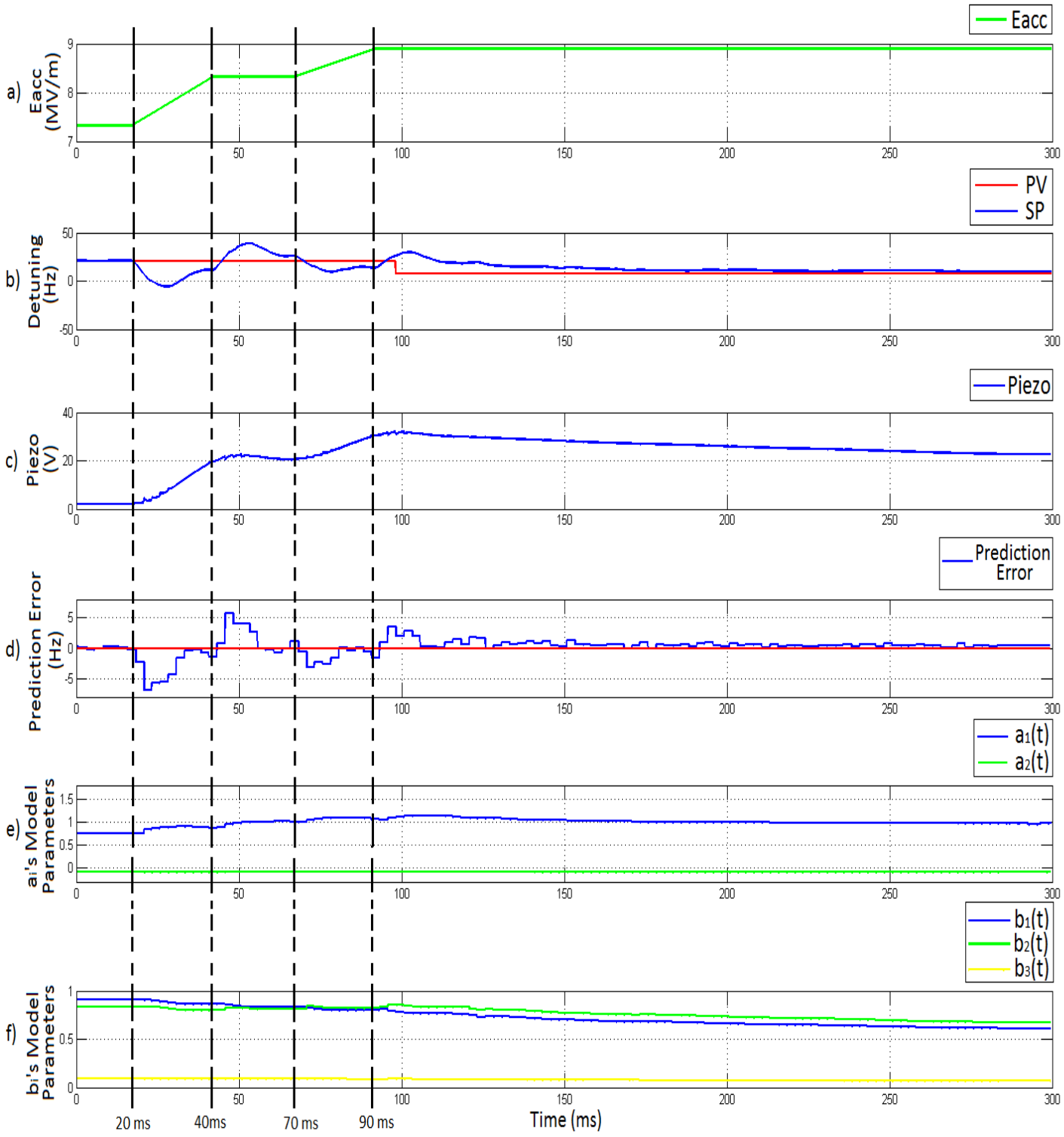

Figure 77. APC for the FTS. Subfigure a) Field inside the cavity. Subfigure b) Cavity frequency detuning and its setpoint. Subfigure c) voltage applied to the piezoelectric actuator. Subfigure d) APC prediction error. Subfigure e) AP model $\hat{\mathbf{a}}_\mathbf{i}(\mathbf{k})$ parameters. Subfigure e) AP model $\hat{\mathbf{b}}_\mathbf{i}(\mathbf{k})$ parameters.

This is an illustrative example of APC performance. When a process dynamic change is produced the error will increase and the adaptation mechanism will identify the change in dynamics making the error return towards zero. At the same time, the predictive control signal compensates the effect of the perturbation that created the process dynamic change driving the process variable under control towards its setpoint.

7.2 MEANS TO AVOID EXCITING RESONANT MODES: NOTCH FILTERS.

Notch filters belong to the family of the Infinite Impulse Response (IIR) filters. A notch filter is a band-reject filter. This means that any signal which is filtered by a notch filter designed for a certain frequency will attenuate its harmonic components at that frequency.

For the implementation of the optimized control strategy second order filters have been considered. The behavior of this kind of filter is determined by the following recursive equation and its coefficients:

$$y(k) = a_1 y(k-1) + a_2 y(k-2) + b_0 u(k) + b_1 u(k-1) + b_2 u(k-2) \quad (7.12)$$

where $u(k)$ is the input value to the filter at the sampling time k and $y(k)$ is the output or filtered signal value at the same sampling time k. a_1, a_2, b_0, b_1 and b_2 are the filter coefficients which need to be correctly adjusted in order to eliminate the desired frequency for the input signal u.

Coefficients in Table 7 define a notch filter designed to eliminate an 80 Hz frequency considering a sampling time of 0.2 ms.

Coeffs. Notch	Value	Coeffs. Cheby Type II	Value
a_1	1.85929	b_0	1
a_2	-0.868712	b_1	-1.98849
		b_2	0.997907

Table 7. Bode Notch filter coefficients for 80 Hz band reject defined for 0.2 ms sampling time.

The recursive filter equation (7.12) with the coefficients defined in Table 7 corresponds to the following discrete transfer function for a sample time of 0.2 ms:

$$N(z) = \frac{z^2 - 1.98849z + 0.997907}{z^2 - 1.85929z + 0.868712} \tag{7.13}$$

The Bode diagram of Figure 78 shows the magnitude attenuation and the phase shift caused by the filter as a function of the frequency of the incoming signal. It can be observed that the maximum attenuation occurs at 80 Hz. It can also be noticed that notch filters not only reject the frequency they have been designed for but they also attenuate frequencies which are located near the design frequency. Although this side-effect can be modified through filter design, certain attenuation at frequencies surrounding the design frequency will not be totally avoided.

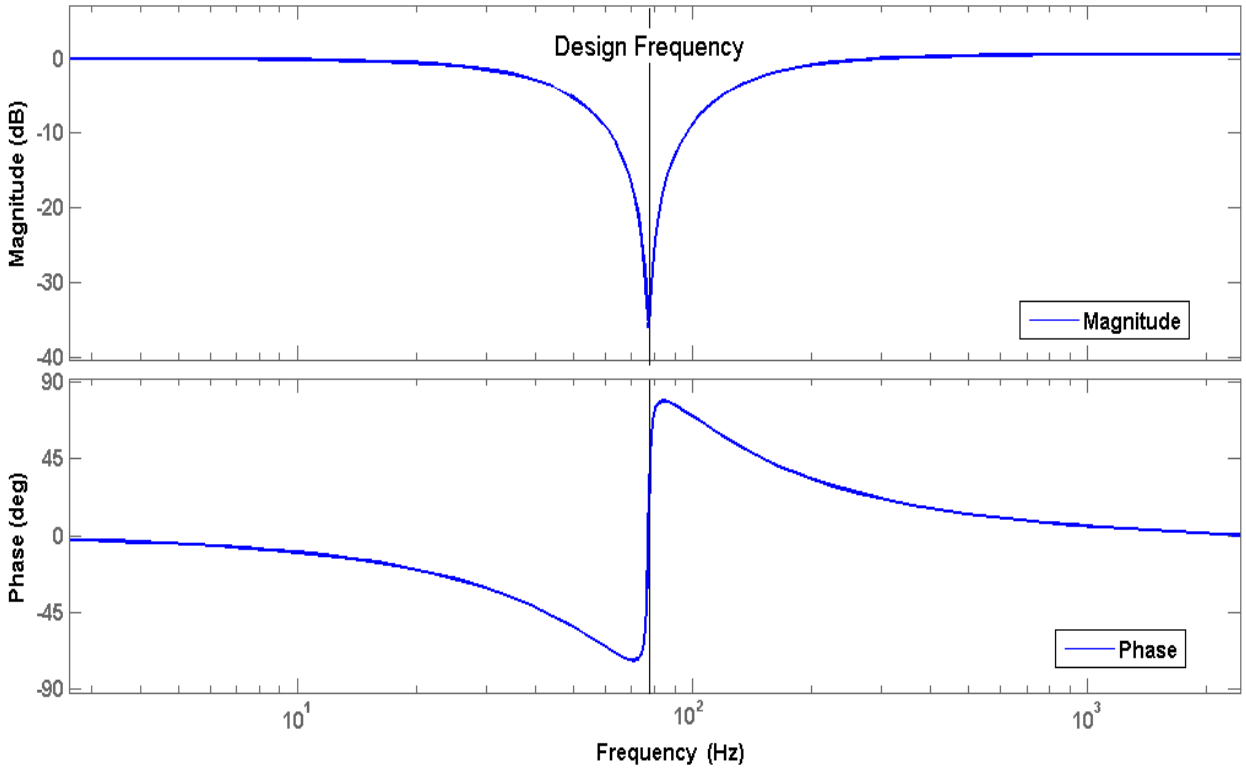

Figure 78. Bode diagram of a notch filter designed for 80 Hz frequency.

Figure 79 shows the classical shape of the step response of a notch filter. In fact it is the step response corresponding to the filter defined by the coefficients in Table 7. This is

illustrative of the “kickback” produced by the notch filter to avoid the presence of determined harmonic components in the step.

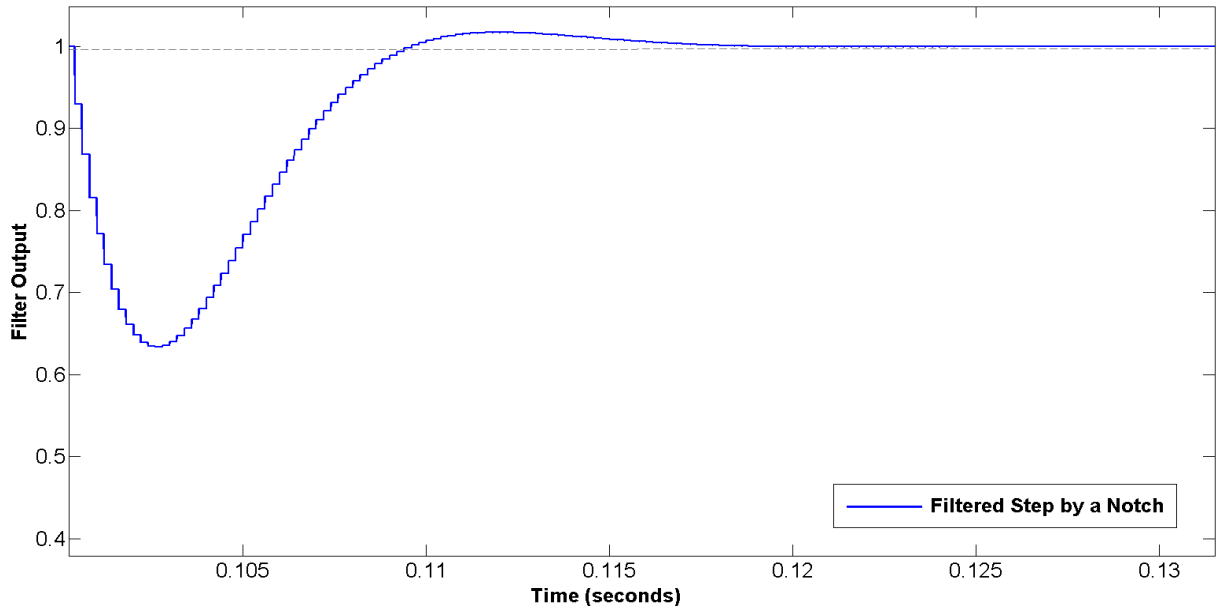

Figure 79. Step filtered with a notch filter designed for 80 Hz.

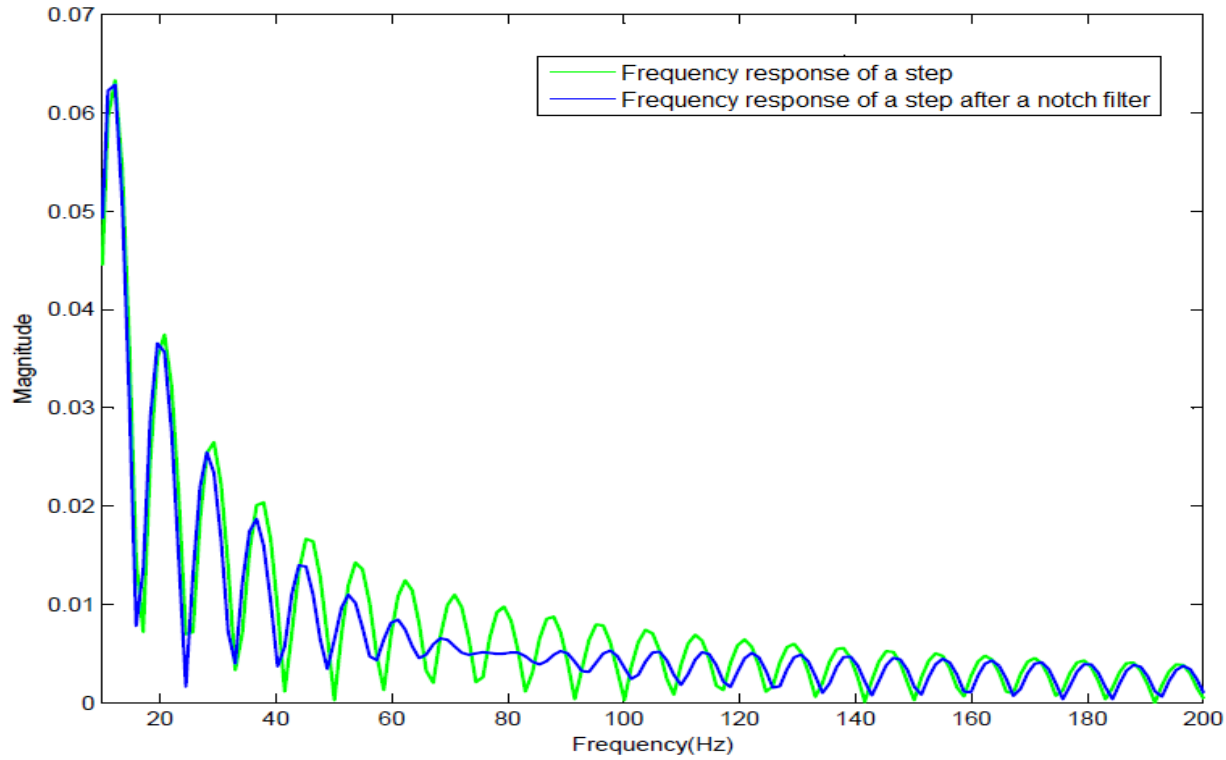

Figure 80. Fast Fourier Transforms (FFTs) of a step and a step filtered with a notch designed for 80 Hz.

In Figure 80 the Fast Fourier Transform (FFT) of a step is depicted in green and shows the magnitude of each harmonic component of the step signal. The same figure presents in blue the FFT of the step filtered by the notch filter defined by Eq. (7.13). Note that the notch filter attenuates the harmonic components surrounding 80 Hz present in the unfiltered step signal.

Thus a notch filter, designed for adequate frequency, placed after the cavity should be capable of eliminating some of the resonant modes observed in Figure 63. Figure 81 shows the transfer function of the cavity (G(s), plotted in Figure 63) and the notch transfer function (N(S)) placed in series to eliminate a resonant frequency at 120 Hz.

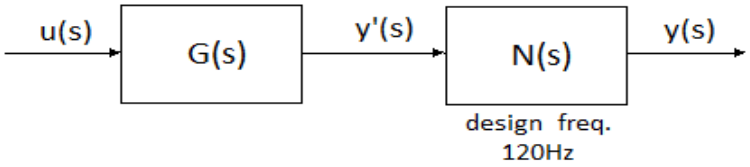

Figure 81. Cavity's and notch filter's transfer function placed in series.

Figure 82 illustrates the behavior of the cavity with and without filtering. In Subfigure 82.a the red line represents the simulated cavity detuning response after a step from 0 to 1V at a sampling time of 0.1 seconds, corresponding to the signal y'(s) represented in Figure 81 but in the time domain. The red line in Subfigure 82.b presents the Fast Fourier Transform (FFT) of this response which shows the resonant modes that have been excited by the step. It must be noted that the main resonant modes correspond to those shown in Figure 63. The simulated cavity detuning (y'(s)) processed by the notch filter designed for 120 Hz (whose attenuation in dBs for frequencies up to 250 Hz is shown in Subfigure 82.c), this is, the filtered cavity detuning that corresponds to y(s) but in the time domain, is represented in blue in Subfigure 82.a. The FFT of the filtered cavity detuning is represented in blue in Subfigure 82.b. Comparing both the detuning FFT and the filtered detuning FFT in Subfigure 82.b, it can be noticed that the notch filter has attenuated the resonant modes that were near 120Hz. The cavity detuning response and its FFT represented in red in Subfigures 82.a and 82.b respectively have shown how the resonant modes of the simulated cavity have been excited by a step input signal with the setup considered in Figure 81.

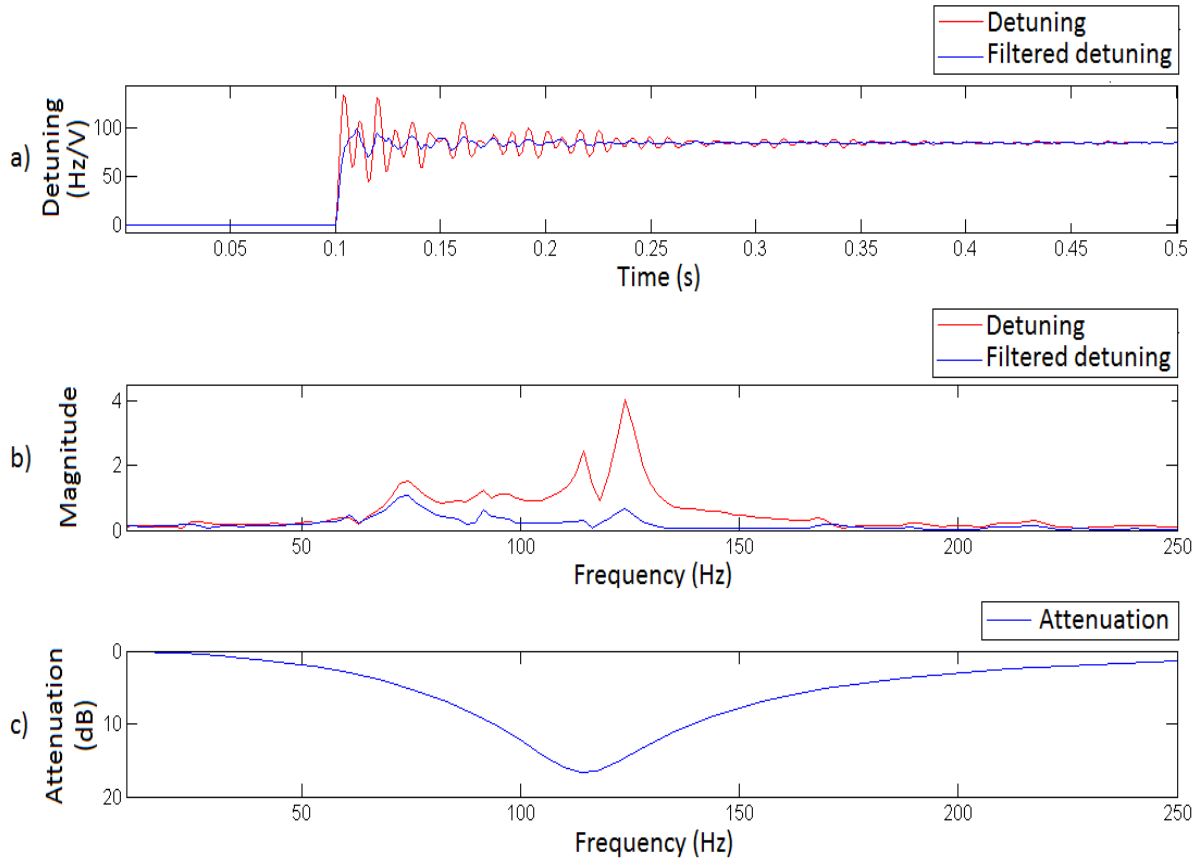

Figure 82. Filtered and unfiltered cavity detuning, Fast Fourier Transforms (FFTs) and filter attenuation. Subfigure a) Resonance frequency detuning and filtered detuning time responses to 1V step in piezo. Subfigure b) FFT responses of detuning and filtered detuning after 1V step in piezo. Subfigure c) Filter attenuation in the frequency range.

However, if the notch filter is placed before the cavity as in the setup shown in Figure 83, the y(s) response to one step in the input signal u(s) will be the same as that obtained by the setup in Figure 81, represented by the blue line in Subfigure 82.a. This is due to the fact that the transfer functions of the whole system shown in Figs. 81 and 83 are identical because of the commutative property.

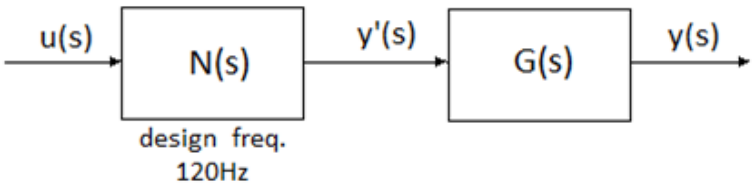

Figure 83. Notch filter and cavity transfer functions placed in series.

It must be noted that the setup of Figure 83 has the advantage that the content in the resonance frequency rejected by the notch filter has already been attenuated by said filter in the input signal to the simulated cavity. Hence the input signal to the cavity will have an attenuated effect on the excitation of the resonance frequency.

The setup shown in Figure 83 is to be considered within the optimized control strategy for the use of notch filters in order to avoid the excitation of resonance frequencies of the cavity by the controller actions.

Integration of Notch Filters in the Optimized Control Strategy

As analyzed previously, the notch filters avoid exciting the resonant modes of the cavity if they are placed before the piezoelectric actuator; i.e. at the output of the controller. In addition to the 120 Hz filter, a notch filter, with a wide rejection-band, has been designed at 80Hz to attenuate the resonant modes found at 73 Hz and at 90 Hz that still remain on Subfigure 82.b.

Thus, a first preliminary optimized control strategy aimed at avoiding the excitation of the cavity resonance frequencies is shown in Figure 84.

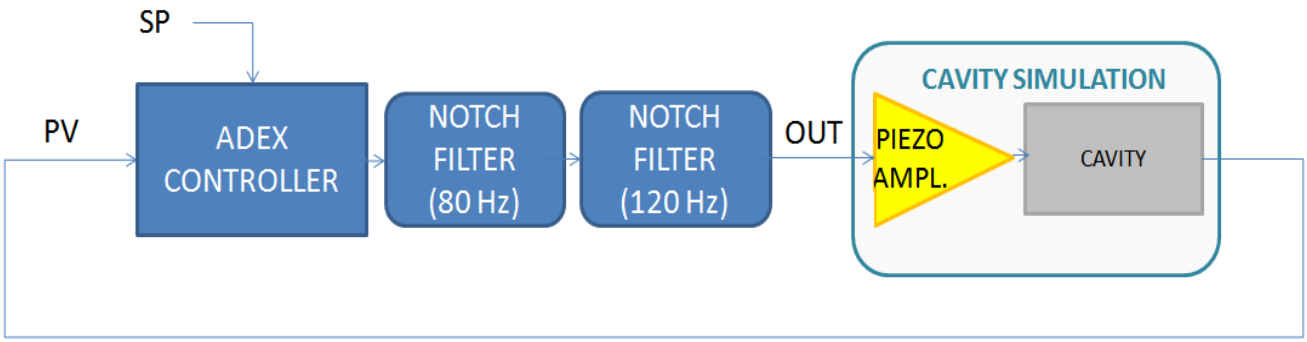

Figure 84. A first preliminary control strategy for the FT loop.

Notch filters avoid exciting the resonant modes of the cavity if they are placed before the piezoelectric actuator, this is, at the output of the controller. Two notch filters at 120 Hz and at 80 Hz, but this last one with a wide rejection-band in order to attenuate the simulated

cavity's resonant modes at 73 Hz and at 90 Hz, have been considered for this preliminary control strategy.

Figure 85 compares the step response without notch filtering in red, shown already in Figure 82, and the step response with the notch filters (considered in Figure 84) in blue.

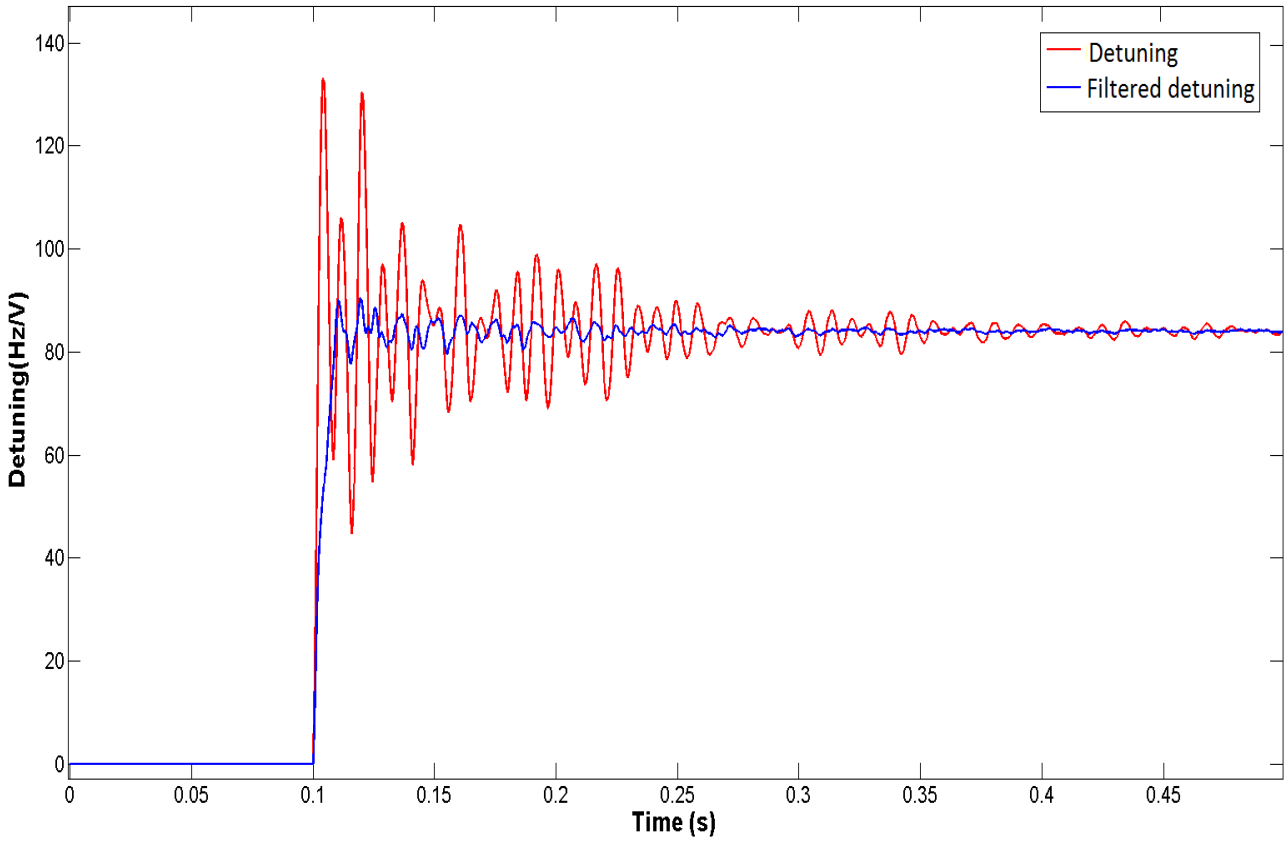

Figure 85. 1V step response of N(s) +G(s): Without (red) and with (blue) notch filters.

However, placing the notch filters after the controller output has certain limitations that must be considered. Imagine a microphonics excitation at 120 Hz on the cavity. The controller would not be able to react against it, as the notch filters would suppress the control action's harmonic component necessary to eliminate this perturbation. Therefore, if this strategy is applied it is necessary to have an additional strategy not affected by the notch filters which can effectively deal with this kind of perturbation.

Additionally, since there will be certain frequencies that the controller will not be able to handle due to the notch filters applied to its outputs, the controller should not generate control actions with components trying to compensate for the content in those frequencies in

the detuning signal. These kinds of components will have no effect on the frequency contents they intend to correct, but may deteriorate the control performance for the rest of the harmonic components of the cavity output variable or detuning. Therefore, it would be advisable to filter the cavity detuning with the same notch filters that filter the controller output. This means changing the first preliminary control strategy shown in Figure 84 to a second preliminary control strategy now shown in Figure 86.

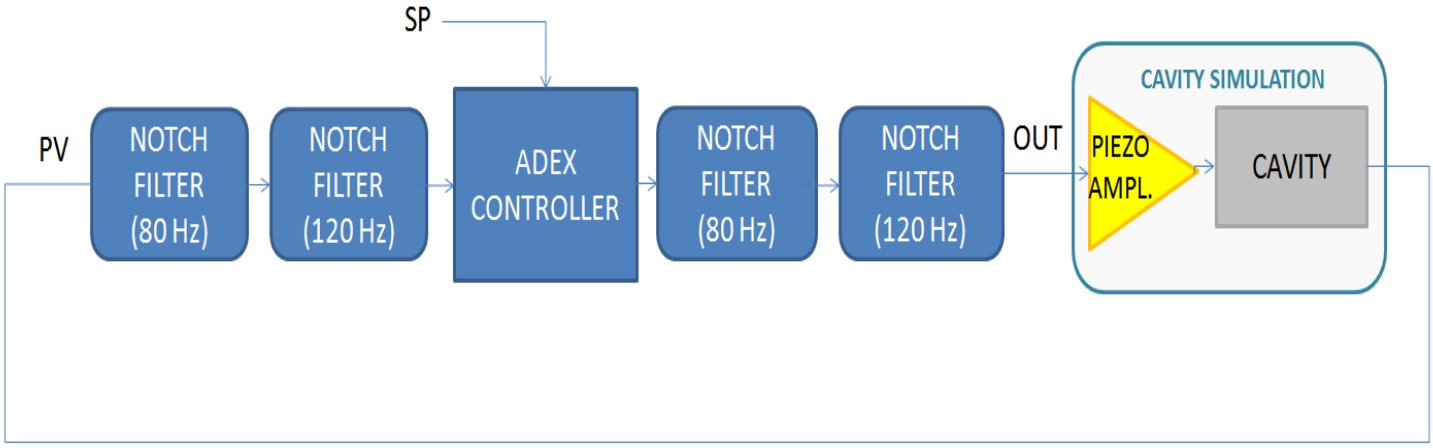

Figure 86. Second preliminary optimized control strategy.

7.3 MEANS TO COMPENSATE FOR EXTERNALLY EXCITED RESONANT MODES: CHEBYSHEV FILTERS.

To attenuate the frequency component of the cavity's resonance frequency detuning that is induced by external perturbations and cannot be compensated by the controller actions when limited by notch filtering, the optimized control strategy integrates Chebyshev filters, as they were introduced in [15], [16] and [17] for this application. This kind of control scheme is represented in Figure 87.

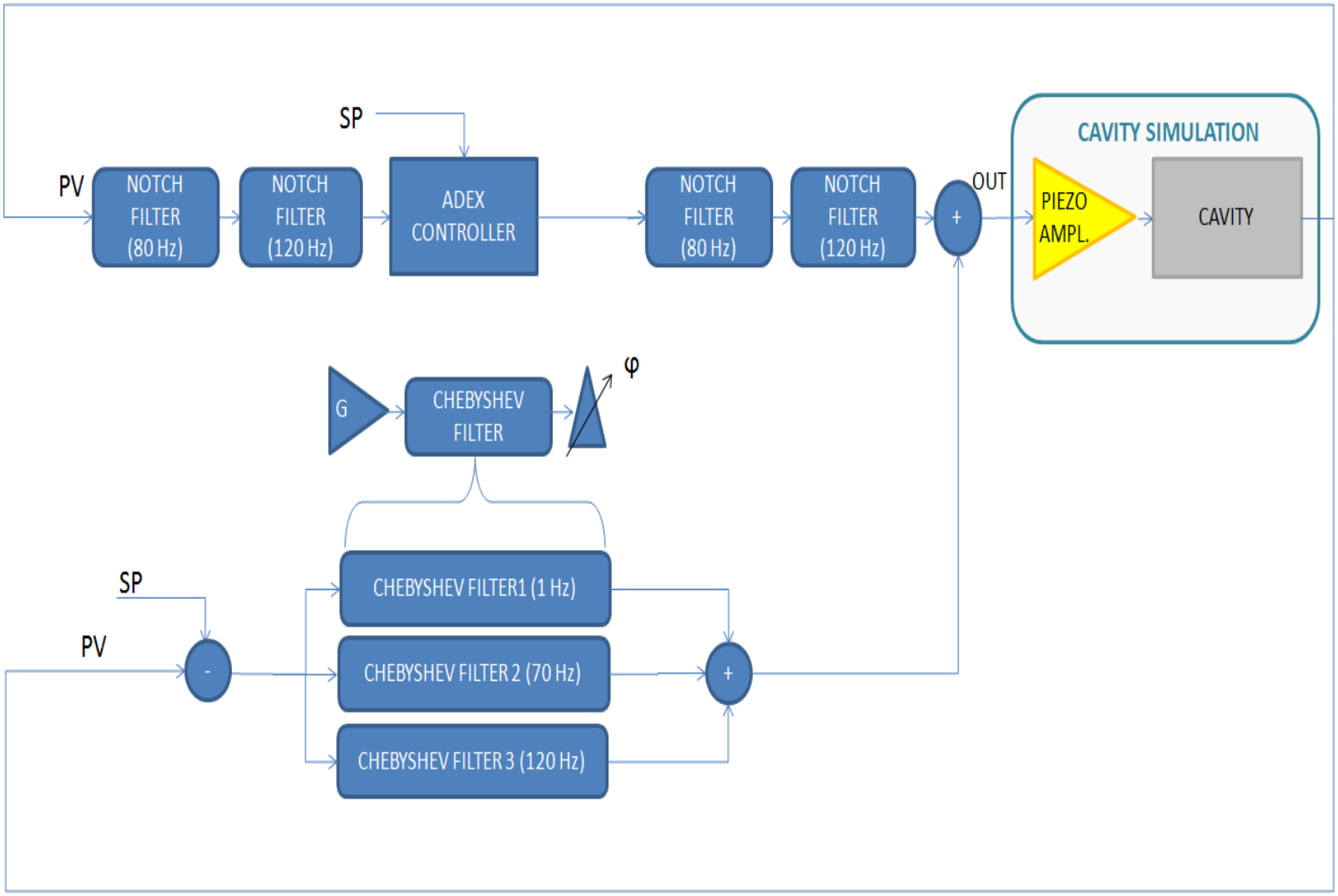

Figure 87. A third preliminary control strategy with notch and Chebyshev filters.

The control strategy represented in the figure integrates Chebyshev type II filters to attenuate those harmonic components of the cavity's resonance frequency detuning that could be induced by external perturbations and cannot be compensated by the controller actions when limited by notch filtering.

Three filters have been considered for the control of the cavity simulation, for microphonics corresponding to 1Hz, 71 Hz and the 120 Hz.

7.4 FEED-FORWARD STRATEGY TO COMPENSATE FOR LORENTZ FORCES DETUNING

An optimized control strategy has to be particularly careful with Lorentz forces, especially when the set points of a cavity ought to be changed. The RF field ramping will cause strong frequency detuning due to Lorentz forces that will deeply affect the FT loop performance.

Nevertheless, there exists available and useful knowledge about the initiation and evolution of the perturbation and on the effect of Lorentz force detuning. On one hand, the FTS can easily receive information from the DLLRF system, indicating when the RF field starts increasing and its evolution. On the other hand, the exact detuning caused by Lorentz forces in stationary regime is given by the equation that was already expressed in (4.42):

$$\Delta f_L = -k_L E_{acc}^2 \tag{7.14}$$

Therefore if, for example, an adjacent cavity failure occurs and the RF field's amplitude has to change from a set point value E_{acc1} to another set point value E_{acc2} in order to compensate, it would cause a detuning in the stationary regime Δf_{12} given by the following Equation:

$$\Delta f_{12} = \Delta f_{L1} - \Delta f_{L2} = K_L(E_{acc1}^2 - E_{acc2}^2) \tag{7.15}$$

If G is the static gain of the cavity detuning after a change in the piezo voltage, then in the stationary regime the detuning produced by a voltage variation is:

$$\Delta f_{12} = G\Delta V_{12} \tag{7.16}$$

Therefore the convenient change in voltage at the piezo to compensate for the Lorentz forces detuning, ΔV_{12}, can be calculated from the difference between equations (7.15) and (7.16):

$$\Delta V_{12} = \frac{K_L(E_{acc1}^2 - E_{acc2}^2)}{G} = K(E_{acc1}^2 - E_{acc2}^2) \qquad (7.17)$$

which leaves the control action that should be applied to the piezoelectric actuator as a function of the change in the field's amplitude $(E_{acc1}^2 - E_{acc2}^2)$, since E_{acc1} is the usual operating reference value, E_{acc2} the RF field's amplitude set point change that can be sent to the FTS, and K $(K = K_L/G)$ can be calculated empirically. Therefore, we can anticipate changes due to Lorentz forces after a cavity failure by reacting to the RF field's amplitude set point change.

This feed-forward strategy modifies the third preliminary optimized control strategy represented in Figure 87 in the manner shown in Figure 88. In this figure, the "Lorentz anticipation block" calculates the necessary ΔV_{12} according to (7.17) to compensate for the Lorentz detuning that will be produced by the LLRF loop when the RF field's amplitude set point changes. Note that the control action produced by the "Lorentz anticipation block" is added up before the notch filters in order to avoid the excitation of the resonant modes of the cavity.

The control strategy shown in Figure 88 determines the ADEX system which has been applied first to the high fidelity simulation anticipating its application to the prototypes of the spoke and elliptical cavities.

An additional consideration is that the control strategy of the ADEX system described by the block diagram of Figure 88 slightly modifies the original control strategy of the cavity which considered two independent systems for the LLRF loop and the FT loop and that was described in Figure 51. This control strategy adds a communication channel between the DLLRF system and the FTS so that the FTS can compensate for setpoint changes in the DLLRF system. This new strategy for the cavity is illustrated in the block diagram of Figure 89.

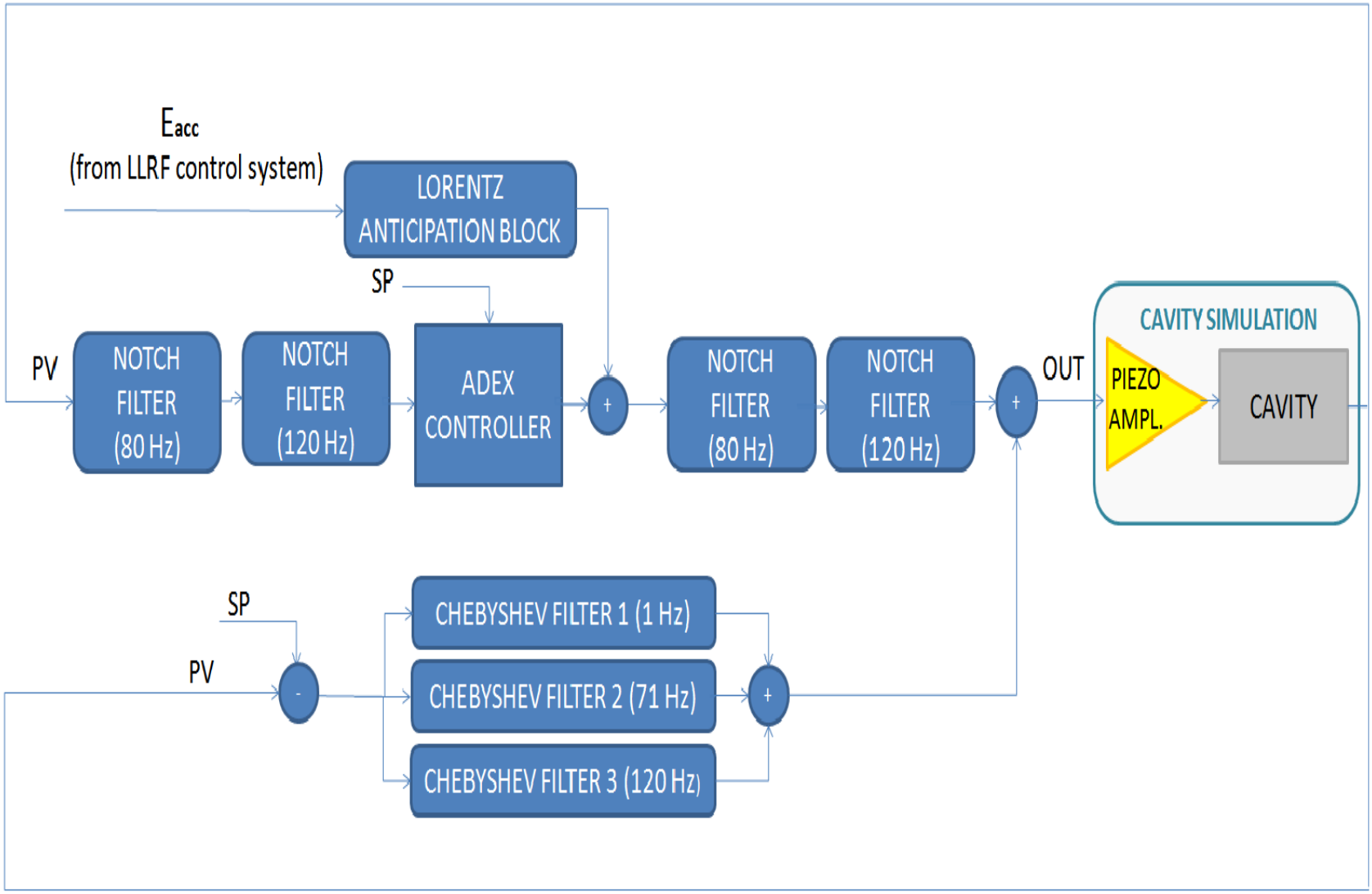

Figure 88. ADaptive predictive EXpert (ADEX) Optimized Adaptive System Design.

The following Chapter 8 presents the results on the control of the CNRS simulated 5 cell elliptical cavity obtained by three different control approaches for the FT control loop:

- The conventional “PID approach”.
- The “PID + Chebyshev filters approach” already considered in [15]–[17].
- The new “Optimized Adaptive Control System” approach.

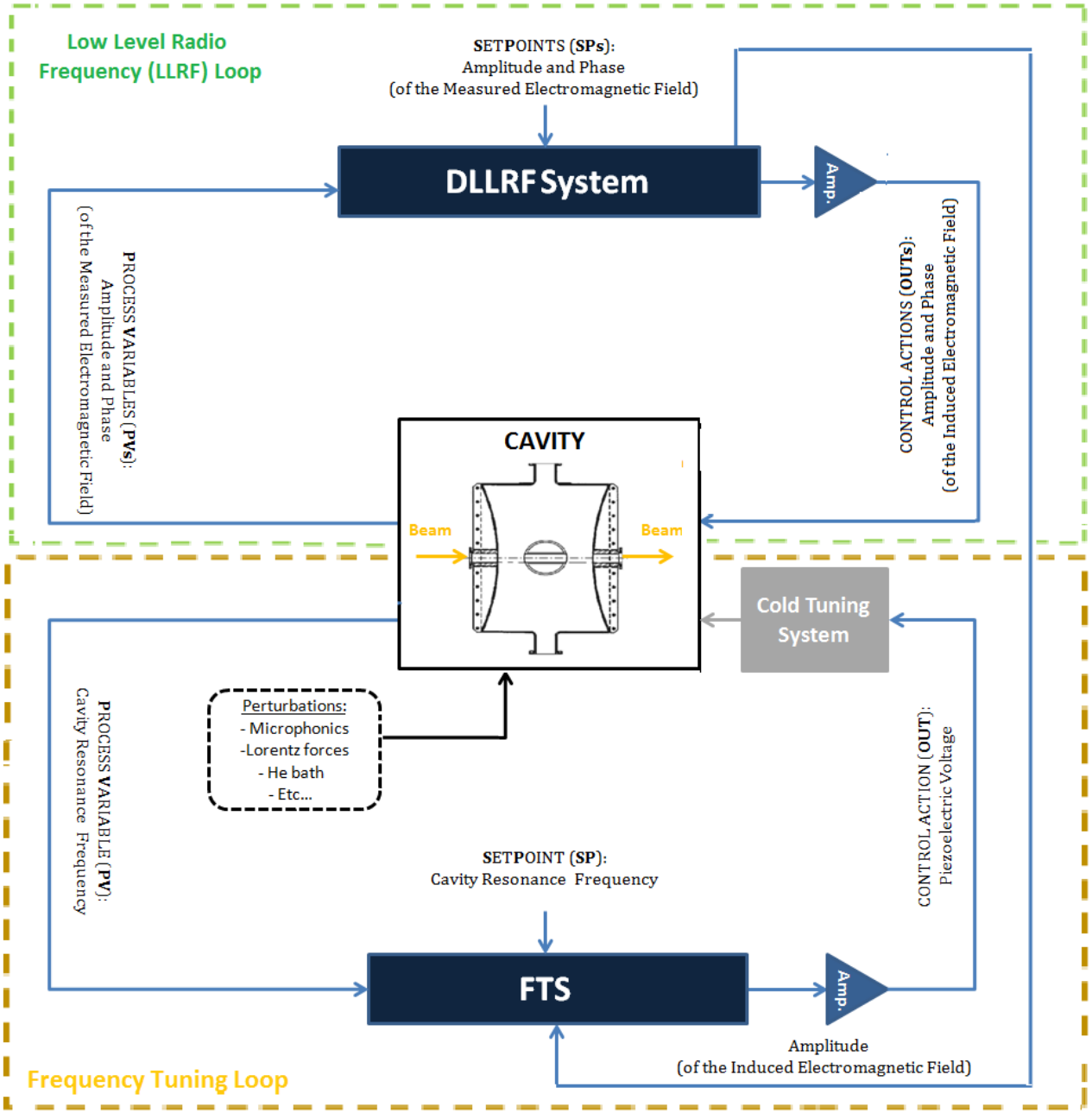

Figure 89. Cavity Control System Strategy modified with a communication channel between DLLRF System and FTS

CHAPTER VIII:

SIMULATION SCENARIO AND RESULTS

Figure 90 shows the main Simulink screen of the Superconducting 704.4 MHz Elliptical Cavity Simulator developed by Centre National de la Recherche Scientific (CNRS) [17] that reproduces the behavior of the prototype of this cavity.

The simulation has been developed in MATLAB Simulink and reproduces the behavior of the processes involved in the beam acceleration and their associated control loops, described in Chapter 4, inside the five cell elliptical cavity. As the time required by Simulink to compute the processes evolution is greater than the necessary time for the real processes evolution to take place the simulation has been time scaled. The scaling can be fixed by the user within certain limits concerning the highest simulation speed. Both vacuum and cryogenics systems are not contemplated under the scope of the simulation and are considered to work ideally thought out all the simulation time. The control loops with the

associated processes contemplated in the simulation are the ones represented in Figure 51. They are the LLRF and the FT control loops.

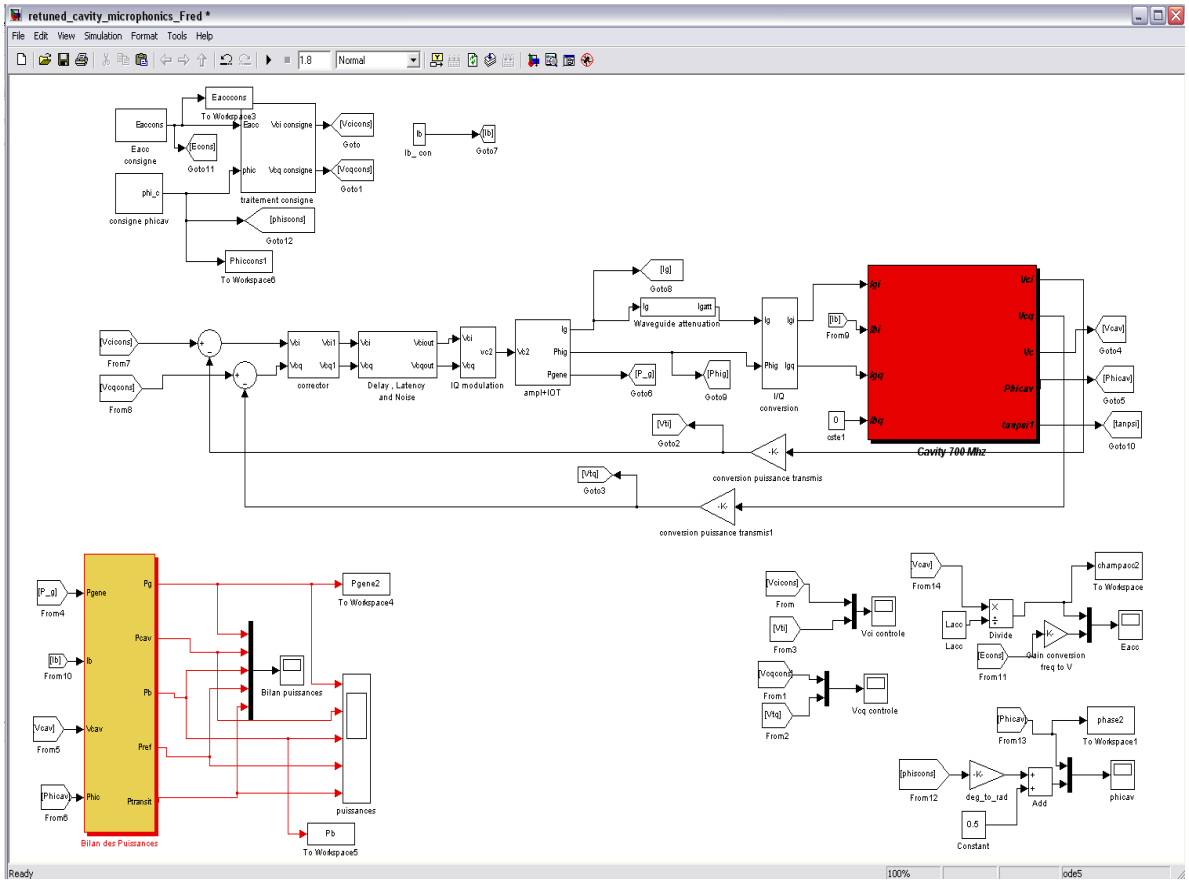

Figure 90. Superconducting 704.4 MHz Elliptical Cavity Simulation's Main Screen

The design of the ADEX Optimized Adaptive Control System is determined by the optimized control strategy described in the previous Chapter 7. It has been programmed in the ADEX control and Optimization Platform (ADEX COP), which is a software platform that facilitates the development and programming of control strategies integrating ADEX controllers, filters and other control tools. ANNEX A is devoted to the explanation of ADEX COP. The basic functioning of ADEX COP, used in the implementation of the ADEX system of this project and others, is represented in Figure 91.

ADEX COP includes a supervisory and configuration system (ADEX SCS) and a control and optimization system (ADEX COS). ADEX COP uses Labview as the graphical integrated development environment (IDE) for the implementation of optimized control strategies. The ADEX SCS allows:

1) The development of optimized control strategies for the ADEX COS, by means of a graphical user interface (GUI) that uses ADEX controllers and logic operators stored in the ADEX COS memory;
2) The creation and configuration of ADEX controllers to be integrated in the OCS. Also, Figure 91, represents schematically the implementation of the ADEX COS, which is described for every control instant in the following steps:

   a) Acquisition of process variables via OPC from the process simulator;
   b) Execution of the OCS capable of calculating the optimized control signals;
   c) Transfer via OPC of the optimized control signals to the process simulator.

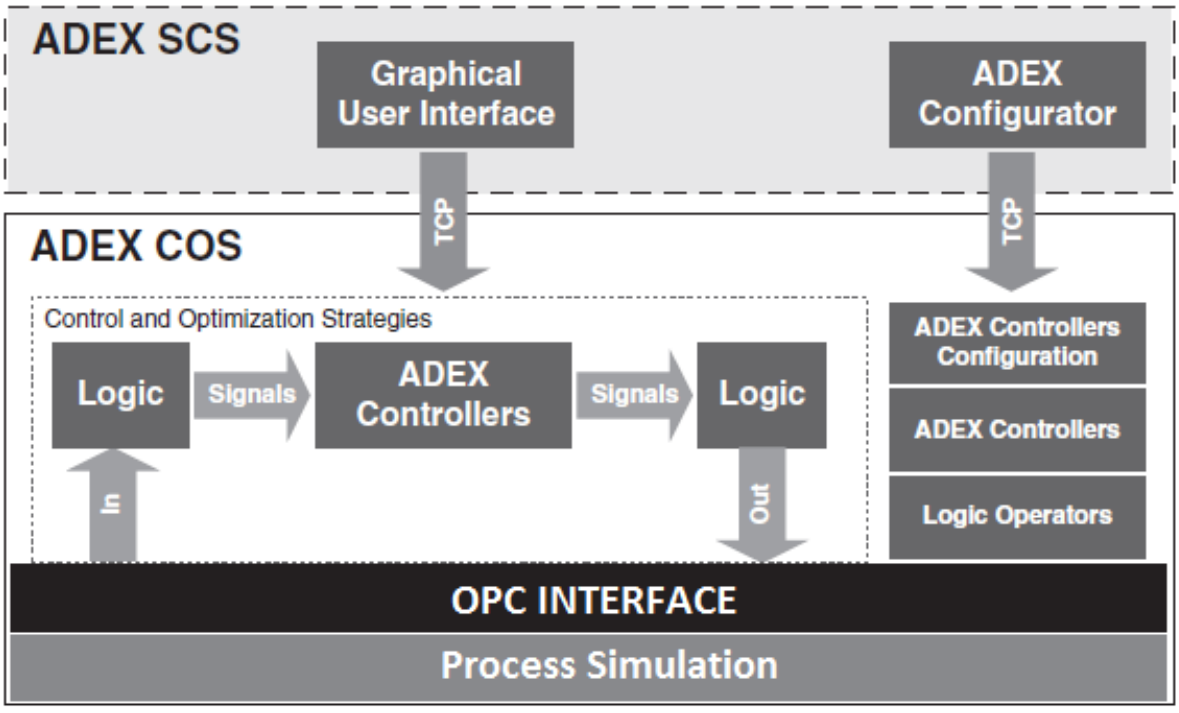

Figure 91. Basic structure of ADaptive predictive EXpert Control and Optimization Platform (ADEX COP)

Regarding the implementation of ADEX controllers, Figure 92 shows the graphical operator that represent ADEX controllers and that it is used in ADEX COP to integrate the ADEX controllers in the optimized control strategy.

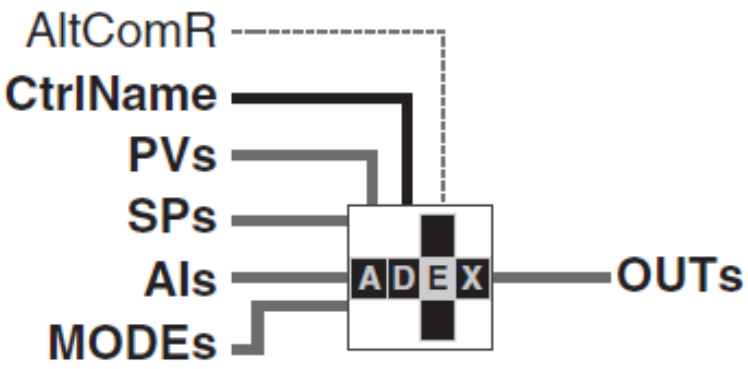

Figure 92. ADaptive predictive EXpert (ADEX) controller graphical operator. ADaptive predictive EXpert (ADEX) controller graphical operator.

The ADEX controllers (explained in depth in ANNEX B together with its configuration in ADEX COP) are designed to be multivariable, which means that their inputs or process outputs (PVs), set points (SPs), and outputs (OUTs) are vectors. Also, the controller receives the information of the actual input (AIs) vector applied to the process in the previous control instant, the mode (MODEs) of operation, the controller name (CtrlName) and a signal (AltComR) indicating that the OPC communication with the process simulator is functioning correctly. Likewise, ADEX COP enables the definition and configuration of the EX and AP domains included in a controller.

As the ADEX system is running on ADEX COP and the time scaled cavity simulation is running on Simulink, these two different environments must exchange process variables values and control signals by means of an OPC communication [124] between both of them, as shown in Figure 93.

While running a simulation both ADEX COP and Simulink are acting as OPC clients. Thus, the simulation writes the values of the process variables every second, after performing the necessary computation, on the OPC server. On the other side, the ADEX COP platform reads these values, executes the control strategy, and writes on the OPC server the pertinent control actions (in this case, only the voltage applied to the piezo). This control action will be read from the OPC server by Simulink and considered for the necessary computation in the

next second. This scheme allowed to establish the necessary interface to tests the control strategy prior to embedding it in the hardware platform that will be presented in Chapter 9.

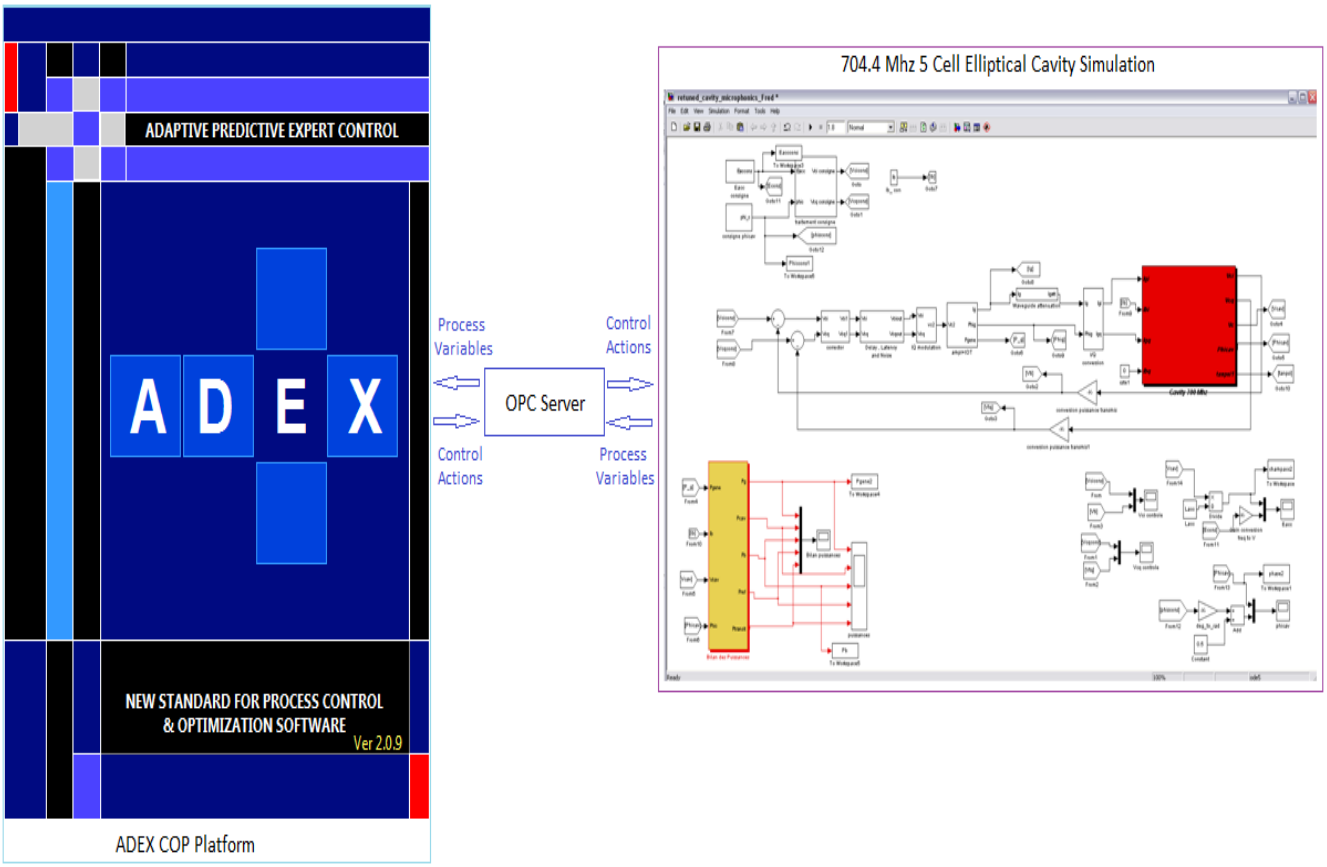

Figure 93. OPC communication between ADEX COP and the Simulink simulation.

8.1 SIMULATED SCENARIO

As mentioned in Chapter 3, the accelerator operation has to be robust against cavity failures. The chosen strategy to recover from a cavity failure is to force the re-tuning of the adjacent cavities to compensate for the failed one. To compare alternative control solutions for the FTS, the scenario of a cavity which has to be re-tuned to compensate for a failure has been chosen because it is considered to be the most stringent scenario for the control systems operation. This retuning scenario is described on Figure 94.

The main steps in the simulation represented by Figure 94 are:

- At time t= 80 ms , the beam is stopped because a failure has been detected in the accelerator.
- Then the new set points for the accelerating fields and phases are sent to the compensation cavity.
- The beam is resumed 130 ms later, once the accelerating fields and phases have been stabilized on the new targets.

In Figure 94, t=0 ms represents a random moment during the usual accelerator's operation. Subfigure 94.a represents the beam intensity (I_{b0}) in the cavity, initially at 4 mA, which is stopped after the cavity failure and resumed 130 ms later at the initial value. When the beam is stopped the accelerating field, E_{acc}, is ramped up into the cavity (Subfigure 94.b). This takes place in two steps to leave some time for the FT loop to compensate for the Lorentz detuning effect caused by the field increase. The phase, ϕ_s, is also changed to a new set point and is ramped to minimize the transient power consumption during the procedure (Subfigure 94.c). Finally, since the cavity set points have changed, Δf_{opt} is also changed according to Equation (4.43); therefore at time t=180 ms the cavity frequency detuning set point is changed to its new optimal value (Subfigure 94.d). Subfigure 94.e shows the simulated effect of the motor in the cavity detuning. The motor will slowly compensate for 375 Hz in the cavity detuning, allowing for the faster piezo compensation to get back to its nominal operating range after the transient provoked by the set point changes.

Both Lorentz forces and microphonic perturbations have been considered throughout this scenario. For microphonics three sinusoidal perturbations have been considered acting at a frequency of 1, 71, and 120 Hz and causing maximum deviations of 10, 10 and 20 Hz in the cavity's frequency detuning.

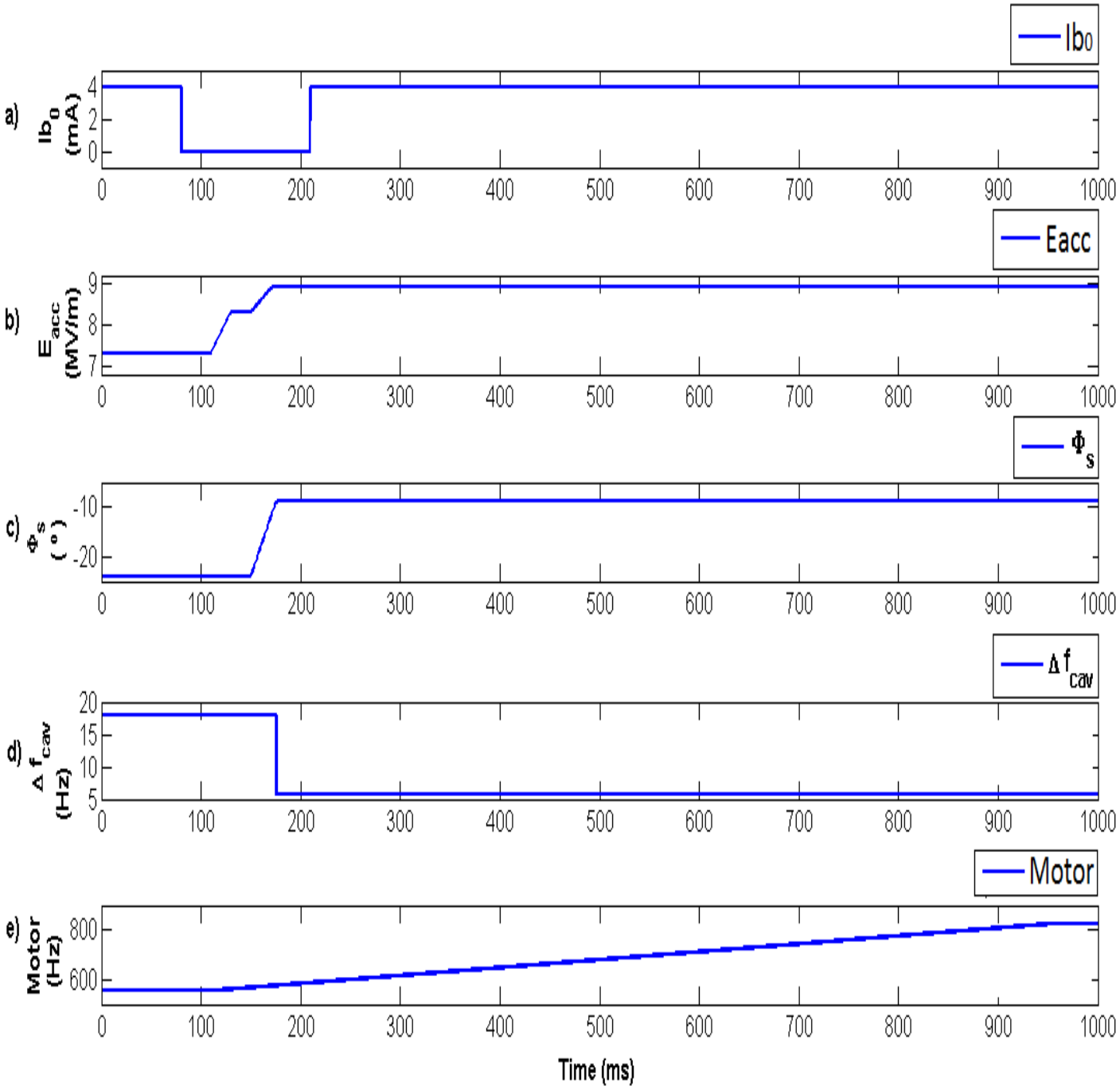

Figure 94. Simulation scenario for the retuning procedure of a cavity. Subfigure a) Beam intensity throughout the simulation. Subfigure b) Field set point throughout the simulation. Subfigure c) Phase set point throughout the simulation. Subfigure d) Frequency detuning set point throughout the simulation. Subfigure e) Detuning caused by the motor's operation throughout the simulation.

8.2 SIMULATED RESULTS

PID Approach

The performance of the FT loop obtained in simulation by a PID controller driving the piezoelectric actuator is illustrated by the experimental results shown in Figure 95.

Figure 95 presents the evolution of the accelerating process critical variables in the cavity during one second of simulation. The abscissa axis is the time scale in milliseconds. The evolution of the amplitude of the field inside the cavity (E_{acc}) is represented by the blue line in Subfigure 95.a, along with the beam intensity (Ib0), represented by the red dotted line. The evolution of the cavity's resonance frequency detuning can be seen in Subfigure 95.b in the blue line, while the red line shows its setpoint. The power consumed to generate the field can be seen in Subfigure 95.c. Finally, the voltage applied to the piezoelectric actuator to drive the cavity's detuning to its set point is represented by the blue line in Subfigure 95.d. The simulated motor effect on the cavity detuning is also shown in Subfigure 95.d but in the red line.

The interpretation from the origin of the subsequent steps is the following:

- When the beam is switched off at 80 ms (Subfigure 95.a) the RF generator power immediately decreases (Subfigure 95.c). Therefore the consumed power is only the power reflected at the cavity entrance and the RF power stored in the cavity.
- Shortly after, the field's amplitude is increased (Subfigure 95.a) and this causes a fall in the cavity detuning (Subfigure 95.b) due to Lorentz forces. Despite PID compensation acting on the piezo (Subfigure 95.d), the drift in the cavity detuning causes the power consumption to rise sharply and saturate at 30 kW (Subfigure 95.a). This causes deviations in the field as can be seen on the detail of Subfigure 95.a. Lack of precision on field control is critical as it has been determined [125] that proper acceleration can be guaranteed with an error smaller than 0.5%.

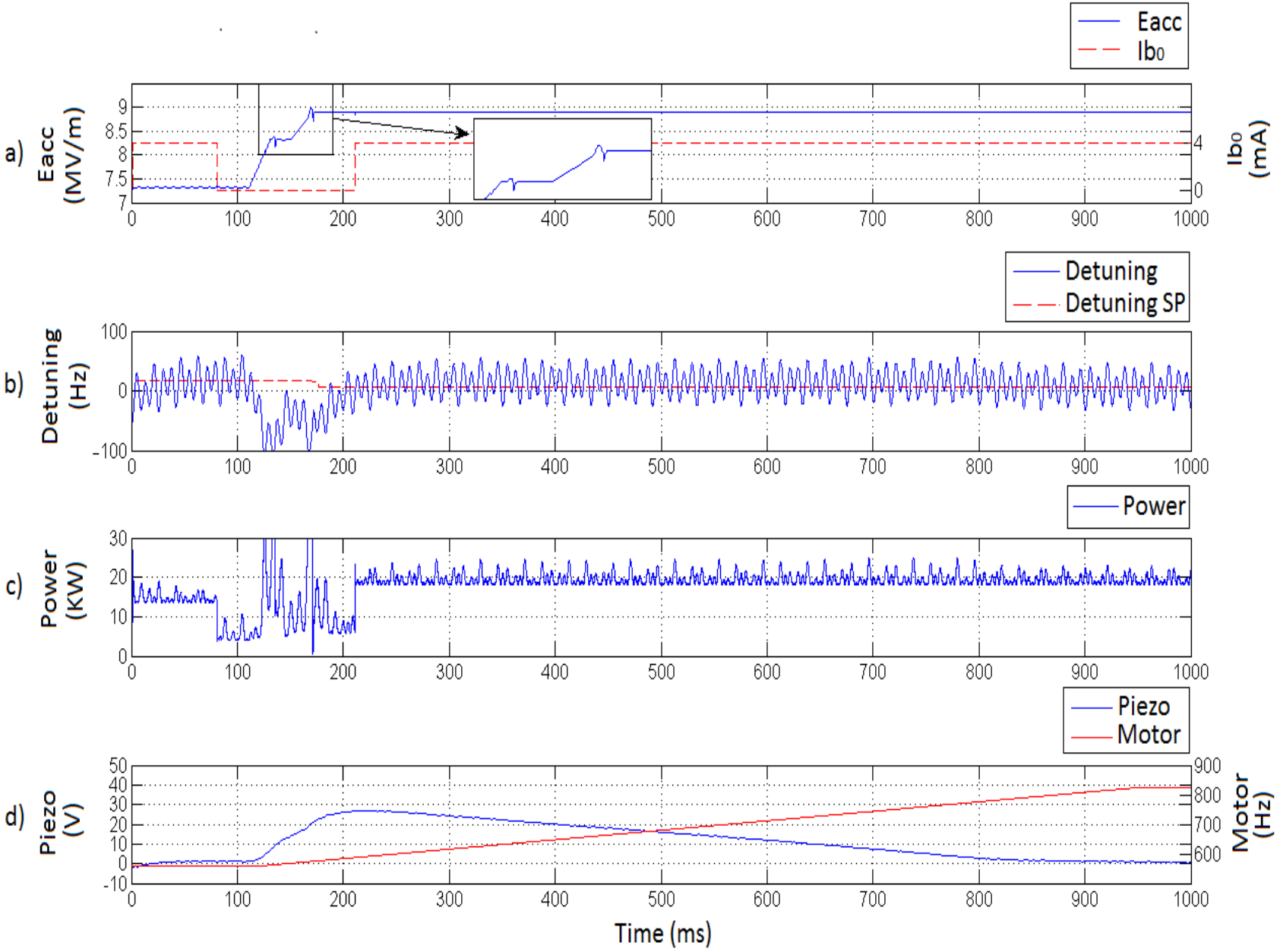

Figure 95. "Proportional Integral Derivative (PID) control approach" performance. Subfigure a) Amplitude of the field inside the cavity throughout the simulation. Subfigure b) Cavity's detuning throughout the simulation. Subfigure c) Power consumption throughout the simulation. Subfigure d) Voltage applied to piezo and motor effect on the cavity detuning.

PID + Chebyshev Filters Approach

The "PID + Chebyshev filters approach" described in [15]–[17] represents a significant enhancement to the control system performance with respect to the previously considered "PID approach". The control strategy used by the "PID + Chebyshev filters approach" is represented by the block diagram previously shown in Figure 64.

Figure 96 presents the results in simulation obtained by this approach for the same experiment previously considered for the PID approach. Figure 96 has the same chromatic criterion and scaling used for Figure 96. It can be noticed that the "PID + Chebyshev filters approach" produce a significant reduction in the detuning oscillations around the set point, which causes a significant drop in power consumption.

Although the control performance in the same scenario is significantly better, it can be noticed that:

- The cavity's detuning experiences a significant deviation from its set point after the cavity failure, due to the growing RF field's amplitude that induces Lorentz forces in the cavity.

- While the stepper motor is compressing the cavity, an offset between the cavity's detuning and its set point is produced such that the PID control action cannot compensate.

It must be noted that requirements for the maximum control errors on the cavity field control are accomplished (0.5 % error on E_{acc} and 0.5° on ϕ_s) with this enhancement.

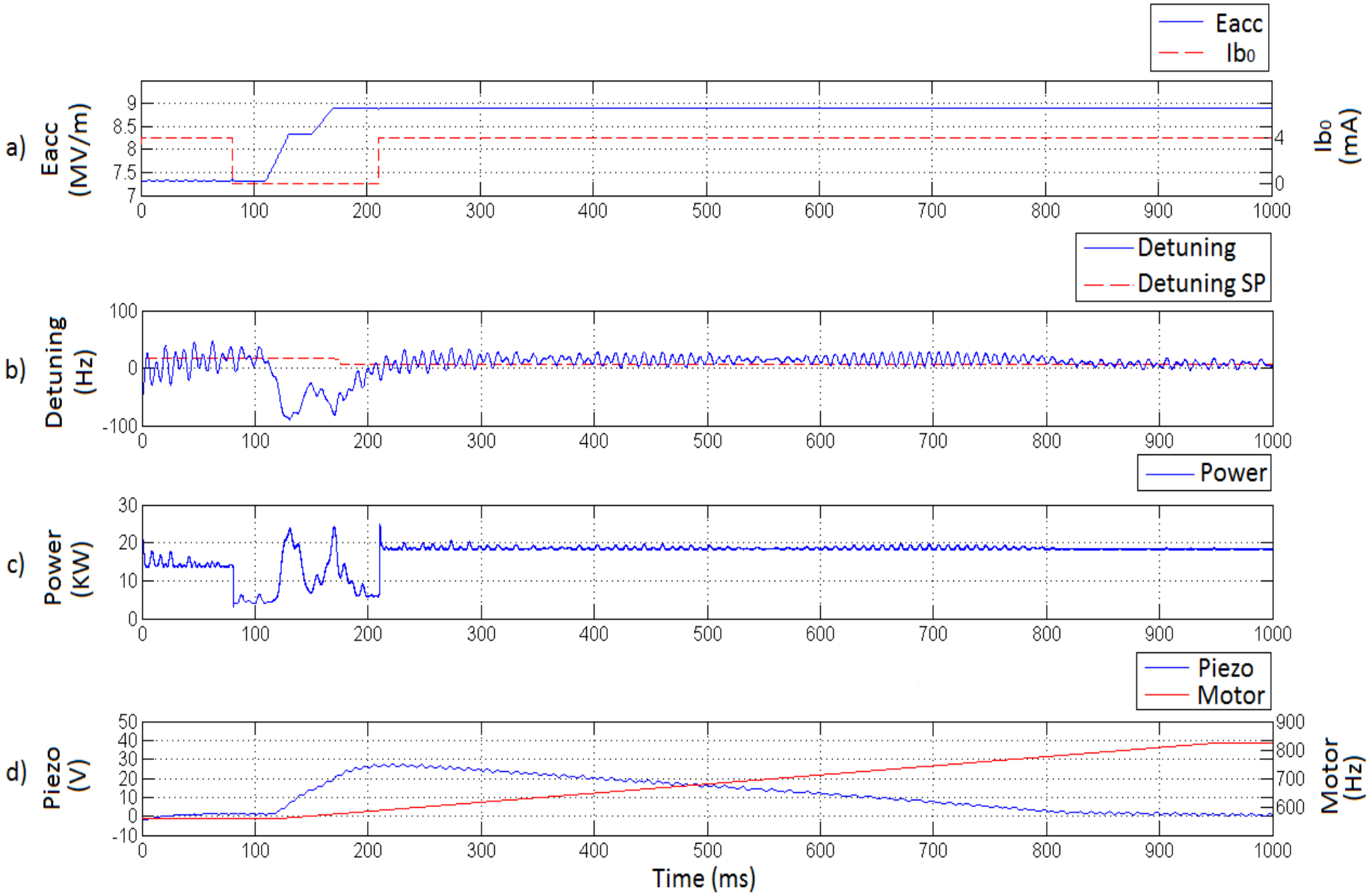

Figure 96. "Proportional Integral Derivative (PID) + Chebyshev filters approach" performance. Subfigure a) Amplitude of the field inside the cavity throughout the simulation. Subfigure b) Cavity's detuning throughout the simulation. Subfigure c) Power consumption throughout the simulation. Subfigure d) Voltage applied to piezoelectric and motor effect on the cavity detuning.

Optimized Adaptive Control System Approach

Figure 97 presents the results in simulation obtained by the ADEX OACS system described by Figure 88 for the same experiment considered previously for the two PID approaches. Figure 97 has the same chromatic criterion and scaling used for Figs. 95 and 96. The ADEX OACS system represented in Figure 88 operated with a Control Period of 2 ms for the Adaptive Predictive Expert ADEX controller and an execution time of 200 ms for the notch and Chebyshev filters, and also for the Lorentz forces anticipation block.

The ADEX controller included an adaptive predictive (AP) domain, an upper expert domain and a lower one. The configuration of the other structure variables of the ADEX controller (already commented in subsection 7.1 of this report) were set up for the AP domain as follows: (i) the adaptive predictive model was of third order with one control period of time delay; (ii) the upper and lower limits on the piezo control signal were -30V and +50V, respectively; (iii) No noise level was considered on the cavity frequency detuning; (iv) the rate of change per control period of the desired process output trajectory was chosen equal to 100 Hz, and (v) the prediction horizon was selected equal to 5 control periods. The ADEX controller upper and lower expert domains determined an expert control action for the piezo when the frequency detuning surpassed the upper level of 300Hz or went under the lower level of -100Hz.

In order to make a qualitative comparison between the results obtained with the ADEX system and the PID based system ("PID + Chebyshev filters approach"), Figure 98 integrates results from simulations recorded in Figures 96 and 97. Subfigure 98.a shows the cavity detuning in both experiences and their setpoint. The detuning under ADEX system control is represented by the green line while with the PID plus Chevyshev filters has been shown in blue, while the setpoint of both is represented by 26 the red line. Subfigure 98.b shows power consumption under ADEX system control represented by the green line, while the power consumption under PID based system control is shown in blue.

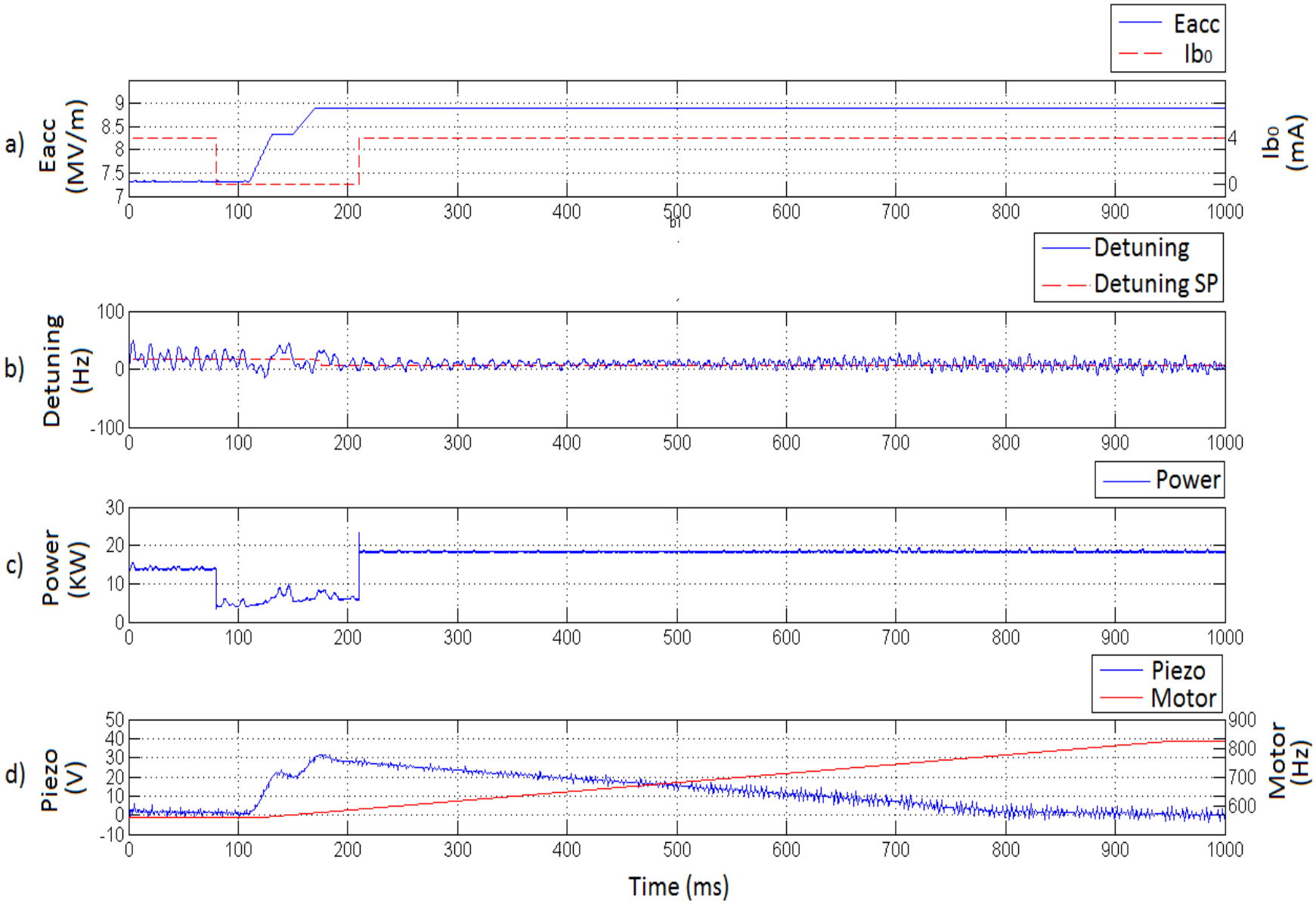

Figure 97. "ADaptive predictive EXpert (ADEX) Optimized Adaptive approach" control performance. Subfigure a) Amplitude of the field inside the cavity throughout the simulation. Subfigure b) Cavity's detuning throughout the simulation. Subfigure c) Power consumption throughout the simulation. Subfigure d) Voltage applied to piezo and motor effect on the cavity detuning.

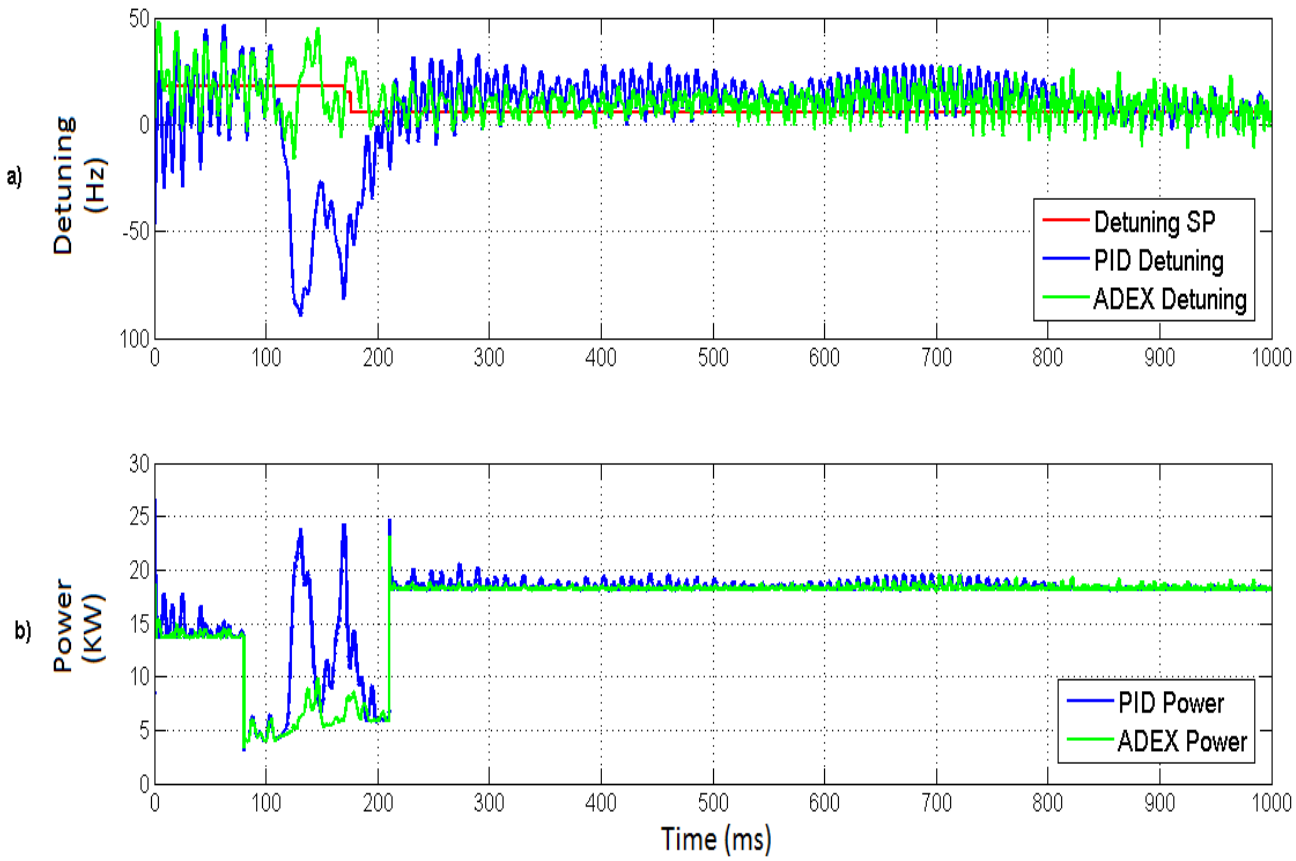

Figure 98. ADaptive Predictive EXpert (ADEX) and Proportional Integral Derivative (PID) based systems' detuning control performance. Subfigure a) ADEX and PID based systems' detuning control performance. Subfigure b) ADEX and PID based systems' power consumption throughout the simulation.

The following remarks can be derived from a comparative analysis using Figure 98:

- A significant reduction in the cavity detuning oscillations around its set point has been achieved by the ADEX system, while the power consumption has also been reduced and is maintained nearly at its minimum throughout the experiment.
- The offset between the cavity detuning and its set point observed under the PID based system, practically disappears under the ADEX system.

On the other hand a statistical analysis yields the following results:

- The mean of the square deviation of the cavity's resonance frequency with the ADEX OACS approach is 15.69 and with the PID approach ("PID + Chebyshev filters approach") it is 25.5. So the mean of the square deviation of the cavity's resonance frequency is improved by 38,5 % with the ADEX OACS approach.

- The mean power consumption with the ADEX OACS approach is 16,300 kW and with the PID approach it is 16,840 kW. There is an approximate power consumption reduction of 3.2 % with the ADEX OACS approach.

Chebyshev bandpass filters have demonstrated capacity to enhance both the ADEX and the PID solution compensating for perturbations which are foreseen in the simulation and that may be encountered in the real tests as they correspond to the mechanical resonant modes of the cavity. However, microphonics have been reported to be an uncertain source of perturbations in several studies [126], [14] currently trying to model and predict their appearance and behavior.

The following section describes the performance of both approaches adding to the simulation the effect of a severe unforeseen microphonic perturbation in order to test their reliability in uncertain operating conditions.

Perturbation in the Simulated Scenario for Reliability Analysis

In this section, a "Perturbed Simulated Scenario" (PSS) will be applied to the cavity both under the PID based control system with Chebyshev filters and under the ADEX system, in order to analyze comparatively the performance of both methodologies for a reliability analysis. The PSS is equivalent to the previously described scenario but an unforeseen microphonic perturbation of 20 Hz frequency occurs with detuning amplitude of 50 Hz on the cavity RF resonance frequency. The results obtained by the execution of the PSS under the PID based system control are presented in Figure 99.

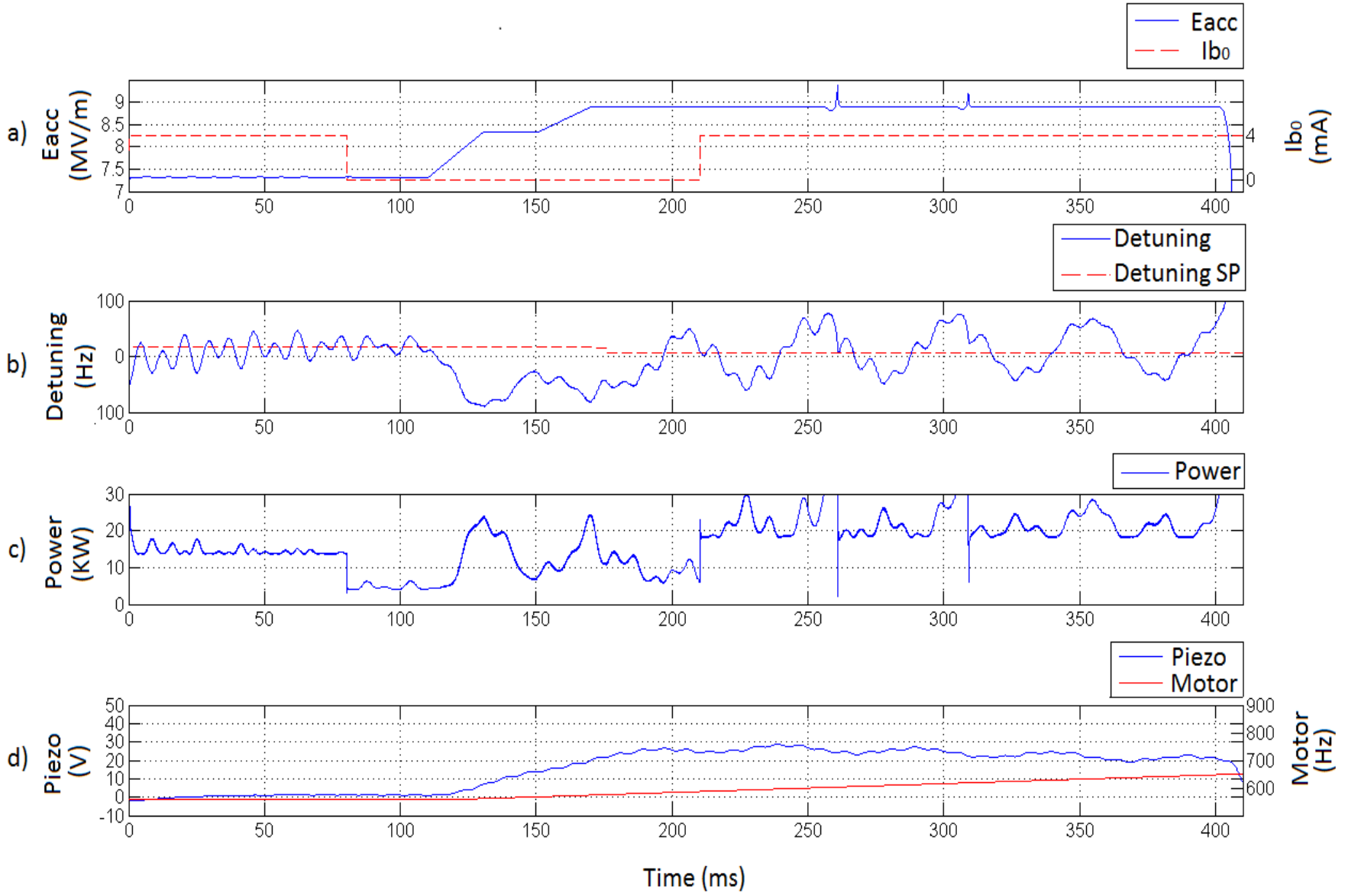

Figure 99. Proportional Integral Derivative (PID) based system's performance under unexpected strong perturbations. Subfigure a) Amplitude of the field inside the cavity throughout the simulation. Subfigure b) Cavity's detuning throughout the simulation. Subfigure c) Power consumption throughout the simulation. Subfigure d) Voltage applied to piezo and motor effect on the cavity detuning.

It can be noticed that Figure 99 is similar to Figure 96 until the beam is turned ON after the variables are stabilized in the simulated scenario (Subfigure 99.a). The explanation of the evolution of the cavity variables in Figure 99 is presented in the following:

- When the beam is switched off at 80 ms (Subfigure 99.a) the RF generator power immediately decreases (Subfigure 99.c). Therefore the consumed power is only the power reflected and the RF power losses in the cavity.

- Shortly after, the field's amplitude is increased (Subfigure 99.a) and this causes a fall in the cavity detuning (Subfigure 99.b) due to Lorentz forces. Despite PID compensation acting on the piezo (Subfigure 99.d), the drift in the cavity detuning increases the power consumption (Subfigure 99.c).

- After the transient, once the field's amplitude has stabilized and the piezo has approached the detuning to its setpoint, the beam has been switched ON again at 220 ms (Subfigure 99.a) raising the power consumption (Subfigure 99.c).

- However, immediately after the beam has been switched ON and the unforeseen external microphonic perturbation is simulated in the system at about 220 ms, strong cyclical oscillations can be observed in the cavity's detuning (Subfigure 99.b). These oscillations are hardly compensated by the voltage that the PID is applying to the piezoelectric actuator (Subfigure 99.d) and the drifts of the frequency from its set point (optimal value that minimizes the power consumption) cause the power (Subfigure 99.c) to increase even more approaching the limit of power supply (30,000 W) three times (270 ms, 320 ms 400 ms). The third time the power supply reaches saturation the RF control system loses control of the cavity and the field drops (Subfigure 99.a). The simulation was interrupted at 410 ms, while it was intended to last 1 sec.

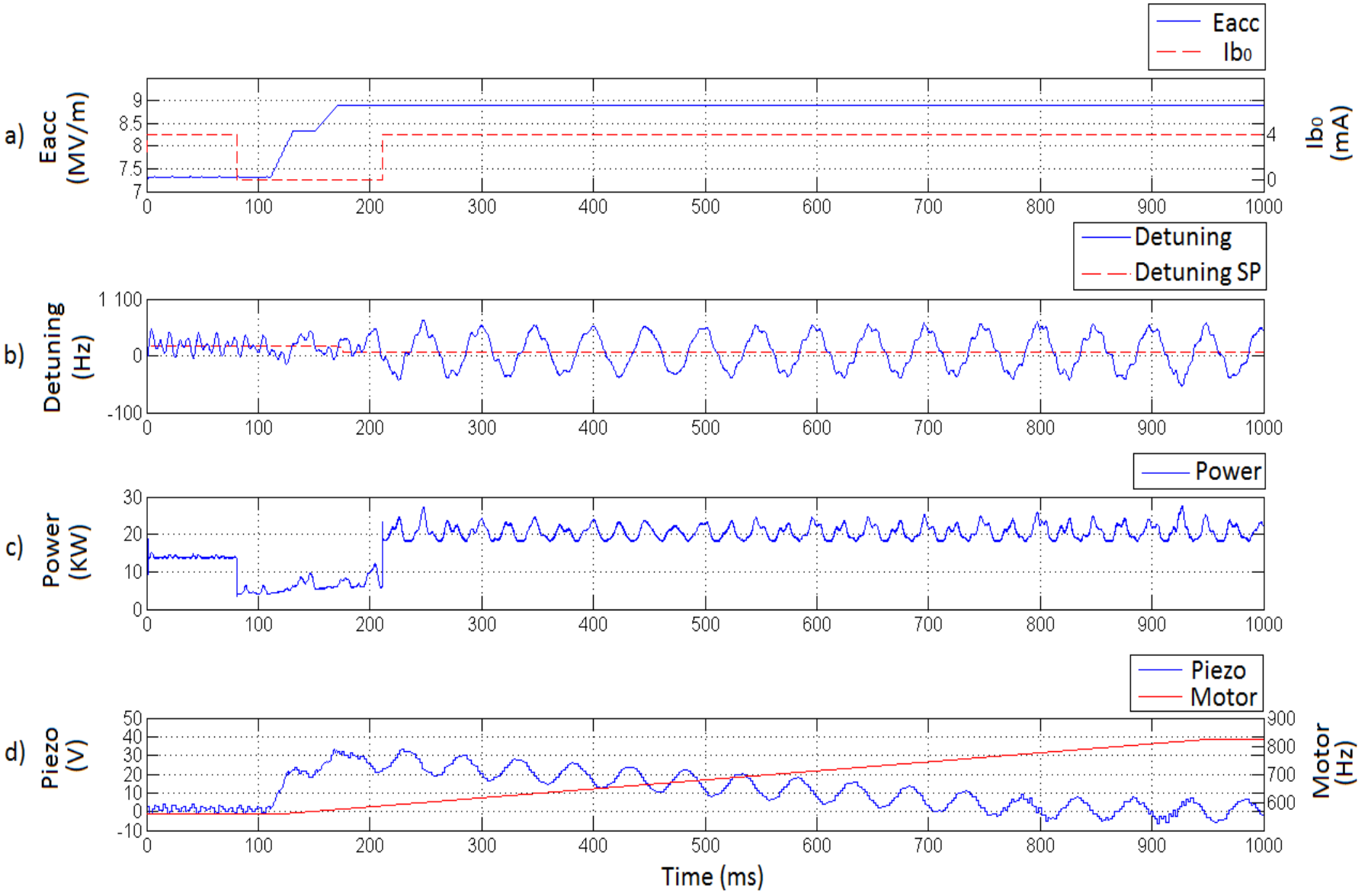

Figure 100. ADaptive predictive EXpert (ADEX) system's performance under unexpected strong perturbations. Subfigure a) Amplitude of the field inside the cavity throughout the simulation. Subfigure b) Cavity's detuning throughout the simulation. Subfigure c) Power consumption throughout the simulation. Subfigure d) Voltage applied to piezo and motor effect on the cavity detuning.

On the other hand, the results obtained by the execution of the PSS under the ADEX system control are presented in Figure 100. It can be noticed that this figure is similar to Figure 97, until the beam is turned ON after the cavity variables are stabilized (Subfigure 100.a). Thus, the evolution of the cavity variables in Figure 100 up to this point is the equivalent to that presented in Figure 97. However, right after the beam has been switched ON and the unforeseen external microphonics perturbation is introduced in the simulation at about 220 ms, strong cyclical oscillations can be observed in the cavity's detuning (Subfigure 100.b). However, the resonance frequency was maintained within operational limits and it completed the simulation without letting the RF system lose control of the field inside the cavity. Also, it can be observed that the power consumption (Subfigure 100.c) and the control action on the piezo (Subfigure 100.d) evolved with limited oscillations around the values previously observed in Figure 97, where the strong perturbation was not present.

A comparative statistical analysis of the "PID + Chebyshev filters approach" and the "ADEX + Chebyshev filters approach" performance in an scenario with an unforeseen severe perturbation (Figures 99 and 100) yields the following results:

- The mean of the square deviation of the cavity's resonance frequency with the "ADEX + Chebyshev filters approach" is 29.66 and with the "PID + Chebyshev filters approach" is 51.98. Thus, the mean of the square deviation of the cavity's resonance frequency is improved by 42.93 % with the "ADEX + Chevychev Filters Approach".
- The mean power consumption with the "ADEX + Chevychev Filters Approach" is 13,780 KW and with the "PID + Chebyshev filters approach" it is 16,270 KW. Thus, there is an approximate power consumption reduction of 15.3 % with the "ADEX + bandpass filters approach".

Obviously the results have been normalized as if the PID "PID + Chebyshev filters approach" had completed the experience. For the uncompleted part of the experience a mean of the cavity resonance frequency and the power consumption between 200 – 400 ms has been considered as the performance the "PID + Chebyshev filters approach" would have had.

Chebyshev filters enhance both the ADEX and the PID solution compensating for perturbations which are foreseen but their performance is vain under unforeseen perturbations. This is logical since they are designed for reacting to a fixed unmobile and sinusoidal perturbation. Thus, the excellence of their performance in the real test can be doubted.

Under these circumstances ADEX maintains the cavity frequency under control while PID may saturate the amplifier and provoke the LLRF system control loss due to the saturation of the power supply which is foreseen to be 30,000 kW.

In this experiment, the ADEX system exhibited more reliability than the PID based System in an uncertain scenario with unforeseen perturbations. In fact, the PID control parameters that had been tuned for the foreseen operating conditions in a context of certainty, failed to maintain control over the critical variables of the process, when an unforeseen perturbation changed the process dynamics. On the other hand, the ADEX system used its adaptive capacity to identify the changing process dynamics introduced by the unforeseen perturbation and self-tune its parameters in real time to minimize the impact of the perturbation. This maintained the cavity in operation.

8.3 CONCLUSIONS FOR THE SIMULATION TRIALS

The previous chapters have described the concept of accelerator driven systems (ADS), the acceleration process that takes place in a superconducting cavity of a linear accelerator (linac) and the complex environment in which this process operates submitted to the effects of the mechanical vibrating modes of the cavity, severe time constraints, perturbations (such as microphonics and Lorentz forces) and a time-varying environment that changes the cavity's dynamics depending on operating conditions.

The need for precise control of this acceleration process cannot be overemphasized since it will determine satisfactory operation of the linac and the operational availability of the whole ADS.

A CNRS simulator of a 704.4 MHz SC cavity has been used to comparatively evaluate the control performance of an ADEX optimized adaptive control system and an alternative PID based control system, as applied to the control of the Frequency Tuning (FT) loop of the cavity. The FT loop controls the cavity frequency detuning and its performance determines the energy required by the low level radio frequency (LLRF) loop for proper operation of the cavity and its operational capacity under certain scenarios, such as an adjacent cavity failure requiring application of the local compensation method or the presence of unforeseen perturbations. The high reliability demanded by the LINAC operation needs optimized and stable control performance of the FT loop in all process environments where cavity operation is physically possible.

The paper has described in detail the control strategies used in the previous PID based control solutions applied to the FT loop and the Optimized Control Strategy (OCS) used in the ADEX system. Notch filters were introduced in the definition of the OCS that, in addition to ADEX controllers, also integrated Chebyshev filters and anticipation of the effects of Lorentz forces when power variations occurred in the cavity field. In this way, the OCS gathered the tools to attenuate the excitation of the cavity's resonance modes by the ADEX controller's actions, minimized the known microphonics induced by external perturbations and compensated in advance for Lorentz forces.

The experimental results in simulation proved the efficiency of the LLRF control loop, under PID control, and the FT control loop, under PID and ADEX control, working together but independently in a standard simulated scenario. The comparative analysis of the results show, in this simulation scenario, that the ADEX system has reduced the frequency detuning deviations from its set point, while power consumption was maintained nearly at its minimum. In a second scenario, an unforeseen external microphonic perturbation of 20 Hz frequency, that caused oscillations with an amplitude of 50Hz in the frequency detuning, was applied to the cavity simulator. This unforeseen perturbation caused the loss of control of the cavity under PID control, while under ADEX control a much more aggressive control action maintained the resonance frequency within operational limits, and the field inside the cavity under control by the LLRF system. These simulation results show how fixed-parameter control/command systems, designed in a context of certainty, where it is assumed that the process dynamics and perturbations acting on the process are correctly modeled and known,

can deteriorate their performance when uncertainties are introduced in the operating context. On the other hand ADEX Optimized Adaptive Control Systems need no accurate knowledge of the process dynamics or its changes with time, or of perturbations acting on the process, and can deal with uncertainty scenarios and unknown perturbations, maintaining desired performance, as this simulation has shown.

The following Chapter 9 describes how the ADEX OACS described by the block diagram of Figure 88 has been embedded into a hardware capable of fulfilling the operational needs such as time constraints and communications with the experimental setups.

CHAPTER IX:

IMPLEMENTATION OF THE ADEX OPTIMIZED ADAPTIVE CONTROL SYSTEM

Throughout the last two Chapters the Optimized Control Strategy (OCS) has been defined and tested in simulation were it has obtained promising results. One of the mayor outcomes of these works is the definition of the execution time constraints for the control strategy using the time scaled simulation. The executions time constraints are not identical for all the parts of the OCS and rather depend on the function of each part. The functions of the different parts of the OCS correspond to a block of the block diagram of Figure 88 and to a specific programming code. As already commented, in the simulation tests the programming code was developed in the control and optimization platform ADEX COP based on Labview which is a programming language developed by National Instruments. Both the simulation and the OCS in ADEX COP were time scaled resulting in an execution period of a second for the filters and Lorentz anticipation block and 10 seconds for every ADEX controller execution. These executions times corresponded, without time scaling, to the required executions times

described in Table 8 for the algorithms related to each of the block diagrams considered in Figure 88.

Functional Block	Required Execution Time
ADEX Controller	**2 ms**
Notch Filters	**200 µs**
Chebyshev Filters	**200 μs**
Lorentz Anticipation	**200 μs**
Overall OCS	**200 μs**

Table 8. Summary of the execution time constraints.

Proper specific HW definition is crucial for the success of the experimental tests. For the implementation of the OACS in a real time fully operational FTS, the adequate hardware had to be conveniently chosen to fulfil the time constraints of Table 8. However time constraints are not the only aspects to be considered.

Additionally, communication (data acquisition and transmission) protocols with the LLRF have to be envisaged as part of the code to be executed and considered in the calculations of the required execution time. Obviously compatibility with the LLRF and the supervisory network are a must. Endurance, robustness and size are important factors. Gathering and analyzing all data related to these issues, the most convenient HW had to be chosen.

9.1 PRELIMINARY HARDWARE DEFINITION

The best way to “plug” the FTS was discussed with IPNO prior to defining the ADEX OACS hardware configuration. At first it was decided that the interface to connect the ADEX OACS would be a dsPIC that would gather the process variables from the existing setup and transmit the control actions to the piezoelectric actuator. Thus, in operation the ADEX OACS would receive the process variables form the dsPIC, compute the optimized adaptive control action and send it back to the dsPIC that would apply it to the piezo. The dsPIC also executes

the PID based control strategy described in Chapter 5. Thus, this setup represented a valid test bench to compare both the ADEX OACS and the PID based system as alternatives for the FTS.

However, the first solution found with this approach resulted in an inconvenient, ostentatious and “messy” configuration as the one shown in the Figure 101 using up to three control boards at the same time.

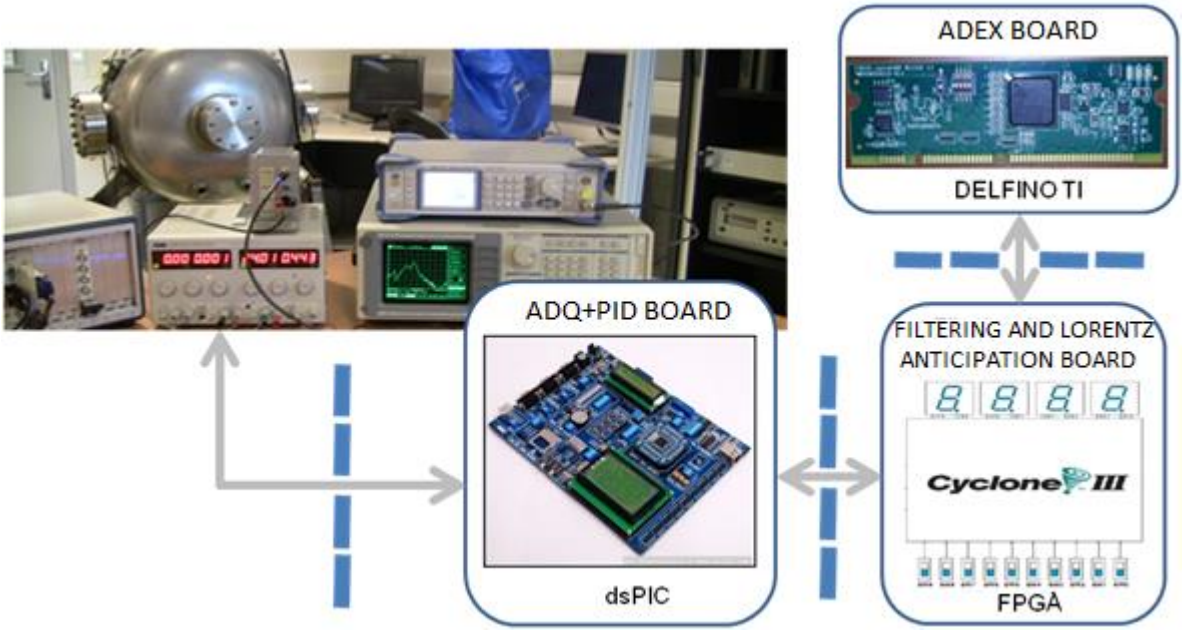

Figure 101. Preliminary hardware definition.

In the figure the preliminary hardware that was defined for the cavities control is presented. In the upper left corner of the figure a picture of the experimental setup represents the cavity, the RF generator, the piezo amplifier and instrumentation related with signal delivery. In this hardware approach each of the boards performed the following tasks:

- The dsPIC board performed the signals acquisition from the process and applied the control actions to the piezo via an amplifier. Running in ADEX mode, it delivered the ADEX signals. Running in PID mode, it executed, the PID control that generated the voltage signal applied to the piezoelectric actuator to control the resonance frequency.
- The Filters and Lorentz anticipation board was a FPGA Altera Cyclone III and is used as a bridge between the ADQ+PID board and the ADEX controller board, and also

to execute the notch and Chebyshev filters and the Lorentz anticipation block in 200 μs. However this board had a scarce memory that limited the number and the order of the filters that could be used.

- The ADEX controller was executed in a DELFINO Texas Instrument processor. In it the ADEX controller generated the optimized control signals to be applied to the piezoelectric actuator, after passing through the FPGA and the dsPIC (running in ADEX mode).

Concerns and doubts about the preliminary hardware definition

Although functional, this preliminary hardware approach was too limited an uncomfortable. The use of this preliminary solution brought forth several concerns and doubts about the chosen hardware. The main concerns about the preliminary hardware are listed in the following:

i. As already commented, more powerful hardware was necessary in the FPGA side. A hardware with sufficient memory and capacity to execute several filters of high order without problems.

ii. The reprogramming flexibility is a must for a start-up and VHDL programming required by the FPGA board cannot be easily reprogrammed in a short period of time and with high success rate.

iii. The solution had to be more compact and less “messy” for reasons related to detecting failures and transport through airports (the hardware developments were made at Madrid they were tested at Paris). When an error arouse it was difficult to know in which of the three boards it might have occurred. This situation was very complex because none of this boards had an appropriate interface to supervise internal values of the programming code. The components used almost “black boxes”.

iv. No operational data could be gathered with this preliminary solution an additional PXI of National Instruments had to be used for this purpose.

9.2 ADVANCES ON HARDWARE DEFINITION

Consequently the hardware approach was completely reinvented. The PID system was separated from the ADEX system and only one of them was used at a time. Figure 102 shows the two separate structures:

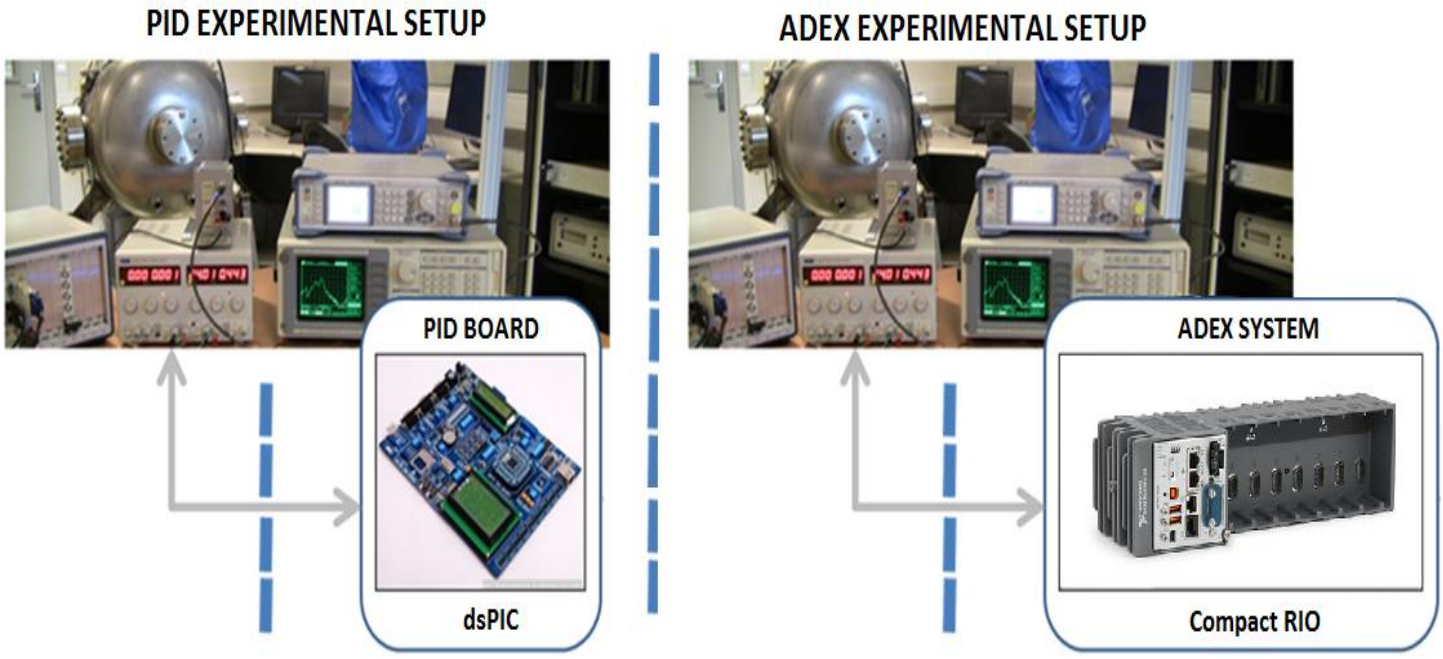

Figure 102. Final hardware definition for trials with PID or ADEX OACS control.

PID System Experimental Setup

To perform the PID control the hardware remained the dsPIC used in the preliminary hardware definition. The dsPIC used by IPNO to perform PID control was an MCU dsPIC33F. This board performed signal acquisition, PID computation and applied the control actions to the piezo amplifier.

The dsPIC33F/E Digital Signal Controllers offers the performance of a DSP with the simplicity of an MCU. The dsPIC33F/E core is designed to execute digital filter algorithms, high-speed precision and digital control loops. The dsPIC33F/E SMPS DSCs provide on-chip peripherals specifically designed for high-performance, digital power supplies. SMPS peripherals include high speed and high resolution PWM, fast ADC and analog comparators.

Key performance points include a computational performance up to 60 MIPS DSC at 3.3V, single cycle 16 x 16 MAC; 40-bit accumulators and dual operand fetches; fast DMA with no cycle stealing; highly integrated motor control, SMPS and audio peripherals.

ADEX System Experimental Setup

On the other hand, to perform ADEX control a Compact RIO 9035 (cRIO-9035) was used [127]. cRIO-9035 combines a 1.33 GHz Intel Atom dual-core processor, a Xilinx Kintex-7 FPGA, and eight slots for C Series I/O modules. The following slots provide flexibility in terms of front-end interfaces and have been used for data acquisition:

- NI 9239 Isolated analog input module ±10 V, 50 kS/s, 24 bits
- NI 9269 Voltage output module ±10V, 100 kS/s, 16 bits

Figure 103 shows both a picture of the cRIO-9035 and of the two slots used. This hardware choice exceeds the capacities of the preliminary hardware and provides the ideal platform to implement the ADEX OACS. Furthermore, this hardware choice responds to all the concerns and doubts listed above in the following ways:

i. cRIO-9035 is based on a Xilinx Kintex-7 FPGA whose main characteristics are described in Table 9.

FPGA type	Xilinx Kintex-7 7K70T
Number of flip-flops	82,000
Number of 6-input LUTs	41,000
Number of DSP slices (18 × 25 multipliers)	240
Available block RAM	4,860 kbits
Number of DMA channels	16
Number of logical interrupts	32

Table 9. Properties of the FPGA installed in the cRIO-9035.

Figure 103. Compact RIO 9035 and acquisition cards (NI 9239 and NI 9269) used to receive and send control signals.

The faster blocks of the Optimized Control Strategy represented in Figure 88 were compiled in this FPGA. The compilation report is shown in Figure 104. In the worst case the percentage of utilization did not exceed 82%. This allows for a 18 % safety margin to include new programming blocks (such as new filters) or extend the existing ones (i.e. increasing the filters order) if needed.

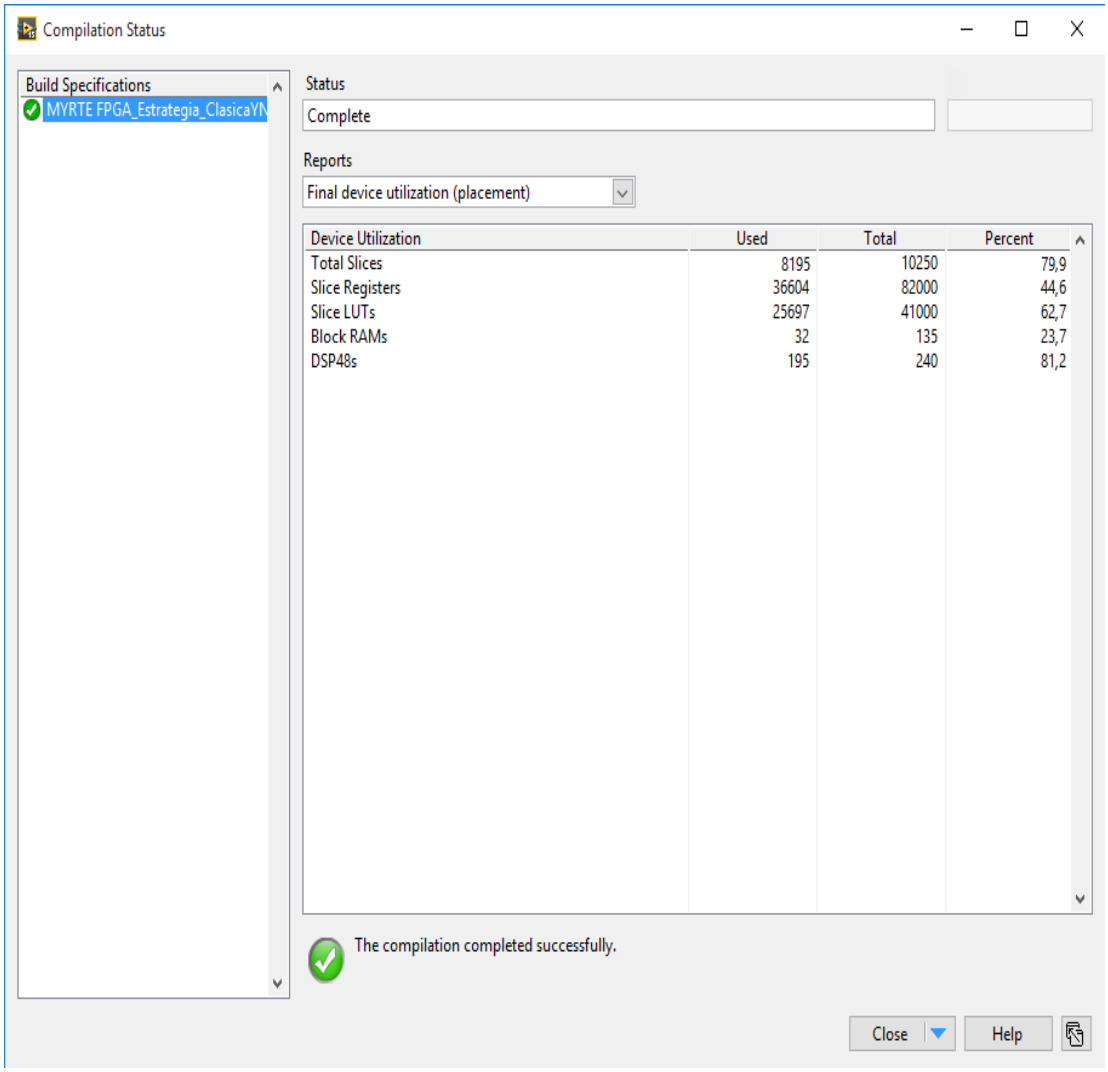

Figure 104. Properties of the FPGA installed in the cRIO-9035.

ii. In cRIO-9035 the reprogramming flexibility is granted by the programming language used which is Labview. Although Labview is slightly adapted to the FPGA and Real-Time (RT) environment for the use with cRIO it is still user-friendly and versatile. The FPGA can be easily reprogrammed in a short period of time with success.

iii. The cRIO-9035 is a compact solution bearing all the algorithms of the ADEX OACS, easy to transport and very transparent allowing for easy failure detection. Figure 105 shows the main engineering screen developed for supervising the operation of the cRIO-9035.

ENGINEERING SCREEN cRIO-9035

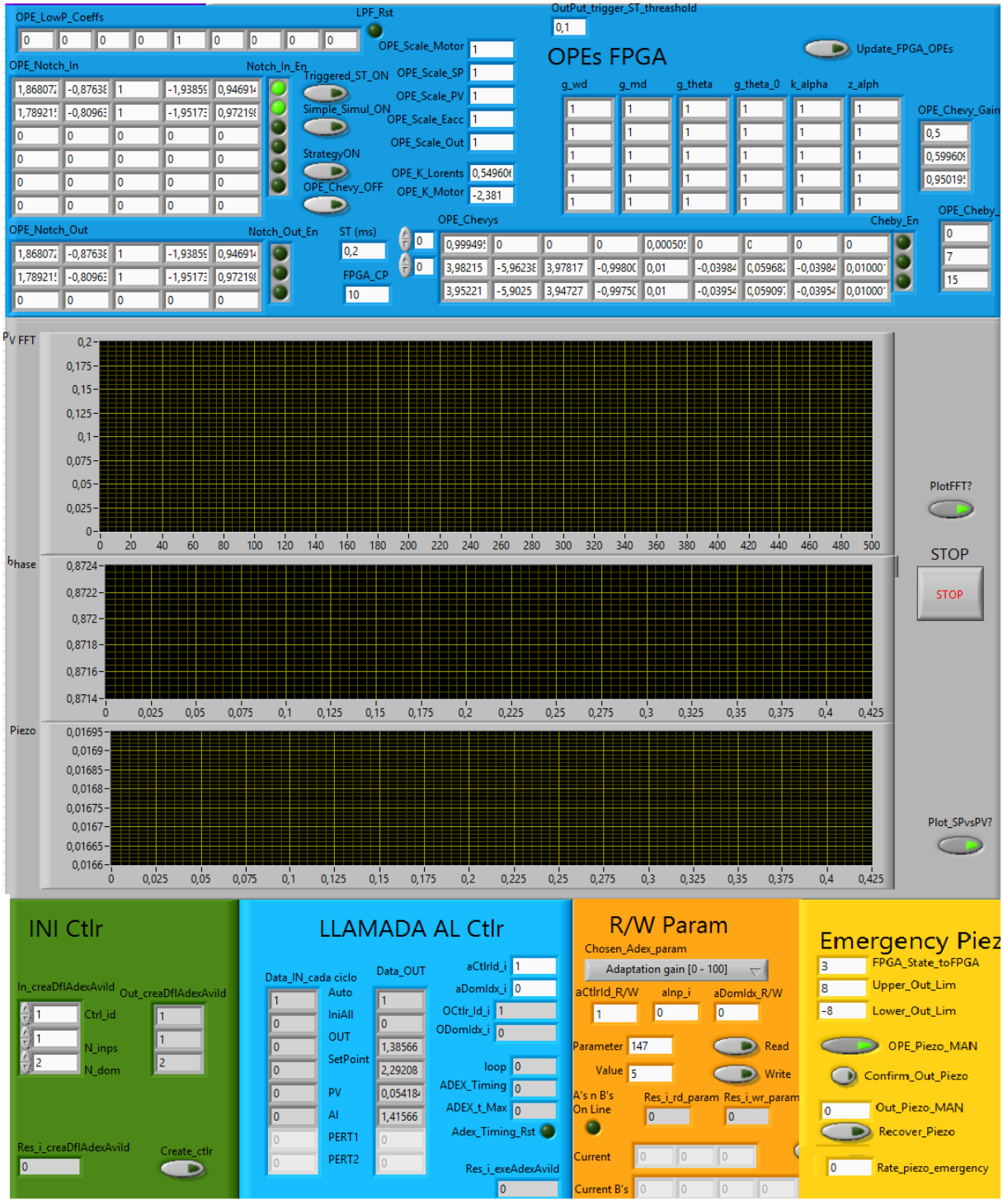

Figure 105. Engineering Screen cRIO-9035.

The program shown in the figure not only follows the process variables evolution (in the charts shown in the middle of the screen) but also alerts the engineer of malfunctioning of a certain part of the code and publishes plenty of signals to facilitate

debugging. For example the blue part at the top publishes information about notch and Chebyshev filters operation. In the lower part the ADEX controller can be manipulated: initialized, called and its configuration variables may be read and written). Finally in the lower right section one can see the emergency actions which would be applied in extreme situations mainly to protect the piezo from extreme control actions that may harm it.

iv. With cRIO-9035 data acquisition and capture is simple and no other equipment apart from the engineering computer (in which the engineering screen shown above would be running) is needed to store this data.

The conclusion was that cRIO-9035 was definitely a better way to proceed for this experimental application. The next subsection will briefly explain the functioning principles of cRIO-9035 and how the Optimized Control Strategy was implemented.

Implementation of the ADEX system in the cRIO-9035

The systems architecture envisaged for the Compact RIO is represented in Figure 106. Compact RIO is illustrated at the center of the figure. At its left a PC has been represented. This is the developers PC which is connected through a network to the cRIO. The PC can serve for two purposes:

i. Develop programs and implement them in the cRIO,
ii. Display signals during the cRIO operation and send commands.

At the right side of cRIO the signals sent and received from the process are represented. Signals received in cRIO from the process are logically process variables measured by sensors. Signals sent by cRIO to the process are the control actions that will modify the value of the process variables. The cRIO performs the acquisition of the process variables and with those signals and the ones received form the display on the PC it computes the new control actions to be sent back to the process. Computation is performed in the cRIO at two different levels:

a) a Real-Time processor capable of performing very complex but "slow" computations, data managing for system monitoring and data registration, and

b) a "Fast" FPGA processor capable of executing simpler algorithms but with incredibly fast speeds (algorithms can be performed in clock ticks of up to 5 ns).

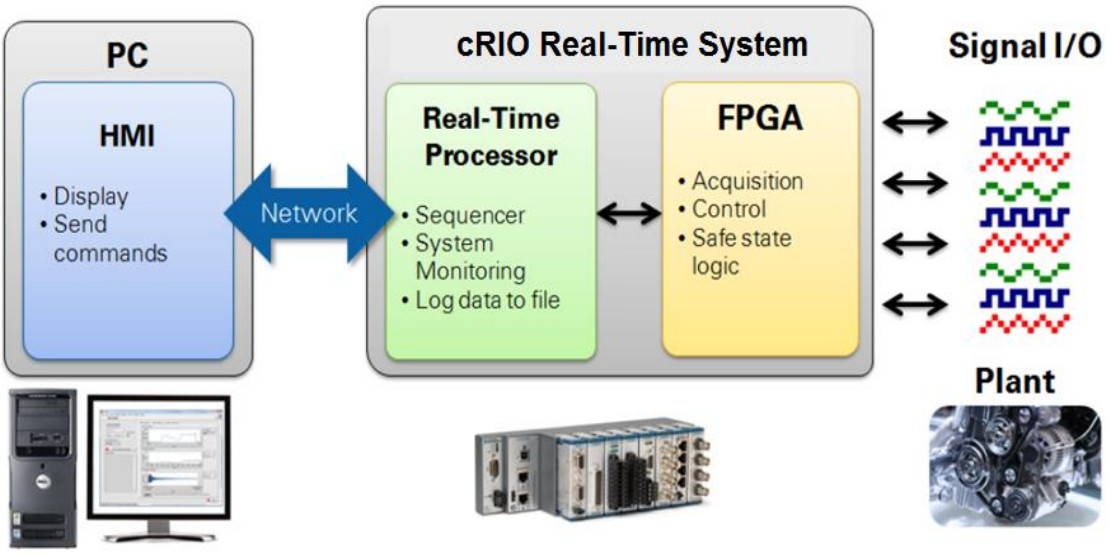

Figure 106. Systems architecture of cRIO-9035.

Fortunately, execution constraints of algorithms represented by the blocks of Figure 88, reviewed in Table 9, match conveniently the configuration of cRIO. This is because the most complex algorithms, which are those related to the ADEX controller are the less restrictive regarding their execution time (ADEX controller must be executed once every 2 ms). Thus, the ADEX controller can executed in the RT processor. Nevertheless, the general formation of the ADEX controller reviewed in Chapter 6 had to be rebuilt ad-hoc for this application as explained in Chapter 7, subsection 7.1, in order to reduce the execution time without losing the controller's performance. Once this modification on the controller was performed thorough tests were made to demonstrate that the RT processor could perform the controller's execution in the given time (2 ms). On the other hand the notch, Chebyshev

and Lorentz anticipation algorithms are much simpler and can be executed on the cRIO FPGA processor meeting the required execution times (200 μs).

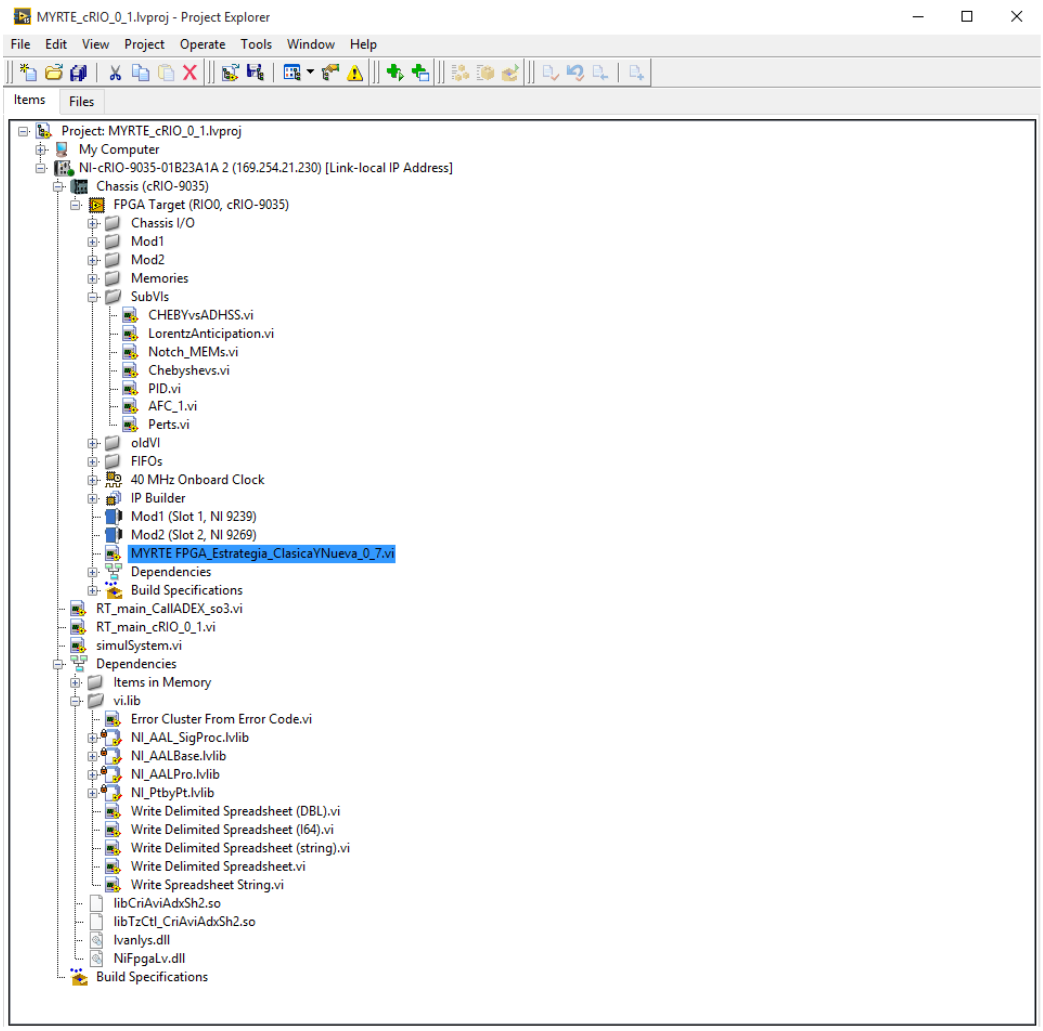

Figure 107 . cRIO-9035 programming project.

The cRIO-9035 programming project that executes the Optimized Control Strategy (OCS) is shown in the above Figure 107. The ADEX controller library was introduced into the RT processor in an archive libCriAviAdxSh2.so which is shown at the end of the tree shown in the figure. The ADEX controller is called in the RT processor code show in Figure 108.

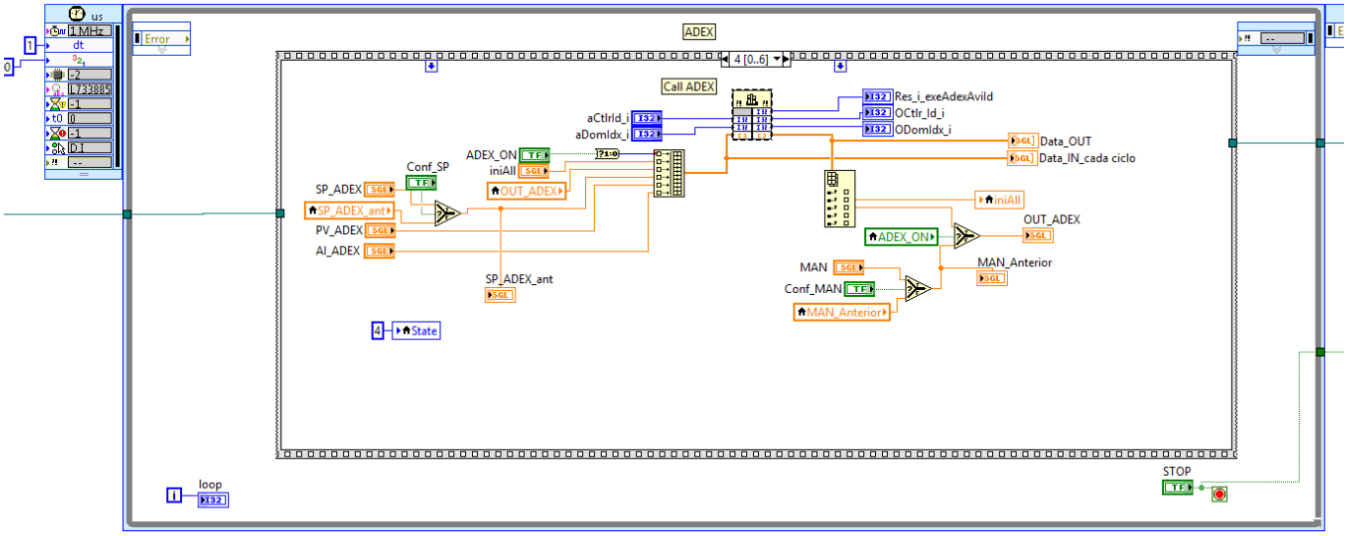

Figure 108. ADEX controller call in the RT program.

The detail of the controller call is shown in the following Figure 109:

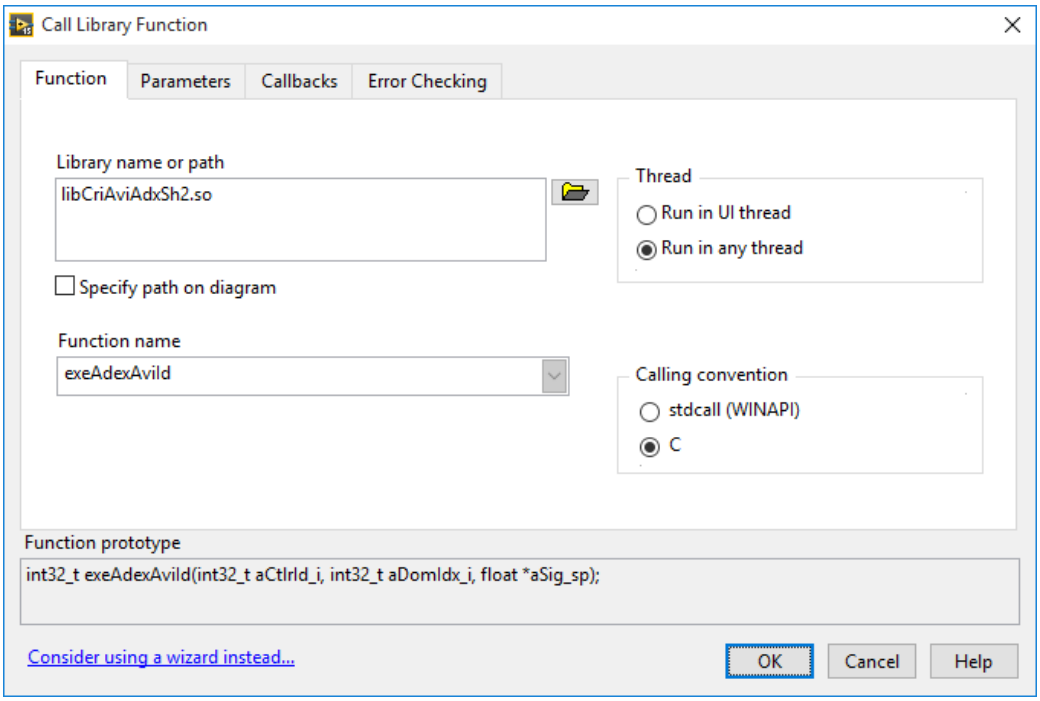

Figure 109. Detail of the ADEX controller call in the RT program.

The RT processor sends the ADEX controller out every 2ms to the FPGA processor which executes its code every 200 μs. The code of the FPGA, including the notch filters, Chebyshev filters and Lorentz anticipation is shown in Figure 110.

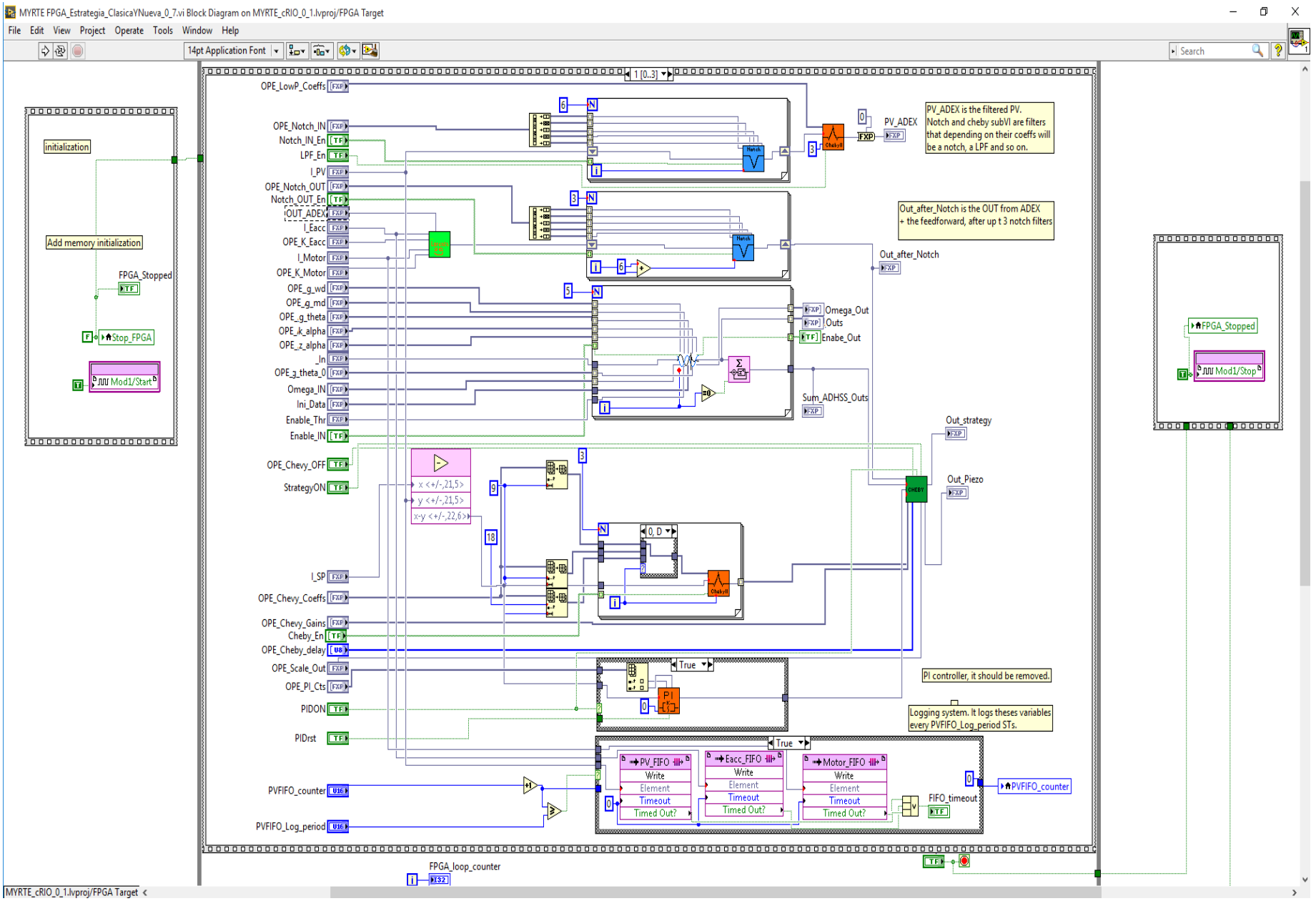

Figure 110. FPGA programming of the Optimized Control Strategy

The cRIO programming has been made in such a way that the FPGA transmits, each execution, a control action across the acquisition board NI-9269 to the piezoelectric amplifier. Once the implementation on the cRIO-9035 was performed, the final step was testing the implementation. In order to this Hardware in the Loop (HiL) tests were performed. In this test the ADEX OACS embedded in the cRIO-9035 was tested against the CNRS simulation using the setup described in Figure 104. This is probably the most complete way to validate the implementation prior to the real experimentation on the cavities. The connection between the cRIO-9035 and the Matlab simulation was made through Ethernet as described in the Figure 111.

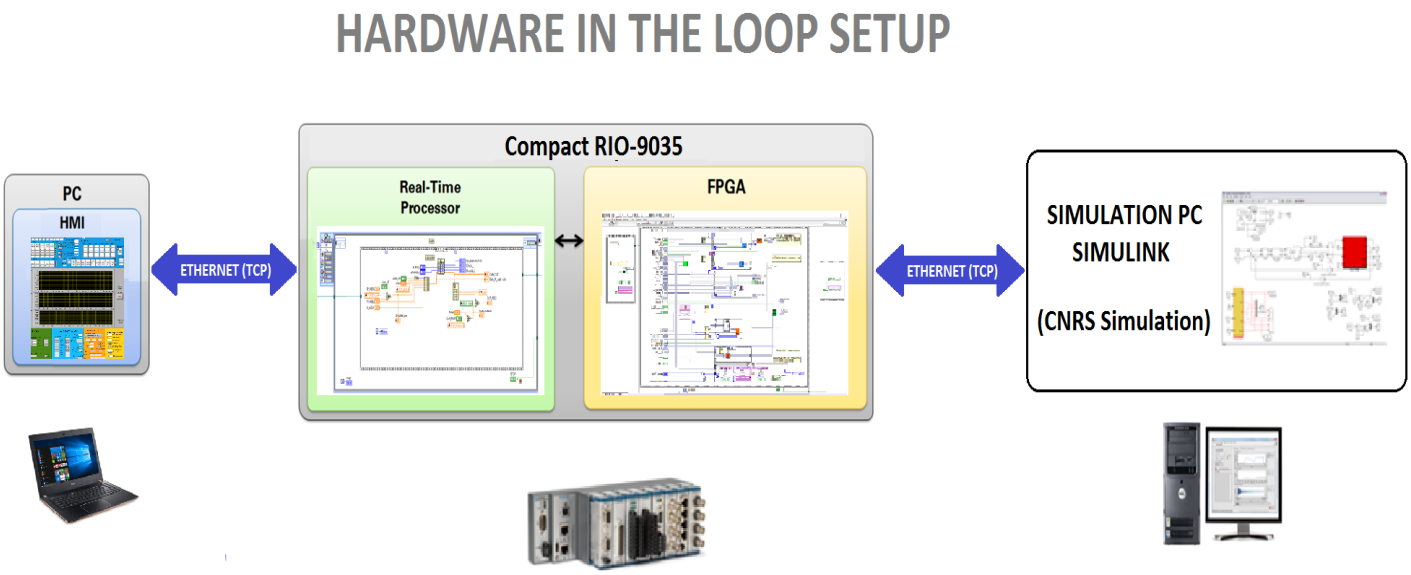

Figure 111. Hardware in the Loop (HiL) setup.

The results obtained when performing these test where identical to those shown in Figure 97. This proved the goodness of the programming but left untested the acquisition boards as the communication with the simulation was not made through them but through Ethernet. However the good functioning of these boards was taken for granted as they had been recently bought. Thus the hardware implementation was validated and ready for the experimental campaign on spoke and elliptical cavities.

Chapter 9 has reviewed the implementation of the ADEX OACS into a cRIO-9035 platform which means the first completion of an OACS for the FTS. Chapter 10 will review the

experimental setups used for the test of the OACS performance and the practical aspects that affected the experimental campaign.

CHAPTER X:

EXPERIMENTAL CAMPAIGN: SETUPS, PRACTICAL ASPECTS AND RESULTS

10.1 GENERAL REMARKS

The main objective of the experimental campaign was to evaluate the joint operation of the Digital LLRF (DLLRF) control system and the FTS control system, including not only the performance of the LLRF and FT control loops, but also that of the rest of the equipment involved. It is important to take into account that the interaction between these systems, the different elements of the equipment and their performances, will affect the individual performance of each of them.

Concerning the FTS, a comparative evaluation of the OACS system and a conventional PID based system, when applied to a 352.2 MHz spoke cavity at room temperature and to a 704.4 MHz SC cavity, was performed. An independent evaluation of the ADEX system

performance was obtained through the simulation results already presented in Chapter 8, but this kind of evaluation would also be of interest in the context of the real application to the cavity.

To approach this evaluation, different trials, all of them without beam loading, where made in different operating conditions (different kinds of cavities, cryogenic, not cryogenic, perturbed operation, not perturbed, etc…). In this context three alternative experimental setups where used to measure the cavity frequency detuning:

- The first experimental setup does not use of a DLLRF. It simply consists on inducing a field at resonant frequency with fixed amplitude and phase into the cavity and measure the phase deviations caused by frequency variations. This setup was used in trials with the room temperature spoke cavity. In this case test where done simulating microphonic perturbations with a dedicated piezoelectric actuator working in parallel with the one used for control.
- The second experimental setup substituted the operation of the DLLRF control system by that of the Phase Locked Loop (PLL) device. The PLL device provides a reliable measurement signal of the cavity´s resonance frequency in a wide range of operation that can be used for the desired evaluation. The tests campaign for this setup included the operation of the FT loop under PID and ADEX control systems, evaluating their performances under the influence of environmental microphonics of different frequencies.
- A third setup considered the final integration between DLLRF control system and the FTS under PID and ADEX control systems. An indirect measurement of the cavity's resonance frequency can be obtained as the difference between the phase of the field inside the cavity and the phase of the field emitted by the DLLRF. In the following this magnitude will be referred to as Cavity Phase Shift (CPS). This third setup is the most similar to the real accelerator's operation, however it presents an important limitation: the relation between the frequency detuning and the phase shift is non-linear and saturates for frequencies outside of the cavity bandwidth.

The fact that the CPS saturates outside a certain range of operation, which is related with the bandwidth of the cavity´s resonance frequency, represents an important limitation for the performance of the FTS as it will later be shown by the experimental tests results. The experimental campaign for this setup included the operation of the FT loop under PID and ADEX control systems, evaluating their performances under the influence of environmental microphonics, the presence of a power increase and perturbations coming from the cryogenic system.

The following sections consider the microphonics spectrum of the real cavity, the resonance modes and their attenuation by notch filters, present the two setups considered during the tests campaign, the results obtained in the different experiments with PLL and DLLRF operations and their discussion.

10.2 PRACTICAL ASPECTS OF THE EXPERIMENTAL CAMPAIGN

Cavity behaviour depends on numerous aspects which have been briefly reviewed by Chapter 3. Some of them are merely constructive and do not affect the dynamic performance of the cavity. However a few of them have a huge impact on the performance of cavities and, without understanding them, proper control and, even more, understanding of the experimental results cannot be attained.

A major aspect affecting the cavity dynamic performance is the cryogenic environment. As already considered in Chapter 3, the cryogenic environment drastically reduces the energy losses on the cavity walls. Its overall effect is reducing the cavity bandwidth and increasing the maximum amplification inside the cavity. A consequence of reducing the bandwidth is shortening the range of frequencies that modify the phase. This effect is represented in the Bode diagram of Figure 112. In this figure two scenarios have been considered, a “room temperature” scenario represented in the Bode diagram by the black line and a cryogenic scenario represented by the blue line. The bandwidth of the electromagnetic resonance is much smaller in the cryogenic scenario Δw_{bw2} than in the room temperature one Δw_{bw1}. This fact has certain implications explained in the following:

i. Obviously, the dynamic relation between the field's amplitude and phase and the actions applied to the CTS will be totally different depending on whether the cavity is working in cryogenic conditions or not.

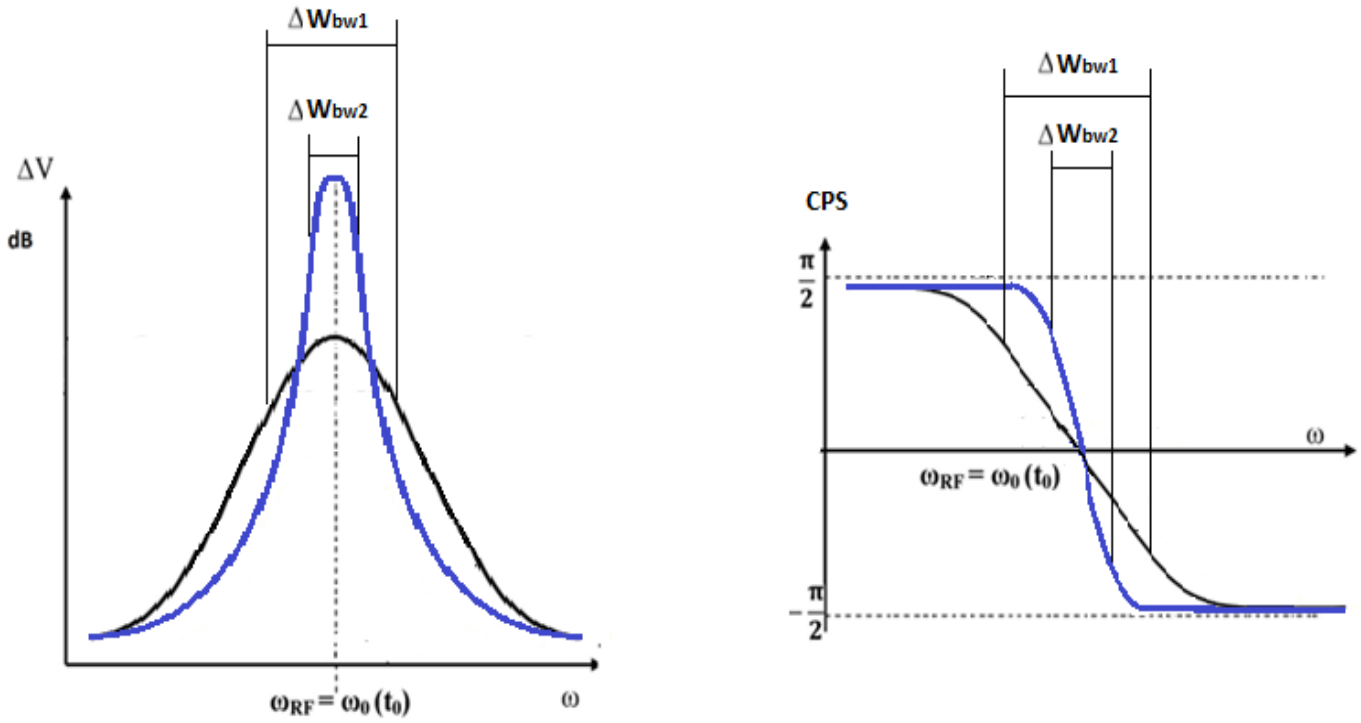

Figure 112. Superconducting effect on a cavity bandwidth.

ii. RF power introduced in the cavity will be limited in the room temperature scenario due to great amount of energy that is lost heating the cavity walls.

iii. A considerably small drift of the cavity's resonance frequency will cause a huge variation of the field amplitude in the cryogenic scenario and a considerably smaller one in the room temperature scenario (approximately 100 times smaller). For this reason microphonics which are very subtle vibrations will have a notable effect in the cryogenic scenario while they will not be very significant in the room temperature scenario.

iv. In the same manner, a drift on the resonance frequency will have a bigger impact in the phase variation in the cryogenic scenario. Thus, in this scenario the phase signal is expected to saturate more easily and maintaining it within the saturation limits will require a very precise control.

Another aspect that deeply affects the cavity dynamic performance are the mechanical resonant frequencies which will limit the CTS actions and that, if not considered in the control system definition, may cause the FTS to lose control due to its own control actions. The resonance frequencies respond to the structure of the cavity and will be therefore different for every type of cavity.

Thus, both cavities have been studied to detect their mechanical resonance frequencies. The next subsections give a deeper description of the setups implemented to measure and control the process variables and present the results of the study of both cavities, characterizing in this way the operating conditions of the trials performed during the experimental campaign.

10.3 FTS EVALUATION SETUPS

Basic setup

As already commented, this setup is the simplest and consequently the less representative of the real operating conditions of the cavity once it has been integrated in the accelerator. The setup is illustrated in Figure 113. This figure shows how an RF generator feeds simultaneously the cavity and a mixer with a wave of 352 MHz of fixed amplitude and phase. The electromagnetic field is measured inside the cavity and transmitted to the mixer that delivers the CPS, resulting from the measurement of both fields, to the FTS. The FTS computes the piezo control signal and sends it to the CTS. In this setup the two piezos of the CTS developed for the spoke cavity (see subsection 4.4 “Cold Tuning Systems”) will be used independently. The first one will be driven by the FTS to control the cavity and the second one will be used to introduce perturbations during the experiments.

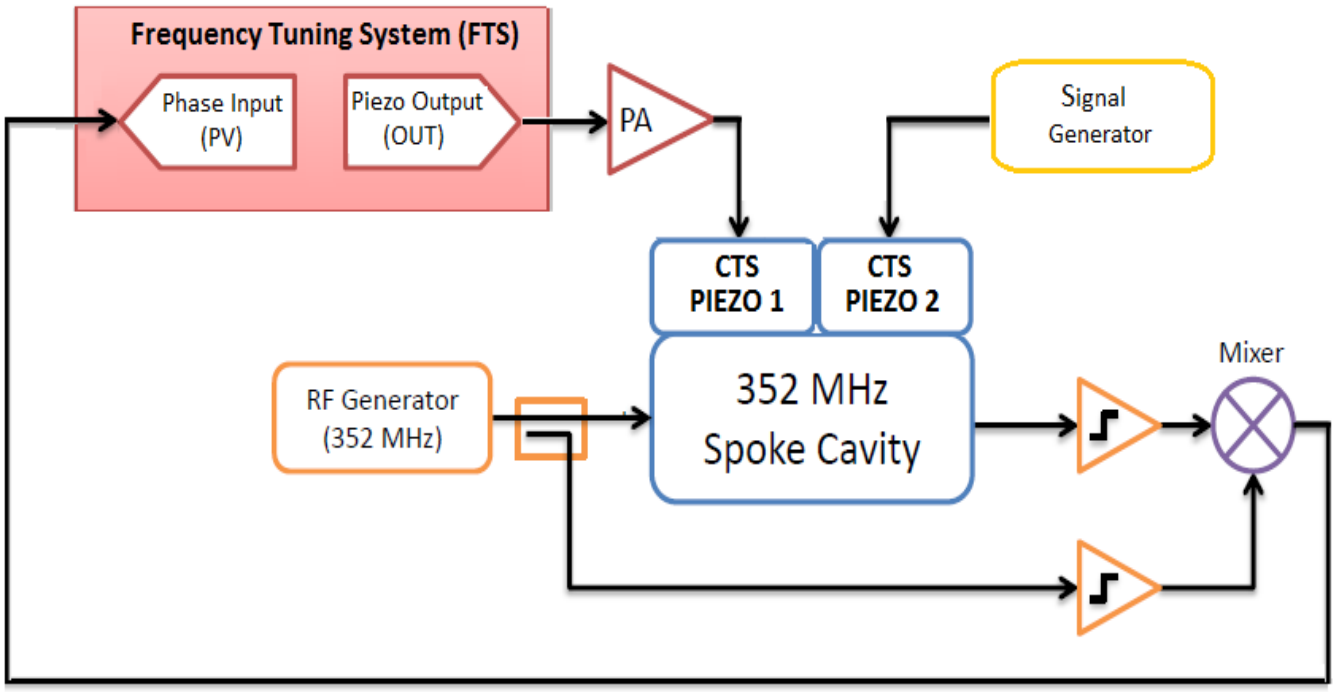

Figure 113. Room temperature tests setup with the 352 MHz cavity without DLLRF.

Setup under Phase Locked Loop (PLL) operation

The second experimental setup was used with the elliptical cavity under cryogenic conditions at 2 K. The Phase Locked Loop (PLL) is a device envisaged for the use in experiments with cavities. Its functioning principle is maintaining the phase fixed at a certain value by modifying the frequency of the wave induced into the cavity. The experimental setup under PLL operation is represented in Figure 114.

In this setup: a) the PLL operation will modify the field induced into the cavity by adjusting its frequency to drive the phase measured in the cavity towards zero, in this way the frequency of the field induced by the PLL tracks the resonance frequency of the cavity; b) this resonance frequency is compared with the nominal frequency, coming from an RF generator, in order to derive the cavity´s frequency detuning; c) the detuning signal is used by the FTS control system to compute the control action to be applied to the piezoelectric actuator (piezo 1), and d) an additional piezoelectric actuator (piezo 2) has been implemented to introduce external perturbations.

It must be noted that during experiments at 2 K there is an additional control loop not represented in this setup: the Helium bath pressure control loop that allows to attain these extremely low temperatures.

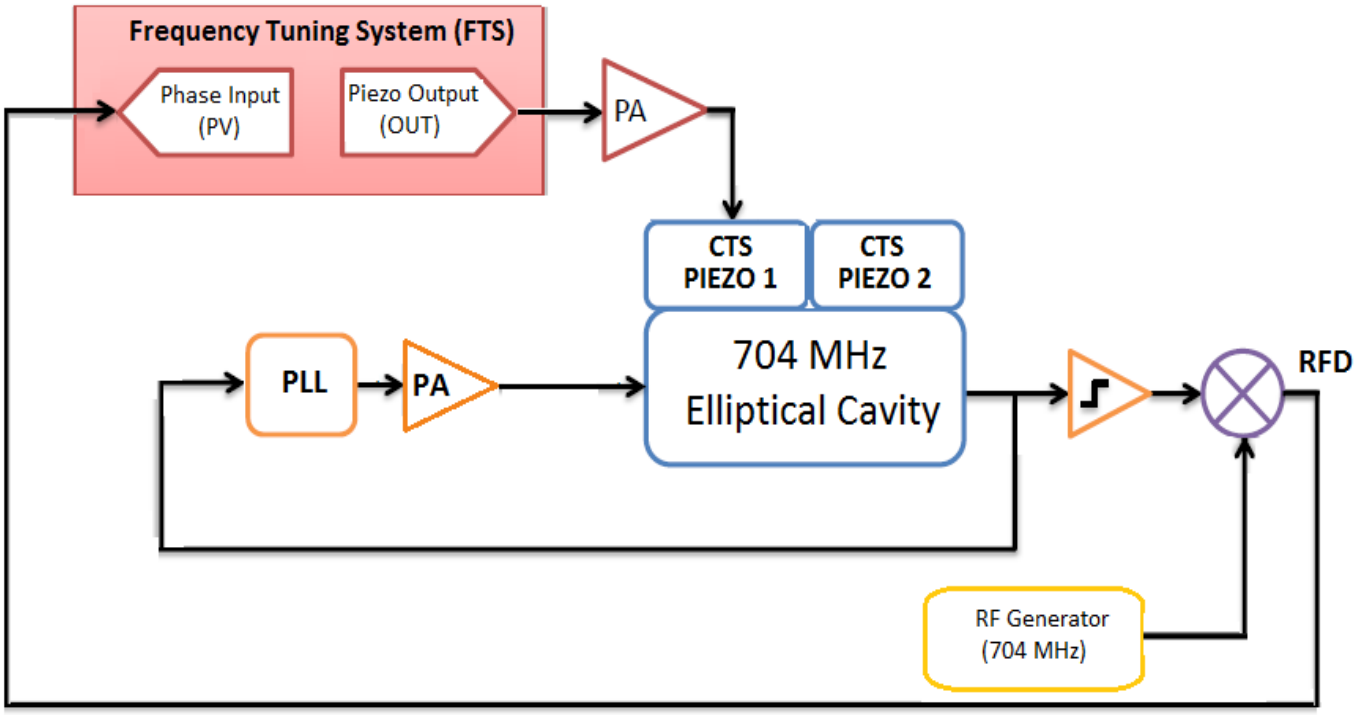

Figure 114. Cold temperature tests setup with the 704 MHz cavity but without DLLRF

Setup under DLLRF operation

The third experimental setup was used with the elliptical cavity under cryogenic conditions at 2 K. The DLLRF, as already considered, will drive the amplitude and the phase of the field measured inside the cavity to their setpoints by adjusting the induced field. In this case the frequency of the fields will remain unmodified at 704,4 Hz. This setup is the most similar one to that of the real cavity operation.

The experimental setup under DLLRF operation is represented in Figure 115. In this setup: a) the DLLRF operation will modify the field induced into the cavity by adjusting its phase and amplitude to drive the phase and the amplitude measured in the cavity to their set points; b) a cavity phase shift (CPS) signal is derived from the difference between the phase

of the induced field and the phase of the field inside the cavity, being the CPS signal representative of the cavity´s frequency detuning; c) the CPS signal is used by the FTS to compute the control action to be applied to the piezoelectric actuator (piezo) that will make the cavity resonance frequency to approach its nominal value.

As considered for the previous setup, the operation of the 704.4 MHz superconducting cavity at 2 K requires of an additional control loop to stabilize the liquid Helium pressure on the cryostat which contains the cavity. Therefore, although this loop is not represented in this setup, during the experiments at 2 K there were up to three control loops acting simultaneously on the cryogenic module: the Helium Pressure loop, the LLRF loop and the FT loop. The pressure variations of the liquid Helium were used as perturbations in some of the experiments with the DLLRF.

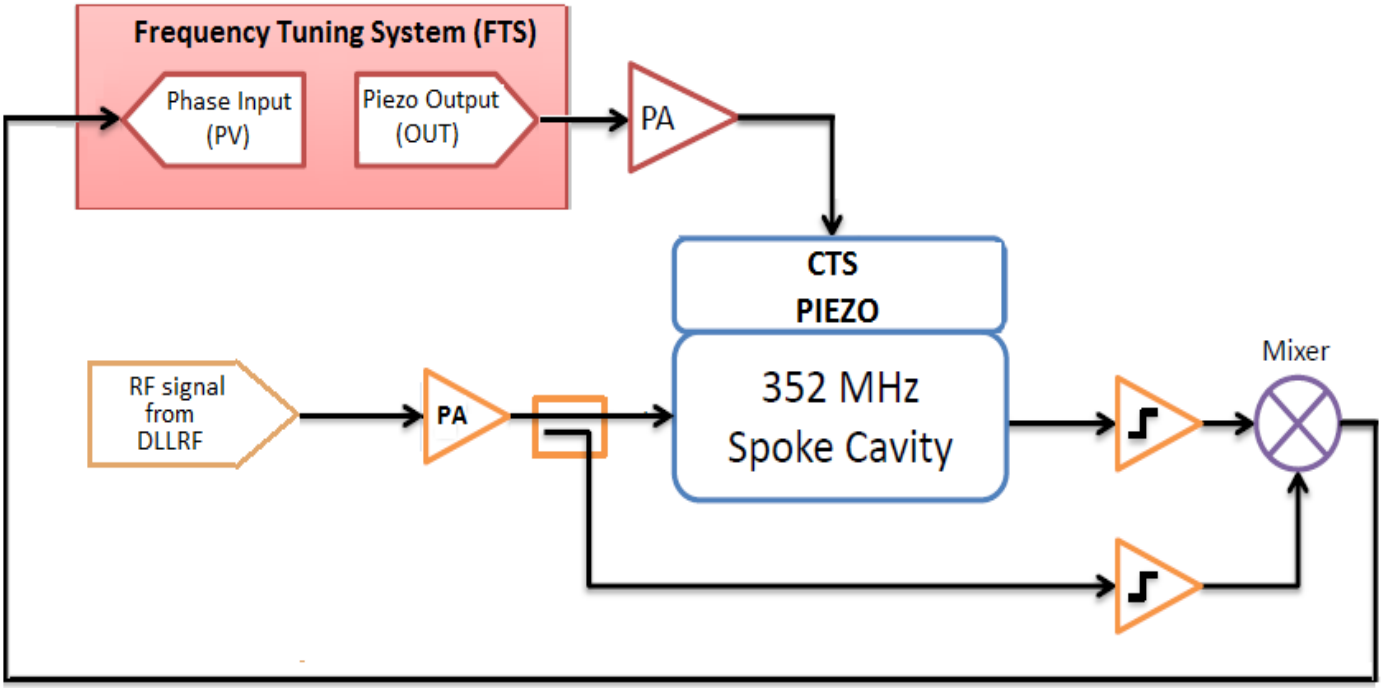

Figure 115. Cold temperature tests with the 700 MHz cavity and DLLRF

10.4 SPOKE AND ELLIPTICAL CAVITIES: MICROPHONICS SPECTRUM, RESONANT MODES AND NOTCH FILTER ATTENUATION

Characterization of the tests with the spoke cavity:

Tests with a single spoke cavity were performed in room temperature condition working with the first setup, the one described by Figure 113. Figure 116 shows the experimental facility in which these tests were performed. At the right of the figure the Spoke Cavity and at left the equipment required for the setups explained above (including amplifiers, signal generators, RF generators, etc.) can be seen.

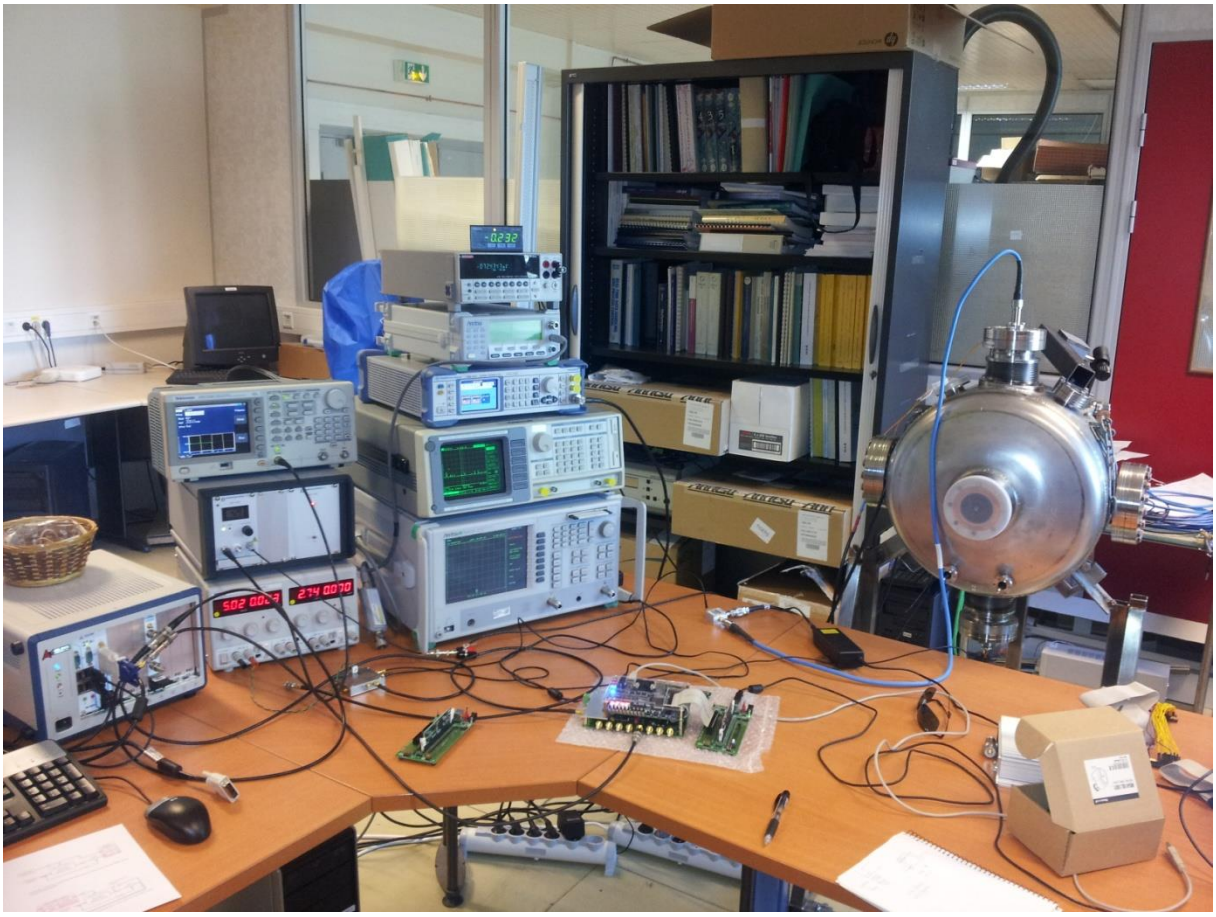

Figure 116. Experimental facility for testing the ADEX OACS prior to the tests at 2 K.

There are several factors that should be considered for the comprehension of this test. In first place the room temperature condition changes completely the process dynamics. Also, that the variable under control is not any more the frequency detuning but the CPS (which is

an indirect measurement of the frequency detuning) will have a significant impact on the dynamics. Therefore the process dynamics will differ from the one observed in the simulations of Chapter 7. Nevertheless, these dynamic changes are expected to be absorbed by the adaptive capacity of the ADEX controller while the PID controller will be appropriately tuned for each trial.

The first record of the CPS performed with this setup is shown in Figure 117. The CPS is a very noisy signal. The origin of this noise may be electrical and come from the mixer or related to microphonics with a very small effect due to the lack of cryogenic conditions. Another explanation for the origin of this noise was that the field in the cavity was very low due to power losses by Joule's effect in the cavity walls. Such a low power RF field might be difficult to measure by the pick-up antenna resulting in a significant amount of noise.

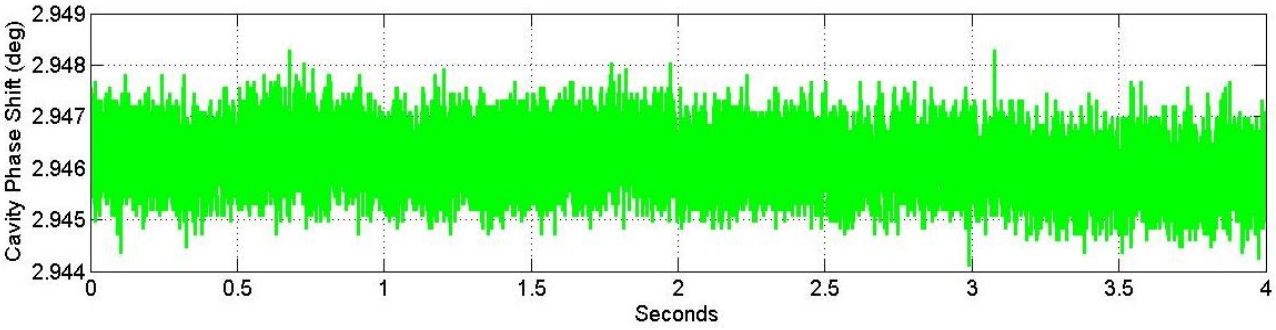

Figure 117. First record of the CPS of the cavity.

However, regarding Figure 117, no outstanding microphonics noise seemed to appear. This was expected because the cavity's sensibility to vibrations is much smaller at room temperature as it was already commented when describing Figure 112. It is well know that for this reason microphonic perturbation only appear in cryogenic conditions. For this reason the Chebyshev filters foreseen both in the ADEX OACS and in the PID based system will not be implemented in the room temperature tests with the spoke cavity.

Even if microphonics are not expected to appear in these tests, the cavity mechanical resonant modes will perturb the control system's operation. In the case of the ADEX OACS, notch filters have been foreseen to mitigate the effect of these perturbations. However the

notch filters that were envisaged for the elliptical cavity will not necessarily work with the spoke cavity as this cavity has different mechanical resonances.

For this reason it was necessary to study the spoke cavity's resonances and find a solution that could compensate for them. In order to do this a step of 20 V was applied to the piezo in order to evaluate the CPS behavior. The results of this experience are shown in Figure 118:

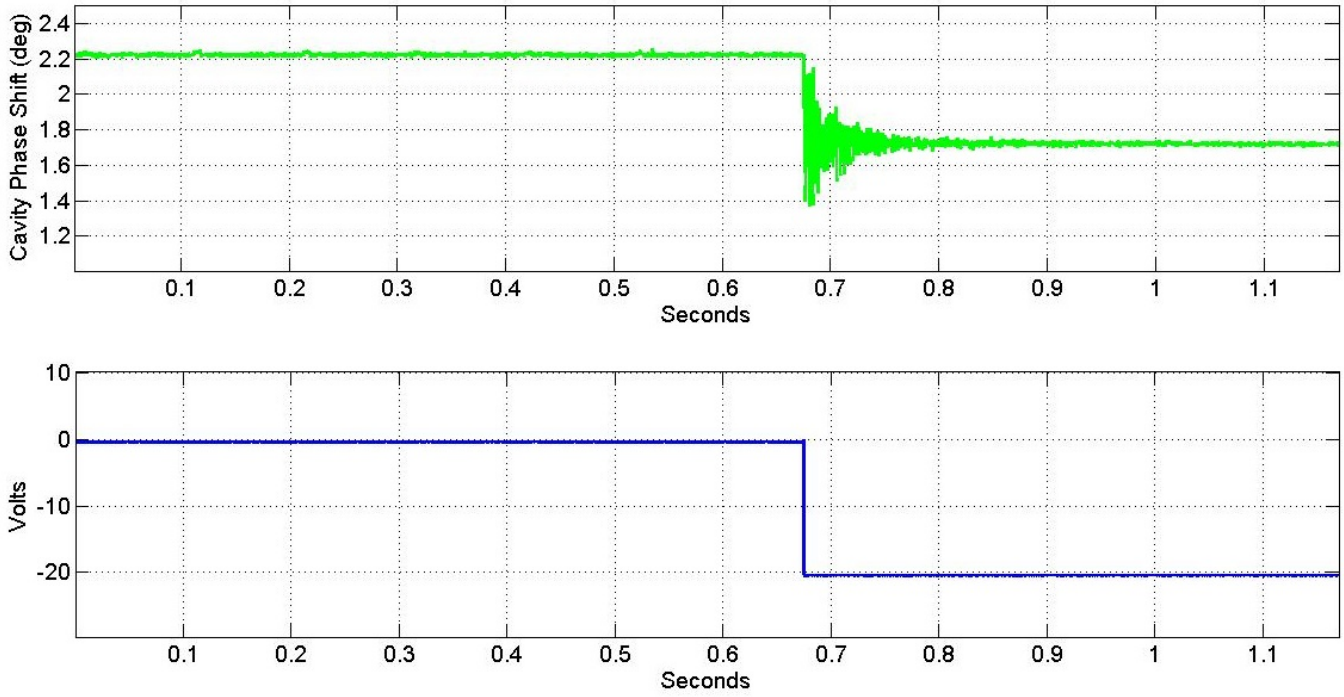

Figure 118. 20 V step applied to the spoke cavity.

Obviously, from the strong and incredibly fast oscillations after the step it can be concluded that the spoke cavity has plenty of mechanical resonant modes just as the elliptical cavity had in the simulation. These modes can be easily identified performing a FFT of the vibrations after the step. The FFT of this response is depicted in Figure 119. The main mechanical resonant modes detected where placed approximately at 313, 341, 422, 590, 871, 903, 1035 and there where even some more at higher frequencies.

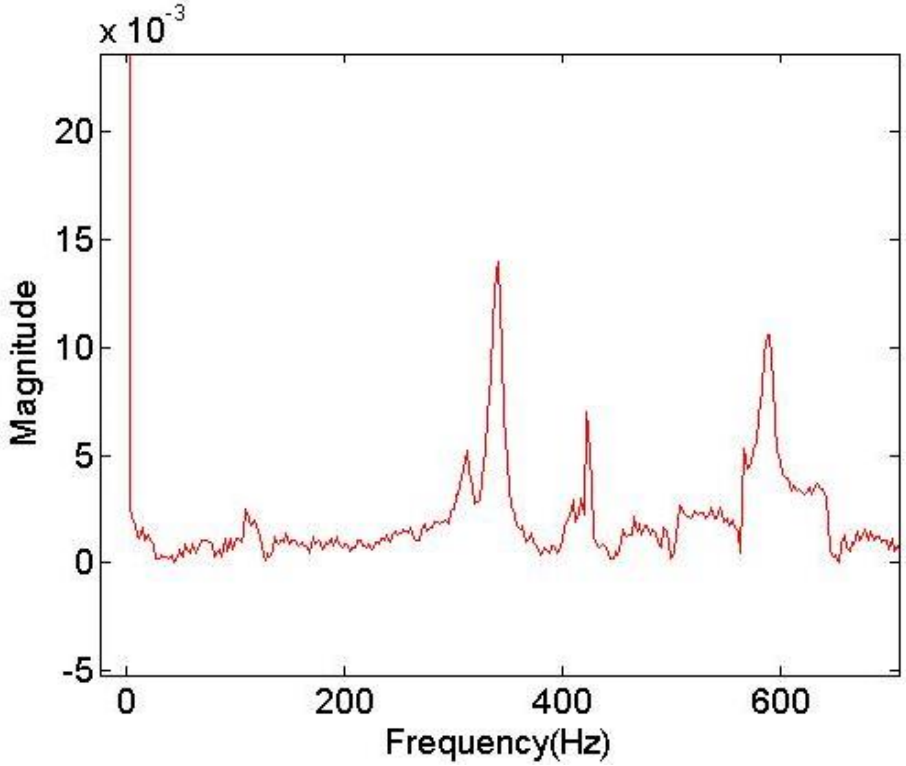

Figure 119. FFT for the detection of the main mechanical resonant modes.

All these mechanical resonant modes correspond to very high frequencies and are very spread apart. Using notch filters to attenuate this resonant spectrum would have required the use of at least 5 filters at frequencies that would most probably have required to use a totally different and even more powerful hardware. The analysis of the resonant spectrum of the spoke cavity concluded that notch filters were not an adequate technique for this kind of cavity. However, in this case the use of lowpass filters seemed convenient.

Two second order lowpass filters corresponding to the following equation in the Laplace domain were developed:

$$F_{LP}(S) = \frac{{w_n}^2}{s^2 + 2\rho w_n + {w_n}^2} \tag{10.1}$$

where w_n is the cut-off frequnacy of the filter and ρ the damping ratio that shall be chosen equal to 1 to have a critically damped filter. The natural frequency has to be chosen adequately to damp the mean mechanical resonant modes of the cavity. If the resonance

frequency is chosen equal to 320 Hz the filter would have the Bode diagram represented in Figure 120. With a filter of $w_n = 320$ Hz the attenuation of resonant modes is more than sufficient and should allow for a good performance of the adaptive controller although finer tuning is possible. In this experiments a double lowpass was implemented for steeper attenuation of high frequencies.

Note that the programming code in the cRIO-9035 does not have to be changed to implement these filters because equation (10.1), expressed in the Laplace domain, has the same structure as equation (7.12), which is expressed in the time domain. Equation (7.12) was already implemented in the cRIO-9035 for the use of the notch filters, thus the only change that had to be performed was modifying the filters coefficients at the upper left side of the engineering screen of Figure 105 to turn the foreseen notch filters into lowpass filters.

After configuring the lowpass filters, a filtered step of 20 V was applied to the piezo in order to observe the effect of the filters after the step. The results are shown in Figure 121. Comparing this figure to the previous one recording a 20 V step without filtering (Figure 118) it seems obvious that the oscillations around the stationary value have been attenuated. However a more precise quantitative assessment of this attenuation can be obtained from the FFT analysis of this step response. The FFT of this response is depicted in Figure 122.

The FFT providing the resonant spectrum of the CPS after a lowpass filtered 20 V step can be compared to the one shown in Figure 119 representing the response to a 20 V step without filtering. The comparison yields that nearly all the resonant modes can be considered negligible after the filtering except for the 341 Hz that has been reduced to almost a third of its original value.

Regarding Figures 118 and 121 it does not seem logical that with almost the same control action on the piezo the responses are so different. However this appreciation is due to the excessive time scale used in both figures and the difference in the response can be better understood when looking closely to the step of Figure 121. For this purpose a zoom of the step signal can be observed in Figure 123.

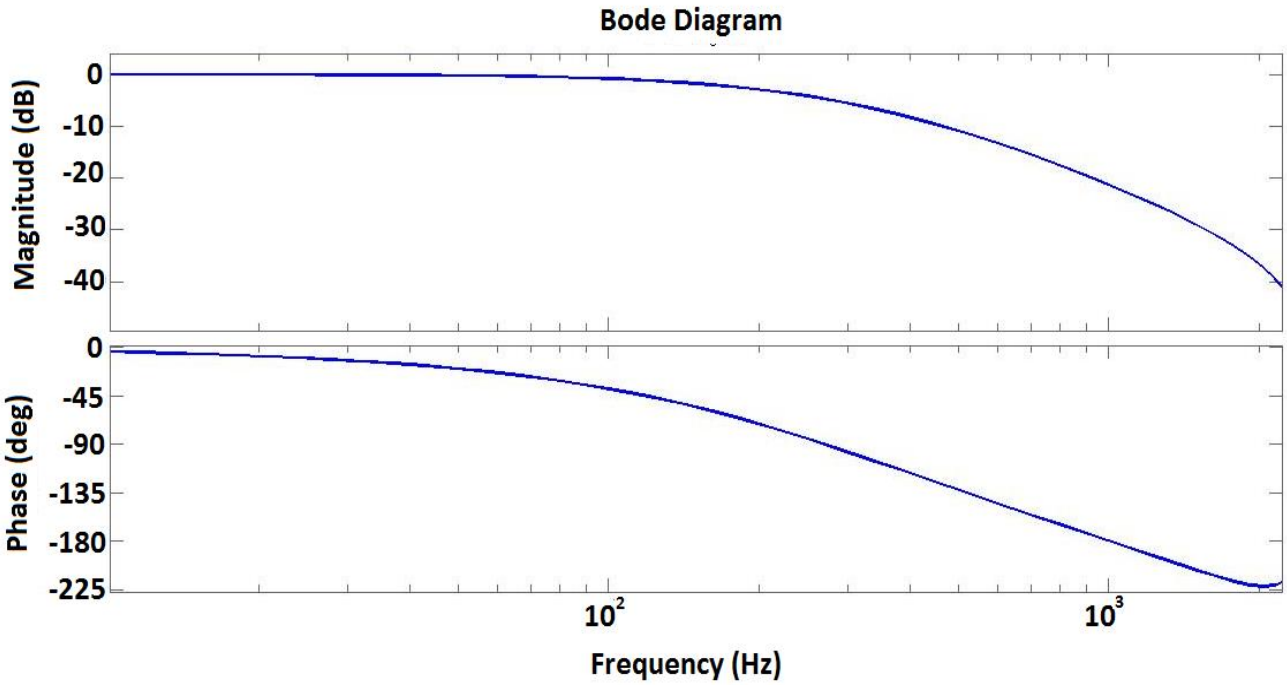

Figure 120. Lowpass filter bode diagram.

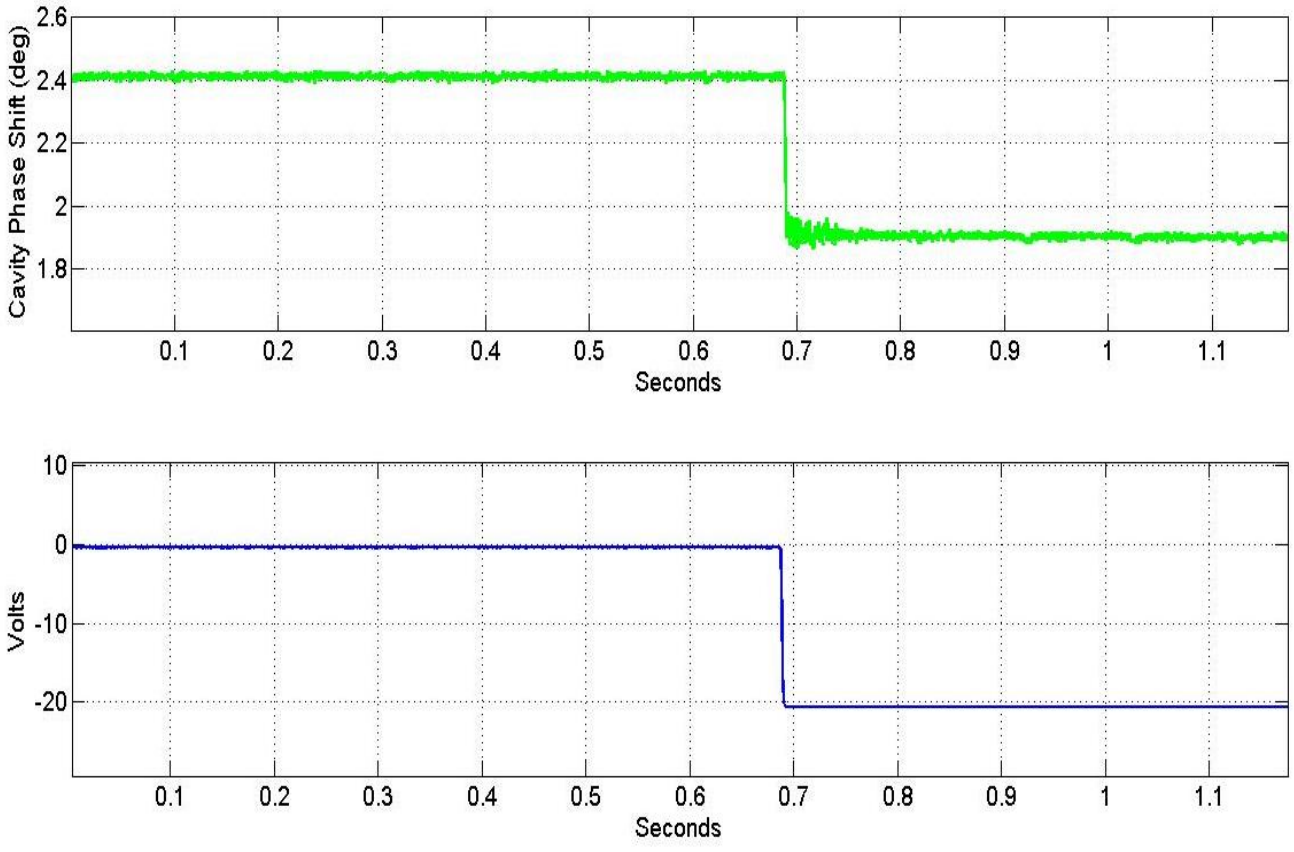

Figure 121. Lowpass Filtered step response in the spoke cavity at room temperature conditions.

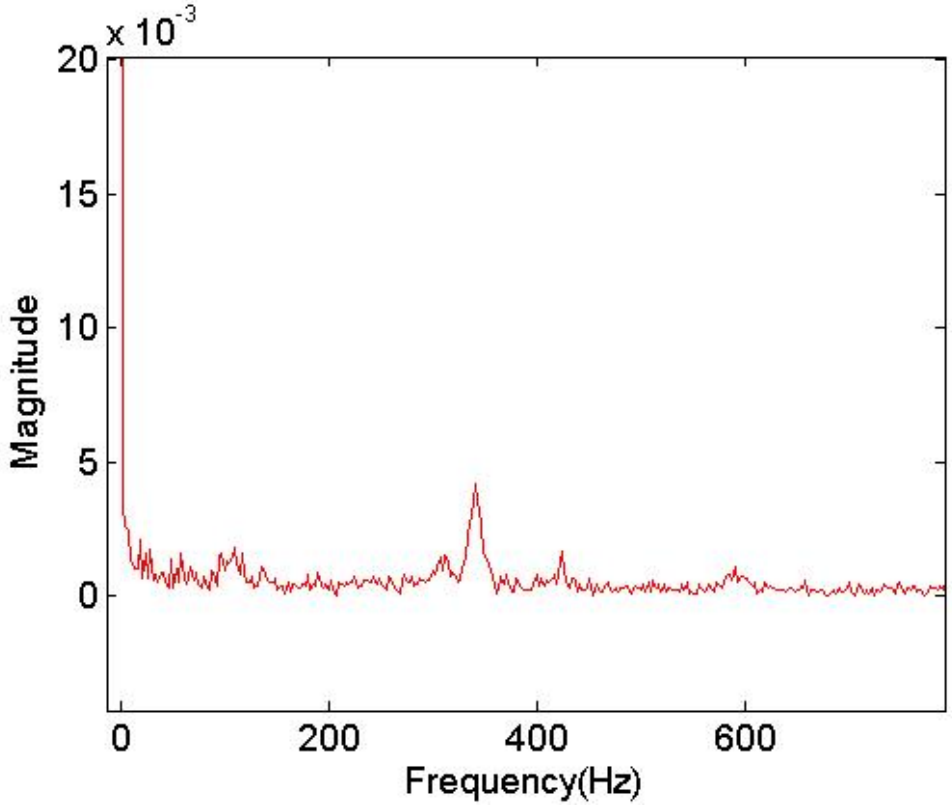

Figure 122. FFT of the lowpass filtered step response.

A closer look to the evolution of the control action applied to the piezo reveals a slow convergence towards the final value as oppose to the instantaneous 20 V step that is applied without filtering. This smooth movement avoids the excitation of the high frequency mechanical resonant modes and allows to attain the results observed in Figure 114. Another aspect that must be considered when analyzing Figure 114 is that the lowpass filters have delayed the step response. This kind of delays deteriorate control performance and could become a problem if they increased notably. Note that the ADEX controller configuration considers a control period of 2 ms and the last three control periods performed in its AP model, taking into account the delay produced by the lowpass filters is around 4 ms and that the CTS performance has a pure time delay of around 1 ms it can be concluded that the AP model is capable of absorbing the dynamics but increasing more the delay is not advisable.

Filters could have been more finely adjusted to reduce even more the mechanical resonant mode at 341 Hz but the results observed in Figure 114 were considered sufficient and a more aggressive filtering (reducing more w_n) would have delayed even more the

response speed. As previously considered this was not considered convenient because of the limits of the ad-hoc ADEX controller used for this application. Thus, it was decided to proceed with the tests with this initial adjustment of the filters.

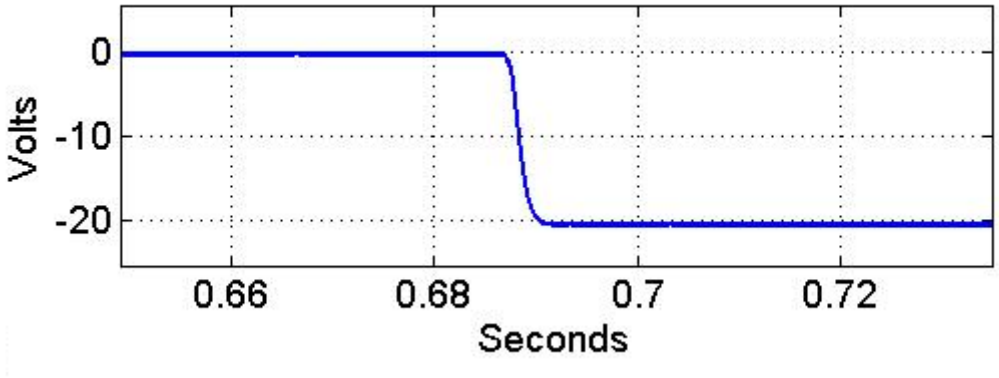

Figure 123. Zoom of the lowpass filtered 20V step response.

Note that if this filters configuration yields a good performance it could be generally applied to any other cavity with the same structure and no further filter adjustment will be needed if this kind of cavity is chosen for mass production.

Characterization of the tests with the elliptical cavity:

Tests with a prototypical elliptical cavity were performed in cryogenic conditions working with the second and third setups which are described by Figures 114 and 115. The second setup considers the use of a PLL and the third one the use of a DLLRF as described in subsection 10.3.

As expected, control trials both with PLL and DLLRF have been affected by the presence microphonics which are produced by external perturbations, such as the noise of pumps or any other environmental vibration. However, their effect surpassed any expectation. Figure 124 shows a 10 seconds record, using the PLL, of the microphonics effect with no other perturbation or control action affecting the cavity.

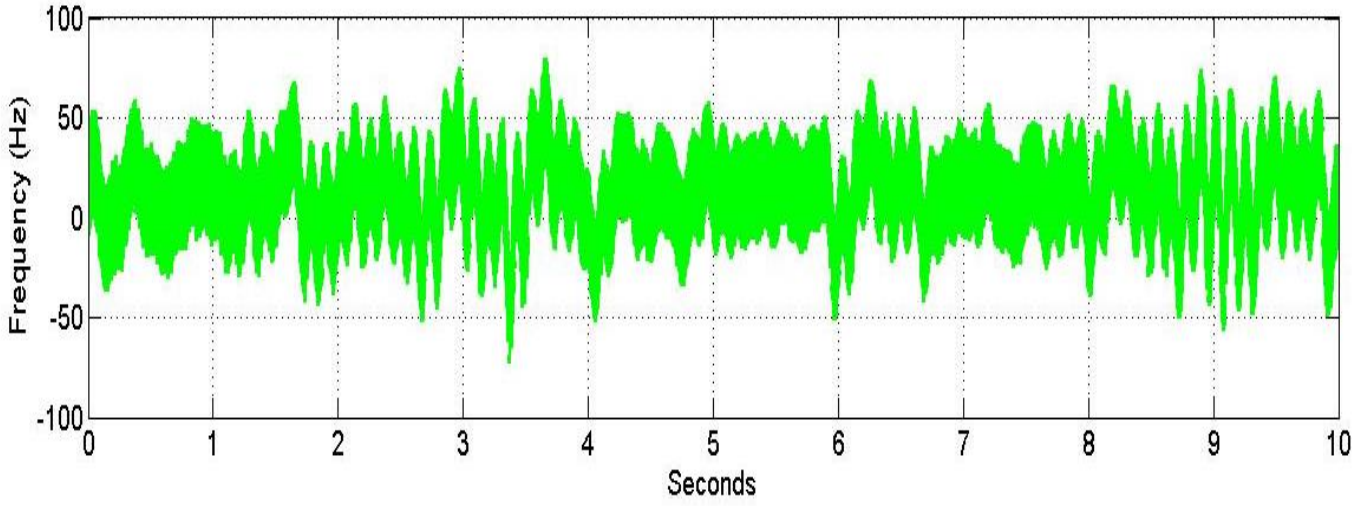

Figure 124. First record of the CPS of the cavity.

This behavior was unexpected. Microphonic perturbations were causing drastic drifts in the cavity detuning of more than ±50 Hz which is more than the estimated bandwidth of the cavity [28].

Furthermore, the microphonic resonating modes kept appearing and disappearing and changing their frequency. Figure 125 shows four different microphonic spectrums obtained from data captured from the cavity, like the one form Figure 124, with no piezo movement or particular perturbation, except for microphonics, affecting the cavity operation. All data captures used to obtain the microphonic spectrums presented in Figure 125 were made within 5 minutes.

The random behavior of microphonics and the speed of its changes made evident that Chebyshev filters that were envisaged for the ADEX OACS and the PID strategies would not work as in simulation were the microphonic perturbations remained at a constant frequency. Chebyshev filters are intended to compensate for microphonic perturbations previously recorded in the facility and have to be tuned for the determined frequency of the perturbation. However, in this case the frequencies of microphonics presented variations of up to 20 Hz within minutes. Hence, the use of Chebyshev filters was discarded.

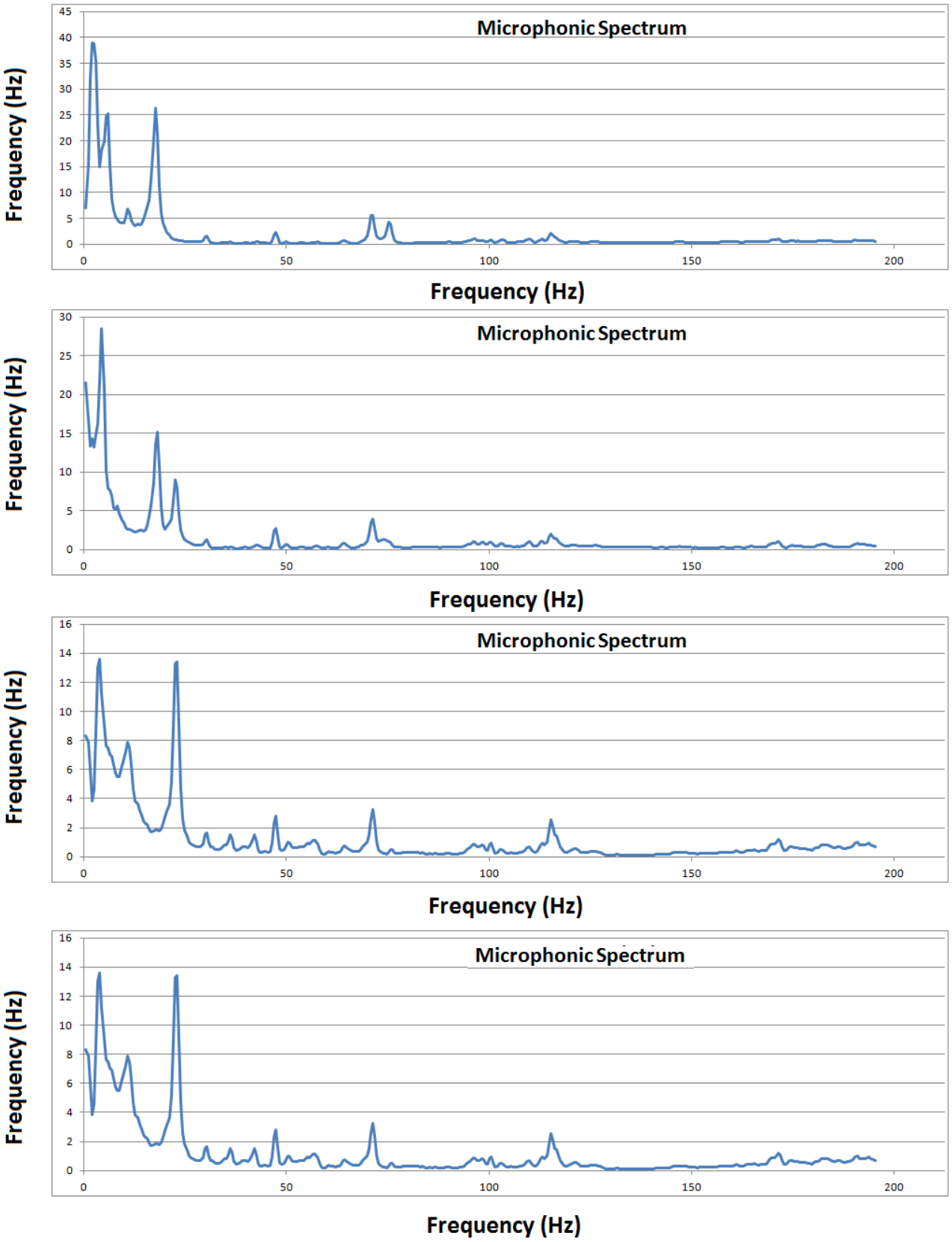

Figure 125. Different microphonic spectrums of the cavity within 5 minutes time.

In a similar manner, a study of the mechanical resonant modes of the cavity was performed. Due to the strong presence of microphonics the way to detect the mechanical resonant modes was to capture data and to calculate the frequency spectrum of the cavity during two consecutive time instants, one before piezo excitation (i.e. a step) and another one after piezo excitation. Figure 126 shows both the resonant modes excited by a step in the piezo (blue) and those that were excited by external microphonics (red) before the piezo movement:

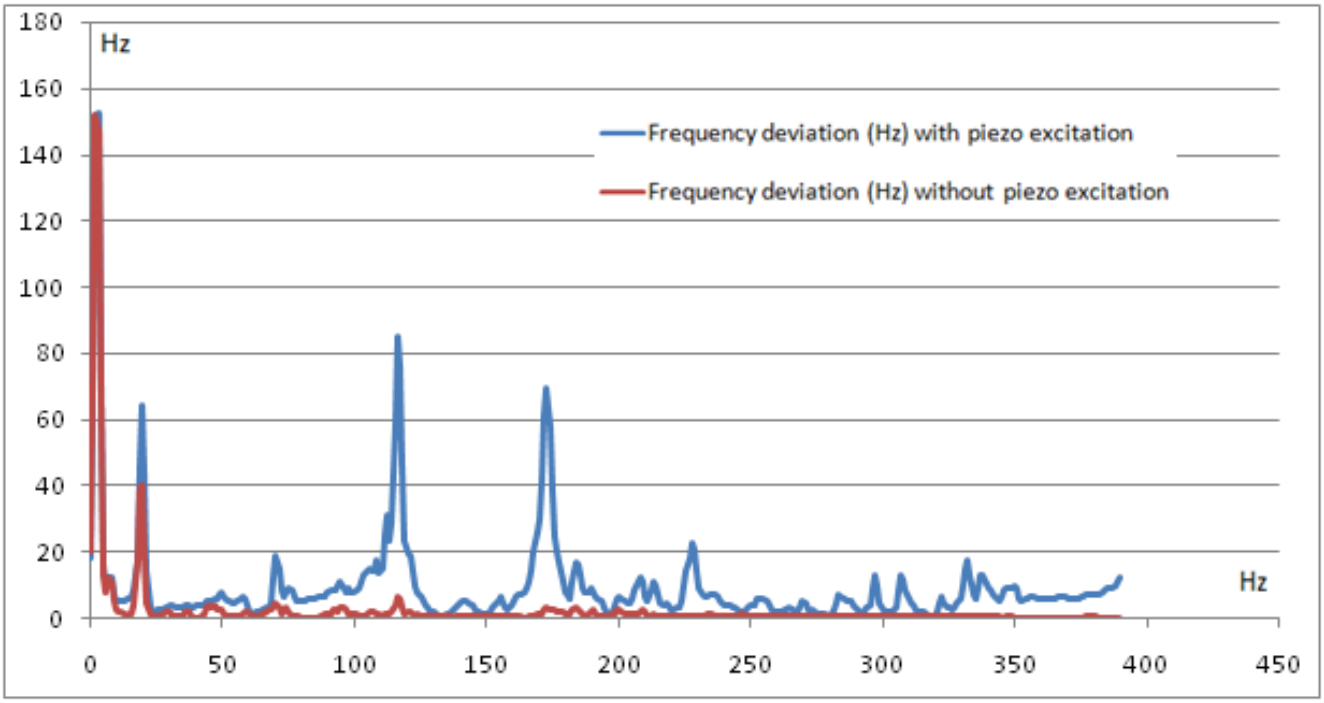

Figure 126. Resonant Modes and Microphonics Spectrum

The red line shows that when the cavity is not excited by the piezo there are still two resonant modes that appear at 2 Hz and at 20 Hz. On the other hand, the blue line shows that the main resonant modes that can be excited by the piezo actuators are placed at 20 Hz, 120 Hz and 170 Hz. This results were consistent and the main resonant modes could be clearly detected even under the effect of strong microphonics.

This cavity features differ from those of the simulated cavity considered in Chapter 8. This chapter presents the control results obtained by the conventional PID system and by the ADEX system for which notch filters have been readjusted to avoid exciting the modes considered in Figure 126. As for the Chevyshev filters which were foreseen to compensate for fast microphonics such as 20 Hz, using them was discarded during the present tests campaign because microphonics at 20 Hz were not fixed in frequency that varied permanently in a range from 16 to 24 Hz.

Figure 127 shows a sequence of steps that have not been filtered with notch filters, while Figure 128 shows the same sequence of steps filtered with notch filters. The same scales and chromatic criterion have been used for both figures. The evolution of the PLL frequency is represented in the upper graph (green) and the evolution of the control action applied to the piezo is represented in the lower graph (blue). This data capture was performed during 5 seconds with a sampling time of 200 μs.

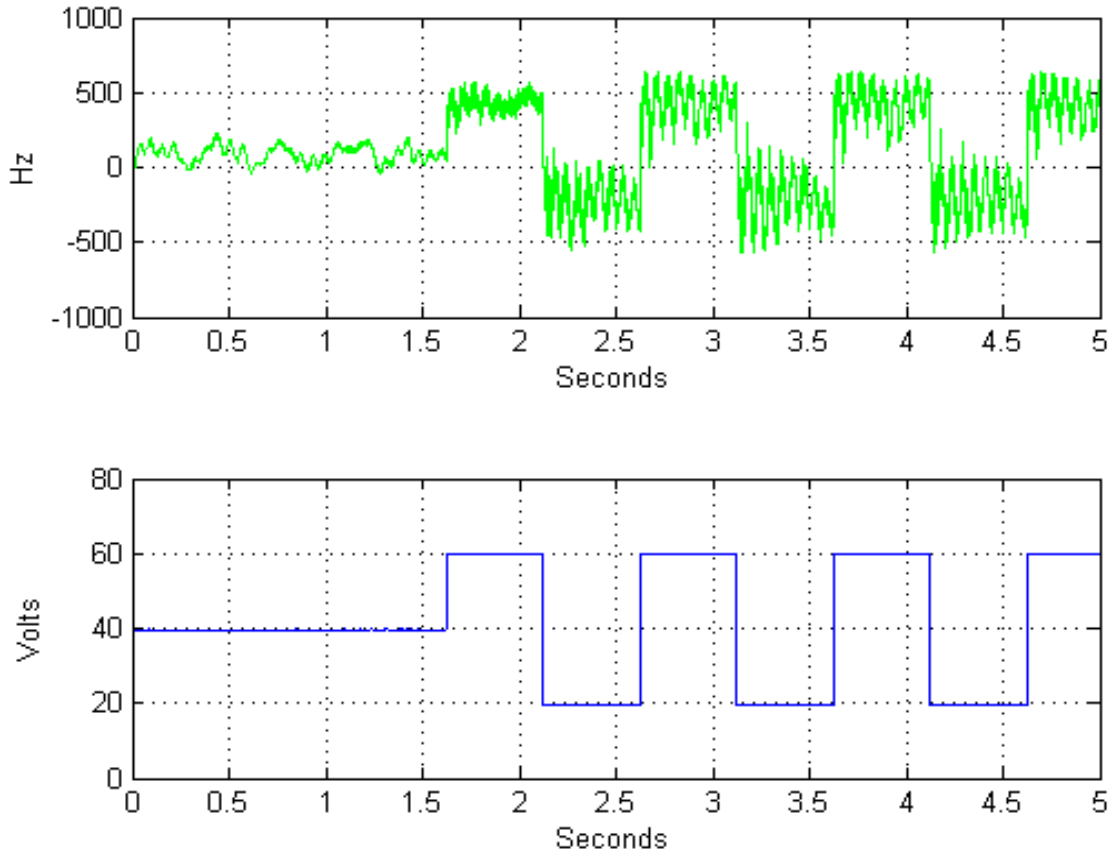

Figure 127. CRFD step response without notch filters

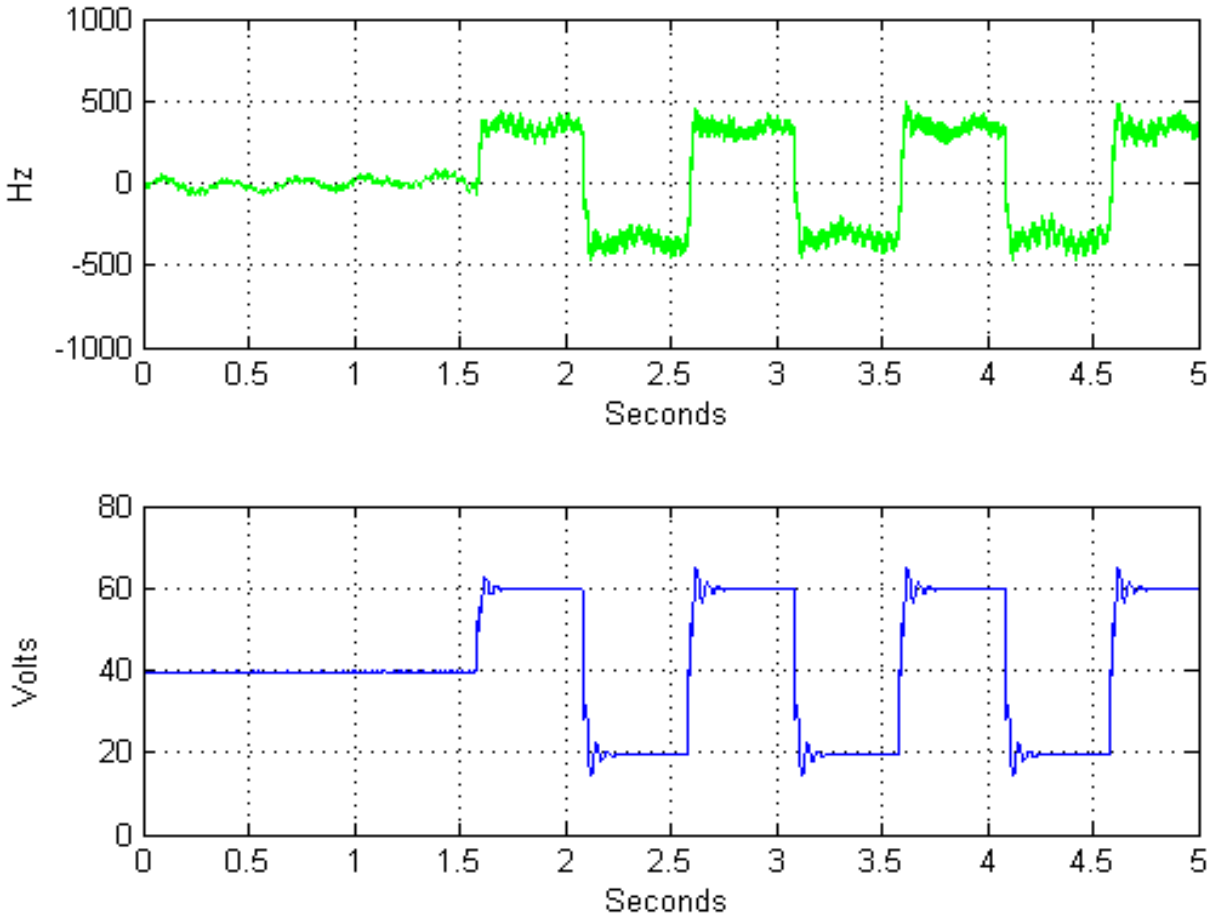

Figure 128. PLL Frequency detuning step response with notch filters.

The data capture of Figure 127, its legend and scales are the same as the ones of Figure 128. A glance at both figures shows that the filtered steps don't excite as many resonant modes from the cavity. Additionally, Figure 129 compares the FFT of both responses in frequency, being the red FFT that of the non-filtered steps and the green one the one of the filtered steps. Looking at the figure it can be noticed that all the resonant modes have been strongly attenuated. These filters have been used in the control strategy of the ADEX OACS system whose performance will be presented in throughout this Chapter.

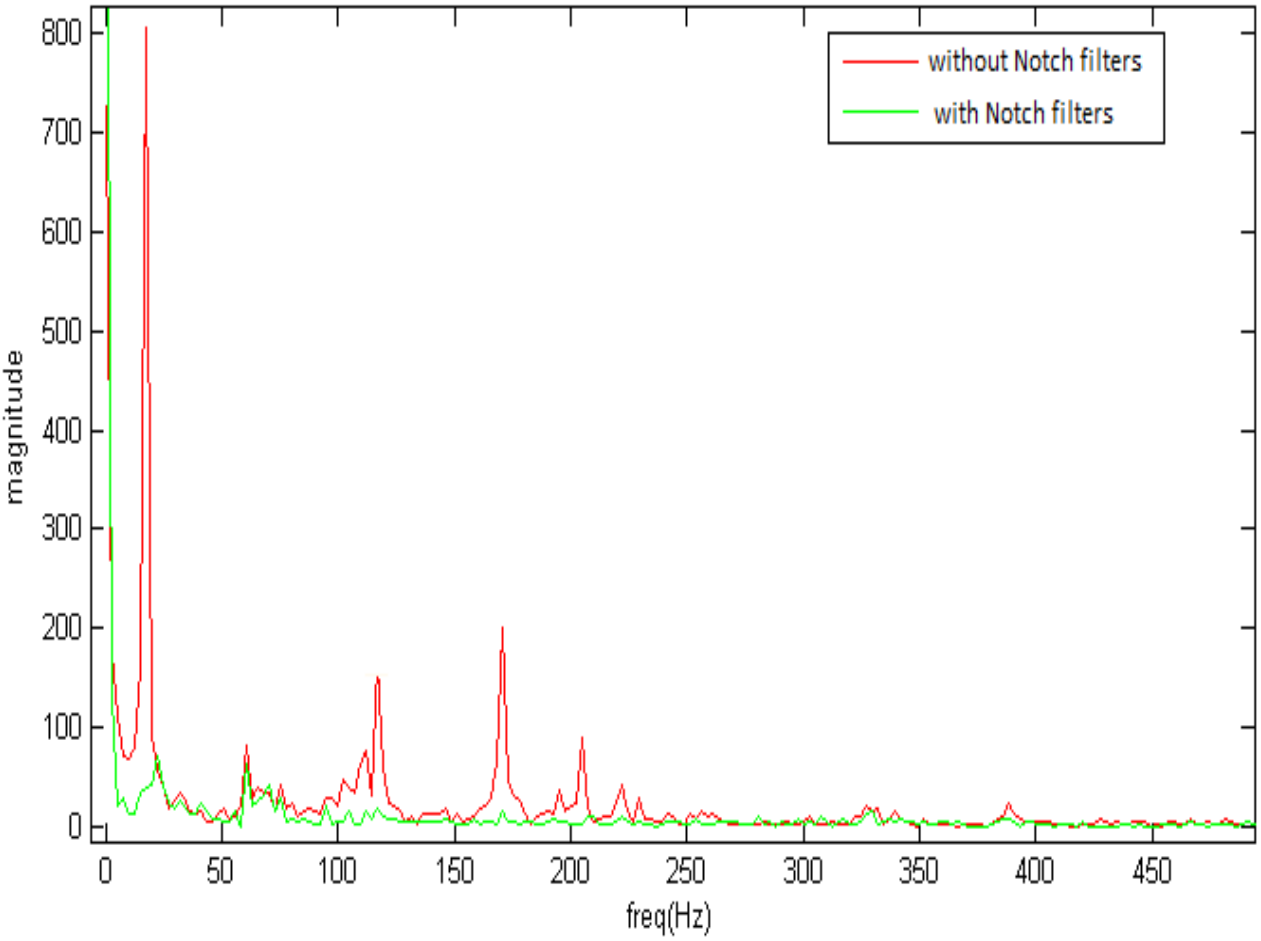

Figure 129. FFT of the step responses with and without Notch filters

When operating with the DLLRF, the variations in the cavity's resonance frequency are directly reflected on the difference between the phase of the cavity's output and the phase of the cavity´s input waves that is to say on the CPS. The non-linear relationship between the CPS and the cavity's resonance frequency w_{RF} is shown in Figure 130.

It can be observed that the linear relationship between the CPS and the resonance frequency is limited to a small region approximately equal to the cavity bandwidth. Outside of this region the CPS saturates and, therefore, is useless for representing the resonance frequency.

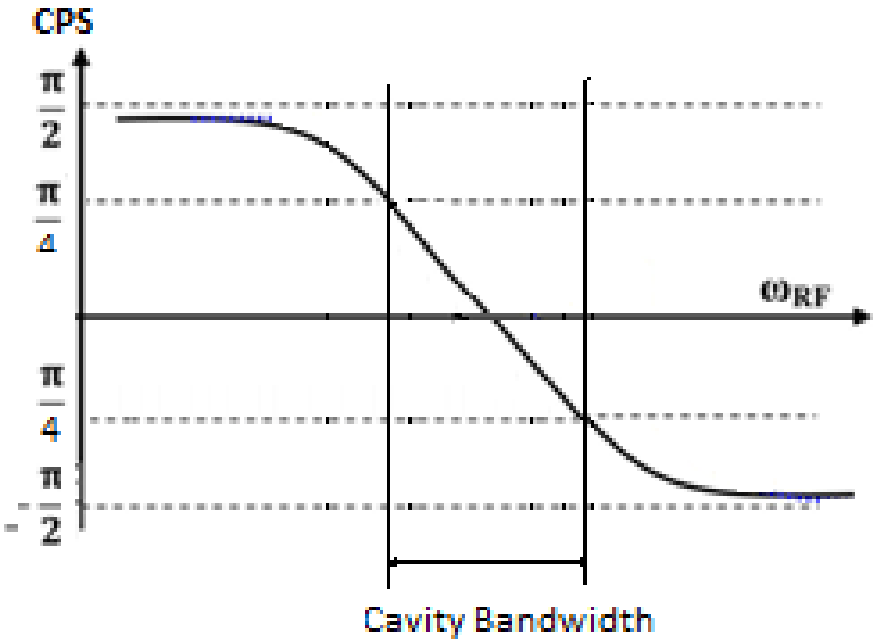

Figure 130. Non-linear relationship between the phase shift and the resonance frequency of the cavity

This feature of the non-linear relationship, common to all accelerating cavities, becomes particularly inconvenient for this cavity when cooled down to 2K for two reasons:

- The bandwidth of the cavity at 2K was considerably smaller than that expected from theoretical calculations and discussed in Section 4.1 of this report. Measurements at 2K confirmed the bandwidth is around 20 Hz [28].
- The "accordion" shape of this cavity makes it very sensitive to environmental vibrations and microphonics. As it may be seen in Figure 125, the resonance frequency of the cavity presents detuning deviations due to microphonics of 150 Hz, which are more than 1,5 times the bandwidth of the cavity.

In this context, the best control system performance would easily saturate the CPS under control. Consequently, results when using the DLLRF are not expected to be very significant, and probably the CPS will be in a saturation condition most of the time.

10.5 EXPERIMENTAL RESULTS

Spoke cavity tests:

The performance of the FTS both with PID and ADEX systems was evaluated in the spoke cavity under room temperature conditions. The setup used for this trials is the one described by Figure 113.

These trials were considered mandatory to test the performance of the systems before their implementation in the cryogenic experimental setups. Note that the duration of cryogenic experimental tests was limited by the available amount of liquid He in IPNOs stock, being the maximum expected length of the tests of two weeks. Besides, there was no possibility of repeating the cold tests in a short period of time, certainly not within the year, due to the extremely expensive costs of liquid He (that allowed to achieve 2 K inside the cryomodule). In this context, all systems involved in the cryogenic tests had to be proven fully performing before starting these tests.

The first experience with the spoke cavity at room temperature consisted simply on trying PID and ADEX control when modifying the CPS offset measurement by 0,15 deg. Figure 131 shows the performance of PID system.

The experiment shown in Figure 131 lasts 1 second as indicated by the time measurement in the x-axis. The green line of subfigure 131.a represents the CPS, while the red line is its setpoint, both measured in degrees, being their scale the one in the y-axis. Subfigure 131.b shows the voltage applied to the piezo in the y-axis during the experiment.

To obtain the result shown in the figure the PID was conveniently tuned. During this tuning there were occasions when the PID system rendered an unstable performance. The unstable performance induced by the PID when badly tuned caused oscillations of increasing magnitude on the CPS and on the voltage applied to the piezoelectric actuator. When this occurred, a strong and acute noise was produced by the oscillations of the piezoelectric. To avoid damaging the piezoelectric actuator the experiment was immediately stoped and a safety protocol that stopped the piezo movement when this situation was detected was

implemented in both ADEX and PID systems. It must be noted that for the ADEX system this was just a caution measure and that this system did not trigger once the safety protocol throughout the whole experimental campaign. With the PID system instabilities occurred nearly immediately when increasing the proportional component. After several trials it was decided that the proportional constant used in the PID would be zero, cancelling thus the proportional component. In a similar manner, the derivative component of the PID reacted very strongly to the high noise of the signal even in stable conditions and was, therefore, considered inappropriate for this control. Thus, the derivative component was also cancelled.

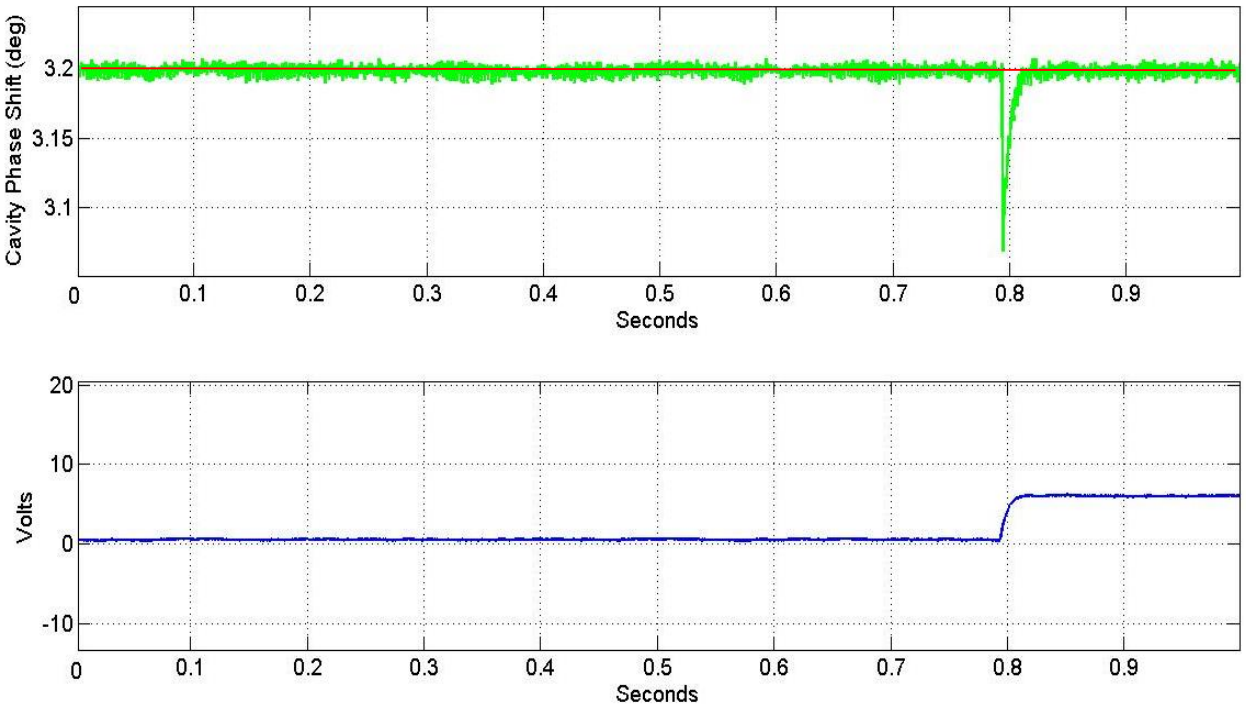

Figure 131. PID control guiding the CPS to its setpoint after a change in its offset.

Figure 132 shows the performance of the ADEX system during a similar experiment to the one shown in Figure 131. The scales and axis of Figure 132 are also similar to those previously considered for Figure 131.

The ADEX performance resulted stable form the very first trial without rendering unstable performance at any moment. This did not happen either at any other tests made during the experimental campaign, be it with the spoke cavity at room temperature or with the elliptical cavity at 2 K.

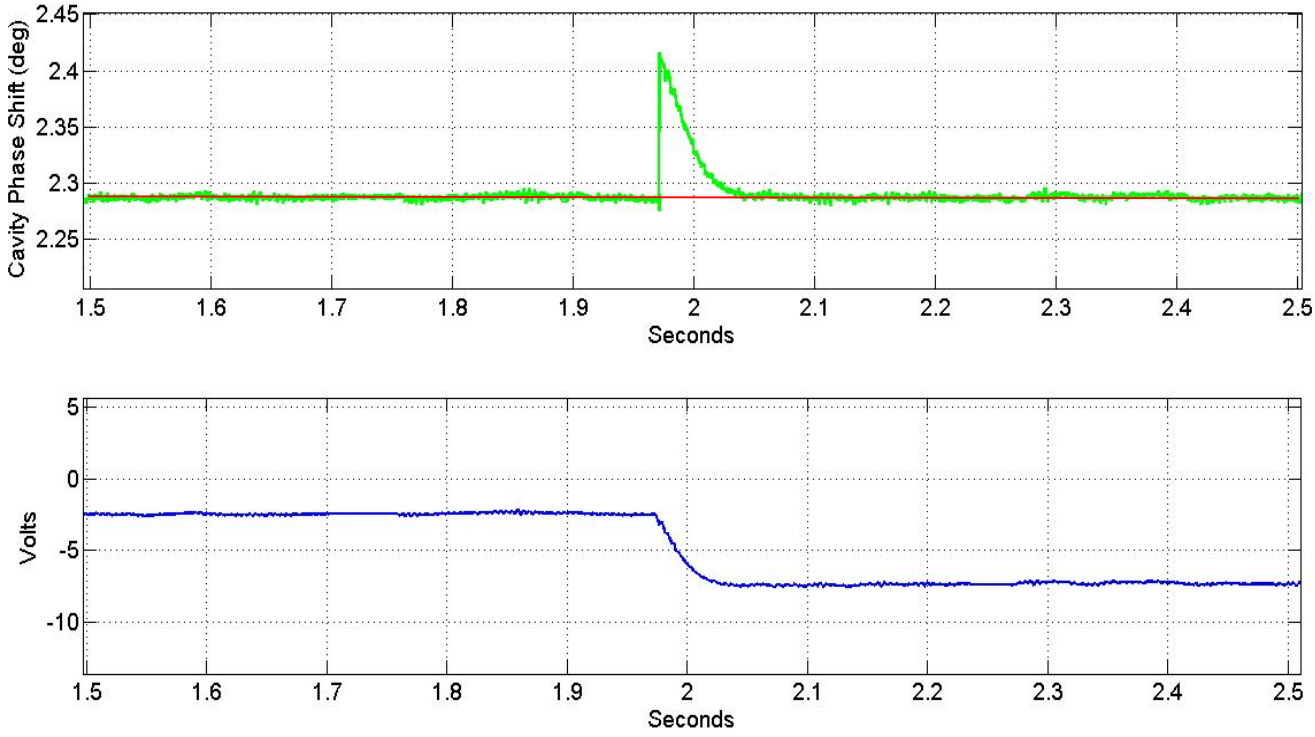

Figure 132. ADEX control guiding the CPS to its setpoint after a change in its offset.

The ADEX performance resulted stable form the very first trial without rendering unstable performance at any moment. This did not happen either at any other tests made during the experimental campaign, be it with the spoke cavity at room temperature or with the elliptical cavity at 2 K.

Comparing both performances, although they are both precise and stable in the guidance of the CPS to their setpoint it must be noted that the PID system provided a faster convergence than the ADEX system (around three times faster).

Regarding these first tests it can be noted that the PID was tuned to obtain an excellent and fast performance while the ADEX controller was not as fast but remained stable throughout the test.

To thoroughly test the performance of both systems with the spoke cavity, a battery of three experiments was designed. These experiments relied on the second piezo of the CTS of the spoke cavity to induce perturbations. The tests performed with PID and ADEX systems are described in Table 10.

No. of Experiment	Perturbations
1	Sinusoidal perturbation of 5 Hz and 2 V acting on the second piezo.
2	Perturbation produced by a sequence of steps 5 Hz and 2 V acting on the second piezo.
3	Sinusoidal perturbation of 30 Hz and 2 V acting on the second piezo.

Table 10: Evaluation experiments in the spoke cavity at room temperature.

The results of this battery of tests are presented and commented in the following subsections. In later sections of this chapter cryogenic tests with PLL and DLLRF are described.

- *Experiment 1*

Figures 133 and 134 present the control performance of both systems, PID and ADEX, under a sinusoidal perturbation of 5 Hz and 2 V. These figures use the same scales and chromatic criterion as the previous ones.

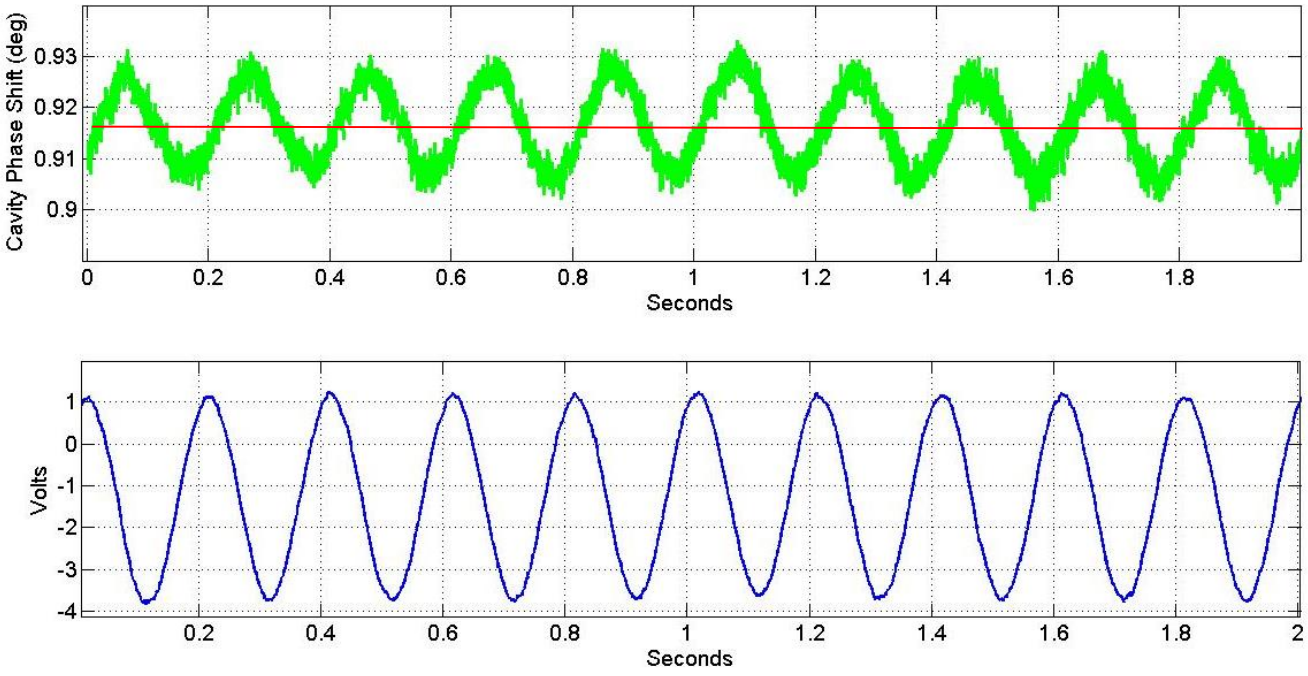

Figure 133. PID compensation for sinusoidal perturbation of 5 Hz and 2 V acting on the second piezo – Experiment 1

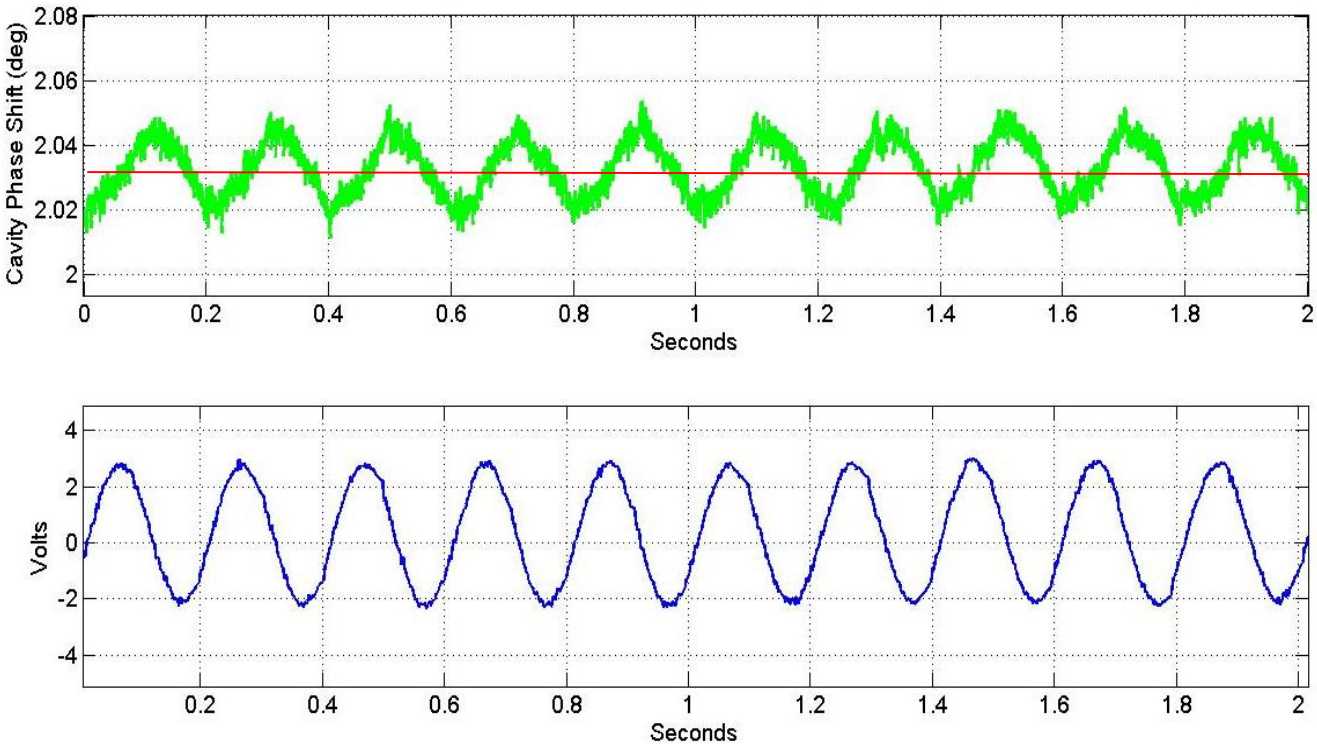

Figure 134. ADEX compensation for sinusoidal perturbation of 5 Hz and 2 V acting on the second piezo - Experiment 1

The PID system was specifically tuned for this scenario. As in the previous case, only the integral component was different to zero. The ADEX controller was self-tuned.

Analyzing the figures it results that both systems obtained a very similar performance. This is not surprising, as logically a carefully tuned PID can obtain an excellent performance as long as no unforeseen perturbation or operating circumstance modifies the process dynamics.

- *Experiment 2*

Figures 135 and 136 present the control performance of both systems under a perturbation composed of a sequence of steps of 5 Hz and 2 V applied to the second piezo. These figures use the same scales and chromatic criterion as the previous ones.

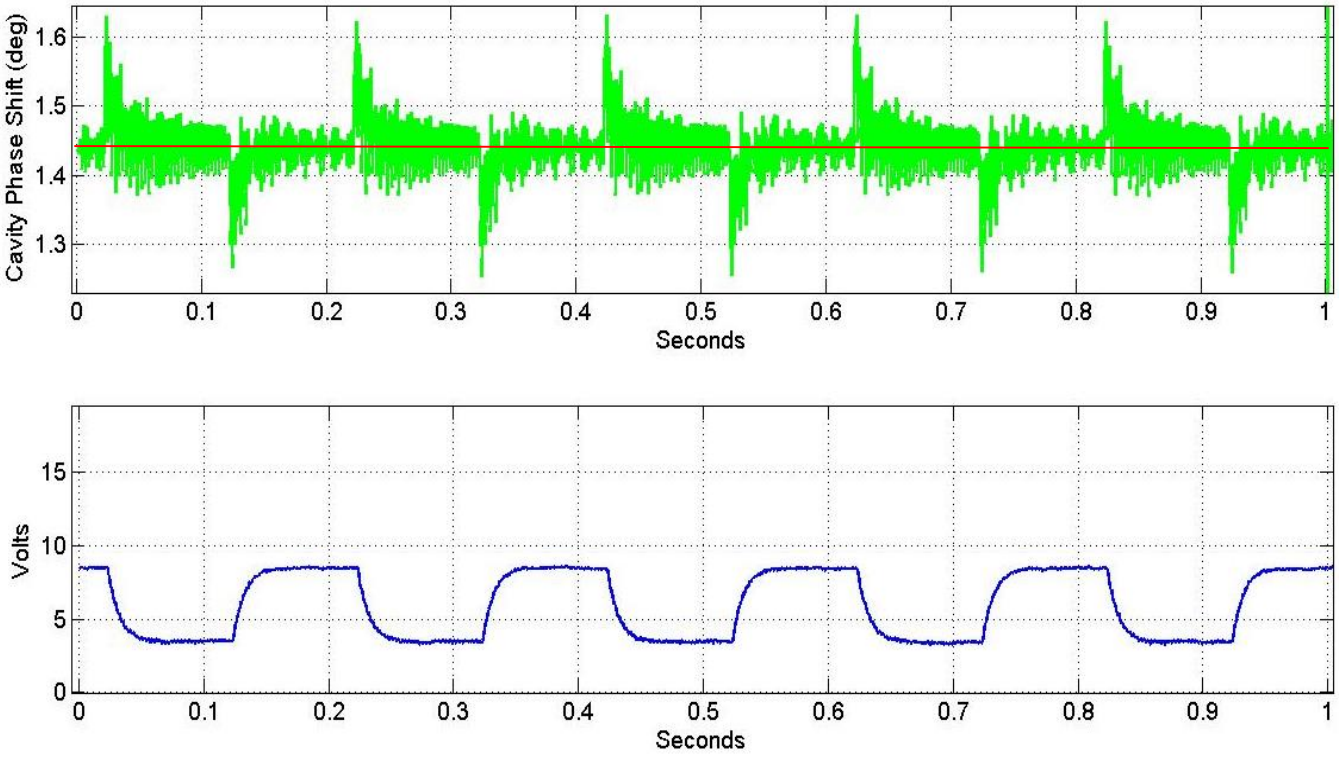

Figure 135. PID compensation for step sequence perturbation of 5 Hz and 2 V acting on the second piezo - Experiment 2

Note that the sequence of steps applied to the second piezo excites strongly the hi-frequency resonances of the cavity. The PID controller was tuned using the integral component as the proportional and derivative ones caused unstable behavior and thus risked damaging the piezo. It is well known that the integral component adds up the error, considering the error as the difference between the process variable, in this case the CPS, and its setpoint. However, the integral sum of the errors result nearly null for a white noise around the setpoint due to its continuous and immediate variation form a positive to negative error, for this reason integral control presents almost no reaction in this case. White noise is somehow similar to the vibrations around the setpoint shown in the figure, in the sense that the integral sum probably results in a value that is approximately zero. For this reason the integral control does not respond to the vibrations produced after the steps of the piezo used to perturb the operation and this vibrations are prolonged until a new step is produced.

As already commented, Figure 136 shows the performance of the ADEX system during this trial.

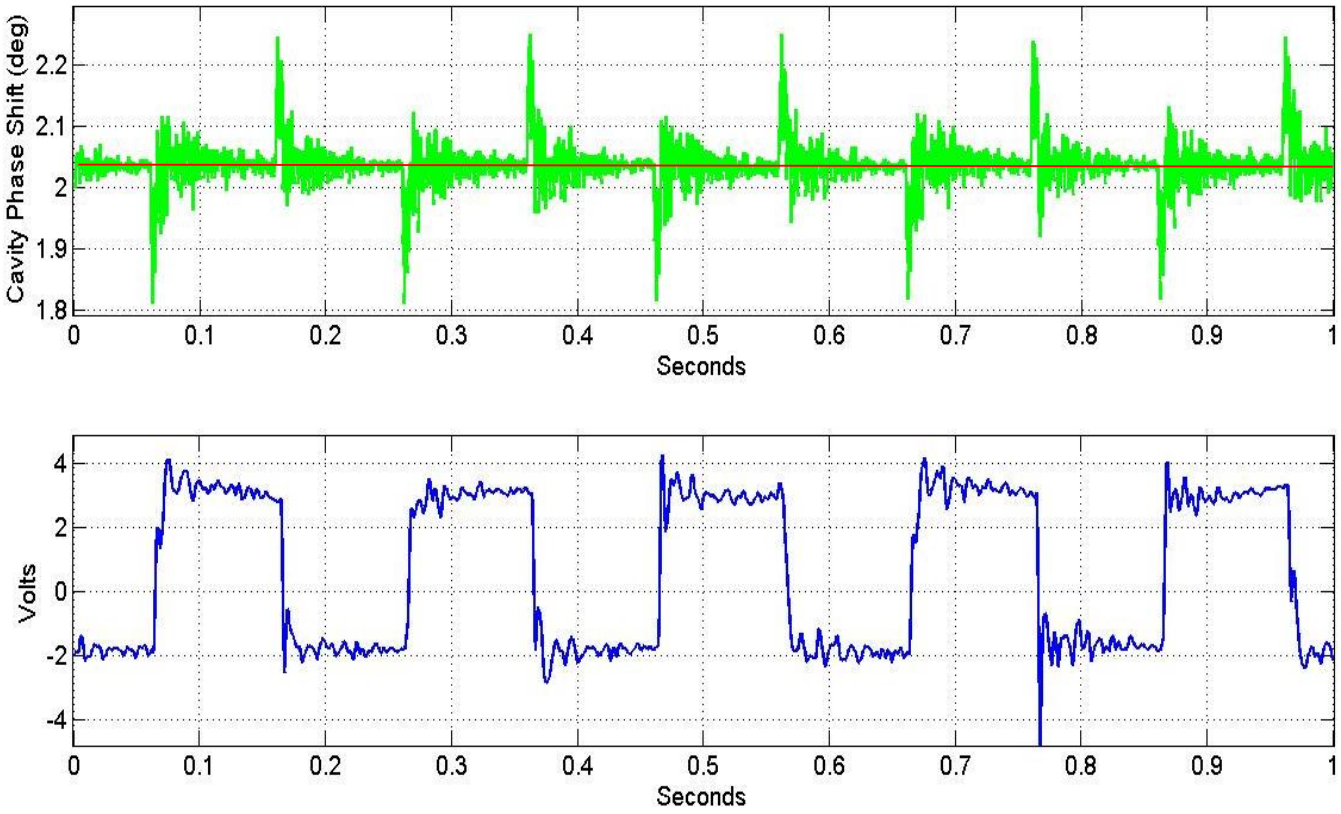

Figure 136. ADEX compensation for step sequence perturbation of 5 Hz and 2 V acting on the second piezo - Experiment 2

The ADEX system tries to counteract the vibrations induced by the steps applied to the first piezo and thus attenuates them. Note that the perturbation induced in the second piezo is a sequence of steps and that a step excites all the frequencies of the resonant spectrum. Therefore, even if the ADEX system does not react nor excite the high resonant modes due to the effect of the lowpass filters, any resonance lower than 250 Hz was conveniently attenuated thus reducing the overall vibrating time. Consequently, the ADEX system achieved in this case a better compensation allowing to stabilize the CPS between steps in piezoelectric actuator used to induce perturbations.

Comparing Figures 135 and 136 it can be noted that ADEX control action is more aggressive than the PID one, in order to compensate for perturbations. This behavior contrasts with the “slow” reaction observed in Figure 136. In this case, under consistent perturbations

the ADEX controller tracked the process dynamics and modified its behavior to enhance control performance.

- *Experiment 3*

This trial is similar to the first one performed but increasing the frequency of the perturbations to test the systems performance at these high frequencies. In particular this experiment considers a sinusoidal perturbation of 30 Hz and 2 V applied to the second piezo.

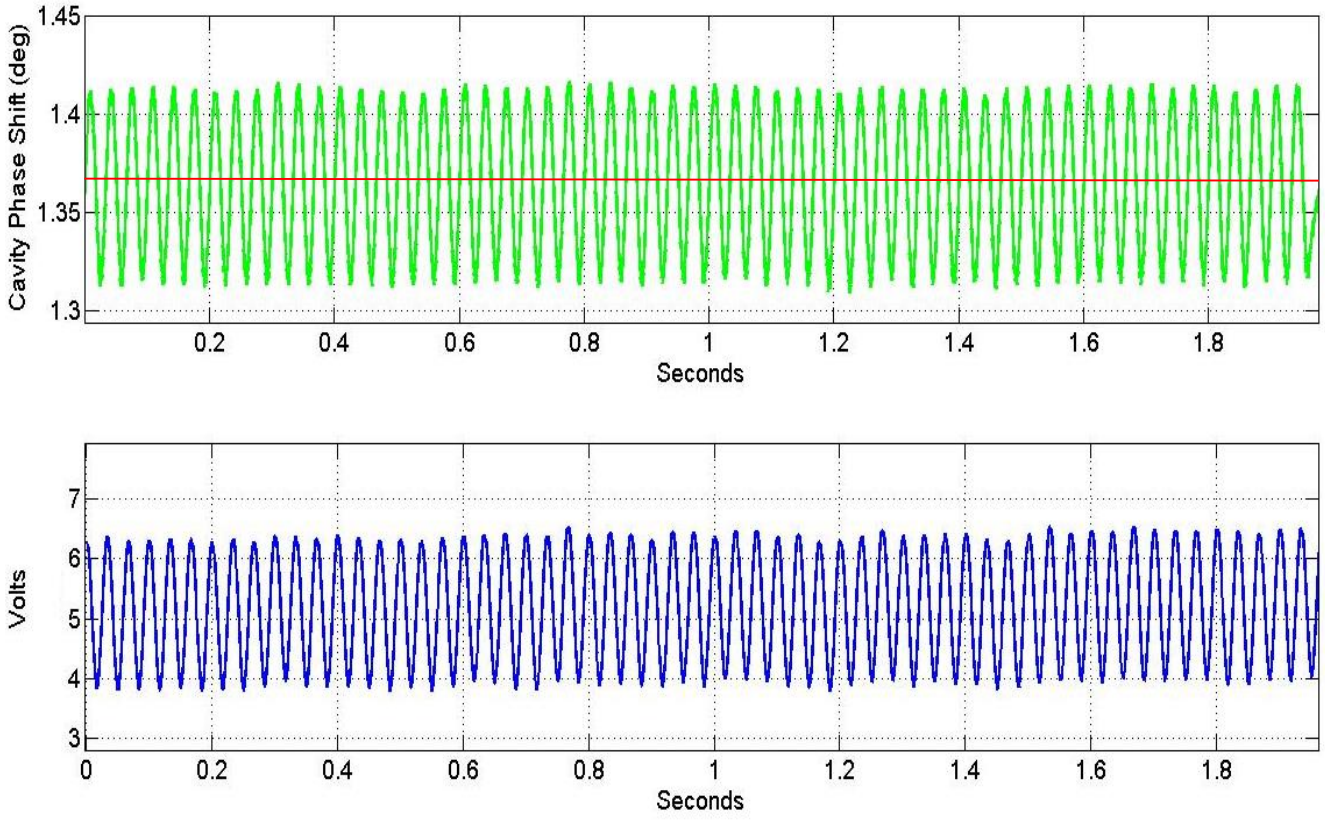

Figure 137. PID compensation for sinusoidal perturbation of 30 Hz and 2 V acting on the second piezo - Experiment 3

Figure 137 shows the performance of the PID system compensation of this perturbation. This figure uses the same scales and chromatic criterion as the previous ones. Once again, in this experiment only the integral component of the PID was functioning.

On the other hand the ADEX system performance is illustrated in Figure 138, which uses the same scales and chromatic criterion as the previous ones. As in the case of the test

with the sinusoidal perturbation of 5Hz and 2 V the performance of both PID and ADEX systems is more or less similar in terms of control precision.

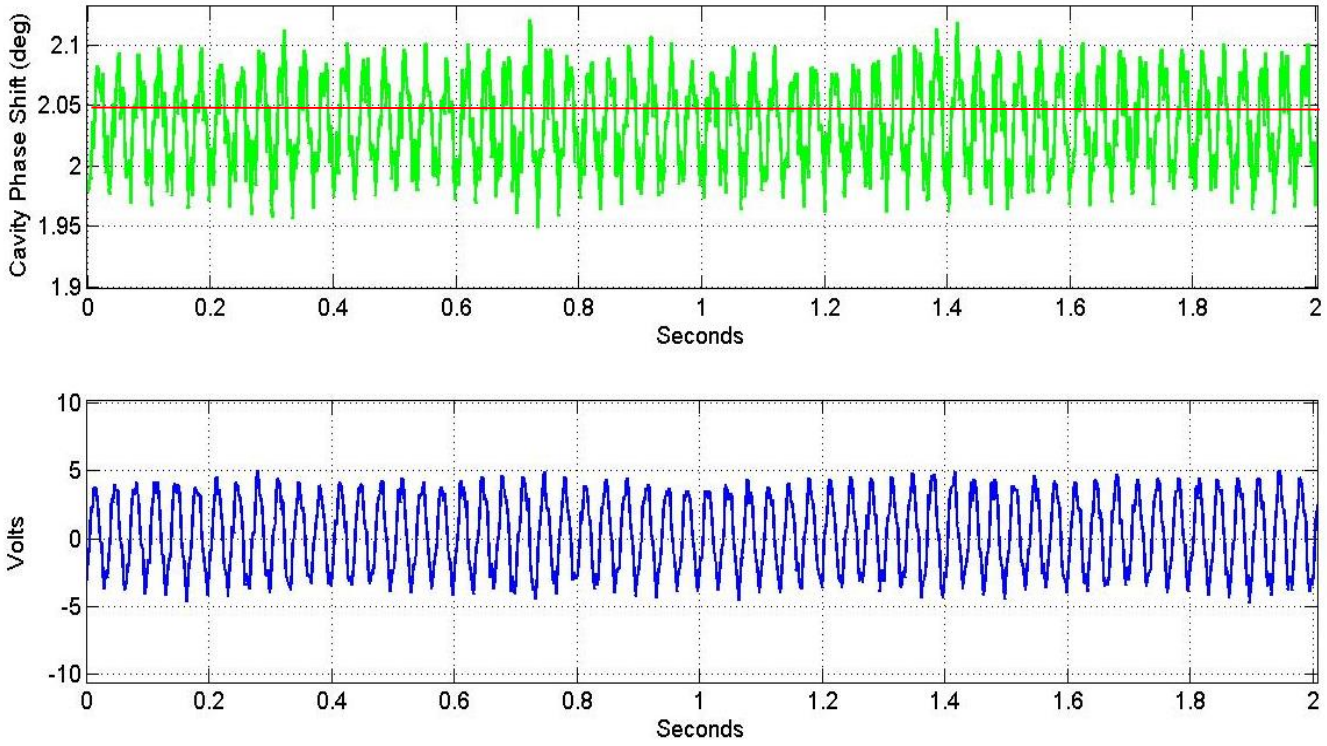

Figure 138. ADEX compensation for sinusoidal perturbation of 30 Hz and 2 V acting on the second piezo - Experiment 3

Conclusions to the spoke cavity tests:

Both ADEX and PID systems proved capable of obtaining an acceptable control performance and guiding the CPS to its setpoint. However instabilities during the tuning of the PID brought forth the need for a safety protocol that stopped the piezoelectric movement when oscillations of the CPS and the voltage applied to the piezoelectric became too strong. This protocol was implemented and tested in the PID system and was considered capable of protecting the piezo from inappropriate control actions. It was also implemented in the ADEX system as caution measure, although the ADEX system never triggered this safety protocol due to the stability of its performance. During the tests, the PID system, when appropriately tuned, seemed to render a faster convergence to the setpoint than the ADEX system. However, in the following tests, i) with a sinusoidal induced perturbation both systems

obtained a similar performance, and ii) in the test with a the perturbation caused by a sequence of steps applied to the second piezo, the ADEX system attenuated the effects of the perturbation and enhanced the results obtained with the PID system.

Acceptable performance of both ADEX and PID systems validated i) the proper functioning of the communications and the connections with the experimental setup and therefore with the appliances to be used in the cryogenic tests, and ii) the correct programing of the systems.

Another main conclusion was that the filtering tools developed for the ADEX system where capable of minimizing the effect of the mechanical resonant modes of a cavity, similarly to how they did when tested in the CNRS simulation of the elliptical cavity. The ease to tune the filters makes possible to attenuate mechanical resonant modes for a determined cavity with very little experimentation and even to perform the filters tuning automatically.

On the other hand, Chebyshev filters remained untested due to the absence of microphonics in the room temperature experiments. Regarding the application of Chebyshev filters in the cryogenic tests, it was considered that the new safety protocol, envisaged to protect the piezoelectric from inappropriate control actions, would also avoid erratic use of the CTS if Chebyshev filters did not work properly. Consequently, it was concluded that both systems were validated and would be implemented and evaluated in the elliptical cavity functioning in a cryogenic environment.

Cryogenic tests under PLL Operation

To evaluate the performance of both alternatives for the FTS, PID and ADEX control systems, 5 experiments for each control technique were applied similarly in both cases, using the experimental setup of Figure 114 characterized by the use of the PLL device, being the cavity´s temperature of 2K.

The 5 experiments considered the presence of microphonics and different external perturbations, which are described in the following Table 11:

No. of Experiment	Perturbations
1	Microphonics
2	Microphonics + a drift of 700Hz in RFD
3	Microphonics + 2 Hz perturbation causing an RFD of 50Hz
4	Microphonics + 4/5 Hz perturbation causing an RFD of 50Hz
5	Microphonics + 8 Hz perturbation causing an RFD of 50Hz

Table 11. Evaluation experiments under PLL operation

- *Experiment 1*

Figure 139 illustrates the control performance of the conventional PID system. The evolution of the frequency is represented in green, with its set point in red, in the upper diagram, while the control action applied to the piezo is represented in blue on the lower one during a 10 seconds data capture with a sampling time of 200 μs.

In the figure the PID system control loop remained closed until second 4, then it was opened. It can be noticed that when the control loop is opened the frequency slightly deviates from its set point, but a comparison with the open loop performance allows appreciating that the PID system, although it compensates for slow frequency drifts, is not so efficient compensating fast variations produced by environmental microphonics. During the first four seconds of PID control the standard deviation of the RFD was 34.71 Hz.

On the other hand, Figure 140 shows the performance of the ADEX system. In this figure the control loop remained closed until second 5, then it was opened. It can be noticed that when the control loop is opened the frequency deviates from its set point, but a comparison with the open loop performance allows appreciating that the ADEX system not only compensates for slow frequency drifts but also compensated partially for fast variations in the frequency due to microphonics. During the first 5 seconds of ADEX control the standard deviation of the RFD was 16.0866 Hz.

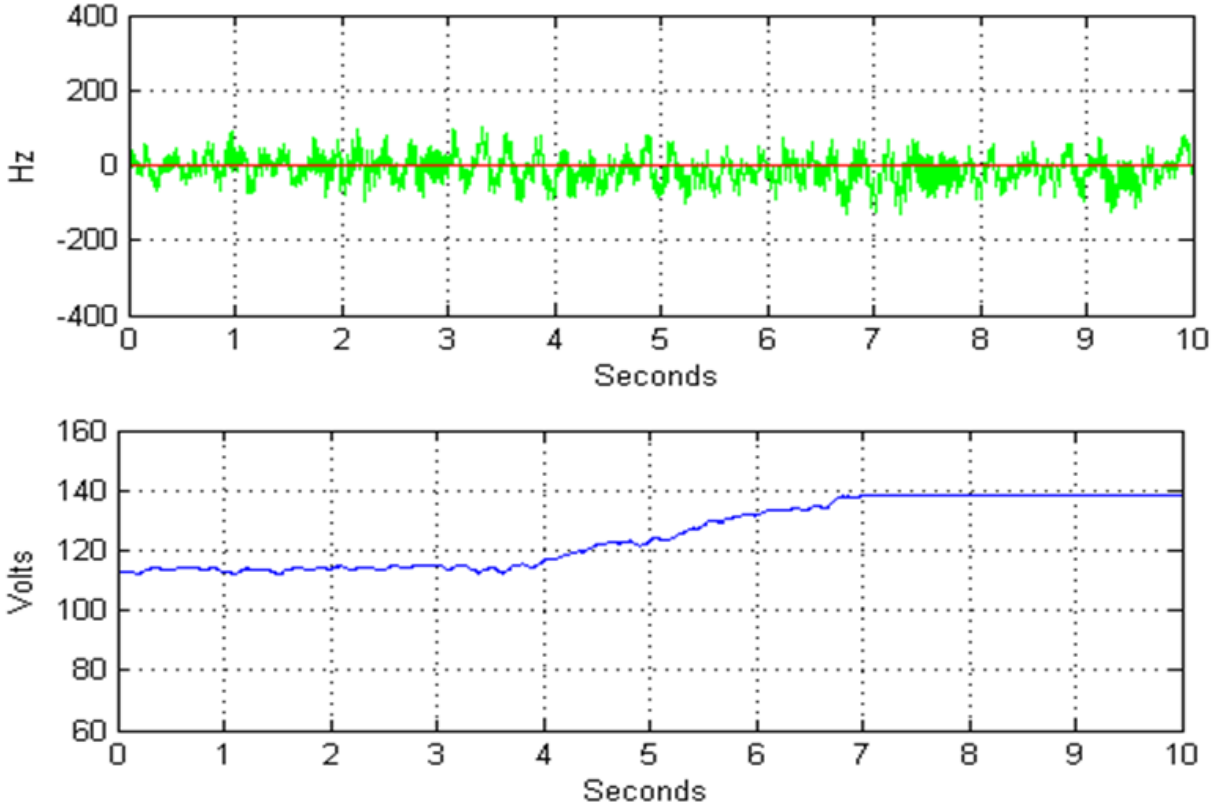

Figure 139. PID performance with PLL – Experiment 1

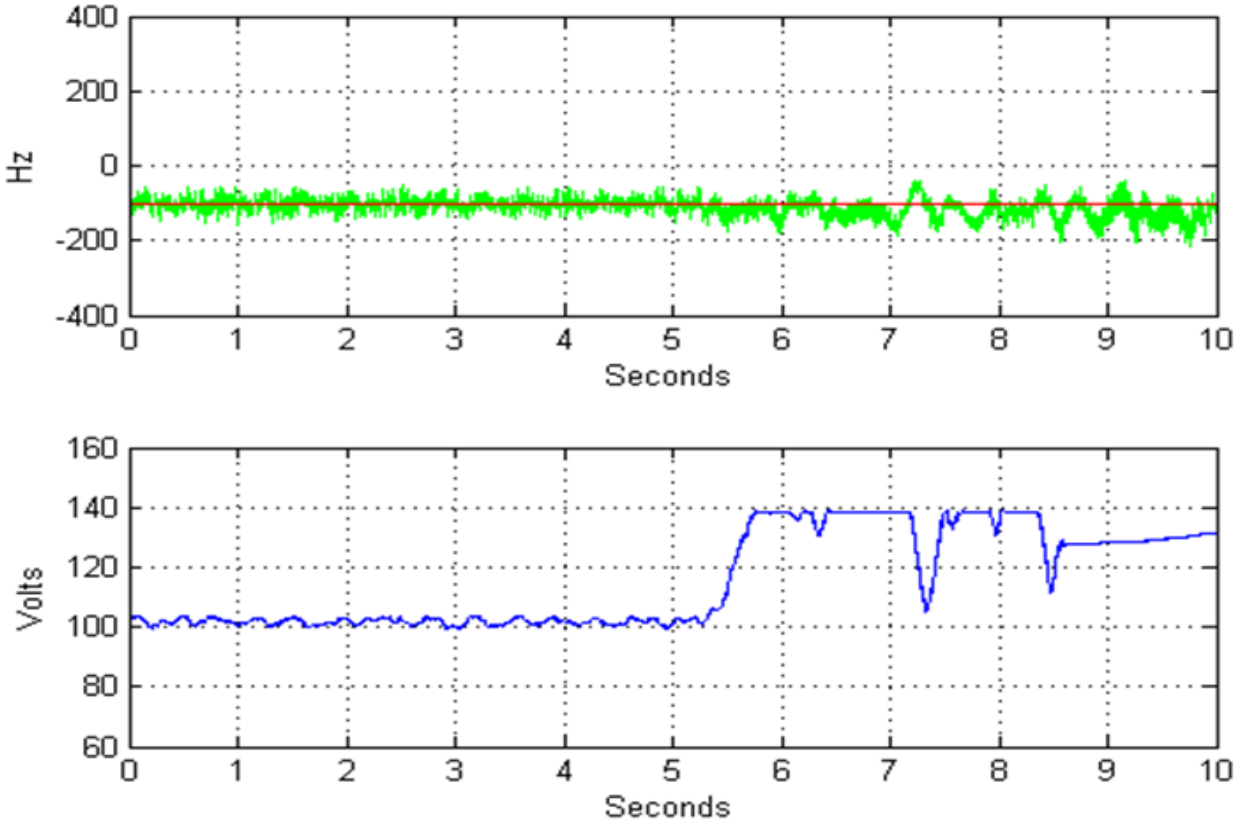

Figure 140. ADEX performance with PLL – Experiment 1

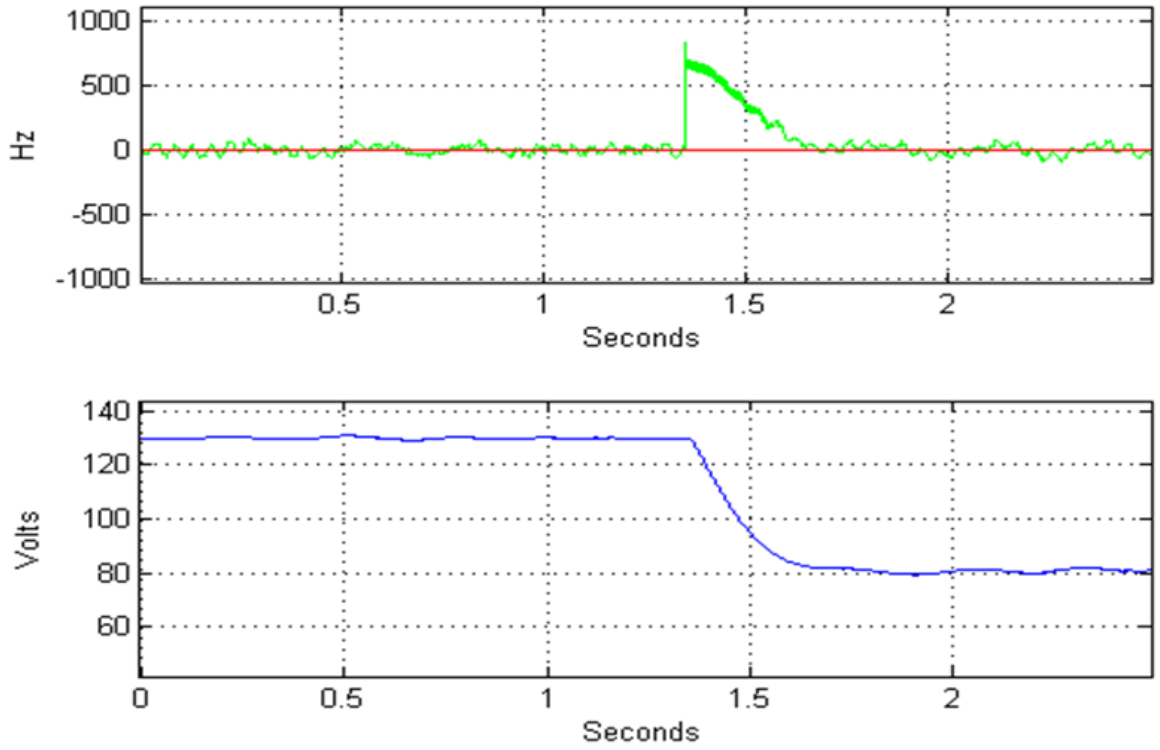

Figure 141. PID compensation for a 700Hz drift with PLL – Experiment 2

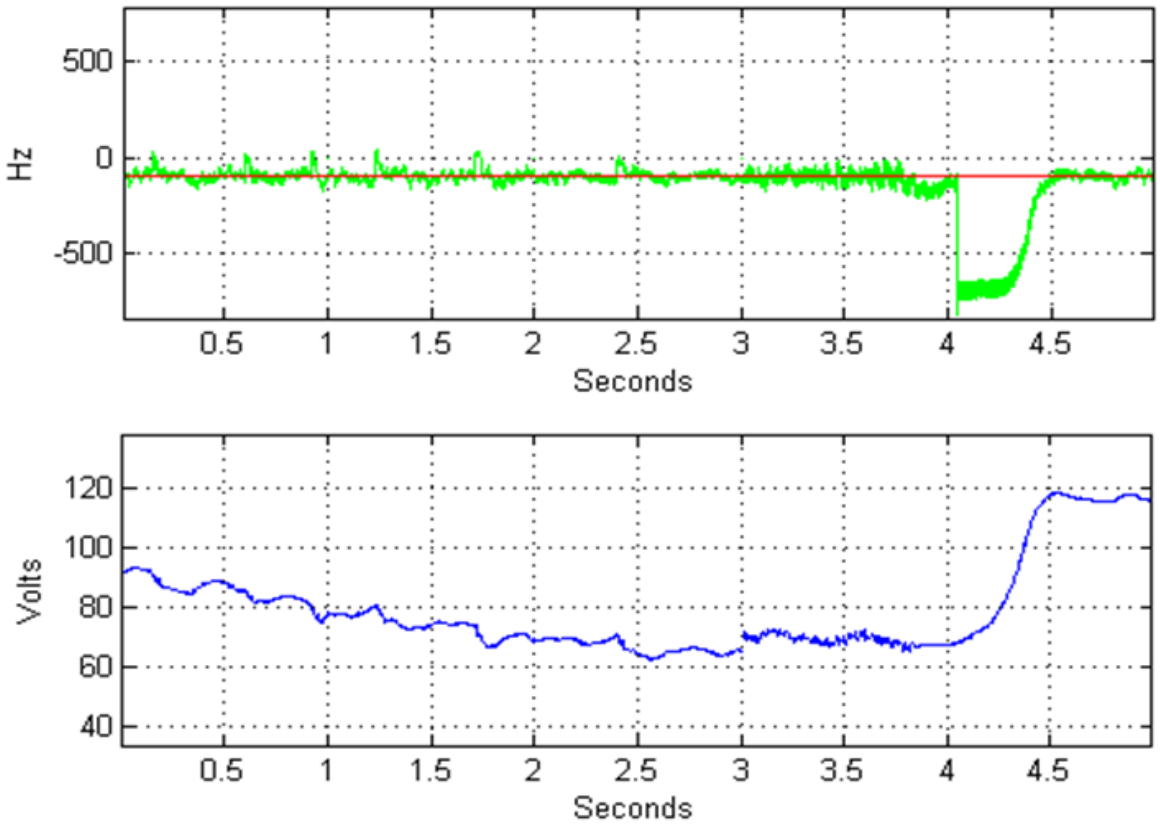

Figure 142. ADEX compensation for a 700HZ drift with PLL – Experiment 2

- *Experiment 2*

Figure 141 shows the PID system compensation for a 700 Hz drift in the frequency. This drift was caused by varying the RF generator frequency output and was afterwards compensated efficiently by the PID control in less than half a sec. On the other hand, Figure 142 shows the ADEX system compensating for the same frequency drift of 700 Hz. This drift was introduced, as in the previous case, by varying the RF generator frequency output. The ADEX system also compensated efficiently this perturbation in less than half a sec.

- *Experiment 3*

Figure 143 shows the PID system compensation for a sinusoidal perturbation of 2 Hz frequency acting on the second piezo and causing a 50Hz resonance frequency detuning. The standard deviation of the resonance frequency detuning was in this case of 60.80 Hz. On the other hand, Figure 144 shows the ADEX system compensation for a sinusoidal perturbation of 2 Hz frequency acting on piezo 2 and causing a 50Hz resonance frequency detuning.

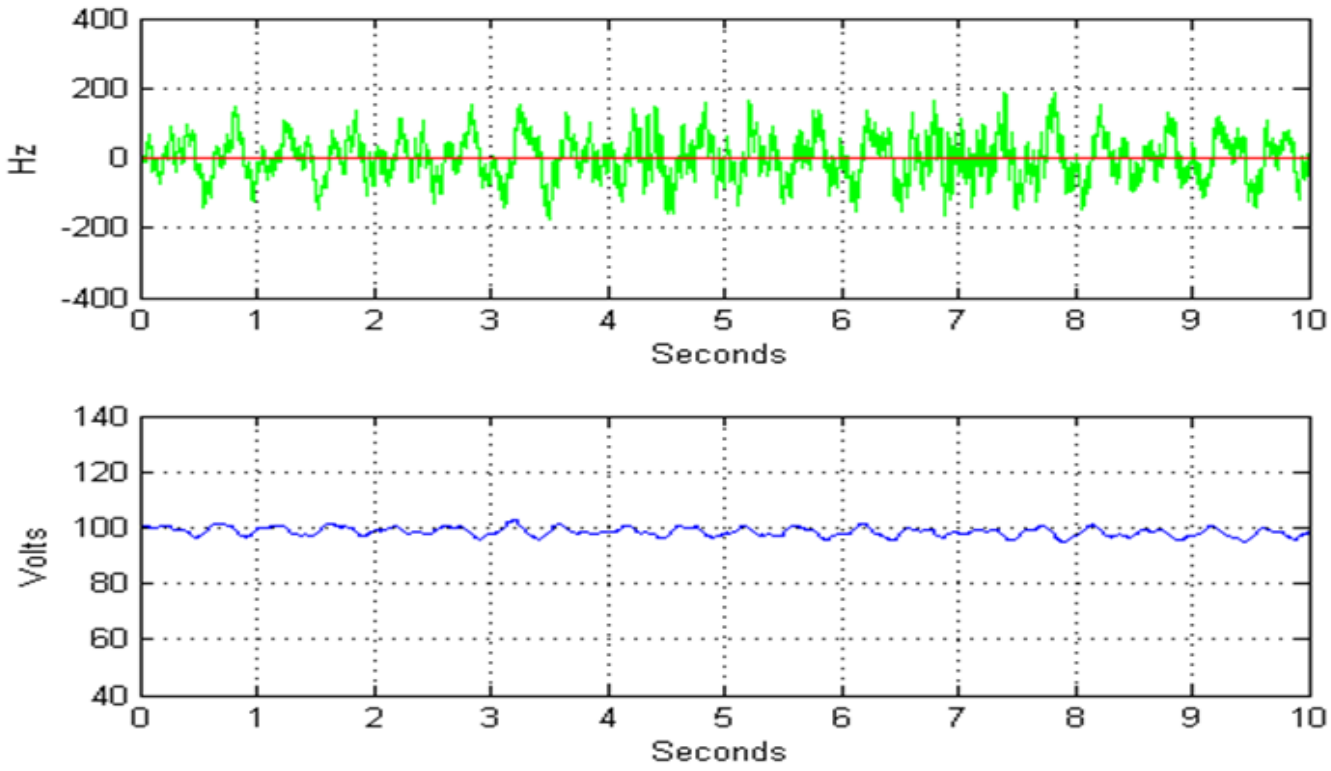

Figure 143. PID compensation of a perturbation of 2 Hz causing an RFD of 50Hz – Experiment 3

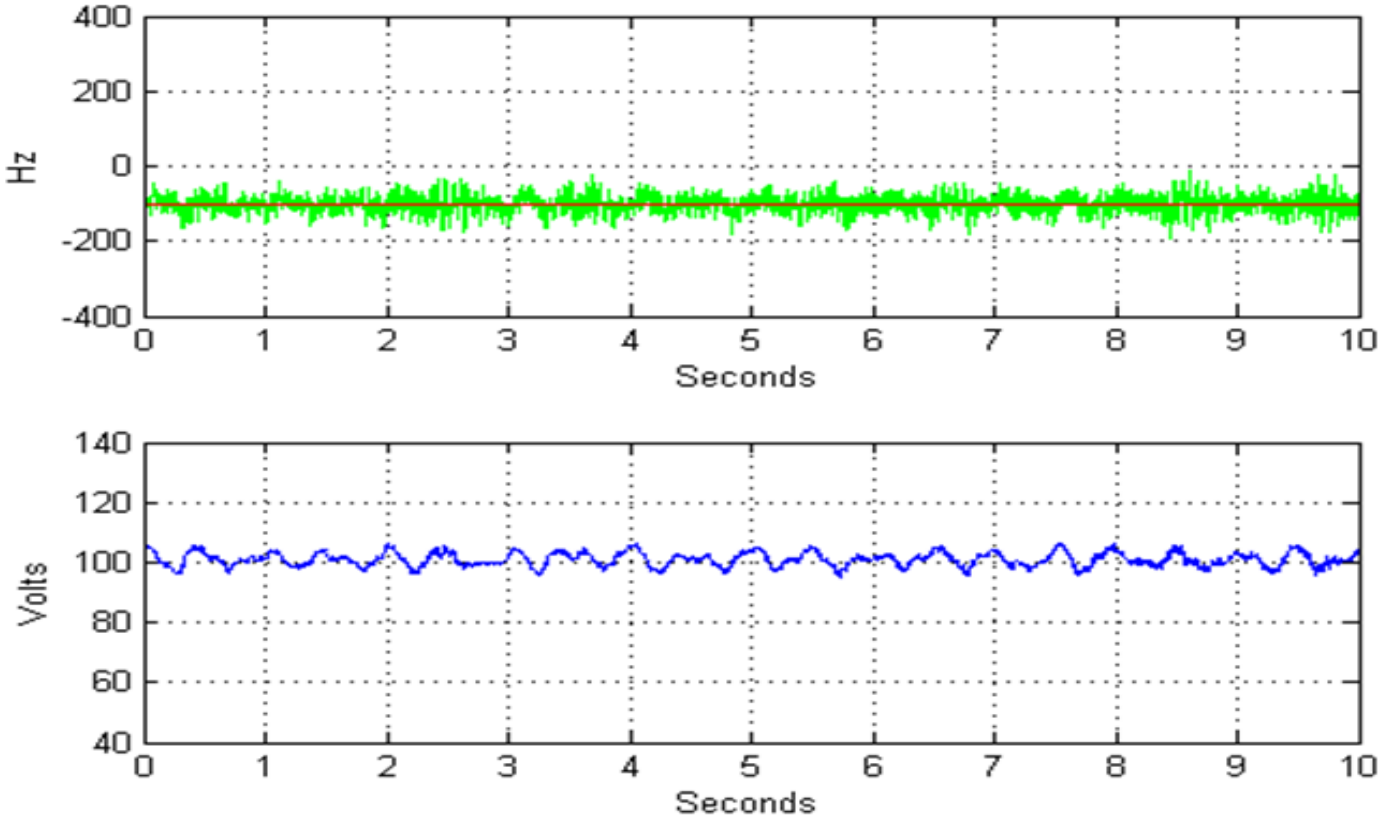

Figure 144. ADEX compensation of a perturbation of 2 Hz causing an RFD of 50Hz – Experiment 3

- *Experiment 4*

Figure 145 shows the PID system compensation for a sinusoidal perturbation of 4 Hz frequency acting on piezo 2 and causining a 50Hz RFD. The standard deviation of the RFD in this case was 52.34 Hz.

Figure 146 shows the ADEX system compensation for a sinusoidal perturbation of 5 Hz frequency acting on the second piezo and causing a 50 Hz resonance frequency detuning. The standard deviation of the resonance frequency detuning is in this case 28.60 Hz.

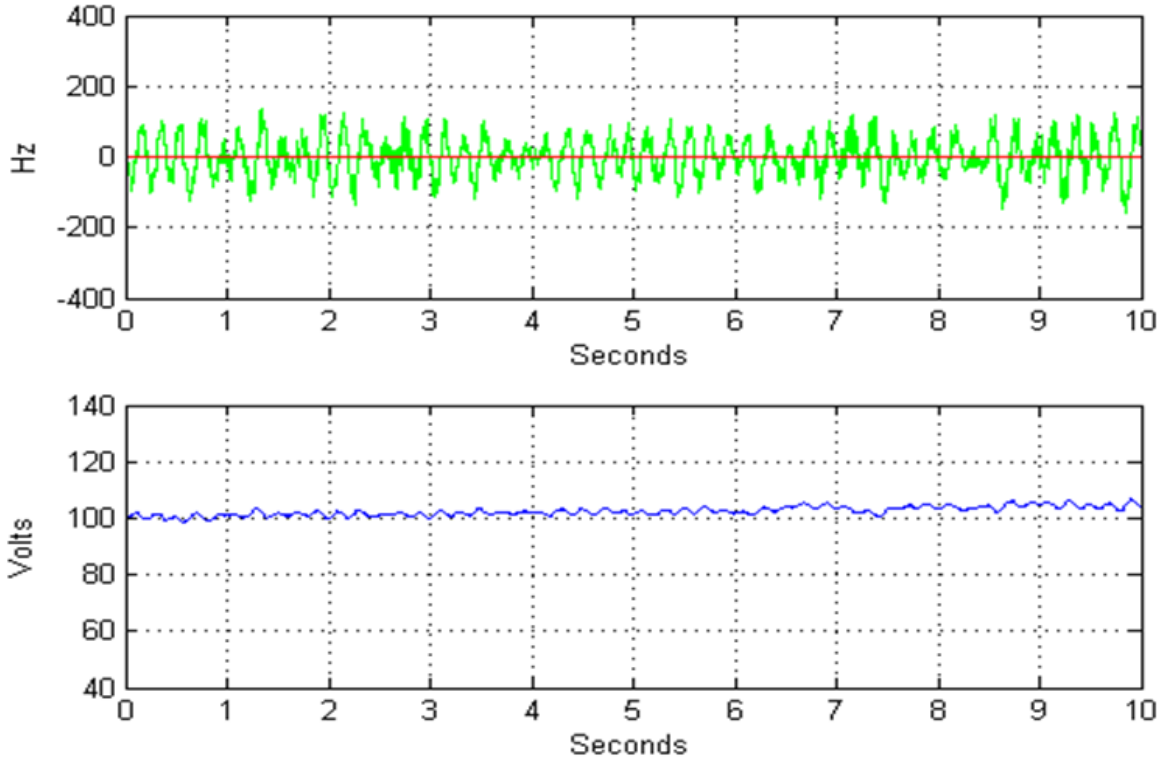

Figure 145. PID compensation of a perturbation of 4 Hz causing an RFD of 50Hz – Experiment 4

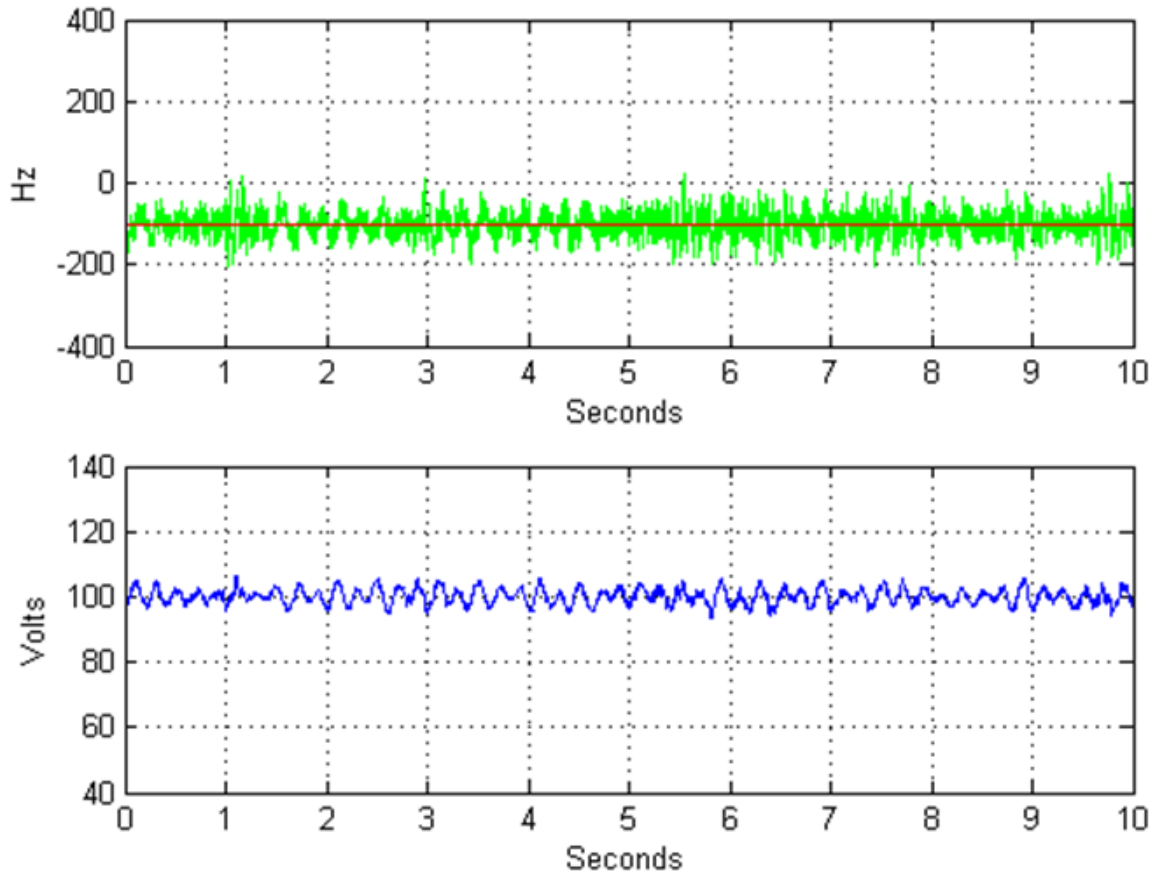

Figure 146. ADEX compensation of a perturbation of 5 Hz causing an RFD of 50Hz – Experiment 4

- *Experiment 5*

Figure 147 shows the PID system compensation for a sinusoidal perturbation of 8 Hz frequency acting on piezo 2 and causing a 50Hz RFD. The standard deviation of the RFD in this case was 67.80 Hz.

On the other hand, Figure 148 shows the ADEX system compensation for a sinusoidal perturbation of 8 Hz frequency acting on piezo 2 and causeing a 50Hz RFD. The standard deviation of the RFD in this case was 47.91 Hz.

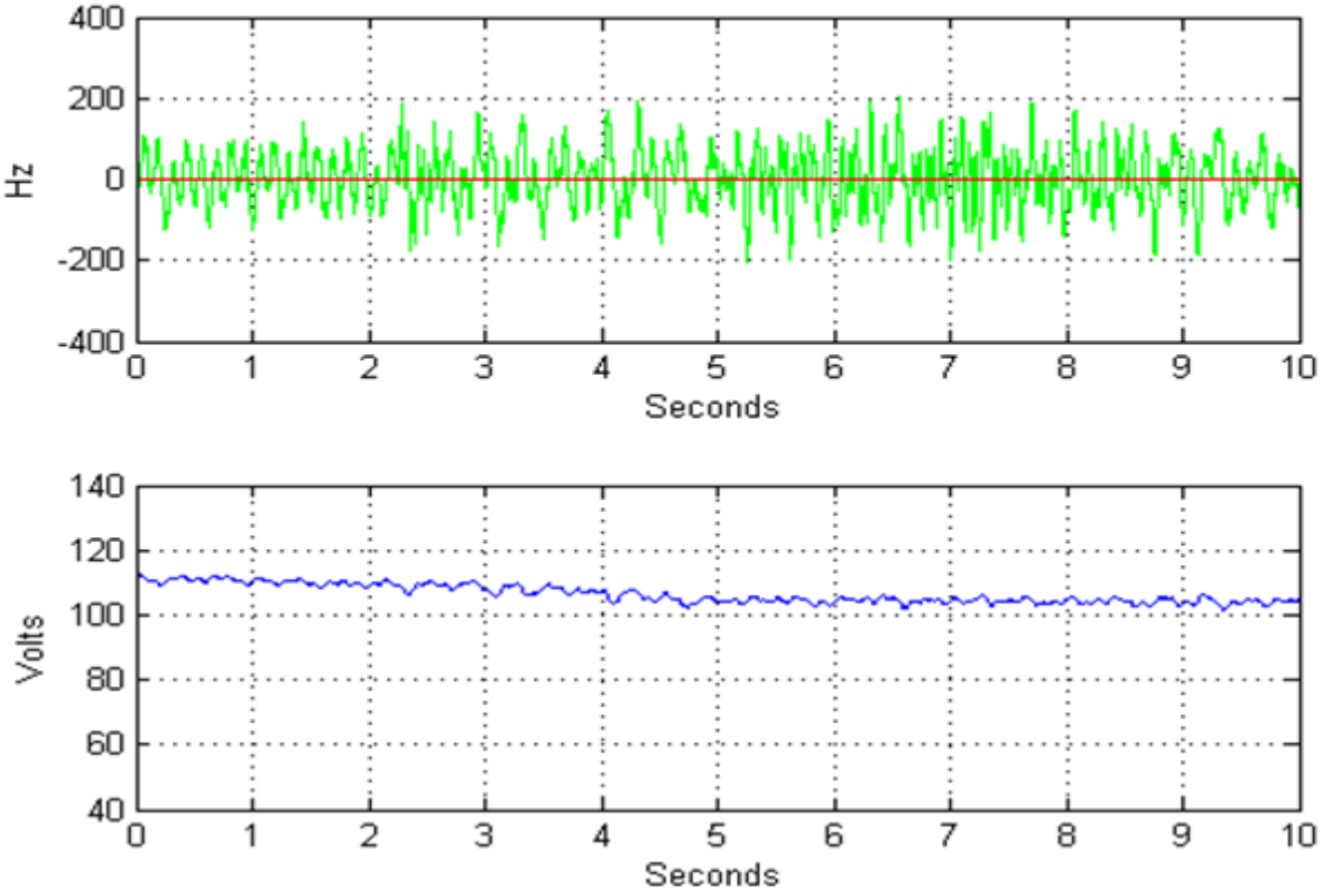

Figure 147. PID compensation of a perturbation of 8 Hz causing an RFD of 50Hz – Experiment 5

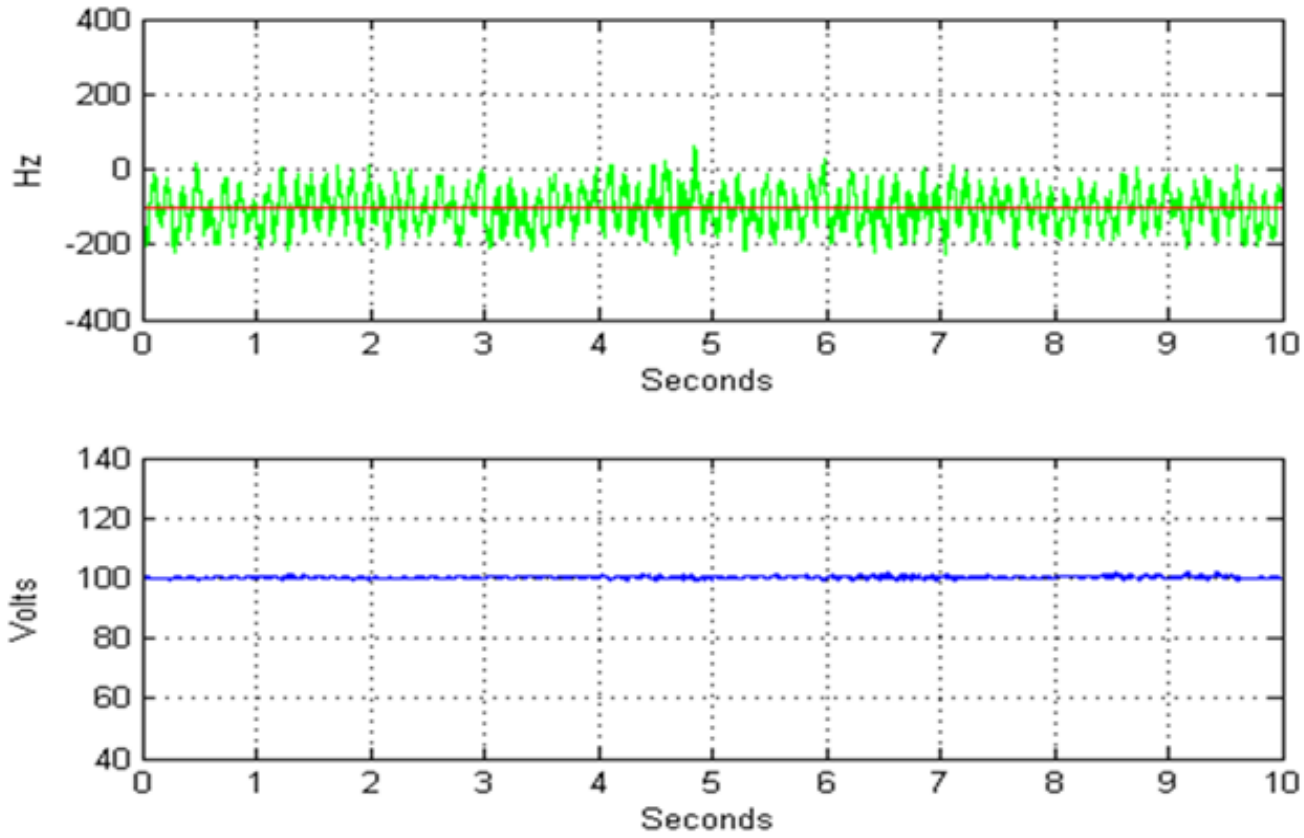

Figure 148. ADEX compensation of a perturbation of 8 Hz causing an RFD of 50Hz – Experiment 5

Conclusions to the tests performed with the elliptical cavity and the PLL:

Both PID and ADEX control have demonstrated their capacity for maintaining the RFD around its set point and compensating efficiently for significant drifts on it, such as a 700 Hz drift shown in Figures 134 and 135. Table 12 presents the RFD standard deviation obtained in the different experiments performed with the setup of Figure 107, under the operation of conventional PID control and ADEX control. The last column of this table presents the percentage of reduction obtained with ADEX control in relation with PID control. The analysis of the results, presented in this table, shows that ADEX enhances stability in normal operating conditions and also under the effect of unforeseen perturbations.

Experiment Nº	PID Control Standard Deviation	ADEX Control Standard Deviation	Standard Deviation Reduction
Experiment 1	34.71	16.09	53,65%
Experiment 2	*	*	*
Experiment 3	60.80	21.18	65,16%
Experiment 4	52.34	28.60	45,35%
Experiment 5	67.80	47.91	29,33%

(*Experiment 2 was useful to analize drifts compensation but its standard deviation depends on experiment time and can, therefore, be an ambiguous result)

Table 12. Evaluation of PID and ADEX performance

These experiments have proven the validity of both alternatives, the PID and the ADEX systems, for the FTS. The results obtained provide, as desired, for an evaluation of the control system performance independent of the interaction with DLLRF control system and the bandwidth of the resonance frequency of the cavity. Particularly, as it can be observed in Table 12, the best standard deviation obtained for the resonance frequency detuning, under PLL operation, was of 16.09 Hz. This means that maximum deviations of the resonance frequency detuning will reach at least in the best conditions of operation the value of 48.27 Hz, that is to say, approximately twice the bandwidth of the cavity´s resonance frequency.

Nonetheless, it must be taken into account that the time for experimentation has been short and, from the experience gained, it must be concluded that there is a lot of room for improvement in relation with the control strategy and the configuration of the controllers themselves.

Experimental Results under DLLRF Operation

- *Preliminary control trials:*

In Section 10.4 of this chapter it was commented that when operating with the DLLRF, the non-linear relationship between the CPS and the cavity's resonance frequency w_{RF} was described by Figure 130. In that figure it could be observed that the linear relationship

between the CPS and the resonance frequency was limited to a small region approximately equal to the cavity bandwidth. Outside of that region the CPS saturates and, therefore, is useless for representing the resonance frequency.

As already commented, in this context, the best control system performance would easily saturate the CPS under control. The kind of results obtained are illustrated in Figs. 149 and 150, where the upper graph shows in the green line the evolution of the CPS and in the red line the evolution of its setpoint while the lower graph shows the evolution of the control action applied to the piezo by the ADEX system.

It can be observed that the ADEX system alternates periods of good performance, around the linear band (Figure 149), with periods of operation away from the linear band, where the phase measurement saturates (Figure 150), depending on the influence of microphonics. The strong influence of microphonics was also present under conventional PID control.

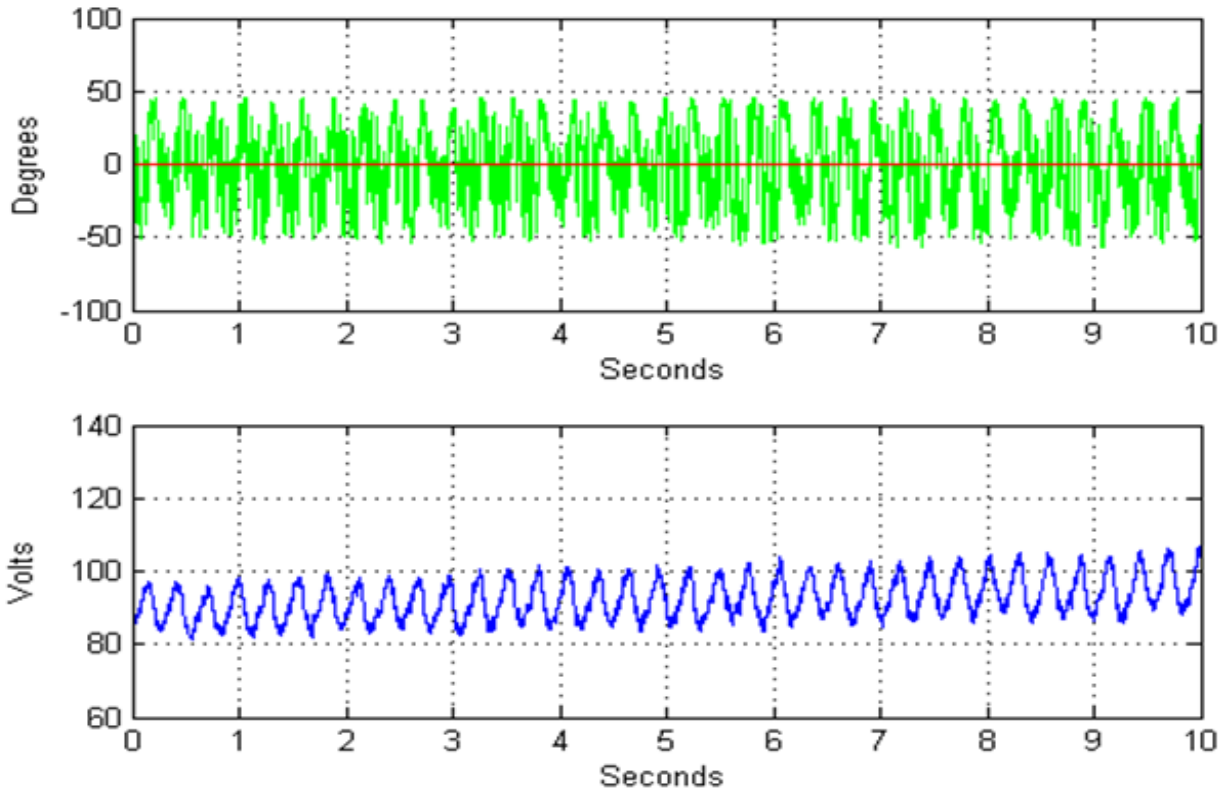

Figure 149. ADEX CPS control

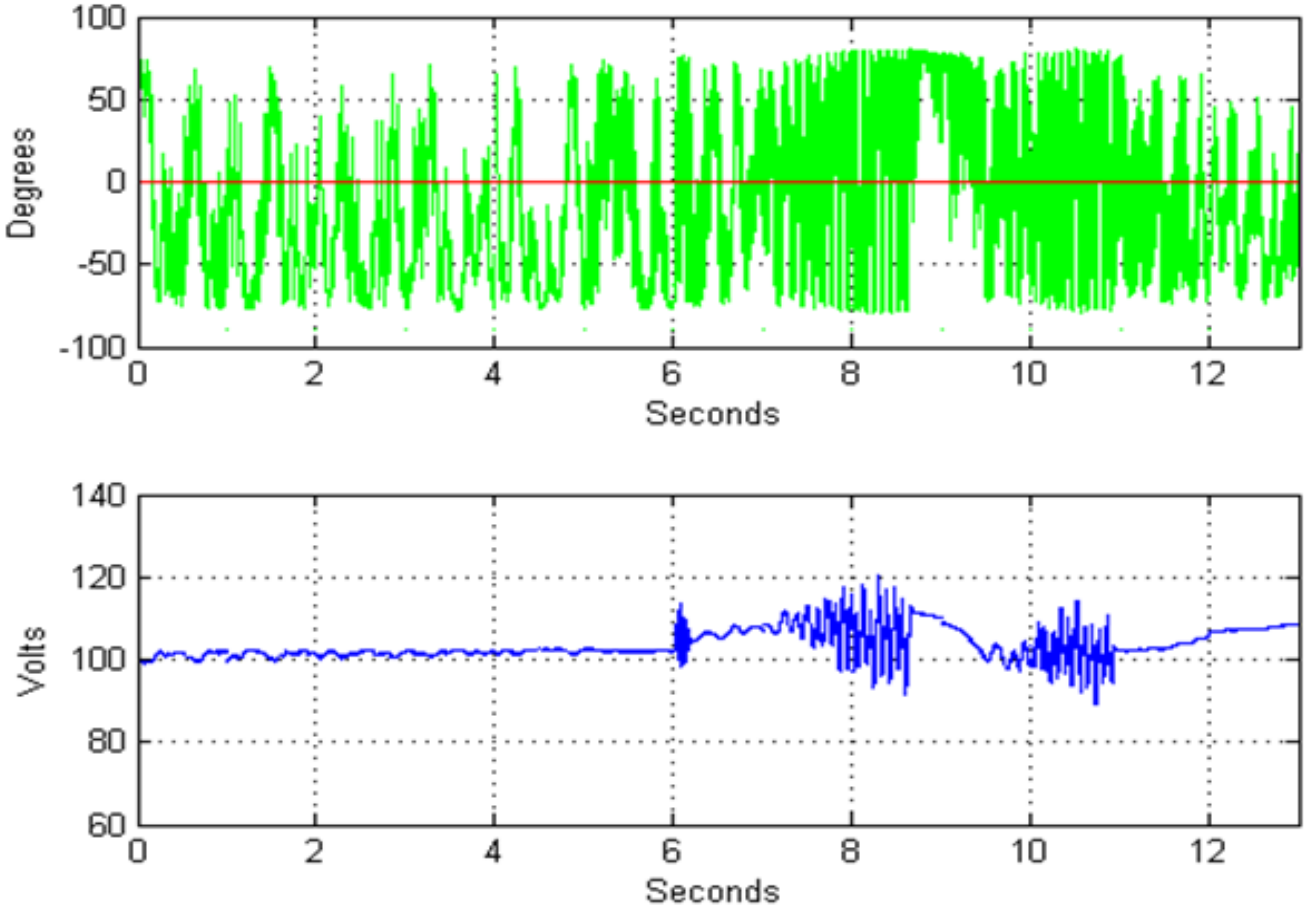

Figure 150. ADEX CPS control with saturations

- *Experimental results in the presence of a power increment*

Figure 151 shows, under ADEX control, how the effect of increasing the power in the DLLRF, producing a 200,000V/m field increment inside the cavity, affects the performance of the FTS. The power increase is produced at sec. 10 of the graph, where the width of the CPS oscillation is augmented. This change in the FTS control performance is most probably due to the excitation of the resonant modes caused by the Lorentz forces generated by the power increase. Figure 152 shows that briefly after the power increase the CPS remains under control around its set point.

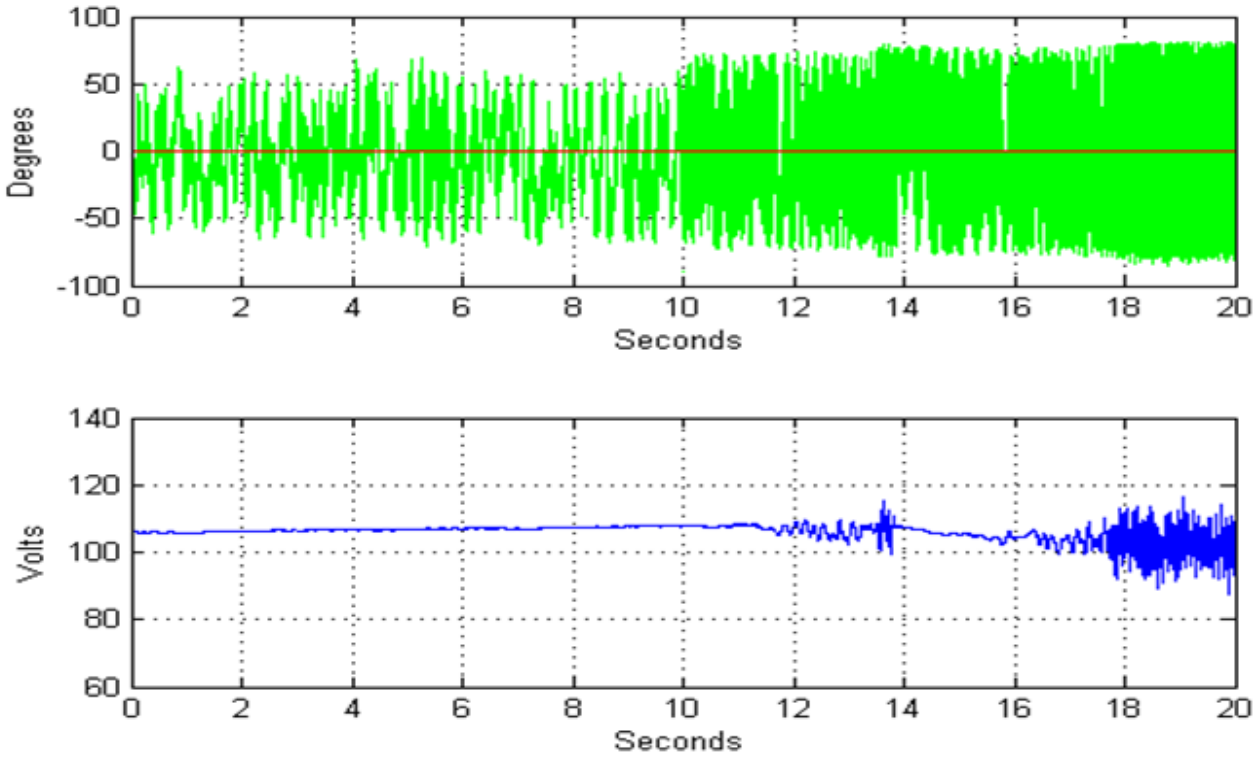

Figure 151. ADEX CPS control in the presence of a Power increment

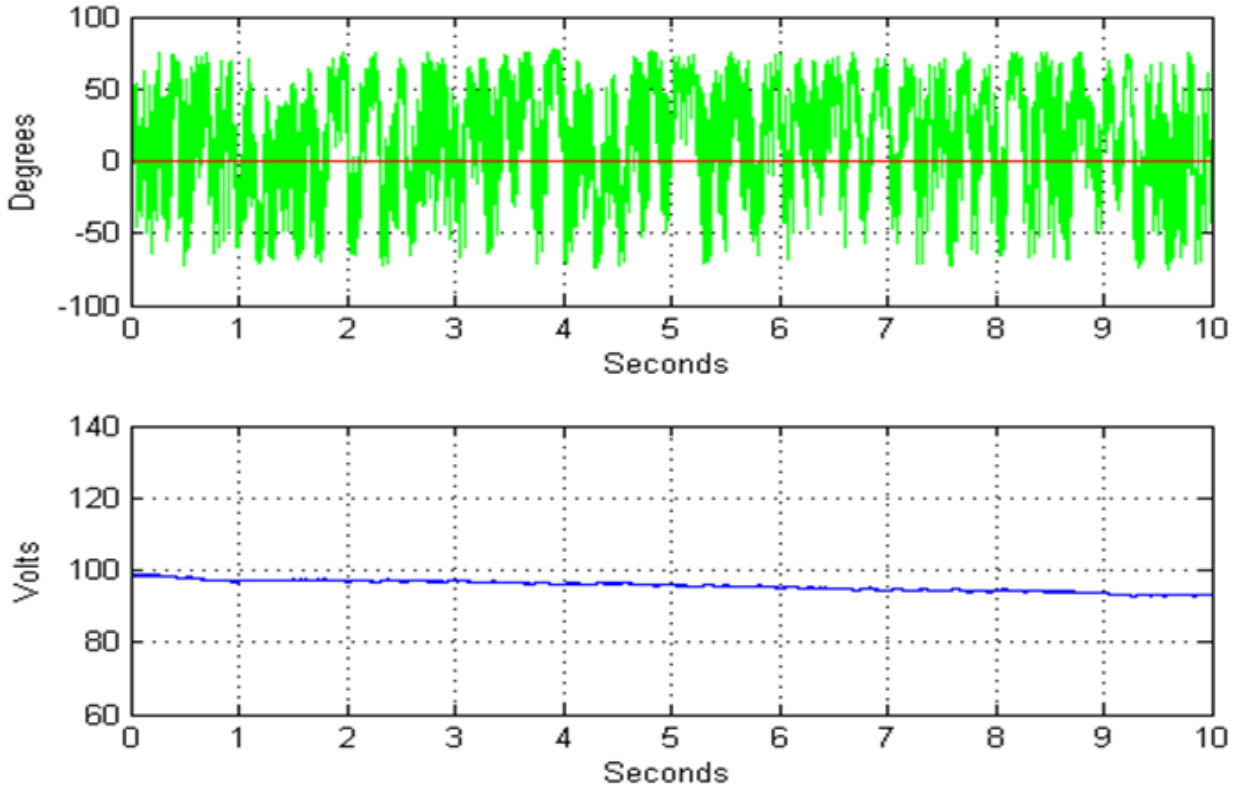

Figure 152. ADEX CPS control after Power increment

- *Control results under the influence of non-high-frequency perturbations*

Once the control systems were tested under the influence of microphonics, it was considered appropriate to get an insight on the long term operation of PID and ADEX systems under the influence of other non-high-frequency process perturbations, such as pressure Helium variations, which can affect control system stability. However, taking into account that the sampling time is 200 μs, the amount of data would be too big to register the phase in long term operation (i.e. 5 minutes). For this reason a sliding five seconds average of the CPS computed every second, that allows evaluating the control performance in long periods, was programmed. In the following this average of the CPS is used to evaluate the performance of PID and ADEX control systems.

- *Conventional PID control*

Figures 153 and 154 show the sliding average of the movement of the piezo and the sliding average of the CPS during approximately 5 minutes of the FTS operation using the PID system. These figures show how the voltage applied to the piezo under PID control maintains the CPS average around its set point. The standard deviation for the CPS average shown in the figure is 17.52 Hz.

Figures 155 and 156 show how PID control reacts to an increase of 2 bars in Helium pressure at 12:41:07 in the time scale, and afterwards how it goes back to its nominal operating point at 12:43:45. This kind of pressure increase and decrease were caused in the pressure loop but they could have as well occurred naturally during the real accelerator´s operation. It can be noticed in Figure 155 that during the Helium pressure changes the CPS control is totally lost.

- *ADEX control*

Figures 157 and 158 show the sliding average of the CPS and the sliding average of the voltage applied to the piezo during approximately 5 minutes of the ADEX system's operation.

Figures 159 and 160 show how the voltage applied to the piezo by the ADEX system maintains the CPS sliding average precisely controlled around its set point. The standard deviation for the CPS average shown in the figure is 10.06 Hz.

Figs. 159 and 160 show how the ADEX system responds to the same perturbations in the Helium pressure that were previously considered under PID control. It can be noticed that the ADEX control action is sharper than that produced by the PID systems and compensates the effect of the Helium pressure variations without losing the CPS control.

Conclusions to the tests performed with the elliptical cavity and the DLLRF:

During the experimentation with the DLLRF in operation, the difficulty for the FTS to maintain the cavity´s phase shift (CPS) within the bandwidth of the cavity has been confirmed, as previously anticipated in Section 4 of this chapter. Neither PID nor ADEX control were capable of maintaining in a permanent manner the CPS out of saturation due to the cavity's narrow bandwidth and the high sensibility of this cavity to microphonics. This is clearly explained by the fact that, during the experimentation with the PLL operation, microphonics causing RFD deviations of 160 Hz, which were 8 times higher than the cavity's bandwidth (≈20 Hz), could be observed.

However, the control performance of the FTS has been reasonable under the circumstances, since the experiments intended to evaluate its performance compensating for microphonics have proven, under PID and ADEX control, the capability of the system to maintain the mean of the CPS under control and centered on the set point. The same result was obtained under ADEX control when the FT loop operation was submitted to the effect of power variations introduced by the DLLRF control system.

In addition, the evaluation of the performance of the FTS in a long term scenario in the presence of microphonics and Helium pressure variations demonstrated the consistency of both control systems on a sliding average of the CPS. The enhancement of stability by the ADEX control system over the PID control system was again confirmed. In the microphonics experiments the standard deviation of the CPS average was reduced from 17.52 to 10.06 Hz (more than 42%). Likewise, the effect of Helium pressure variations under PID control made the CTS lose control of the CPS, which did not happen under ADEX control.

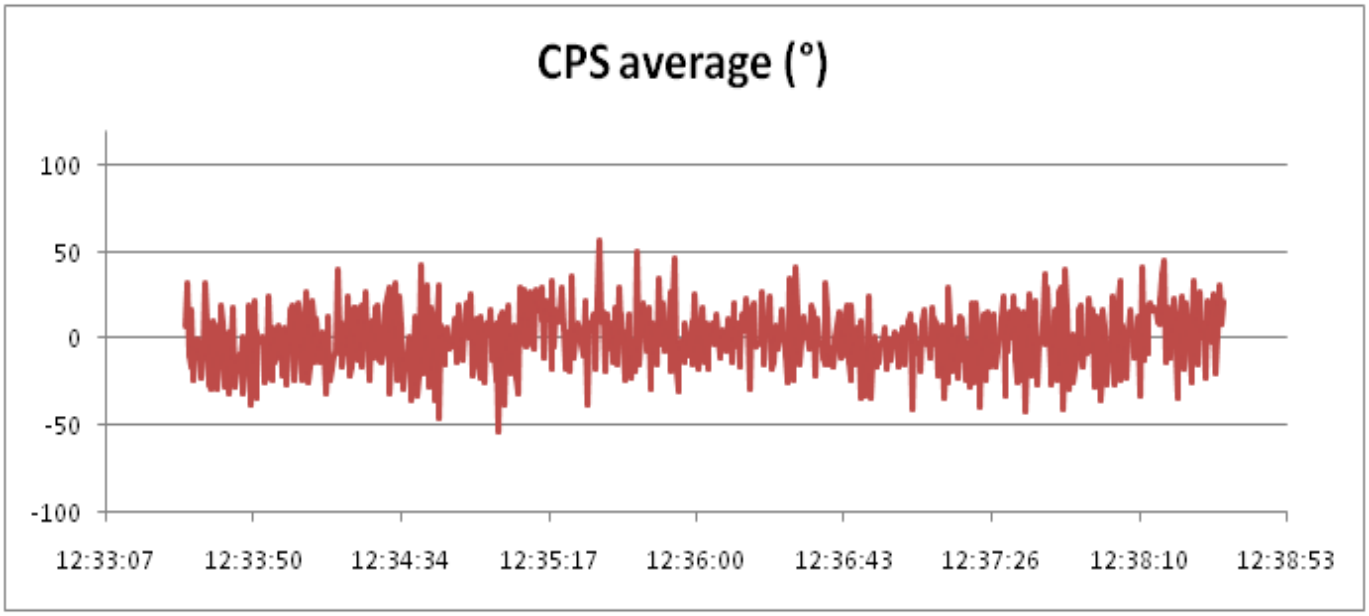

Figure 153. CPS average under PID Control

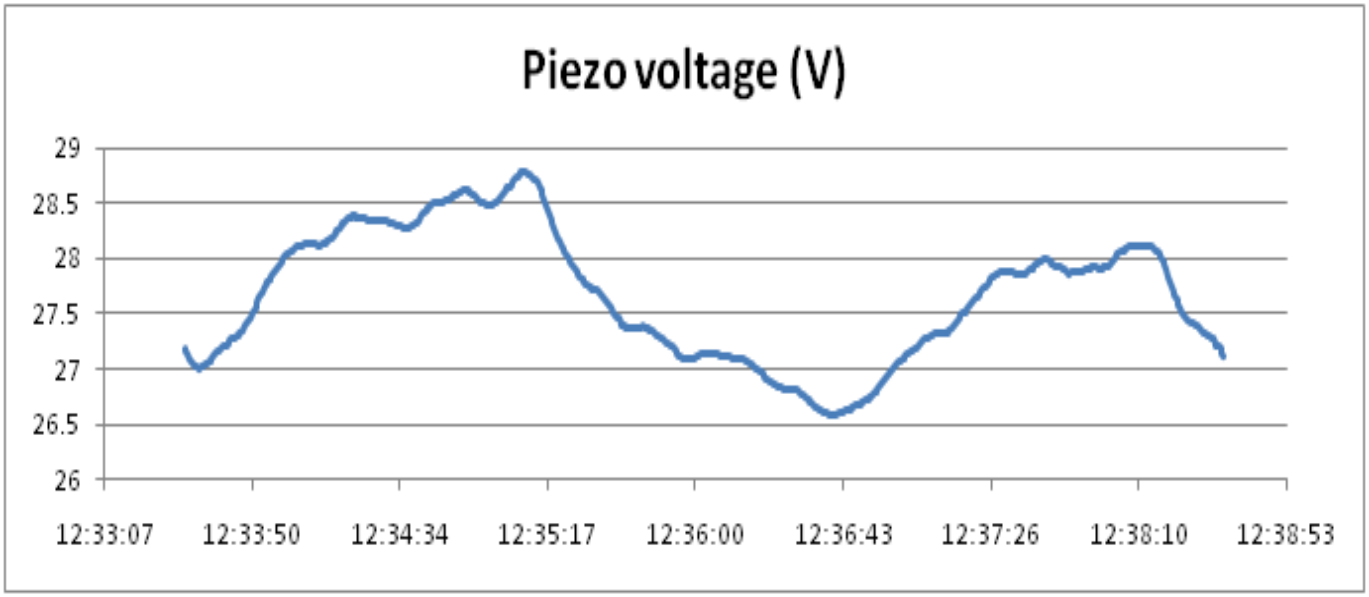

Figure 154. Piezo Movement under PID Control

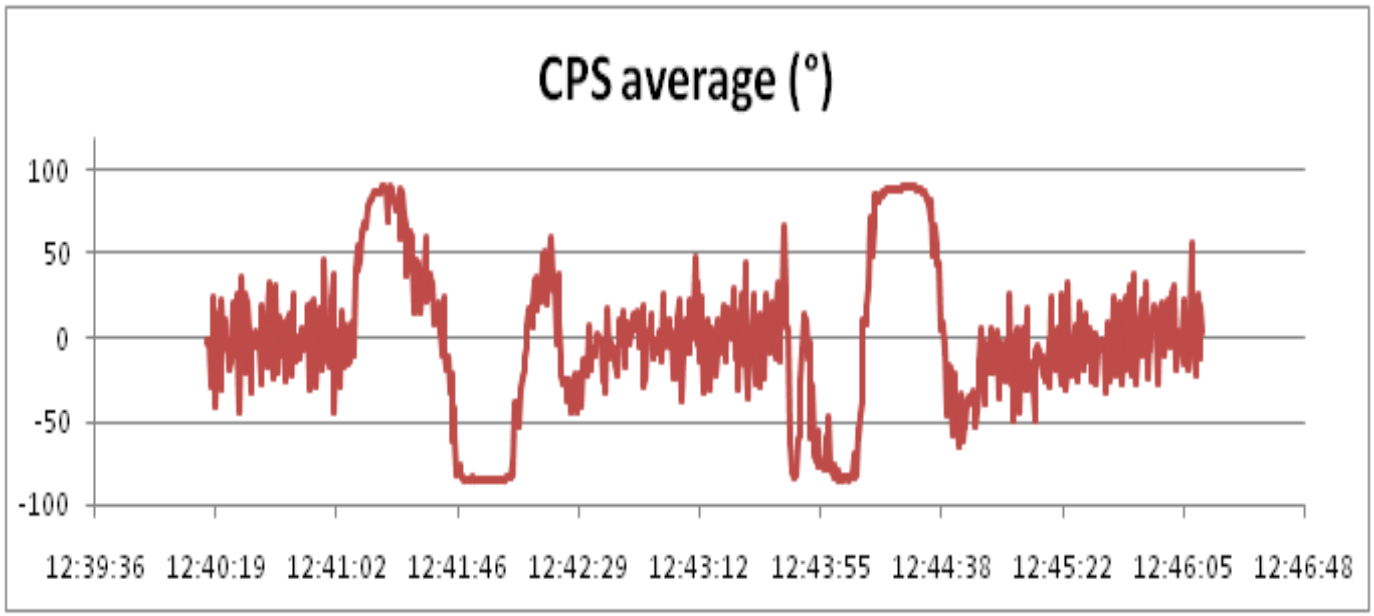

Figure 155. CPS average under PID control in the presence of Helium pressure variations

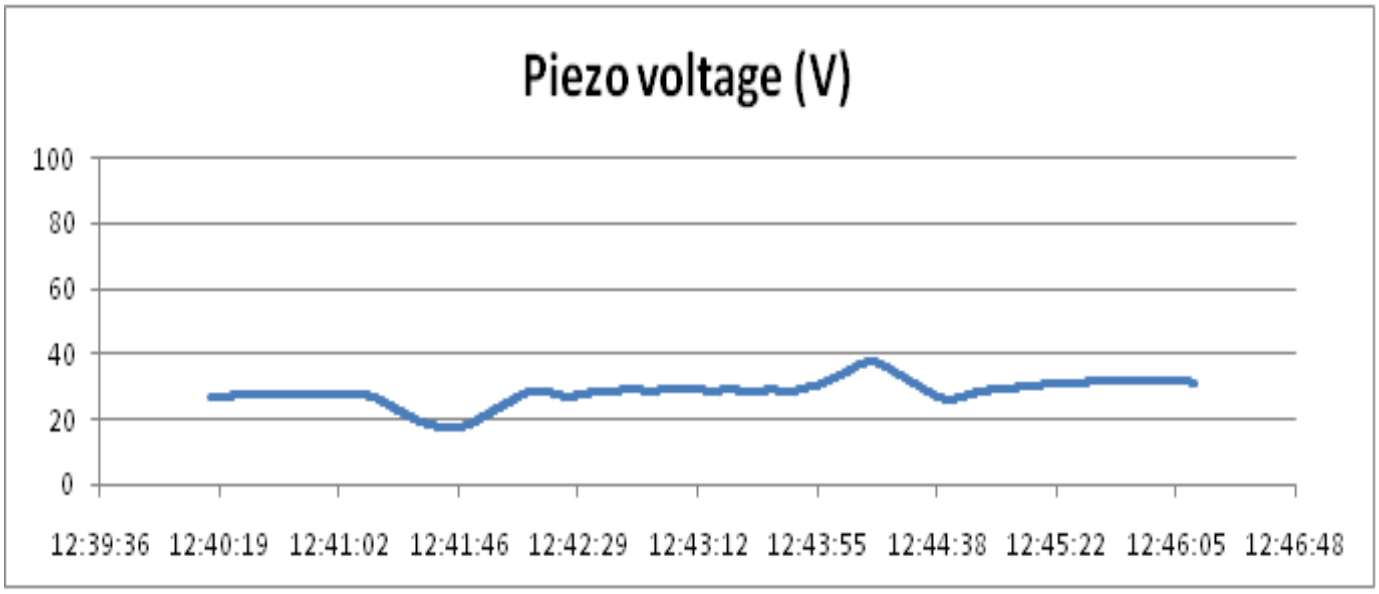

Figure 156. Piezo movement average under PID control in the presence of Helium pressure variations

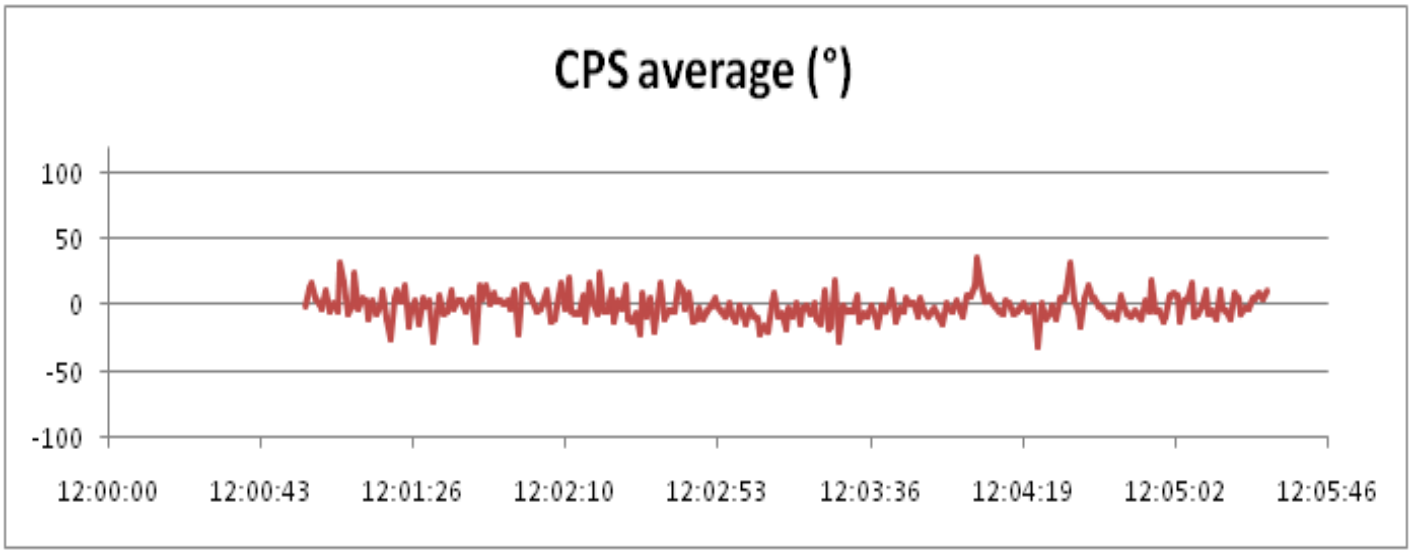

Figure 157. CPS average under ADEX Control

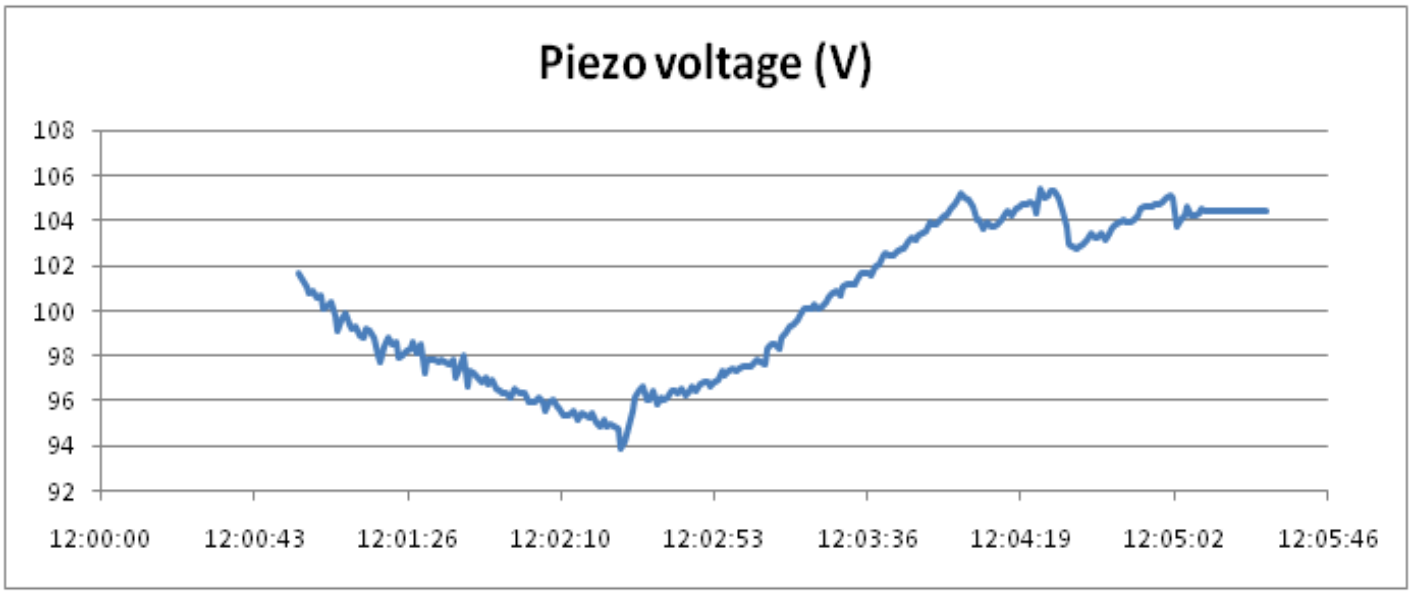

Figure 158. Piezo movement average under ADEX Control

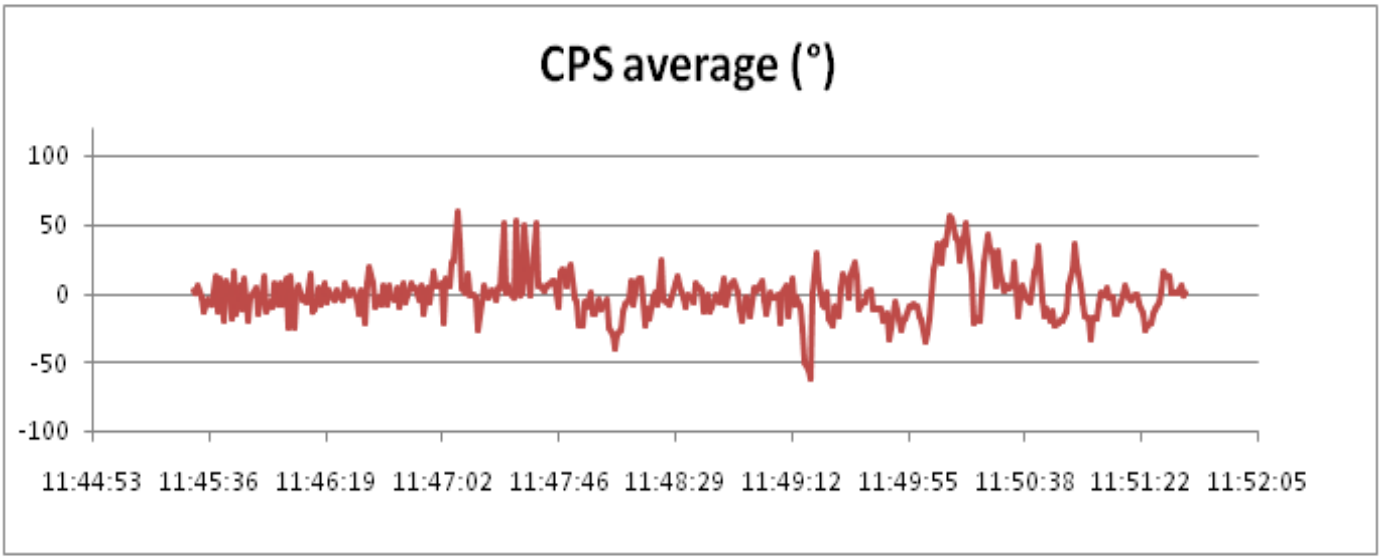

Figure 159. CPS average under ADEX control in the presence of Helium pressure variations

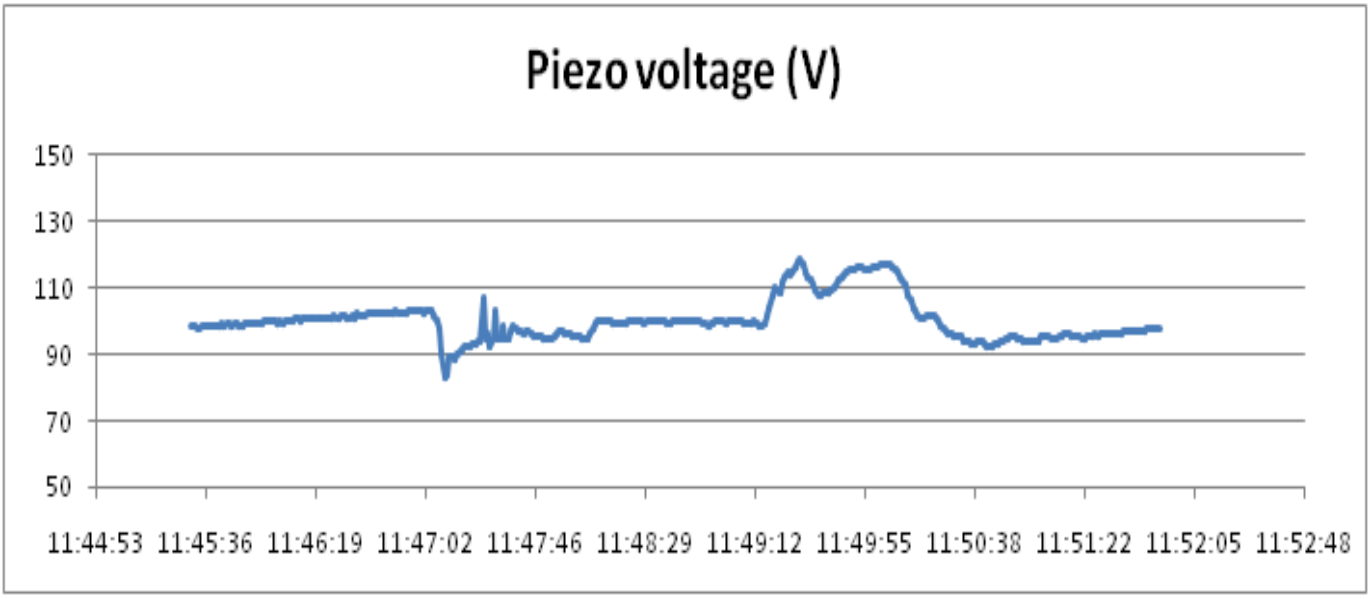

Figure 160. Piezo movement average under ADEX control in the presence of Helium pressure variations

10.6 CONCLUSIONS OF THE EXPERIMENTAL CAMPAIGN

The test campaign was planned to apply the alternative PID and ADEX control systems proposed for the FTS to the elliptical cavity at 2 K. It was first applied in a setup that did not considered the operation of the DLLRF control system, but the operation of the Phase Locked Loop (PLL) device. This device provides a reliable measurement signal of the cavity´s resonance frequency in a wide range of operation that can be used for an evaluation of the FTS performance independently of the DLLRF control system operation.

Under this setup, both PID and ADEX control demonstrated their capacity for maintaining the resonance frequency detuning around its set point and compensating efficiently for significant drifts on it. Notch filters worked as expected, but Chebyshev filters were not applied due to the variations found experimentally in the frequency of the microphonics. The results showed that ADEX enhances stability in normal operating conditions and also under the effect of unforeseen perturbations. However, the best standard deviation obtained for the resonance frequency detuning, under PLL operation, was of 16.09 Hz. This means that deviations of the frequency detuning will reach at least in the best conditions of operation the value of 48.27 Hz, that is to say, approximately bandwidth of the cavity´s resonance frequency (≈20 Hz).

During the experimentation with the DLLRF in operation, the difficulty of the FTS to maintain the cavity´s phase shift (CPS) within the bandwidth of the cavity was confirmed. Neither PID nor ADEX control were capable of maintaining in a permanent manner the CPS out of saturation due to the cavity's narrow bandwidth and the high sensibility of this cavity to microphonics.

However, the control performance of the FTS has been reasonable under the circumstances, since the experiments intended to evaluate its performance compensating for microphonics have proven, under PID and ADEX control, the capability of the system to maintain the mean of the CPS under control and centered on the set point. The same result was obtained under ADEX control when the FTS operation was submitted to the effect of power variations introduced by the DLLRF control system.

In addition, the evaluation of the performance of the FTS in a long term scenario in the presence of microphonics and Helium pressure variations demonstrated the consistency of both control systems on a sliding average of the CPS. The enhancement of stability by the ADEX control system over the PID control system was again confirmed. In the microphonics experiments the standard deviation of the CPS average was reduced from 17.52 to 10.06 Hz. However, the effect of Helium pressure variations under PID control made the CTS lose control of the CPS, which did not happen under ADEX control. This result confirmed again in the cryogenic setup for the operation of the CTS the higher reliability of the ADEX control system.

The concluding remarks of the experimental campaign are the following:

1. The evaluation of the performance of the CTS control system, both under PID and ADEX control was satisfactory in simulation and in the real application with PLL operation.

2. The evaluation of both alternatives for the FTS, working together with the DLLRF control system, was reasonable under the circumstances, given the cavity´s narrow bandwidth and high sensitivity to microphonics.

3. ADEX system enhanced the stability and control precision of the Frequency Tuning and demonstrated to be a reliable control system under unforeseen perturbations that made the PID control system to lose control of the cavity´s variables.

4. Although the tests campaign was short, the knowledge acquired during the development of this task and the results obtained, confirm that there is a lot of room for improvement, in the design of the cavity and the FTS control system. In this sense Chebyshev filters, that have been worthless for the elliptical cavity control should be substituted by alternative adaptive techniques capable of tracking time-varying microphonic perturbations.

CONCLUSIONS AND RESEARCH PERSPECTIVES

This thesis is the culmination of a PhD program in industrial technologies and within this wide thematic area it presents a study that has merged two forefront research disciplines: particle acceleration and advanced control methodologies. Among the original contributions presented, the introduction and adaptation of the innovative Adaptive Predictive Expert (ADEX) Control methodology to the particle acceleration field and, namely, to the Resonance Frequency Detuning (RFD) of accelerating cavities, must be highlighted. Similarly, this thesis has presented the first application of FIR filters (notch and lowpass) between the control actions and the instrumentation, in this case the Cold Tuning System (CTS), to avoid pernicious excitation of resonant modes. It must be noted that this technique has been proven successful and has a generic nature valid for processes presenting undesirable resonance mode excitation. Finally, this thesis has evaluated the use of Chebyshev filters for microphonic compensation, but this technique did not seem valid to cancel or attenuate the variable microphonics found during the test campaign.

During the first part of this PhD endeavor, the CNRS´s model of the 704.4 MHz elliptical cavity has been used to estimate the execution times required for the ADEX controller and

develop an optimized control strategy for the software and hardware + software implementation of an Optimized Adaptive Control System (OACS).

As already commented, notch filters were introduced in the definition of the optimized control strategy that, in addition to ADEX controllers, also integrated Chebyshev filters and the anticipation of the effects of Lorentz forces when power variations occur in the cavity field. In this way, the optimized control strategy gathered the tools to attenuate the excitation of cavity´s resonance modes by the ADEX controller's actions, minimize the known microphonics induced by external perturbations and compensate in advance for Lorentz forces.

The experimental results in simulation proved the efficiency of the Low Level Radio Frequency (LLRF) control loop, under PID control, and the FTS control loop, under PID and ADEX control, working together but independently in a standard simulated scenario. The comparative analysis of the results obtained in simulation yields that a significant reduction in the resonant frequency detuning (RFD) oscillations around its set point has been achieved by the OACS, while the power consumption is maintained nearly at its minimum throughout all the experiment. Additionally, an unforeseen external perturbation of 20 Hz frequency, that caused oscillations of 50Hz in the RFD, was applied to the simulated scenario. This unforeseen perturbation caused the loss of control of the cavity under PID control, while under ADEX control a much more aggressive control action maintained the resonance frequency within its operational limits and the field inside the cavity controlled by the LLRF system.

These results can be explained by the fact that unforeseen perturbations, not only deviate the variables under control, but also change the processes dynamics, which makes fix-parameters controllers, such as the PID, detune their control actions. ADEX controllers adjust themselves to changes in the process dynamics and, therefore, can deal with uncertainty scenarios and unforeseen perturbations, increasing in this way significantly the reliability of the control system.

Prior to the cold tests, room temperature trials where performed in a spoke cavity to validate the hardware + software operation of both the PID based and the OACS Frequency Tuning Systems (FTS). After this validation, cold tests where planned to apply both FTSs to the prototype of the elliptical cavity at 2K. Two setups where used, the first one did not considered the operation of the LLRF system, using instead a Phase Locked Loop (PLL) device. This device

provides a reliable measurement signal of the cavity´s resonance frequency in a wide range of operation that can be used for an evaluation of the FTSs performance independently of the LLRF control system operation. Under this setup, both PID and ADEX control demonstrated their capacity for maintaining the RFD around its set point and compensating efficiently for significant drifts on it. Notch filters worked as expected, but Chebyshev filters were not applied due to the variations found experimentally in the frequency of the microphonics. The results showed that ADEX enhances stability in normal operating conditions and also under the effect of unforeseen perturbations. However, the best standard deviation obtained for the RFD, under PLL operation, was of 16.09 Hz. This means that deviations of the RFD will reach at least in the best conditions of operation the value of 48.27 Hz, that is to say, more than twice the bandwidth of the cavity´s resonance frequency (20 Hz).

During the experimentation with the LLRF in operation, the difficulty for the FTSs of maintaining the cavity´s phase shift (CPS) within the bandwidth of the cavity was confirmed. Neither PID nor ADEX control were capable of maintaining in a permanent manner the CPS out of saturation due to the cavity's narrow bandwidth and the high sensibility of this cavity to microphonics. Thus, the elliptical cavity could be modified/stiffened for future advances in the MYRRHA development.

However, the control performance of the FTS has been reasonable under the circumstances, since the experiments intended to evaluate its performance compensating for microphonics have proven, under PID and ADEX control, the capability of the system to maintain the mean of the CPS under control and centered on the set point. The same result was obtained under ADEX control when the FT loop operation was submitted to the effect of power variations introduced by the LLRF control system.

In addition, the evaluation of the performance of the FTSs in a long term scenario in the presence of microphonics and Helium pressure variations demonstrated the consistency of both control systems on a sliding average of the CPS. The enhancement of stability by the ADEX control system over the PID control system was again confirmed. In the microphonics experiments the standard deviation of the CPS average was reduced from 17.52 to 10.06 Hz. However, the effect of Helium pressure variations under PID control made the CTS lose control of the CPS, which did not happen under ADEX control. This result confirmed again, in the real setup for the operation of the FTS, the higher reliability of the ADEX control system.

Thus, throughout the test campaign the goodness of the ADEX methodology and the FIR filters, namely notch and lowpass, to compensate for unforeseen perturbations and avoid the excitation of resonant modes respectively was validated. Regarding the unsuccessful implementation of Chebyshev filters for microphonics compensation it is clear that further research effort is necessary to define a new adaptive compensation mechanism to substitute these filters. This mechanism shall be capable of tracking the frequency and magnitude of time varying microphonics in order to compute the adequate control signal to cancel these perturbations when applied to the CTS.

Finally, it must be noted that this PhD thesis has introduced Adaptive Predictive Expert ADEX control methodology in the particle acceleration domain and its results have attracted the attention of researchers and institutes collaborating in the MYRRHA project and in the accelerator's community. There are numerous possible applications of this technology in the MYRRHA or in other accelerators (GENEPI2, LIPAc,…) which are currently being considered or carried out (see ANNEX C). These new applications of the ADEX technology will require of new studies, developments and designs of control strategies, some of which could be the subject of future PhDs.

ANNEX A:

THE ADEX CONTROL AND OPTIMIZATION PLATFORM

This annex presents the ADEX Control and Optimization Platform (ADEX COP) used to develop ADEX systems and its connection to processes which have local control and use OPC, DDE, MODBUS, CAN, DIM or other industrial protocols and buses. The software structure of ADEX systems is shown in Figure A1. The two principal elements shown are the SUPERVISOR and the PROCESSOR. The two programs run independently of each other but are connected via a TCP communication.

As can be appreciated in Figure A1, the PROCESSOR is the part which uses an I/O connection to communicate with the process under control, executes the control and optimization schemes (COS), and sends the control action to the process. The I/O communication can be made directly via I/O cards or other standards such as the ones already commented. The PROCESSOR maintains a database, on hard disk, of the ADEX controller configurations applicable to the COS, and optionally, the history of variables used by ADEX COP. The PROCESSOR uses a TCP server which is connected with one or more SUPERVISORS which can be executed in the same computer as the PROCESSOR or in remote computers in

the same network. The TCP server responds to read/write requests for PROCESSOR parameters from the SUPERVISOR, thereby enabling the monitoring and configuration of the former.

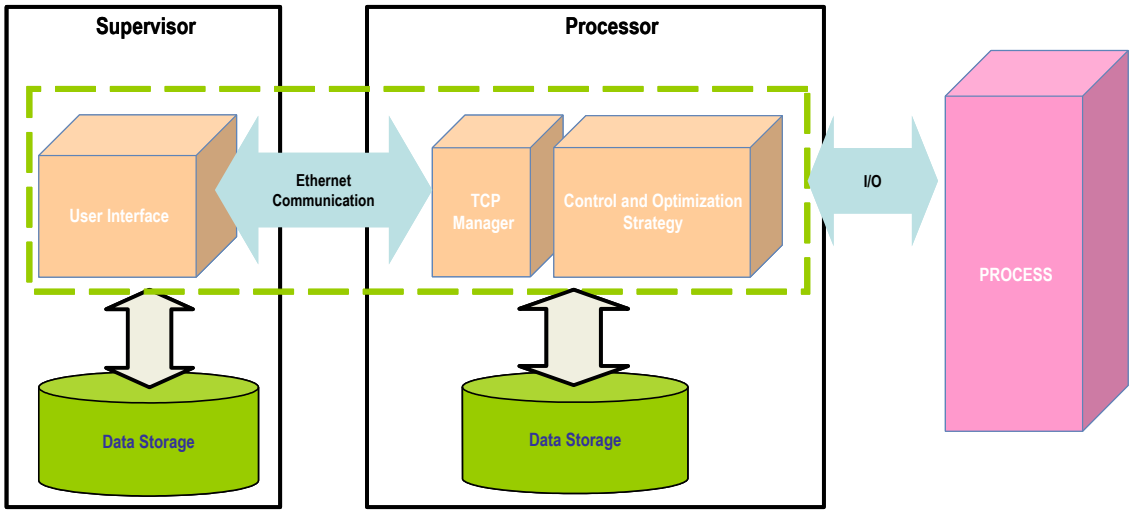

Figure A1. ADEX Systems structure

The SUPERVISOR provides a Graphical User Interface (GUI) for the control system. It is not needed for the functioning of the PROCESSOR and can remain on standby while it is not required. As can be seen in Figure A1, the SUPERVISOR has facilities for accessing and storing variables in the same way as the PROCESSOR. However, it should be noted that these variables can only be stored while the SUPERVISOR remains active.

Communication with the local control system

Figure A2 shows how an ADEX system can be connected to a process already controlled by a local control system which uses an OPC server. As can be seen, the ADEX system reads the variables required for optimization via the OPC server of the local control system. Based on this information, the ADEX system executes the COS which generates the optimized control actions, sends these to the local control system and applies them to the process via OPC.

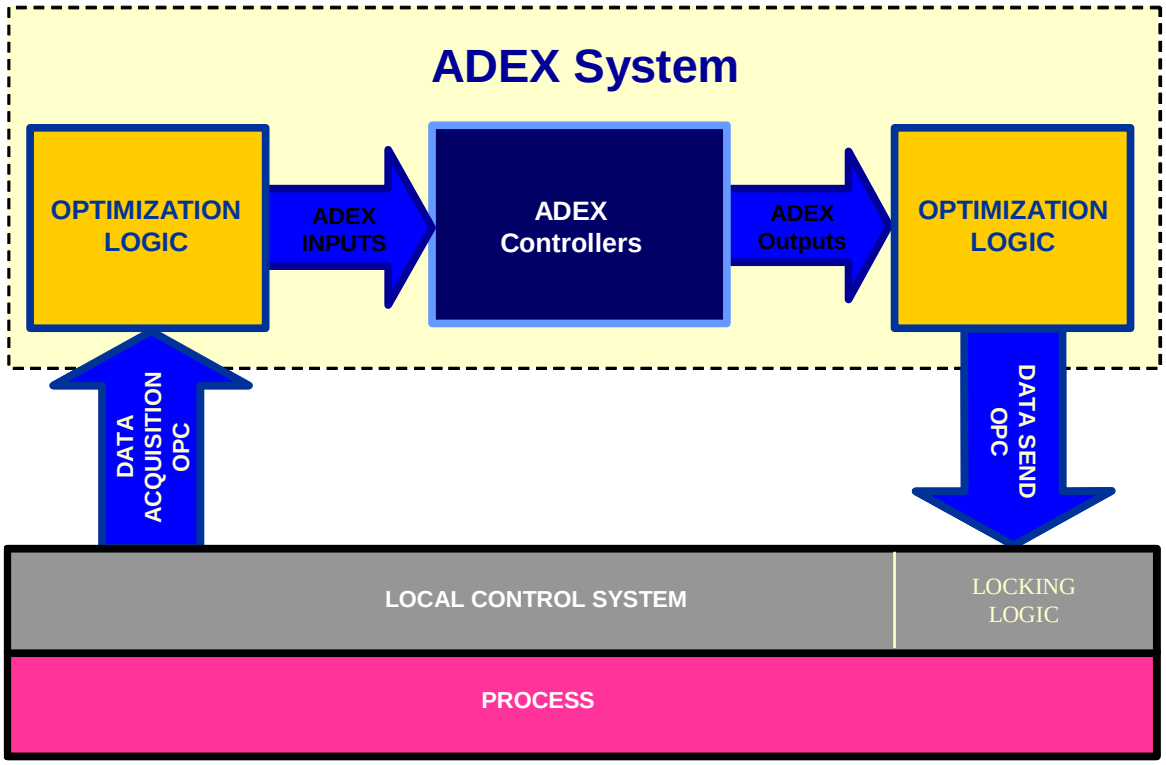

Figure A2. Communication with the local control system

In this way, modifications to the local control system are minimized and programming reduced to the following:

- A switch enabling the GUI of the local control system to choose whether to apply the local or ADEX generated control variable.
- A locking logic which monitors the switching of a variable defined in the OPC server which will be modified by ADEX at regular time intervals. In this way, the local control system will monitor the correct functioning of the OPC connection at all times and be able to revert to local control in the event of a communication failure. These variables are generated automatically by the ADEX COP 2.0 platform.

This form of integration requires very little engineering effort on the local system and enables the full control of the operator by offering the option of reverting to the previous functionality or switching to the new ADEX system at any time

ADEX COP 2.0

ADEX COP 2.0 is a software platform which enables the development, storage and execution of different ADEX systems. The executable code generated from each development can be duplicated for use in other identical applications within the Windows environment in accordance with the appropriate permissions or licensing agreements.

ADEX systems developed within ADEX COP 2.0 comprise the following three elements.

- PROCESSOR: Executable file containing all the software facilities required for process control and optimization. This includes data acquisition, the COS which contains the ADEX controllers and all the necessary system support intelligence.
- SUPERVISOR: This comprehends an executable file which implements the GUI thereby enabling the monitoring and real time update of the configuration and operation of the optimization system.
- SIMULATOR: ADEX COP 2.0 also provides facilities for developing a simulation model of each process to be optimized. This can be used to test and validate the COS developed for the PROCESSOR within the ADEX COP environment. During this validation phase, the PROCESSOR will connect with the simulation module instead of the plant.

Utilities of ADEX COP 2.0

Once the ADEX system has been developed, the resulting PROCESSOR is a stand-alone tool capable of controlling process variables on its own. The SUPERVISOR can be used to monitor and modify certain process variables as required and both programs can run on separate computers provided they are connected by a network.

At the start of a new ADEX system development using the Platform, the initial screen will appear as shown in Figure A3. At the bottom of the screen are three tab options which provide access to the three main utilities of ADEX COP; PROCESSOR, SUPERVISOR and SIMULATOR. These are described in the following sections.

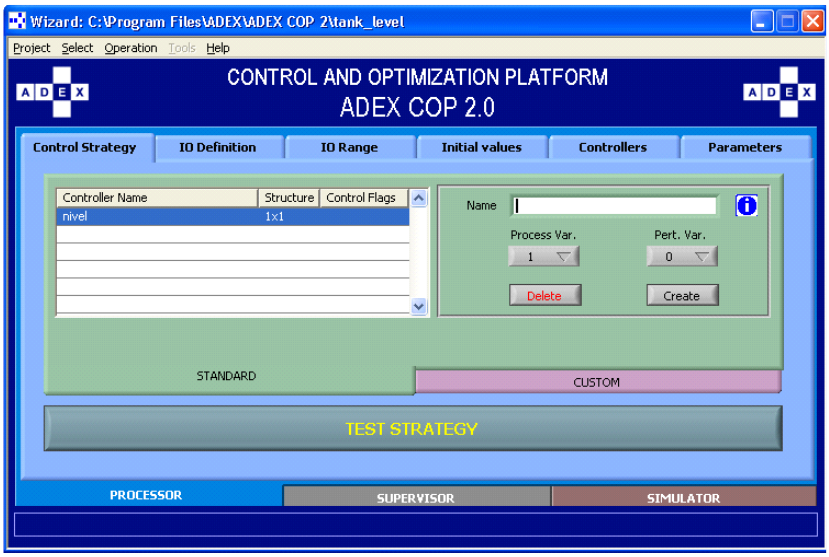

Figure A3. Utilities of ADEX COP 2.0

i) *Processor Utility*

This ADEX COP 2.0 utility guides the user, step at a time, through the development of the PROCESSOR part of the ADEX system. The designer can access these steps via the tab options which appear at the top of the screen as shown in Figure A3. These options are:

- Control Strategy definition
- IO definition. Assign the method of acquiring each external variable
- IO Range. Establish the value range of each external variable.
- Initial Values. Establish the initial values for each of the defined variables in the Control Strategy .
- Controllers. Initial configuration of the ADEX controllers as defined in the Control Strategy.
- Parameters. Definition of the parameters relating to the data capture and PROCESSOR code execution periods.

In some cases, as was previously mentioned, the solution to a control problem may require a COS which incorporates the use of ADEX controllers together with a COL

(complementary optimization logic) to be applied to the input and output signals. In other cases, the solution may consist of simply connecting the ADEX controllers to the relevant process variables. In view of this, ADEX COP 2.0 offers two solutions to the definition of the COS and both can also be combined in the same project.

ii) *Supervisor Utility*

ADEX COP 2.0 enables the development of the SUPERVISOR component of ADEX systems. The SUPERVISOR function enables the monitoring and operation of the ADEX system under development, and in particular, shows values measured by the instrumentation being used such as set points, or any other information included in the PROCESSOR as required by the designer. This information can be presented either numerically or graphically.

iii) *Simulator Utility*

This utility enables the development of simulation code for the validation of the ADEX system PROCESSOR. In a similar way to the development of control and optimization strategies, it is possible to associate simulated processes to the controllers in “Standard” or “Custom” mode as described above.

Custom Strategy (Processor Utility)

The custom strategy is used to develop complex control schemes in order to deal with specific control or optimization issues. These integrate complementary optimization logic (COL) and ADEX controllers in the ADEX COP 2.0 platform.

To develop a custom strategy in the ADEX COP 2.0 platform the graphical programming language Labview is used to develop the Custom Optimization Strategy (COS). Access is available to general programming functions of Labview, in addition to the options which the platform ADEX COP 2.0 incorporates in the menu of Labview functions.

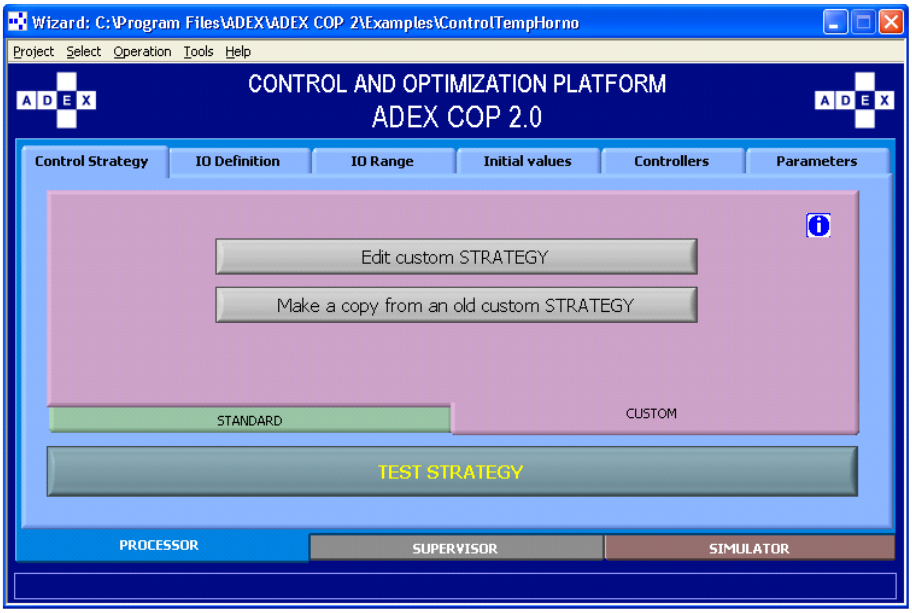

Figure A4. Selection screen for the custom strategy

The button <<Edit custom STRATEGY>> will open the program of Labview strategy.vi which enables the development of control logic. Alternatively, a copy of an existing strategy can be generated which will serve as a reference model for the new one by selecting <<Make a copy from an old custom STRATEGY>>. Inside the Block Diagram of Strategy.vi, the strategy can be edited using the submenu of functions ADEX>> PROCESSOR and the general functions of Labview.

Logic Diagrams

Once the Strategy.vi program is opened, the edit box window named Block Diagram is displayed as shown in Figure A5. Inside the edit box, a default cycle counter is generated which is used by the PROCESSOR to control the program once the project is under execution.

To edit the strategy, there exists a menu of Labview functions. Functions appear grouped according to their purpose. For example, inside the Arithmetic & Comparison menu there is a submenu called “Numeric” in which all Labview functions related to the manipulation of numbers (add, subtract, multiply, etc) can be found. This is shown in Figure A6. Together with the general functions of Labview, ADEX COP 2.0 integrates its own menu of functions which are divided in the same way as the Platform: PROCESSOR, SUPERVISOR and SIMULATOR. In the case of editing the custom strategy, it is necessary to go to the functions grouped inside the PROCESSOR.

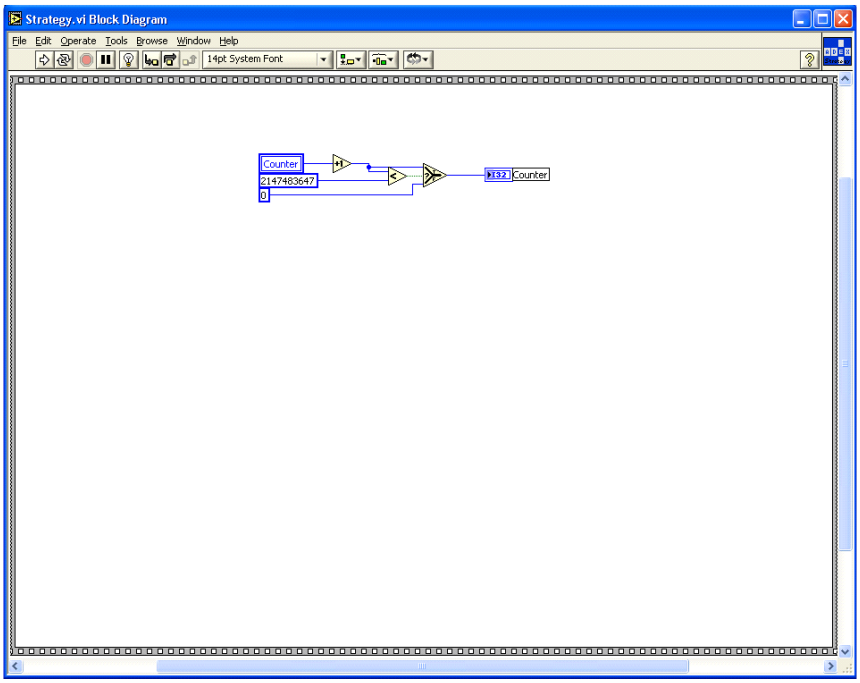

Figure A5. Editing box in Labview for the custom strategy

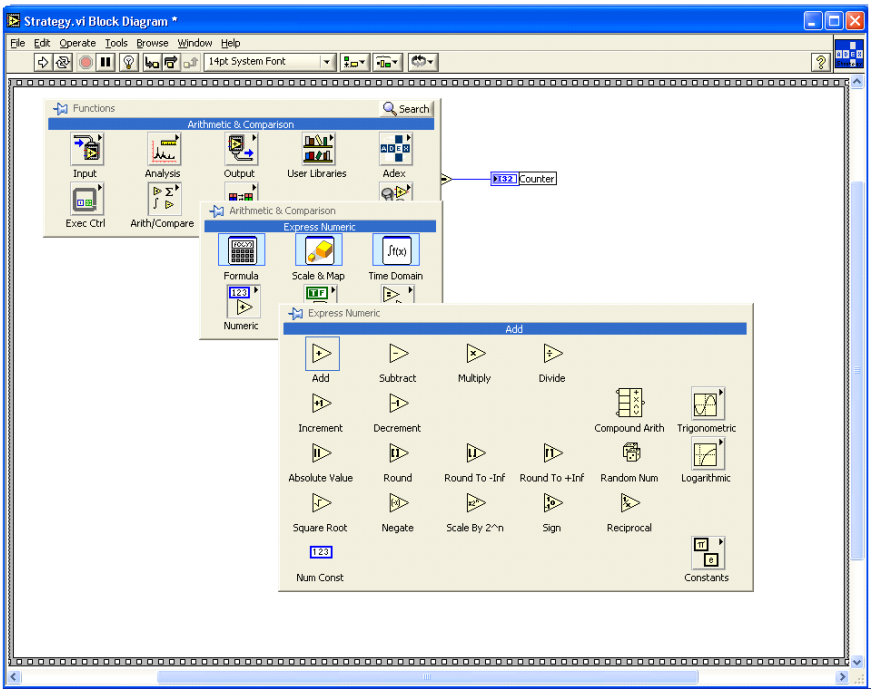

Figure A6. Diagram of the Labview functions menu

Processor Menu

To edit the custom strategy, the PROCESSOR functions are necessary and these are divided into two submenus: Connectors and Controllers.

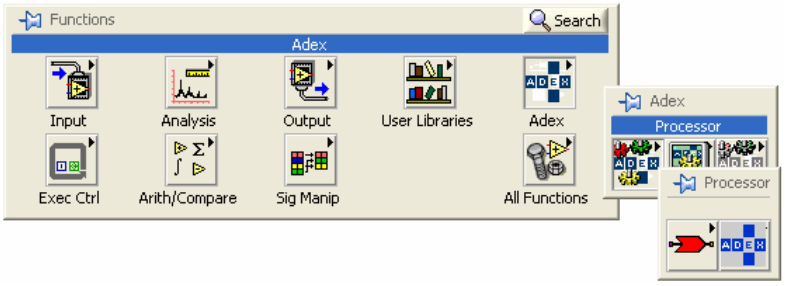

Figure A7. Menu of ADEX processor functions

To begin with, this section will outline the subject of the connectors which are graphical programming elements used to define the input and output variables of the project. This includes the type of data being communicated, whether digital or analogue and the communication type i.e. field, memory or operator variable.

To define a variable, the following actions are needed:

- Activate the function menu on the editing box.
- Move across to the menu ADEX>>Processor>>Connectors and select the type of connector corresponding to the variable to be defined.
- Locate the connector inside the editing box of the custom strategy.
- Generate an alphanumeric constant so that it can subsequently be assigned as the variable name and connect it to the input CODES of the connector.
- Edit the constant generated in the previous step with the corresponding variable name. These names are the identifiers which the programmer determines the relation to the actual physical addresses, and in the case of field variables, these are created in the I/O section in same way as for the standard strategy.

It is important to indicate that all of the connectors are designed to manipulate vectors of the input and output in such a way that only one connector is used for each type of variable. This will help generate code with a minimum execution time and will be critical as the number of inputs and outputs increases. All the variables used in the project must be defined in Strategy.

The remaining explanation is the insertion of the ADEX controllers in a custom strategy to complete the control and optimization scheme (COS). To add an ADEX controller, the following must be carried out:

- Activate the function menu on the editing box.
- Move across to the menu ADEX>>Processor>>Controllers and select the ADEX icon.
- Position the ADEX controller inside the editing box.

Connect the controller terminals. Figure A8 shows the connections of the ADEX controllers with the input/ output terminals required for the strategy.

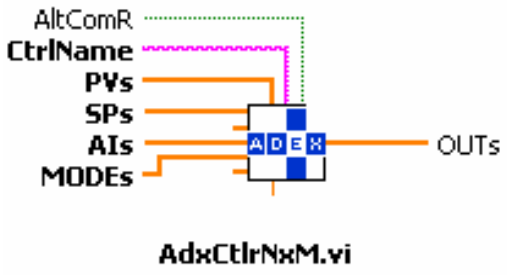

Figure A8. Connections of the ADEX controller

It is important to mention that the controllers are designed to be multivariable which means that the inputs and outputs are vectors and for this reason they frequently require the functions of Labview: “build array” to convert numbers to vectors, and “index array” to convert vectors to numbers. Both functions can be found in the submenu All Functions>> Array of the menu of functions.

Finally in Figure A9 an example of a custom strategy is displayed in which it can be seen that the use of the Labview graphic language enables the definition of the COS in an intuitive way since the schematic diagram directly generates the executable code.

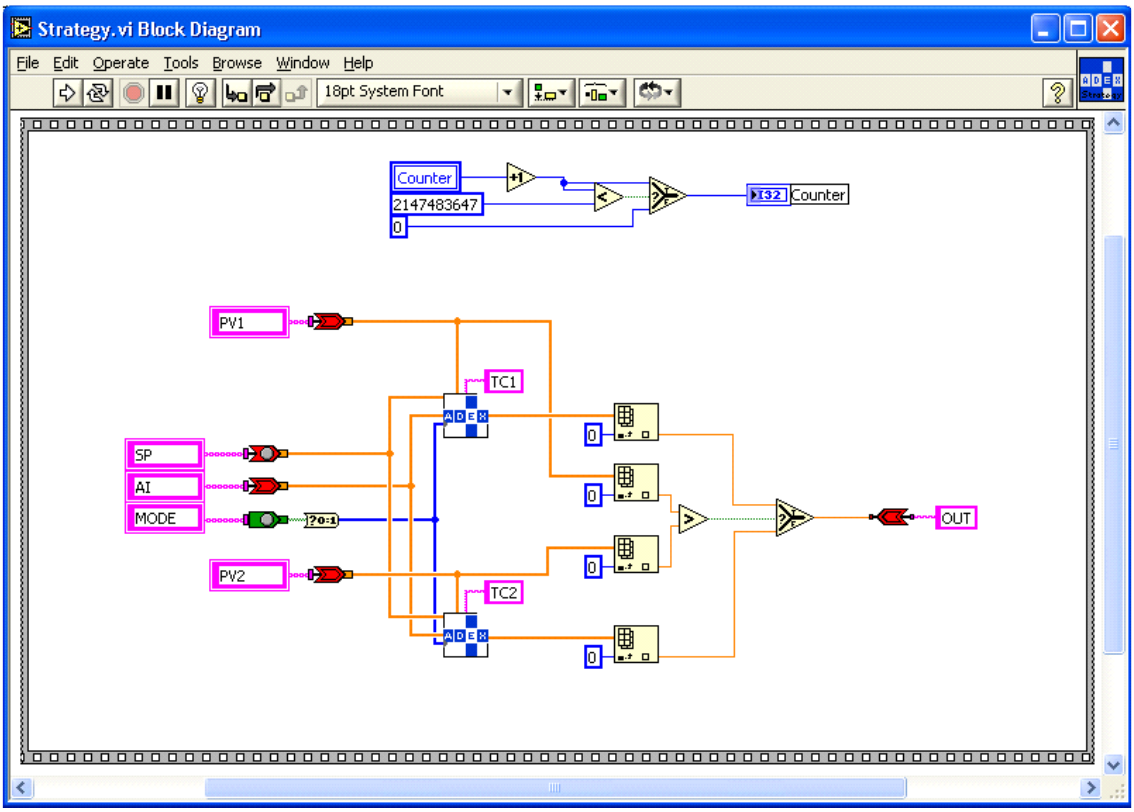

Figure A9. Example of a custom control strategy

Once the custom strategy editing is completed, return to the ADEX COP and test the strategy by selecting <<TEST STRATEGY>> shown in Figure A4. The platform will extract the group of variables defined using the connectors in the Strategy.vi and put them into the options of the PROCESSOR configurator.

With the custom strategy defined, the next step is to characterize of the field variables, this includes; defining the path to get the variables; establishing the ranges for the field variables; establishing the initial values for the operator and memory variables; configure the ADEX controllers and define the strategy operation parameters. All this can be done in the Processor menu of ADEX COP 2.0 and is explained in the following:

➔ I/O path definition:

Many of the variables used in the strategy are generated externally, i.e. temperature measurement in a furnace. For this reason, it is necessary to link external variables to the variables used by the PROCESSOR. This is normally accomplished using different communication protocols and drivers. At the present time, OPC, DEE, DIM, MODBUS and CAN protocols are used in ADEX COP 2.0. The PROCESSOR utility enables data acquisition of variables via the option tab "IO Definition" which, when activated, displays the variable acquisition screen shown in Figure A10. A list of digital inputs is shown by default.

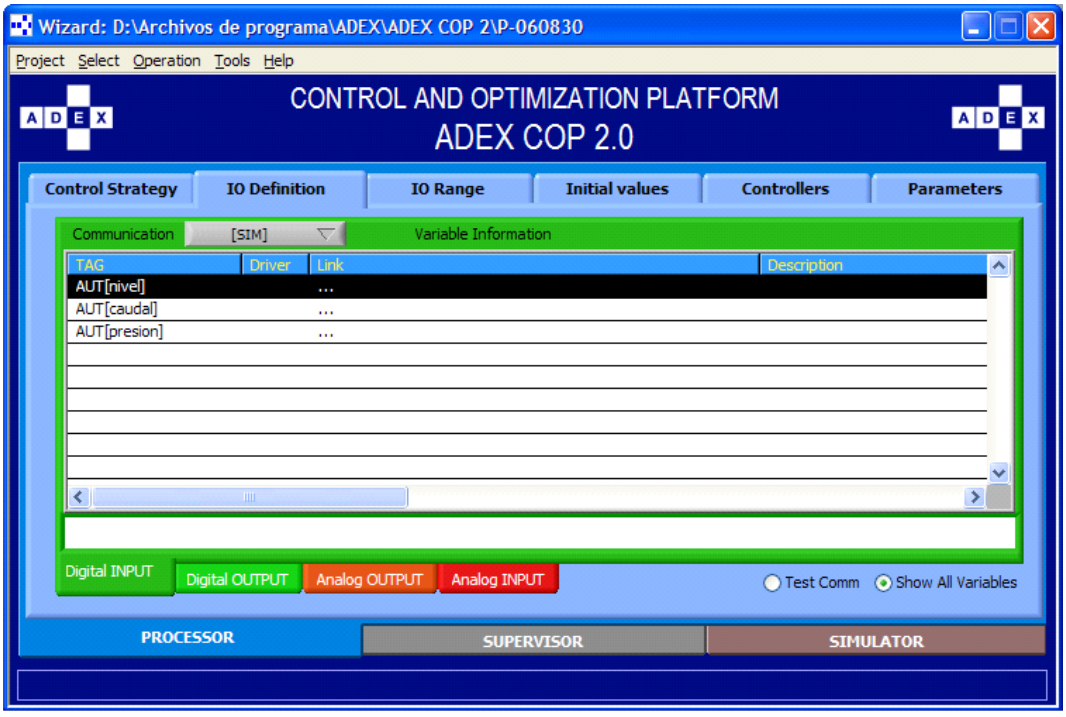

Figure A10. Acquisition of field variables

In the lower left part of the I/O definition screen, the four types of variables likely to be acquired are displayed as option tabs. Those are: Digital Input, Digital Output, Analog Output, and Analog Input. Clicking on the first option tab to the left (Digital Input shown activated in Figure 13), also displays the window with the list of fields corresponding to 'Digital Input'. The first column shows the Tags or identifiers of the Digital Input variables created via the previous "Control Strategy" option tab. The three digital input variables shown on the

screen, MODE[Level], MODE[Flow Rate], and MODE[Pressure], are the modes of operation of the respective controllers, which logically have to be determined externally. In the example shown, the variables have been obtained from the SIMULATOR as can be seen from the Driver column which is shown with the label [SIM]. The other two columns are; “Link” which determines the address of the remote machine and connection point for the acquisition of the data in question (which in the case of the SIMULATOR coincides with the name of the variable); and “Description”, where descriptive text can be added for clarity if necessary.

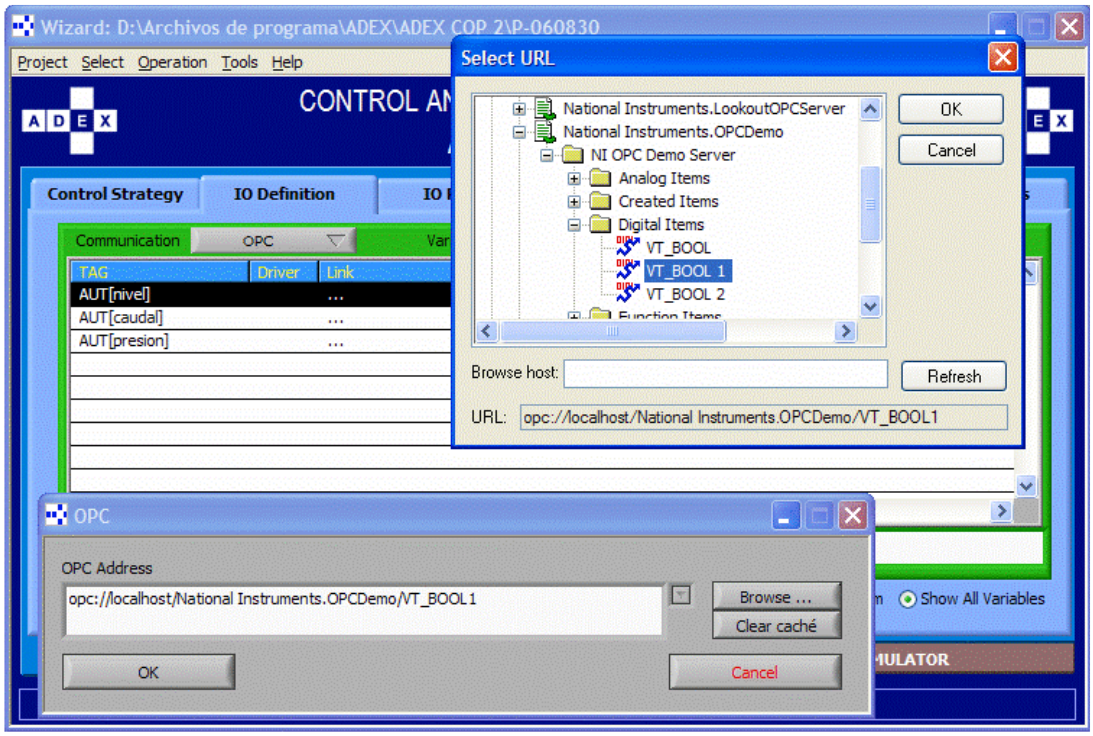

Figure A11. Acquisition of variables via OPC

To establish, for example, an OPC communication it is necessary to assign a variable to a point on an OPC server. The assignment is carried out by setting the OPC driver in the grey tab displayed to the right of “Communication”, as shown in Figure A11. To change or set the assignment of a determined variable it has to be indicated in the list. The system will open a browser allowing the selection of an OPC point in any server which is found in the network as shown in Figure A11. Once the appropriate points in the OPC server are selected for all variables the communication I/O path definition is done.

➔ Establishing field variable ranges (I/O Range)

Accessing the option “IO Range” of the PROCESSOR utility, a screen for setting the ranges of input and output analogue variables as shown in Figure A12 is displayed. It can be seen that the option tabs corresponding to the digital variables are deactivated.

This screen displays a window of fields called “Range of measurement” in which the left hand column are lists of the variables already defined. Four columns are available for the input of maximum and minimum permissible values along with columns for Eng. Min and Eng. Max values which are the engineering limits applicable to ADEX COP calculation.

The system uses a linear transform to adjust the offset and the change of scale. It is possible to use negative values to carry out an inversion of the external variable reading.

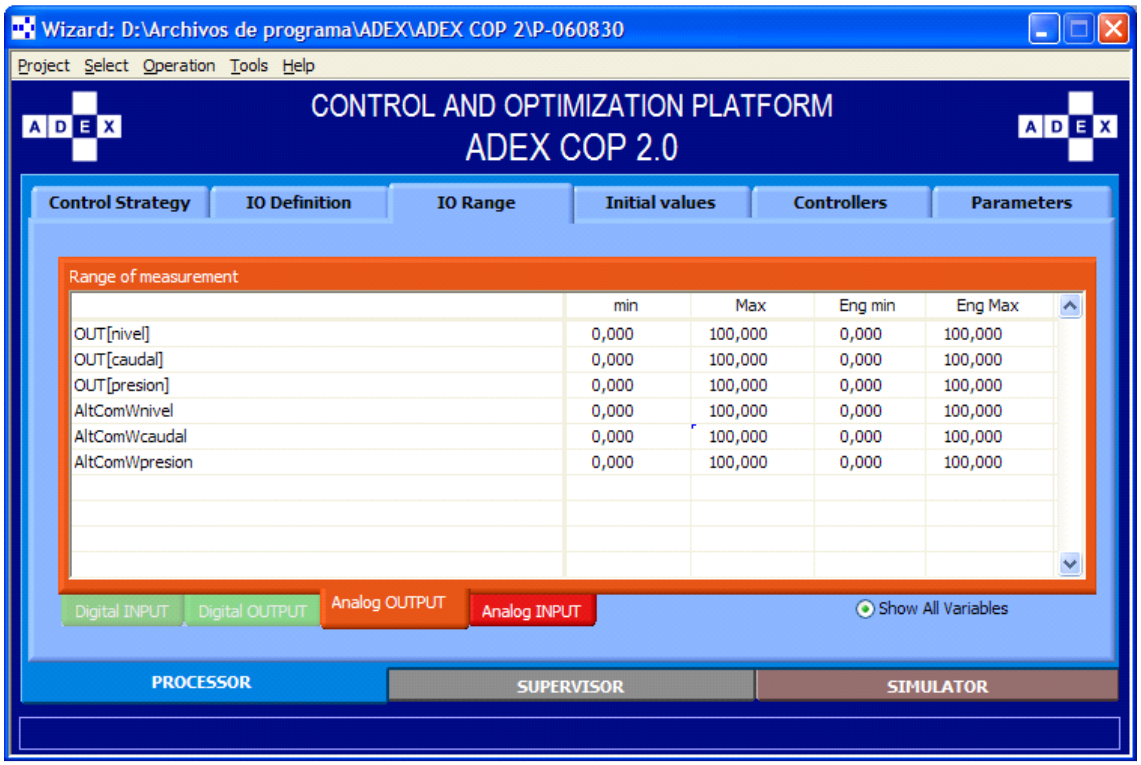

Figure A12. Definition of ranges for analogue I/O variables

The default values in the Platform are 0, 100, 0, 100 which means that the external variables do not require transformation or offset for use within ADEX COP.

➔ Initial Values of variables in operation and in memory

Apart from the input/ output variables used to relate the ADEX system with the process, other types of internal variables are required for the functioning of the system. These are memory and operating variables.

Memory variables are those used to store intermediate data for internal calculations and are accessible for reading from or writing to any of the function blocks of the ADEX system (PROCESSOR, SUPERVISOR or SIMULATOR). The operating variables are those which are generally written from the SUPERVISOR and are sent as set points or function parameters to the PROCESSOR.

The memory or operation variables are normally initialized as 0 for both digital and analogue values unless specified otherwise. Initial values can be set by selecting the "Initial Values" option tab of the PROCESSOR Utility and displaying the screen as shown in Figure A13.

Figure A13. Definition of initial values

ADEX COP automatically lists the names of the memory and operating variables in the left hand column corresponding to each of the variable types, accessible via the appropriate tab option. These variables are generally used in the definition of Custom Strategies (see

Section 7), and this usage initially indicates its type. The two columns “Value” and “Description” enable the designer to assign appropriate initialization values, such as functional description, to each of these variables whenever convenient.

➔ Configuration of ADEX Controllers

Selecting the option “Controllers” of the PROCESSOR Utility reveals a screen with a list of all the controllers used in the control strategy as shown in Figure A14. The name of the controllers defined in Strategy.vi are listed in the column at the left side, the I/O structure corresponding to each one is listed in the column at the right. In addition, associated with each of the controllers, there is a symbol which indicates whether the controller can be configured initially from this screen. These symbols are as follows:

√ OK: The controller has been initialized correctly and can be configured.

X NOK: The controller has not been initialized due to an error. It cannot be configured.

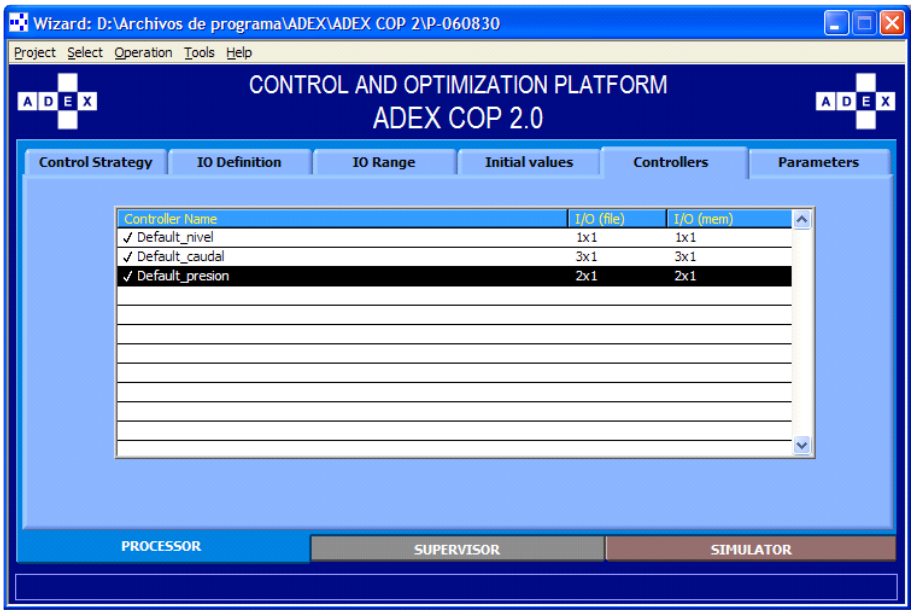

Figure A14. List of controllers to be configured

To configure the controllers which appear as “OK”, it is only necessary to double click on the controller and the configuration window will appear showing the values and status. Clicking on the controllers the controller configuration screen appears allowing to set the initial structure variables of the controller (further details about the controller, the controller’s configuration interface and its structure variables are given in ANNEX B).

➔ Definition of parameters

Selecting the tab option “Parameters” of the PROCESSOR utility enables to specify the parameters which determine the data acquisition times and the PROCESSOR code execution times. The parameters are:

i) Cycle time: Period of time in which the PROCESSOR reads the external variables, executes the COS and writes the output variables or control actions. These actions are repeated cyclically.

ii) Time out: Maximum time ADEX COP will wait to declare a test failure in the event that a fault in the programming causes a delay in carrying out the strategy test. Ten times the cycle time is recommended.

iii) History: This variable specifies if historical data is to be saved on the machine which executes the PROCESSOR program. It is set 1 for yes and 0 for no.

iv) LogDays: To avoid filling the storage space completely, this variable defines the number of days history desired to be stored, after which data will be overwritten. If this variable is not relevant if the ‘History’ variable is set to 0.

v) Verbosity: This variable enables operational events to be stored. These events are stored in the subdirectory logs of the system installation directory. The system saves events which have a certain level of importance and the level is selected using this parameter. The lowest value 0 means save all minor events while the highest value 2 is limited to system errors.

vi) Debug: With this option set at 1, the system will open a window corresponding to the front panel of the strategy in Labview so that debugging can be carried out.

Graphical User Interface (Supervisor Utility)

In the following the method for generating the SUPERVISOR program will be described. The purpose of the SUPERVISOR program is to provide a means for the user to start up, monitor and operate the developed project in real time. For the SUPERVISOR, the main points of interest are the manipulation of operation variables and/or memory variables to display instrumentation values, actuator values, and set points. This information is presented in a numerical and graphical manner which needs to be formatted.

To generate the graphical user interface of a project, the ADEX COP 2.0 integrates an editing window into which objects (Labview graphical screens) can be inserted in order to create a panel containing a group of graphical objects with its corresponding program code. These objects will carry out the function of the SUPERVISOR.

Each object can be created using the general functions of Labview in conjunction with the functions of ADEX COP 2.0 available in the function menu ADEX>>Supervisor. The steps required to define the user interface are presented in the following:

- Select SUPERVISOR>> Graphical User Interface >>Create new OBJECT
- Assign a name to the new object <<New Object>>
- Press OK

This action will open a program in Labview with the assigned name of the object.

The graphical screens are generated by applying all the development techniques of Labview. All the variables used in the strategy and in the simulation can be accessed using the connectors. These connectors are to be found in the tools menu of ADEX within the submenu ADEX>>Supervisor. The use of connectors is analogous to those used in the custom strategy. Figure A16 shows an example of the development of a SUPERVISOR object.

Once the definition of all the objects has been completed, they must be incorporated into the GUI and visually organized as explained in the following.

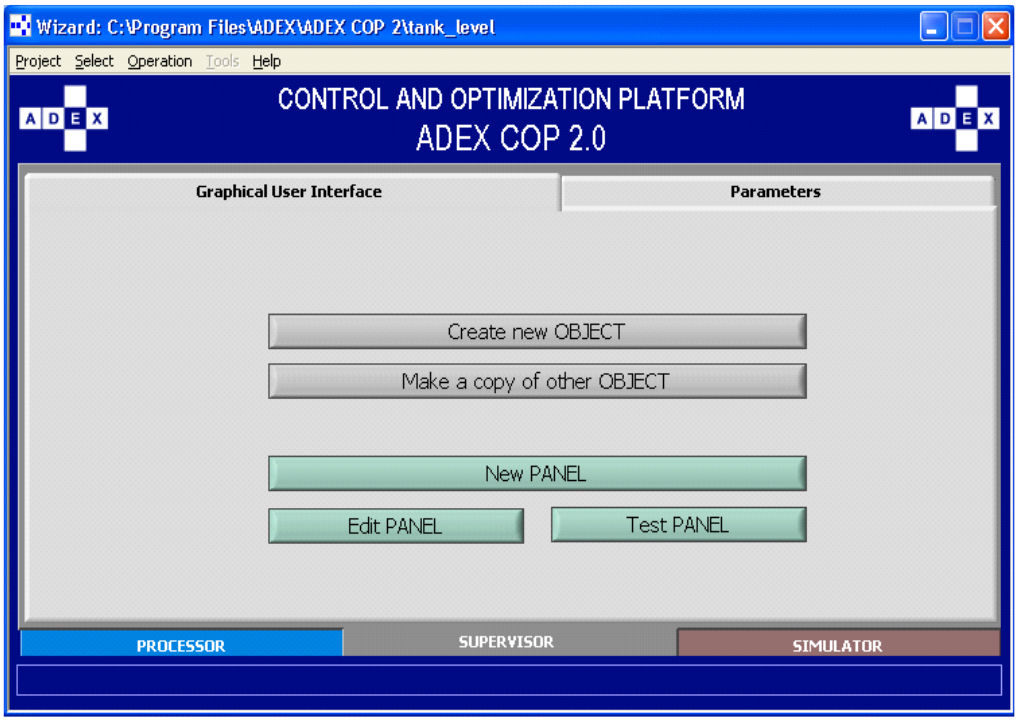

Figure A15. Screen for editing the graphical interface.

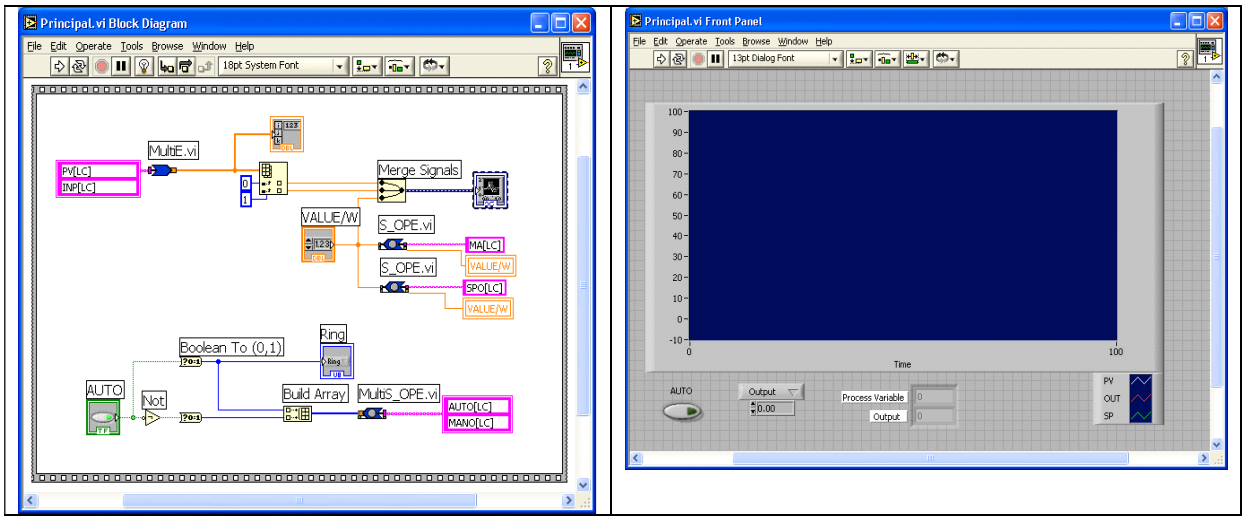

Figure A16. Example of the creation of a supervisor interface

Definition of the panel

The panel is a window which includes the objects previously created. The application panel can be launched form the screen of Figure A15 by selecting <<EDIT PANEL>> or, <<NEW PANEL>> if the existing panel is to be erased and a new one started.

Once the panel editor window appears, it is possible to work directly with the object. For a new panel, only the application logo will be found. The screen menu shown in Figure A17 allows to erase or insert an object.

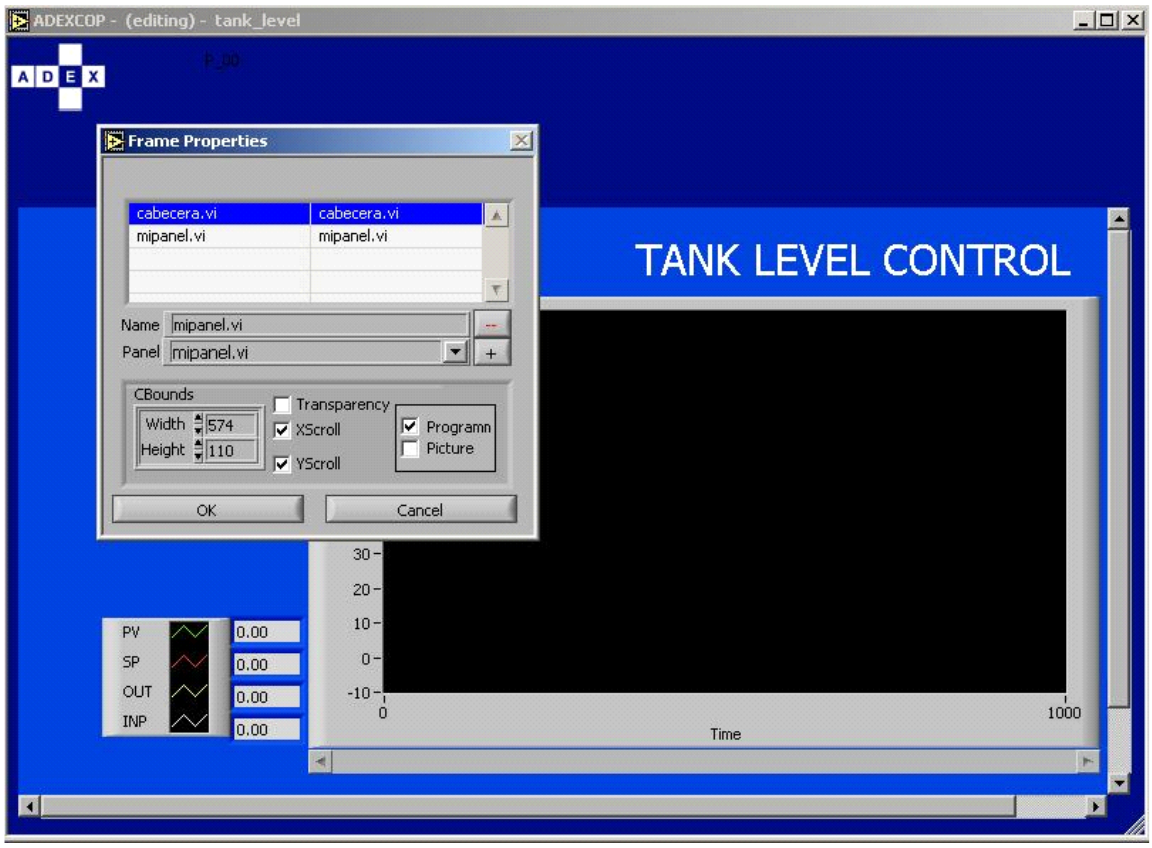

Figure A17. Modifying object properties.

The object properties such as the background color and dimensions can then be edited. The objects appear with a shaded grey area when they are able to be moved around on the screen.

Simulation (Simulator Utility)

In order to test the execution of the controllers and the control logic, the function of a SIMULATOR can be incorporated. The objective of this tool is to link the process of simulation to COS created in the processor utility in such a way that the control behavior can be analyzed and possible errors can be corrected in a safe environment.

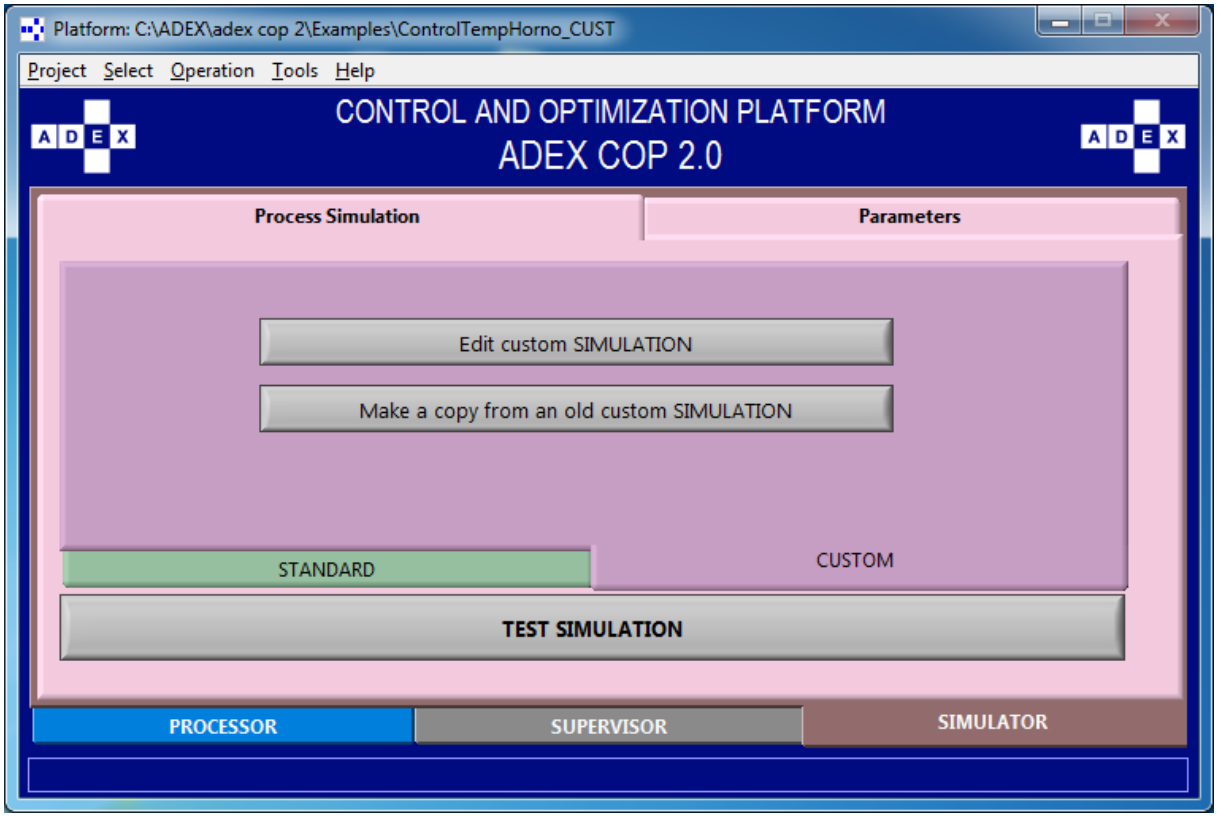

Figure A18. Simulation development screen.

Definition of Process Simulation

In a way similar to the generation of strategies, the environment enables the design of a simulation. The simulation is developed in a Labview VI called simulation.vi, which can be accessed by selecting the option SIMULATOR>>Process Simulation>>CUSTOM>> Edit custom SIMULATION.

To illustrate the process of developing a custom simulation, an example will be explained of a first order linear process simulation which responds to equation (A.1). In the particular case of this example the process is simulated with a transfer function (A.2) representing a process with a gain of 2 and a time constant of 5 seconds. The sampling period is 1 second.

$$y_k = a_1 y_{k-1} + b_1 u_{k-1} \tag{A.1}$$

$$G_p(s) = \frac{2}{5s+1} \tag{A.2}$$

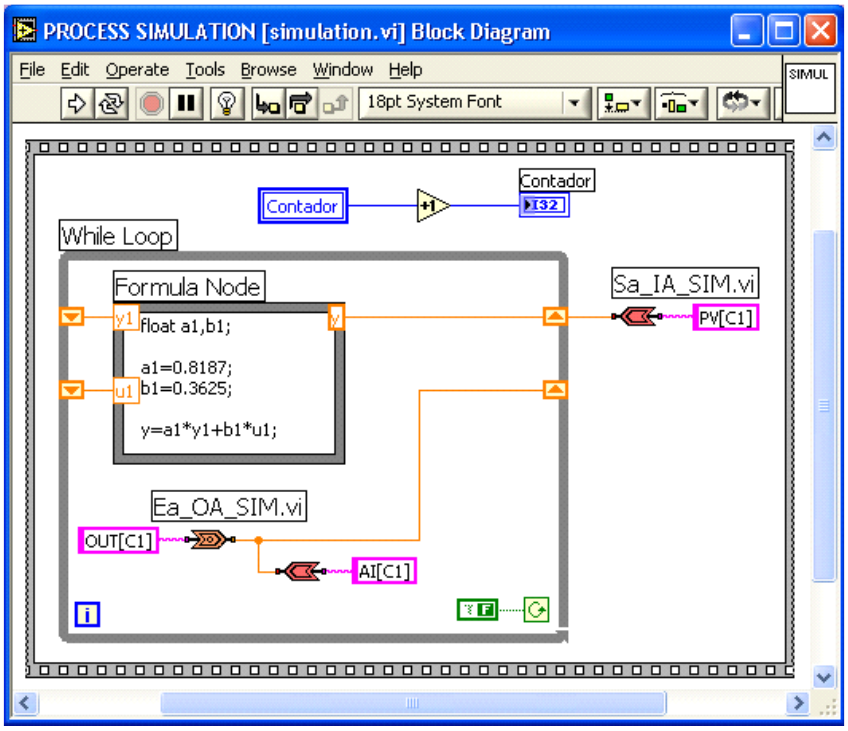

Figure A19. Simulation of a first order linear process.

Figure A19 shows a simulation scheme carried out in Labview using general functions and ADEX simulation connectors located inside the menu ADEX>>Simulation>>Connectors. In this figure it can be seen that the "While" cycle with the shift register enables the storage of the previous values of the process variable "y" and the control action "u". In addition, the

“Formula Node” containing the formula (written in C programming language) allows process parameters, or even the simulated process structure, to be easily changed.

At the end, the simulation.vi must be saved in Labview and tested in ADEX COP by pressing TEST SIMULATION which the button is shown in Figure A18.

Compilation and execution of a project

Once all the parts of a project have been developed in accordance with the previous concepts, some further databases must be built so that PROCESSOR, SUPERVISOR and SIMULATOR (if active) can work in the execution phase. This stage is developed from ADEX COP by selecting the option “Test & Build” in the operation menu. First of all, however, using the option “Elements”, it is necessary to specify whether the database functions to be created are for the PROCESSOR, the SUPERVISOR or the SIMULATOR. For this the following steps need to be taken.

- From the Tools bar of the Platform, the Operation>>Elements menu must be selected to ensure that the elements required to be verified are marked as seen in Figure A20.

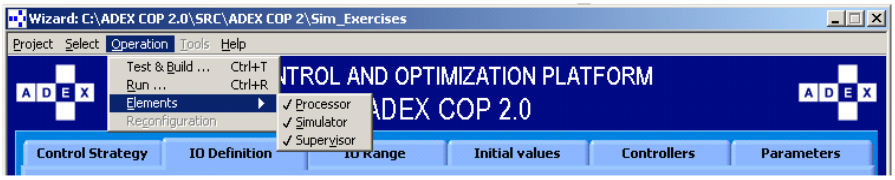

Figure A20. Project compilation and execution menu

- Selecting Operation>>Test & build the project compilation window can be opened as seen in Figure A21.

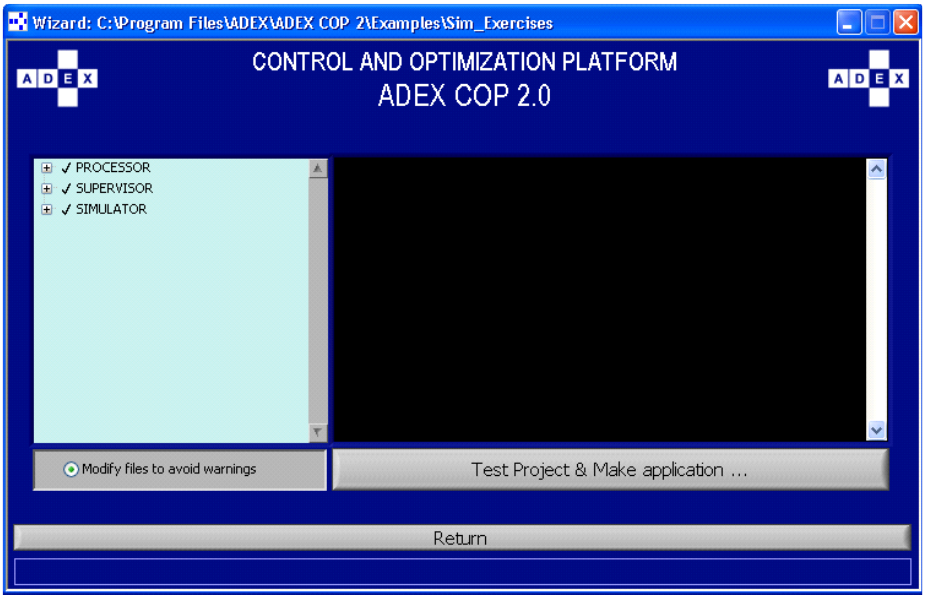

Figure A21. Project compilation window

The option “Test & Build” shown in the figure displays an environment of the status of the compilation and information related to different parts of the three functional blocks in a way that is easy to see whether there are errors, and where they can be found.

Pressing <<Test Project & Make application>> initiates the project database construction and generates a report such as the one shown on Figure A22.

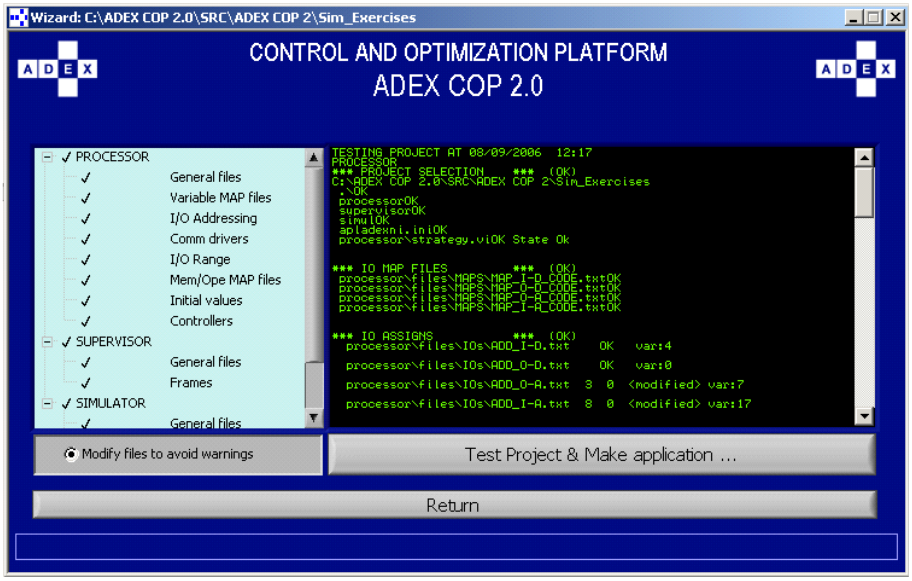

Figure A22. Project compilation report

Once this development has been concluded without errors, on the main screen, selecting “Operation: Run” (see Figure A23) from the menu, launches the execution of the elements which are selected (see Figure A20).

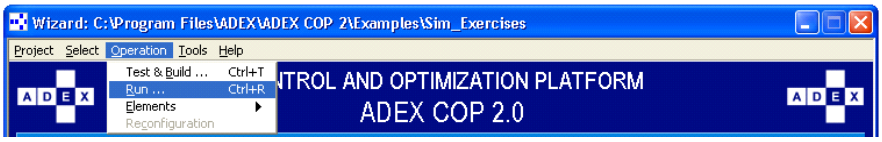

Figure A23. Execution of a project

ANNEX B:

ADAPTIVE PREDICTIVE EXPERT CONTROLLER CONFIGURATION

It should be remembered that the structure of the multivariable controllers MIMO can be understood as a group of MISO controllers containing the same number of controllers as variables in the process to be controlled. Hence, in the configuration process, there is always a MISO controller selected for configuration within the ADEX controller. An ADEX controller with only one PV, only one OUT and with either one, more or no PERTS, is a particular case within this general formulation. The ADEX configuration interface assumes:

- That the user will first configure an AP domain for each of the MISO controllers which will be called AP-C ('C' for 'Central domain' i.e. between upper and lower domains). The limits of these domains will, by default, be those of the corresponding ranges of the PV.
- The user will be able subsequently to configure 1 or 2 AP additional domains for each MISO controller, called AP-U (Upper) and AP-L (Lower) taking into account that establishing the limits should correspond to those of AP-C. For this purpose, the

user will change to the Configuration Domain to set the relevant limits for that domain.

- The domains defined will always cover the corresponding ranges of the PV.

Once the desired domains are configured, the user can continue to configure the Expert Domains. For each of the MISO controllers, an EX-U (Upper) domain can be defined with a range above the PV and conversely, an EX-L (Lower) domain can be defined with a range below the PV.

In order to change the default values of each controller configuration the configuration screen is displayed as shown in Figure B1. All the parameters will have default values.

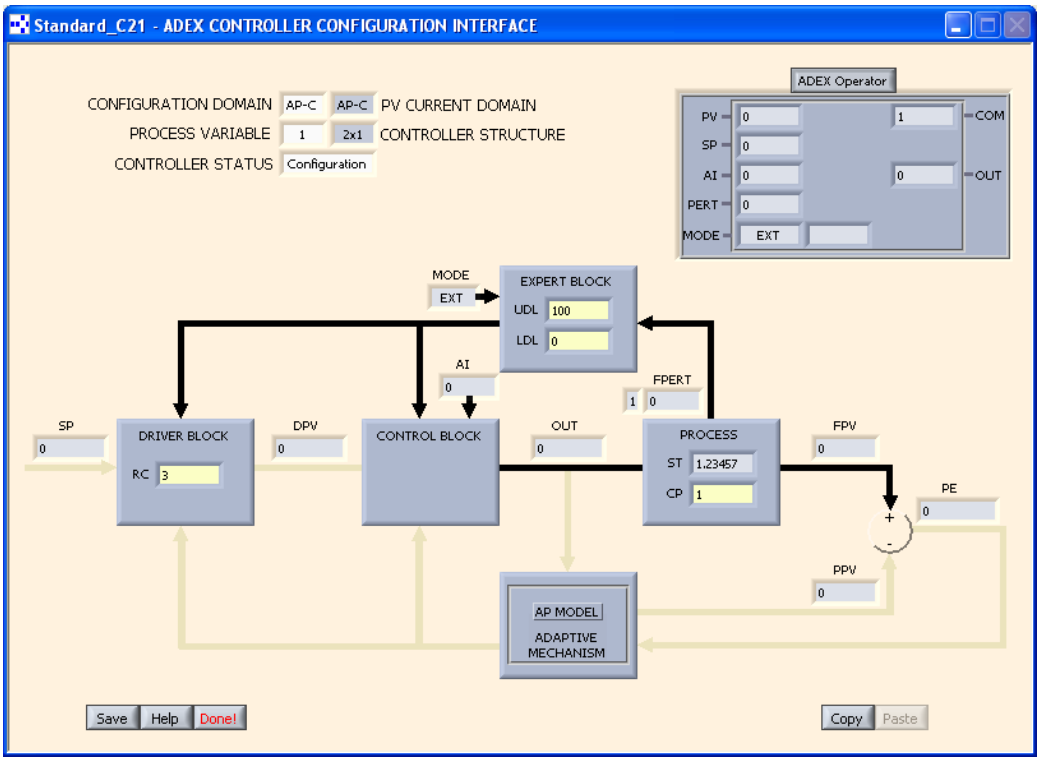

Figure B1. Configuration interface of the ADEX controllers

Note that any of the MISO controllers selected is by default PV_1 and referred to as "PROCESS VARIABLE 1", as shown in Figure 1, since it is a single controller.

The top left hand corner of the figure shows the "CONFIGURATION DOMAIN" and the "PV CURRENT DOMAIN" for the selected MISO controller. The configuration domain box

enables the user to select any of the other domains (which are displayed in the list when the box is clicked) for configuration.

As shown in the figure the ADEX controller blocks are the following: PROCESS, EXPERT BLOCK, DRIVER BLOCK, CONTROL BLOCK and the AP MODEL ADAPTIVE MECHANISM. The first three of these blocks display the parameters of the selected MISO controller which are configurable by the user. These are:

➔ PROCESS: Two defaults values are presented:

ST - Sample Time

CP - Control Period for the AP-C domain as shown in Figure 1.

These parameters are common to all the MISO controllers and the ADEX controller will always use the values set for PV_1 (MISO 1).

➔ EXPERT BLOCK: Two default values are presented:

UDL - Upper limit of the expert domain.

LDL - Lower limit of the expert domain.

➔ DRIVER BLOCK: One default value is presented:

RC - Rate of Change. This is the maximum rate at which the variable should change in time.

When the EXPERT BLOCK, DRIVER BLOCK, CONTROL BLOCK and the AP MODEL ADAPTIVE MECHANISM are double clicked, configuration windows are displayed for each one. As is explained in the following sections, the user can determine the desired function for each of the blocks by replacing the default values. As can be seen, the ADEX blocks are represented by option tabs which are permanently active when they are relevant to the domain of the selected configuration or otherwise, they remain inactive and are dimmed.

The principal real time variables of each MISO controller are shown in smaller windows in Figure B1 and are outlined below:

➔ The MODE variable, which together with the variable PV of the current domain, determines basically the type of operation of the Expert Block for the corresponding MISO system.

The MODE variable, which together with the variable PV of the current domain, determines basically the type of operation of the Expert Block for the corresponding MISO system.

➔ The set-point (SP) which is input to the Driver Block and the desired process variable (DPV) which is output from the Driver Block and input to the Control Block.

➔ The output from the Control Block (OUT) to be applied to the Process, the perturbation which acts on the process (FPERT) and the Filtered Process Variable (FPV) output from the process.

➔ The Predicted Process Variable (PPV) which is output from the AP MODEL and,

➔ the Prediction Error (PE) are both shown when the operation is functional.

The lines showing the interrelationships between the ADEX blocks. These lines appear black when the interrelation is active between the blocks for the selected MISO system. Otherwise they are dimmed. As shown in Figure B1, the MODE variable is EXT or “External”. Only the lines in the upper part of the screen are shown in black and therefore active. In this case, the Expert Block determines that the Driver Block and the AP Model adaptive mechanism remain inactive. It also has determined the functioning of the Control Block which produces an OUT equal to the AI.

There is an option ADEX Operator shown in Figure B1 which when double clicked, displays an Operator scheme, showing the values of the Operator I/O variables of the ADEX

controller in real time, in relation to the selected MISO controller. This window is shown in the top right hand of Figure B1.

Controller Status

In order to monitor the status of each controller once ready for operation, and to show if there are any execution errors, a configuration window is displayed with an indicator called "CONTROLLER STATUS" (see Figure B1). The user can change the status of the controller by changing this value. The next section explains the four possible values:

- ➔ Configuration - Under this status, the internal functions of the controller are being defined/ configured and so it is not available for operation. This is the initial status assigned as soon as the controller is created.
- ➔ Ready - This status indicates that the controller is already configured and ready for operation. This status can be set by the user by clicking on the box beside "Controller Status" (shown in the top left corner of Figure 18) whenever the controller configuration process is complete.
- ➔ Operation - Indicates that the controller is functioning as part of he control and optimization scheme. This status is assigned automatically by ADEX COP when the COS is in operation and in communication with the local area network.
- ➔ Connecting - This status is transitory and assigned automatically by ADEX COP when communication between the controller or the COS and the local area network has been lost.

Configuration of the AP Domains

- Process block

The parameters which are configured within the Process Block are common to all the MISO controllers and are established in the configuration of the MISO controller for PV_1 which determines its value for the whole of the ADEX controller as explained in the following:

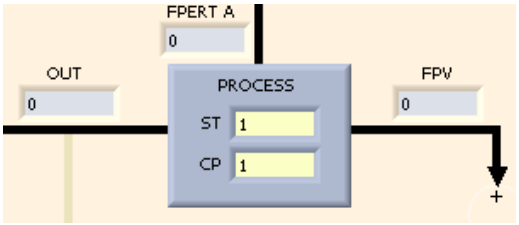

Figure B2. Process block

➔ ST - Sample Time, which determines the frequency with which the ADEX controller receives information, particularly the current values of the PV measurements from the output vector of the process, the perturbation signal 'PERT', the input vector 'AI' and the vector of operating mode 'MODE'. The sample period is the execution time period of the logic schemes which execute the PROCESSOR cycle time, and its value is displayed in seconds in this field.

➔ CP - Control Period, determines the number of sample periods between two control actions generated by the ADEX controller when under automatic control. The value can be established through the keyboard or via the logic of the control scheme. The procedure is as follows:

- If the user types in a positive number, the period of control is defined in terms of sample periods.

- If the user types in a zero, the control period will be determined by the logic scheme and transferred via the corresponding operator 'pin' in the logic scheme.

- If the user types in a negative number, the control instant will occur when the ADEX controller detects a change in the signal sent via the operator pin mentioned above. A control instant will take place if it is detected that there has not been a change following the set number of sampling periods since the last control instant.

In general, it would be convenient to use shorter sampling periods in order to receive as much information as possible about the process. This information can be used to obtain a convenient filtered process variable (FPV) from the process variable vector. In a SISO process, the selection of the control period must take into account the response time of the process, for example, approximately 95% of the time it takes for a process variable (PV) to stabilize after the application of a step change in control signal (OUT). A reasonable value for the control period various normally between 1/10 and 1/40 of the response time. In this case, since the process response time may be different for different MISO controllers, the choice of a common control period needs to be a compromise between both response times.

- Control Block

The Control Block shown in Figure B1, is configured with the parameter configuration window shown in Figure B3. On the left hand side, the window shows a column of variables which form part of the Control Block for the selected MISO controller. In this case, the variables, from top to bottom, are PV, OUT and PERT where PV and OUT are the corresponding variables of the process and output of the controller MISO, and PERT is an input variable which has an influence on the evolution of the process variable. Each one of these variables has associated parameters which can be configured by the user in this window.

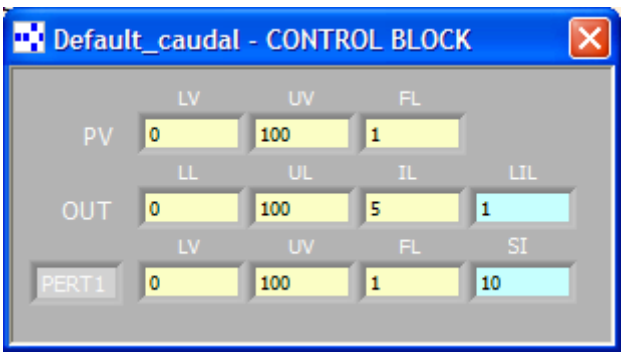

Figure B3. Parameters defined in the control block

The parameters related to the variable PV of the process are:

- ➔ LV - Lower value, which is the bottom of the range of values measurable by the process.
- ➔ UV - Upper Value, which is the top of the range of values.

- ➔ FL - Filtered constant. The filtered value of the process variable at the sampling instant k FPV(k) is obtained by measuring the value PV(k), using FL as follows:

$$FPV(k) = FL * PV(k) + (1 - FL) * FPV(k - 1) \qquad (B.1)$$

If PV(k) is contaminated with measurement noise, the use of this first order filter (B.1) produces a better estimate of the process variable FPV(k).

The parameters related to the output OUT of the controller MISO are:

- ➔ LL - Lower limit for the controller output.
- ➔ UL - Upper limit for the controller output.
- ➔ IL - Incremental limit for the controller output.
- ➔ LIL - Lower incremental limit for the controller output. This reduced control limit is applied when the process is in steady state close to the set point.

It is important to note that special attention must be paid to define a variation range for the actual range of the controller when introducing these limits, that is, a range of variation in which any change in the value of OUT_n has a particular and unique effect on the process variable PV_n of the process.

The parameters related to the perturbations are the same as those related to PV except the LIL which does not exist and therefore is substituted by:

- ➔ SI - Significant increment. This is the absolute value of the increment in PERT which if it occurs, relieves the controller of the limit LIL, although the PV

continues close to the SP. This allows the controller to respond with a greater control action and thereby reduce the impact that PERT would otherwise have on PV.

If the MISO controller corresponding to the other PV is selected and the Control Block button clicked, the same window will appear, but this time with the values of this MISO controller.

- Adaptive Mechanism

The parameter configuration window of the adaptive mechanism is shown in Figure B4. If the MISO controller selected corresponds to that of PV_1. The detailed information relating to the variables, whose names are shown to the far left, is displayed in each line of parameters and these variables can be selected by means of a pop-up menu as shown in Figure B4.

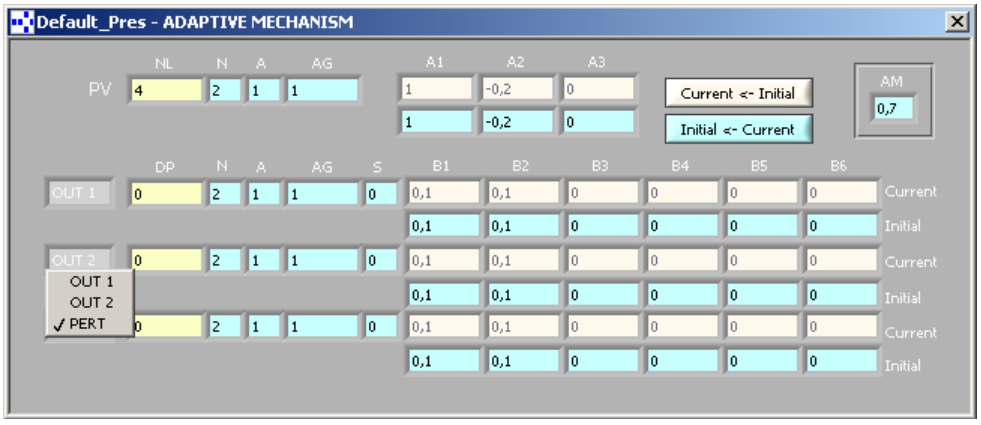

Figure B4. Adaptive mechanism parameters

These variables are considered by the Adaptive Predictive model and are used by the MISO controller in the adaptive mechanism defined as follows:

$$PV_1(k|k-1) = A_1(k-1) * PV_1(k-1) + A_2(k-1) * PV_1(k-2) + \cdots$$
$$\ldots + B_1(k-1) * OUT_1(k-1-DP) + B_2(k-1) * OUT_1(k-2-DP) + \cdots$$
$$\ldots + C_1(k-1) * OUT_2(k-1-DPC) + C_2(k-1) * OUT_2(k-2-DPC) + \cdots$$
$$\ldots + D_1(k-1) * PERT(k-1-DPD) + D_2(k-1) * PERT(k-2-DP) + \cdots \quad (B.2)$$

$PV_1(k|k-1)$ represents the estimated value of PV_1 in the control instant k, obtained from the previous available instant $k-1$. As a consequence, this estimated PV_1 is obtained from the value of the adaptive predictive model parameters (AP) A_i, B_i, C_i, and D_i and the measured values of PV_1, OUT_1, OUT_2 and $PERT$ at the $k-1$ instant and at the previous instants. DP, DPC and DPD are integers which represent the delay in control periods in which a change in OUT_1, OUT_2 and $PERT$ respectively produce a change in the value of PV_1.

The estimated $PV_1(k|k-1)$ above can differ from $PV_1(k)$, the measured value of PV_1 at instant k, with an estimation error of $\varepsilon(k)$ as given by

$$\varepsilon(k) = PV_1(k) - PV_1(k|k-1) \qquad (B.3)$$

The values of the parameters A_i, B_i, C_i, and D_i at instant $k-1$ are changed at the instant k by the adaptive mechanism using functions of the form:

$$\begin{aligned} A_i(k) &= A_i(k-1) + a\ function\ of\ \varepsilon(k) \\ B_i(k) &= B_i(k-1) + a\ function\ of\ \varepsilon(k) \\ C_i(k) &= C_i(k-1) + a\ function\ of\ \varepsilon(k) \\ D_i(k) &= D_i(k-1) + a\ function\ of\ \varepsilon(k) \end{aligned} \qquad (B.4)$$

These functions are defined in such a way that $\varepsilon(k)$ tends rapidly to zero. This adaptation only happens when a statistical criteria indicates the $\varepsilon(k)$ is due to a error in the model (lack of precision in A_i and B_i) and not caused by noise in the measurements or unknown perturbations

The parameters related to the process variable PV_1, shown in the window displayed in Figure B4 are as follows:

- ➔ NL - Noise Level indicating the maximum variations which can be found in the measurement of PV_1 while OUT_1, OUT_2 and PERT are constants and the process is in a steady state. These variations can be caused by measurement noise which occurs in the PV and also by the dynamic effect of other variables not taken into account in the AP model.

- ➔ N - Appears in the row of parameters associated with the PV and also in the row of a parameters associated with OUT. In the first case it is the number of parameters A_i taken into consideration in the AP model while in the second, it is the number of B_i parameters. The remainder of the AP model parameters shown, but not considered, are effectively ignored and treated as though their values were zero.
- ➔ A - This parameter is also presented in the rows of PV and OUT parameters. The value can be 0 – disabled or 1 – enabled, and refers to the enabling of the adaptation mechanism for the A_i and B_i parameters respectively.
- ➔ AG - Adaptation Gain. As in the case of N and A, this parameter appears in the PV_1 and the OUT_1 rows. Sometimes, it is possible to improve the function of the adaptive mechanism by changing the internal range of the variation of some I/O variables in the AP model simply for reasons of adaptation. The internal range of variation is defined by default as a percentage above the range of variation in the variable defined in engineering units. The parameter AG will change the internal range of variation in PV_1 or OUT_1, multiplying the default by AG to obtain the adjusted range value.
- ➔ Current A_1, A_2, A_3 - The values of these parameters represent the current value of adaptation generated by the adaptive mechanism for the corresponding Ai parameters of the AP model. The user cannot change them unless the button [Current ← Initial] is clicked to revert the current A_1, A_2, and A_3 parameter settings to their initial values.
- ➔ Initial A_1, A_2, A_3 - The values of these parameters are those introduced at the very beginning by the user to initialize the AP model prior to putting the adaptive mechanism into action. The user can replace the initial values at any time, by replacing them with the current values clicking on [Initial ← Current].

The parameters related to the output OUT_1 of the selected MISO controller shown in Figure B4 are as follows:

- ➔ DP - Delay Periods. A change in OUT_1 will require a certain number of control periods before a change will start to develop in PV_1. This number of control periods minus 1 is what is termed a delay period.
- ➔ N, A, AG - The values of these parameters are important for OUT_1 and related to the parameters B_i in the AP model, equivalent to what has already been described for PV_1.
- ➔ S - Sign (+/-) of the static gain of the process which will be made equal to 1 if the response of PV1 is positive and if an increment in the output from the controller OUT1 is also positive. Otherwise, the S will be made equal to -1. The value of S is used internally to diagnose an undesirable result in the 'current' functioning of the Adaptive Mechanism. When the current values of AP model parameters are working satisfactorily, the derived static gain will be positive. To ensure this, the value of S is used as a multiplier for the Bi parameters. When the derived static gain is negative, the parameters inside the AP model may be re-initialized. The user can disable this internal test by setting the value of S to 0.
- ➔ Current B_1 a B6 - The values of these parameters represent the current value of the adaptation generated by the adaptive mechanism for the corresponding parameters Bi of the AP model. The user cannot change this unless the button [Current ← Initial] is clicked to reset the current values back to initial (B1 to B6).
- ➔ Initial B1 a B6 - The values of these parameters are introduced by the user to provide initial values for the Bi parameters of the AP model before the adaptive mechanism comes into action. The user can replace them at any time by clicking on the [Initial ← Current] button.

Parameters for the rest of the OUTs and PERTs work similarly to the ones explained above.

- ➔ AM - Adaptive Mechanism. This parameter adjusts the speed of adaptation of the AP model between 0 (no adaptation takes place) to 1 (maximum speed of adaptation) with intermediate speeds between.

Finally, it is important to note that if the MISO controller corresponding to PV_2 is selected, the window shown in Figure B4 will appear the same but with all the parameters corresponding to PV_2.

- Expert Block

The variables displayed in the Expert Block are shown in Figure B5:

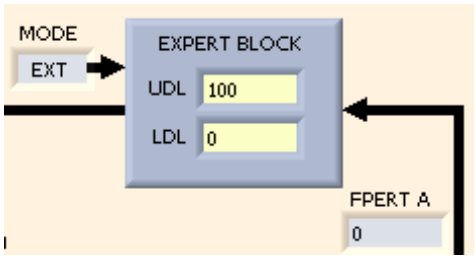

Figure B5. Expert block

The two main parameters to configure the expert block are the following:

- ➔ UDL - Upper Domain Limit. This defines the value of the upper limit of the process variable. The system uses limits to define appropriate responses to the value of the process variable PV in terms of a corresponding OUT.
- ➔ LDL - Lower Domain Limit. This defines the value of the lower limit of the process variable. Both the lower and upper limits will be wider (if an Expert Domain is defined) or equal (if there is no Expert Domain defined) to the limits set for the AP domains.

Other parameters of the Expert Block are displayed in the following configuration window:

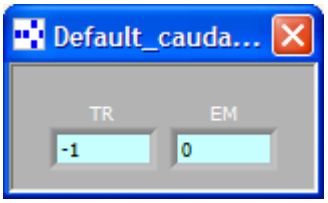

Figure B6. Expert block parameters

The window shown in Figure B6 enables to configure the following parameters:

- TR - Time of Residence. The value introduced in this box determines the number of control periods which the AP model needs to acquire the minimum data (I/O values) sufficient to allow the calculation of a control signal. The default value is -1 and in this case, the system itself calculates the minimum number of control periods necessary to fill out all the variables of the AP model with significant data before carrying out the calculations. If the value assigned to TR is less than the minimum number, the AP model will start to carry out calculations assuming that previous variable values of the AP model are the same as the most recent ones where there is no information available.
- EM - Entry Mode. The value of this parameter determines which values will be taken by the current parameters of the AP model when the output value of the selected MISO process passes from a particular domain to the selected AP configuration domain. There are 4 different options which correspond to the following EM values:

  0 – Leaving the value at zero (default value), the Expert Block reinitializes the current parameters of the AP model in accordance with the initial values assigned for the selected domain.

  1 – The Expert block will reinitialize the values of the current AP model parameters in accordance with the latest current values of the selected domain.

  2 – If the PV comes from an AP domain, the current parameters of the AP model maintain the latest current values from that domain. If the PV comes from an Expert Domain, the values of the current parameters reset themselves to their initial values automatically.

3 – If the PV comes from an AP domain, the current parameters maintain the latest current values obtained in that AP domain in the same way as described in point 2. If the PV comes from an Expert Domain, the values of the parameters also maintain the latest values in the selected domain.

- Driver Block

The Driver Block has a small box inside labeled “RC” as shown in Figure B7:

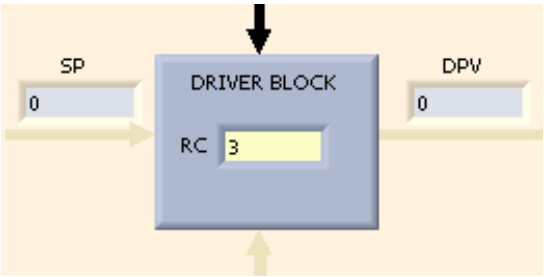

Figure B7. Driver block

➔ RC - Rate of Change. This parameter limits the rate of change of the trajectory which drives the process output towards the set point. The value of the RC is introduced in the form of engineering units per control period.

Other parameters of the driver block can be configured in the window shown in Figure B8:

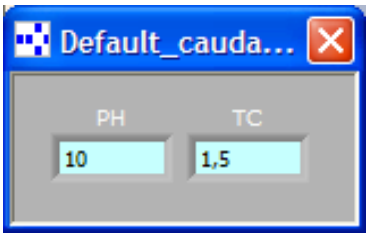

Figure B8. Parameters of the driver block

This window of the driver block enables the user to set the following parameters:

➔ PH - Prediction Horizon. This parameter defines the number of future steps (control periods), starting from the current control instant and projected along the desired output trajectory of the process. The corresponding process control signal for the OUT of the selected MISO system is calculated in such a way that the predicted variable is equal to the desired variable at the end of the prediction horizon.

➔ TC - Time Constant. This parameter determines the time constant, in control periods, of the default desired trajectory generated by the driver block from a second order model with a static gain and damping factor of 1. For example, if the TC is equal to 1.5 control periods, the desired process output will be delayed nearly 9 control periods required for a variable to reach the set point without overshooting.

- ADEX Operator

The ADEX Operator tab is displayed in Figure B9.

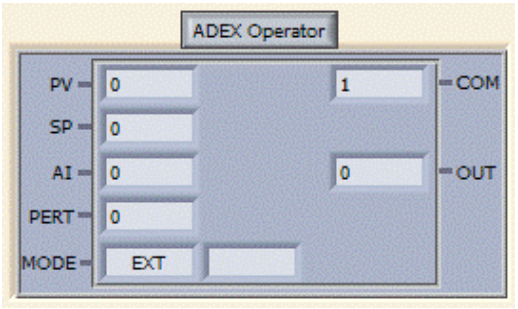

Figure B9. Diagram of the ADEX operator

It can be seen in the diagram that the ADEX Operator shows I/O values of the selected MISO controller in real time which are, in this case, PV_1, SP_1, AI_1, PERT and OUT_1. If the MISO controller number 2 was selected, the variables would have the number 2 attached (PV_2, SP_2,

AI_2 and OUT_2. In addition, it can be seen that the ADEX operator displays two MODE variables. The left hand MODE variable is the signal received from the COL while the right hand one is an internal MODE variable which the user can put into “Auto” by clicking with the mouse. If this last option is taken, the control mode continues “External”, that is, the control signal OUT follows the actual input signal AI generated by the COL, but it puts into action a mode “Internal AP Control”.

The AP internal mode initiates the function of Adaptive Predictive Control, i.e. the Driver Block, the Control Block and the Adaptive Mechanism, although the Adaptive Predictive Control signal is not applied yet to the process. This mode of internal operation can be understood as a kind of “training” for the Adaptive Predictive Control before it is applied to the process. This allows the user to observe the evolution of the parameters and variables of the controller such as, for example, see how the Prediction Error (PE) tends to zero, and how the AP model converges on specific values. In this way, the user can easily adjust the system before the application of the AP control signal and ensure it is working appropriately and correctly.

Similarly, while the controller is under Auto control, the operator will be able to activate an “Internal Manual” (MAN) mode from the ADEX Operator, and an “Internal Set point” (INT.SP) to control the selected MISO controller. In the first instance, the operator can determine the output OUT of the controller by changing the corresponding field “OUT” of the ADEX controller from the keyboard. In this mode, the value of OUT will remain a constant if the operator does not change its value.

Under the “Internal Set point” mode, the operator can force the value of the Internal Set point (INT. SP) field which will become the new controller set point.

- Configuration of other AP Domains

Once the configuration of the AP-C domain has been completed, the user can configure other AP domains choosing the domain to be configured, upper (AP-U), central (AP-C) or lower (AP-L), as shown in Figure B10.

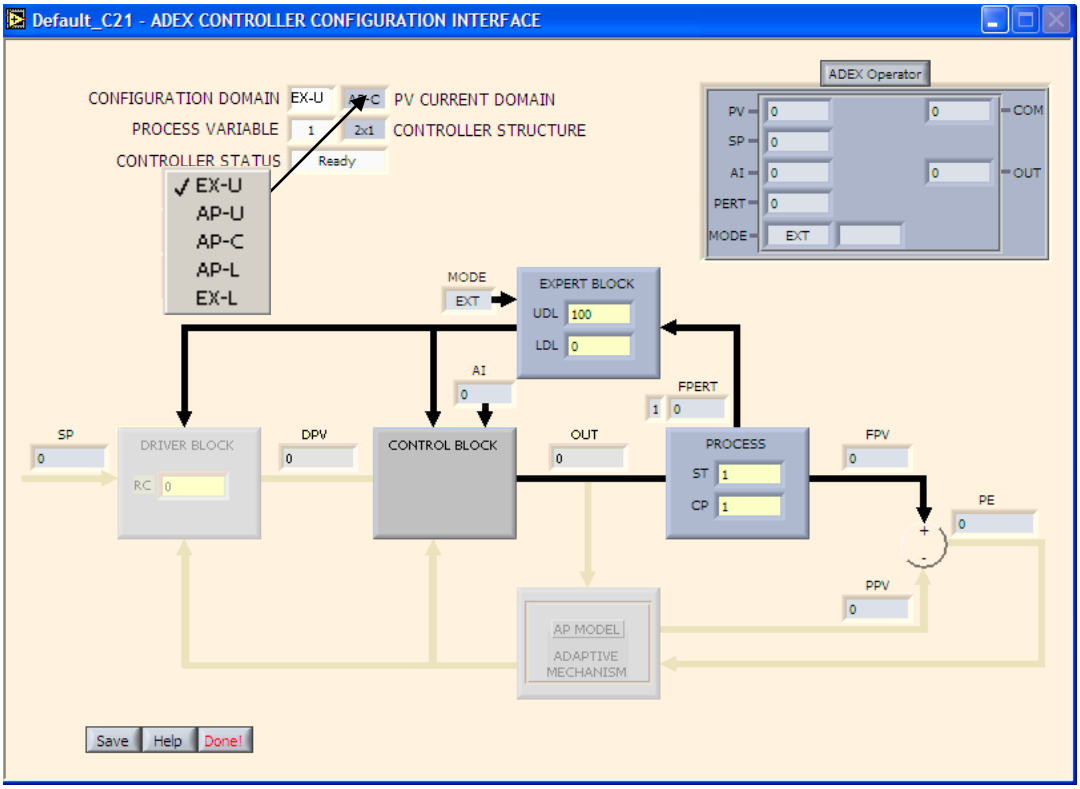

Figure B10. Configuring expert domains

- Configuration of the Expert Domains

The user can configure an Expert Domain by selecting it in the window shown in Figure B10. Choosing for example the EX-U domain, the system will display a screen like that shown in Figure B11.

The value of the parameters shown in the Expert Block can be changed by the user in order to determine the upper (UDL) and lower (LDL) limits of the Expert Domain selected. The user can change the values of the Sampling Time (ST) and the Control Period (CP) for the selected domain in the Process Block as has been previously explained.

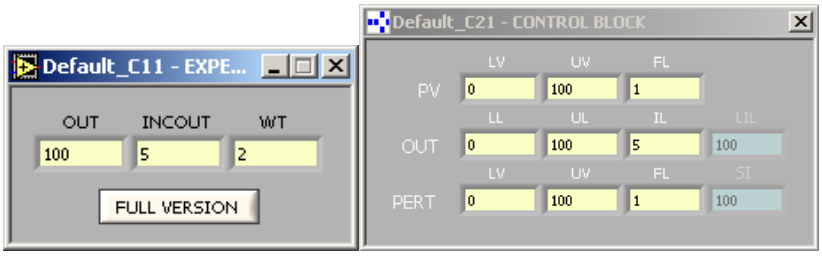

Figure B11. Configuration of the expert domain

The control block will now display the configuration windows shown in Figure B11. The window to the right shows the default values of the range and filter variables (LV, UV and FL) in relation to the process variable (PV) and the ranges and incremental limits (LL, UL, IL) in relation to the output variable (OUT) and perturbations if relevant (PERT). The user can make changes to all the parameters of the selected domain. These have all been described in previous sections.

The window to the left of Figure B11 shows the parameters of expert control. A button is displayed which changes the number of parameters used by the expert block. In a reduced version, only three are used and these are explained as follows in the context of the expert block:

- ➔ OUT - This is the value of the control signal which the ADEX controller, under Automatic mode, generates first while the selected PV is in the Expert Domain under consideration.
- ➔ INCOUT - This value will be added to the above control signal periodically if PV1 does not leave the expert domain.
- ➔ WT - Waiting time. This is the value of the time period in seconds which the system will wait prior to carrying out the incremental action in the control signal mentioned above in INCOUT.

Choice of Structure Variables

As described before, ADEX methodology is applied to multivariable processes by decomposing internally the ADEX multivariable controllers into a set of n multi-input single-output (MISO) ADEX controllers. The selection criteria for the main structure varibles of the

controller is presented hereafter and is valid for single-input single-output and multivariable controllers.

- Control & Sampling Period

The selection of the control period for a MISO ADEX controller should be done, if possible, in the light of the dynamics of the process variable PV itself, and with particular attention to the response time of the loop, a concept which is illustrated in Figure 12. Response time is defined as the time the process variable takes to enter a range (from ±5% of the value of the increment of PV) around its stationary state value, in response to a step in the OUT control signal. It is assumed that the step in the value of OUT will begin from a stationary state of the process.

If the control period is very short with respect to the response time, the successive measurements of PV at the different control instants will contribute little information about the variation of PV, and, even worse, may contain measurement noise. Moreover, the bi parameters of the AP model tend to zero as the control period diminishes. This makes the validity of prediction more sensitive than is desirable to identification errors and measurement noises. Likewise, the time delays of the different inputs of the MISO ADEX controller (DP), which are accounted in control periods, may excessively increase. It would be advisable to maintain these time delays under or equal 6 control periods.

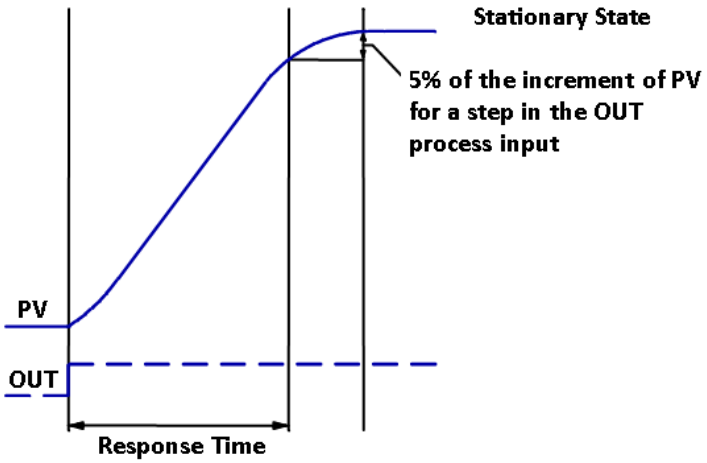

Figure B12. Response time of a process

If the control period is significantly long with respect to the response time, deviations of the PV produced during a control period cannot be correct until the next control instant arrives and this may take too long. Also, if the control period and sampling period are equal, information which would be useful for control purposes may be lost, since the variation of PV may be captured at intervals which will be too widely spaced, ignoring what happens between those intervals.

For all of the reasons set forth above, it is not advisable to choose a control period that is either very short or excessively long relative to response time. In practice, it is recommended a control period for a MISO ADEX controller between 1/5 and 1/40 of the response time. The sampling period should be selected according to filtering criteria so that, if strong filtering is suitable, the sampling period should be short compared with the control period. Within the context of an ADEX multivariable controller, including more than one MISO ADEX controller, a compromise must be made for the control period selected.

- Noise level

The noise level must be adjusted precisely. However, because the control action is moderated when PV is inside the noise level band, if the latter is unnecessarily broad, it can give rise to unacceptable deviations of PV with respect to the set point SP. In general, the process variable PV will tend to be in a band which, relative to the setpoint, will be lower than the noise level band.

Moreover, it must be taken must take into account that when the set point changes, the noise band will center itself around the new SP. If this change is not greater than the width of the noise level band, the process variable can remain inside it and, as a result, the control action will be moderated. The result may be that the PV does not converge towards the new SP.

- Number of AP Model Parameters.

If the time delays of the MISO ADEX controller inputs are fixed, the selection of number of parameters N for the different input/output AP model signals is simple; in most cases it will

be made equal to 2. However, if the time delay is variable for the control signal, a number of parameters for this signal will be chosen which will allow the adaptive mechanism to adjust the corresponding bi parameters to follow the variations of the time delay. To illustrate this procedure, let us consider a simple single-input single-output process in which the time delay of PV with respect to OUT can vary between 0 and 2. In this case the following predictive model could be used:

$$PV(k+1|k) = A_1(k) * PV(k) + A_2(k) * PV(k-1) + B_1(k) * OUT(k) + B_2(k) * OUT(k-1) + B_3(k) * OUT(k-2) \quad (B.5)$$

where N = 2 for PV, N = 3 for OUT and DP = 0.

If the actual time delay of the process (without considering the inherent time delay of discrete processes) is equal to zero, the identification mechanism will give the parameter $B_1(k)$ a value other than zero. Nonetheless, if the actual time delay of the process becomes equal to 2, identification will generate a model like this one:

$$PV(k+1|k) = A_1(k) * PV(k) + A_2(k) * PV(k-1) + 0 * OUT(k) + 0 * OUT(k-1) + B_3(k) * OUT(k-2) \quad (B.6)$$

That is, B1 and B2 will have been made equal to 0, revealing that the actual time delay is equal to 2. Therefore, to retain at least one B_i which is not equal to zero, DP and N for OUT must be chosen in the following manner:

➔ DP = DPmin

➔ N ≥ DPmax - DPmin + 1

where DPmin and DPmax are the minimum and maximum limits, respectively, of the range of possible variation of the actual time delay.

- Initial Values for the AP Model Parameters

Let us consider a stable linear single-input single-output process described by the following equation:

$$PV(k+1|k) = A_1(k) * PV(k) + A_2(k) * PV(k-1) + B_1 * OUT(k) + B_2 * OUT(k-1) \quad (B.7)$$

Assuming initial values equal to zero, the process gain can be calculated from the permanent response PVperm to a step in the control signal OUTstep, by means of $G = PV_{perm} / OUT_{step}$. Since equation (B.7) will also be verified when the steady state is reached by the process, after the application of said step in the control signal, it may be written:

$$PV_{perm} = A_1 PV_{perm} + A_2 PV_{perm} + B_1 OUT_{step} + B_2 OUT_{step} + B_3 OUT_{step} \quad (B.8)$$

Therefore, by dividing both members of (B.8) by OUTstep:

$$G = A_1 G + A_2 G + B_1 + B_2 + B_3 \quad (B.9)$$

Thus,

$$G = A_1 G + A_2 G + B_1 + B_2 + B_3 \quad (B.10)$$

$$G = \frac{\sum B_i}{1 - \sum A_i} \quad (B.11)$$

The preceding equation can be useful to us for establishing some initial or default values for the AP model parameters which would comply themselves with a experimental estimation of the process gain.

Assuming an AP model is described by equation (B.7) and that the process has a gain equal to 1, the following values could be taken as initial values for the parameters of the predictive model: $A_1(0) = 1$; $B_1(0) = 0.1$; $A_2(0) = -0.2$; and $B_2(0) = 0.1$.

In fact, these are typical initial or default values for the predictive model of ADEX controllers. If the gain were different from 1, it would be sufficient to multiply all the B parameters by the value of the gain to obtain a predictive model with the appropriate gain.

In general, the adaptive mechanism of ADEX controllers will find the appropriate value for the predictive model parameters by itself. Nevertheless, for reasons of common sense and to facilitate adaptation, it is obviously a good idea to initialize the parameters of the predictive model in such a way that the model has a gain that is approximately equal to or greater than the process gain, so that the first control signals are correctly moderated when the model is not yet adapted. Further, the rational choice of other structure variables, such as the prediction horizon considered in the next section, makes the ADEX controller performance robust and tolerant of errors in the identification of predictive model parameters.

As a general rule, it should be borne in mind that, if the control period tends toward zero, the Bi parameters of the process will also tend toward zero. Moreover, when the control period tends toward to the response time, the B_1 parameter tends toward the gain G, and the rest of the A_i and B_i parameters tend toward zero. This dependency of the parameter values on the control period is inherent to the mathematical representation of the process, and may be observed in parameters identification performed by the adaptive mechanism of ADEX controllers.

An analogous consideration is valid for the choice of the initial or default values of the parameters related to other inputs signals within the AP model a MISO ADEX controller.

- Prediction Horizon

When the prediction horizon (PH) is small, the process variable PV is constrained to follow closely the desired trajectory, without taking into account the actual dynamics of the process. On the other hand, when the PH is bigger the process variable can reach the desired values with more flexibility taking into account the actual process dynamics.

Thus, the selection of PH depends on how rigorously the process variable PV should follow a given path or desired trajectory. If PH is small or equal to 1 (its minimum value), the possible measurement noise in PV(k) can introduce high frequency contents in the control signal OUT.

Also, it is important to consider that the prediction horizon must compensate for the variations of pure time delays when they occur. As considered previously, for a process time delay which varies between DPmin and DPmax, the structure variable DP will be set equal to DPmin and the difference with the actual time delay of the process will be absorbed by a certain number of parameters B which become equal to zero. In this case the PH must be chosen in the following way:

$$PH \geq DP_{max} - DP_{min} + 1 \qquad (B.12)$$

This is due to the fact that when the actual process time delay becomes equal to DPmax, if inequality (B.12) is not verified, the prediction instant k + DP + PH will be previous to the instant k + DPmax + 1, that is the first instant in which the control action OUT applied at instant k will have an effect on the process variable PV, and as a consequence the application of predictive control will not be possible.

An analogous consideration must also be made for the choice of PH in relation with other input signals with variable time delays within the AP model of a MISO ADEX controller.

ANNEX C:

EXTENSIONS IN THE APPLICATION OF THE ADEX METHODOLOGY TO PARTICLE ACCELERATORS

This PhD thesis has introduced Adaptive Predictive Expert ADEX control methodology in the particle acceleration domain and the results presented attracted the attention of researchers and institutes collaborating in the MYRRHA project and in the accelerator's community. This annex reports the first extension of the application of the ADEX methodology to new processes comprised in the MYRRHA accelerator, namely to the control of the current produced by the injector.

One of the branches of the MYRRHA linac injector is being presently developed at "Laboratoire de Physique Subatomique et Cosmologie de Grenoble" (LPSC Grenoble). Recalling "Chapter 3: The MYRRHA ADS", each branch of the injector will be composed of an Electron Cyclotron Resonance (ECR) source, that will produce a 30 keV beam, a focusing and diagnostics "Low Energy Bem Transfer" (LEBT) line, a Radio Frequency Quadrupole RFQ allowing to convert the continuous particle flow produced by the source into bunches with a repetition rate of 352,2 MHz, and a series of "Crossbar-H-Type" accelerating the beam up to 17 MeV.

So far the injector branch has been developed up to the LEBT. The scetch of Figure C1 shows the main parts of the injector that have been developed:

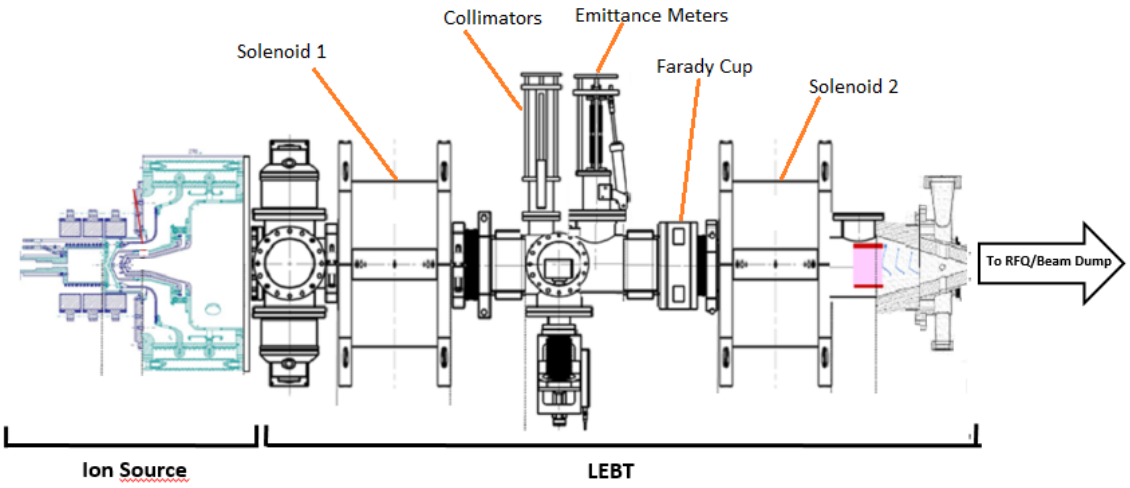

Figure C1. Scetch of the Injector at LPSC

As shown in the figure the first component of the injector is the ERC ion source. The ion source is composed of chamber where a gas flow, mainly Hydrogen, is introduced. Simultaneously, a strong RF field is induced in the cavity. This field is capable of dragging the electrons, thus freeing protons which are collected in a 30 keV beam and delivered to the LEBT.

The LEBT is then composed of a couple of focusing solenoids, a collimator device that narrows the proton beam, an emittance meter, used to characterize the average spread of particle coordinates in phase space, and a Faraday cup, that measures beam current. The LEBT is intended to work in vacuum, however a small Argon flow intended to study the effect of residual gas is allowed. This Argon flow also allows to “watch” with the help of a camera the proton beam, this is shown in Figure C2.

It is foreseen that the experimental setup described, depicted in Figure C1 will be “plugged” to the RFQ in the facilities of SCK·CEN in Louvain La Neuve. However, currently, the output of this setup ends in a beam dump.

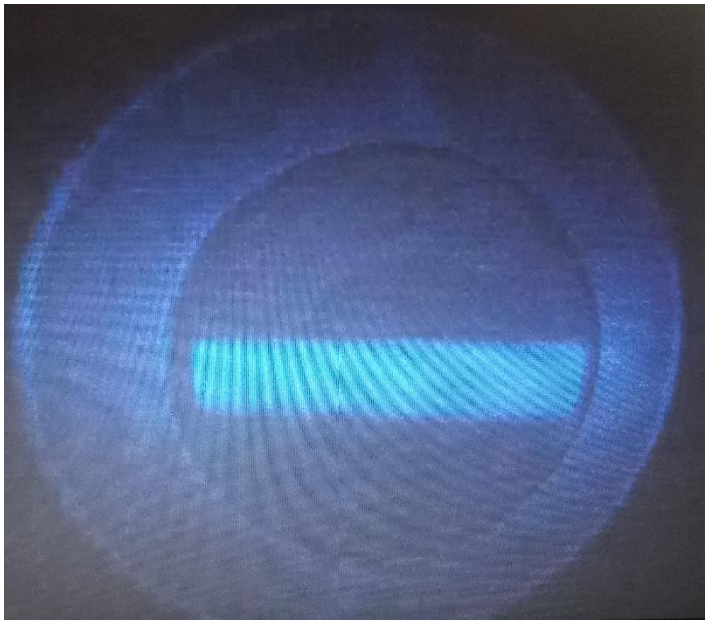

Figure C2. Proton beam recorded by a camera. Brightness coming from fluorescent Argon.

The importance of the Faraday cup must be noted as it is the main diagnostic of the beam, measuring the amount of protons produced by the ion source. In order to validate the measurements of the Faraday cup, a second beam current measurement was installed in the beam dump. Logically, this second measurement will disappear with the beam dump once the RFQ is assembled.

In the context of the MYRTE project it was decided that an ADEX system would be installed to perform the control of the current produced by the ion source. The control strategy envisaged was to control the beam current, with either the Faraday cup measurement or the beam dump measurement, by acting on the power of the RF source. This simple control strategy is represented in Figure C3.

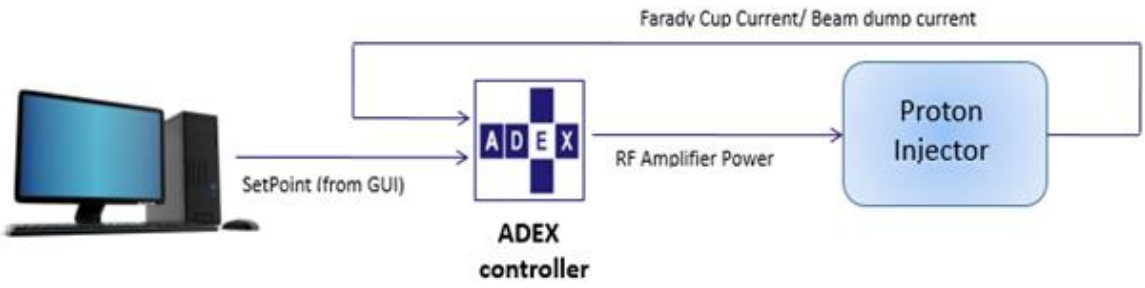

Figure C3. ADEX controller application the proton injector current control.

The injector is intended to produce a 4 mA beam in nominal condition, however, there is a certain range of currents that can be delivered by the ion source. To select the current value during operation the beam current setpoint can be chosen by the operator form a GUI, as shown in Figure C3. The GUI was provided by the ion source developer, Pantechnik S.A., together with a full automation system that drives the starting and safety procedures. The existing automation system of the ion source works in a Compact Rio (cRIO) of National Instruments. A scetch of this setup is shown in Figure C4.

Figure C4. Automation setup of the ion source.

Pantechnik's CompactRIO provides the following functions:

→ Captures data from the proton injector and serves it to the GUI.
→ Bears start-up and security algorithms.
→ Transfers the operator's commands introduced in the GUI to the proton injector.

On the other hand, Pantechnik's GUI:

→ Shows relevant information to the operator.
→ Allows the operator to command the machine.

For logical standardization purposes it was decided that the implementation of the ADEX system would also be performed in a cRIO. Thus, a cRIO based ADEX process control

platform for building Real-Time control applications, which assures deterministic behavior, was developed. When implemented in the proton injector this platform allowed for:

- → Real-time capture of process variable's values from the injector automation system.
- → Real-time execution of control algorithms.
- → Real-time invoice of control actions to the injector.
- → Respect all security and safety procedures.

The implementation scheme performed is shown in Figure C5.

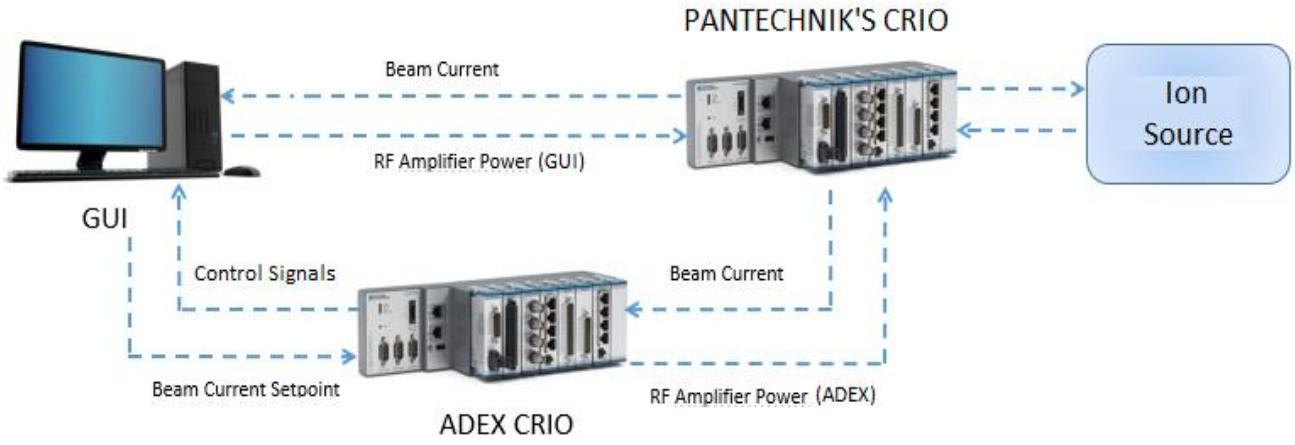

Figure C5. ADEX cRIO platform implementation in the existing automation setup of the ion source.

As shown in the figure, ADEX cRIO gets the beam current measurements from Pantechniks cRIO and the current setpoint from the GUI. With these inputs ADEX cRIO computes the RF amplifier power to drive efficiently the beam current to its setpoint, which is sent back to Pantechnik's cRIO. Pantechniks cRIO then applies the RF amplifier power computed by the ADEX cRIO platform to the ion source without interfering with the safety procedures. All this actions are performed in real time, meaning that a deterministic behavior is assured.

Additionally, ADEX cRIO exchanges control signals with the GUI related the operation of the ADEX system. Thus the operator can activate and deactivate ADEX control and choose

if the process variable under control will be the current measured by the Faraday cup or by the beam dump. In order to do this minor modifications, shown in Figure C6, were performed in the GUI. Figure C6 also shows a detail of the modifications added in the GUI's operator screen.

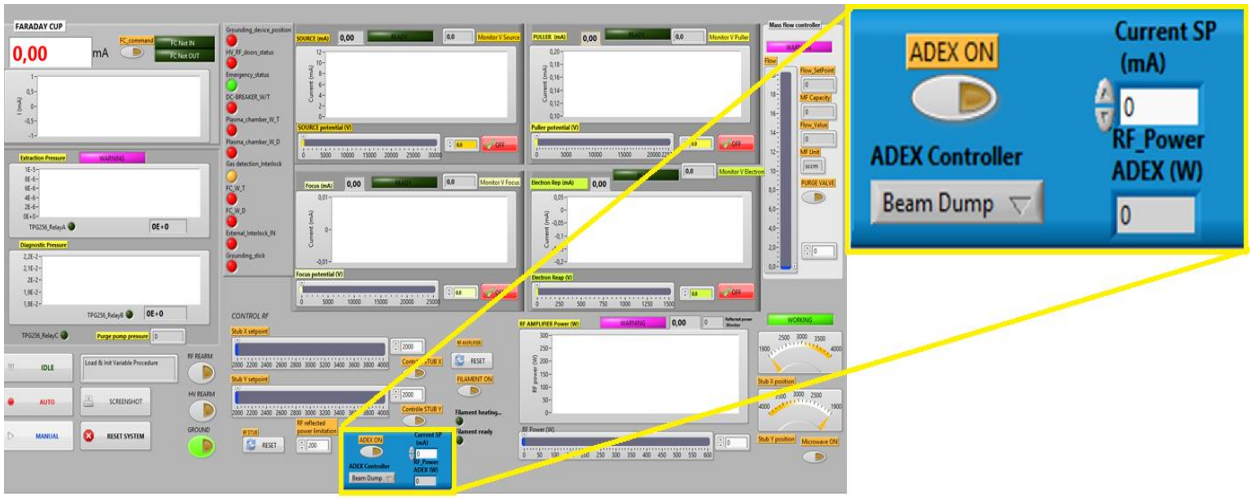

Figure C6. Graphical User Interface (GUI) screen and modification for the ADEX system implementation.

At the left side of the figure, the GUI developed by Pantechnik is shown. The modifications performed to implement the ADEX system have been highlighted and zoomed at the right side of the figure. These modifications consist on a button to switch the ADEX system ON or OFF, a field to introduce the current setpoint (current SP), a field to read the RF power computed by the ADEX system and a tab to choose the process variable to be controlled between the two possible options: the beam dump current and the Faraday cup current. It must be noted that when the ADEX system is switched OFF the RF power applied to the ion source is the one manually introduced in the GUI by the operator.

In the following the results of ADEX control with the setup described by Figure C5 will be shown and discussed. Several experiments were performed to evaluate the ADEX system that can be classified according to Table C1.

Experiment Nº	Description
Experiment 1	ADEX control of the beam dump current
Experiment 2	ADEX control of the Faraday cup current
Experiment 3	ADEX control of the Faraday cup current under the effect of perturbations
Experiment 4	ADEX control in long runs

Table C1. Experiments performed with the ADEX system in the MYRRA injector.

Experiment 1

Several trials were made controlling the beam dump current with the ADEX system. Figure C7 shows an example of the performance of the ADEX system and its response to setpoint changes.

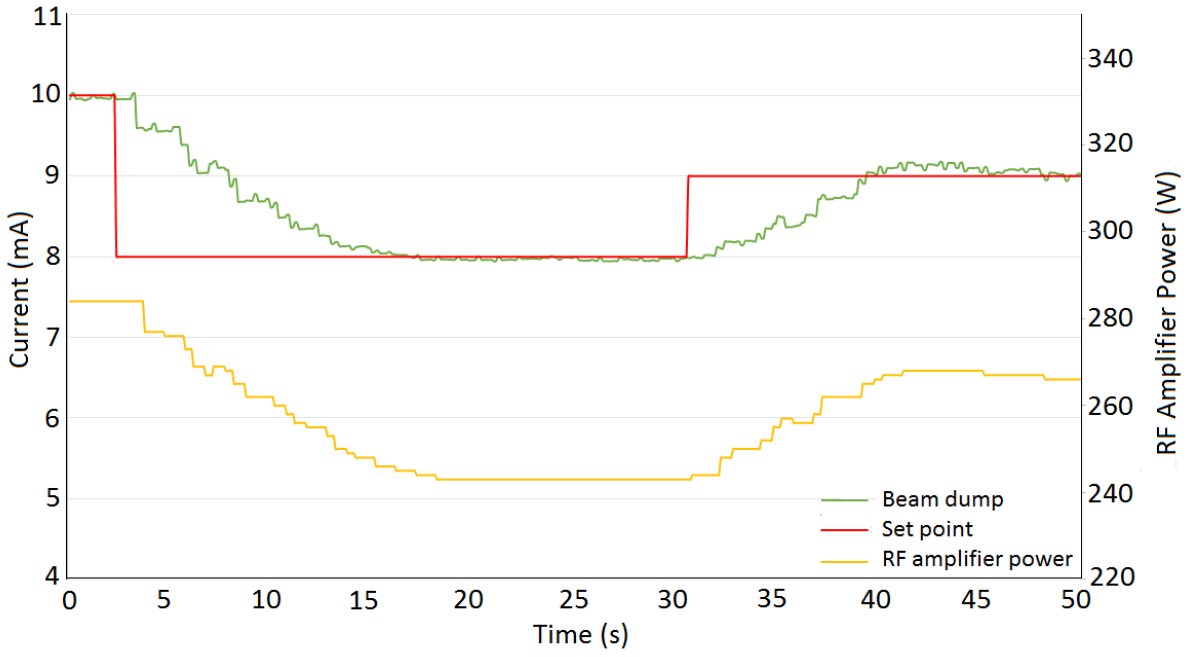

Figure C7. ADEX system performance controlling the beam dump current.

In the figure the beam dump current evolution is depicted in the green line being its set point the red line. Their scale is at the left side of the figure measured in mA. The RF amplifier power applied to the gas chamber and computed by the ADEX system is represented

by the yellow line, being its scale the one at the right side measured in W. The time scale can be found in seconds in the x-axis. The figure shows how the ADEX system is capable of driving the beam dump current to its set point after every setpoint change with stability and precision.

Experiment 2

Trials were also performed controlling the Faraday cup current with the ADEX system. Figure C8 shows an example of the performance of the ADEX system in this case and its response to setpoint changes.

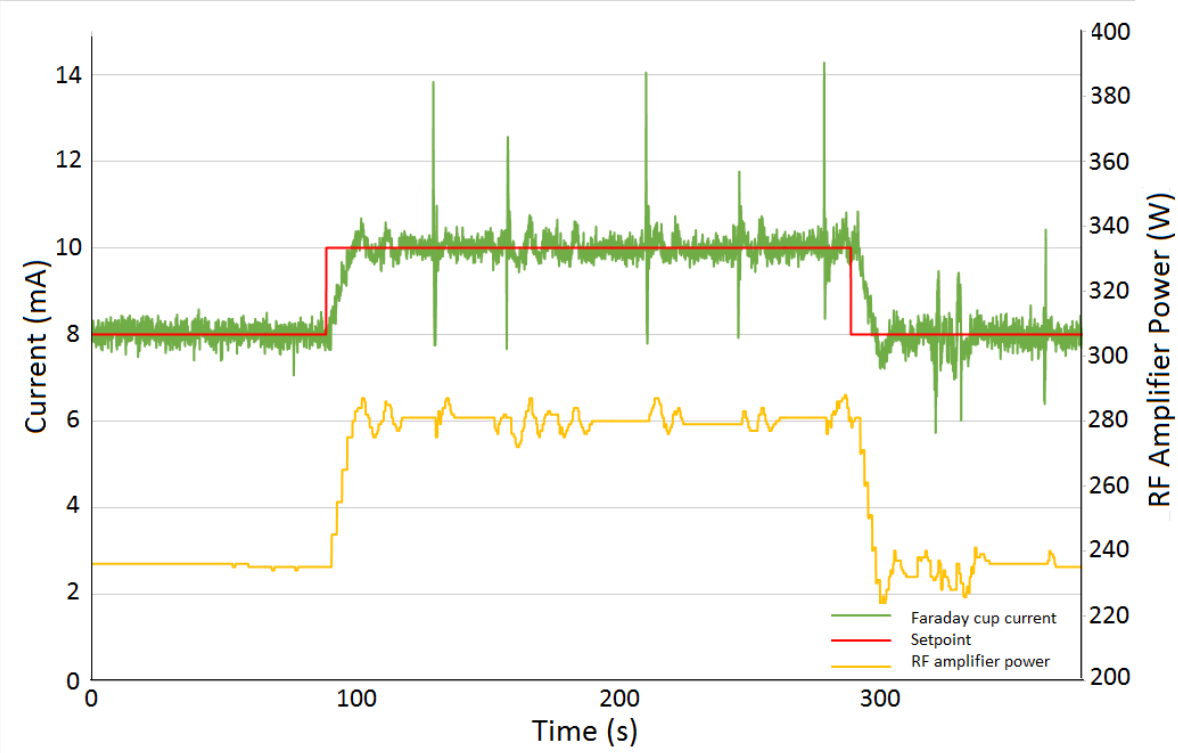

Figure C8. ADEX system performance controlling the Faraday cup current.

The chromatic criterion and the scales are similar to those considered for the previous figure changing the beam dump current for the Faraday cup current. It must be noted that the Faraday cup current is noisier than the beam dump current. Additionally it has pronounced spikes which cannot be considered noise. Their origin has not yet been identified but it seems to be some kind of perturbation in the electric signal. Logically this circumstances cause some deterioration on the control performance. Nevertheless, despite this inconveniences the

ADEX system continues to drive the current to its setpoint with stability and precision. It must be noted that no adjustment had to be made in the controller to achieve this result.

Experiment 3

After the previous tests and still with the ADEX system controlling the Faraday cup current, perturbations were introduced by changing the gas pressure in the LEBT approximately from 1e-5 to 1e-4 mbars and vice versa. Results shown in Figure C9 can give an idea of the compensation capacity of the system.

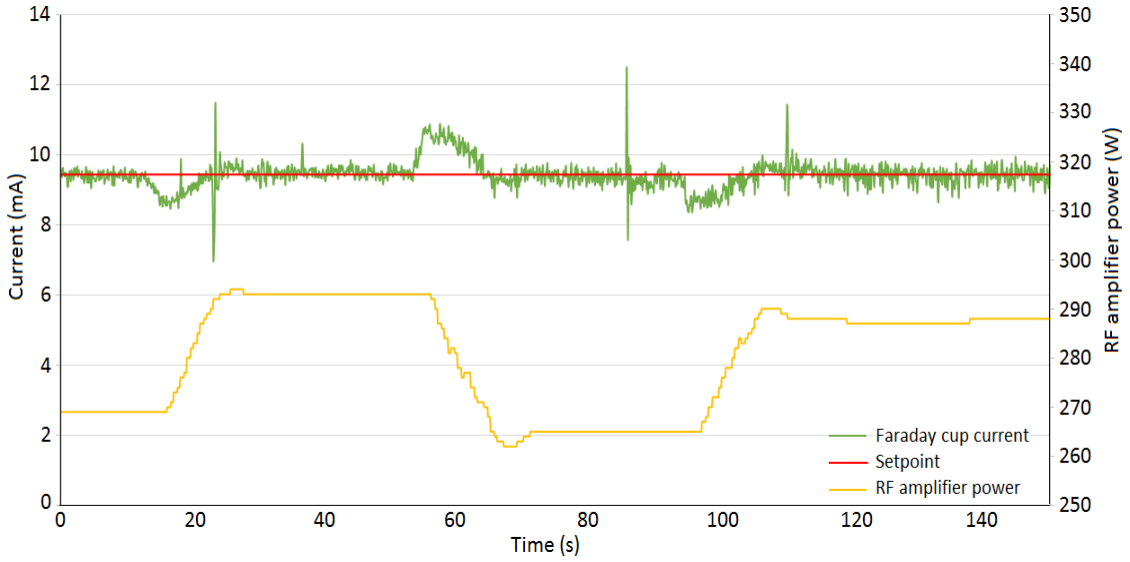

Figure C9. ADEX system performance controlling the Faraday cup current under gas pressure perturbations.

This figure has similar scales and chromatic criterion to that considered for Figure C8 and shows how the ADEX system compensates for gas pressure variations. It must be noted that gas pressure variations are small (≈1 e-5 to 1 e-4 mbars), however these pressure variations have a significant influence in the process. This is illustrated on Figure C10 that shows the influence of the gas pressure on the beam transmission, which is the relation between the current measured on the beam dump and the one generated by the ion source.

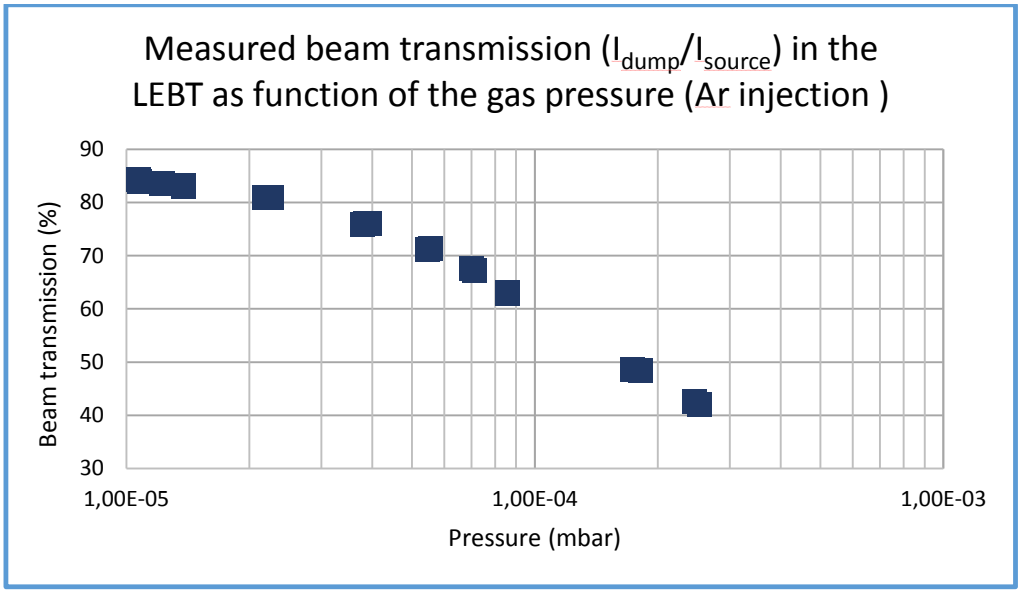

Figure C10. Effect of the gas pressure variation on the beam transmission [128].

Experiment 4

Experiment 4 consisted in recording the ADEX system performance in a long run. The following Figure C11 shows the ADEX system performance in a long run of the MYRRHA injector.

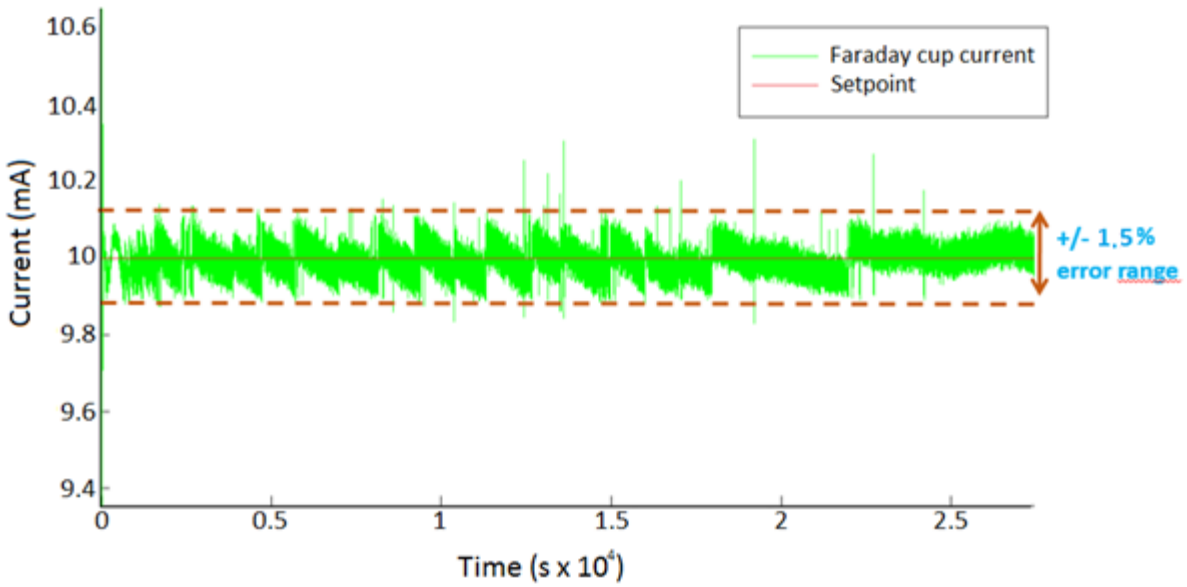

Figure C11. ADEX system.

The standard deviation computed from the data shown in Figure C11 is of 0.042 mA. This is a fairly good result. However, it must be noted that the current evolution shape seems that of a saw. This shape is due to the fact that there is a necessary minimum increment between control actions for the RF power amplifier to follow the commands of the ADEX system and this limits the control performance. Probably a different setup would have yield a better result with the ADEX system developed for this application.

Nevertheless, as already considered, this results are very satisfactory and have opened the alternative to reproduce the ADEX system in the GENEPI2 accelerator, also belonging to Laboratoire de Physique Subatomique et Cosmologie (LPSC).

REFERENCES

[1] “World Energy Outlook 2014”, ISBN 978-92-64-20804-9, Paris, Nov. 2014. Available online (last accessed 06/05/16)
http://www.worldenergyoutlook.org/weo2014/

[2] NEA/OCDE, “Nuclear energy today. Second edition.” ISBN 978-92-64-99204-7, Nov.2012. Available online (last accessed 06/05/16)
http://www.oecd-nea.org/pub/nuclearenergytoday/6885-nuclear-energy-today.pdf

[3] D. Struwe and J. Somers, “Overview of activities in europe exploring options for transmutation”, NUKLEAR, JRC-ITU, Karlsruhe, Germany, Tech. Rep., Oct. 2008.
Available online (last accessed 06/05/16)
http://cordis.europa.eu/pub/fp7/fission/docs/euradwaste08/papers/paper-8-overview-of-activities-in-europe-d-struwe_en.pdf

[4] E. M. G. Romero, “Rational and added value of P&T for waste management policies”, Project PATEROS, Sixth Framework Programme, Karlsruhe, Germany, Work Package 1, Deliverable 1.1, Mars 2007, Research and training on nuclear energy, Coordination action.
Available online (last accessed 06/05/16)
http://pateros.sckcen.be/en/Deliverables

[5] “P&T european roadmap for sustainable nuclear energy (PARTEROS)”, Contract Number:FP6-036418. Available online (last accessed 06/05/16)
http://pateros.sckcen.be/en

[6] “EUROpean research programme for the TRANSmutation of high level nuclear waste in an accelerator driven system (EUROTRANS)”, Contract Number: FI6W-CT-2004-516520.
Available online (last accessed 06/05/16)
http://cordis.europa.eu/project/rcn/85226_es.html

[7] “EUROpean research programme for the PARTitioning of minor actinides and some long-lived fission products from high active wastes issuing the reprocessing of spent nuclear fuels (EUROPART)”. Contract Number-. FI6W-CT-2003-508854. Available online (last accessed 06/05/16)
http://cordis.europa.eu/project/rcn/74122_en.html

[8] “Preliminary Design Studies of an eXperimental Accelerator-Driven System (PDS-XADS)”, Contract Number: FIKW-CT-2001-00179.
Available online (last accessed 06/05/16)
http://cordis.europa.eu/project/rcn/58635_en.html

[9] “MYRRHA Accelerator eXperiment, research & development programme (MAX)”, Contract Number: 269565.
Available online (last accessed 06/05/16)
http://cordis.europa.eu/result/rcn/54795_en.html

[10] T. Kandil, H. Khalil, J. Vincent, T. Grimm, W. Hartung, J. Popielarski, R. York, and S. Seshagiri, “Adaptive feedforward cancellation of sinusoidal disturbances in superconducting RF cavities”, *Nuclear Instruments and Methods in Physics Research A*, no. 550, pp. 514520, 2005.
Available online (last accessed 06/05/16)
https://people.nscl.msu.edu/~hartung/phptry/papers/Linac04TUP76.pdf

[11] A. Neumann, W. Anders, S. Klauke, J. Knobloch, O. Kugeler, and M. Schuster,“Characterization of a piezo-based microphonics compensation system at hobicat”, *Proceedings of EPAC 2006*, Edinburg, Scotland, 2006, pp. 408-410.

[12] A. Neumann, “Compensating microphonics in SRF cavities to ensure beam stability for future free-electron-lasers”, Ph.D. dissertation, Humboldt-Universitat zu Berlin, July 2008.
Available online (last accessed 06/05/16)
http://edoc.hu-berlin.de/dissertationen/neumann-axel-2008-07-21/PDF/neumann.pdf

[13] T. Grimm, W. Hartung, T. Kandil, H. Khalil, J. Popielarski, C. Radcliffe, J. Vincent, and R. York, “Measurement and control of microphonics in high loaded-q superconducting RF cavities”, *Proceedings of LINAC 2004*, Lubeck, Germany, 2004, pp. 763-765.
Available online (last accessed 06/05/16)
http://accelconf.web.cern.ch/AccelConf/l04/PAPERS/THP66.PDF

[14] K. Przygoda. “Development of Control System for Fast Frequency Tuners of Superconducting Resonant Cavities for FLASH and XFEL Experiments”. PhD thesis, Technical University of Lodz, Poland, 2010.
Available online (last accessed 17/09/17)

http://cds.cern.ch/record/1349300/files/EuCARD-DIS-2011-001.pdf

[15] M. Luong, “Microphonics analysis and compensation with a feedback loop at low cavity gradient”, Commissariat l’Énergie Atomique (CEA), Tech. Rep., Oct. 2007.
Available online (last accessed 06/05/16)
http://irfu.cea.fr/Phocea/file.php?class=std&&file=Doc/Publications/Archives/dapnia-07-185.pdf

[16] F. Bouly, J. L. Biarrotte, and C. Joly, “Low level radio-frequency developments toward a fault-tolerant linac scheme for an accelerator driven system”, *XXV Int.Linear Accelerator Conf.*, Tsukuba, Japan, 2010, pp. 244-246.
Available online (last accessed 06/05/16)
https://accelconf.web.cern.ch/accelconf/LINAC2010/papers/mop082.pdf

[17] F. Bouly, “Etude d’un module accélérateur et de ses systèmes de régulation pour le projet MYRRHA”, Ph.D. dissertation, Université Paris Sud - Paris XI, November 2011. Available online (last accessed 06/05/16)
https://tel.archives-ouvertes.fr/tel-00660392/file/VA2_BOULY_Frederic_03112011.pdf

[18] G. Devanz, P. Bosland, M. Desmons, E. Jacques, M. Luong and B. Visentin, “Compensation of Lorentz force detuning of a TTF 9-cell cavity with a new integrated piezo tuner”, *Proceedings of EPAC 2006*, Edinburg, UK, 2006.
Available online (last accessed 06/05/16)
http://accelconf.web.cern.ch/AccelConf/e06/Pre-Press/MOPCH140.pdf

[19] J. M. Martín-Sánchez, “Adaptive Predictive Expert Control System”, US Patent PCT/IB00/01 368, 2003.
Available online (last accessed 06/05/16)
http://www.adexcop.com/archivos/Patente%20EE.UU%202003.pdf

[20] J. M. Martín-Sánchez and J. Rodellar, “ADEX optimized adaptive controllers and systems: from research to industrial practice”. ISBN 978-3-319-09794-7. Springer, 2015.

[21] A. Nevado, I. Martín-Hoyo, and F. Mur, “Design and application of a steam temperature optimizer in a combined cycle”, *International Journal of Adaptive Control and Signal Processing*, vol. 26, no. 10, pp. 919-931, 2012.

[22] R. Estrada, A. Favela, A. Nevado, A. Raimondi, and E. Gracia, “Control of five sulphur recovery units at PEMEX Cadereyta refinery”, *Third IEEE Seminar for Advanced Industrial Control Applications (SAICA 2009)*, Madrid, Spain, 2009, pp. 79-88.

[23] A. Nevado, I. Martín-Hoyo and R. Requena, “ADEX control of steam temperature in a combined cycle”, *2010 IEEE International Energy Conference (ENERGYCON2010)*, Manama, Bahrain, 2010, pp. 137-142.

[24] R. Pérez, A. Geddes and A. Clegg, “Adaptive predictive expert control of superheated steam temperature in a coal-fired power plant”, *International Journal of Adaptive Control and Signal Processing*, vol. 26, no. 10, pp. 932-944, 2012.

[25] J. M. Martín-Sánchez, “Adaptive predictive control system”, US Patent 4,197,576. 1980. Available online (last accessed 06/05/16)
http://www.adexcop.com/archivos/PatenteEEUU1980.pdf

[26] J. M. Martín-Sánchez and J. Rodellar, “Adaptive predictive control: from the concepts to plant optimization”. **ISBN-13:** 978-0135148617. Prentice Hall, 1996.

[27] J. M. Martín-Sánchez, J. M. Lemos and J. Rodellar, “Survey of industrial optimized adaptive control”, *International Journal of Adaptive Control and Signal Processing*, vol. 26, no.10, pp.881-918, 2012.

[28] J. L. Biarrotte, M. E. Yakoubi, F. Chatelet, N. Gandolfo, C. Joly, J. Lesrel, H. Saugnac, A. Bosotti, R. Paparella, P. Pierini, F. Bouly, and I. Martín-Hoyo, “Commissioning of the max 700 MHz test stand”, *27th Linear Accelerator Conference (LINAC 2014)*, Geneva, Switzerland, 2014, pp. 610-612.
Available online (last accessed 13/09/17)
http://accelconf.web.cern.ch/AccelConf/linac2014/papers/tupp080.pdf

[29] A. Burke, “Uranium”. ISBN: 978-1-5095-1071-9. Polity Press, 2017.

[30] “Physics and safety of transmutation systems. A status report.”, Nuclear Energy Agency (NEA), Tech. Rep., 2006.
Available online (last accessed 27/02/18)
https://www.oecd-nea.org/science/docs/pubs/nea6090-transmutation.pdf

[31] K. Nishihara, H. Oigawa, S. Nakayama, K. Ono and H, Shiotani, “Impact of Partitioning and Transmutation on High-Level Waste Disposal for the Fast Breeder Reactor Fuel Cycle”, *Journal of Nuclear Science and Technology*, vol. 47, no. 12, pp. 1101-1117, 2010.

[32] “The potential impacts on repository safety from potential partitioning and transmutation programme”, Nuclear Energy Agency (NEA), Tech. Rep., Jan. 2003.
Available online (last accessed 13/09/17)
https://www.oecd-nea.org/rwm/docs/2003/rwm-igsc2003-2.pdf

[33] F. Bouly, M. Baylac, D. Bondoux, J. Belmans, D. Vandeplassche, N. Chauvin and F. Gérardin, “Commissioning of the MYRRHA low energy beam transport line and space charge compensation experiments”, *Proceedings of IPAC2017*, Copenhagen, Denmark, 2017, pp. 1226-1229.

[34] MYRRHA website.
Available online (last accessed 13/09/17)
http://myrrha.sckcen.be/

[35] J. L. Biarrotte, “Etude de cavités supraconductrices pour les accélérateurs de protons de forte puissance”, Ph.D. dissertation, Université Paris Sud - Paris XI, December 2000.

[36] J. L. Biarrotte and A.C. Mueller, “WP1.3 final report: Accelerator design, performances, costs & associated roadmap”, EUROpean Research Programme for the TRANSmutation of High Level Nuclear Waste in an accelerator Driven System, Tech. Rep., March 2010.
Available online (last accessed 13/09/17)
http://ipnwww.in2p3.fr/MAX/images/stories/design/5._EUROTRANS_accelerator_finalreport_D1.74_march2010.pdf

[37] J. L. Biarrotte, F. Bouly, S. Bousson, T. Junquera, A.C. Mueller, G. Olry, E. Rampnoux, R. Gobin, M. Luong, D. Uriot, H. Klein, H. Podlech, S. Barbanotti, P. Pierini and D. De Bruyn, “Accelerator R&D for the European ADS demonstrator”, *Proceedings of PAC09*, Vancouver, Canada, 2009, pp. 668-672.

[38] J. Galambos, T. Koseki and M. Seidel, “Commissioning strategies, operations and performance, beam loss management, activation, machine protection”. *Proceedings of Hadron Beam*, Nashville, USA, August 2008, pp. 489-492.

[39] H. Takei et al., “Comparison of beam trip frequencies between estimation from current experimental data of accelerators and requirement from ADS transient analyses”, *Proc. of the 5th HPPA workshop*, Mol, Belgium, May 2007, pp. 181 – 194.

[40] B. Giraud, L. Cinotti and B. Farrar, “Preliminary engineering requirements on accelerators for ADS”, *Proc. of the 2nd HPPA workshop*, Aix-en-Provence, France, November 1999.

[41] G. Rimpault, P. Richard, L. Mansani, F. Frogheri, A. Woaye-Hune, S. Ehster-Vignoud, S. Larmignat, A. Mueller, J.L. Biarotte, C. Artioli, et al., “General Synthesis Report of the Different ADS Design Status. Establishment of a Catalogue of the R&D needs”, EUROTRANS - Commissariat l’Énergie Atomique (CEA), Tech. Rep., July 2010.
Available online (last accessed 14/09/17)
https://hal.inria.fr/hal-01084509/document

[42] “RCC-MR 2007: Design and construction rules for mechanical components of nuclear installations”, User Manual, 2007.
Available online (last accessed 14/09/17)
http://www.afcen.com/en/publications/rcc-mrx

[43] D. Vandeplassche, J. L. Biarrotte, H. Klein, H. Podlech, “The MYRRHA linear accelerator”, *Proc. IPAC 2011*, San Sebastian, Spain 2011, pp. 2718 - 2720.

[44] J-L. Biarrotte and D. Vandeplassche, “Analysis of the XT-ADS accelerator design & detailed work programme”, Deliverable 1.1 of the Euratom FP7 MAX project, April 2011.

[45] C. Zhang et al., “From Eurotrans to MAX: new strategies and approaches for the injector development", *Proc. IPAC 2011*, San Sebastian, Spain.

[46] C.M. Piaszczyk, “Operational Experiences at Existing Accelerator Facilities”. *Proceedings of the Workshop on Utilisation and Reliability of High Power Proton Accelerators*, Oct. 1998, Mito, Japan, page 163.

[47] S.H. Kim and J. Galambos, “High power operational experience at the Spallation Neutron Source”. *Proceedings of the TCADS Workshop*, Karlsruhe, Germany, pages 243-250. AEN-NEA, Nuclear Energy Agency (NEA), 2010.

[48] D. Mäder, H. Klein, H. Podlech, U. Ratzinger,M. Vossberg and C. Zhang “Development of CH-cavities for the 17 MeV MYRRHA-injector”, *Proceedings of PAC09*, Vancouver, Canada, 2009, pp. 668-672.
Available online (last accessed 13/09/17)
https://accelconf.web.cern.ch/accelconf/IPAC2011/papers/weps038.pdf

[49] J. L. Biarrotte, D. Uriot, F. Bouly, J. P. Carneiro, and D. Vandeplassche, “Design of the MYRRHA 17-600 MeV superconducting linac”, *Proceedings of SRF2013*, Paris, France, 2013, pp. 129-132.
Available online (last accessed 13/09/17)
http://ipnwww.in2p3.fr/srf2013/papers/mop018.pdf

[50] J. L. Biarrotte, M. Novati, P. Pierini, H. Safa, and D. Uriot, “Beam dynamics studies 12 for the fault tolerance assessment of the PDS-XADS linac”, *Proceedings of EPAC2004,* Lucerne, Switzerland, 2004, pp. 1282-1284.

[51] F. Bouly, J. L. Biarrotte, and D. Uriot, “Fault tolerance and consequences in the MYRRHA superconducting linac”, *Proceedings of LINAC14*, Geneva, Switzerland, 2014, pp. 297-299.
Available online (last accessed 13/09/17)
http://accelconf.web.cern.ch/AccelConf/linac2014/papers/mopp103.pdf

[52] Mathworks Matlab Simulink website.
Available online (last accessed 13/09/17)
https://www.mathworks.com/products/simulink.html

[53] D. Vandeplassche and L. Medeiros, “The linear proton accelerator for the MYRRHA-ADS”, Centre de l’énergie nucleaire (SCK·CEN), Tech. Rep. 2013.
Available online (last accessed 16/09/17)
https://www.unamur.be/sciences/philosoc/revueqs/textes-en-ligne/rqs_2013_184_1-2_myrrha

[54] R. Salemne, “MYRRHA: a multipurpose Accelerator Driven System for Research & Development”. *Accelerators for future spallation sources: ESS, MYRRHA and the ISIS upgrde*, United Kingdom, Cockcroft Institute, Dec. 2013.
Available online (last accessed 27/02/18)
https://eventbooking.stfc.ac.uk/uploads/accelerators_for_future_spallation_sources___ess__myrrha_and_the_isis_upgrade1363967784/salemme---cockcrof-institute.pdf

[55] J.D. Cockcroft and E.T.S. Walton: Experiments with high velocity positive ions. II-the disintegration of elements by high velocity protons. *Proceedings of the Royal Society of London*. Series A, 137(831):229, 1932.

[56] R.J. Van de Graaff : A 1,500,000 volt electrostatic generator. *Phys. Rev*, 38, 1931.

[57] R.P. Feynman, R.B. Leighton and M. Sands, "The Feynman Lectures on Physics, Mainly Electromagnetism and Matter, Volume II". ISBN-13: 978-0465024940. Addison Wesley Longman, 1998.
[58] G.O. Boudouris : Cavités électromagnétiques. Dunod, 1971.

[59] N. Marcuvitz, "Waveguide handbook". Peter Peregrinus Ltd, on behalf of Iee, 1986.

[60] F. Bouly, "Proton linacs as ADS drivers", *Status of Accelerator Driven Systems Research and Technology Development EUCARD2 Workshop*, Meyrin (CERN), February 2017.

[61] H. Padamsee, J. Knobloch and T. Hays, "RF Superconductivity for accelerators", ISBN: 978-3-527-40842-9. Wiley series, 1998.

[62]. U. Kelin and D. Proch, Proc. "Confenrence on Future Possibilities for Electron Accelerators", Charlottesville, USA, Jan. 1979.

[63] D. Longuevergne : "Etude et test d'un module accélérateur supraconducteur pour le projet Spiral 2". Ph.D. Paris 11, Orsay, 2009. Nov. 2009.

[64] G. Olry. "Etude d'une cavité accélératrice supraconductrice Spoke pour les accélérateurs de protons de forte intensité". Ph.D. dissertation. Université Paris-Diderot - Paris VII, 2004. France.

[65] G. Olry, J-L. Biarrotte, T. Junquera, J. Lesrel, C. Mielot, H. Saugnac, P. Maccioni and M. Gauthier "Design and Industrial Fabrication of β=0.35 spoke-type cavity", *Proceedings of EPAC 2002*, Paris, France, 2002, pp. 2271-2273.
Available online (last accessed 13/09/17)
https://accelconf.web.cern.ch/accelconf/e02/PAPERS/THPDO035.pdf

[66] J.C.Slater, "Microwave Electronics", *Reviews of Modern Physics*, vol. 18, no.4, pp. 441-512. Oct. 1946.

[67] Cryoperm website.
Available online (last accessed 13/09/17)
http://www.cryopermshielding.com/

[68] T. Schilcher, "Vector sum control of pulsed accelerating fields in Lorentz force detuned superconducting cavities", Ph.D. dissertation, DESY, 1998.
Available online (last accessed 13/09/17)
https://bib-pubdb1.desy.de/record/291638/files/schilcher.pdf

[69] N. Gandolfo, “Système d’accord à froid pour les cavités accélératrices supraconductrices”, Institut de Physique Nucléaire d’Orsay (IPNO), Tech. Rep. 2007.

[70] R. Paparella, “Fast frequency tuner for high gradient SC cavities for ILC and XFEL”, Ph.D. dissertation, Laboratorio Acceleratori e Superconduttività Applicata (LASA), 2006.
Available online (last accessed 13/09/17)
http://cds.cern.ch/record/1118577/files/care-thesis-08-001.pdf

[71] P. Pierini, N. Panzeri, A. Bosotti, P. Michelato, C. Pagani, R. Paparella, “Report on tuner design ”, Laboratorio Acceleratori e Superconduttività Applicata (LASA), Tech. Rep. 2006.
Available online (last accessed 13/09/17)
wwwsrf.mi.infn.it/publications/papers/2006/file/CARE-Note-2006-003-HIPPI.pdf

[72] I.D. Landau. “A survey of model reference adaptive techniques. Theory and application.” *Automatica*. 1974, vol 10, no. 4, pp. 353 – 379.

[73] J.A Richalet, J.L. Rault and R. Pouliquen. “Identification des processus par la méthode du Modèle”. Gordon & Breach, 1971.

[74]. K.J Ästrom and P. Eykhoff. “System identification, a survey”. *Automatica* 1971, vol. 7, no. 2, pp.123–162.

[75]. J.M. Mendel. “Discrete techniques of Parameter Estimation - The Equation Error Formulation”. ISBN 13: 9780824714550. Marcel Dekker, 1973.

[76]. I.D. Landau. “Sur une méthode de synthèse des systèmes adaptatifs avec modèle utilisés pour la commande et l’identification d’une clase de procédés physiques”. Thèse d’État des Sciences Physiques. PhD Thesis, Université de Grenoble 1973.

[77]. V.M.Popov. “Hyperstability of Control Systems”. ISBN 978-3-642-65656-9. Springer-Verlag, 1973.

[78]. I.D. Landau. “A generalization of hyperstability conditions for model reference adaptive systems”. *IEEE Trans. Automatic Control.* 1972; vol. 17, no.2, pp. 246–247.

[79]. I.D. Landau. “Design of model reference adaptive systems using the positivity concept”. *Proc. 3rd IFAC Symposium on Sensitivity, Adaptivity and Optimality,* Ischia, Italy, 1973 pp. 307–314.

[80]. I.D. Landau and J.M. Martín-Sánchez. “Sistemas adaptivos discretos con Modelo de Referencia. Analisis y Sintesis a partir de la teoria de la hiperestabilidad”. *Proc. Of Automatica Congress*, Barcelona, Spain, 1972.

[81]. J.M. Martín-Sánchez. “Contribución a los sistemas adaptativos con modelo de referencia a partir de la teoría de la hiperestabilidad”. Ph.D Thesis, Universidad Politécnica de Cataluña, Barcelona, Spain 1974.

[82]. J.M. Martín-Sánchez. “A new solution to adaptive control”. *Proceedings of the IEEE*, 1976, vol. 64, no. 8, pp. 1209 – 1218.

[83]. K.J. Ästrom and B. Wittenmark. “On self-tuning regulators”. *Automatica* 1973, vol. 9, no.2, pp. 185 – 199.

[84]. D.W. Clarke and P.J. Gawthrop. “Self-tuning controller*”. Proc. IEE-D* 1975, vol. 122, no. 9, pp. 929 – 934.

[85]. J.M. Martín-Sánchez and S. L. Shah, “Multivariable Adaptive Predictive Control of a Binary Distillation Colum”, *Automatica*, 1984, vol. 20, no. 5, pp. 607-620.

[86]. C.R. Johnson and M.G. Larimore. Comments on “A New solution to adaptive control”. *Proc. of IEEE* 1977, vol. 65, pp. 587.

[87]. J.M. Martín-Sánchez. Reply to comments on “A new solution to adaptive control”. *Proc. of IEEE* 1977, vol. 65, pp. 587 – 588.

[88]. J.M. Martín-Sánchez. Adaptive Predictive Control System (CIP), European Patent No. 0037579. 1980.

[89]. G.C. Goodwin, P.J. Ramadge and P.E. Caines. “Discrete time multivariable adaptive control”. *IEEE Trans. Automatic Control* 1980, vol.25, no. 3, pp. 449–456.

[90]. A.S. Morse. “Global stability of parameter adaptative control systems”. *IEEE Trans. Automatic Control* 1980, vol. 25, no. 3, pp. 433–461.

[91]. K.S. Narendra, Y.H. Lin and L.S. Valavani. “Stable adaptive controller design. Part II: Proof of stability”. *IEEE Trans.Automatic Control* 1980, vol. 25, no. 3, pp.440–448.

[92]. H. Elliott. “Direct adaptive pole placement with application to nonminimum phase systems”. *IEEE Trans. Automatic Control* 1982, vol. 27, no. 3, pp.720 – 722.

[93]. G.C. Goodwin, P.J. Ramadge and P.E. Caines. “Discrete-time stochastic adaptive control”. *SIAM Journal on Control Optimization*. 1981, vol. 19, no. 6, pp. 829 – 853.

[94]. B. Egardt. “Stability of Adaptive Controllers”. ISBN 978-3-540-09646-7.Springer-Verlag, 1979.

[95]. B.B. Peterson and K.S. Narendra. “Bounded error adaptive control”. *IEEE Trans. Automatic Control* 1982, vol. 27, no. 6, pp. 1161–1168.

[96]. C. Samson. “Stability analysis of adaptively controlled systems subject to bounded disturbances”. *Automatica* 1983, vol. 19, no. 1, pp. 81–86.

[97]. J.M. Martín-Sánchez. “A globally stable APCS in the presence of bounded unmeasured noises and disturbances”. *Proceedings of the 21st IEEE CDC, IEEE*: Orlando, Florida, 1982, pp. 761–769. Also in *IEEE Transactions in Automatic Control*, vol.29, no. 5, pp. 461-464, 1984.

[98]. J.M. Martín-Sánchez, S. I. Shah and D.G. Fisher. “A stable adaptive predictive control system”. *International Journal of Control* 1984, vol. 39, no.1, pp. 215–234.

[99]. G. Kreisselmeier. “Adaptive control via adaptive observation and asymptotic feedback matrix synthesis”. *IEEE Trans. Automatic Control* 1980, vol. 25, no. 4, pp. 717 – 722.

[100]. G.C. Goodwin and K.S. Sin. “Adaptive control of nonminimum phase systems”. *IEEE Transactions in Automatic Control* 1981, vol. 26, no. 2, pp.478–483.

[101]. J. Rodellar. “Diseño Optimo del Bloque Conductor en el Sistema de Control Adaptativo Predictivo”. Ph.D Thesis, Universidad de Barcelona 1982.

[102]. B.D.O. Anderson and R.M. Johnstone. “Global adaptive pole positioning”. *IEEE Trans. Automatic Control* 1985, vol. 30, no. 1, pp. 11–21.

[103]. A.O. Cordero and D.Q. Mayne. “Deterministic convergence of a self-tuning regulator with variable forgetting factor”. *IEEE Proc. D: Control Theory Appl.* 1981, vol. 128, no. 1, pp. 19–23.

[104]. B.D.O. Anderson, R.M. Johnstone. “Adaptive systems and time-varying plants”. *International Journal of Control* 1983, vol. 37, no. 2 pp. 367–377.

[105]. P.E. Caines. “Stochastic Adaptive Control: Randomly Varying Parameters and Continually Disturbed Controls”. *Proc. IFAC Congress*, Kyoto, Japan, 1981.

[106]. G.C. Goodwin, D.J. Hill, X. Xianya. “Stochastic adaptive control for exponentially convergent time-varying systems”. *Proc. 23rd IEEE CDC*, Las Vegas, Nevada, USA, 1984.

[107]. J.M. Martín-Sánchez. “Adaptive control for time variant process”. *International Journal of Control* 1986, vol. 44, no. 2, pp. 315 – 329.

[108]. P.E. Caines, H.F. Chen. “On the Adaptive Control of Stochastic Systems with Random Parameters: A Counterexample”. *Proc. of ISI Workshop on Adaptive Control*, Florence, Italy, 1982.

[109]. I.D.Landau. “Adaptive control”. ISBN-0824765486. Marcel Dekker, 1979.

[110]. C.A. Desoer and M. Vidyasagar. “Feedback Systems: Input and Output Properties”. ISBN: 978-0-12-212050-3. Academic Press, 1975.

[111]. C.E. Rohrs. “Adaptive control in the presence of unmodeled dynamics”. Ph.D Thesis, Department Electronics Engineering Computation Science, MIT, Cambridge 1982.

[112]. L. Praly. “Robust model reference adaptive controllers. Part 1.” *Proc. 23rd IEEE Conference on Decision and Control*, 1984, pp. 1009–1014.

[113]. G. Kreisselmeier and B.D.O. Angerson. “Robust model reference adaptive control”. *IEEE Transactions in Automatic Control* 1986; vol. 31, no. 2, pp. 127–133.

[114]. W.R. Cluett, J.M. Martín-Sánchez, S.L. Shah and D.G. Fisher. “Stable discrete-time adaptative control in the presence of unmodeled dynamics”. *IEEE Trans. Automatic Control* 1988; AC-33, pp. 410–414.

[115]. J.M. Martín-Sánchez and J. Rodellar. “Adaptive predictive control: Limits of stability”. *International Journal of Adaptive Control and Signal Processing* 1997, vol. 11, no. 4, pp. 263–284.

[116]. J.M. Martín-Sánchez and J. Rodellar. “Adaptive predictive expert control: Methodology, Design and Application” (in Spanish). ISBN: 9788436250947. UNED, 2005.

[117]. J.M. Martín-Sánchez, D.G. Fisher, S.L. Shah. “Application of a multivariable adaptive predictive control system”. Proceedings of the Second Workshop on Applications of Adaptive Theory, Yale University, New Haven, 1981; pp. 138–148.

[118]. L. Ljung. “System Identification: Theory for the User”. ISBN-13: 978-0136566953. Prentice Hall, 1987.

[119]. J.M. Martín-Sánchez. “Adaptive Predictive Expert Control System”. International Patent Application. Application No: PCT/US00/17836, Priority Date: June 28, 1999.

[120]. J.M. Martín-Sánchez. “Adaptive Predictive Expert Control System”. European Patent. EP 1200882:B1. 2003.

[121]. J.M. Martín-Sánchez. “Special Issue: Industrial Optimized Adaptive Control”. *International Journal of Adaptive Control and Signal Processing* 2012. Vol. 26, no.10.

[122] R. M. De Keyser, P.G Vande Velde and F. A. Dumoriter, “A comparative study of self-adaptive long-range predictive control methods*”, Proceedings 7th IFAC symposium on identification and control*, York, UK, 1985, pp. 1317-1322.

[123] D. Clarke and C. Mohtadi, “Properties of generalized predictive control”. *Proceedings 10th IFAC world congress*, Munich, Germany, 1987, pp. 63-74.

[124] “OPC foundation” website.
Available online (last accessed 06/05/16)
https://opcfoundation.org/

[125] A. Mosnier, “Control of SCRF cavities in high power proton linac”, *Proceedings of EPAC 4* 2002, Paris, France, 2002, pp. 179 -183.
Available online (last accessed 06/05/16)

http://irfu.cea.fr/Phocea/file.php?class=std&&file=Doc/Publications/Archives/dapnia-02-190.pdf

[126] R. Rybaniec, V. Ayvazyan, L, Butkowski, L. Opalski, S. Pfeiffer, K. Przygoda, H. Schlarb and C. Schmidt. "Microphonic Disturbances Prediction and Compensation in Pulsed Superconducting Accelerators". *6th International Particle Accelerator Conference (IPAC 2015)*, May 2015. Richmond, Virginia, USA, pp. 2997 – 2999.
Available online (last accessed 17/09/17)
http://accelconf.web.cern.ch/AccelConf/IPAC2015/papers/wepmn032.pdf

[127] The CompactRIO platform website.
Available online (last accessed 17/09/17)
http://www.ni.com/compactrio/

[128] F. Bouly, "Status MYRRHA LEBT Experiment". MYRTE work package meeting, Madrid, Spain, 2017.